NASA/CP—2008–215252

39th Aerospace Mechanisms Symposium

Compiled by
E.A. Boesiger
Lockheed Martin Space Systems Company, Sunnyvale, California

Proceedings of a Symposium held at the
Von Braun Center, Huntsville, Alabama,
Hosted by Marshall Space Flight Center
and Lockheed Martin Space Systems Company,
Organized by the Mechanisms Education Association
May 7–9, 2008

May 2008

The NASA STI Program…in Profile

Since its founding, NASA has been dedicated to the advancement of aeronautics and space science. The NASA Scientific and Technical Information (STI) Program Office plays a key part in helping NASA maintain this important role.

The NASA STI program operates under the auspices of the Agency Chief Information Officer. It collects, organizes, provides for archiving, and disseminates NASA's STI. The NASA STI program provides access to the NASA Aeronautics and Space Database and its public interface, the NASA Technical Report Server, thus providing one of the largest collections of aeronautical and space science STI in the world. Results are published in both non-NASA channels and by NASA in the NASA STI Report Series, which includes the following report types:

- TECHNICAL PUBLICATION. Reports of completed research or a major significant phase of research that present the results of NASA programs and include extensive data or theoretical analysis. Includes compilations of significant scientific and technical data and information deemed to be of continuing reference value. NASA's counterpart of peer-reviewed formal professional papers but has less stringent limitations on manuscript length and extent of graphic presentations.

- TECHNICAL MEMORANDUM. Scientific and technical findings that are preliminary or of specialized interest, e.g., quick release reports, working papers, and bibliographies that contain minimal annotation. Does not contain extensive analysis.

- CONTRACTOR REPORT. Scientific and technical findings by NASA-sponsored contractors and grantees.

- CONFERENCE PUBLICATION. Collected papers from scientific and technical conferences, symposia, seminars, or other meetings sponsored or cosponsored by NASA.

- SPECIAL PUBLICATION. Scientific, technical, or historical information from NASA programs, projects, and missions, often concerned with subjects having substantial public interest.

- TECHNICAL TRANSLATION. English-language translations of foreign scientific and technical material pertinent to NASA's mission.

Specialized services also include creating custom thesauri, building customized databases, and organizing and publishing research results.

For more information about the NASA STI program, see the following:

- Access the NASA STI program home page at <http://www.sti.nasa.gov>

- E-mail your question via the Internet to <help@sti.nasa.gov>

- Fax your question to the NASA STI Help Desk at 301–621–0134

- Phone the NASA STI Help Desk at 301–621–0390

- Write to:
  NASA STI Help Desk
  NASA Center for AeroSpace Information
  7115 Standard Drive
  Hanover, MD 21076–1320

NASA/CP—2008–215252

39th Aerospace Mechanisms Symposium

Compiled by
E.A. Boesiger
Lockheed Martin Space Systems Company, Sunnyvale, California

Proceedings of a Symposium held at the
Von Braun Center, Huntsville, Alabama,
Hosted by Marshall Space Flight Center
and Lockheed Martin Space Systems Company,
Organized by the Mechanisms Education Association
May 7–9, 2008

National Aeronautics and
Space Administration

Marshall Space Flight Center • MSFC, Alabama 35812

May 2008

Acknowledgments

The high quality of this symposium is a result of the work of many people, and their efforts are gratefully acknowledged. This extends to the voluntary members of the symposium organizing committee representing the eight NASA Field Centers, Lockheed Martin Space Systems Company, and the European Space Agency. Appreciation is also extended to the session chairs, the authors, and particularly the personnel at Marshall Space Flight Center responsible for the symposium arrangements and the publication of these proceedings. A sincere thank you also goes to the symposium executive committee who is responsible for the year-to-year management of the Aerospace Mechanisms Symposium, including paper processing and preparation of the program.

TRADEMARKS

Available from:

NASA Center for AeroSpace Information
7115 Standard Drive
Hanover, MD 21076–1320
301–621–0390

This report is also available in electronic form at
<https://www2.sti.nasa.gov>

TABLE OF CONTENTS

TABLE OF CONTENTS (Continued)

TABLE OF CONTENTS (Continued)

SYMPOSIUM SCHEDULE

WEDNESDAY, 7 MAY 2008

7:30 Wednesday Presenters' Breakfast – Embassy Suites Hotel Redstone Boardroom

8:00 **CHECK-IN AND REFRESHMENTS** – Von Braun Center South Hall Meeting Rooms

8:30 **INTRODUCTORY REMARKS** – Von Braun Center South Hall Meeting Rooms
Donald McQueen, Jr., Host Chairman
NASA Marshall Space Flight Center, Huntsville, AL
Edward Boesiger, Operations Chairman
Lockheed Martin Space Systems, Sunnyvale, CA

CENTER WELCOME
NASA Marshall Space Flight Center, Huntsville, AL

9:00 **SESSION I—ACTUATORS & MOTORS** – Von Braun Center South Hall Meeting Rooms
Chris Kalogeras, Session Chair
Boeing Satellite Systems, El Segundo, CA

- Linear High-Force "Step and Repeat" Piezoelectric Motors
  Jeffrey Paine, M. Johns, J. Sesler, M. Stefanick & J.A. Kennedy,
  Dynamic Structures and Materials LLC, Franklin, TN

- Development of a High Resolution Rotary Actuator for an Antenna Trimming Mechanism
  Jérôme Brossier, Xavier Jeandot, Yannick Baudasse, David Grima & Fabrice Champandard,
  Thales Alenia Space, Cannes, France

- Implications of Underdamped Stepper Mechanism Performance and Damping Solution Methodology
  Shane Brown & Scott Starin, Ball Aerospace & Technologies Corp., Boulder, CO

- Large Scale Magnetostrictive Valve Actuator
  James Richard, Elizabeth Holleman & David Eddleman, NASA Marshall Space Flight Center, Huntsville, AL

- Design and Development of a Miniaturized Double Latching Solenoid Valve for the Sample Analysis at Mars Instrument Suite
  James Smith, NASA Goddard Space Flight Center, Greenbelt, MD

- A New Structural Bonding Process for Ferromagnetic Sheet Stacking used in Electric Motors
  Christophe Casteras, CNES, Toulouse, France; Bruno Bonduelle, SOTEREM, Castanet Tolosan, France; Frederic Martin, CLIX Industries, Toulouse, France

11:45 **LUNCH BREAK** – Box lunch is provided

1:00 **SESSION II—BEARINGS & TRIBOLOGY** – Von Braun Center South Hall Meeting Rooms
Ralph Carruth, Session Chair
NASA Marshall Space Flight Center, Huntsville, AL

- Evaluation of Perflouropolyether Lubricant Lifetime in the High Stress and High Stress-Cycle Regime for Mars Applications
  Jason Herman & Kiel Davis, Honeybee Robotics Spacecraft Mechanisms Corp., New York, NY

- Mars Science Laboratory Rover Mobility Bushing Development
  Benjamin Riggs, Jet Propulsion Laboratory, Pasadena, CA

- Space Shuttle Orbiter Atlantis Liquid Oxygen Pre-Valve Detent Roller Cracking Investigation
  Elizabeth Holleman, David Eddleman & James Richard, NASA Marshall Space Flight Center, Huntsville, AL; Rebecca Jacobs, Jacobs Engineering Science & Technical Services Group, Huntsville, AL

- Measuring the EHD Film Thickness in a Rotating Ball Bearing
  Peter Ward, Alan Leveille & Peter Frantz, The Aerospace Corporation, El Segundo, CA

- Scanning System Development and Associated Bearing Cage Instability Issue
  Manfred Schmid & Christian Hehr, EADS Astrium GmbH Satellites, Friedrichshafen, Germany

3:30 **BREAK**

3:45 **SESSION III—RELEASE & SENSORS** – Von Braun Center South Hall Meeting Rooms
John Bohner, Session Chair
The Aerospace Corporation, El Segundo, CA

- Launch Lock Mechanism Design Fault Tree Use and Coatings Study
  Daniel Villa & Gustavo Toledo, Sandia National Laboratories, Albuquerque, NM

- Lessons Learned Designing a Spherical Satellite Release Mechanism
  Ryan Hevner, Planetary Systems Corp., Silver Spring, MD

- Wear Life Testing of a Mission Critical Separation Interface
  Jonathan Wood & Joseph de la Fuente, Lockheed Martin Space Systems Company, Sunnyvale, CA

- Circular Hall Transducer for Accurate Contactless Angular Position Sensing
  Laurent Sache, Mikael Sjöholm, Daniel Bommottet & Volker Gass, RUAG Aerospace, Nyon, Switzerland; Serge Reymond, Pavel Kejik & Radjan Popovic, Ecole Polytechnique Fédérale de Lausanne, Lausanne, Switzerland; Lionel Gaillard, European Space Research and Technology Centre, Noordwijk, The Netherlands

- Electrically Powered Separation Nuts
  Barney Little, Hi-Shear Technology Corporation, Torrance, CA

- A Radiation-Hardened, High-Resolution Optical Encoder for Use in Aerospace Applications
  Pat Kreckie, MicroE Systems, Natick, MA

- A Novel Grabbing/Latching Mechanism Without Moving Parts
  Brian Gore & Gary Hawkins, The Aerospace Corporation, El Segundo, CA

6:30–
9:30 **RECEPTION & DISPLAYS** – Von Braun Center
Invited component suppliers display current products and provide tutorials

THURSDAY, 8 MAY 2008

7:30 Thursday Presenters' Breakfast – Embassy Suites Hotel Redstone Boardroom

8:00 Light Refreshments – Von Braun Center South Hall Meeting Room

8:30 **SESSION IV—DOCK & DEPLOY** – Von Braun Center South Hall Meeting Room
Gérard Migliorero, Session Chair
ESA/ESTeC, Noordwijk, The Netherlands

- Docking System Mechanism Utilized on Orbital Express Program
  Scott Christiansen & Troy Nilson, SpaceDev Inc., Louisville, CO

- Ultra Light Self-Motorized Mechanism for Deployment of Light Weight Space Craft Appendages
  Cornel Bösch & C. Pereira, RUAG Aerospace, Wallisellen, Switzerland; R. John, T. Schmidt, K. Seifart & H. Sparr, HTS GmbH, Coswig, Germany; J. Lautier, ESA-ESTeC, Noordwijk, The Netherlands; T. Pyttel, University of Applied Sciences, Friedberg, Germany

- Development of the Aquarius Antenna Deployment Mechanisms and Spring/Damper Actuator
  Joel Johnson, Jet Propulsion Laboratory, Pasadena, CA

10:00 **BREAK**

10:15 **SESSION V—ANOMALY INVESTIGATIONS** – Von Braun Center South Hall Meeting Rooms
Joe Pellicciotti, Session Chair
NASA Goddard Space Flight Center, Greenbelt, MD

- Deflection Analysis of the Space Shuttle External Tank Door Drive Mechanism
  Michael Tosto & Robert Lindberg, National Institute of Aerospace/University of Virginia, Hampton, VA; Bo Trieu & Drew Hope, NASA Langley Research Center, Hampton, VA; Brent Evernden & Kenneth Wong, NASA Johnson Space Center, Houston, TX

- Failure of the Trailing Umbilical System Disconnect Actuator on the International Space Station
  Adam Gilmore & Laura Merritt, NASA Johnson Space Center, Houston, TX; Chris Schmitt & V.J. Bolton, The Boeing Company, Houston, TX

- The Mars Climate Sounder In-Flight Positioning Anomaly
  Bruno Jau & David Kass, Jet Propulsion Laboratory, Pasadena, CA

11:45 **LUNCH BREAK** – Box lunch is provided

1:00 **SESSION VI—MARS & WAY TO GET THERE**
Neil Otte, Session Chair
NASA Marshall Space Flight Center, Huntsville, AL

- Icy Soil Acquisition Device for the 2007 Phoenix Mars Lander
  Philip Chu, Jack Wilson & Kiel Davis, Honeybee Robotics Spacecraft Mechanisms Corp., New York, NY; Lori Shiraishi & Kevin Burke, Jet Propulsion Laboratory, Pasadena, CA

- Sample Manipulation System for Sample Analysis at Mars
  Erik Mumm, Tom Kennedy, Lee Carlson & Dustyn Roberts, Honeybee Robotics Spacecraft Mechanisms Corp., New York, NY

- A System for Suspending and Vibration-Isolating a Large Spacecraft for Testing in Vacuum
  David Keinholz, CSA Engineering Inc., Mountain View, CA

- Gas Strut Separation Alternative for Ares I
  Brian Floyd & James Owens, NASA Marshall Space Flight Center, Huntsville, AL

- Evaluation of Separation Mechanism Design for the Orion/Ares Launch Vehicle
  Kevin Konno, Daniel Catalano & Thomas Krivanek, NASA Glenn Research Center, Cleveland, OH

3:45 **BREAK**

4:00 **SPECIAL PRESENTATION** – MSFC Launch Vehicles, History, Lessons Learned, Projections to ARES
Bob Ryan, NASA Marshall Space Flight Center (retired)

The presentation will cover the history of MSFC launch vehicles including Redstone, Saturn, Space Shuttle, and NLS/NGLT. Issues discussed will focus on technical integration, uncertainties and margins, risks and trades. A discussion of the Ares mission configurations will lead to projections of possible issues on the ARES I and V configurations.

5:30–
10:30 **SYMPOSIUM BANQUET AT U.S. SPACE & ROCKET CENTER**

5:30 Bus leaves Embassy Suites to Rocket Center
Spacedome IMAX Theater – “Magnificent Desolation”
Dinner under the Saturn V
Tour the museum
10:00 Bus leaves Rocket Center for hotel

FRIDAY, 9 MAY 2008

7:30 Friday Presenters' Breakfast – Embassy Suites Hotel Redstone Boardroom

8:00 Light Refreshments – Von Braun Center South Hall Meeting Room

8:30 **SESSION VII—POSITIONERS** – Von Braun Center South Hall Meeting Room
Scott Tibbitts, Session Chair
SpaceDev Inc., Louisville, CO

- Focus Mechanism for Kepler Mission
  Kraig Koski, Ball Aerospace & Technologies Corp., Boulder, CO

- Precision Linear Actuator for Space Interferometry Mission (SIM) Siderostat Pointing
  Brant Cook, David Braun, Steve Hankins, John Koenig & Don Moore, Jet Propulsion Laboratory, Pasadena, CA

- Development of a Low-Cost Fine Steering Mirror
  Steve Wassom & Morgan Davidson, Space Dynamics Laboratory/Utah State University Research Foundation, North Logan, UT

10:00 **QUICK MID-SESSION BREAK**

- Cryogenic Focus Mechanism for the Spitzer Space Telescope
  William Schade, Ball Aerospace & Technologies Corp., Boulder, CO

- Development of a Spacecraft Antenna Pointing Gimbal
  Chuck Monroe & Peter Rossoni, NASA Goddard Space Flight Center, Greenbelt, MD

11:15 **SPECIAL PRESENTATION**: An Overview of Orion CEV Mechanisms
Lance Lininger, Orion Service Module Mechanism Design Lead, will give a preview of all the mechanisms on the Crew Exploration Vehicle. May see these again as the topic of a paper in the future!

11:45 **TECHNICAL SESSIONS CONCLUSION**

- Herzl Award Presentation
- Closing Remarks

12:00 **LUNCH BREAK** – Box lunch is provided

1:30 **BUSES DEPART HOTEL FOR TOUR**

2:00–
4:00 **FACILITY TOUR at ULA or MSFC**

SYMPOSIUM ORGANIZING COMMITTEE

Donald H. McQueen, Jr., Host Chair, NASA MSFC

Stuart H. Loewenthal, General Chairman, Lockheed Martin
Edward A. Boesiger, Operations Chairman, Lockheed Martin

Carlton L. Foster, NASA MSFC
Claef F. Hakun, NASA GSFC
Christopher P. Hansen, NASA JSC
Wayne Jermstad, NASA JSC
Gérard Migliorero, ESA/ESTeC
Alan C. Littlefield, NASA KSC
Edward C. Litty, JPL
Fred G. Martwick, NASA ARC
Wilfredo Morales, NASA GRC
Robert P. Mueller, NASA KSC
Fred B. Oswald, NASA GRC
Minh Phan, NASA GSFC
Donald R. Sevilla, JPL
Mark F. Turner, NASA ARC
Robin Tutterow, NASA LaRC
James E. Wells, NASA LaRC

SYMPOSIUM ADVISORY COMMITTEE

Obie H. Bradley, Jr., NASA LaRC (retired)
Ronald E. Mancini, NASA ARC (retired)
Stewart C. Meyers, NASA GSFC (retired)
William C. Schneider, NASA JSC (retired)

Linear High-Force "Step And Repeat" Piezoelectric Motors

J.S.N. Paine*, M.E. Johns*, J.J. Sesler*, M.T. Stefanick* and J.A. Kennedy*

Abstract

Dynamic Structures and Materials, LLC (DSM) has designed a patent-pending piezoelectric linear motor for demonstration in two aerospace applications related to the operation of a cryogenic 2" isolation valve and an environmental controls air handling system for next-generation space vehicles. The scaleable actuator technology provides a combination of force, stroke, and speed not previously demonstrated in other piezoelectric motor developments. The IMPULSE PiezoMotor™ technology is presented as a viable and superior replacement for heritage pneumatic, hydraulic, and electromagnetic actuation devices. A key feature of the IMPULSE PiezoMotor™ technology resulting from its friction-based drive architecture is a power-off-lock characteristic (fails in last position). A description of the mechanism and key performance parameters (step size, drive force, and resolution/accuracy), influence of materials on friction/wear, and power requirements are discussed.

Introduction to Piezoelectric Motors

A development effort to produce linear proportional electromechanical actuators for valve control has resulted in a new class of linear actuation mechanisms based on piezoelectric prime movers. The piezoelectric driven actuators are based on a step and repeat motor topology that enables relatively large strokes compared to typical piezoelectric driven actuators. This paper describes the mechanism and how it operates as well as discusses design and performance issues relative to using this device in precision motion control applications.

Linear "Step and Repeat" piezoelectric motors or SRMs are electro-mechanical energy transducers that convert electrical energy to mechanical motion through the expansion of piezoelectric ceramic materials. Piezoelectricity is the ability of certain crystals to generate a voltage in response to applied mechanical stress. The piezoelectric effect is reversible in that piezoelectric crystals formed into thin layers and stacked with electrodes can expand a small amount when subjected to an externally applied voltage. Typical expansion of these "stacks" can be on the order of 0.1 to 0.2% of length (i.e. a 20 mm long sample will extend ~ 20 to 40 microns (0.001 to 0.0016") at an applied voltage of 100 to 200 VDC. Figure 1 illustrates the expansion for a simple prismatic piezoelectric ceramic stack actuator. The expansion can occur at very fast response times (20+ kHz) and relative high force (50 MPa). This high force can be harnessed to produce very high bandwidth actuators and motors.

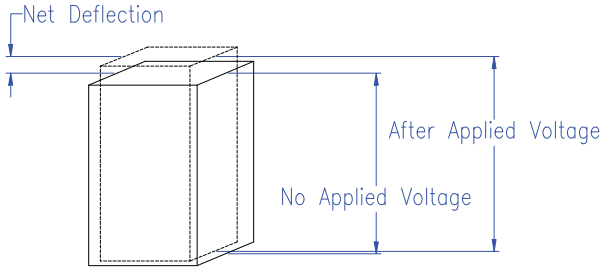

Figure 1 – Exaggerated Expansion Of A Piezoelectric Stack In The Column Direction

* Dynamic Structures and Materials, LLC, Franklin, TN

Piezoelectric stacks are the core components of DSM's SRM actuators. Since the single move displacement of piezoelectric ceramic stacks is very small, SRMs consist of a mechanism to convert many small steps into a single continuous move equaling the sum of the small steps. Generally, controlled intermittent friction is used as the means of transferring the displacement of the piezoelectric ceramic stack to the output shaft or slider's continuous motion. Spanner (2006) classifies piezoelectric motors into two classifications: quasistatic, and ultrasonic motors. Quasistatic motors are further characterized by those that operate on a clamping principle or inertial principle. DSM's SRM actuators are quasistatic clamping motors. A typical clamping motor operation is described in Figure 2, which follows from the Inchworm® Motor patented by Burleigh Instruments, Inc. in 1975 (May, 1975). The motor has two sets of piezoelectrically actuated mechanical clampers that alternatively grip (by applied friction) either end of the output shaft. The extender moves the clamps relative to each other and the external frame to advance the shaft either to the right or left as the sequence dictates. Through the process of clamping and unclamping the clamp elements and stepping the extender, the shaft advances.

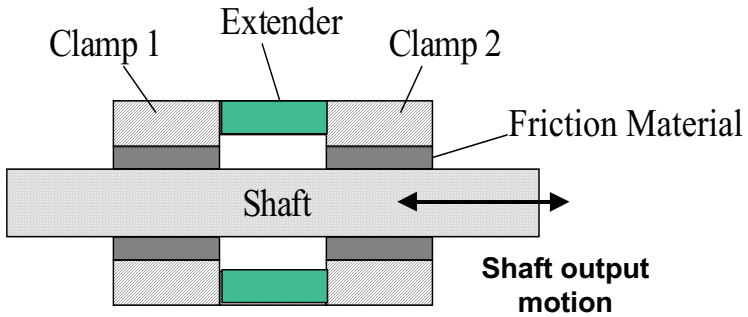

Operating sequence
1) actuate clamp 1
2) release clamp 2
3) extend shaft
4) actuate clamp 2
5) release clamp 1
6) contract mid section
7) repeat

Velocity control
step size - voltage
# of steps - frequency

Figure 2 – Operating Steps Of A Step And Repeat Motor After The Patent By May (1975)

Numerous piezoelectric motors have been developed in the last 6 years through a DARPA initiative called the Compact Hybrid Actuator Program or CHAP. Three motors demonstrated reasonably high levels of mechanical output power when compared to previous generations. Of the three motor actuators, the Kinetic Ceramic (2004) unit is the most powerful - achieving up to 40Watts of mechanical power. An advanced Burleigh unit (Burleigh, 2005) has approximately 600 times more power than the current Inchworm® motor but it produces only 2.5 Watts of mechanical power. In the UCLA MADD device (Carman et al, 2001), silicon microteeth are used but are limited in strength resulting in a 1.1-Watt maximum output. The Kinetic Ceramic motor delivers approximately 40 Watts of mechanical power through a hydraulic interface that requires hydraulic tubing and valving to deliver motion to the load.

Description of DSM's High-Force SRM Mechanism

DSM's SRM design uses a spring-biased clamper plate mechanism and other proprietary innovations within the motor to significantly improve drive force relative to current commercial SRMs. Shown in Figure 3 are the components of DSM's motor architecture. The minimal components include an extender element, a single active clamp, a static clamp, friction interface components, and the novel clamper plate. While DSM's current designs can all be operated with only one active clamp, most use two active clamps to increase the motor drive force. The extender resides directly in the moving shaft and advances the clamp element relative to the non-moving frame. In this configuration, DSM's design is an inversion of the traditional step and repeat motor with the clamper elements moving with the shaft while the location of the clamper plate remains stationary. DSM has also created a motor configuration with fixed clampers that uses the novel clamper plate and has an extender with a friction interface at each end. Either configuration with the novel clamper plate design offers higher drive forces than traditional SRM mechanisms and a means for self-compensating for temperature change and clamping surface wear.

The clamper plate provides a constant clamping force to the motor actuator enabling zero power hold. The clamping plate is on a pivot and it therefore transfers the clamping force from the active clamp to the static clamp – leading to an operating condition where the clamping force is always present. DSM's architecture also provides a much more consistent and significantly higher clamping magnitude than in the traditional step and repeat motor. For example, DSM recently developed a high-force IMPULSE PiezoMotor™ with approximately 2000 N peak force (called IMPULSE 2000 for short) and 20 mm/s peak unloaded speed. Compare this to a COTS piezomotor linear actuator from EXFO (2007) with 9.8 N peak force and 1.5 mm/s peak speed. For low-force applications and a small package, DSM is developing an IMPULSE 30 (30 N of force) with 32 mm/s drive speed.

IMPULSE PiezoMotor™ mechanism details and factors that affect the force and step size are presented relative to the components shown in Figure 3. Experimental testing results are also discussed.

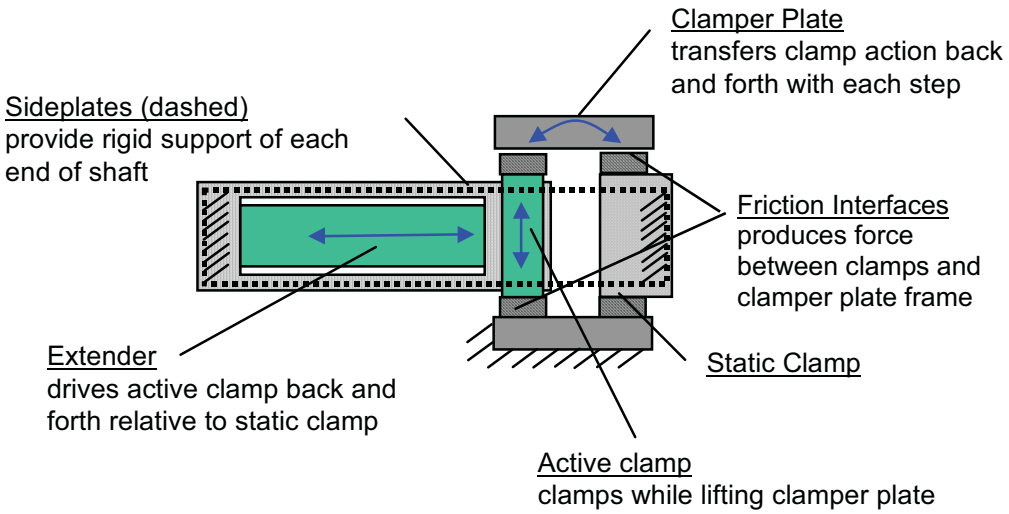

Figure 3 – Operational Components And Mechanisms In DSM's Step And Repeat Motor

Motor Drive Force

The first factor in determining motor drive force is the force capacity of the piezoelectric stack in the extender element. DSM uses two common piezoelectric stack cross-sections of 3.5 x 3.5 mm^2 and 10 x 10 mm^2. The extension force capacity of these stacks is approximately 650 and 5000 N respectively at 50 MPa of drive pressure. DSM has designed the motor's peak drive force to coincide with approximately 20% of the extender stack capacity. Therefore a design maximum for DSM's IMPULSE PiezoMotor™ with a single 3.5 x 3.5 mm^2 piezoelectric extender stack would be 130 N of drive force. To obtain up to 2000 N of drive force, DSM's IMPULSE PiezoMotor™ uses two side-by-side 10 x 10 mm^2 stacks. Figure 4 is a picture of an IMPULSE 2000 prototype motor that was delivered to a NASA valve contractor for testing with a propellant isolation valve and the IMPULSE 30 prototype.

The second factor in motor drive force is the clamping force applied by the clamper plate to the active and static clamp components. The clamping force is applied via a spring that biases the clamped plate down onto the active and static clamps. The resulting clamping force is proportional to the spring force. The product of the clamping force magnitude and coefficient of friction of interacting components dictates the driving force for the motor. The size of the spring force that can be applied to the clamper plate is dictated by the size of the piezoelectric stack used in the active clamp. A key aspect of motor design is balancing the amount of spring force with the size of the active clamp piezoelectric stack. Through careful experimentation and analysis, DSM has derived a proprietary process for sizing the spring force and piezoelectric stack for maximum driving force.

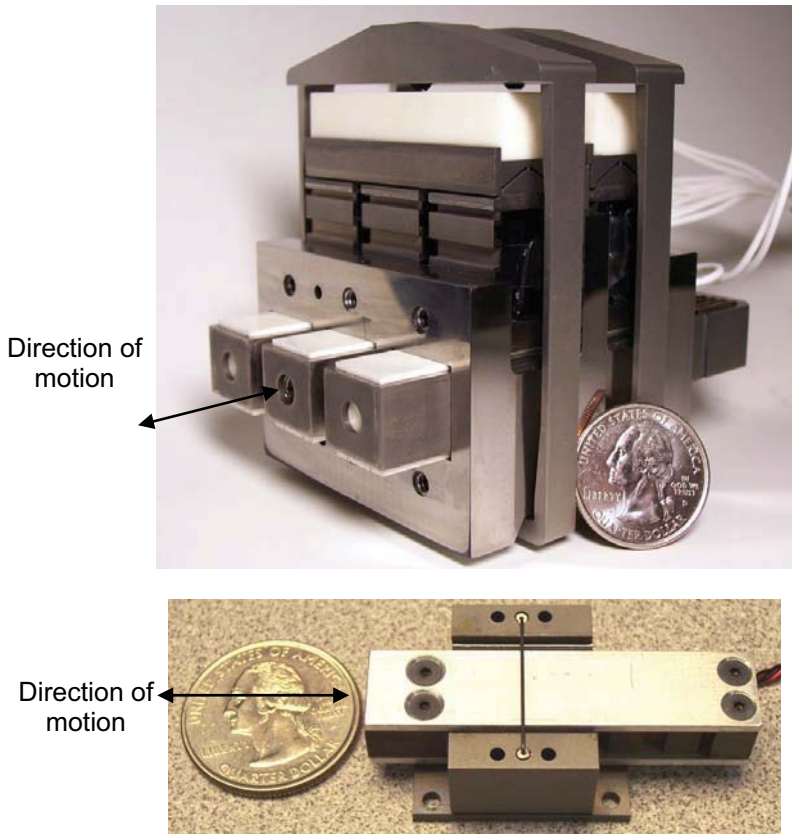

Figure 4 - Prototype Deliverable Of DSM's 2000 N IMPULSE Piezomotor™ (IMPULSE 2000) At Top And DSM's IMPULSE 30 At Bottom

A third factor in motor drive force is the friction coefficient of interfaces between the ends of the clamps and the clamper plate frame. DSM has found that the drive force is linearly proportional to the friction coefficient of the two materials in contact. Therefore, increasing the coefficient of friction between the two materials leads to an increase in drive force. DSM has performed a detailed experimental study of interface materials friction coefficients. A summary of this study is included in the next section.

Figure 5 shows the motor step size versus drive force for one of the IMPULSE 2000 prototypes and for two different IMPULSE 1000 prototypes that have been produced for NASA applications. The results were generated by driving a friction load with the motors while recording step size. Peak drive force scales approximately with the size of the clamp stacks used in the motors and with friction coefficient differences in the two systems. In this graph, the IMPULSE 2000 has more than twice the projected blocked force of the IMPULSE 1000 actuators. The IMPULSE 2000 has twice the piezoelectric clamp stack size of the IMPULSE 1000 and a coefficient of friction that is approximately 50% greater. While it is difficult to attribute specific quantitative differences to clamp size difference versus coefficient of friction, DSM has found that the trends are consistent. When a motor has twice the clamp stack size of a previous version, the available drive force can be double. When friction coefficient increases, the drive force follows.

Step Size and Drive Speed

The curve of the IMPULSE 2000 step size (Figure 5) shows a no load step of 27 microns and a near linear drop to 8-micron step size at a friction load of 2000 N. For all three prototypes, the step size consistently decreases with an increase in friction force. The difference in the step size of the two

IMPULSE 1000 motors reflects the variability in the friction between these early prototypes and the importance of achieving consistent fit and finish in the motors at the micron tolerance level.

Generally, the motor step size is dictated by the length of the piezoelectric stack used in the extender and the external load applied to the extender. Since the piezoelectric stacks are effectively spring elements, when the extender stack expands against a load, the compressive reaction force effectively reduces the stack's step size. The nature of the load also affects step size. A weight directly applied to the end of the extender will cause the extender to compress and slip backward during clamper transitions when moving against the weight. A friction load will stay in place and simply diminish the extender stroke as a function of the friction magnitude. A spring-type load will compress the extender to reach force equilibrium during each step and will release the stored energy backward during each clamper transition. In this manner, the step size becomes dependent not only on the magnitude of the external load, but also the direction and type of load.

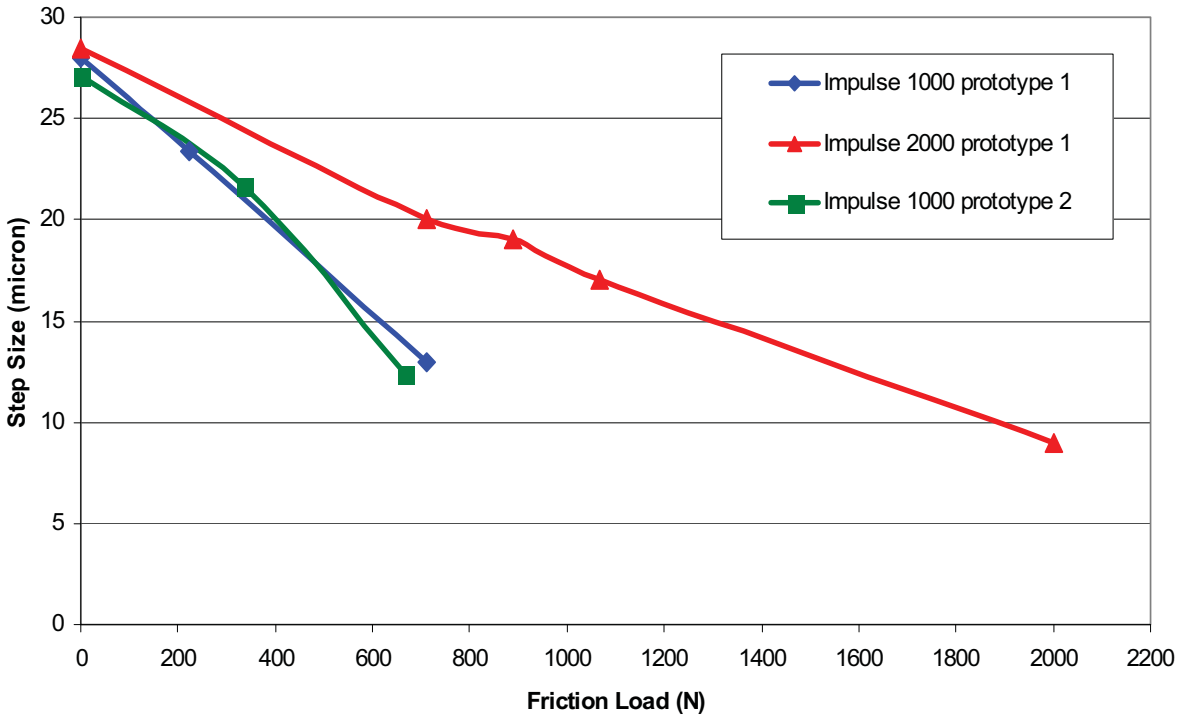

Figure 5 - Step Size Vs. Drive Force (Friction Load) For The IMPULSE 2000 And 1000 Prototypes

For example, the ideal step size and measured step size for DSM's IMPULSE 30 is shown in Figure 6. The unloaded step size of the extender using a 3.5 x 3.5 x 18 mm^3 long piezoelectric stack is 23 microns. The stiffness of this extender element is approximately 29 N/micron. Pushing a static load (weight) with this extender reduces ideal step size by the slope of the curve (i.e. 29 N static load reduces the stroke by 1 micron). This ideal step size ignores the compliance of other frame components and the non-ideal nature of the friction force that permits the motor to function. The compliance of the motor frame is a linear value that can be placed in series with the extender compliance. The non-linear friction effects are more difficult to predict but follow a recognizable trend. At this point in the SRM development, DSM has structural techniques that can be applied to reduce the motor frame compliance but has not completed a predictive model. Instead, each motor is designed with a balance of mass and stiffness to achieve the application objective while recognizing that the force versus step size response may be far from ideal.

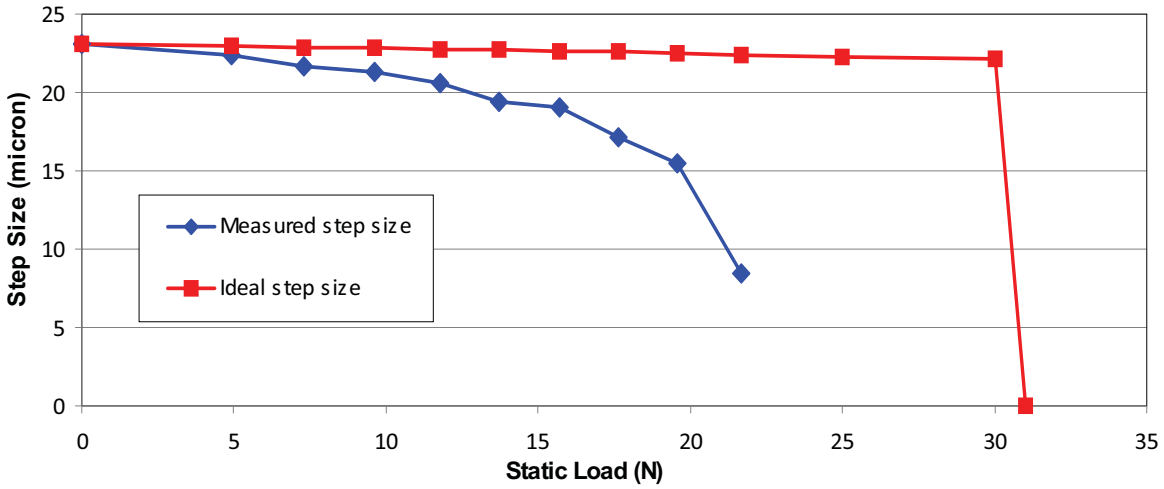

Figure 6 - Step Size Vs. Drive Force (Static Load) For The IMPULSE 30 Prototype

Drive speed is the product of the motor step frequency (number of steps per second) and the extender step size. The motor step frequency is the rate at which the electronics driver sequences the piezoelectric extender and clamper elements through the entire motor step cycle. Typical quasistatic clamping motors require that all three piezoelectric elements (extender and two clamps) oscillate through a complete square or triangle wave period without overlap in the rise or fall segments. DSM uses a special motor electronics driver that can produce six rise and fall segments fast enough to drive a 6-segment full step in less than 125 microseconds or step rate of 8000 Hz.

In practice, DSM has been able to operate motors up to 80 mm/s. The limitation results from the natural frequency of internal motor components (clamps and extender elements) being too low to respond to the highest possible step frequency. DSM can run the IMPULSE 30 and IMPULSE 2000 at approximately 2600 and 2000 steps per second respectively. The limitation in the IMPULSE 30 is the natural frequency of the extender element moving the lumped mass of the extender frame and active clamp elements. The limitation of the IMPULSE 2000 stems from the limitation in maximum piezoelectric stack preload that currently can be applied to the extender piezoelectric elements.

The fact that the piezoelectric actuator is controlled by a sequence of driving waveforms means that the motion profile can be optimized for different step frequencies within portions of the overall motion profile. This characteristic is valuable for proportional control applications.

Characteristic Impulse Force Profile

An interesting aspect of the IMPULSE PiezoMotor™ technology is the profile of the force that results during the step action. The extension step of the IMPULSE PiezoMotor™ may produce significant impact force on undamped loads. To quantify this effect, DSM tested three coupling conditions at a drive step rate of 800 motor steps per second (800 Hz). The resulting force profile measured by a high-stiffness load cell in-line with the motor extender and ground is shown in Figure 7.

At the point in the extender waveform where the extender advances the load cell into a solid aluminum block a very sharp resonance peak of 2000 N peak to peak occurs. The RMS average force is approximately 2200 N. This demonstrates the rapid hammering effect that the piezoelectric prime mover can produce against very stiff elastic loads. Placing layers of rubber between the extender and the aluminum block softens the hammering effect as shown by the blue and red curves. The impulse peaks for the 1/8th inch rubber (blue) are 1100 N peak to peak and approximately 1750 N RMS average. The impulse peaks for the 1/4th inch rubber (red curve) are 600 N peak-to-peak and approximately 1400 N RMS average.

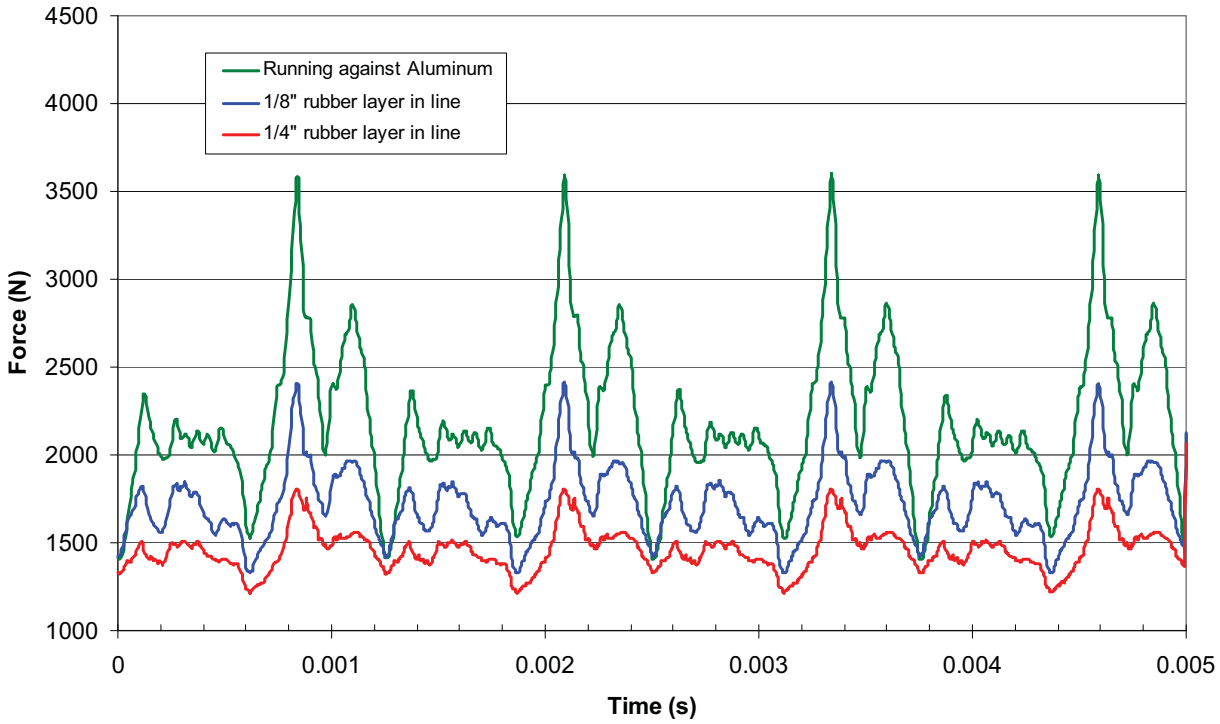

Figure 7 – IMPULSE 2000 Peak Output Force Profile With Three Different Coupling Configurations To Ground As Measured By An "In-Line" Load Cell

It is interesting to note that twice the thickness of the rubber (red curve) appears to reduce the impulse peaks to ½ the value of the blue curve. The drop in impulse peak-to-peak values appears to follow the thickness of the rubber layers. In this experiment, black neoprene rubber was used for the damping barrier but other damping and spring materials have been tested with similar results.

Characterizing the Friction Interface Materials

Because the IMPULSE PiezoMotor™ architecture is a friction-based drive mechanism, DSM has performed extensive experimental work with various material sets to understand the static and dynamic friction response. DSM has also investigated how wear affects surface roughness properties for the friction interface materials. For the IMPULSE PiezoMotor™ technology to operate properly, the friction interface materials must be very flat and smooth or have a very low surface roughness. Since the active clamp elements have stroke levels on the order of 10 to 20 microns, surface roughness values that are greater than 1 micron (40 microinch) can be significant. Additionally, the design goal is to achieve high friction at the interface materials in order to produce a high level of motor drive force. DSM has also determined that to maintain a rated load capacity, the surface roughness, flatness and parallelism of the friction pair must be maintained to an acceptable level throughout the useful life of the actuator. Therefore, minimizing wear is also a design goal.

Working with University of South Florida (Mudhivarthi, 2006) and Brigham Young University, DSM has performed a number of friction materials characterization studies for piezomotor applications. The testing consists of a series of physical tests on numerous friction pairs that was designed to simulate the loads, motions and conditions typical to the various motor applications. DSM has tested friction pairs including various combinations of steels, ceramics and surface treated steels. High-cycle wear tests were performed and optimum friction pairs for this application were identified based on high friction, low wear and low roughness. Much of this data is repeated from the work that DSM funded at University of South Florida (USF) that is recorded in the Mudhivarthi (2006) paper.

Test Method for High Cycle Friction Testing

Typical loads and speeds used in the testing were set to force and speed levels that corresponds to the drag that the friction materials would experience during a sliding transition. During a clamp move, the friction materials experience force levels up to 6000 N but with the expectation that no sliding will occur. To characterize the materials' initial hardness and surface roughness, both values were measured before any wear testing and recorded for all specimens. DSM requested eighteen material pairs to be tested by USF listed in Tables 1A and 1B.

The interaction of the friction pairs in a piezoelectric motor was simulated using a Universal Micro-Tribometer with custom fixtures. The lower test specimen (50x12x1.2 mm^3) and fixture were fixed. The upper test specimen (25x12x1.2 mm^3) and fixture provided normal loading and reciprocating sliding motion using the upper vertical and lateral positioning systems of the tribometer.

Each pair was subjected to the following test procedure:

1. Clean test surfaces with acetone before each test
2. Photograph test specimens and measure surface roughness of test specimens
3. Measure initial friction force with sliding velocity of 0.5mm/s and sliding displacement of 2mm for 3 steps with 1 sec rests in between steps
4. Perform a test sequence on the tribometer for N cycles where N is 100, 500, 10,000, 50,000, 100,000, 200,000, or 300,000, until the test is stopped due to failure or poor friction response.
    a) Set upper specimen near center of contact area of lower specimen
    b) Set normal contact force to 44.5 N (10 lb)
    c) Move upper specimen to the left 5 mm at sliding velocity of 7.5 mm/s
    d) Move upper specimen to the right 5 mm at 7.5 mm/s
    e) Repeat steps c thru d for N-1 times
5. Photograph test specimens, measure surface roughness and assess wear of test specimens

Test Results for High Cycle Friction Testing

An example of a typical friction coefficient versus time plot for a solid Croblox® sample against a 52100 steel sample is shown in Figure 8. Contrary to conventional thought, each plot in Figure 8 indicates that the initial breakaway friction (static) is less than the moving friction (dynamic). DSM attributes this characteristic to the very smooth nature of the interfacing surfaces and their lack of mechanical interaction.

Tables 1A and 1B show the test results for the coated friction interface materials and solid friction interface materials respectively. The tungsten carbide (WC) coated specimens against either a Croblox® gage block or a ceramic gage block showed very low friction. The Croblox® is a chromium carbide material from Starrett Gage Company. The diamond like carbon (DLC) coating also indicated very low friction against the ceramic gage block. These tests were therefore cancelled after only a few cycles. The response of the other coated material friction pairs in Table 1A indicate that within 40,000 cycles, the coating had abraded enough that is was decided to stop the test. The coatings were generally 2 to 5 microns (80 to 200 microinch) thick. Therefore, surface roughness on the order of 2 microns (80 microinch) is an indication that the coating thickness might be completely worn away. Generally, after abrasion on the surfaces exceeded 2 microns (80 microinch) the test was stopped. The trends indicate that the surfaces with higher initial coefficient of friction (COF) had greater abrasion after fewer cycles.

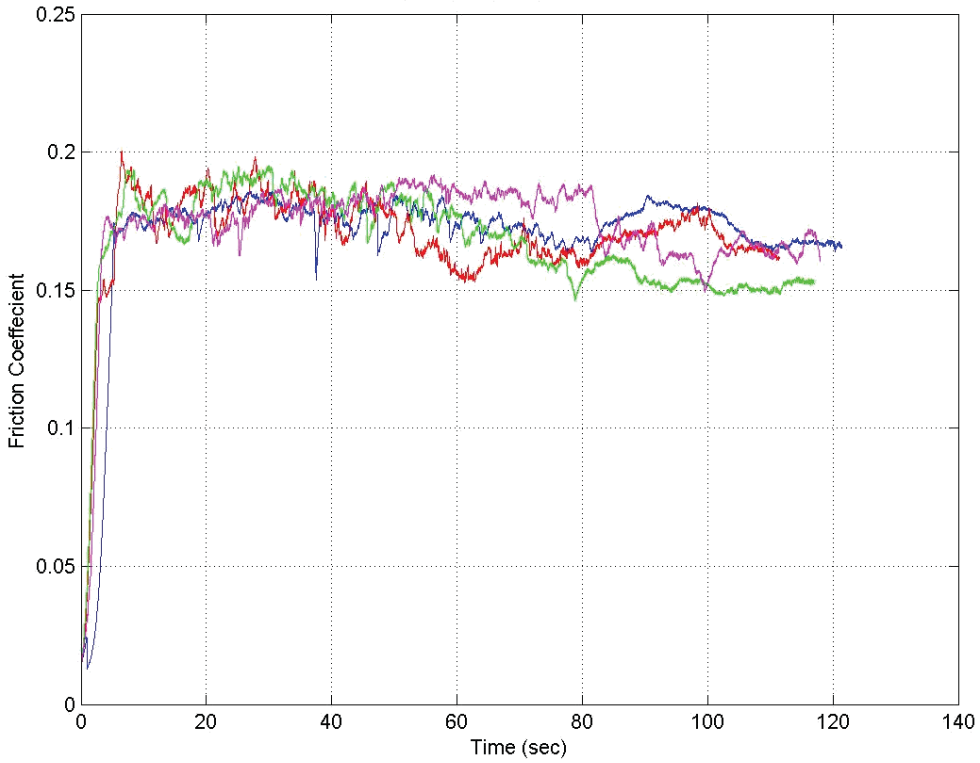

Figure 8 - Friction Versus Time Plot For A Solid Croblox® Against A Solid 52100 Steel Specimen

Table 1A - High Cycle Tests Summary For Coated 52100 Steel Friction Interfaces
(repeated from Mudhivarthi, 2006)

No.	Material Pair	COF	Post Test Condition
1	TiN / TiN	0.18-0.22	Coating removal/severe abrasion after 600 cycles; Rtm=41-364 μin
2	MoST / MoST	0.10-0.32	Severe coating removal after 100 cycles; Rtm=45-177 μin
3	WC / ceramic gage block	0.09	Cancelled due to low friction
4	WC / 52100 steel gage block	0.18-0.21	Abrasion after 20,000 cycles; Rtm=33-65 μin
5	WC / Croblox® gage block	0.11	Cancelled due to low friction
6	DLC / ceramic gage block	0.09-0.11	Cancelled due to low friction
7	DLC / 52100 steel gage block	0.13-0.15	Abrasion after 40,000 cycles; Rtm=14-96 μin
8	Tetrabond / ceramic gage block	0.17-0.21	Abrasion after 20,000 cycles; Rtm=79-94 μin
9	Tetrabond / 52100 steel gage block	0.32-0.36	Severe abrasion after 10,000 cycles; Rtm=79-156 μin
10	TiN / A2 steel	0.16-0.24	Severe abrasion after 10,000 cycles; Rtm=280-1,257 μin

The solid material friction interface pairs (Table 1B) performed very well in terms of wear and surface roughness. The steel feeler gages cycled against each other were the only pair that manifested severe abrasion after a relatively low number of cycles. Compared to the coated specimens, the solid friction interface materials had much lower abrasion and lasted to levels of 300,000 cycles in the case of ceramic on ceramic. When comparing the response of the materials, DSM found that the following pairs had reasonable coefficient of friction levels in the range of 0.12 to 0.18 and indicated very mild abrasion:

- Sapphire on 52100 steel gage block (test no. 14) at 0.13 to 0.15 COF,
- Sapphire on ceramic gage block (test no. 15) at 0.15 to 0.17 COF,
- 52100 steel gage block on ceramic gage block (test nos. 12 and 17) at 0.12 to 0.17 COF, and
- Ceramic gage block on ceramic gage block (test no. 18) at 0.13 to 0.15 COF.

For environments where resistance to corrosion is an issue, the two different ceramic pairs would perform better than either of the two pairs with steel. Fine particles generated during testing of the 52100 steel gage block on ceramic gage block were found to be oxidized and some of the fine abrasive scratches in the steel also showed oxidation.

Table 1B - High Cycle Tests Summary For Solid Material Friction Interfaces
(repeated from Mudhivarthi, 2006 with updates*)

No.	Material Pair	COF	Post Test Condition
11	Steel feeler gage / steel feeler gage	0.30-0.60	Severe abrasion after 600 cycles; Rtm= 1.4 – 3.1 μm (57-123 μin)
12	52100 gage block / ceramic gage block	0.14-0.17	Mild abrasion after 200,000 cycles; Rtm= 0.1 – 1.2 μm (4 - 47μin)
13	Croblox® gage block / ceramic gage block	0.13-0.2*	Cancelled due to low friction
14	Sapphire / 52100 steel gage block	0.13-0.15	Mild abrasion after 40,000 cycles; Rtm= 0.1 – 0.2 μm (5 - 10 μin)
15	Sapphire / ceramic gage block	0.15-0.17	Mild abrasion after 40,000 cycles; Rtm= 0.08 – 0.2 μm (3 - 7 μin)
16	Croblox® gage block / 52100 steel gage block	0.15-0.2*	Abrasion after 10,000 cycles; Rtm= 0.08 – 1.1 μm (3 – 46 μin)
17	52100 steel gage block / ceramic gage block	0.14-0.2	Mild abrasion after 200,000 cycles; Rtm= 0.08 – 1.4 μm (3 – 55 μin)
18	Ceramic gage block / ceramic gage block	0.13-0.15	Mild abrasion after 300,000 cycles; Rtm= 0.08 – 0.1 μm (3 – 5 μin)

Example of Wear at the Friction Interface

To characterize the material wear of friction surfaces within a prototype piezoelectric motor environment, DSM assembled an extender element using two 52100 steel gage blocks separated by a piezoelectric extender stack. The extender was actively driven within an early IMPULSE PiezoMotor™ prototype frame. The mating friction surfaces contacting the extender's steel gage blocks were fabricated from a hard ceramic. Following a cumulative travel distance of 10 km, surface profile scans were made on the extender's blocks in order to quantify material loss. The mating ceramic surfaces were not profiled. The surface scans were performed along the direction of the lines indicated in light blue in Figure 9.

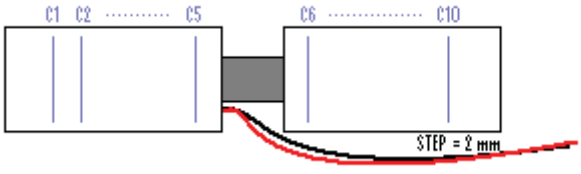

Figure 9 - Sketch Of Extender Assembly Used In Long Endurance Friction Wear Testing

Figure 10 illustrates the surface height measured with a profilometer for each of ten scans. Note the original flatness of the block on the outside edges. Over the course of ten kilometers, as much as ~8 microns of depth in the steel was worn away in certain locations, but the average material loss appears closer to 4-5 microns of depth. One attractive feature of DSM's IMPULSE PiezoMotor™ patent-pending

architecture is its ability to compensate for this material loss, thus avoiding a decrease in the motor's available driving force.

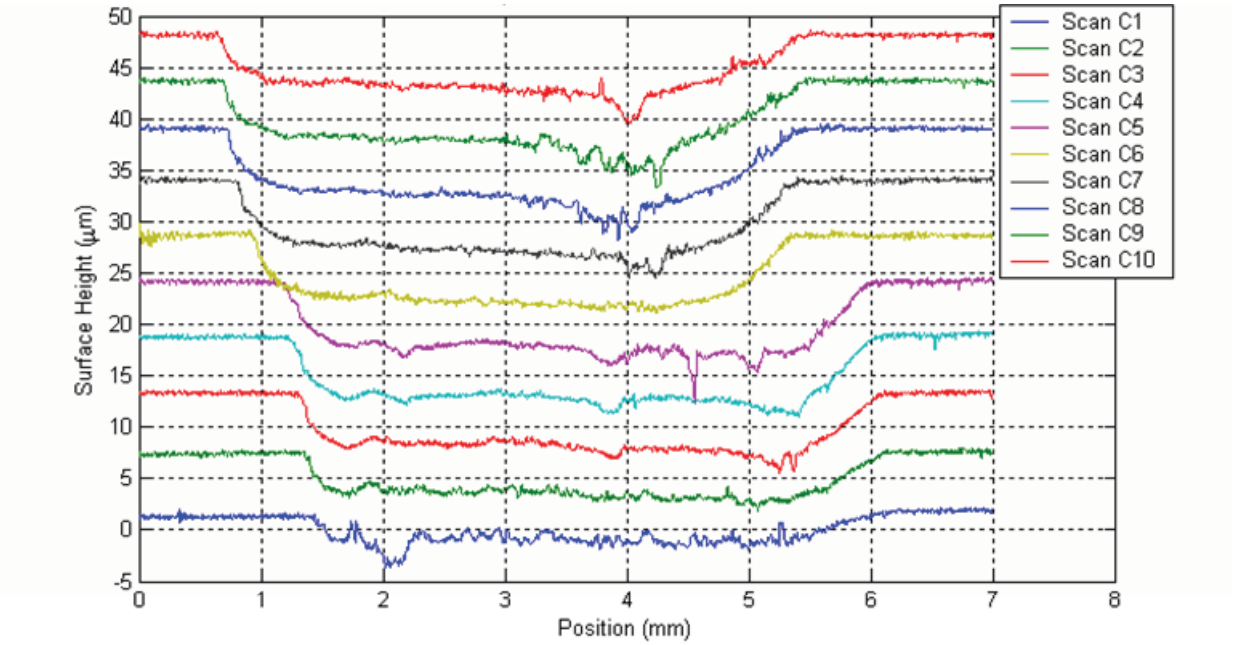

Figure 10 - Surface Heights For Each Of Ten Scans Across The 52100 Steel Extender Components After 10 km Of Cumulative Linear Travel In A Prototype Piezoelectric Motor

Conclusions from the Study of Friction Interface Materials

A number of coated and solid friction interface materials have been studied and tested. The solid friction materials held up substantially better than the coated friction materials. Three types of materials held up notably well: a ceramic gage block; a hardened 52100 bearing steel; and, a sapphire substrate. All indicated very little abrasive wear in a friction test at over 40,000 wear cycles. Of particular interest is the nature of the coefficient of friction in the hardened specimens. Regardless of the initial COF, all of the materials migrated to a similar range of 0.11 to 0.18 COF after sufficient wear cycles had occurred.

Accuracy and Resolution of the SRM Mechanism

As described previously, the step size of DSM's SRM mechanism is dependent on the size of the load applied to the motor output. The accuracy of the step size is therefore dependent on the load magnitude and the consistency of the load. Generally, DSM recommends that these mechanisms be used with an encoder or other type of position feedback device to provide a means of updating the position to the controller and closing the position loop on a specific target.

In a recent example of using an IMPULSE 1000 to drive a NASA valve, DSM closed the loop on a position target using an LVDT device for feedback. An LVDT produces a linear variable voltage as a function of position over the travel length. In this application, the SRM was used to drive the valve to a set location (voltage). The controller is programmed to stop the motor at the nearest step position within a designated deadband around the voltage position target. In this case, the resolution of the position control is approximately one motor step or less than 25 microns.

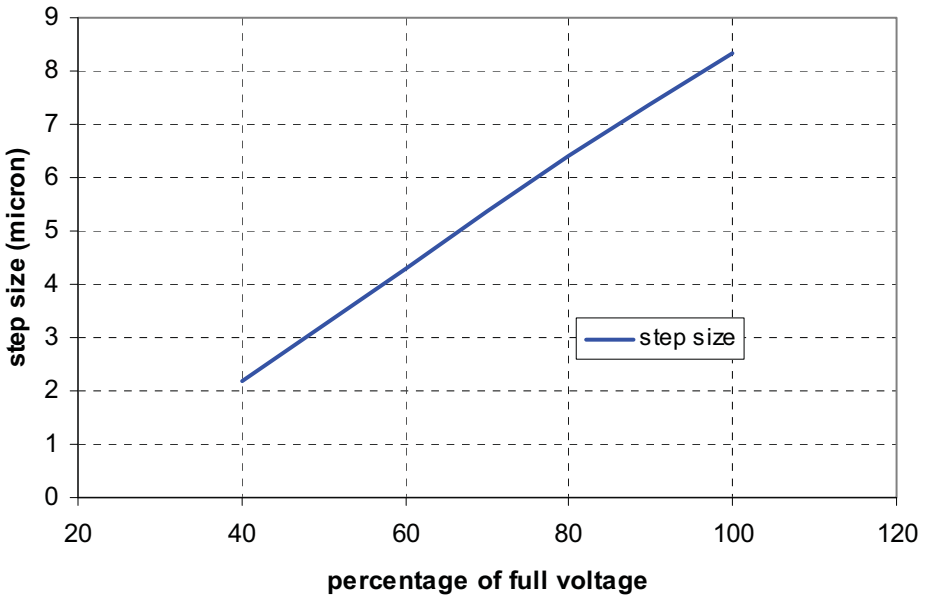

Figure 11 – Demonstration Of Partial Stepping On An Early SRM Prototype

In another demonstration to test the capability for producing micro-stepping in an IMPULSE PiezoMotor™ device, DSM ran an early "light duty" SRM with a variable voltage on the extender. Figure 11 shows the resulting step size as this motor was driven a few steps to characterize the step size. The partial step size follows the voltage applied to the extender in a linear and proportional manner indicating that overall resolution of the motor might be made smaller using proportionally smaller extender steps.

Measurements of Electrical Power Input to the IMPULSE PiezoMotor™

Using an accurate data acquisition setup, DSM engineers measured the electrical power going into each channel of the IMPULSE 30 prototype as a function of drive voltage, step rate and static load (weight) applied to the output of the motor. Two different drive voltages, multiple drive step frequencies and multiple static load values were tested. The outcome of the testing is captured in Figure 11. DSM used linear amplifier electronics in this study to make the measurements; current and voltage signals are better captured with linear amplifiers instead of motor electronics. With the linear amplifiers, the step rate was limited to 500 steps per second.

To make a measurement of output power efficiency, DSM measured the output mechanical power of the motor while pulling a range of static loads (weights). DSM found that the efficiency was very low since the extender stack has much more mechanical force capacity than can be manifested by the clamping elements. In other words, the main pushing stack of the motor can produce 130 N (30 lbf) of drive force but is only called upon to produce up to 30 N (7 lbf) of drive force because of clamp limitations. Since DSM's motors are friction limited, the excess capacity of the extender simply goes to waste.

Figure 12 shows the electrical power used to drive the motor as a function of static load (weight) that the motor is lifting. The electrical power measurements were made for each channel (extender and clampers) along with the motor displacement for 25 steps at 200 steps per second while lifting the indicated mass. The mechanical power is the product of lifting force and motor velocity. At 200 Hz, the velocity is approximately 4.5 mm/s under zero weight. Velocity decreases with increased lifting mass as indicated by the green displacement line. The peak mechanical power correlates with lifting around 1800 grams (3.5 lbm).

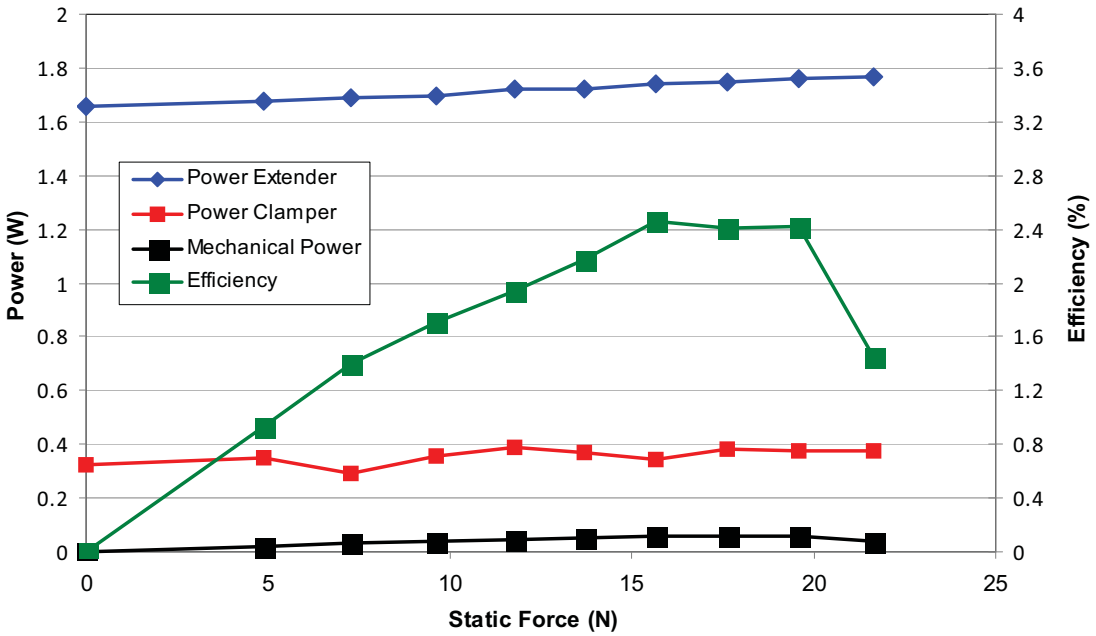

Figure 12 – Electrical Power Used In DSM's IMPULSE 30 At 200 Hz Step Rate

From this data, DSM gains information regarding how the electrical power is used in the motor actuator. First, the clamp stack electrical power does not vary as a function of the mass that the motor is lifting. The extender channel electrical power shows only a small correlation with the increased mass and even with no lifting mass, the extender uses over 1.6 Watts of power. The small increase in extender power correlates with the increase in mechanical power indicating that any work that the extender is required to produce while lifting mass requires proportionally more electrical power.

The mechanical power increases with the lifting force until the motor drive force becomes friction limited. Once the lifting force exceeds the available friction force, the motor begins to slip during its forward motion and the mechanical power decreases. The efficiency is the measure of the output mechanical power divided by the total electrical power applied to the motor. Peak efficiency numbers are approximately 2.5%. DSM estimates that there are two reasons for the low efficiency numbers. The first involves the oversized nature of the extender stack used in the motor. The second reason involves the electrical properties of the particular piezoceramic material that this motor uses.

Using a smaller extender stack can cause the motor efficiency to increase since the motor drive force is friction limited not limited by the extender stack size. Another method for increasing the efficiency of the motor would be to use piezoelectric ceramic materials that are by composition more efficient than the soft PZT materials used in the current motor prototype. The current motor prototype uses piezoelectric ceramics with a loss factor of over 5% and a relatively high amount of capacitance. DSM is considering the use of piezoceramics with less than 40% of the loss factor and approximately 50% of the capacitance of the soft piezoelectric ceramics. DSM estimates that this might lead to a doubling of the current efficiency numbers.

Piezoceramic motors have a significant advantage in duty cycle over electromagnetic motors. In actuator duty cycles where holding maneuvers are required, DSM's motors use only the quiescent power that is required to maintain the drive electronics in a ready state. The piezoelectric motors do not require any power to hold position. Therefore, even 18 Watts of power for the 10 to 20 ms used to make a move does not require significant battery energy. With the same setup, DSM measured the power as a function of step rate for the IMPULSE 30 SRM. The power was measured for step rates up to 500 steps per second and then extrapolated for higher frequencies. DSM found a direct linear correlation between electrical power going into the motor and step rate.

Conclusions

In the IMPULSE PiezoMotor™ technology, DSM has developed a new class of high force piezoelectric SRM mechanisms. The operation of the motor and the drive force, step-size, and characteristic step impulse profile are presented. Compared to conventional step and repeat motors, DSM has produced a family of devices with substantially greater drive force. Results from a study of various potential friction interface materials yields a set of materials with suitable wear performance and with coefficients of friction that are in the range of 0.15 to 0.18. Modulating the voltage on the SRM extender to obtain smaller steps is demonstrated as a means to increase the step resolution of the output. To demonstrate the electrical to mechanical conversion potential in the SRM mechanisms, DSM performed an experimental study that involved lifting various weights and measuring resultant speed. For the current family of actuators, drive efficiency is around 2.5%. A means of obtaining higher levels of drive efficiency is discussed. Measurements also indicate that the electrical power increases proportionally to the motor step rate.

The proposed actuators offer the following significant advantages over conventional electromagnetic actuator technologies.

- the ability to withstand higher (200°C) and lower (-150°C) temperatures,
- zero power draw during hold maneuvers,
- the ability to carry a significant side load,
- greater impact resistance due to the solid-state nature of their construction,
- fewer number of components that leads to a more reliable system,
- lack of required lubricants for improved storage characteristics, and,
- a much smaller form factor for the same level of force.

References

Spanner, Karl, 2006, “Survey of Various Operating Principles of Ultrasonic Piezomotors, Proceedings of Actuator 2006, June 9, 2008, Bremen, Germany.

Carman, Dunn, Friedmann, Hahn, Ho, Kim 2001, “Developing Innovative Actuator Devices for Use on Rotocraft Systems” U.S. Army Research Office.

Burleigh, 2005, “Prototype Actuators”, The Power of Precision, Burleigh, An EXFO Company.

Kinetic Ceramics, 2004, “High Pressure Piezoelectric Pump”, Kinetic Ceramics website: http://www.kineticceramics.com/pdf_files/turnkey_pzt_systems.PDF

EXFO, 2007, Inchworm Motors W-800/810, Web page specification sheet at http://www.exfo-lifesciences.com/nano/app_notes/IW-800.pdf

May, William, 1975, “Piezoelectric Electromechanical Translation Apparatus, U.S. Patent 3902084, Aug. 26, 1975.

Mudhivarthi, S., D. P. Hess, 2006, “Wear data from friction pairs for microscale piezoelectric actuators”, in Tribotest, Volume 11, Issue 1 , Pages 1 – 10, Published online 9 Mar 2006.

Development of a High Resolution Rotary Actuator for an Antenna Trimming Mechanism

Jérôme Brossier*, Xavier Jeandot*, Yannick Baudasse*, David Grima* and Fabrice Champandard*

Abstract

The High Resolution Rotary Actuator (HR²A) product is one of the main components of the Antenna Trimming System (ATS) developed for a commercial satellite. The mechanism needs to deploy and point the reflector around two axes and is composed of two HR²A in a gimballed configuration. It operates in a closed loop system using an RF beacon on the ground. This assembly is called MADPM, Multimedia Antenna Deployment and Pointing Mechanism. These mechanisms are located between the spacecraft structure and the reflector. The positions and orientations of these mechanisms on the spacecraft result from an architecture layout analysis, dealing with deployment and pointing objectives. The HR²A mechanism is developed to be able to steer a large reflector along a wide deployment angle (up to 180° with steps of 0.02°), to point it with a small output resolution (0.002° each step) and to perform a large number of micro cycles. The mechanism is qualified and 6 flight models have been built in parallel of the qualification and are now assembled on the spacecraft.

Introduction

Initially, system engineers required that the mechanism shall be able to perform a high and not well defined number and type of cycles. The first choices of technology were therefore based on this main requirement. This requirement disqualifies automatically all the links with tribological contact. After more work with system engineers and in order to be able to qualify this type of product, the number and types of cycle were determined for the generic Thales Alenia Space platform. It appeared that the need still required a technology and design with no risk with regard to the life time. Moreover, the mechanism will have to be able to deploy the reflectors up to 180° of motion. Aiming at reducing the number of actuators, we decided to use the same actuator for deployment and for pointing. The background of Thales Alenia Space mechanism product line with very large number of cycles led us to use the heritage of the Scan Drive Unit Actuator. The Scan Drive Unit actuator is a part of the SEVIRI instrument of METEOSAT Second Generation spacecraft and has been fully developed by Thales Alenia Space. This mechanism is a linear actuator constituted mainly by a stepper motor, a spindle, ball bearings and potentiometer. The peculiarity of this mechanism is to be fully sealed and filled with oil. As a rotational movement is required to deploy a reflector, it was necessary to have another mechanism able to transform a linear movement into a rotational movement without risk with regards to life time. It is in this framework that the HR²A has been successfully developed by Thales Alenia Space.

Mechanism Description

The High Resolution Rotary Actuators is made of different components based on several innovative ideas.

- A high life time capability linear drive unit.
- A high life time capability reducer, that realizes, with the same linear kinematic input, a large amplitude rotating movement (deployment), following by a small amplitude rotational movement, with a high accuracy (fine pointing).
- A specific guiding (and crossing) system, with flexible blades, that provides stiffness and loads capabilities.

* Thales Alenia Space, Cannes, France

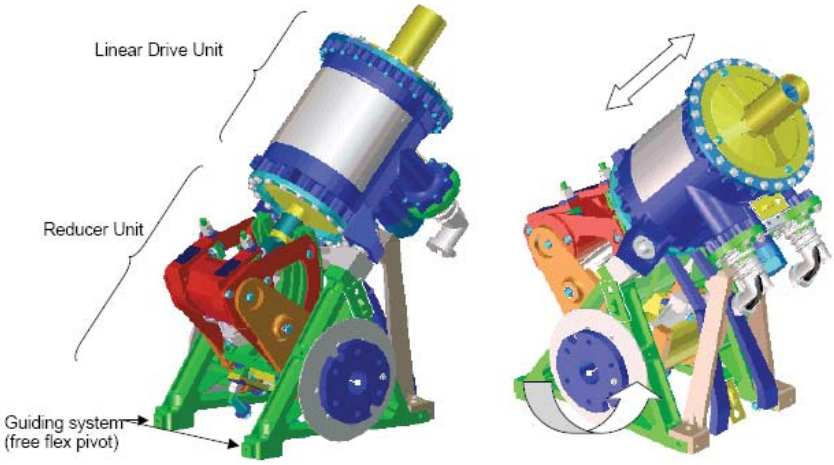

Figure 1. High Resolution Rotary Actuator

The linear drive unit is composed of:

- a redundant two-phase permanent magnet stepper motor
- a redundant rotational potentiometer (fine)
- two linear potentiometers (nominal and redundant) (coarse)
- a roller screw
- ball bearings
- metallic bellows
- ring metallic joints
- oil
- hard stop

The reducing unit is composed of:

- metallic strap
- free flex bearing
- ball bearings
- hard stop
- two outputs

Three patents are filed for this product.

- 1st innovative idea: the reducer : (Patent: Folio 652805)
- 2nd innovative idea: combined guiding: (Patent: Folio 652667)
- 3rd innovative idea: The specific crossing guiding with flexible blades (also called free flex pivot) (Patent: FR0753521 27/02/2007):

The system requires deployment and then pointing around two axes. To fulfil this function, two HR²A are mounted together in a gimballed configuration to form the MADPM; the layout is shown in Figures 2 – 4.

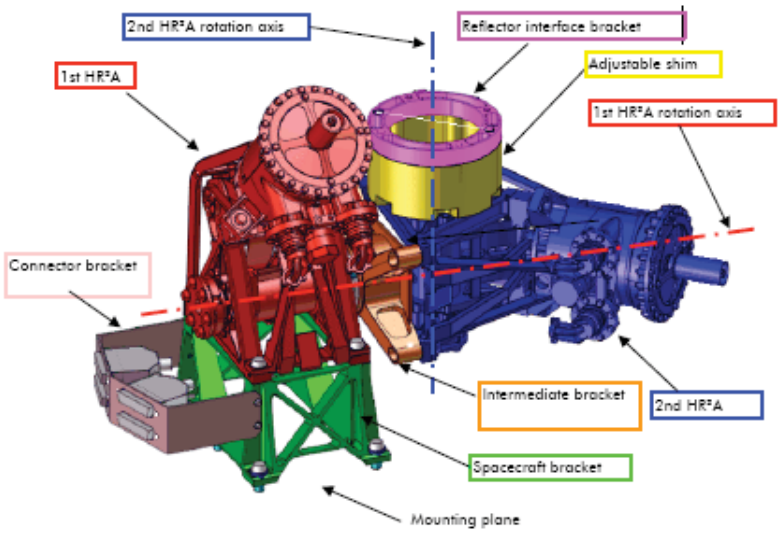

Figure 2. MADPM layout in deployed configuration

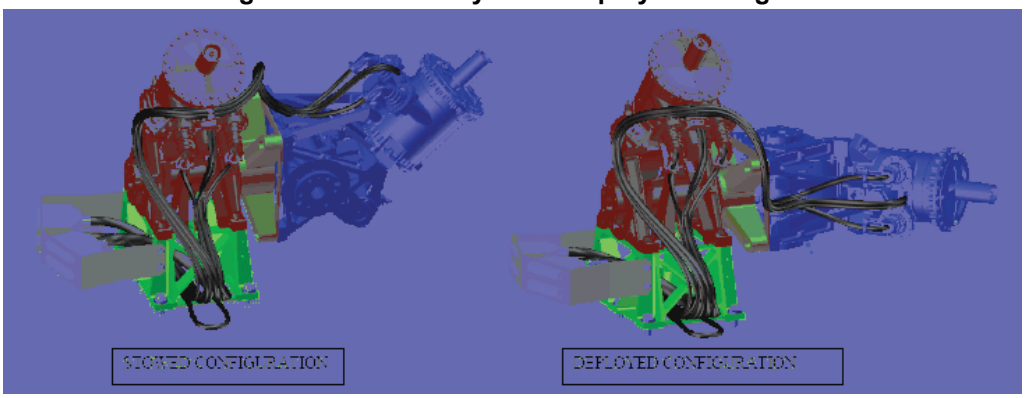

Figure 3. MADPM stowed and deployed configurations

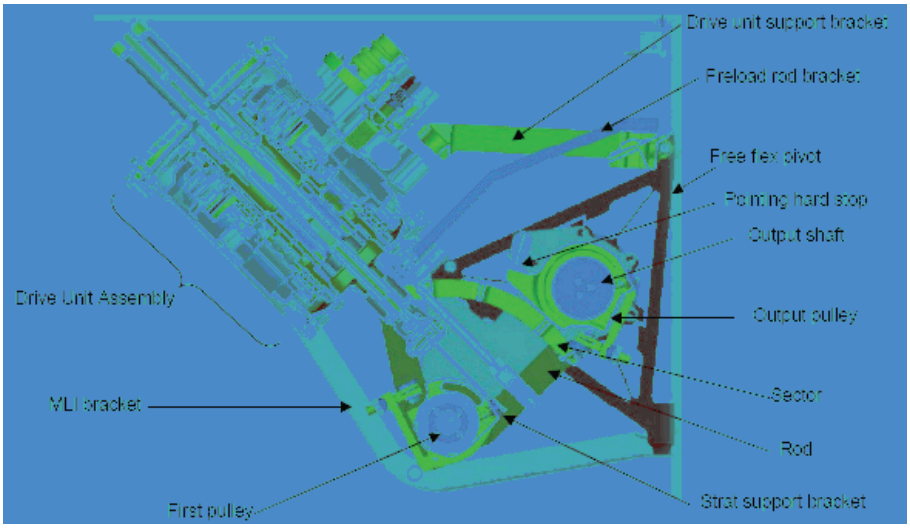

Figure 4. Mechanism Kinematic

Deployment

Once the reflector is released, the stepper motor of the linear drive unit is powered on. The stepper motor drives the bolt of the roller screw in rotation. As the screw is stopped in rotation by the bellows, the screw moves in translation. The linear drive unit output step is equal to 2.2 10^{-3} mm/step. The rotational potentiometer is linked to the stepper motor rotor to provide fine position. The linear potentiometer is linked to the screw to provide coarse position.

- The strap support bracket, linked to the linear drive unit output moves in translation.
- Straps unwind and wind at the same time around the first pulley.
- The first pulley radius is 20 mm.
- The sector with a higher radius (63 mm) turns in the same movement. Its straps unwind and wind in the same time around the output pulley.
- As a consequence, the output step is equal to: $\theta_{output} = \frac{63mm}{20mm} \times \frac{0.0022mm}{20mm} = 0.00035rad = 0.02° / step$

End of deployment:

At 1.25° before the operational deployment position, a pointing hard stop on the output pulley comes in contact with the rod. As the rod supports the first pulley and sector, the rotational movement of both is stopped with respect to the rod. There is no more movement of the first pulley ball bearing and output pulley ball bearings. As the linear drive unit continues to push the strap support bracket, the rod unsticks from the preload rod bracket and moves the free flex pivot. The output rotational movement is obtained by bending of the three blades of the free flex pivot. The end of deployment is when the potentiometers give the right value. This position corresponds to a rotation of the free flex pivot of 1.25°.

In pointing phase

In this phase, the linear drive unit can move in two ways. The free flex pivot is always bending. The operational range is ±1° (specification) but might be increased up to ±1.25° (design margins). The output step value is given by the distance between the output rotation axis and the axis of the linear drive unit (63 mm). The range of HR²A movement is limited thanks to the hard stop inside the drive unit.

$$\theta_{output} = \arctan\left(\frac{\Delta l_{linear\_output}}{63mm}\right) = \arctan\left(\frac{0.0022mm}{63mm}\right) = 0.00202° / step$$

Linear Actuator Description and Maturity

The linear drive actuator is a sealed linear actuator with a complete oil bath. This technology enables a high number of micro-cycles in a harsh thermal environment. The movement is performed due to the screw of a spindle. The nut of the spindle is linked to the rotor of a stepper motor. A redundant rotational potentiometer gives the position of the stepper motor (fine potentiometer). A redundant linear potentiometer gives the position of the screw (coarse potentiometer). The combination of both potentiometers' information gives the position of the screw with accuracy inferior to the step. Power and measurements are sent by two hermetic connectors, one nominal, and one redundant. The dynamic sealing is performed by metallic bellows (which stop the spindle screw in rotation) and static sealing due to metallic joints.

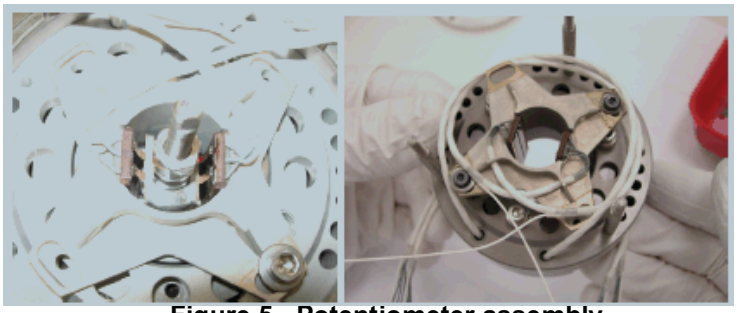

Figure 5. Potentiometer assembly

The stepper motor, the spindle, the potentiometers, the oil, the ball bearings, the bellows, the joints and the hermetic connectors are procured elements and represent 90% of linear the drive unit.

Both bellows at the front and back of the linear drive actuator are the same in order to have no variation of volume inside the mechanism. However, it is still necessary to have a volume balancer due to the thermal expansion of the oil. Actually, the inside volume of the mechanism is constant but the mechanism is not fully filled of oil. The volume not used by the oil if filled with a neutral gas. The oil / gas ratio is calculated such that the maximum pressure is not exceeded at temperature.

Figure 6. Metallic bellow

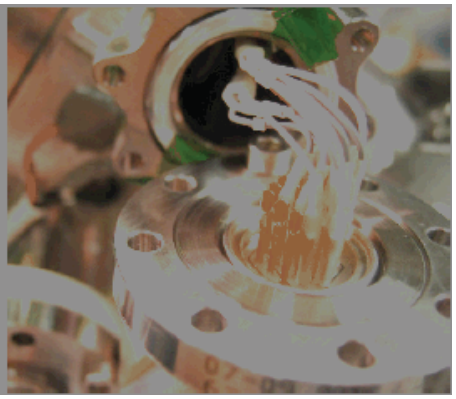

Figure 7. Hermetic connector

The oil is the same as the one used on the heritage Scan Drive Unit mechanism. It has the main characteristic to not have emulsions even in a moving bath. It can survive the radiation environment without degradation.

The screw of the spindle has a diameter of 12 mm. The spindle is composed of 7 rollers with a solid preload. The solid preload allows a reversibility limit higher than the elastic preload. The lubrication environment of the spindle has no effect on the reversibility limit. The main requirements to the supplier were the reversibility and the resistive torque.

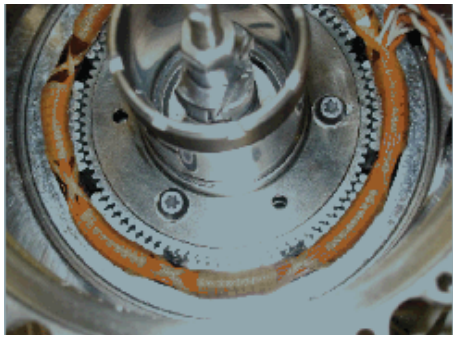

Figure 8. Stepper motor and roller screw assembly

The ball bearings are super duplex back-to-back mounted with a solid preload.

The main characteristics measured for this unit are:

- sealing: $<1.10^{-9}$ atm-cm^3/s under helium at 50000 Pa
- linear resolution of 0.0022 mm/step
- linear range: 24 mm
- Torque margin >3
- Maximum load capability = Reversibility load. (This is due to the duty cycle voltage command of the stepper motor)
- Qualification Temperature: [-50°C; +100°C], the drive unit temperature is maintained up to 10°C with its own thermal control.
- Vibration: 25g mounted in HR²A configuration
- Velocity: nominal 2.1 mm/mn, tested successfully up to 26 mm/mn
- Mass <2 kg

The linear drive unit has been fully qualified and six flight units are on one spacecraft.

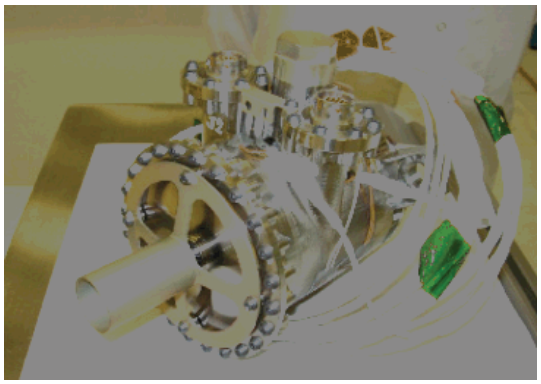

Figure 9. Stepper motor and roller screw assembly

Reducer unit

The reducing unit is a mechanism that transforms the linear movement of the drive unit to a rotational movement with accuracy and high stiffness, with an output range of 180° for deployment and ±1° for pointing. The output step resolution is 0.02° for the deployment and 0.002° for the pointing. In the range of pointing, the design of the mechanism is free of any tribological link to ensure a high cycle life time. There is no movement of ball bearings. The transformation of the translation in rotation is performed by metallic straps winding and unwinding on a pulley.

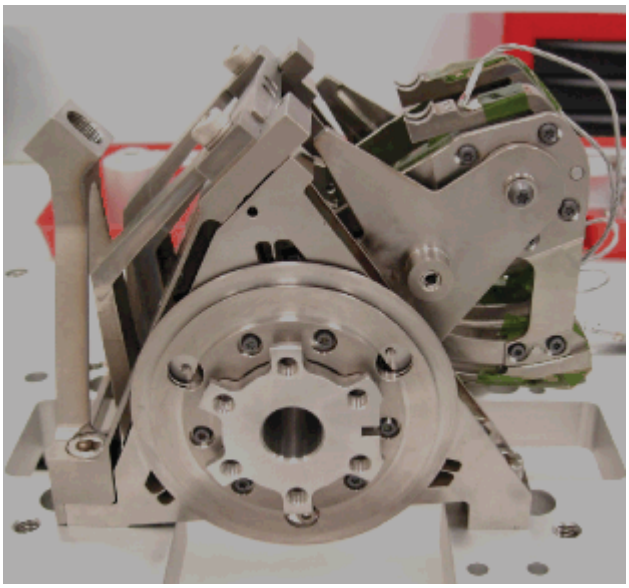

Figure 10. Reducer unit assembly

Design development and qualification plan

At linear drive unit level

This product was based on the heritage of the Scan Drive Unit mechanism. All the suppliers have been kept to reduce the risks with regard to the chemical environment of the oil and gas. But due to the re-packaging of the mechanism, all the supply units have been reduced in size. The main concern was the internal wiring of the mechanism. Indeed, the number of cables was more important than heritage number because there was no coarse potentiometer on the Scan Drive Unit. These cables had to be routed in a far more compact design compared to heritage. That is why a mock up of the linear drive unit in Plexiglas was built to verify the internal cable routing. This mock up allowed validation of the internal design of the drive unit.

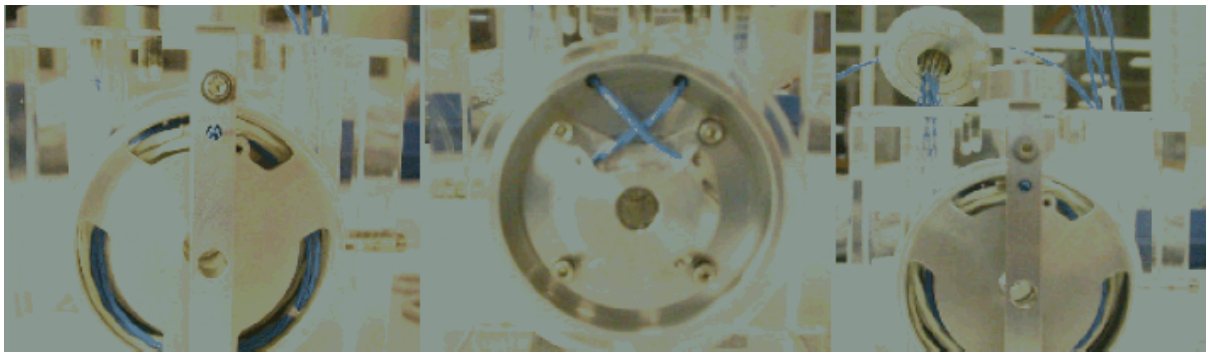

Figure 11. Mock up of the drive unit internal cabling

Once the QM was assembled and tested, six flight linear drive units were assembled in parallel and submitted to a complete acceptance test including functional and mechanical characterization tests (sealing, motorization margin, reversibility, motion range, max output load, power consumption…).

At reducer unit level

Due to very stringent planning constraints, the delivery schedule imposed from the start of the project forced production of the flight hardware in parallel of the QM model. It was therefore decided to verify the capability of the metallic straps and the free flex pivot new design to perform the number of cycles required at the earliest stage. Mock-ups were built to validate the design.

Metallic strap mock up

Strap design:
One of the issues with the strap design wais the resistance of the interface under strap load. Either the interface is held by friction, or is held by opposition. In the first case, we need to know the friction coefficient and the tension in the screw to guarantee the link. In the second case, we need only to verify the capability of the strap under peening and solicitation under clevis but we are limited by the thickness of the strap.

The first mock up test was to verify the threshold tension load for which the stiffness behavior of the metallic strap winding on a pulley is linear.

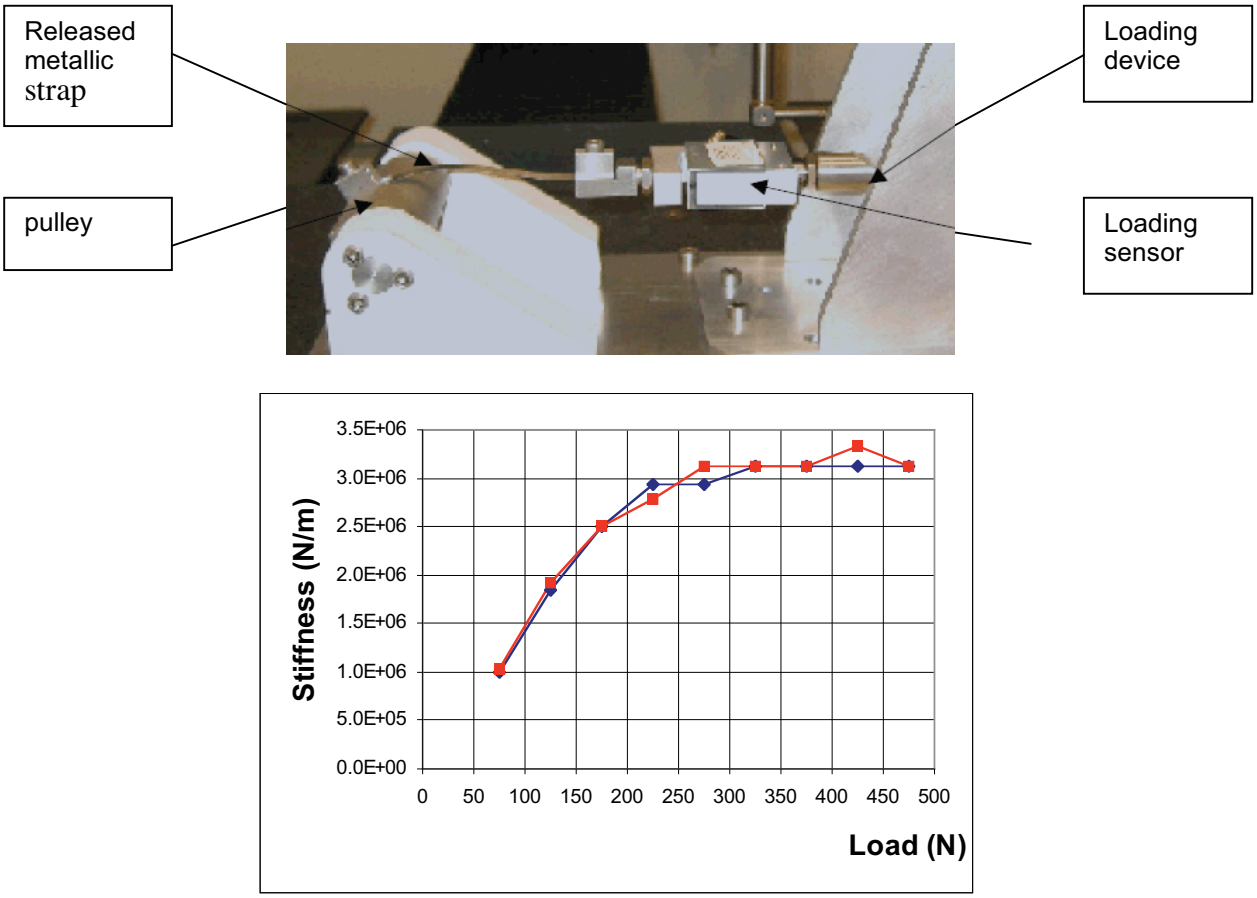

Figure 10. Metallic strap stiffness behavior

This test showed that the strap must be tightened to a minimum of 300 N to have linear behavior. This is due to the local bending around the output of the strap with the pulley.

The second mock up objective was to verify the capability of the strap in life time. During the life time, the straps wind and unwind locally on a pulley. So the strap sees constant stress due to tension and an oscillation stress due to the wind and unwind on the pulley.

Before and after life test, a dye penetrant test was performed on the strap to verify the non presence of crack.

Free flex pivot mock up

Due to the design, the behavior of the free flex under an imposed rotation is non linear. So we needed to verify by test the predicted behavior with regard to stiffness, the back torque and the buckling.

The first mock up consisted of three sample blades fully identical to the flight one to verify if the non linear model was good.

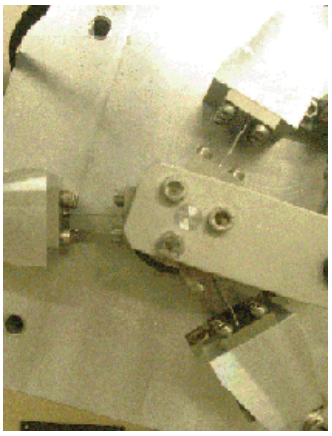

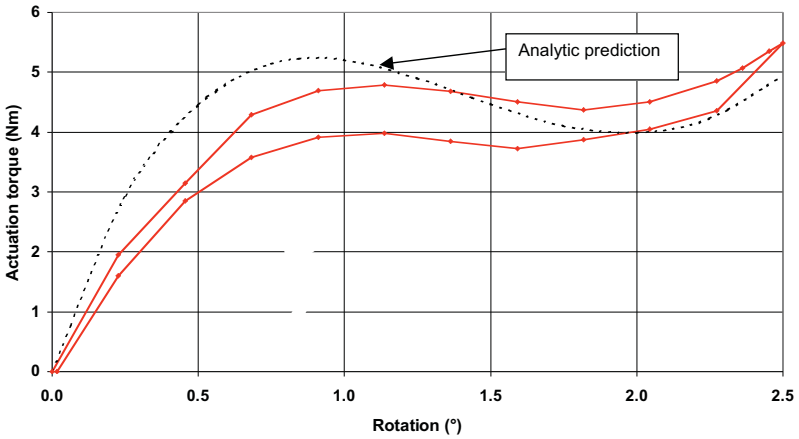

Figure 13. Free Flex mock up 1

Figure 14. Free flex stiffness behavior correlation

The second mock up consisted of a free flex fully representative of the flight one. The objective of this test was to verify the limit of buckling of this design when it was submitted to a bending moment. For this, the free flex was equipped with a strain gauge all along both sides of the three blades. The test is performed in imposed displacement and the buckling is detected when the strain gauge signal becomes non linear.

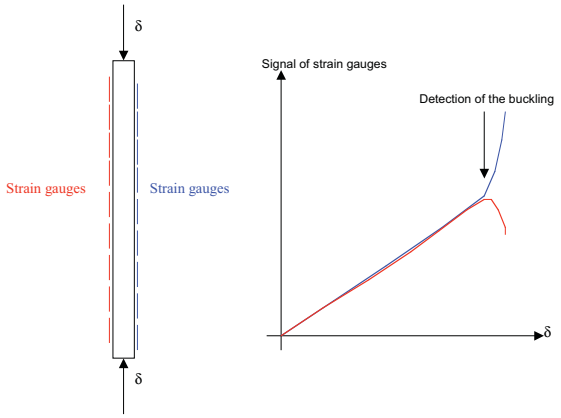

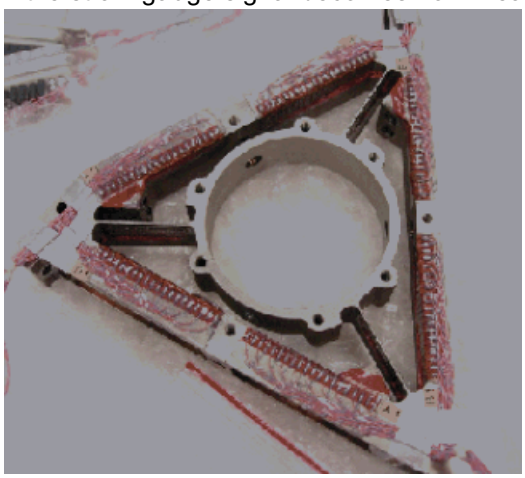

Figure 15. Detection of the free flex buckling

Figure 16. Free flex equipped with strain gauges

The results obtained confirm the prediction.

At HR²A level

The objective of the development was to qualify the MADPM with only one HR²A. That is why the following test plan has been performed with some particularity for the vibration and shock test.

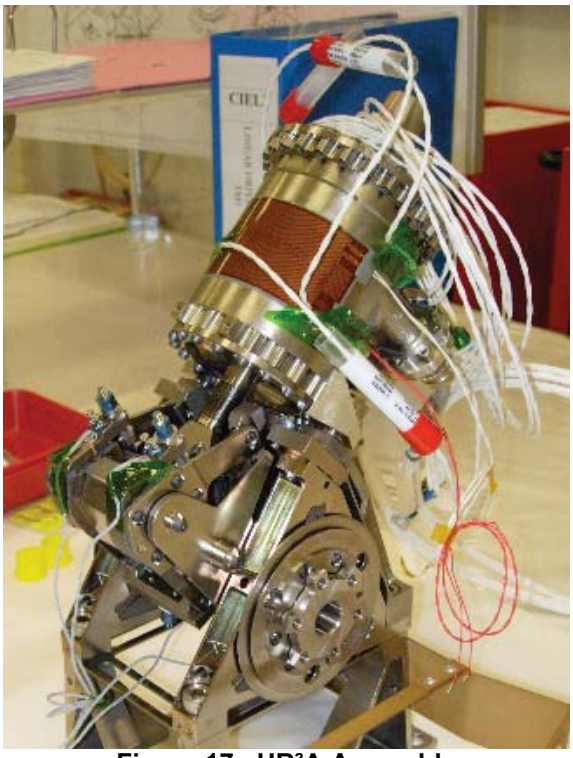

Figure 17. HR²A Assembly

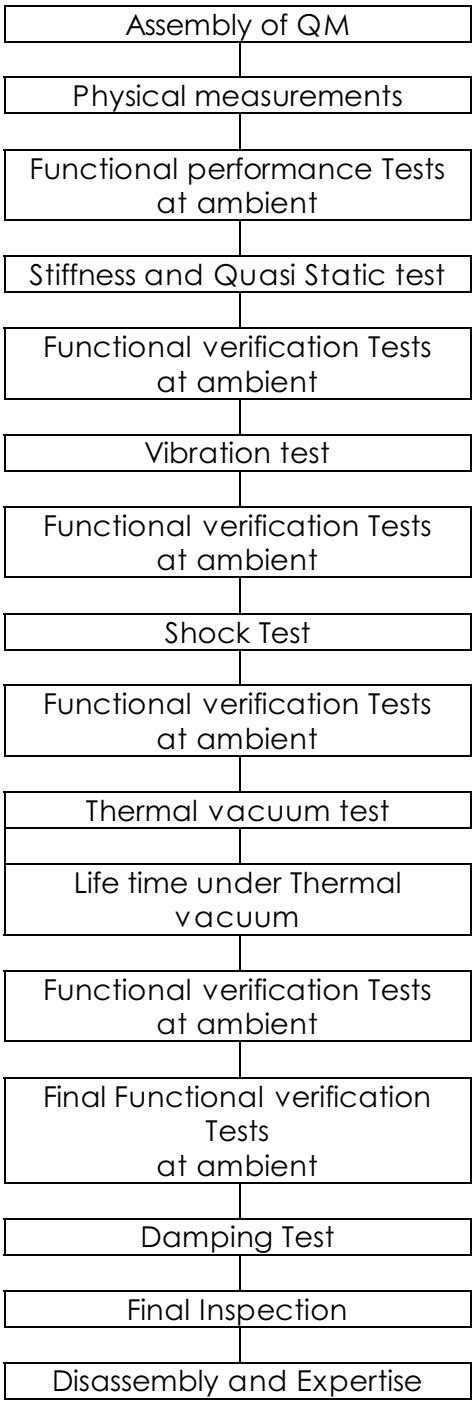

Vibration and shock test

The HR²A was tested in vibration in three configurations. The first configuration corresponded to the HR²A in position 1 on the MADPM and loaded by the HR²A in position 2. The HR²A in position 2 was simulated by a dummy mass representative in mass, Cdg position and inertia. This dummy mass was connected to the test support thanks to a tool representing the reflector arm stiffness.

The second configuration corresponded to the HR²A in position 2 on the MADPM. In this configuration, the HR²A QM was submitted to the envelope level of the configuration one and the level seen by the interface of the dummy mass of the first configuration.

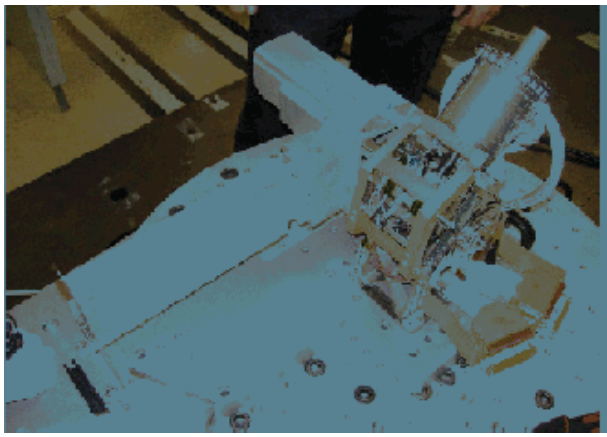

Figure 18. First vibration configuration test

Figure 19. Second vibration configuration test

The third configuration corresponds to the HR²A vibration configuration of the complete flight model. In this configuration, the HR²A QM only saw low level sine. This allowed a comparison of the flight model behavior with the qualification model. This configuration is close to the first one with no spacecraft bracket.

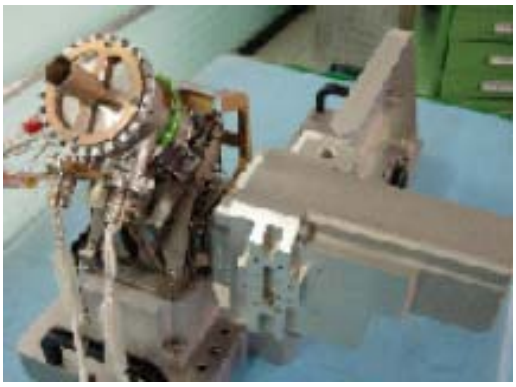

Figure 20. Third vibration configuration test

At MADPM level

In order to deploy and then point around two axes, two HR²A are mounted together in a gimbal configuration to form the MADPM; the layout is the presented in Figure 21. Figure 22 shows the MADPM (Multimedia Antenna Deployment and Pointing Mechanism) assembly and on the spacecraft (3 flight unit on the same spacecraft)

Figure 21. MADPM without and with MLI

Figure 22. Three MADPM on the same spacecraft

Lessons Learned

One of the main challenges was to develop a new mechanism and deliver flight hardware in 24 months. The design of the HR2A is far from the heritage design. The first lesson learned was that the schedule challenge was made possible only because technologies involved in the design concept were well assessed before the development (blades, straps, oil bath, sealing).

The second lesson learned concerns the suppliers. Major design evolutions compared to the heritage were analyzed deeply and led to no surprise for this development. Due to the size reduction needed, some components were slightly modified. Suppliers were kept unchanged compared to the heritage for all components. New requirements ended up being not well taken into account due to lack of close communication and reviews with the suppliers.

The third lesson learned concerns the way to manage FM hardware integration in parallel to QM assembly and testing. A QM is a first model and always needs some adjustments. It was decided to tackle the FM deadline with two rules:

- allow assembly or test step on FMs only when the QM operation step had been performed and return of experience well taken into account
- the engineering manager is part of the production tiger team and work in the clean room on both QM and FM models

The bet was that even though the QM planning was drifting due to first adjustment needed, the FM delivery date would be kept by having clear production file and learning experience of the operators. It was challenging not to delay some QM testing in order to deliver the flight models more quickly.

The fourth lesson learned concerns the difficulty of comprehension of the design (detailed kinematics, consequences of failure modes …). To help the understanding, we built a Plexiglas mock up. Thanks to this mock up, most of the points raised were more easily addressed. This mock up helped to understand and solve the difficulties met during integration. It also eased the communication with the final customer during design reviews.

Implications of Underdamped Stepper Mechanism Performance and Damping Solution Methodology

Shane Brown* and Scott Starin*

Abstract

When driving a stepper motor the control method of stepping the motor has a significant impact on the performance of the mechanism. When driving a stepper motor system with unipolar or wave method of control, the back-emf generated in the open, unregulated coil creates a stepper motor system that provides significantly less inherent damping compared to full bipolar control. Less damping results in higher overshoot, ringing, and potentially exciting mechanical resonances resulting in fatigue. In addition, a significantly underdamped system, particularly with significant load inertia, raises many concerns with mechanism life and performance. The mechanism described herein utilizes a Rotary Accelerometer (RA) for step counting as well as state-of-health monitoring [1]. Another consequence of an underdamped mechanism using accelerometers is that the RA data is of limited or no value, due to high overshoot acceleration. This paper presents a proven design approach to damp a stepper motor driven in a unipolar, wave fashion, or a system with significant inertia mismatch between the motor and the reflected load.

Introduction

Ball Aerospace & Technologies Corp. (BATC) is involved in a proprietary space vehicle application that has several mechanisms. One of the mission critical applications is a single degree of freedom mechanism consisting of a geared stepper motor actuator coupled to a balanced load inertia, to be referred to here after as the mechanism. The load of the mechanism must be controlled to precision interval locations and have full 360° of operation (no hard stops). A geared stepper motor was selected because of the precision response, simple controls, and proven heritage and reliability.

For various reasons, a three-phase stepper motor with an integral Rotary Accelerometer (RA) was selected for the actuator. We believed the mechanism was simple enough that an Engineering Development Unit (EDU) was not required. However, for calibration of the control electronics, a representative EDU mechanism was produced simultaneously with the flight hardware. During the electronics calibration procedure anomalous performance of the mechanism was observed, resulting in the inability of the control electronics to process the RA feedback signal as originally intended. We believed the erratic performance of the mechanism was a mechanical reliability concern, due to significant overshoot, operational resonance and mechanical ringing.

This paper details the troubleshooting, analysis and test simulation process, as well as the ultimate course of action taken to resolve the performance issue. We also detail the implications of the stepper motor drive control methods and the effects they have on mechanism performance. In addition, we detail the requirements for interfacing with, and signal processing of, the RA signal for step verification. Time was critical in the decision making and rework process because flight hardware was received, and all viable solution options required an in-process modification to the flight hardware. Because of these schedule needs, several solutions that would have been plausible for the initial design phase, were no longer viable, and are not fully discussed in this paper.

The Mechanism

Mechanical Description

* Ball Aerospace & Technologies Corp., Boulder CO

The mechanism drive system consists of a three-phase stepper motor with an integral RA and gear-head with a 96:1 gear ratio (N). The gear-motor is coupled to a drive shaft with a flexible coupling. Both the motor and the drive shaft are secured to the flexible coupling with match-drilled pins. A preloaded, separated bearing pair supports the drive shaft; and the drive shaft in turn supports the balanced load inertia. Because the load is balanced, the detent torque of the stepper motor is sufficient to hold the load in place during launch and no launch lock is necessary. Figure 1 shows a schematic of the drive system.

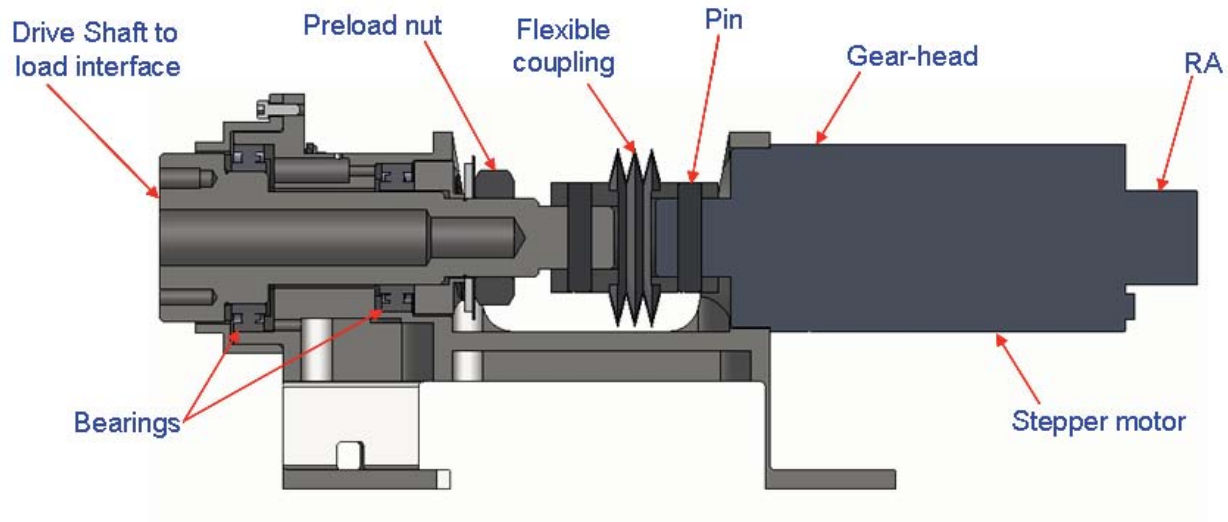

Figure 1. The Drive

The total mass of the suspended load is 1.36 kg and the mass moment of inertia of this rotating load (J_L) is 0.027 kg•m^2. When reflected through the gear-head, the load inertia (J_{LM}) [3] is:

$$J_{LM} = (J_L) / N^2 = (0.027 \text{ kg•m}^2) / 96^2 = 2.9 \text{ X } 10^{-6} \text{ kg•m}^2 \text{.....(1)}$$

The mass moment of inertia of the 3.8-cm (1.5-inch) diameter stepper motor (J_M) is 2.8 X 10^{-5} kg•m^2. The inertia factor (J_F) [3] is defined as:

$$J_F = (J_M + J_{LM}) / J_M \text{.....(2)}$$

For this system the inertia factor is 2.64. A good rule of thumb is that the inertia factor of a stepper motor system should be less than three. Additionally, torque margin was calculated to be 126% using a factor of 3 for all friction values, meeting the MIL-A-83577 requirement of 125% for mechanism at their Critical Design Review. Analysis indicated a functional design.

Position Knowledge

Several options were considered to provide rotational feedback of the mechanism, including contacting and non-contacting switches, encoders, potentiometers and RAs. Contacting switches were ruled out because they are inherently limited life items, while encoders and potentiometers were eliminated because of their relatively large size. The RA was selected over the non-contacting switches, such as Hall Effect sensors, because the RA was easier to mechanically integrate to the system since it is integral to the motor, requires fewer lead wires, has higher reliability numbers, higher positional knowledge and is easier for software to implement.

The RA provides the added feature of monitoring the heath of the drive system. If the peak acceleration decreases, the drive is degrading; and this knowledge can enable the operations team to modify their use of an on orbit mechanism before it fails. A technical disadvantage of using a RA for feedback is that it derives position of the motor shaft, not the output of the gear-head shaft. As a result the accuracy of the position feedback provided by the RA is limited by the backlash of the gear-head, which for our application was sufficient for positional knowledge. There is also a procurement disadvantage, as the technology is patented by CDA InterCorp, and thus is only available from one supplier. There are other

suppliers with acceleration feedback technology, but they require DC excitation, which results in additional power loss and performance variation with supply voltage fluctuations.

EDU Performance

The EDU was necessary for calibrating and determining the gains in the electronics to determine proper step verification. More on this process will be discussed later in the paper. The Responsible Engineer for the control electronics observed the proper direction of rotation and displacement for stepping the actuator, however, the observed output of the RA showed significant overshoot and ringing of the stepper motor. Figure 2 shows the RA output from a single step of this development unit.

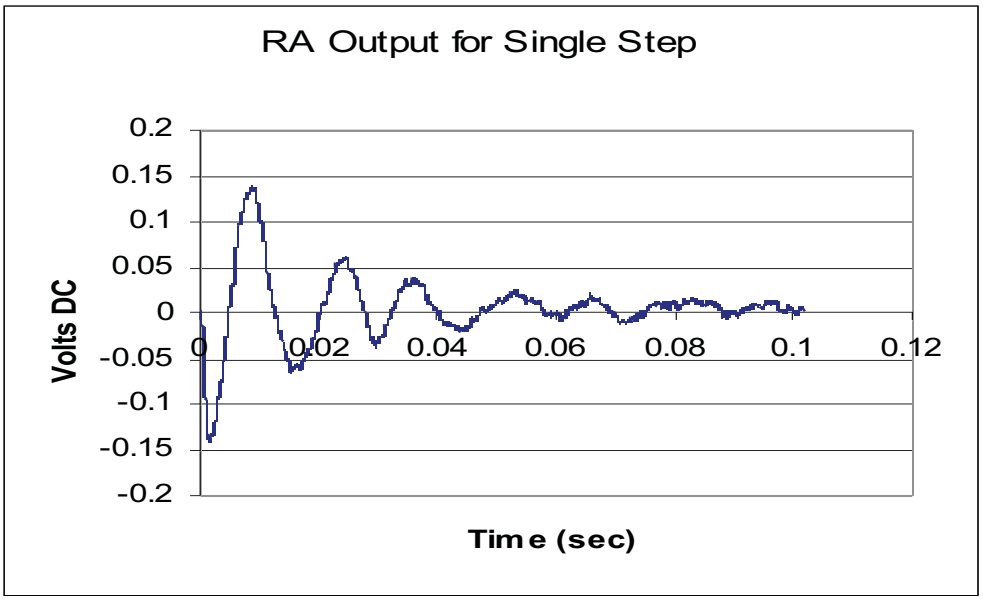

Figure 2. Oscilloscope Output of the Underdamped EDU Mechanism

This plot of data captured with an oscilloscope shows the significant overshoot and ringing of the mechanism. Figure 3 shows the RA output of 6 steps being driven at the operational pulse rate of 26 Pulses Per Second (PPS).

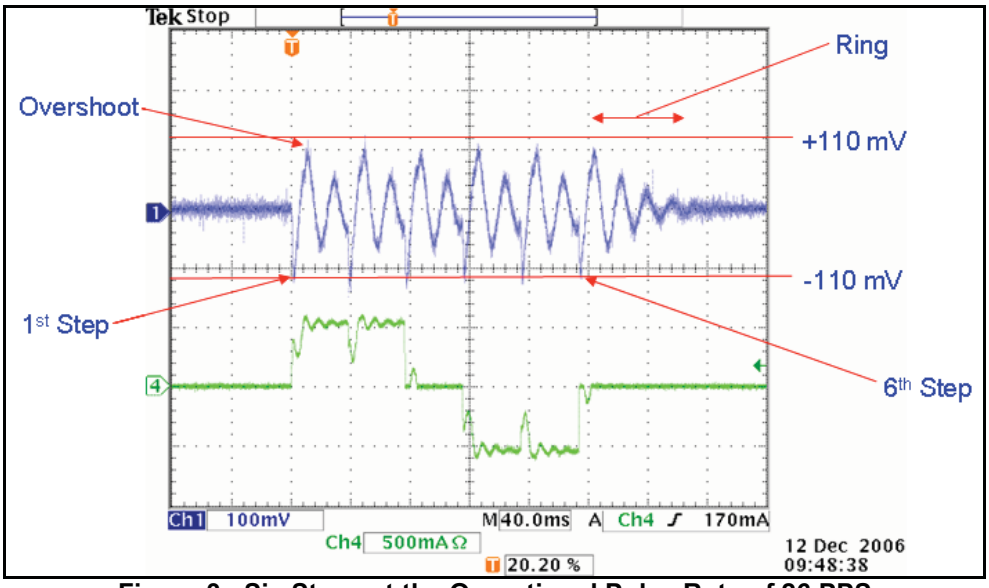

Figure 3. Six Steps at the Operational Pulse Rate of 26 PPS

This oscilloscope trace shows that the motion of the mechanism was erratic and significantly underdamped. The ringing was both audible and visible in the lab, raising the concern that loads might be high enough to cause a premature mechanical failure of the drive. The specific concerns of the team centered on if a resonance was excited a bearing retainer could fail, or the gears could micro-pit due to the vibration and reversing. Also problematic in this performance was that the overshoot acceleration voltage was nearly equal to the primary step voltage. Our "Original Transition Voltage Counting" method yielded false positional information as the threshold voltage is realized at the primary step as well as the overshoot. The processed logic would falsely determine the motor was simply stepping back-and-forth between two pulses. (Original Transition Voltage Counting is described in the later section Processing the Rotary Accelerometer Signal.)

Investigation of the Problem

Engineering Review Board Process

Due to schedule constraints, EDU testing and flight assembly occurred concurrently. By the time, the EDU testing showed that the designed method for step verification did not work as intended, the flight stepper motor had already been received, almost all of the mechanisms piece parts had been completed and the flight electronics were in fabrication. Re-work of flight hardware was going to be required to solve this problem, thus an Engineering Review Board (ERB) was convened to determine the best system solution for the program. The first step in the ERB process was to brainstorm every possible root cause. Figure 4 shows the fishbone diagram developed by the ERB team as a result of this brainstorming effort.

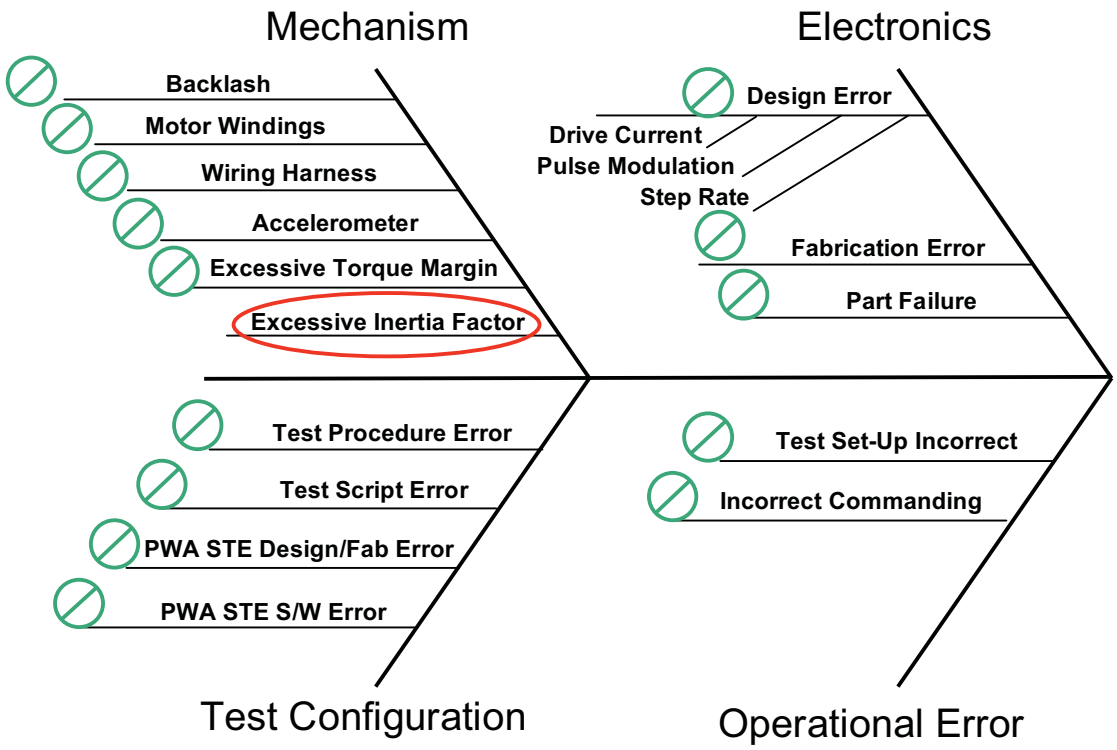

Figure 4. ERB Fishbone Diagram

An audit of the EDU electronics and Special Test Equipment's documentation and certification logs determined the electronics were built to print and certified. Review of the test procedure and set-up eliminated the test procedure and operator error. Review of test data supplied by the motor supplier eliminated backlash, motor windings and the accelerometer. A pin-to-pin test of the wire harness verified its manufacture. Torque margin of the EDU was measured using the RA to be greater than 400%, however, when a reduced voltage was applied to the EDU the system still exhibited significantly underdamped actuation. Therefore, excessive torque margin was eliminated. While the inertial factor of 2.64 was below the desired value of three, because the rotating mass was so large, at 1.36 kg, the initial determination of the ERB was that the system was under-damped because the inertia factor was too high, and the trade table of solutions for this problem was created.

A Note On Torque Margin

Torque margin is measured using an RA by increasing the load friction until the drive begins to miss steps; the ratio between the nominal RA output and the RA output when a step is missed is the torque margin [1]. For the measurements made using the EDU, the load inertia was increased by applying hand pressure to the rotating load, and an operational torque margin of greater than 400% was measured. The calculated torque margin at CDR was estimated to be 126%. This large discrepancy between the calculated and actual margins is a result of performance projection without hardware to empirically test our CDR analysis. Standards require the assumption of worst case gear-head efficiency, motor detent torque, and most significantly a factor of safety on all friction values. This is sufficient justification for using EDUs early in a system's development. Actual torque margin measurements can be made, potentially enabling the use of a smaller stepper motor or increasing efficiency by reducing power consumption.

Troubleshooting and Root Cause Determination

Table 1 below delineates the trades considered for solving the excessive inertia factor problem. We sought the most technically robust solution that minimized cost and schedule impacts to the program. The trades were complicated by the fact that both flight and EDU hardware were in house, and any change to the mechanical configuration required an in-process change to existing hardware.

Table 1. Trade Consideration Table

Area	Modification	Advantages	Disadvantages
Electrical	Use RA to produce contour current.	No change to mechanism. Lowest risk option.	Significant changes to electronics to add compensation network.
Electrical	Increase or decrease step rate to optimize stepping characteristic.	No change to mechanism, "only" FPGA modification.	Does not solve mechanical resonance problem.
Electrical	Contour pulse waveform to attenuate acceleration (Miller effect)	No change to mechanism.	Significant power loss increase, minimal performance advantage.
Electrical	Modify pulse verification logic to ignore overshoot pulse.	No change to mechanism, "only" FPGA modification.	Does not solve mechanical resonance problem.
Electrical	Short Redundant windings while primary is operated (and vice versa)	Minor electronics change	If relays or open winding failure underdamped situation would persist.
Electrical	Add delta configuration load resistors across bridge to provide inherent damping.	No change to mechanism.	Board layout modification required to accommodate large power resistors. Increase in power loss on board.
Mechanical	Increase gear ratio (N) to minimize Inertia Factor	Not many.	Modify mechanism hardware and electronics FPGAs. System velocity requirements could not tolerate slower operation.
Mechanical	Reduce load inertia to minimize Inertia Factor	No change to electronics or software	Significant modification to mechanism with minimal performance benefits.
Mechanical	Modify winding configuration to Delta.	No change to electronics or software	Requires in-process upgrade of EDU and Flight hardware. If motor winding opens, damping benefit lost.
Mechanical	Add Shorted Coils in Motor to approach critical damping	No change to electronics or software	Requires in-process upgrade of EDU and Flight hardware

The first three mechanical solutions were quickly eliminated because the change would violate other operational requirements. Using the RA contour current was also quickly removed from the trade space because of the significant changes required to the electronics. This method uses the motor peak acceleration to attenuate the supply voltage or current [5]. While this is the “elegant” solution, and the circuitry is relatively simple, a modification to the board layout and the additional tuning required was schedule prohibitive. The best solution, from a cost and schedule standpoint, was changing the step rate to optimize stepping characteristics, so this was tested first.

Decreasing the pulse rate did not change the overall performance of the system, and was thus eliminated, but increasing the pulse rate did yield some interesting results. It was found that the system did have a “sweet spot” at half the resonance of the ringing, approximately 64 Hz. If the system was driven at 64 PPS, each subsequent step coupled with the bounce of the previous step (see Figure 5). However, this solution was eliminated for two reasons: First, it would require a late modification of the flight FPGA once the flight mechanism had been built and its resonance determined; second, the difference between the peak voltage of the first step and the subsequent overshoots was too small. The threshold voltage is determined by a resistor, and as this resistor drifts due to temperature changes and/or end of life degradation the threshold voltage will drift accordingly. Our analysis showed that we needed a much greater delta between the peaks of the pulse and the overshoot.

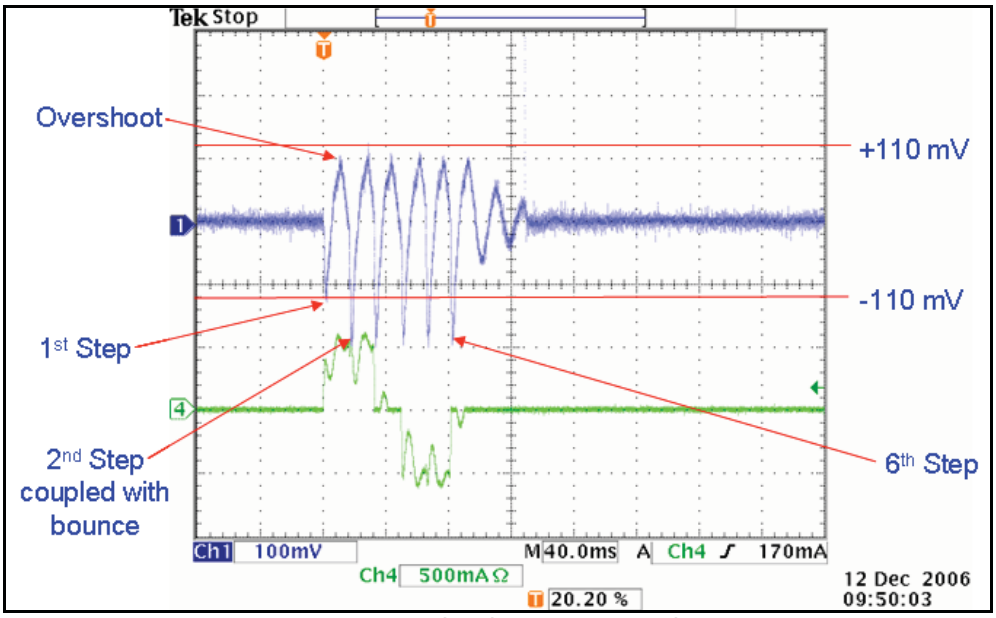

Figure 5. Six Steps at 64 PPS

Another interesting result was that when the system was driven faster than half the resonance of the ringing the amplitude of the acceleration of the second step decreased (see Figure 6). This behavior was consistent for all rates greater than 64 PPS. Finally, if the system was driven at any rate between the operational pulse rate of 26 PPS and the sweet spot of 64 PPS, the only change was that there were fewer bounces the closer the rate got to 64 PPS.

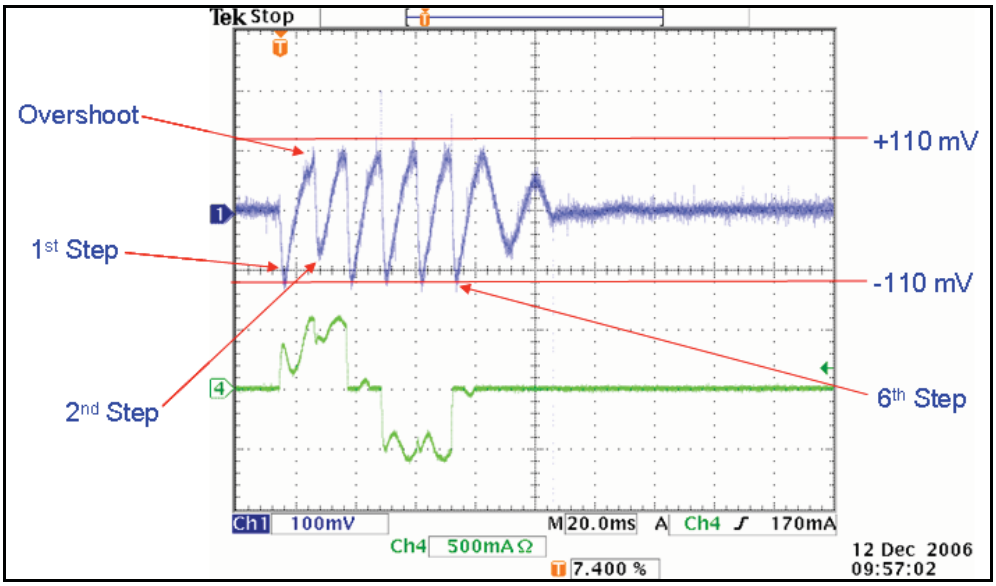

Figure 6. Six Steps at 92 PPS

The next best, solution from a cost and schedule standpoint, was minor modification of the electronics, therefore our testing moved onto shaping the pulse to reduce the acceleration. One of the modifications tested was to add large capacitors to the drive circuitry to “soften” the edges of the voltage pulses. This technique is known as the “Miller Effect”. Several one µF capacitors were added, and while there was some benefit to the mechanical resonance, the underdamped situation still persisted. Also power losses on the electronics board increased, and there was no “real estate” on the board to add the sizable capacitors. Therefore, this option was eliminated. This, and other methods, did reduce the audible noise

of the system, but all still resulted in insufficient difference between the pulse and overshoot signals of the RA, and we still had a concern about mechanism fatigue.

The final step of testing was to run the drive with the load inertia removed. When this was done, there was no change in the performance of the system. This was the "Ah-ha!" moment of our testing. Our initial most probable root cause was incorrect, for if the system had an excessive inertia factor, removing the load inertia would have solved the problem. We now realized that we had an underdamped stepper motor system and believed our wave drive method was the root cause. To validate our new root cause we shorted the redundant winding of the EDU by tying the three redundant lead wires together. With the shorted windings we now had the critically damped system that we had originally expected based on component level testing of the stepper motor by the supplier. While we had known that the supplier had performed their component level testing of the stepper motor using a bi-polar driver, we had not understood the implications of our different drive methods. (Wave and bi-polar drive methods are described in the later section Method of Three-Phase Control.)

Homing in on the Solution

Three methods of damping the system were evaluated. The first was modifying the electronics to short the redundant side windings when driving with the primary side and to short the primary side windings when driving with the redundant side. The system requirement that the mechanism be one fault tolerant eliminated this solution. If one of the primary windings failed open, causing the system to switch to the redundant side, the damaged primary windings would be unable to provide the required damping.

The second was adding delta configuration load resistors across the bridge to provide damping. This method was ruled out because it required a new layout of the printed wire assembly to accommodate the large load resistors. The added power loss on the board was also a disadvantage. However, empirical testing of various load resistors across the redundant winding allowed us to determine the magnitude of damping desired to achieve adequate damping and robust step counting.

This left us with our final option, developing a new motor with additional shorted coils that would act as an integral eddy current damper. This solution had the advantage of being transparent to the electronics, but it did have significant cost and schedule ramifications for the mechanism. Schedule issues were alleviated by changing the assembly sequence of the mechanism. Communication provided by the ERB process kept program management and effected disciplines informed and participating in the decision making process. Cost impacts were understood and accepted.

The Solution

Calculated Solution

Once we decided to incorporate the internal damping via redundant shorted coils, we needed to revise the motor torque constant and determine the requirements for the shorted damping coils. From EDU actuator torque margin testing with the RA, we determined we could reduce the motor torque by 50% and still be well above the 100% torque margin required for flight hardware by MIL-A-83577. From the shorted load resistor testing conducted, we determined that the mechanism required at least 15% of a fully shorted winding to provide enough damping for reliable stepping and robust RA signal processing.

The EDU motor had the following performance criteria for primary and redundant:

- Motor Torque Constant (Kt) = 0.205 Nm/Amp
- Winding Resistance (Ω) = 40 Ohms
- Motor Constant (Km) = 0.0324 Nm/$\sqrt{}$watt
- Holding Torque at Minimum Voltage (Th) = 0.092 Nm
- Damping Rate with fully shorted redundant windings (Bm) = 1.048 X 10^{-3} Nm-sec/rad

One of the many advantages of working in SI units is the simple determination of the damping rate of a motor with shorted coils. The damping rate is equal to the motor constant, squared, if units are Nm/$\sqrt{}$watt (Bm = Km^2) [2]. This first order relationship is applicable for shorted alternator analysis. The equation

becomes more complicated at high velocities, but for applications where the rotor velocity is below 200 rad/sec, this relationship is valid.

$$Bm \approx Km^2 \quad \ldots\ldots(3)$$

Armed with this information, we calculated what winding modifications were required to achieve reduced holding torque and increased damping, by adding a separate set of shorted windings. The reduction of one gage of magnet wire reduces the volume of the turns and increases DC Resistance by 26%. Since we wanted to reduce torque constant as well, we needed to reduce the number of turns into the motor phases. A straight reduction in turns will reduce the torque constant by the same percentage. Table 2 describes the original EDU performance (EDU#1) and our desired "New" motor performance.

Table 2. Motor Design Characteristics Comparison

Parameter	Units	EDU#1 (Baseline)	"New" Motor (EDU#2 & Flight)	Comment
Torque Constant	Nm/Amp	0.205	0.164	20% reduction in number of turns = 20% reduction in torque constant
Turns Reference	Reference	100%	80%	
Winding Resistance	Ohms	40	45	Use magnet wire size 1.5 AWG finer than baseline
Percentage Pack for power windings	Reference	100%	57%	20% less turns, and 1.5 gage finer wire ($100 \bullet 0.8 \bullet 1.26^{-1.5}$)
Motor Constant	Nm/√watt	0.0324	0.0244	Kt / √R
Holding Torque at 18 VDC	Nm	0.092	0.066	~30% reduction in torque desirable.
Stall Power at 35 VDC	Watts	30.6	27.2	~10% reduction in power

Reducing the power winding pack (slot fill percentage) to 57% of EDU#1, allows us to use up to 43% of the slot area as shorted coil damping windings. Table 3 compares the shorted coil requirements and performance to the power winding for EDU#2 and Flight versions.

Table 3. EDU#2 & Flight Motor Performance Relative to EDU#1

Parameter	Units	Power Winding	Shorted Coil	Comment
Turns Reference (Percentage of EDU#1 turns)	Reference	80%	80%	Use same percentage of turns on shorted coils as primary power. **Note:** This is not a requirement.
Resistance	Ohms	45	63	1.5 wire sizes finer than the power winding ($45 \bullet 1.26^{1.5}$)
Motor Constant	Nm/√watt	0.0244	0.02066 (Ref)	Reference only, used to calculate damping rate
Shorted Coil Damping Rate	Nm-sec/rad	N/A	4.27×10^{-4}	Two sets of damping coils working together
Percentage Pack of EDU#1 Slot Fill	Reference	57%	40%	Providing an overall slot fill of 97% with respect to EDU#1

All of our desired characteristics are met with this scenario. The torque margin reduces from 400% to 214% with the new proposed motor, and the damping rate with the shorted coils is 40% of a fully shorted redundant winding. If there is a failure of one set of coils, the damping rate will be 20% of a fully shorted winding set, still within our desired requirements, so our new motor is one fault tolerant. Since we have sufficient of torque margin, we wanted to add as much damping as possible.

In order to simulate the "New" motor performance, we conducted a test with our EDU test set. We set the supply voltage down to 12.6V to simulate the new motor at 18V, our minimum voltage, and we added shorting resistors across the redundant winding to simulate the magnitude of damping of the "New" motor's shorted windings. Figure 7 shows a scope trace of our test set simulation. This plot shows significant difference between the primary pulse RA signal and the overshoot. Additionally, the mechanical performance of the system was adequately damped and torque margins were exactly as predicted from the previous analysis.

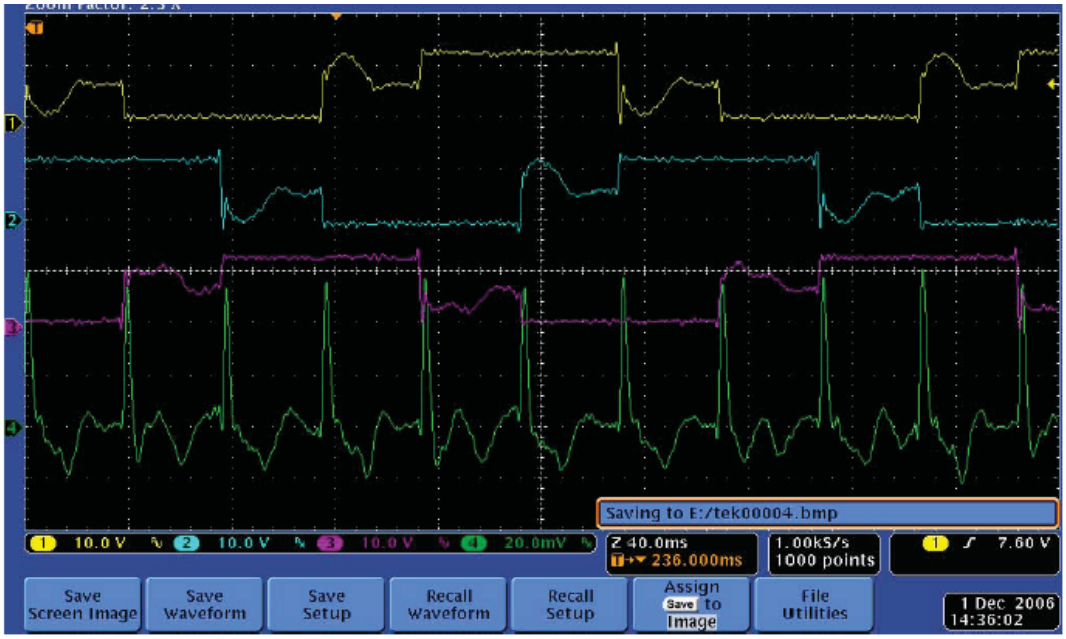

Figure 7. Performance Simulation of the Stepper Motor with Integral Eddy Current Damper

Step Performance Simulation

Stepper motors perform like classical underdamped second order systems. It is a straightforward procedure to analyze the RA output to determine the step kinematics of a mechanism by varying the Damping Ratio (ζ) and time factor ($\Delta\tau$) of classical second order response equations. This allows us to correlate actual performance to theoretical step performance.

Motor position (θm) of a second order response system may be simulated from the following equation [4]:

$$\theta m_t = \mathrm{E}\left[1 - \frac{e^{-\zeta \bullet t}}{\beta} \bullet \sin(\beta t + \phi)\right] \quad \text{.....(4)}$$

Where:

- θm_t = Motor Position at time "t" in radians
- E = Step Angle in radians
- ζ = Damping Ratio (dimensionless $0<\zeta<1$)

$$\beta = \sqrt{1-\zeta^2} \quad \text{.....(5)}$$

$$\phi = \cos^{-1}(\zeta) \quad \text{.....(6)}$$

$$\psi = \tan^{-1}\left(\frac{\zeta}{\sqrt{1-\zeta^2}}\right) \quad \text{.....(7)}$$

Equation 4 is a time-normalized equation. You may establish a new time base by varying a "time factor" ($\Delta\tau$). Simply vary the time base of the simulation to achieve an equivalent crossover time as observed from the empirical data. You may then calculate the velocity (ω) by taking the derivative of position with respect to time ($d\theta/dt$), and the acceleration by taking the derivative of velocity with respect to time ($d\omega/dt$). Then vary ζ and $\Delta\tau$ in a spreadsheet until your model matches the observed acceleration data from the RA. From this process, you have detailed kinematical position, velocity and acceleration information of the mechanism simply by matching the model to the observed acceleration signals.

Referring back to Figure 2, the oscilloscope output of EDU#1 for a single step of the mechanism with load inertia, in order to simulate the performance, we used the equations above to match the overshoot and settling characteristics. Figure 8, is our simulation with the damping ratio and time factor noted.

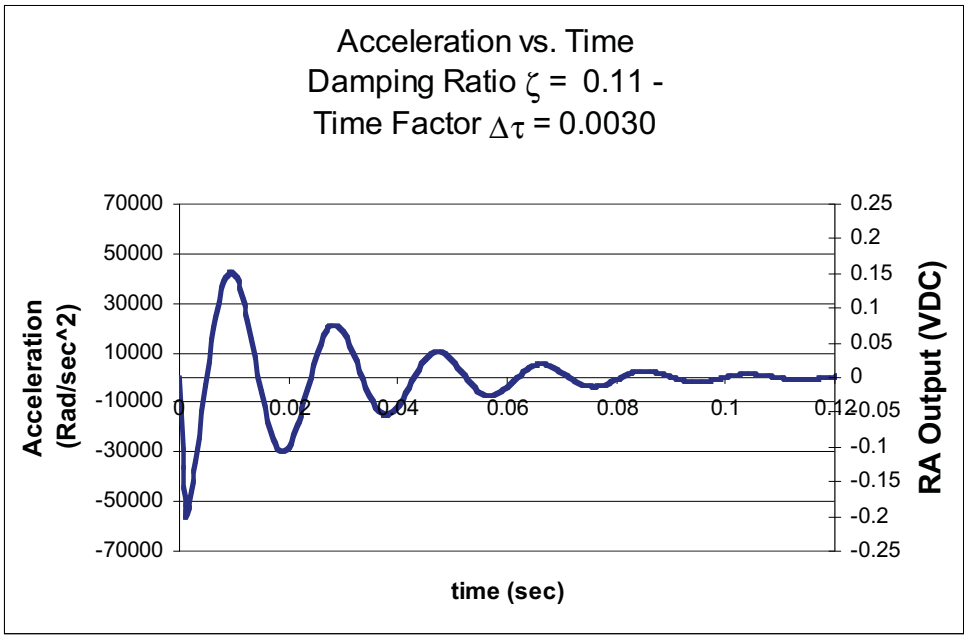

Figure 8. Simulation of EDU#1 Acceleration Profile

EDU / Flight Modifications

The elegance of this design change was that it was transparent to the rest of the system, both mechanical and electrical. The new motor had the same electrical interface and would be controlled as originally planned. The new motor had the same mechanical interface, the same envelope and would meet our torque margin requirements. Additionally, in order to minimize both the cost of and the time to fabricate the new flight motors, the existing flight motors' gear-heads were reused. The performance of the motor supplier, CDA InterCorp, during this re-build effort was extraordinary: delivering two flight motors only eight weeks after the contract was signed. The total time from discovery of the problem until the new motors were received was just under five months. Because other parts of the assembly were able to proceed in parallel, the actual schedule delay to the mechanism was only two months. The program was able to plan accordingly and there was no impact to the overall system schedule.

Modified Actuator Performance

The modified actuators with integral eddy current damping performed better than expected. The magnitude of the acceleration, measured torque and inherently damped characteristics were as predicted, or better than predictions. The scope shot in Figure 9 shows the motor phase voltages along

with the new mechanism acceleration profile, with the internal damping. Notice how the RA signal shows a distinct pulse per step with minimal overshoot providing desired monitoring characteristics. Robust acceleration characteristics, minimal overshoot and consistent performance highlights the improved mechanism. This scope trace was taken at nominal voltage (+24VDC) and pulse rate. The acceleration signal is raw and unfiltered. The difference between the overshoot pulse and the first transient pulse is a robust 400%, making the step counting reliable and consistent. Most importantly, the stepping characteristic was smooth, quiet and dependable. The erratic motion and audible rattle was no longer present.

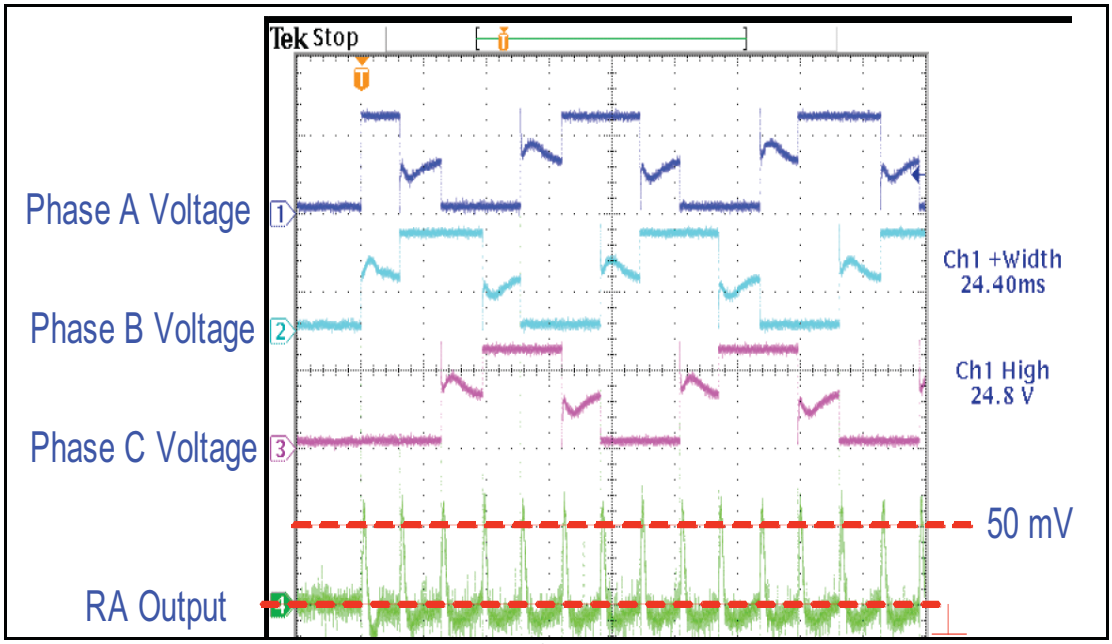

Figure 9. Flight Actuator Performance with Internal Damping

Table 4 delineates the difference in performance between the original, EDU#1, and the new, EDU#2 and Flight, units. From our kinematical analysis, we detail the differences in performance from our initial EDU#1 and "final" configuration. Most notable in the differences in performance, are the reduction in Peak Positional Overshoot, which reduced by 47%, and the Peak Velocity Overshoot, which reduced from -113 rad/sec (-1079 RPM), down to -22 rad/sec (-210 RPM). Since the kinetic energy varies with the square of the velocity, the Overshoot Velocity Kinetic Energy was reduced by an astonishing 96%.

Table 4. Motor Performance Comparison

Parameter	Units	EDU#1	EDU#2 and Flight	Comment
Power (Max)	Watts	29	25.6	At Maximum Voltage (34VDC), Lower = Better
Torque Margin	%	>400%	>200%	At Minimum Voltage (18VDC) Higher not necessarily better
Peak Positional Overshoot	**%**	**72%**	**25%**	**At Maximum Voltage (34VDC), Lower = Better**
Peak Velocity at Motor (during step transient)	rad/sec	161	108	At Maximum Voltage (34VDC), Lower = Better
Peak Velocity Overshoot at Motor	**rad/Sec**	**-113**	**-22**	**Kinetic Energy at Velocity Overshoot Reduced by 96%**

Reaction Torque at Load During Peak Acceleration	Nm	13.4	9.6	At Maximum Voltage (34VDC), Lower = Better

Drive Methods and Control Electronics

Method of Three-Phase Control

We decided to use three-phase stepper actuators, due to several tangible benefits such as fine step resolution, simple electronics with fewer power switching Field-Effect Transistors (FETs) and increased torque capacity under high friction conditions. There are many ways to control stepper motors, but the most common are wave and bipolar operation. Wave operation (also known as "Line-to-line" or 2/3 phase) and bipolar (also known as two-leads-tied or 3/3 phase) are represented in Figure 10.

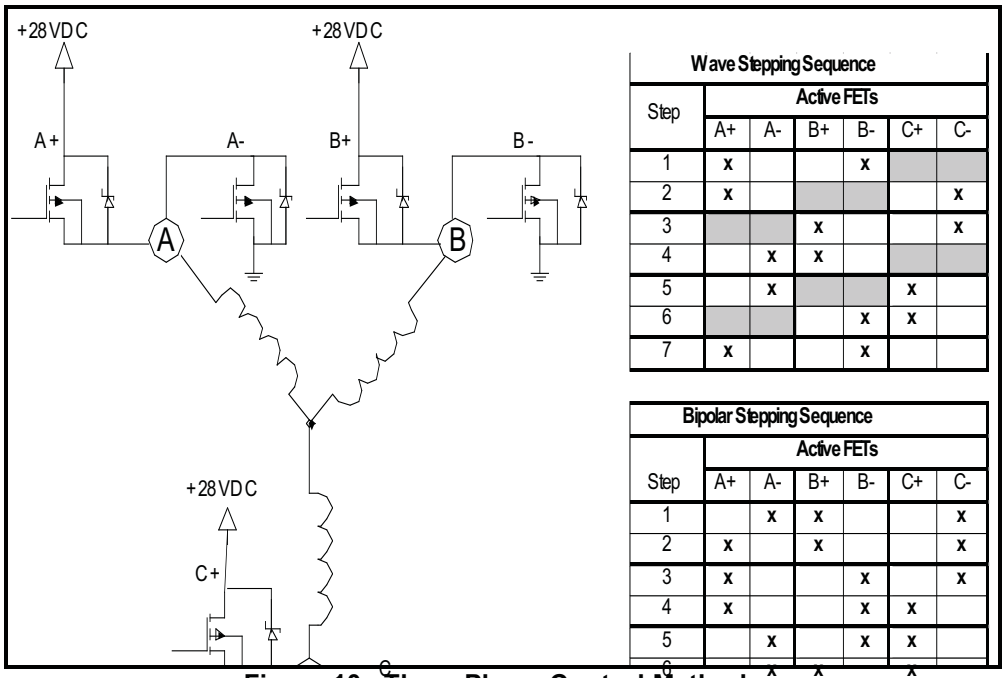

Wave Stepping Sequence

Step	Active FETs					
	A+	A-	B+	B-	C+	C-
1	x			x		
2	x					x
3			x			x
4		x	x			
5		x			x	
6				x	x	
7	x			x		

Bipolar Stepping Sequence

Step	Active FETs					
	A+	A-	B+	B-	C+	C-
1		x	x			x
2	x		x			x
3	x			x		x
4	x			x	x	
5		x		x	x	
6		x	x		x	

Figure 10. Three Phase Control Methods

For wave operation, two of the three phases are active at one time. In the Stepping Sequence Chart, we see that for the first step, Phase A is connected to the +28V through the A+ FET, and Phase B is connected to ground through the B- FET. Under this condition, current is flowing from A through B to ground. Phase C is open and is not connected through either FET. For the transition from step one to step two, Phase A remains connected to +28V, but now Phase C is connected to ground through C- FET and Phase B is open. The terminology of wave comes from this open leg shifting, and is analogous to two-phase wave operation. Referring back to Figure 7, this is a scope trace of the three phase stepping sequence of a wave drive with a regulated power supply, notice how the voltage in the open leg oscillates during the overshoot transient. This is the back-emf circulating and causing the underdamped characteristics when no damping coils are present.

For bipolar operation, all legs are active during each stepping sequence. For bipolar step one, Phase B is "high" through the B+ FET, and both A and C are connected to ground through the A- and C- FETS respectively. At the second pulse, Phase B and C do not change state, but Phase A transitions from ground to +28V. This *controlled and continuous* reversal of current flow is why we call this method bipolar, and is analogous to two-phase bipolar operation.

Control Method Trades

For either control method, during the transition of each pulse, you should *never* have the situation where the high and low side FETs of a common node (e.g. A+ and A-) are simultaneously active. If they were to

be active at the same time, the current flow would bypass the motor and “shoot-through” from the supply voltage directly to ground, failing the FETs. Wave operation offers the advantage of not having to worry about “break-before-make” of the power stage FETs, while with bipolar operation you must “break” the active FET before “making” the next active FET. Therefore, the wave control method offers higher reliability and fewer failure modes compared to the bipolar operation. This was the discriminating factor in our selection of wave control for this space flight stepper motors.

An operational dilemma arises from the wave operation because there is an unregulated phase at each step, resulting in underdamped operation. For example, transitioning from step one to step two under the wave scenario, the current flowing in phase B is instantaneously cut-off from ground. At that instant, an L•di/dt transient voltage is generated in reaction to the state change. The transient current flows through the B+ diode back into the supply voltage. Additionally, the motor back-emf generated from the stepper motion is allowed to flow freely in this unregulated winding, until step 3 when it is driven to the +28 voltage. The combination of the transient current and the back-emf result in an inherently underdamped control system. For bipolar operation, at each step of the control sequence all legs are actively controlled to either +28V or ground. There are no “free-wheeling” legs to allow transient currents to create an underdamped condition. This difference was found to be the root cause of the significantly underdamped condition of the mechanism.

Another observation of the various testing was the variation of performance whether the voltage supply was regulated or not. Notice the leg voltage measurements in Figures 3, 5 and 6. These voltages came from a non-regulated supply. You can clearly see the impact of the back-emf on the voltage during the step transient. Now notice the phase voltages on Figures 7 and 9. These voltages are generated on the regulated voltages in the control electronics. Notice the difference between the regulated and unregulated voltages during the step transients. The unregulated supply voltages “bounce” with the step transients, while the regulated voltages do not vary with the step transient. The differences in these voltage supplies will also affect the step characteristics; therefore, the voltage supplies used during testing should match the conditions the mechanism will see under flight conditions.

Processing the Rotary Accelerometer Signal

As previously discussed, we implemented an RA in the system for pulse step verification. The associated electronics to process the RA may be as sophisticated or as simple as desired, depending on the flexibility and capabilities required in the system. The charter for the RA in our system is pulse verification and state of health monitoring. For basic pulse verification a simple amplifier and comparator circuit is all that is required. An example of this circuitry is shown in Figure 11 [1]. The RA enables step verification by producing a voltage pulse that exceeds a specified threshold voltage each time the motor steps with the sign of the pulse indicating whether a clockwise or counter-clockwise step is taken. This method of step verification is called Original Transition Voltage Counting [1]. Figure 12 shows a single step of an adequately damped stepper motor system with a well-defined pulse for step verification. This trace was actually taken by the actuator supplier of the EDU#1, driven at our nominal *power*, with a *bipolar drive configuration*. Notice the significant damping characteristic as compared to a single step of a wave controller, as shown in Figure 2, with equivalent power input.

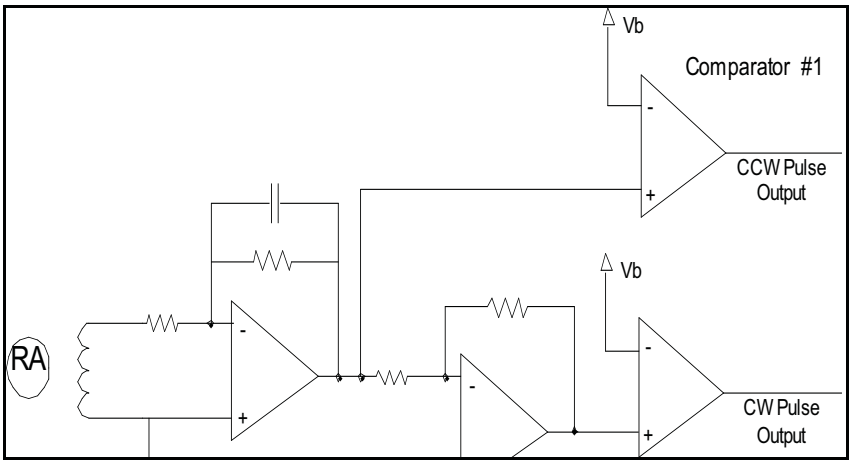

Figure 11. Simple Transition Voltage Counting Circuitry

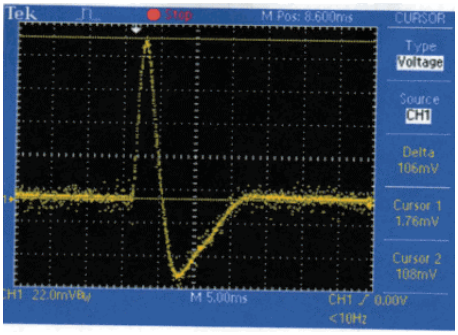

Figure 12. Oscilloscope Output of an Adequately Damped Single Step

Conclusion

The first and most obvious conclusion is that EDUs proved invaluable to the process. EDU testing enabled the discovery of the underdamped condition at a stage in the process when corrective action did not negatively affect the program. Thanks to cooperation and teamwork between the Mechanisms, Electrical Engineering, System Engineering and Reliability Teams, as well as a responsive supplier, there was no impact to the program master schedule, even with a major in-process modification to the actuator.

The most significant lesson learned is that the drive control methodology and power supply regulation have a much more significant impact on mechanism performance than anticipated. Wave or unipolar drive methods result in a much more underdamped system, when compared to bipolar drive methods. Additionally, power supply voltages in test sets must duplicate on-orbit conditions, whether the supply is regulated or unregulated, because the supply voltage type affects the fundamental step kinematics and damping.

We discussed detrimental implications of an underdamped stepping mechanism, and the reasons to require an adequately damped system. We covered many common industry practices and potential options that could yield desired damping and mechanism characteristics. We took advantage of an excess of torque margin capacity within the motor, and used shorting coils to provide desired damping and mechanism performance. Our solution was efficient and robust, making use of existing technologies and capabilities while maintaining critical schedule requirements.

The utilization of a Rotary Accelerometer (RA) proved extremely useful in characterizing performance and troubleshooting potential solutions. Determining operational torque margin and conducting the simple kinematical analysis of the mechanism performance were also integral to the development and solution process. Utilization of an RA in the design increased mechanism reliability, improved position knowledge, verified step performance, and provided state of health information for this mission critical application.

Acknowledgements

Special thanks are extended to Erik Wilkinson, Charlie Hamp, Kiley Jones, Scott Miller, Richard Maxwell, Randall Whitaker, and the whole Mechanism, Electronics and Reliability teams at BATC that supported the testing, evaluation, review and solution process. Additional thanks and recognition go to CDA InterCorp for their responsive service and capabilities.

References

1. Starin, Scott, and Crosno, Fred, "System Characterization and Motor Step Verification through Rotary Acceleration Signals," 36th Aerospace Mechanisms Symposium, May 2002.

2. Starin, Scott and Neumeister, Jeff, "Eddy Current Damper Simulation and Modeling", Proc. 9th European Space Mechanism and Tribology Symposium, Liege 21 Sept. 2001, ESA SP-480, September 2001.

3. CDA InterCorp, "Stepper Motor Engineering Reference Data", © 2000

4. Ramakant Gayakwad and Leonard Sokoloff, "Analog and Digital Control Systems", Prentice Hall, Engelwood Cliffs, NJ 07632, © 1988.

5. Starin, Scott and Rodriguez, Tony, "Soft Stepping and Disturbance Compensation Through Rotary Acceleration Signal Processing", Proc. 10th European Space Mechanism and Tribology Symposium, San Sebastian, Spain, 24-26 September, 2003, ESA SP-524, September 2003.

Large Scale Magnetostrictive Valve Actuator

James A. Richard*, Elizabeth Holleman* and David Eddleman*

Abstract

Marshall Space Flight Center's Valves, Actuators and Ducts Design and Development Branch developed a large scale magnetostrictive valve actuator. The potential advantages of this technology are faster, more efficient valve actuators that consume less power and provide precise position control and deliver higher flow rates than conventional solenoid valves. Magnetostrictive materials change dimensions when a magnetic field is applied; this property is referred to as magnetostriction. Magnetostriction is caused by the alignment of the magnetic domains in the material's crystalline structure and the applied magnetic field lines. Typically, the material changes shape by elongating in the axial direction and constricting in the radial direction, resulting in no net change in volume. All hardware and testing is complete. This paper will discuss: the potential applications of the technology; overview of the as built actuator design; discuss problems that were uncovered during the development testing; review test data and evaluate weaknesses of the design; and discuss areas for improvement for future work. This actuator holds promises of a low power, high load, proportionally controlled actuator for valves requiring 440 to 1500 newtons load.

Introduction

Magnetostrictive materials change dimensions when a magnetic field is applied; this property is referred to as magnetostriction. Magnetostriction is caused by the alignment of the magnetic domains in the material's crystalline structure and the applied magnetic field lines. Typically, the material changes shape by elongating in the axial direction and constricting in the radial direction, resulting in no net change in volume.

The response is proportional to the applied field strength and occurs in microseconds. Most metals exhibit this property. Nickel, for example, increases in length (strain) by approximately 40 parts per million in a sufficiently strong magnetic field. Materials which produce strains greater than 600 PPM are known as "giant" magnetostrictive or "smart" materials. Terfenol-D, produced by Etrema Products, Inc., produces strains from 800 to 1200 PPM in fields as low as 2000 Oersteds (Oe) and is, currently, the only commercially available magnetostrictive material. Even though this is considered to be "Giant" scale magnetostriction, the net motion is only 0.025 mm per 25 mm of material

The load carrying ability of the material is limited by the maximum stress the material can withstand; therefore, the load density is far greater than conventional actuators power systems. Current solenoids are limited to about 2.3 MPa, pneumatic systems to about 10 MPa and hydraulic system to 20 MPa. The yield strength of magnetostrictive materials is over 69 MPa, giving it a load density that is 3 times the best available. The material is only limited by the small stroke.

Discussion

Approach: The approach was to build a mechanical advantage system that will utilize a magnetostrictive actuator to operate a large valve (25-mm size) at high flow demand. ER33 hoped to demonstrate the valve will be as fast as a solenoid valve, precise as a hydraulic valve and lighter than either for its size.

Accomplishments: All hardware and testing is complete. The valve performance was acceptable, but strokes were not as predicted.

* NASA Marshall Space Flight Center, Huntsville, AL

Following the proposed plan, hardware for the magnetostrictive valve design (designed using ER funds prior to this effort), shown in Figure 1, was built within the first year of the effort. However, the valve could not be reasonably modified as an actuator, so a new design was developed. The newly designed actuator, shown in Figure 2, used lessons learned and some concepts from the original valve design.

Figure 1. Original Valve Design

Figure 1. New Valve /Actuator Design

Early testing revealed that Terfenol –D does not hold up well to high frequency responses. The material is very brittle and susceptible to cracking and fracture if improperly side loaded. Results of testing are shown in Figure 3. Also, the small motions in the actuator require machining to close tolerances, precise shimming to achieve correct preloads to obtain proper strain (elongation), and large magnetic biasing to maintain the proper pre-load on the material to prevent hysteresis. Figure 4 shows that the Terfenol D material hysteresis decreases and strain increases with preload. The design allowed for these adjustments in the preload using shims under the pre-load springs.

The material was loaned to a local contractor to perform tests to verify the response of the material to preload. The contractor presented data, shown in Figure 5 that differed from the theoretical data supplied by the material vendor, shown in Figure 4. This data was incorporated into the new design. The contractor derived curve, Figure 5, shows the hysteresis in the material measured as a load is applied to the end of a bar of Terfenol D. This is a plot of magnetic field line angles from the normal (axial) direction. The angle is directly related to the inverse relationship of magnetic input for a force output.

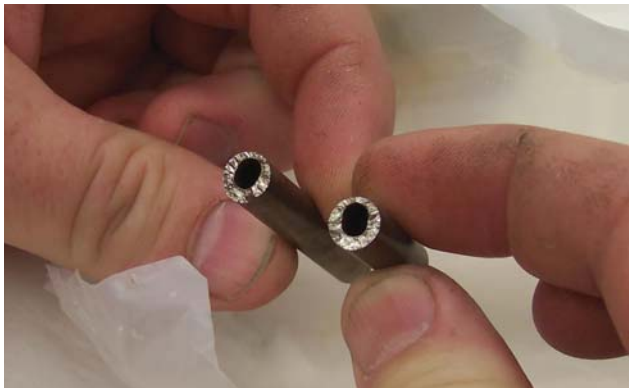

Figure 2. Terfenol-D Is Very Brittle.

After incorporating preliminary test results into the design, the fabricated hardware was assembled, as shown in Figure 6, and tested. During testing, several issues were discovered. The stroke of the valve was measured as 0.14 mm on the arm (multiplied) versus the expected stroke of 0.38 mm. Figure 7 shows the displacement measurement recorded during test. Investigation revealed that the magnetic field suggested by the vendor for magnetic biasing of the material was too high and caused the crystalline structure to begin to exhibit strain (elongation) before the electric field was applied. The magnets were eliminated and the valve coil repositioned resulting in a stroke of 0.22 mm, just over half the predicted stroke. Perhaps, using weaker magnets for the biasing would increase the stroke of the material, but time did not allow for this to be done.

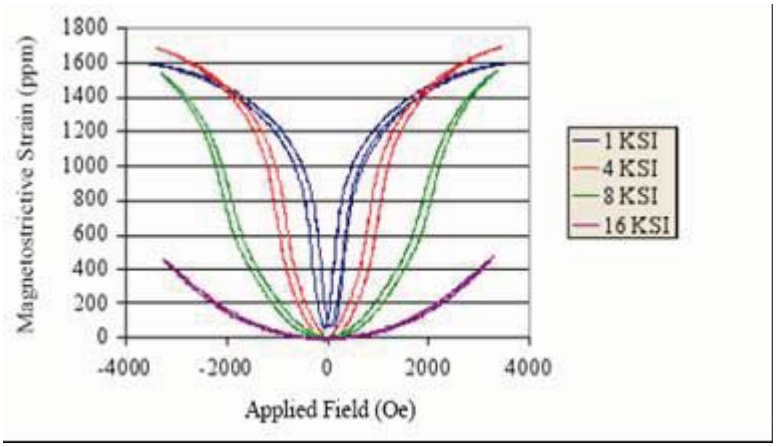

Figure 4. Material Hysteresis vs. Preload

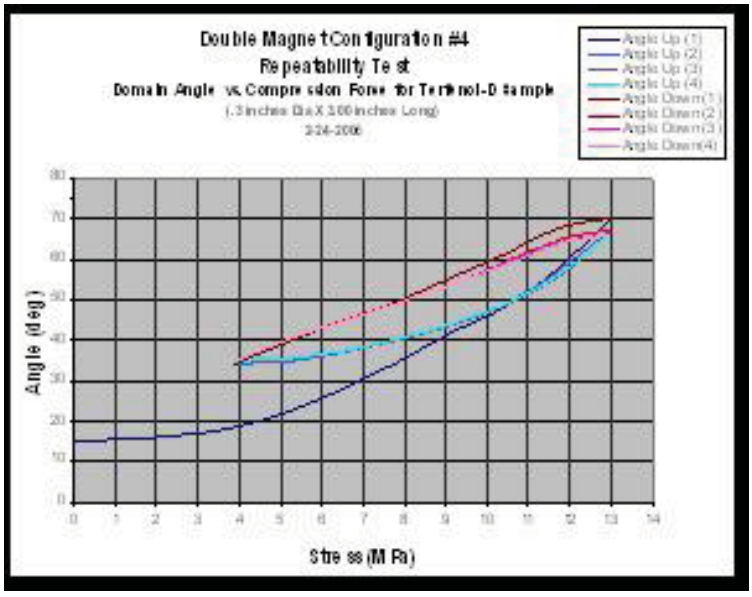

Figure 5. Measured Hysteresis

Figure 6. Final Valve Assembly

Figure 7. Original Displacement

Per design, the length of the coil was approximately half the length of the magnetostrictive material. The concept was to use the end effects of the shorter coil to provide strain to the material out side the coil, so the coil was centered on the material. This concept was not ideal and a new coil was ordered, but time did not allow testing with the new coil. During a review of the magnetic flux path design with a local vendor, it was suggested that the design may not accommodate an ideal path and the valve was "leaking" magnetic field strength. A possible solution to this issue is to replace the aluminum-bronze shield surrounding the coils with a new shield made of a magnetic material. These three changes, weaker magnets, a longer coil and a different shield material, could be easily incorporated into the design if time and budget allowed.

Planned Future Work: No current program has expressed interest in the technology. CLV is working to a low risk, existing technology approach. Future programs, such as LSAM, have inquired, but no technical risks have been identified where this technology would be useful. A Space Act Agreement with Orion will continue and ER33 plans to apply for some Innovative Partnerships Program funds to expand this development.

Publications and Patent Applications: ER33 has submitted a patent application for the magnetostrictive valve. The local company that performed the load testing on the materials has entered into a Space Act Agreement with MSFC to develop this into a marketable regulator for space craft application. Being proportional, fast, and small, this valve has the potential to be an electrical regulator and could provide a regulator system that has little or no change in regulation regardless of the required flow demand. This would improve pressure feed reaction control system performance, better control purges, allow active pressure control in propellant tanks, and a number of other advantages.

Conclusions

The data obtained during this effort has proven that the concept actuator design has merit, shown the valve design must be carefully controlled, and that the preload, coil design and flux path issues are critical to obtain the required stroke and repeatability. The valve met all design requirements except stroke. This problem has been evaluated and solutions developed, but not proven. The design could be modified to incorporate these improvements and regain the lost stroke.

Therefore, the concept has been shown to work, the multiplying lever system worked perfectly and the valve concept shows potential.

Additionally, newer materials are available that have larger strokes (Terfenol-D has 1200 PPM, newer materials have 5000 PPM potential). The design provided has proven that the use of magnetostrictive materials in valves is a viable concept. More time and better magnetic flux path design is needed to fully utilize the capabilities of this material.

Design and Development of a Miniaturized Double Latching Solenoid Valve for the Sample Analysis at Mars Instrument Suite

James T. Smith*

Abstract

The development of the in-house Miniaturized Double Latching Solenoid Valve, or Microvalve, for the Gas Processing System (GPS) of the Sample Analysis at Mars (SAM) instrument suite is described. The Microvalve is a double latching solenoid valve that actuates a pintle shaft axially to hermetically seal an orifice. The key requirements and the design innovations implemented to meet them are described.

Introduction

This paper outlines requirements, design and development activities of the SAM Microvalves. The SAM instrument suite will be an integral part of the Mars Science Laboratory rover, and the Microvalves will control the gas flow within the SAM instrument suite.

There are 44 in-house Microvalves in SAM, as well as several Microvalves supplied by the sole outside provider of this technology. The decision to develop and build in-house Microvalves was primarily based on past delivery performance of the outside vendor coupled with the high number of valves needed for this mission. Additionally, improvements in mass and reliability were goals of this design effort.

Background

NASA's Goddard Space Flight Center has used Microvalves on several missions in the past (e.g. Galileo, Cassini/Huygens), but never in the quantity required for SAM. Over the past several decades, only one vendor has been able to meet the difficult requirements for the Microvalve, but this vendor has had difficulties meeting delivery schedules. Due to the large number of valves required for SAM, the decision was made to develop an in-house design.

The effort began as an Internal Research and Development project in 2004, and is currently in the flight qualification phase.

Driving Requirements

The primary requirement for the Microvalve is the leak rate. The valve is required to have a helium leak rate across the valve seat and through the outer case of less than $1x10^{-10}$ atm.cc/sec. This drove the design of the pintletip as well as the use of bellows to isolate the gas flow. Also, the materials for the components in the gas flow must be chemically inert so they do not influence the scientific measurements.

Another key requirement was that the valves must be able to survive the qualification temperature range of -60°C to +225°C, and be capable of operation from -40°C to +195°C. This requirement further limited material selection.

In order to reduce mass over current technology, the valves were designed to be welded into their respective manifolds as opposed to a bolted configuration. This requirement drove the design of the "floating" pintletip, as well as the use of an explosion welded Inconel to Titanium bellows housings.

* NASA/Goddard Space Flight Center, Greenbelt, MD

Since there are a several Microvalves supplied by an outside vendor used on SAM, there was a requirement that the in-house Microvalve operate of the same drive circuitry. This requirement drove the design of the solenoid, as well as the position sensor.

Microvalve Design Overview

A Microvalve is a double latching solenoid valve that actuates a pintle axially to hermetically seal an orifice to control gas flow. A permanent magnet latches the valve in either the open position or closed position with the power off, and a solenoid is energize to change the state of the valve.

In order to achieve the required leak rate, a diamond turned Vespel pintletip is pressed into a lapped and polished titanium valveseat when the valve is closed. The load is applied to the pintletip via a pintle shaft. The load on the pintle shaft is generated by a stack of disc springs that are compressed by an armature. The armature compresses the disc springs when it is magnetically latched in the closed position by a permanent magnet. The amount the disc springs are compressed is controlled by adjusting the gap under the armature that is present at the moment the pintletip first contacts the valveseat. This gap will be closed by the magnetic force of the permanent magnet. The adjustability is discussed in a later section.

A bellows is used to isolate the sample gases and obtain the outer case of leak rate of less than $1x10^{-10}$ atm.cc/sec. The bellows are made of SS321 and are electron beam welded at each end to Inconel 718. The bellows were designed to have a low spring rate because the force generated by the bellows when the valve is in the open state acts against the magnetic latching force that holds the valve open.

To control the magnetic flux path (see Figure 4), alternating rings of Inconel and Hiperco are brazed together and then machined on a lathe to allow for a sliding fit with the armature. The brazing compound used was selected to be below the annealing temperature of Hiperco so the brazing process would not degrade the performance of the assembly.

To reduce friction, both the brazed assembly and the armature are coated with Dicronite, a modified tungsten disulfide dry lubricant. Additionally, the armature and the pintle shaft are nickel coated to prevent similar metals from having a sliding contact surface.

Specifics of the pintletip design, the solenoid design, and the adjustability feature are discussed in more detail in later sections.

<u>Valve Specifications</u>
Mass: 20 grams
Height: 35.5 mm (26.5 mm above manifold surface)
Diameter: 14.73 mm
Power: 18 volts (Since the valve operates on a pulse from a capacitor, voltage is the constraint)
Helium Leak Rate (valveseat): < $1x10^{-10}$ atm.cc/sec (instantaneous), $2x10^{-9}$ atm.cc/sec (steady state)
Helium Leak Rate (case): < $1x10^{-11}$ atm.cc/sec
Operational Temperature Range: -60°C to +220°C
All materials in gas flow are chemically inert
Valve Orifice (diameter): 1.778 mm
Pintle Travel: 0.762 mm
Actuation Time: < 1 millisecond

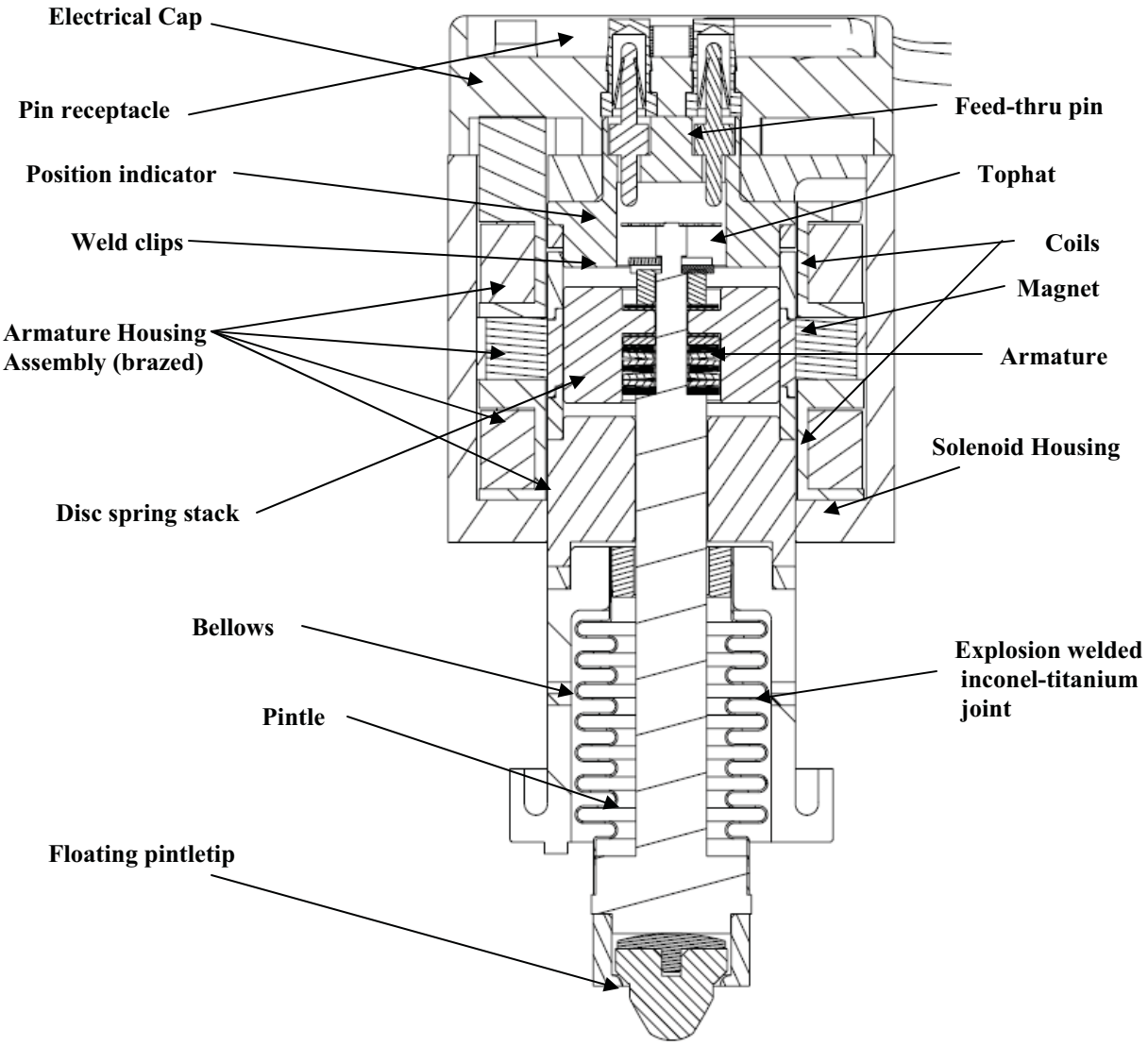

Figure 1 - Microvalve Cross Section

Floating Pintletip

The pintletip for the Microvalve is made from Vespel 22 due to the inert nature of the material, as well as the high operational temperature of Vespel. The part is fabricated on a lathe to the rough dimensions, and then finished on a diamond turning machine to impart a curved surfaced upon the 60-degree cone as shown in Figure 2 (the outside line represents the rough cut part, with the inside line representing the finished, diamond turned part). By creating a curved surface, the pintle tip will “self seat” when pressed into the cone shaped valveseat like a ball in a cone.

Through experimentation it was determined that a radius of curvature of 0.381 cm (0.15 in) was ideal. After the pintletip is diamond turned, it is hand polished with an extremely fine polishing cloth. Each pintletip is screened to ensure the required leak rate can be achieved. It should be noted that the leak rate of less than $1x10^{-10}$ atm.cc/sec is the instantaneous leak rate, and that the Vespel will permeate helium at a leak rate of about $2x10^{-9}$ atm.cc/sec when subjected to helium for an extended period of time (between 5 to 30 minutes).

In order to facilitate the “self seating” action, the pintletip is free to rotate about all three axis, and free to translate in two directions, with the only constraint being the movement along the axis of travel (the Z-axis as shown in Figure 3). The pintletip “floats” in the pintle collar, which is welded to the pintle shaft. The backer plate applies the load from the pintle shaft when the valve is closed, and the plate itself has a curved surface to allow for rotation as the pintle seats itself into the valveseat. The “floating” feature also allows for some misalignment between the axis of the pintle shaft and the axis of the conical valveseat. This is critical since the valveseat is part of the manifold, and the valve is welded into the manifold, which limits alignment capabilities.

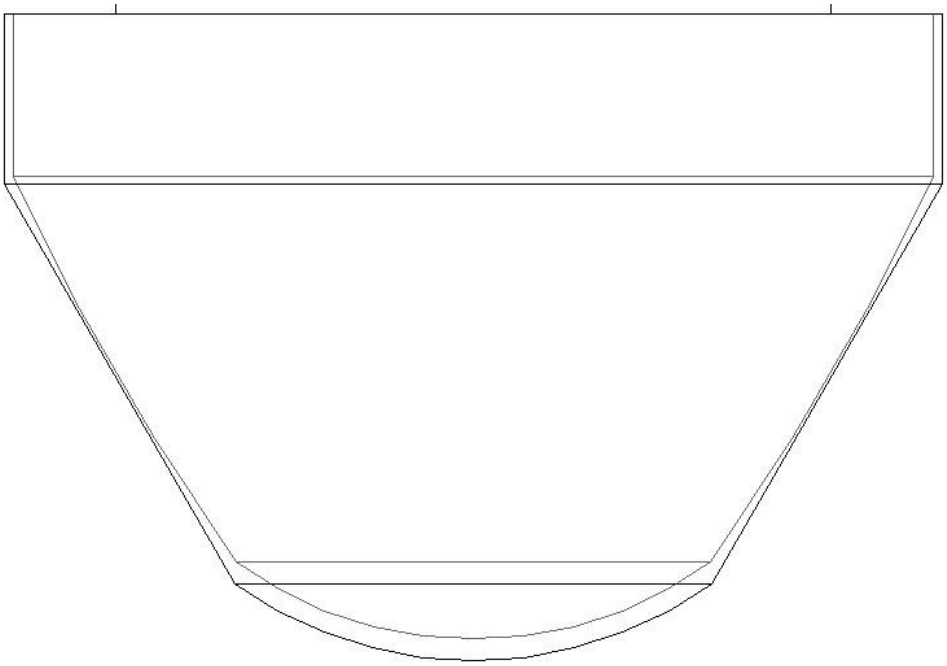

Figure 2 - Pintletip Profile

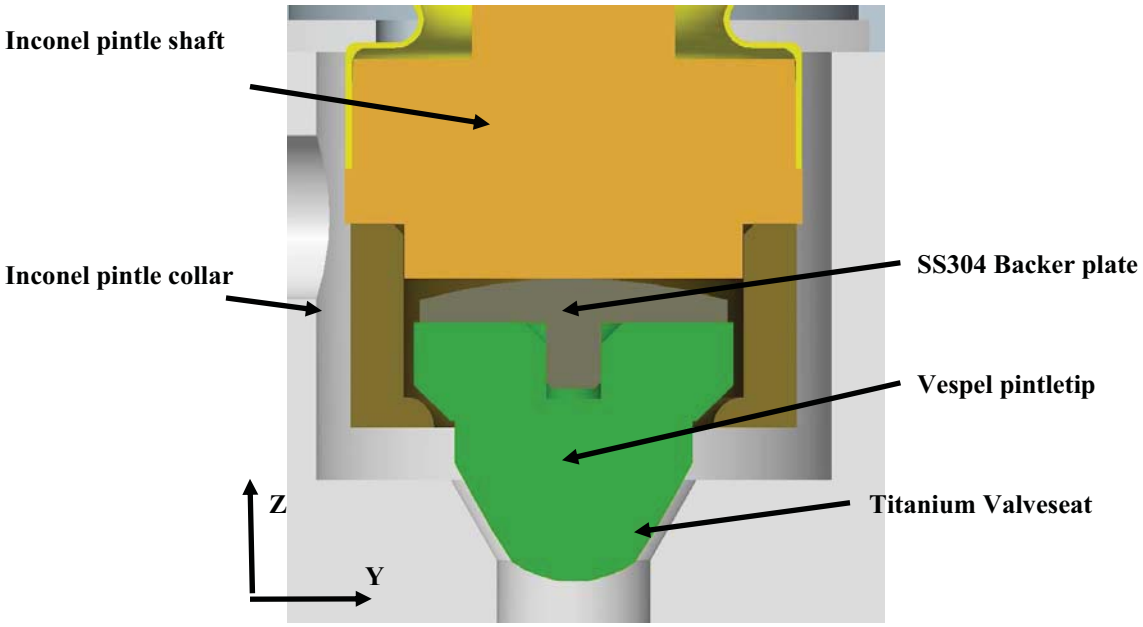

Figure 3 - Floating Pintletip Cross Section

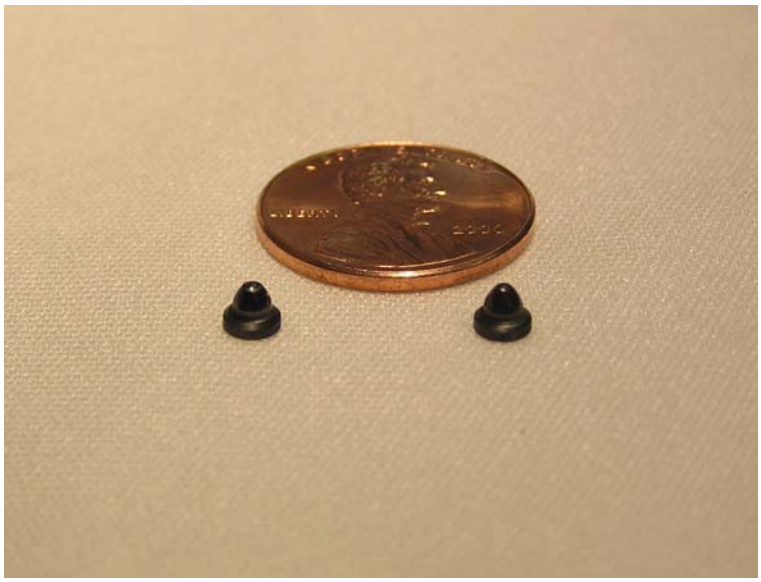

Figure 4 - Sample Pintle Tips

Solenoid Design

The solenoid consists of two coils wound with H-APTZ magnet wire, a radially magnetized Samarium Cobalt magnet, and a Hiperco 50A housing (see Figure 5). The flux path shown in Figure 4 is for the valve in the closed position. The magnet allows for the valve to remain either open or closed with no power supplied to the solenoid. The solenoid is energized by the discharge of a capacitor, and the valve changes state in less than 1 millisecond.

One of the key features of the in-house design is that the solenoid is removable. The ability to replace a solenoid without replacing the whole valve allows for increased reliability in the welded design. If a solenoid were to fail during acceptance testing or any pre-launch operations, the faulty solenoid could be easily swapped out for a new one without machining the valve out of the manifold.

To increase the durability of the coils in the solenoid they are encapsulated with Duralco 4460.

The bobbins that the coils are wound around are ultrasonically machined out of Magnesia partially stabilized Zirconia. This process allows for tolerance control within 0.0254 mm (.001 in) since the ceramic material is machined in the hardened, not green state. The material is very strong, has an extremely high dielectric strength, and has a compatible CTE for the required temperature range.

The wires for each coil are terminated at copper pins by laser welding. The pins are supplied bonded into glass barrels with Kovar sleeves, and these assemblies are bonded into the towers on the ceramic top bobbin.

Another feature of the solenoid design is that the coils can be run either in parallel for redundancy, or in series to reduce the require size of the capacitor to change the valve state. The only change necessary to switch the mode of operation is a change in the wiring of the electrical cap that interfaces with the wiring harness to the drive circuitry. For SAM, the coils are run in series.

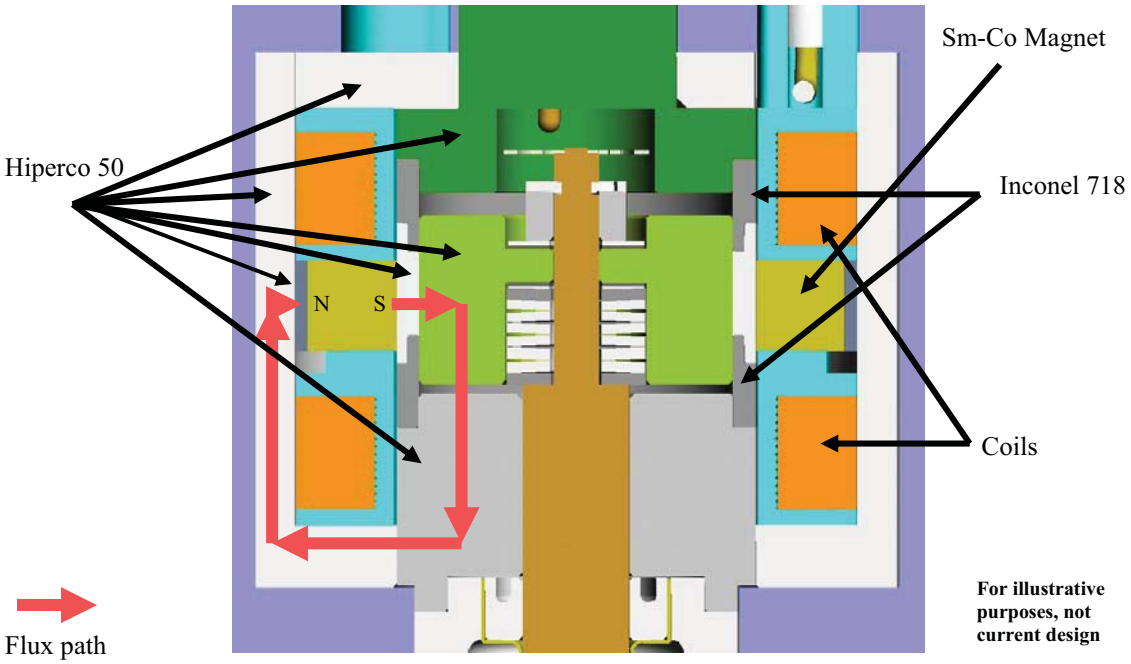

Figure 5 - Solenoid Cross Section

Adjustability for Tolerance Stack-up

Since the components of the Microvalve are small, the tolerances of standard machining become more obvious as a percentage of overall dimensions. For example, on the pintle backer plate shown in Figure 3, the shaft that aligns the part to the pintle tip is only 0.4064 mm (0.016 in) in diameter. The standard tolerance of ±0.127 mm (0.005 in) would be over 50% of the overall dimension! While tolerances in the range of 0.00254 mm to 0.0127 mm (0.0001 in to 0.0005 in) are achievable, they come at a cost. In order to achieve meet the design intent and keep cost relatively low, most tolerances were set to 0.0254 mm to 0.0508 mm (0.001 in to 0.002 in).

The downside is that those tolerances still result in variation from valve to valve during assembly. For the disc springs to apply the correct load to the pintle shaft when the valve is closed the amount the disc springs are compressed must be controlled to within 0.0254 mm (0.001 in). Therefore there has to be adjustability to control the amount of compression. Figure 5 shows how adjustment shims are used to increase or decrease the gap. Each stack of disc springs is calibrated so that the amount of compression required for a desired force is known within 0.0127 mm (0.0005 in).

The measurements shown below are taken during assembly, and the adjustments are made for each valve. After the adjustments are made, weld clips (not shown in Figure 6) are tack welded into place, and the valve is actuated and leak checked to verify the performance. Once verify, the weld clips are permanently welded into place and the tophat is welded onto the valve.

Position Sensor

The Microvalve is designed to have a resistance based position sensor (shown in Figure 1). A flexure contacts a pin when the valve is in the open state and creates a path to ground though the valve case. This design was selected because of the requirement that the valve use the same electronics as current technology. That meant that there was only one wire to use, and that position sensing circuit was based on a resistance measurement.

- **h_{gap} controls the amount the disc springs compress**
- **By measuring h_{arm}, d_{cavity}, and d_{arm} you can determine h_{gap}**
- **h_{gap} can be controlled by moving the shims (SS304) from on top to below the armature and vice versa**

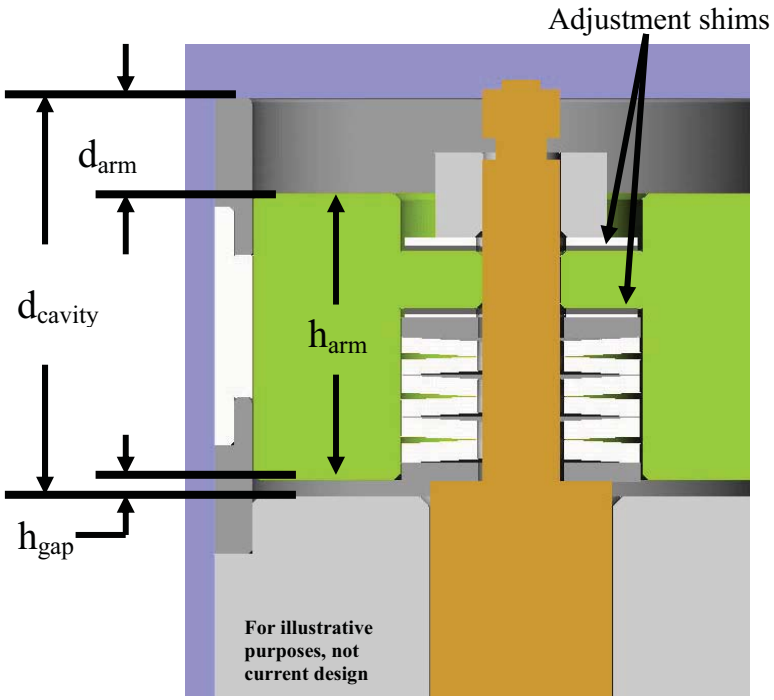

Figure 6 - Disc Spring Compression Adjustability

However, a recent failure with several of the flexures themselves has caused this feature to be removed from the current design used on SAM. The project was not depending on position knowledge for any of the command sequences, and would only use the knowledge for diagnostics. Therefore, due to the extremely tight schedule for SAM, the decision to remove the flexure was reached easily.

It is known that the flexures yielded during actuation, but the exact cause is not yet known. The flexures are designed to see 0.0762 mm (0.003 in) of deflection when the valve is open. Life tests were performed on the flexures where they were deflected 0.127 mm (.005 in) for 10,000 cycles followed by an additional 1,250 cycles at 0.1778 mm (0.007 in) of deflection with no yielding or decrease in reactionary load (~.22 N @ .1778 mm deflection).

One possible cause could be an overshoot of the pintle shaft during the opening of the valve where the flexure would see excessive deflection before settling to the static position. However, preliminary testing indicated there is less than 0.0254 mm (0.001 in) of overshoot, which would not explain the yielding.

Another issue to be investigated is that the valve actuates in less than 1 millisecond, and the shock event may be affecting the flexure. The rate of deflection during the life test performed was so slow it could be considered quasi-static.

Due to the schedule for SAM, this means that there will be no position indicator. However, alternate methods for determining position with just one wire are currently being investigated for future use. One method would be to measure the change in inductance of the top coil that would result from the movement of the armature. Another method would look at the back EMF present when the valve is commanded to close and see if it differs depending on the current state of the valve. For example, is the back EMF higher when you command a valve closed that is already closed than it is if was open?

Testing

The first batch of four (4) Qualification Valves has successfully completed both the vibration and thermal vacuum portion of the qualification test program.

The vibration test consisted of a pre low level sine sweep, a 14.1-grms GEVS specification random vibration, a 60-g sine burst, and a post low level sine sweep.

The thermal vacuum test was run as follows:

- Eight cycles from -60°C to + 225°C at a hard vacuum; the valves were cycled 5 times at each extreme and leak testing
- Eight cycles from -60°C to + 225°C in a CO_2 atmosphere at 10 kPa (100 mBar); the valves were cycled 5 times at each extreme and leak testing

The failure with the position sensor was discovered during the TV testing, so the life test was not run on this batch of valves.

A second batch is about to begin its qualification testing as soon as possible. This batch will undergo the full suite of tests, including life testing. The random vibration levels will be higher since the test levels have been updated by the project, but the increased energy is at frequencies low enough not to be a concern.

Additionally, a multitude of component testing was performed over the last two years, including, but not limited to: thermal cycling of the solenoids followed by high pot testing, life testing of the bellows, pressure testing of the bellows, life testing of the disc springs, thermal cycling followed by strength testing of the brazed joints, strength testing of weld samples for all welded joints.

Conclusion

The Microvalve has gone from a research and development effort to a flight design in the past three and a half years. The first 19 flight valves have already been welded into flight manifolds, and the remaining 25 will be assembled over the next two months. The qualification program has been successful to this point, and additional testing will begin as soon as possible. The failure of the position sensor was a disappointment, but the project considered the loss acceptable. More work needs to be done to either fix the current position sensor design or come up with a new method of position knowledge for future use of the Microvalve.

Acknowledgements

The author would like to acknowledge Marvin Noreiga, Bob Abell, Brett Louis, Yury Flom, Russell Rowles, Dan Harpold, John Bischell, Steve Price, Donneise Briscoe, Carl Strojny, Charlie Fleetwood, Dan Carrigan, Armando Morell, and Lee Niemeyer, as well as the entire SAM team at NASA Goddard Space Flight Center. Without all of their assistance the development of the in-house Microvalve would not have been possible.

Figure 7 - Flight Microvalves Welded into a Flight Manifold

A New Structural Bonding Process for Ferromagnetic Sheet Stacking used in Electric Motors (Rotors, Stators…)

Christophe Casteras*, Bruno Bonduelle** and Frederic Martin***

Abstract

A new structural bonding process has been developed for the assembly of the thin iron sheet stacking used in electrical motors. This process, based on screen printing technology, improves the stack cohesion and allows very precise geometrical dimension machining. A stator has been assembled based on such a structurally bonded stack, and it has been submitted to a complete qualification test sequence similar to an existing space-qualified stator with a potted stack. Process development, test results, and comparisons are presented hereafter.

Introduction

A new onset of brushless DC motors for space was developed at SOTEREM for a satellite platform application. This electrical motor is a large and powerful one, whose performance at high rotation speeds is disturbed by eddy current. To lower the eddy current, ferromagnetic thin sheet stacking must be used for the stator. The potting employed to maintain this stack was already qualified but was deemed difficult to produce and has some industrial constraints for large diameter stators.

So, in parallel, a structural technique of bonded assembly was developed by CLIX Industries under CNES funding, to solve the stator ferromagnetic sheet stacking issue. The objectives were to increase cohesion and rigidity, to reduce the structural mass, to increase electromagnetic performance, to improve the workability of stacking without delamination, and finally to obtain better manufacturing precision. The difficulty with the structural bonding technique is to obtain very thin uniform adhesive joints (of about few microns), which increases the iron/insulator ratio and generates an insulating layer at any point to limit iron losses.

The first part of the article presents a new process that relies on a technique of adhesive serigraphy adapted to adhesive rheology properties. Screen printing technology is used for assembling thin ferromagnetic sheet stacks with structural bonding. This technology makes the depositing of very thin and regular adhesive films on to the elementary parts of a stator stack possible. All kinds of resins can be applied including structural adhesives with a wide range of viscosities and tacks.

In addition, this structural bonding technology makes stacks machinable. An original method of wire electro-erosion machining was developed to cut out the stacks (insulating layer & conductor sheet) after gluing. This technique makes it possible to avoid tolerance issues of elementary components and to increase precision of the final stator geometry.

The second part of the article presents the test results of the evaluation campaign towards space and launch environment that has been performed on the motor equipped with the previous potted stator. A comparison with a similar space-qualified stator, based on a varnished structurally bonded stack, is also given.

* CNES, Toulouse, France
** SOTEREM, Castanet Tolosan, France
*** CLIX Industries, Toulouse, France

First Part: Development of a New Stack Bonding Process

Technical context

A laminated stator (Figure 1) generally consists of a thin sheet stacking (ferromagnetic material) with notches designed for windings (Figure 2). The central opening of the ring is intended to house the rotor. The resins used for bonded stacking are often winding impregnation varnishes and in all cases synthetic resins with very low viscosity.

Low viscosity is a necessary characteristic because it facilitates sheet capillary impregnation and stack pressing. In addition, these resins correspond to the electric motor industry's standard norms both in thermal and dielectric terms. However, these resins have adhesive and mechanical properties often unsuited to stator bonding and to its mechanical environment.

Figure 1. Brushless DC motor stator : 18001-2 (SOTEREM)

Figure 2. Thin sheet stacking with notches

Sometimes, delamination of the metal stack may occur either during motor manufacturing or handling, in general because of excessive stress or shock. Delamination may also be due to defective adhesion or lack of adhesive. During stack pressing, for example, disparities of sheet thicknesses and of oxidation treatment can create localized contact points between sheets where fluid resin is pressed out. Lack of adhesive is, of course, related to the intensity of applied pressure and to affinities between ferromagnetic sheets and resin (viscosity and wettability).

Sheet stack bonding is one of the main improvements in stator manufacturing. Using structural bonding for stack assembling can reduce the risk of delamination through mechanical or thermal constraints or shocks. It also means that stacking reinforcements, such as housing, bolting or welding are no longer necessary. Furthermore, rigidified stacking is much more machinable.

Screen printing

Screen printing is a printing method that can also be used to deposit all types of resins and, in particular, structural adhesives with high mechanical properties within a wide range of viscosities and tacks (1 to 400 000 mPa). Adhesive is pushed through a silkscreen (Figures 3 & 4). The screen consists of a fabric tightened over a rigid framework. The characteristics of the taffeta screening depend on thread diameter and spacing. Screening is selected according to rheological adhesive characteristics and required adhesive volume.

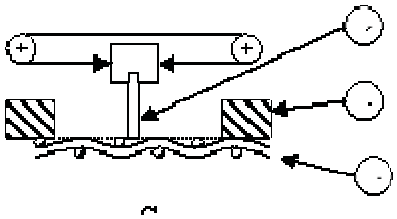

Figure 3. Screen printing method

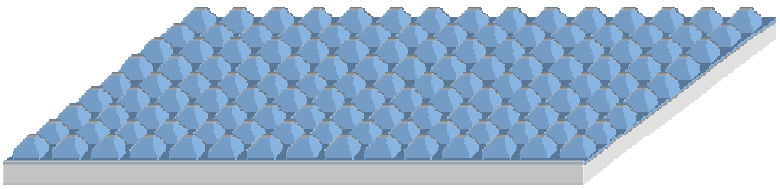

Figure 4. Depositing of thin adhesive film

Deposited adhesive films are very thin (from 1 to 20 microns), regular and repeatable. Thickness adjustment is very precise (±3%).

Adhesive selection depends on the ferromagnetic material that is to be assembled and on the life constraints of the product. The resin chosen for the serigraphy of the electric motors is a structural adhesive with high shear and peeling strength (rigidity and adherence).

Initially, sheets have a simple annular shape. They are screen printed then piled on top of each other with a pressing tool, which guarantees precise assembly height (Figure 5).

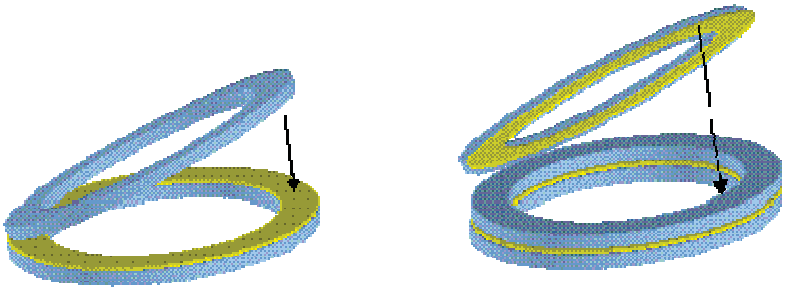

Figure 5. Sheets are piled on top of each other

Due to the thinness of the adhesive film, the stack has a very good iron / [iron + insulator] ratio (nearly 97%). For this application, the selected adhesive, which has a strong viscosity and a high tack, does not flow easily between sheets. So, the interlaminary space thicknesses are very homogeneous and regular. In addition, lack of adhesive due to air bubbles or sheet defects does not occur.

The "Structural adhesive bonding" of sheets with the silkscreen method aims to give them improved rigidity and make them machinable, without any risk of delamination. Moreover, stack machining precision is better than the precision of already machined assembled sheets. Good electro-magnetic performance results from good geometry.

Stack machining

When the stacking is polymerized, it can be machined. The machining method used is wire electro-erosion, which is a precise and safe technology. Indeed, notches are well aligned and assemblies are not at all stressed.

While the use of structural adhesives is a benefit to final stator rigidity and machining, the insulator layers are a problem for electro-erosion machining. Electro-erosion is based on capacitor discharges between an electrode wire and the part being machined. Each plate must be connected to the generator. The discharges generate micro-plasmas (locally about 10000°C) and sublimate all the materials (ferro-magnetic and synthetic resin).

The technique, used to make electro-erosion compatible with sheet stacking, consists of coating inner and outer slices with an electro-conductive resin to ensure that all metallic sheets have the same potential.

Electro-erosion does not create degradation of the structural adhesive joints. The resulting geometry of the stack is very precise; inner and outer diameters are coaxial, notches are aligned, and their geometry is symmetrical (Figure 6).

Figure 6. Stack Geometry

Second Part: New Bonded Stator Assembling and Validation Testing

To check the impact of the structurally bonded stack on motor performance, the second phase of development consisted of the following steps:

- manufacturing of a fully wound stator based on the structurally bonded stack
- testing a frameless motor, consisting of the bonded stack stator and an associated rotor, through a complete validation test sequence.
- for comparison, testing of a similar space-qualified motor.

Stator manufacturing

The structurally bonded stack presented in the first part has been designed and manufactured in order to replace an existing space stator with the same stator geometrical dimensions and interfaces based on the same lamination sheet materials and design. It has been equipped with exactly the same windings as the existing referenced stator. However, it has been impregnated with a varnish that complies with space outgassing standards. Figure 1 shows the finished stator manufactured with the bonded stack. Figure 7 shows the existing referenced stator and the structurally bonded stack. Figure 8 shows a detail of the existing referenced stator.

Figure 7. Existing Referenced Stator and the Structurally Bonded Stack

Figure 8. A Detail of the Existing Referenced Stator

The differences between both stators are summarized in Table 1

Table 1. Stator Differences

	Existing space stator	Structurally bonded stack stator
Lamination sheet	Same material Same design	
Stack	Synthetic resin bonded stack	Structurally bonded stack
Coils	Same wires Same windings	
Coating and finish	Resin compound molding in order to protect windings, and increase stator rigidity	Varnish impregnation

One of the specificities of these stators, driven by the space application, is that fixation onto the equipment is done directly on the stack; this implies that the stack outer diameter must be designed with very stringent tolerances (diameter ±0.02 mm and concentricity tolerance in the range of 0.02 mm). Such constraints explain why the qualified stator had been designed with a rigid compound, which guarantees efficient winding protection, but also drastically increases mass.

For the new structurally bonded stator, and thanks to its good mechanical properties, development has been oriented towards a lighter version without any compound. This raises potential criticalities with regards to stator flexibility and to winding protection. To take into account the high flexibility of the non-molded stator, the development effort required adaptation of existing processes and the introduction of stiffening tools. The finished stator had a small ovalization, which was easily corrected by a shaping tool, making the average diameters and concentricity fully compliant with the required tolerances.

Stator Testing and Characterization

The stator is a part of a brushless frameless motor (DC three-phased motor). The other part is a rotor equipped with permanent Samarium Cobalt magnets. For characterization of the new developed stator and in order to compare with existing space referenced stator, both stators associated with the same rotor have been successively submitted to the same complete test sequence (Figure 7). The tested environmental conditions are those which are required for a space application on a satellite platform at qualification level. From the test results, the main characteristic variations between the two stators are given in Table 2.

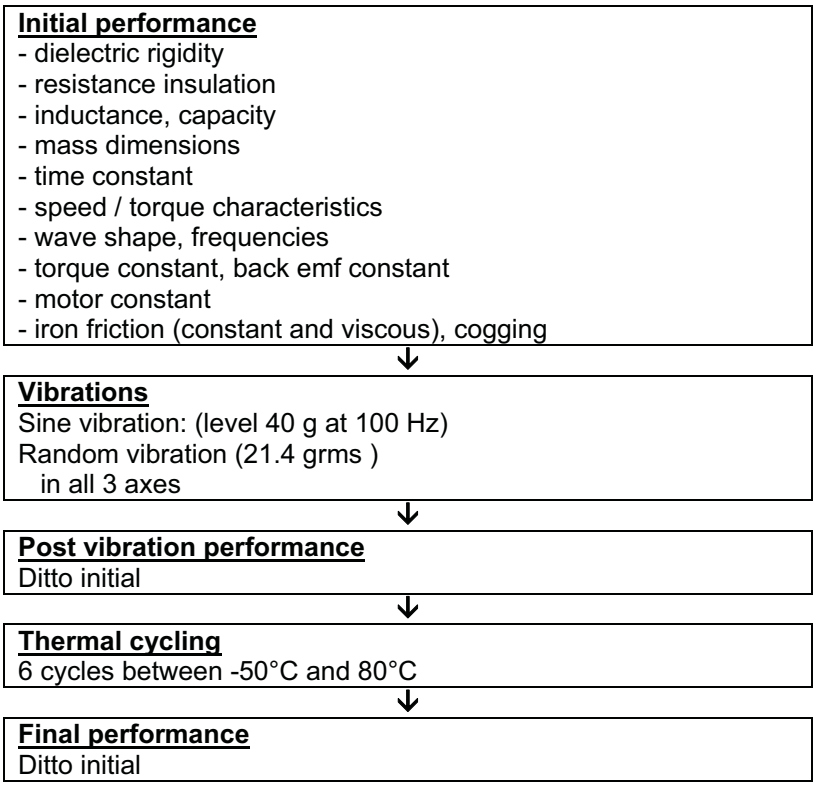

Figure 7. Test Sequence

Table 2. Stator Test Results

	Existing space stator (A)	New structurally bonded stator (B)	Variation (B) / (A)
Torque constant	4.24 Nm/A	4.27 Nm/A	+0.8 %
Back EMF constant	4.18 V/rad/s	4.24 V/rad/s	+1.4 %
Dry iron losses	0.0301 Nm	0.0158 Nm	-47.5 %
Viscous iron losses	0.0008 Nm.s/rad	0.0013 Nm.s/rad	+ 62.5 %
Cogging	0.0621 Nm	0.0257 Nm	- 58.6 %
Motor constant	0.888 Nm/√w	0.897 Nm/√w	+1 %
Mass	1820 g	1484 g	-18.5 %

It can be seen that:

- the general performance (torque constant, motor constant) is equivalent; no significant variation.
- dry friction and cogging are lower; this might be the result of better insulation between the iron sheets and to the good final geometry quality of the new bonded stator.
- drastic mass reduction, due to the suppression of the molded compound, which results from the better mechanical behavior of the structural bonding.

Conclusion

Stack structural bonding is possible using the screen printing method. The goal of this type of bonding is to rigidify stackings and improve their cohesion. Serigraphy also guarantees optimal insulation between sheets. It makes it possible to machine stacks with electro-erosion, which gives them a precise and stable geometry.

Many advantages result from this process:

- Stiffness / geometry stability → better electro-magnetic performance, less dry iron losses (around 50% of friction reduction), weak cogging (around 60% of cogging reduction).
- Rigidity /cohesion → no reinforcement: lightness (around 20% of mass reduction), compactness, reduction in number of parts, protection against delamination.
- Sustainability / reliability → constancy of performance, protection of insulating layers.

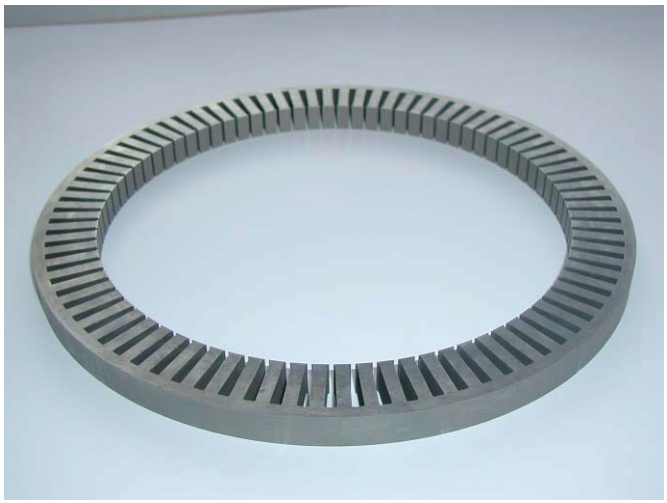

Figure 8. Thin Sheet Stacking with Structural Bonding

Process patented under patent n°: FR 2888390, EP 06778850.5

Evaluation of Perflouropolyether Lubricant Lifetime in the High Stress and High Stress-Cycle Regime for Mars Applications.

Jason Herman* and Kiel Davis*

Abstract

The successful operation of long-life, highly loaded mechanisms used for planetary exploration or autonomous structures assembly will depend upon the ability to effectively lubricate rolling-element bearings. As new tools are developed (i.e. drill, abraders, robotic manipulators, etc.) that interact with their environment in a more direct manner, lubricants will be pushed past the bounds that current scientific literature has published. This paper details results from bearing lubrication lifetime testing performed in support of Honeybee Robotics' development of the Mars Science Laboratory (MSL) Surface Removal Tool (SRT). This testing was done due to the lack of available data in research literature that is applicable to the lubrication regime the SRT bearings are being designed for. Based on the test results, the chosen bearing arrangement can be used for the SRT Grind Shaft bearings with the use of a Braycote Micronic 601EF grease-plate with a 10 vol% grease slurry fill (50/50 wt% Braycote Micronic 601EF and Brayco 815Z). This arrangement showed no signs of detrimental degradation over the course of the 3x life test. The purely grease-plated bearing ran at a consistently higher torque and showed signs of failure beginning at ~2.2 x 10^7 revs (~6.3 x 10^7 stress-cycles) with a torque over-limit failure at ~4.5 x 10^7 revs (~1.3 x 10^8 stress-cycles). Barring cold-start torque margin limitations, it is recommended that any long-life bearing application include some vol% grease-pack in addition to a standard grease-plate to reduce parasitic torque and increase bearing life. While these results are specific to a particular environment and loading condition, they demonstrate the extended capabilities of a commonly used flight lubricant outside of the range that is published in current research literature.

Introduction

In 2009, the National Aeronautics and Space Administration (NASA) plans to launch the Mars Science Laboratory (MSL) spacecraft that will include a roving vehicle and payload designed for a surface mission of one Martian year (~669 Martian sols or ~687 Earth days) at a yet to be selected landing site. During the nominal surface mission, the vehicle will be expected to traverse multiple kilometers and payload instruments and tools will be required to perform dozens and in some case hundreds of operations. The combination of MSL's mission life requirement and potentially extreme surface environment at higher latitudes is unprecedented for the Mars Exploration Program. As a quick comparison, NASA's Viking landers, Pathfinder Sojourner rover, Mars Exploration Rovers (MER) Spirit and Opportunity and the Phoenix Lander (currently en route) were all designed for surface missions of 90 sols or less. Instruments and tools of past missions were designed for dozens of hours of operation as opposed to hundreds of hours as is the case with MSL. While many of the past landed Mars missions have far exceeded their design life, the same (if not more stringent) reliability assurance requirements apply to MSL mechanism designs. At a fundamental component level, MSL's mechanism design challenges exceed those of past landed Mars missions by nearly an order of magnitude. In other words, what worked for MER will likely not work for MSL.

MSL originally planned to carry a Surface Removal Tool (SRT) as part of its payload for brushing and grinding rock surfaces in a manner similar to the MER Rock Abrasion Tool (RAT) [1]. The desired performance improvements over the MER RAT led to an increase in both grinding loads and lifetime requirements (see Table 1). Outside of designing a longer lasting grinding bit, the most significant challenge faced by the design team was to develop a drive train design that would meet the life requirements given all of the constraints. Specifically, the bearings, which supported the grinding bit shaft,

* Honeybee Robotics Spacecraft Mechanisms Corporation, New York, NY

were identified as the highest risk components as they saw the most severe combination of loading conditions and stress cycles.

Table 1: MER RAT & MSL SRT Desired Performance

	MER RAT	MSL SRT
Minimum Grinding Operations	3	> 80
Grind Area (min. diameter)	45 mm	35 mm
Grinding Bit Speed	3000 rpm	750 rpm
Grinding Bit Torque	28 mNm	140 mNm
Grinding Bit Down Force	20 N	100 N
Grinding Operation Duration (max)	3 hr	4 hr
Mass	685 grams	< 3.5x RAT
Volume	1463 cu. cm.	< 3.5x RAT
PF Min. Operating Temperature	-70 C	-135C
PF Max. Operating Temperature	+30 C	+ 70C

This paper describes the MSL SRT grinding bit bearing design and the measures taken to reduce the risk associated with this component. The early part of the SRT design phase was spent developing the grinding bit and in turn deriving requirements for the drive train components including loads, speeds, and maximum allowable size. Once these basic grinding bit bearing requirements stabilized, attention turned to selecting the specific bearing geometry, material and lubricant. After surveying the literature, consulting experts in the field and performing many analysis iterations, a final bearing design was selected. The final design featured New Hampshire Ball Bearing (NHBB) 19-mm angular contact bearings (DB configuration) made from SAE 52100 steel with cotton phenolic retainers. The bearing pair was lubricated with a combination of perflouropolyether (PFPE) based oil and grease (specifically, Castrol Brayco 815Z oil and Braycote micronic 601EF grease) – the recipe is described later in the paper. To verify the design, a test program was conducted which successfully demonstrated a 3x life capability under Mars conditions.

Bearing Design and Lubricant Selection

The SRT grinding bit bearing configuration is shown in Figure 1. When grinding, the bearing pair must react cutting forces and loads imparted at the gear mesh. Requirements analysis yielded six distinct SRT operating modes to be considered. These six modes, shown in Table 2, had varying durations, speeds and loads totaling ~20 x 10^6 bearing revolutions (~60 x 10^6 stress cycles) at 1x life. The bearing design would need to survive 3x life to pass qualification test requirements.

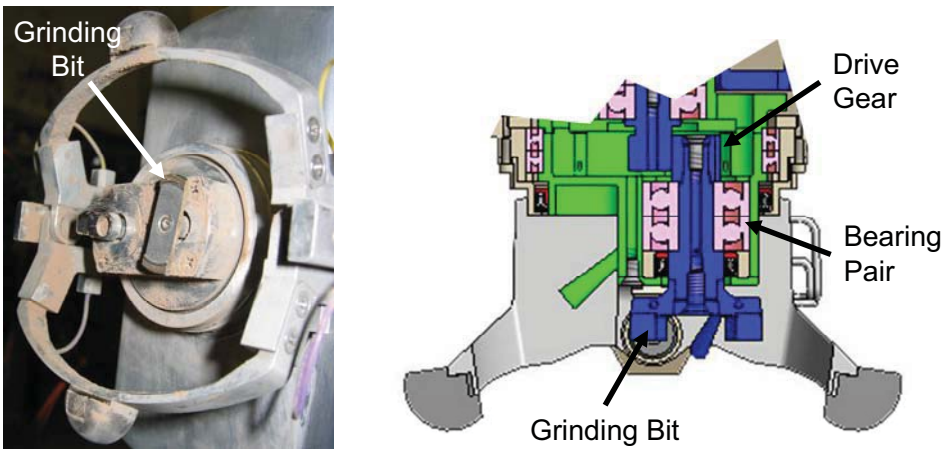

Figure 1: Grinding Bit Bearing Configuration

Grinding operations accounted for more than 75% of the bearing revolutions and early analysis using COBRA EHL indicated that mean Hertzian stress levels would approach between 1.38-2.06 GPa (200-300 ksi) during the grinding mode. While this satisfied standards for allowable bearing material contact

stress (e.g., AIAA S-114-2005), it posed a concern from a lubricant degradation perspective as the contact stress levels appeared to be beyond the published capability of viable spacecraft lubricant options.

Table 2: SRT Operating Modes

Operating Mode	3x Ops. Required	3x Life (hours)	Bit Load (N, mNm)	Bit Speed (rpm)	3x Bit Bearing Revolutions
Grinding: Difficult Rock	90	360	100, 143	750	16.2×10^6
Grinding: Medium Rock	36	144	50, 76.5	750	6.5×10^6
Grinding: Easy Rock	126	504	25, 43	750	22.8×10^6
Brushing Rock	600	150	10, 10	1500	13.5×10^6
Seek-Scan *(locates surface)*	852	85	10, 10	60	0.3×10^6
Calibration *(homes device)*	852	85	0, 0	60	0.3×10^6

The specifications for the selected grinding bit bearing are shown in Table 3. This represented the largest bearing that could be accommodated by the design. A partial ball complement was chosen over a full complement in order to keep parasitic friction as low as possible. Just as important, this bearing was available in quantity from a distributor with a lead time that met the schedule.

There was a concern that grinding chatter might damage the bearing if the balls were allowed to become unloaded during the grinding process. Thus, a 124.6 N (28 lbf) preload was selected for the duplexed (back-to-back) pair so that all balls would remain loaded under worst case grinding conditions. With this preload, analysis showed that the maximum mean contact stress in the bearing pair ranged from 1.28 GPa (during Calibration mode) to 1.59 GPa (during Grinding Difficult Rock).

Table 3: SRT Grind Bit Bearing Specifications

Specification	Value
Manufacturer	NHBB
Part Number	MER-1960SD501 DB
Type	Angular contact
Configuration	Inner-race relieved
Outer Diameter	19 mm
Inner Diameter	6 mm
Width	6 mm
Ball Diameter	3.572 mm
Ball Complement	8
Initial Contact Angle	15
Total Raceway Curvature	0.08
Tolerance Level	ABEC 7
Ball & Raceway Material	SAE 52100 Steel
Cage Type	Full-enclosed
Cage Material	Cotton-phenolic

Allowable Parasitic Torque

The total bearing drag at the beginning life was expected to be less than 14 mNm. The SRT grind actuator was sized with enough torque margin to handle parasitic drag up to 28 mNm from the grinding bit bearings during the grinding mode towards the end of life.

Lubricant Considerations

Figure 2 shows how the SRT grinding bit bearing contact stress and stress cycle requirements stack up relative to several examples of common spacecraft dry and wet lubricant performance. The chart was created using data from [2][7][8][9][10][15]. It is clear that even at 1x life and at the lower end of the contact stress range, the SRT grinding bit bearings are operating in a regime beyond the known capability of these lubricants. One caveat is that this is a two-dimensional chart that does not consider drag torque or speed. Also, in the case of the Brayco 815Z, the chart reflects testing done with 440C or 52100 steel

bearings with phenolic cages – thus Brayco 815Z performance with ceramic (S_3N_4) or ceramic coated (TiC) balls or additives, which is known to be improved, is not shown. Finally, failure criteria vary. Polymerization of the PFPE lubricant does not necessarily constitute a failure for the SRT bearings if there is an adequate reservoir for re-supply of the contact zone with unaltered oil. Likewise, with regard to the MoS_2-Ni data, a 40x increase in torque also might not constitute failure for the SRT bearings depending on the running torque at the beginning of life. It does convincingly show however, that both lubricant systems will undergo significant degradation before the SRT achieves 1x life.

The preference was to be capable of operating the SRT at -135° C without the use of heaters, although "heat-to-use" was an option. To enable operations at the cold end of the temperature range, dry-film lubricant options were considered. In addition to much lower drag at cold temperatures, other benefits of using a dry-film lubricant include negligible vapor pressure, little surface migration, and valid accelerated-life testing [4]. Specifically, the design team considered coating the balls and races with molybdenum disulfide co-sputtered with nickel (MoS_2-Ni) and replacing the phenolic retainer with one made of reinforced, MoS_2-containing PTFE (Rulon® AMR). However, MoS_2-Ni dry film coatings were ruled out for the following reasons:

- Relevant existing research indicates that SRT bearing contact stresses significantly exceed the known capability of MoS_2-Ni coatings. It seemed likely that the initial surface coating on the balls and races would quickly be worn away.
- Unlike a wet lubricant (grease), dry film coatings possess a very limited ability for lubricant replenishment in the contact zone for rolling-element bearings once the initial coating has worn away. Some replenishment may occur as wear particulate from the retainer migrates to the contact zone. By contrast, when mixed to the proper ratio, the grease thickener will not migrate excessively and over the life of the component it will slowly release oil to the contacting metal parts.

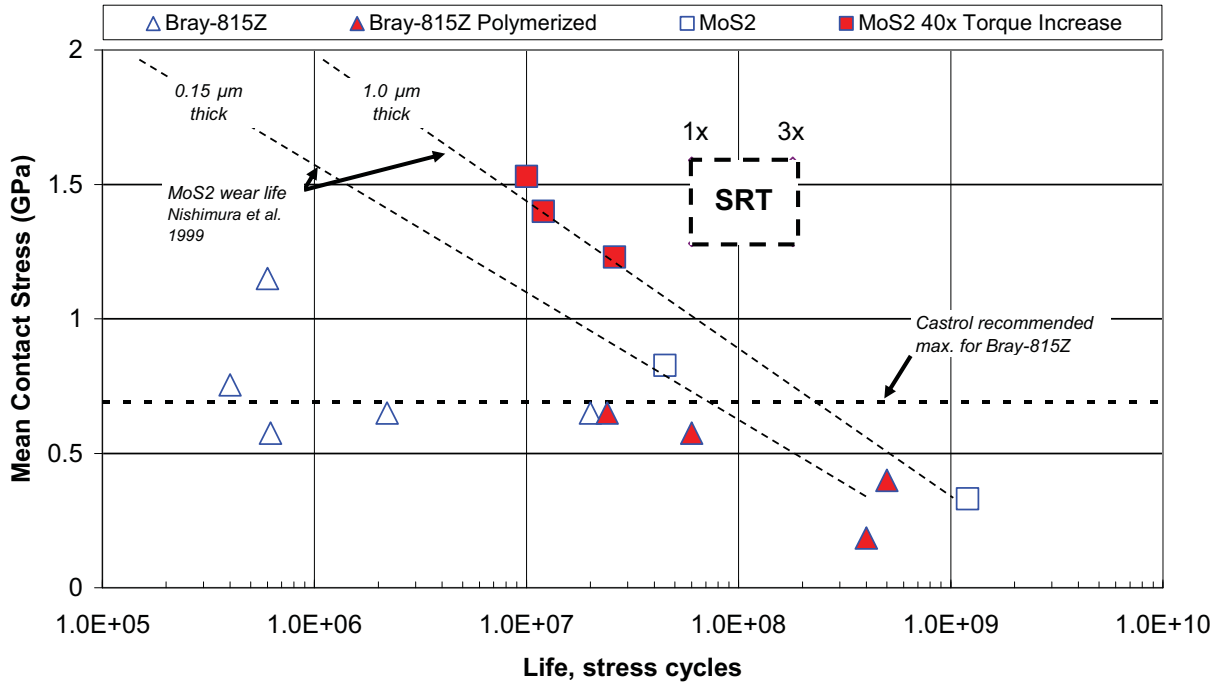

Figure 2: SRT Grind Bearing Contact Stress & Stress Cycle Requirement

For these reasons, it was decided to adopt a "heat-to-use" approach and use a wet lubricant (grease). During surface operations, heaters would warm the mechanism to -55° C if necessary before turning on the SRT actuators. However, the protoflight test program would require the mechanism to be demonstrated at -70° C. A PFPE lubricant (Brayco 815Z oil-based grease) was selected over MAC-based

or PAO-based based lubricants primarily because it offers the lowest kinematic viscosity at the cold end of the temperature range and has a comparable vapor pressure.

The well-documented Achilles' heel of PFPE lubricants is their tendency to rapidly degrade due to catalytic chemical breakdown of the oil's polymeric structure when used with common bearing materials (e.g., 440C stainless steel). All polymer molecules are subject to degradation under high mechanical shear and in a lubricant, high shear loads will act to rip apart the molecular chains. PFPE fluids react with bearing surfaces producing "a friction polymer, which, in turn, reacts with existing oxides to produce metallic fluorides [that] are effective, in situ solid lubricants, which reduce friction and prevent catastrophic surface damage" [4]. Unfortunately, these metallic fluorides act as catalysts that speed up the breakdown of PFPE oils – they are Lewis acids (electron acceptors) that catalytically attack and pull the polymer's molecular structure apart. It is the worst under boundary lubrication conditions where there is a large area of metal-on-metal contact and more of these fluorides are created. PFPE Z-fluids, which perform better at low temperatures, are even more vulnerable to this phenomenon since they possess a more linear structure (straight polymer chains as opposed to branched). To effectively inhibit the degradation of PFPE fluids one must "prevent the catalytic action of strong Lewis acids on the functional surfaces" [3]. There are two ways to reduce the catalytic action. First, one can minimize or avoid operating in a boundary contact regime by a combination of reducing contact stress, increasing operating speeds, keeping temperature down and avoiding lubricant starvation – the goal should be to guarantee the bearing will operate in a elastohydrodynamic (EHD) regime with virtually no metal-on-metal contact. The second option is to use alternative materials (e.g., ceramics, additives) that possess a lower reactivity with the PFPE fluids. However, this was not viable since the schedule could not be met.

PFPE Lubrication Evaluation

Lubrication modes include EHD, boundary contact, or the mixed regime (see Table 4). For long bearing life, especially for those lubricated with PFPE fluids, it is important that the bearing not be operated in the boundary contact regime for significant amounts of time. The SRT grinding bit bearing lubricant film parameter (Λ) was calculated using both COBRA EHL software and manual calculations to determine the operating lubrication regime [5]. Figure 3 shows the lubricant film parameter for the most severe operating mode (Grinding Difficult Rock).

Table 4: Fluid Lubrication Regimes

Lubrication Regime	Lubricant Film Parameter (Λ)
Full Separation / EHD	$\Lambda > 3.0$
Acceptable EHD	$\Lambda > 1.5$
Mixed	$1.0 < \Lambda < 1.5$
Boundary Contact	$\Lambda < 1.0$

Full ball-raceway separation occurs at $\Lambda > 3.0$; however one can assume very little asperity contact, and therefore EHD, for $\Lambda > 1.5$ [5]. As shown in Figure 3, the bearings will most likely be operating in a full EHD regime at room temperature (20° C) assuming the bearings are well lubricated. As lubricant is depleted and the contact surfaces become starved, the bearing will begin to operate in a mixed regime and ultimately boundary contact will occur. The analysis showed if the bearing was operating in a starved condition at temperatures exceeding ~20° C, there was a high likelihood of boundary contact[**].

[**] One exception was the brushing load case, which is run at 1500 rpm. The analysis showed that the bearing would operate in the EHD regime across the temperature range.

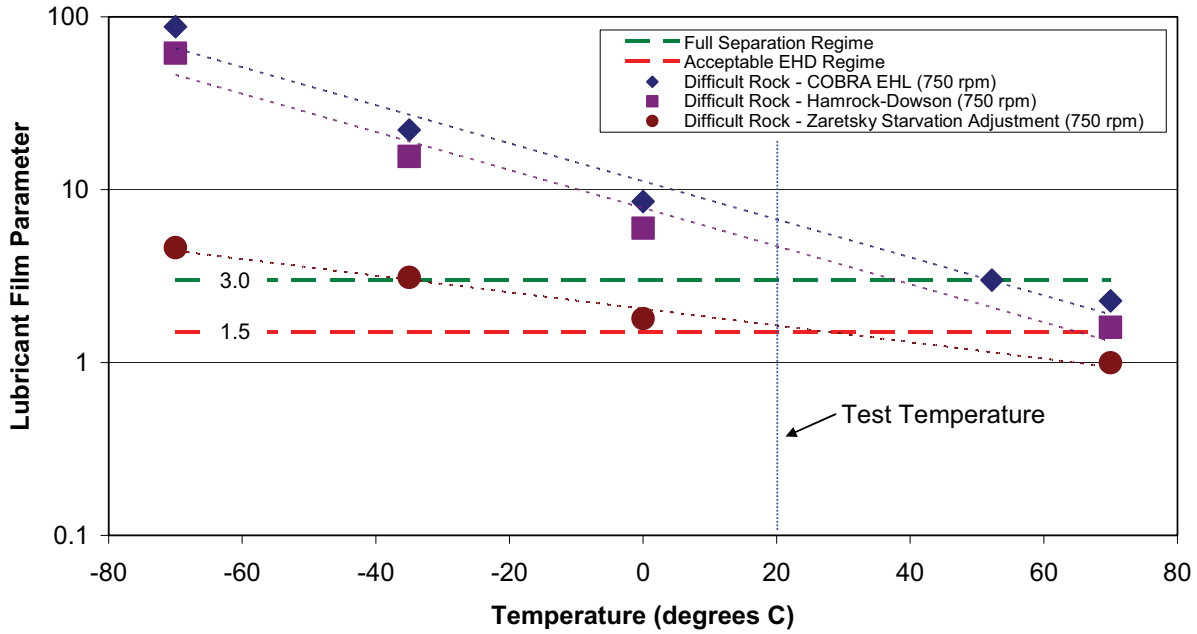

Figure 3: Lubricant Film Parameter versus Temperature

The remaining question with regard to the bearing and lubrication design was how much lubricant to use. To minimize parasitic torque, especially at temperatures less than -45° C where Brayco 815Z viscosity starts to increase dramatically, grease plating the bearings would be ideal. However, this means the bearings would likely be starved for lubricant and the analysis showed that boundary contact was extremely likely at the higher end of the temperature range. When considering that local self-heating of the bearing would elevate temperatures even more, boundary contact seemed practically guaranteed. It was decided that a verification test must be performed to demonstrate that the bearing design would survive the 3x-life requirement. Room temperature (20° C) was selected as the test temperature for convenience and because it represented a reasonable maximum ambient based on past RAT experience – very rarely was the RAT operated at ambient temperatures above 20° C. Finally, a decision was made to test two bearing sets side by side. One bearing set would be grease plated only, while the other set would be grease plated and filled to 10 vol% with a grease/oil slurry.

Experimental

Test Bearings

The NHBB bearings (MER-1960SD501 DB) used for the test were procured from a distributor, the Intercontinental Bearing & Supply Company (IBSCO). These bearings had been precision ground for a preload of 27 N (6 lb). The bearings were also lubricated with a MIL-L-6085C synthetic diester oil (Winsorlube L-245X). Several steps were necessary to make the bearings suitable for the SRT bearing life test.

First, the Winsorlube oil needed to be replaced with Brayco 815Z. IBSCO handled this process – a process they considered proprietary and certified by NHBB. Because the bearing featured a phenolic retainer, there was significant concern about the re-lubrication process. The concern stems from the fact that porous cotton phenolic retainers, if not sufficiently saturated, can absorb oil from the bearing contact zone [12][13][14]. It is evident from these reports that typical vacuum impregnation processes used in industry cannot fully saturate cotton-phenolic retainers. The retainers continue to absorb oil over the course of years until fully saturated. Furthermore, once fully saturated, there is no significant transfer of oil from the cage to a poorly lubricated raceway or ball. Therefore, it is very important to saturate the retainer with as much oil as possible to minimize the sink effect and prevent a premature starved condition. Members of the design team were permitted to witness the process and bearing mass measurements

taken at various points of the process yielded an estimated average of 19.5 mg of Brayco 815Z oil absorbed by each retainer[+]. This represented a >5 wt% increase to the retainer, which satisfies one spacecraft standard [11], and nearly 85% saturation assuming a 5% porosity.

Second, two bearing sets were grease-plated using a 10/90 wt% grease-plate solution of Braycote micronic 601EF and Fluoroclean X100. The bearings were delivered with a thin coating of Brayco 815Z and grease plating with this solution ensured that the 52100 steel components were coated with the grease's corrosion inhibiting additive (sodium nitrite). Grease plating was accomplished by pouring enough Fluoroclean X100 into a clean glass jar to fully cover a bearing. The Fluoroclean mass was recorded to allow for a calculation of the amount of Braycote Micronic 601EF to add. Once the Braycote micronic 601EF was added and mixed into solution, the grease-plate solution was ready for use. Each bearing was dipped in the solution for 5-10 seconds, placed on a Class 100 clean bench for 10-20 minutes; followed by an oven bake at 66˚C for 60 minutes. Once the bearings were cooled, they were stored until needed.

Third, one of the bearing sets was filled an additional 10 vol% with a 50/50 wt% mixture of Braycote micronic 601EF and Brayco 815Z oil. The 50/50 mixture had a lower viscosity than pure grease allowing for cold-temperature operation on Mars. A CAD model was used to estimate the empty space inside the bearing to allow for determination of the correct mass of the 50/50 slurry to add. A total of 170 mg of the slurry was added to bearing pair using a syringe.

Finally, in order to achieve the desired preload, a shim was added between the outer races of each bearing pair. To determine the proper shim thickness, measurements were made on the bearings to verify the preload deflection of the bearing pair and correlate COBRA software preload predictions.

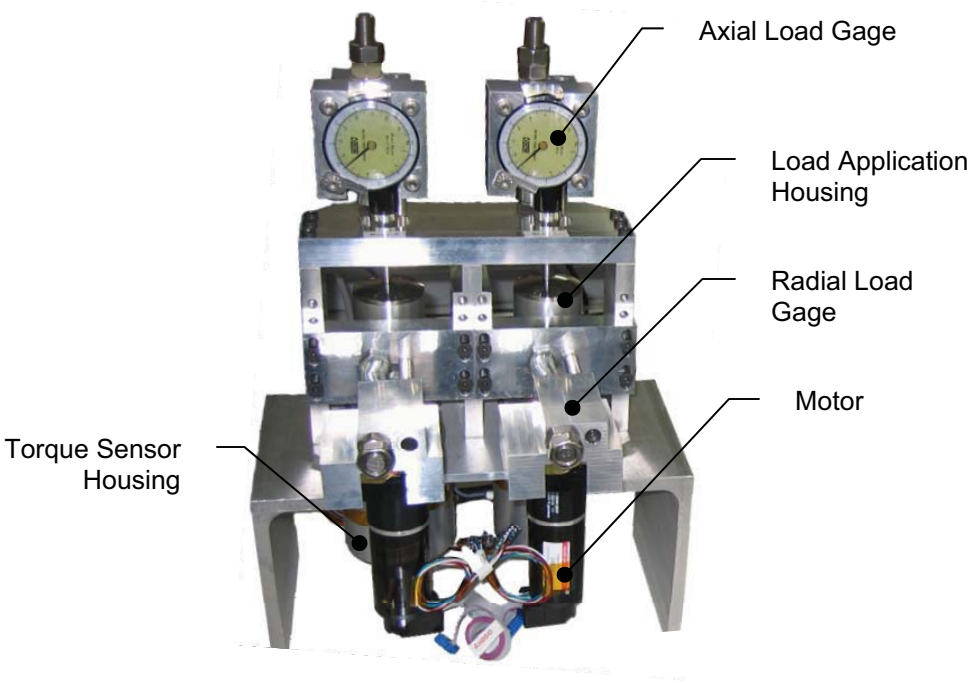

Figure 4: Bearing Test Stand

[+] Subsequent analysis performed by NASA JPL showed that some amount of the Winsorlube remained in the retainer post-processing, however the analysis procedure requires refining to determine the exact amount.

Test Apparatus

The bearing test stand (Figure 5), capable of simultaneously testing two bearing configurations, consisted of housing and shaft components for mounting and loading the test bearings, mechanical force gages, brushless DC drive motors, and torque sensors. Each test bearing set was mounted on a "non-rotating" shaft (shown in Figure 5) which was rotationally grounded through its torque sensor – in this way, the drag torque in the bearing could be directly measured. To achieve the desired combined bearing load case, independent axial and radial loads were applied to the non-rotating shaft by adjusting load screws with in-line dial force gages. The position at which the radial load was applied could be adjusted in order to achieve the desired moment. A tapered roller bearing between the load application housing and the non-rotating bearing shaft attempted to rotationally isolate the shaft from the loading gages so that bearing drag torque is reacted only by the torque sensor.

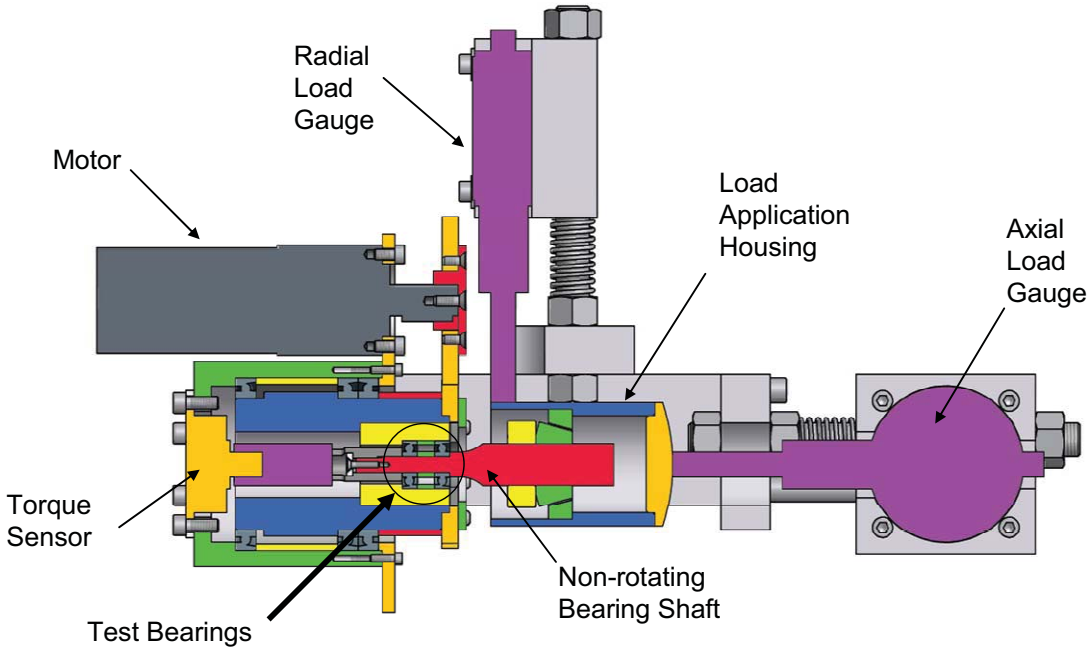

Figure 5: Bearing Test Stand Cross-Section

The entire test stand was placed in a small vacuum chamber with gas feed-thrus and an automatic control system. The controller maintained the chamber pressure at between 0.27-1.6 kPa (2-12 torr) and with each pump cycle replenished the CO_2 atmosphere by injecting a small amount of the gas.

Test Procedure

Testing was broken up into six blocks; each block representing one-half of the total required bearing life. At the conclusion of the test, three times the required life would be demonstrated. Each block was broken up into four load cases (shown in Table 5) representing expected operating conditions. This methodology allowed the various load cases to be spread across the entire life. Conducting each load case test run consisted of the following steps:

- Run 1st pre-test diagnostic to verify that test fixture was functioning properly;
- Adjust applied bearing shaft loads & configure test fixture in vacuum chamber;
- Run 2nd pre-test diagnostic to verify that loaded system was functioning properly;
- Purge (CO_2) and evacuate chamber to 0.27 kPa (2 torr);
- Run test at case loads and speed for the specified amount of time;
- Break chamber, unload bearing shaft and run post-test diagnostic to confirm that test fixture was still functioning properly.

Table 5: Four load cases run for each test block

	Load Case #1	Load Case #2	Load Case #3	Load Case #4
SRT Op. Mode	Calibrate / Seek-Scan	Brushing Rock	Grinding Easy & Medium Rocks	Grinding Difficult Rocks
Max. Mean Stress	1.28 GPa	1.28 GPa	1.39 GPa	1.59 GPa
F axial	0 N	10 N	37.5 N	100 N
F radial	6.8 N	10.9 N	27.7 N	52.3 N
Moment	0.19 Nm	0.25 Nm	0.73 Nm	1.67 Nm
Speed	220 rpm	1500 rpm	750 rpm	750 rpm
Op. Mode Duration	464 minutes	1500 minutes	6489 minutes	3600 minutes
Bearing Revs	1.02×10^5	2.25×10^6	4.87×10^6	2.7×10^6
Stress Cycles	2.97×10^5	6.52×10^6	1.41×10^7	7.82×10^6
Block N Duration	13292 minutes = 221.5 hours (or 0.5x required life)			

Results and Discussion

Data and Naming Convention

Data collected during the test included average, minimum and maximum bearing torque (torque sensor), bearing speed and motor current. Data was stored once every two minutes. The average torque was calculated from a 4 Hz buffer filled over the two-minute storage period. The minimum and maximum torque values represent the minimum and maximum torque sensor signal over that same two-minute storage period. Finally, the grease-plated bearings are designated Bearing Pair 'A' (BP-A) while the grease-plated plus grease-filled bearings are designated Bearing Pair 'B' (BP-B).

The average torque sensor data from all six blocks of the bearing lubrication life test are shown in Figure 6. Note that a single block represents 0.5x required lifetime and is approximately 9.92×10^6 revolutions (2.87×10^7 stress cycles). Other than catastrophic events, it was difficult to see gradual trends in the average torque signal for a couple reasons. First, adjusting the load case four times per test block complicates the torque signal (i.e., running torque should change with bearing load) and introduces set-up error. While the set-up procedure was consistently followed, small variations in load could produce noticeable differences in the torque sensor signal. Second, it is suspected that the tapered bearing between the load application housing and the non-rotating bearing shaft introduced a certain amount of error that varied with the load case. Friction in the tapered bearing would subtract from the amount of torque registered on the torque sensor. That being said, trend information can be seen pretty clearly by looking at the torque noise in the bearing. Torque noise is the difference between the maximum and minimum torque levels.

Bearing Pair 'A' (BP-A) – grease-plate only

From Figure 6, it is evident that over the length of the test that BP-A (blue line) ran with a higher parasitic torque than BP-B (red line). Through 2x life (3.97×10^7 revs), the average torque for BP-A was between 5 and 10 mNm. Figure 7 shows the torque noise in BP-A. After 1.1x life (2.2×10^7 revs) the noise in the bearing pair started to steadily increase. At approximately 2.3x life (~4.5×10^7 revs) there was a significant spike in the torque exceeding the 28-mNm limit that stopped the test. After increasing the limit and restarting the test, the noise and average torque continued to increase rapidly until a catastrophic torque increase stopped the test for good just before 3x life.

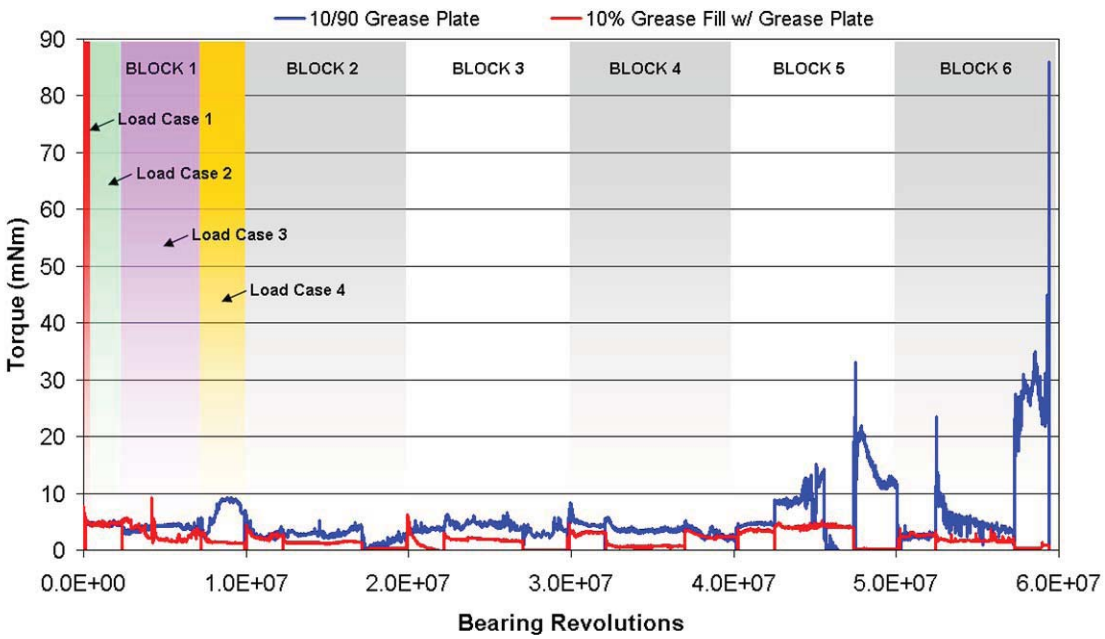

Figure 6: Bearing Life Test Data

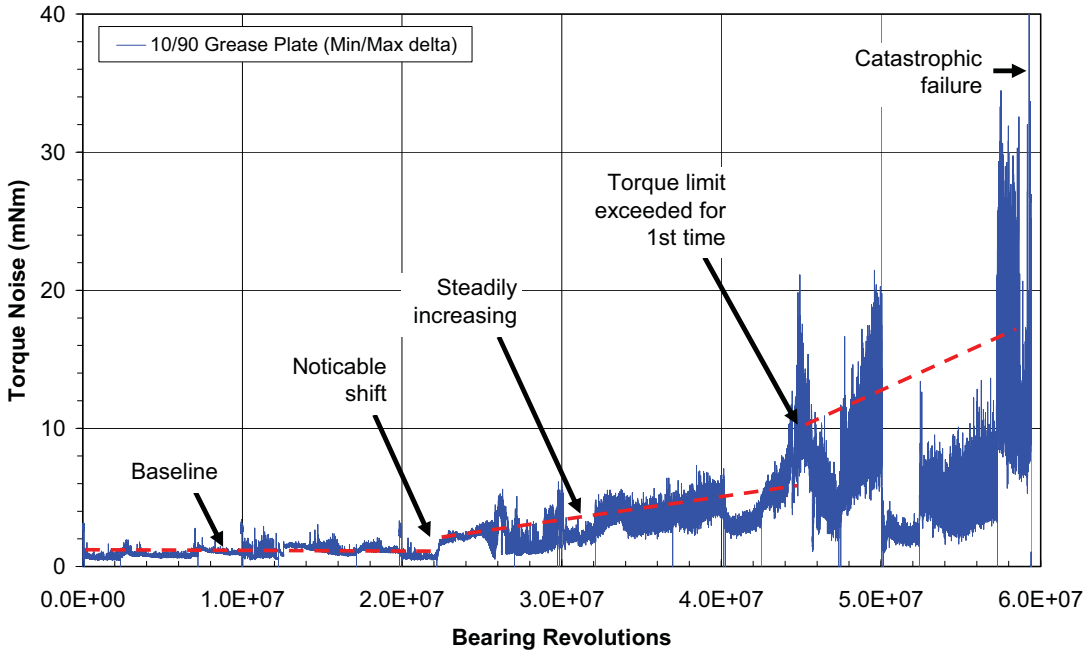

Figure 7: Torque Noise in Grease-Plated Bearing (BP-A)

Following the test, the fixture was disassembled and it was noted that BP-A was no longer preloaded even though the preload fastener was still tight – a gap of 0.64 mm was measured between the outer races. Upon removing the bearings from the fixture, the races separated with very little force – the bearing are non-separable by design. A substantial amount of brownish-black debris was present on BP-A and many of the fixture components near the torque sensor (see Figure 8). It was determined that this debris was generated by frictional wear between the stainless steel torque sensor coupling (Figure 8, right image) and the aluminum cylinder that housed the outer races of BP-A. The races of BP-A had worn so much that the non-rotating bearing shaft was permitted to cock several degrees. This allowed the

components to rub together generating debris that contaminated the bearings. Without being able to pinpoint exactly when this began, it's likely based on the torque signature that the race wear became severe enough to allow rubbing some time during Load Case 2 of Block 5 leading to the first torque over-limit event.

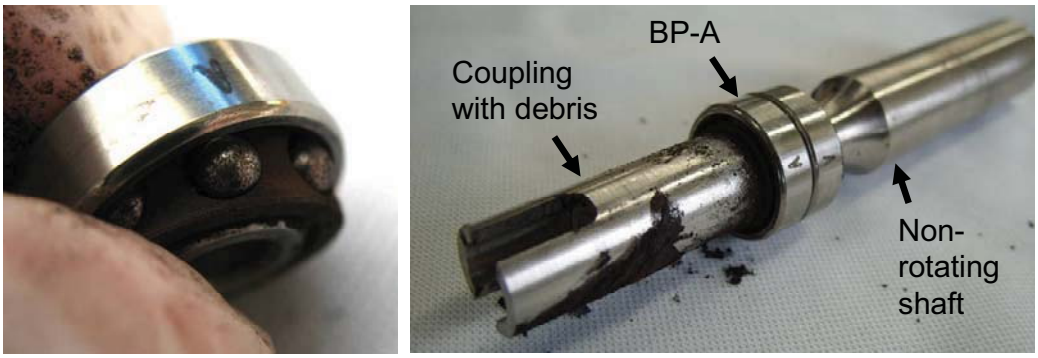

Figure 8: Post-Test BP-A (Left – hand separable bearing; Right – shaft with particulate)

Further BP-A lubricant observations were not possible due to the excessive contamination by wear particulate shown in Figure8. However, further inspection of the bearing components was conducted using a stereomicroscope. Prior to this inspection, BP-A components were soaked in methylene chloride for 90 minutes. The solution was agitated manually to aid in removing any particulate captured within the bearing cavities. Following the methylene chloride soak, the bearing components were cleaned with isopropyl alcohol and the metallic components were run through a 3-stage ultrasonic cleaning procedure. Microscopic inspection showed that noticeable wear tracks were present on both the inner and outer races (see Figure 9). Very heavy wear existed at two distinct circumferential locations on the inner race while there was more evenly distributed wear on the outer race. This was to be expected since the outer race was rotating and the inner race was stationary with respect to the applied load. With the possible exception of very minor pitting, the balls appeared to be in decent shape. The phenolic retainer also did not exhibit significant wear.

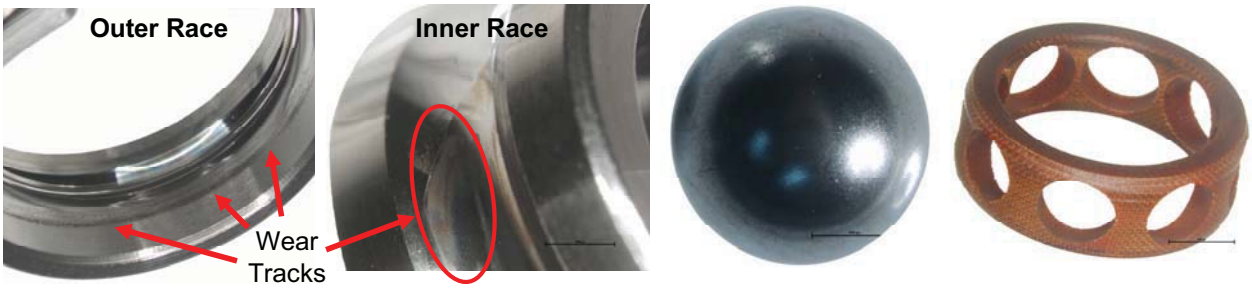

Figure 9: BP-A Components Post-Test (clean)

Bearing Pair 'B' (BP-B) – grease-plate plus 10 vol% grease fill

Through 3x life (5.96 x 10^7 revs), the average torque remained at approximately 5 mNm or less – however, it is suspected that the tapered bearing affected the torque sensor signal at the higher load cases (3 and 4). BP-B also ran much quieter than BP-A for the totality of the test with the torque noise averaging between 1-2 mNm. At 2.6x life (5.25 x 10^7 revs), the first hints of wear started to appear in the torque noise signal with the noise spiking no higher than 4 mNm.

During disassembly of the fixture to remove BP-B after the test, no noticeable axial or angular play was found in the test shaft. There was no gap between the outer races of the duplexed pair. When rotated by hand, the bearing pair ran smoothly. A visual inspection confirmed that there was still an oil-grease slurry in the bearing (Figure 10). The bearing pair was weighed before and after the test to determine the amount of lubricant lost. The total mass loss was 56 mg representing 33% of the original 170 mg of slurry

added to the bearing before the test. This loss could be due to either the migration of oil from the bearing due to surface wetting or inertial forces or could represent a mass decrease due to the catalytic degradation of the PFPE lubricant. A combination of both loss mechanisms is likely.

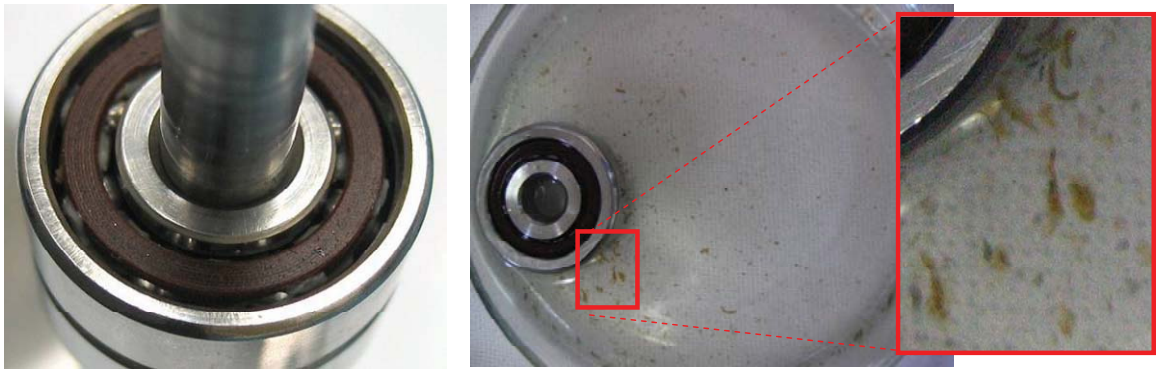

Figure 10: BP-B Bearings Post-Test (Left – Grease-fill; Right – Flouroclean X100 soak)

A single bearing from BP-B was soaked in Fluoroclean X100 for ~20 hours to remove the remaining lubricant and any wear debris internal to the bearing. Initially, a small amount of translucent brownish particulate came out of the bearing (Figure 10, right). After 20 hours, most of the particulate had broken up and dissolved. The brownish particulate (sometimes likened to "brown sugar") is a telltale sign that the PFPE lubricant was breaking down as a result of the catalytic chemical reaction [16].

Once clean, a slit was cut into the outer race to allow for disassembly. Photographs of the bearing components were taken and are shown in Figure 11. Evenly distributed wear tracks can be seen on both the inner and outer races. The inner race does show slightly heavier wear signs at a given location in a similar manner to BP-A components; however of a much lesser degree. As with BP-A, the balls and retainer did not exhibit any significant wear.

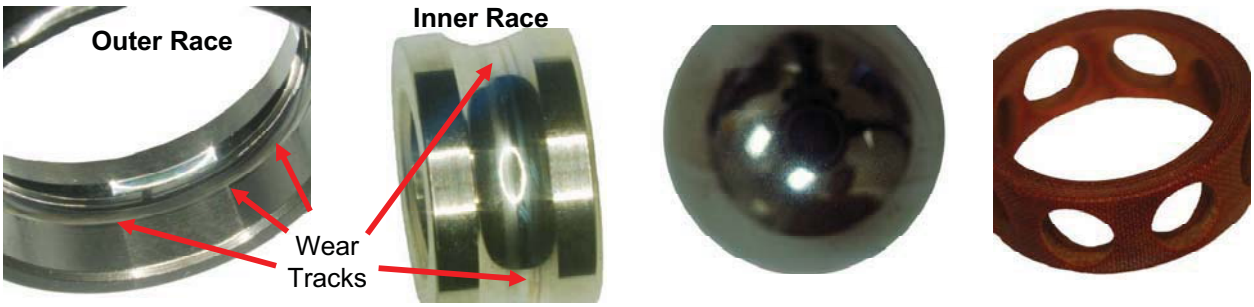

Figure 11: BP-B Components Post-Test (clean)

As shown above, bearing pair 'B' (10 vol% grease-fill) ran with a lower parasitic torque and did not display any severe signs of boundary contact type wear other than some degradation of the lubricant (brown sugar). This is due to the lack of a starved condition which kept $\Lambda > 1.5$ and allowed operation in the EHD regime. Bearing pair 'A' (grease-plate only) shows intermittent increases in parasitic torque anywhere from two to six times nominal operating torque. These torque anomalies are followed by a sudden drop back down to nominal torque values. As the test progressed, these anomalies increase in frequency and severity. A similar torque signature has been documented previously and was characterized by significant wear patterns at the ball-cage and raceway-cage interfaces [6]. Also noted in [6], is that the cause of this type of failure is oil starvation and injection of additional oil during these events caused a decrease in parasitic torque to nominal levels.

Conclusions

Based on the test results discussed above, the chosen bearing arrangement with the use of a Braycote micronic 601EF grease-plate with a 10 vol% grease slurry fill (50/50 wt% Braycote micronic 601EF grease and Brayco 815Z oil) meets the SRT grinding bit shaft 3x life requirement (~6 x 10^7 revs or 1.73 x 10^8 stress cycles). This arrangement showed minimal signs of degradation over the course of the life test. In contrast, the purely grease-plated bearing does not meet the requirement. The purely grease-plated bearing ran at a consistently higher torque and showed signs of failure beginning at ~2.2 x 10^7 revs (~6.3 x 10^7 stress-cycles) with a torque over-limit failure at ~4.5 x 10^7 revs (~1.3 x 10^8 stress-cycles). Barring cold-start torque margin limitations, it is recommended that any long-life bearing application include some vol% grease-pack in addition to a standard grease-plate to reduce parasitic torque and increase bearing life.

PFPE lubricants, such as Brayco 815Z oil, can be used in the high stress, high stress-cycle regime depending on the application. In the case of mechanisms that have sufficient torque margin, PFPE lubricants can be pushed beyond the currently documented allowable stress conditions. More research is necessary in the field of PFPE lubrication for space and planetary exploration applications where mechanisms tend to be less about precision and more about ruggedness. Data does exist; however test conditions and geometry are not always well documented and many test results are applicable only to Hertzian stress levels below 0.69 GPa. There exist many possibilities to further the abilities of PFPE lubricants and bearing life in general, including the use of hybrid bearings or specialty steels. Carefully documented research will be paramount to future exploration missions that require long life for tools such as abraders, drills and other rugged mechanisms that may operate continuously under high loads.

Acknowledgements

The authors would like to thank all of the SRT program technicians, machinists, designers, engineers and managers at Honeybee Robotics and JPL for their commitment to developing this device. Specifically, the authors would like to thank Mark Balzer of JPL and Jeff Lince of the Aerospace Corporation for their time and technical insights.

This work was performed under a contract with Jet Propulsion Laboratory, California Institute of Technology, for the National Aeronautics and Space Administration. References herein to any specific commercial product, process or service by trade name, trademark, manufacturer, or otherwise does not constitute or imply its endorsement by the United States Government or the Jet Propulsion Laboratory.

References

[1] NASA's Mars Exploration Program. 09 Oct. 2007. NASA. 09 Oct. 2007 <http://mars.jpl.nasa.gov/>

[2] Lince, Jeff. Aerospace Corp. Teleconference. March 2007.

[3] Conley, P. L. and J. J. Bohner, "Experience With Synthetic Fluorinated Fluid Lubricants", *Proc. 24th Aerospace Mechanisms Symp.*, NASA CP-3062, 1990.

[4] Jones, W. R., and M. J. Jansen, "Lubrication for Space Applications", NASA Glenn Research Center, NASA CR-2005-213424, 2005.

[5] Tribology for Aerospace Applications. Ed. E. V. Zaretsky, Illinois: STLE, 1997.

[6] Fleischauer, P. D., "Tribology in the Space Environment", Aerospace Corp., El Segundo, CA, Report No. TR-97(8570)-2, 1997.

[7] Suzuki, M. and M. Nishimura, "Tribological characteristics of ball bearings lubricated with a sputtered molybdenum disulphide film in a vacuum under a high thrust load", Proc. 5th European Space

Mechanisms and Tribology Symposium, ESTEC, Noordwijk, The Netherlands, 28-30 October 1992 (ESA SP-334, April 1993)

[8] Nishimura, M. and M. Suzuki, “Tribological characteristics of solid-lubricated ball bearings operated for 10,000 hours in a vacuum”, Japanese Journal of Tribology, 43(3) (1998) 361-374.

[9] Loewenthal, S. H., R.G. Chou, G. B. Hopple, and W. L. Winger, “Evaluation of Ion-Sputtered Molybdenum Disulfide Bearings for Spacecraft Gimbals”, Tribology Trans., 37(3) (1994) 505-515.

[10] am_Braycote_601_EF_Mic_USA_English_pds.pdf, <http://www.castrol.com>

[11] “The oil impregnation of phenolic resin based materials used in the fabrication of ball-bearing cages”, ESA PSS-01-712

[12] Bertrand, P. A. “Coray 100 Oil Absorption into Cotton-Phenolic Ball-Bearing Retainers”, Aerospace Corp., El Segundo, CA, Report No. TOR-0091(9975)-4

[13] Bertrand, P. A. “Oil absorption into cotton-phenolic material”, Materials Research Society Vol. 8 No. 7, Jul. 1993, Aerospace Corp., El Segundo, CA.

[14] Bertrand, Carre and Bauer, Aerospace Corp, TR-94, “Oil Exchange Between Ball Bearings and Cotton-Phenolic Ball-Bearing Retainers”

[15] Nishimura, M. and M. Suzuki, “Solid-lubricated ball bearings for use in a vacuum”, Tribology International 32 (1999) 637-647.

[16] Space Mechanisms Lessons Learned Study. 07 Jan. 2008. NASA. 18 Dec. 2007. <http://www.lerc.nasa.gov/WWW/spacemech/vol1.html>

Mars Science Laboratory Rover Mobility Bushing Development

Benjamin Riggs*

Abstract

NASA's Mars Science Laboratory (MSL) Project will send a six-wheeled rover to Mars in 2009. The rover will carry a scientific payload designed to search for organic molecules on the Martian surface during its primary mission. This paper describes the development and testing of a bonded film lubricated bushing system to be used in the mobility system of the rover.

Introduction

The MSL Rover Mobility System contains several pivots that are tightly constrained with respect to mass and volume. These pivots are also exposed to relatively low temperatures (-135°C) during operation. The combination of these constraints led the mobility team to consider the use of solid film lubricated metallic bushings and dry running polymeric bushings in several flight pivot applications.

A test program was developed to mitigate the risk associated with using these materials in critical pivots on the MSL vehicle. The program was designed to characterize bushing friction and wear performance over the expected operational temperature range (-135°C to +70°C). Seven different bushing material / lubricant combinations were evaluated to aid in the selection of the final flight pivot bushing material / lubricant combination.

Background

The mobility team recognized during the rover preliminary design phase that the large size and mass of the new vehicle required a fresh look at the design approach for many of its pivots. The rover required pivots that could tolerate intermittent, low speed (<2.5 rpm) dithering motion at operational temperatures that precluded the use of wet lubricants. After an extensive trade study that assessed mass, complexity and volumetric efficiency the team decided to pursue main pivots based on primarily on flanged bushings. Flanged bushings provided a simple, robust, mass-effective solution to the design challenges associated with the highly loaded main mobility pivots.

With the general design approach selected the team accelerated its search for viable material/lubrication options for the bushings. A large number of material and lubrication options were considered for use in the pivots including various bronze bushing alloys, zinc aluminum, polymeric materials, and coated stainless steel. Although a number of these materials had merit the team selected coated, gall-resistant stainless steel bushings for the initial test series on the basis of compressive strength, gall resistance in the event of lubricant failure and published coated coefficient of friction information. Isolating a bushing material also allowed for a manageable set of bushing material, mating surface and lubricant combinations during testing. Three candidate bonded film lubricants with inorganic binders were selected to coat the stainless steel bushings during the initial test series.

Testing

The unproven combination of bonded film lubricants and bushing materials in the rover mobility pivots required testing to enable their use on the flight vehicle. Friction and wear performance data was also desired to enable more accurate modeling of the pivots in dynamic simulations. These factors led the design team to plan a multiphase test series to select a final bonded film lubricant and characterize the friction and wear performance of the bushings over the pivot operational temperature range.

* Jet Propulsion Laboratory/California Institute of Technology, Pasadena, CA

Phase One: Initial Ring on Cylinder Testing

Since the second phase of the test series involved a relatively complex, flight-like pivot and test apparatus there was a desire to "start simple" and get some initial data on the candidate bonded film / bushing systems before resources were committed to the more elaborate, follow-on setup. Due to looming review dates and a desire to get the initial test series completed quickly the team investigated various bushing test resources at other facilities. Fortunately a preexisting developmental bushing test setup at NASA/Glenn Research Center (GRC) was located that could be slightly modified to complete the desired initial testing of the bushing / lubricant systems. The GRC team quickly reconfigured their setup and test samples were fabricated so that testing could begin.

The testing consisted of loading PTFE infused hard anodized 7075 rings & PTFE infused Ti6Al4V rings against various bonded film coated stainless steel shafts to produce a projected bearing stress of approximately 6895 kPa (1000 psi). The test fixture rotated the coated shaft against the ring in a constant dithering motion of ±2 degrees. Testing was performed in lab air at 40% relative humidity for the first 69 cycles then in a CO_2 purged glove box for the remainder of the 4200 total cycles (all at 23°C). Friction torque was measured throughout the test so that coefficient of friction values could be calculated at the completion of testing. Three samples of each material combination were tested during the series. The summarized results of the GRC test series are listed in Table 1 [1].

Table 1: Phase One Bushing Test Results

Ring Material	Shaft Material / Coating	Mean Coefficient of Friction for 3 Tests
Al 7075-T7351 with PTFE hard anodized coating	Stainless steel coated with MoS_2 based bonded film lubricant with "phosphate-like" binder	0.084 std dev 0.028
Al 7075-T7351 with PTFE hard anodized coating	Stainless steel coated with PTFE based bonded film lubricant with "phosphate-like" binder	0.120 std dev 0.020
Al 7075-T7351 with PTFE hard anodized coating	Stainless steel coated with MoS_2 based bonded film lubricant with silicate binder	0.139 std dev 0.054
Ti6Al4V with PTFE anodic coating	Stainless steel coated with MoS_2 based bonded film lubricant with "phosphate-like" binder	0.070 std dev 0.031
Ti6Al4V with PTFE anodic coating	Stainless steel coated with PTFE based bonded film lubricant with "phosphate-like" binder	0.194 std dev 0.047
Ti6Al4V with PTFE anodic coating	Stainless steel coated with MoS_2 based bonded film lubricant with silicate binder	0.145 std dev 0.005
Al 7075-T7351 with PTFE hard anodized coating	Bare stainless steel	0.266 std dev 0.070
Ti6Al4V with PTFE anodic coating	Bare stainless steel	0.212 std dev 0.048

Phase Two: Application Specific Bushing Testing

Phase Two of the Bushing Test Series was designed to characterize bushing friction and wear behavior in a flight-like pivot assembly over the expected mobility operational temperature range (-135°C to +70°C). Several different bushing materials and coatings were tested during this test series to allow the team to select the best combination for the flight mobility pivots based on data from a representative pivot.

Test Setup

The bushing test hardware was designed to mimic a portion of the MSL Rover's Main Differential Pivot (MDP). The flight pivot assembly is comprised of two flanged bushings located between a central pivot shaft and a hollow cylindrical housing (Figure 2). In the test assembly (Figures 1 & 3) the central pivot shaft was attached to a fixture comprised of an aluminum block, several C-channel sections and a baseplate. The cylindrical housing was attached to a driveshaft driven by a motion controlled DC servomotor through several flexible shaft couplings and a torquemeter. This torquemeter was used to measure the friction torque generated in the pivot assembly during testing.

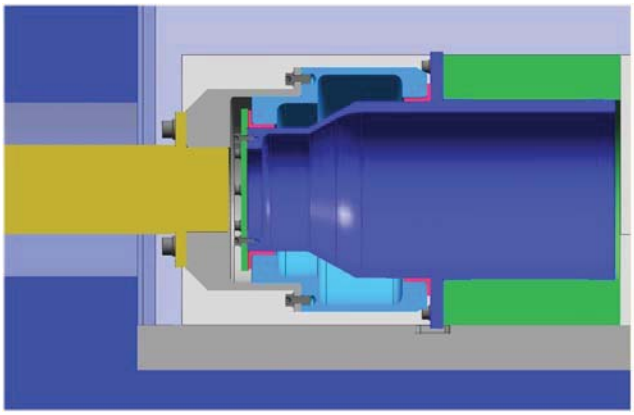

Figure 1: Test Assembly

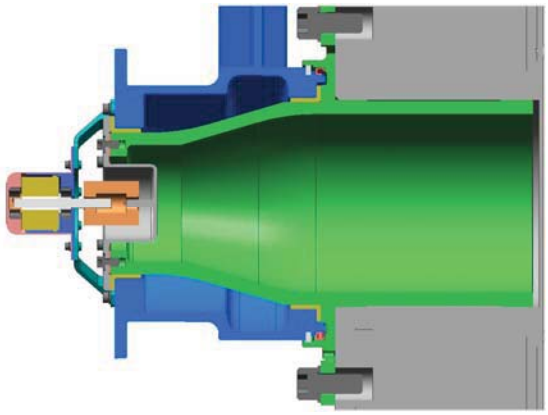

Figure 2: Flight MDP Assembly

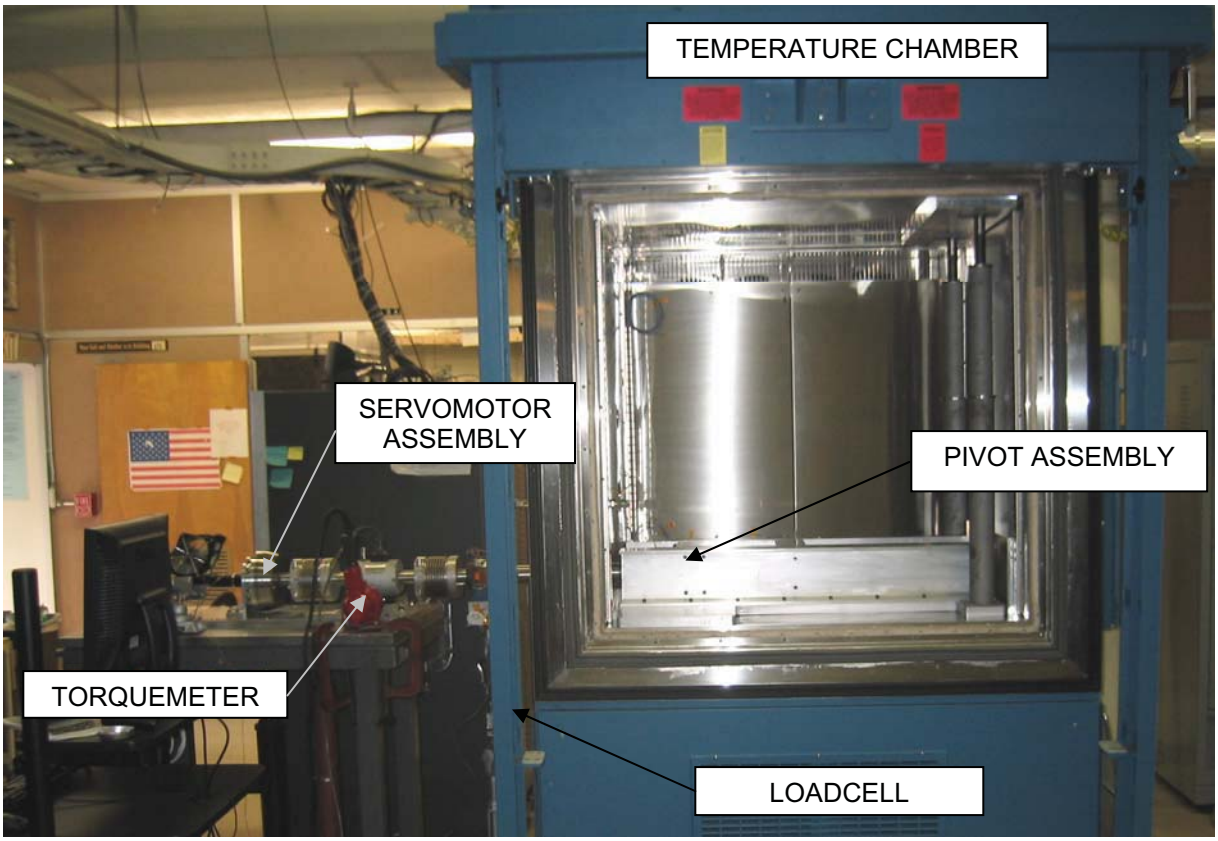

Figure 3: Bushing Test Hardware in Temperature Chamber

A pillow block assembly, turnbuckle, and grounded load cell string were attached to the driveshaft to apply a known moment on the pivot assembly during testing. This known moment produced reaction loads on the bushings roughly equivalent to those expected during vehicle traverse on Mars.

The DC servomotor rotated the driveshaft and cylindrical housing through a specific dithering angular motion profile during bushing testing. This motion profile was developed to replicate the oscillating motion of the Flight Main Differential Pivot.

The pivot assembly, comprised of the bushing pair, central pivot shaft and cylindrical housing, was mounted inside a temperature chamber that was used to drive the assembly through a specific temperature profile. The chamber also provided a humidity-controlled, dry nitrogen environment throughout testing. During test planning the option of testing in a CO_2 environment was discussed. Although the CO_2 environment would have been preferred as the Martian atmosphere is predominantly CO_2, the cost and schedule impact associated with that testing was prohibitive. The team also felt that testing in dry Nitrogen would yield acceptable results based on test data from the Phase One Testing at GRC.

Bushing Material / Lubrication Description

Seven different bushing material / bushing lubricant combinations were evaluated as part of the test series. Two MoS_2-based bonded film lubricants were selected for the test series, a bonded film with a "phosphate-like" binder and a bonded film with a silicate binder. These lubricants were coupled a stainless steel alloy based on its anti-galling characteristics in the event of coating failure. Polyamide-imide and polyimide samples were added to the test series after initial testing of the first bonded film sample revealed less than ideal bushing wear behavior. These two polymeric bushing materials were selected based on their suitability for the low temperature, dry running flight pivot environments.

All bushing samples were run against either 7075-T7351 Aluminum or Ti6Al4V shafts and housings that matched potential flight pivot materials. The aluminum shafts and housings were coated with a PTFE infused hard anodized coating. All titanium parts were coated with a PTFE infused anodic coating. Both of these coatings were applied to provide a hard, low friction, wear resistant bearing surface. Table 2 summarizes the bushing material and lubricants used for each test in the series:

Table 2: Phase Two Testing Material Matrix

Test Date	Housing & Shaft Material	Bushing Material	Bushing Coating
6/29/06	Al 7075-T7351 with PTFE infused hard anodized coating	Stainless steel	MoS_2 based bonded film lubricant with silicate binder
9/18/06	Al 7075-T7351 with PTFE infused hard anodized coating	Stainless steel	MoS_2 based bonded film lubricant with "phosphate-like" binder
9/25/06	Al 7075-T7351 with PTFE infused hard anodized coating	Polyamide-imide	None
10/24/06	Al 7075-T7351 with PTFE infused hard anodized coating	Polyimide	None
12/12/06	Al 7075-T7351 with PTFE infused hard anodized coating	Polyamide-imide	Braycote 601 Greaseplate
1/29/07	Ti6Al4V with PTFE infused anodic coating	Stainless steel	MoS_2 based bonded film lubricant with "phosphate-like" binder
2/7/07	Al 7075-T7351 with PTFE infused hard anodized coating	Stainless steel	None

Test Temperature / Cycling Profile

The bushing test temperature profile was generated to provide friction torque data throughout the expected pivot operational temperature range with an emphasis on the low side of range. The low temperature bias was selected as overall bushing clearance variances were most extreme at the low end of the temperature range. Also, low temperature friction and wear data for the bonded films and polymeric materials tested was very limited. The bushing test temperature profile and bushing test temperature/dither summary are listed in Table 3.

Table 3: Phase Two Bushing Testing Dither Cycle / Temperature Profile

Number of Dither Cycles	Temperature	Comments
10	+23°C	Initial check out, chamber door open
200	+23°C	Chamber door closed, N2 purge on
30	+47°C	
30	+70°C	
30	+47°C	
30	+23°C	
30	-9°C	
30	-43°C	
30	-73°C	
30	-105°C	
20	-120°C	Cycles added to prevent ice formation on feedthru
10	-130°C	Cycles added to prevent ice formation on feedthru
4720	-135°C	
30	-105°C	
30	-73°C	
30	-41°C	
30	-9°C	
200	+23°C	

Dither Cycling Profile

The dithering motion profile run during the bushing testing was formulated based on the output of Matlab code written by Jaime Waydo [2]. Her *Dither Analysis Code* calculated the main pivot (differential) dither angles produced by rock encounters during a simulated 60-kilometer vehicle traverse in a 20% rock field. The code output dither angle amplitude events for the 60-km traverse as shown in Table 4.

Table 4: Dither Event Count for 60 km Vehicle Traverse in 20% Rock Field

Main Pivot Dither Angle (θ) Range	Number of events for 60 km traverse	% of Total
θ < 5 degrees	3252	78%
5 degrees < θ < 15 degrees	450	11%
15 deg < θ < 20+ degrees	439	11%

Based on this output a simplified test dither cycle profile was formulated. The profile was based on three distinct dither amplitude cycles, a small angle cycle (±2 degrees), a medium angle cycle (±10 degrees) and a large angle cycle (±20 degrees). When these groupings were mapped to the frequencies generated by the Matlab code the following profile was developed. A 10-cycle set started with a ±20-

degree dither cycle followed by four ±2-degrees dither cycles, one ±10-degree dither cycle, and finally four more ±2-degrees dither cycles. The final test dither cycle profile is plotted in Figure 4

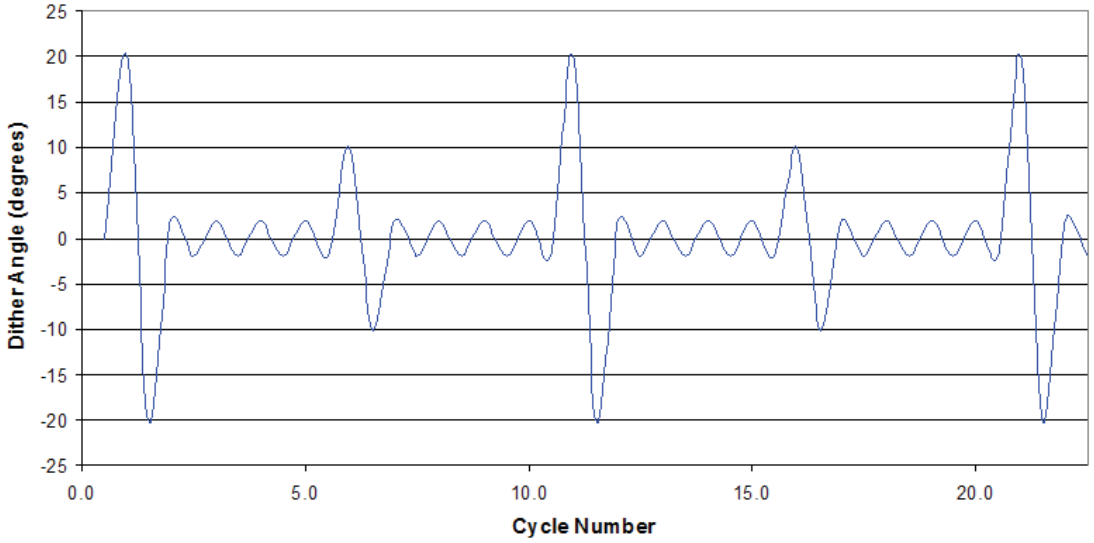

Figure 4: Bushing Test Dither Cycling Profile

This dither cycle profile was repeated until the total number of cycles planned at each temperature target was reached and the drive assembly was paused. The total number of dither cycles run for each test was based on a 60 kilometer total scaled to 80 kilometers (or four times the current 20-km mission traverse distance requirement). This scaling yielded a total bushing test dither cycle number of 5520 (for a 4x test).

The maximum angular rate of the servomotor output was set to 2.5 RPM for the duration of the dither testing. This angular rate was selected based on a combination of actuator/torque capabilities and expected maximum differential articulation rates during traverse.

Bushing Loading

The radial loads placed on the test bushings were intended to replicate a subset of those imparted on the flight MDP bushings during the primary mission of the vehicle. Dynamic loading of the bushings due to the touchdown or multi-wheel drops during traverse was not factored into the load calculations for the test bushings. Only the six wheels flat, 1G, 30 deg vehicle roll Adams model output values scaled to 3/8g equivalent loading were used to determine the target loading for bushing testing. The flight bushing radial loads and test loads are listed in Table 5. Also listed is the average bearing stress on the bushings due to radial loading and approximate contact stress values based on formulas from Roark's Formulas for Stress and Strain [3].

Table 5: Bushing Loading Summary

Bushing Location	Radial Bushing Load (N)	Average Bearing Stress (kPa)	Contact Stress (kPa)
MDP Inboard Bushing	5383	3.6 (0.520 ksi)	14.5 (2.1 ksi)
Test Inboard Bushing	6427	4.3 (0.622 ksi)	15.9 (2.3 ksi)
MDP Outboard Bushing	5127	4.9 (0.708 ksi)	17.9 (2.6 ksi)
Test Outboard Bushing	5267	5.0 (0.727 ksi)	18.6 (2.7 ksi)

The loading method employed in the bushing test setup did not allow the applied radial load to be matched for both the inboard and outboard bushing. As such the loading in the inboard test bushing was slightly higher than the target flight MDP inboard bushing radial load.

Although the moment-carrying load path for the flanged bushing pair was assumed to be purely radial for the loading calculations listed in Table 5, actual bushing loading in the test assembly proved that this assumption was at least partly flawed. The most significant bushing wear in the initial tests was on the edge of the thrust face of the bushing indicating that at least part of the moment applied to the test setup was being reacted out on the thrust faces of the bushings. This result was not altogether unexpected as the test pivot assembly geometry does have a redundant moment carrying capability through the thrust faces of the bushings. The radial gaps in the pivot required due to dissimilar coefficient of thermal expansion values between the gall resistant stainless steel bushing material and the pivot structure allowed this redundant load path to be possible. Although the loading produced in test setup is still thought to be representative of the flight environment, exact contact stress value determination for the bushings was significantly complicated by this non-ideal loading. If this tribological combination is selected for future designs careful thought should be employed to produce at design with a more tightly constrained load path.

Results

Friction Torque

The friction torque measurements obtained during the bushing test series are plotted in Figures 5 through 11. Housing temperature (shown in red) during the measurements was also plotted on a secondary axis for reference. Each plot was generated with the same scale on the X and Y axes to permit a quick visual comparison of the friction torque profile for each test.

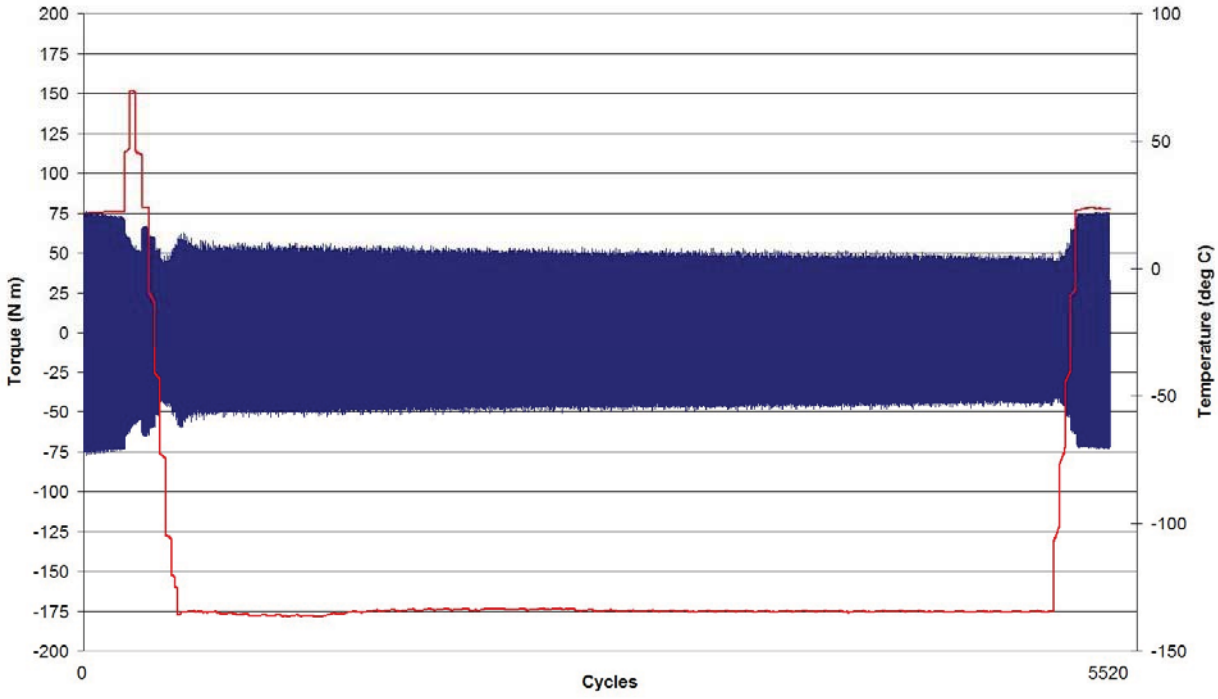

Figure 5: Friction Torque Plot
"Phosphate-like" Binder MoS_2 Bonded Film Coated Bushings vs. Anodized Aluminum)

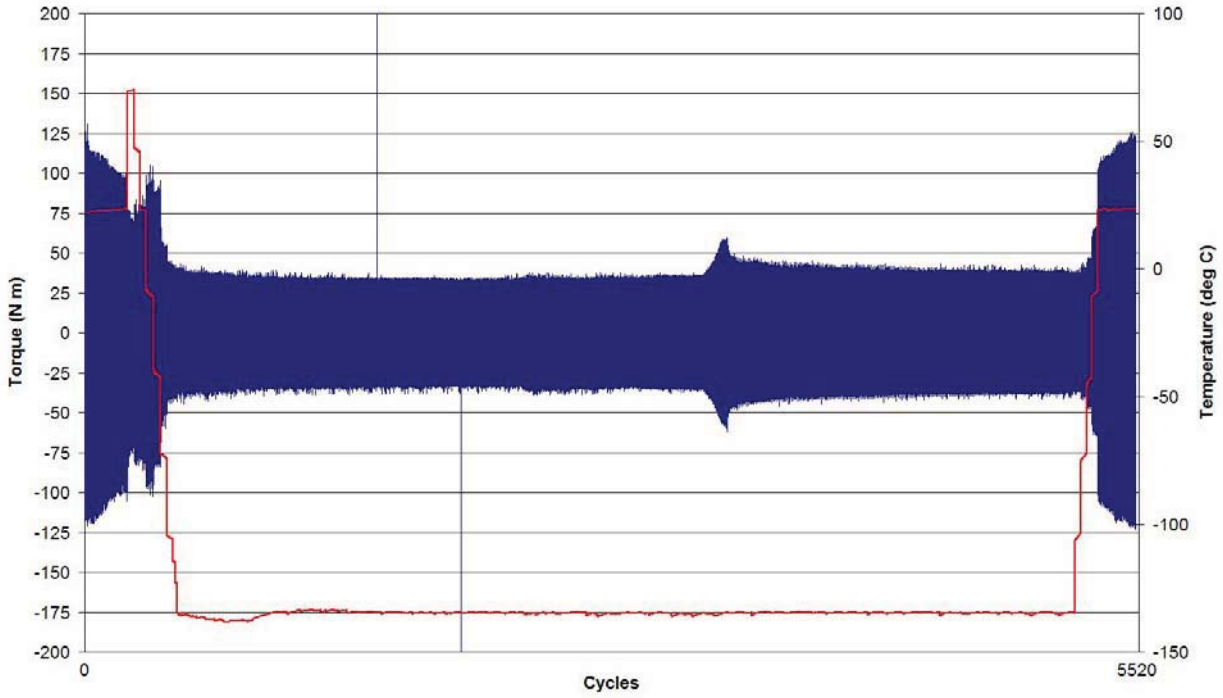

Figure 6: Friction Torque Plot
Silicate Binder MoS_2 Bonded Film Coated Bushings vs. Anodized Aluminum)

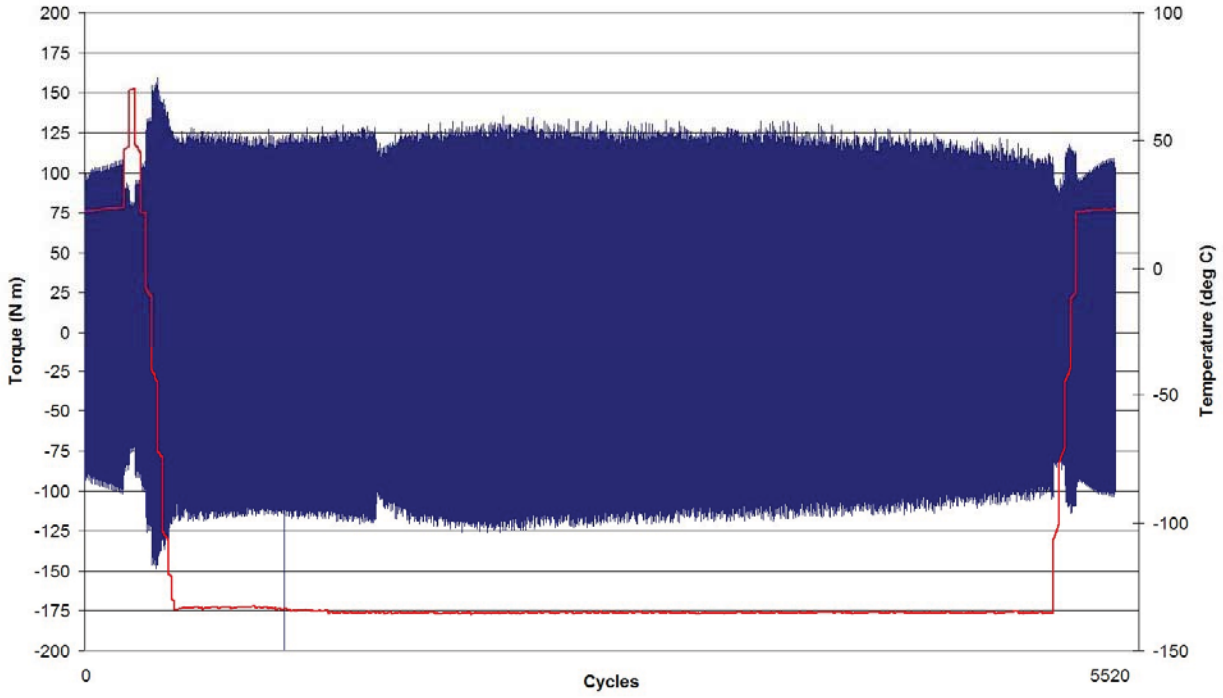

Figure 7: Friction Torque Plot
Polyamide-imide Bushings vs. Anodized Aluminum

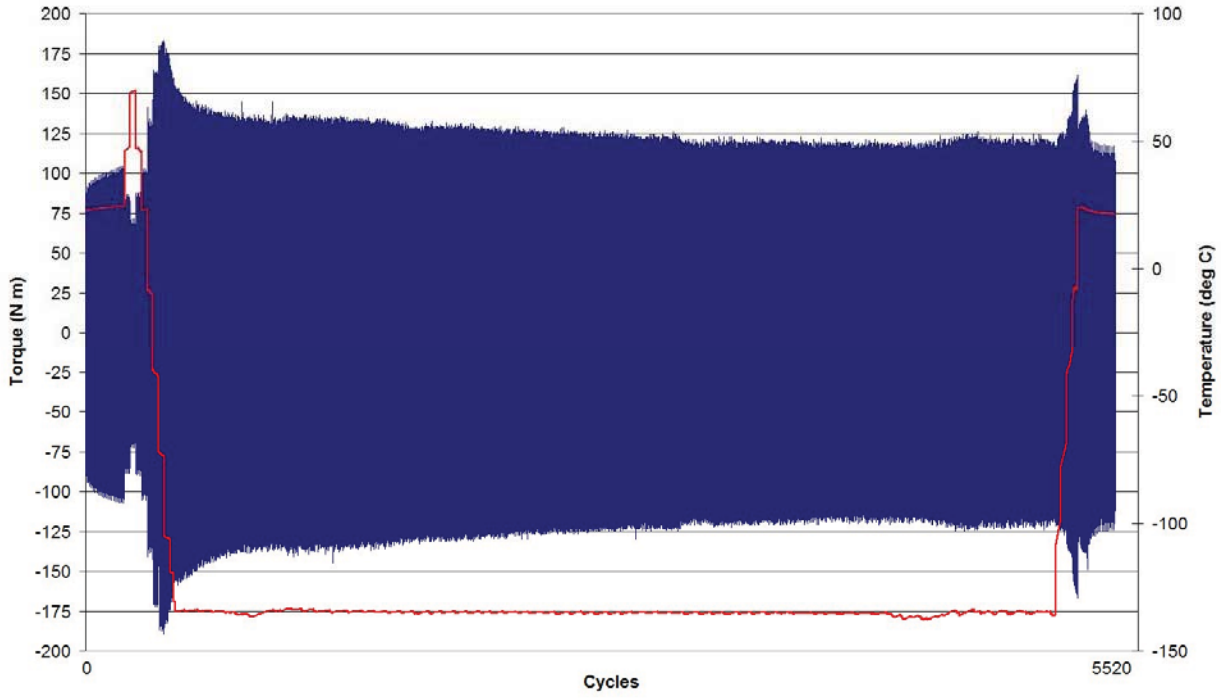

Figure 8: Friction Torque Plot
Polyimide Bushings vs. Anodized Aluminum

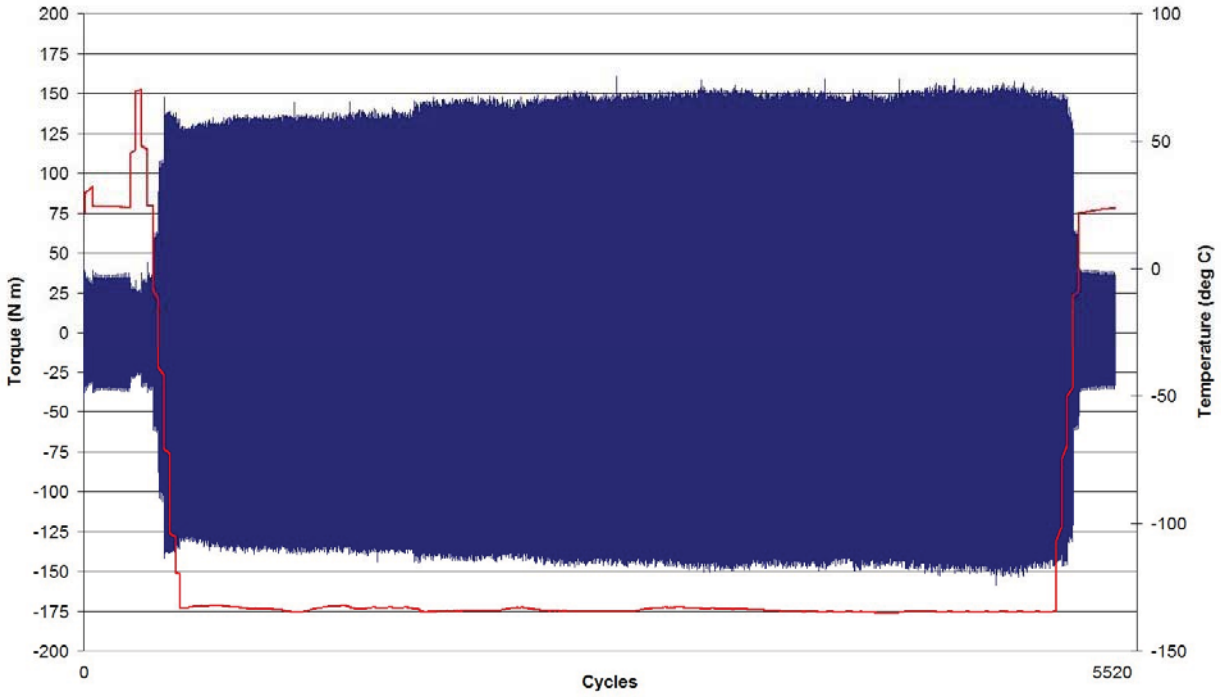

Figure 9: Friction Torque Plot
Polyamide-imide Bushings Greaseplated w/ Bray 601 vs. Anodized Aluminum

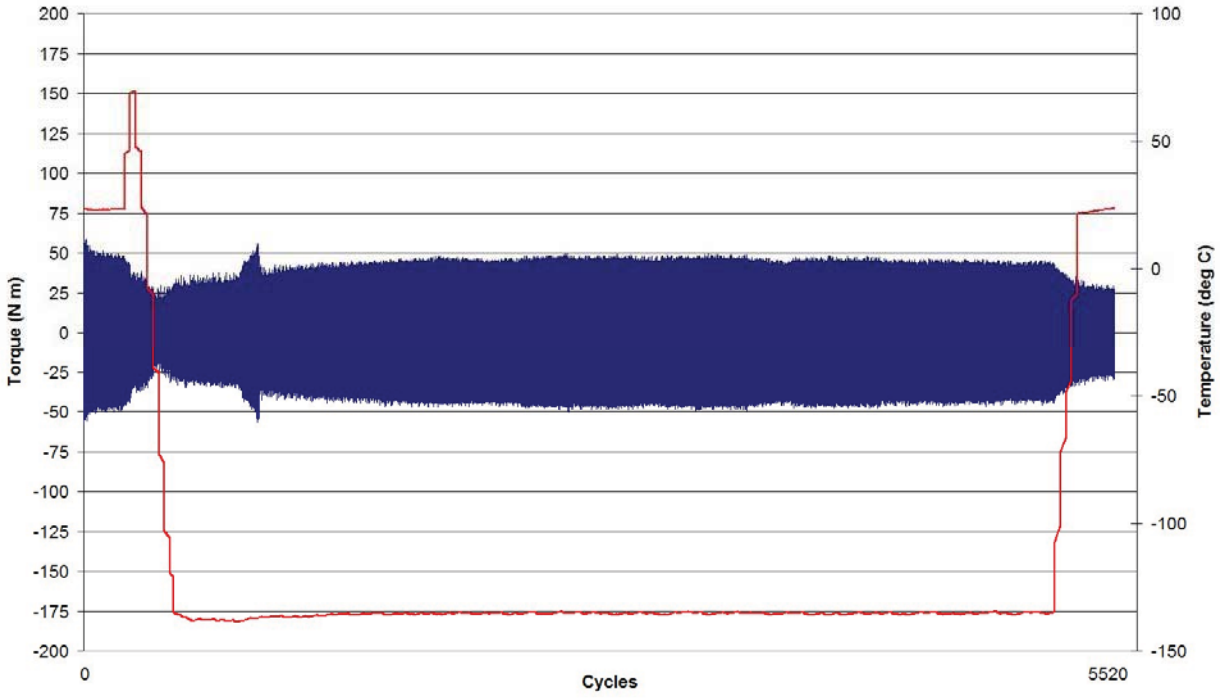

Figure 10: Friction Torque Plot
"Phosphate-like" Binder MoS_2 Bonded Film Coated Bushings vs. Titanium

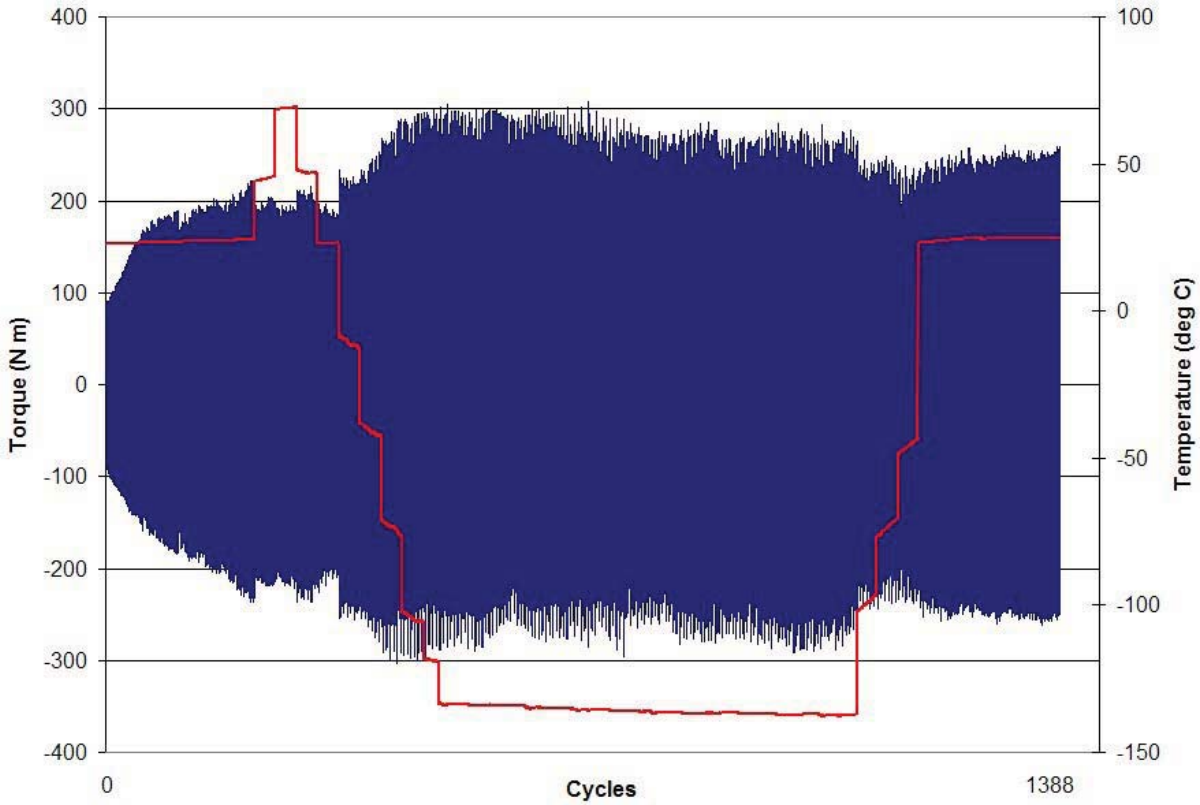

Figure 11: Friction Torque Plot
Bare Stainless Steel Bushings vs. Aluminum

Figure 12 illustrates the maximum (absolute value) friction torque, minimum (absolute value) peak friction torque, minimum peak torque at -135°C, and the difference between the maximum friction torque and minimum peak torque for each bushing test.

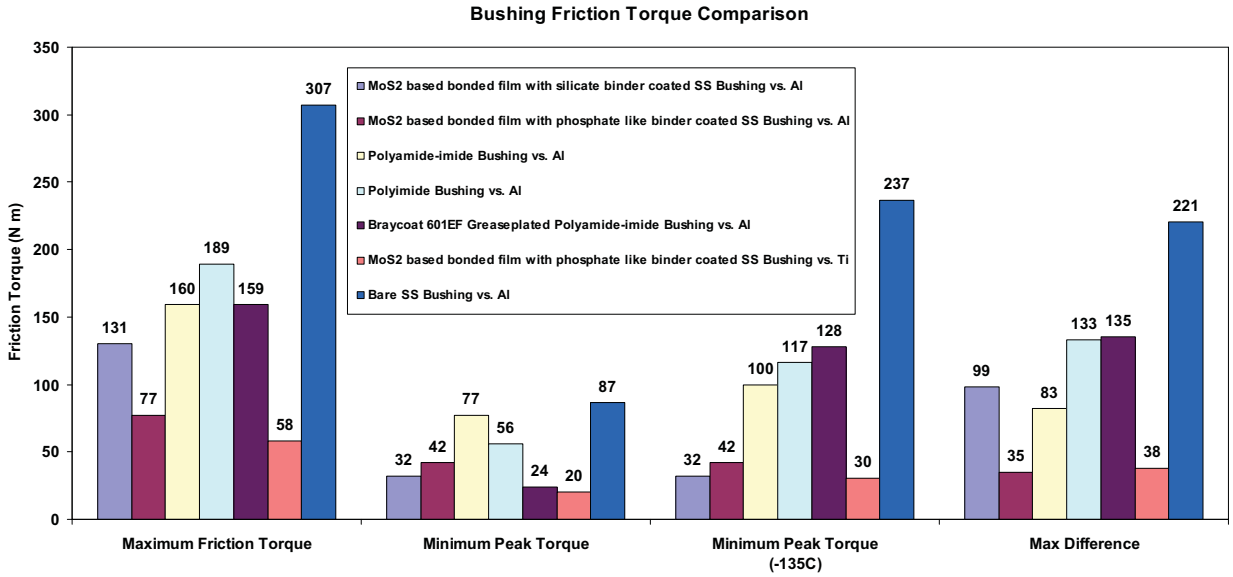

Figure 12: Bushing Friction Torque Comparison

One striking result of the bushing test series was the wide variation of friction torque over the test temperature profile. This variation was somewhat surprising as the coefficient of friction values for both bonded films and polymerics are not considered to be highly sensitive to temperature variation. If the coefficient of friction values were stable over temperature another mechanism must have been responsible for the friction torque variation during the testing. One possibility is that the mismatched, CTE induced, variable gaps between the shaft, the bushings, and the housing changed the contact geometry enough over temperature to produce the torque variation.

Another possible cause for the wide friction torque variation over temperature would be a test setup related systematic error. The setup for this test series was complex and involved the interaction of several large elements over a significant temperature range. The turnbuckle adjustments made to maintain a constant load on the driveshaft may have inadvertently altered the desired loading on the bushings. Although this is a possibility, the adjustments would not explain all of the torque variation over temperature.

In addition to the torque variation over temperature one sample also encountered an unexplained torque anomaly during testing. About midway through the cold dwell during the silicate binder MoS_2-bonded film test a torque ripple event occurred. The friction torque climbed steadily for several hundred cycles until peaking then abruptly self-correcting. It is difficult to definitively state what the cause of this event was given that the samples were not accessible at the time. That being said it was clear after disassembly of the pivot that a large amount of wear debris was generated during this test. The large volume of wear debris in the pivot could have shifted during the test and partially restricted the motion of one of the bushings. After some period of time the wear debris blockage could have cleared returning the assembly to a pre-event state. It is unknown whether this was an isolated event during just this test or this would be a repeatable behavior. The limited number of samples tested during this series does not provide any statically significant data to assess the repeatability of the behavior. None of the other samples exhibited this behavior during testing.

A review of the summary chart in Figure 12 illustrates the wide maximum friction torque variation between different bushing systems. The best performing bushing system with respect to maximum friction torque and maximum torque difference appears to be the “phosphate-like” binder MoS_2-based bonded film

coated stainless steel samples. The other MoS_2-based bonded film coated sample also exhibited good overall friction torque behavior compared to the polymeric samples.

An additional test was added during the test series to assess whether adding wet lubrication to the polyamide-imide bushings would improve the friction torque performance of that system throughout the operational temperature range. A set of polyamide-imide bushings was greaseplated with Braycote 601 and assembled in a test pivot to get hard data on the impact of adding the wet lube to the system. The results indicated there was a distinct benefit above -50°C but at lower temperatures the increased viscosity of the lubricant negatively impacted the performance of the bushing system by increasing the friction torque (compared to the unlubricated polyamide-imide samples).

Minimizing friction torque in the flight mobility pivots over temperature was desired to ensure the rover's suspension system articulates properly while traversing obstacles. Excessive drag in the pivots could significantly impair the mobile performance of the vehicle. This concern led the team to closely consider measured friction torque behavior in the selection of the final flight bushing material.

Wear

Relative bushing wear performance was also assessed as part of this test series. The nested configuration of the pivot assembly bushings prevented incremental wear monitoring during testing but thorough inspections were possible after each test.

Establishing a valid wear metric to quantify pivot assembly component wear has proven to be difficult. Some researchers have based wear rates on the volume of material lost during testing but this type of wear scar measurement was thought to be too complex for this application. With this in mind an alternative wear assessment approach was adopted involving photography of wear scars, profilimetry, and SEM microscopy.

JPL contracted with the Aerospace Corporation to analyze the worn bushing test samples [4,5]. The Aerospace Team photographed, provided SEM microscopy images, and performed profilimetry on the samples. A subset of the post test sample photographs taken by the team are shown in Figures 13 & 14. The overall wear performance of the samples was mixed with the bonded film coated samples exhibiting isolated but significant wear and the polymeric samples showing relatively light overall wear.

The MoS_2-based bonded film samples with the silicate binder performed most poorly with respect to wear generating large quantities of wear debris and significant wear scars on the outboard bushing. These wear scars were troubling as the lubricant film was completely worn away leaving metal to metal contact between the corner of the bushing and the contacting parts. Metal transfer occurred in this region as stainless steel particles were detected in the contacting end plate during the Aerospace Corp. analysis of the test samples. Measurable wear of the closeout plate itself was also documented in the analysis.

The MoS_2-based bonded film samples with the "phosphate-like" binder faired better during testing. Significant wear was limited to a small band on the corner of the coated outboard bushing. Stainless steel was exposed in that region but produced minimal wear on mating end plate in contrast to the silicate binder MoS_2 bonded film results.

Wear of the polyamide-imide and polyimide samples was very light. The team found that wear analysis of the polymeric materials was somewhat challenging as they are not coated so manufacturing scars look similar to wear scars.

The results of the wear assessment were in marked contrast to the friction torque results where the bonded films outperformed the polymerics. This was a troubling development as the team had hoped to find one superior bushing system that had both good friction torque performance and superior wear behavior. In the end, the team adopted a compromise position selecting the best performer with respect to friction torque accepting the non-ideal wear performance associated with that bushing system (MoS_2-based bonded film with "phosphate-like" binder).

Silicate binder MoS_2 bonded film coated Stainless

Phosphate-like binder MoS_2 bonded film coated Stainless

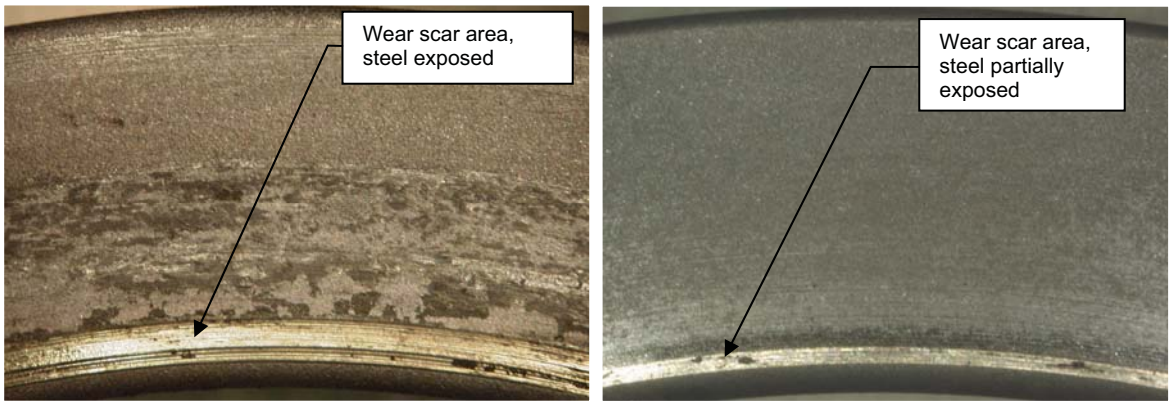

Figure 13: Post-Test Photos of Smaller, Outboard Bushing

Silicate binder MoS_2 bonded film Test

Phosphate-like binder MoS_2 bonded film Test

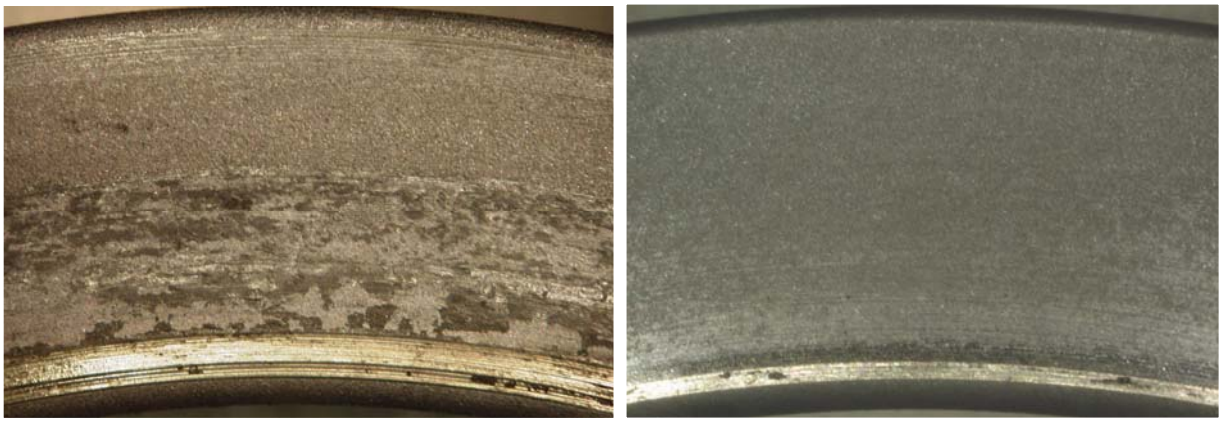

Polyamide-imide Test

Polyimide Test

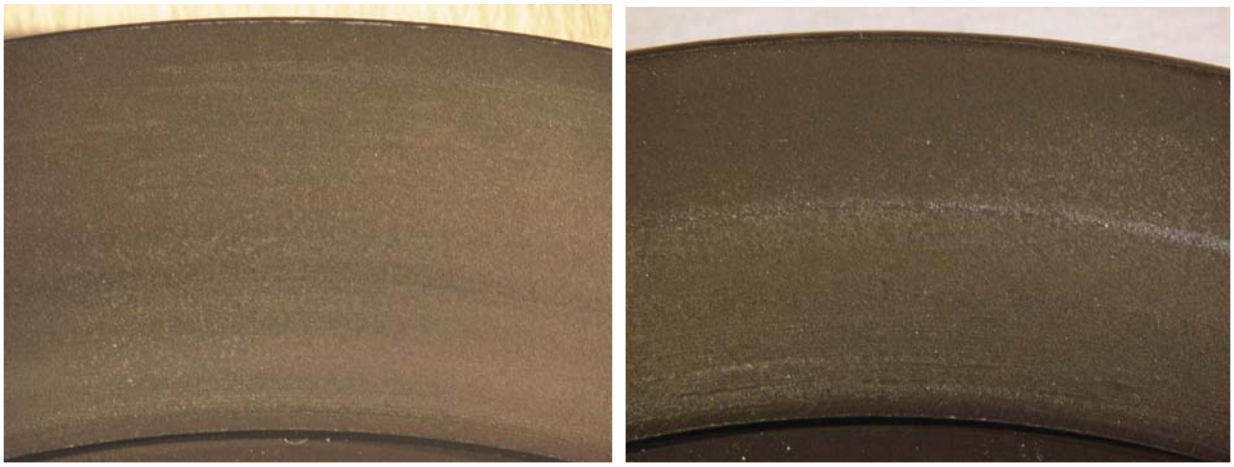

Figure 14: Post-Test Photos of Wear on Aluminum Pivot End Plates

Conclusion

The stated objectives of the bushing test series were to characterize the friction and wear performance of several candidate bushing/coating materials in a flight-like application and evaluate the behavior of these materials over the MSL operational temperature range. Both of these objectives were met during the testing and subsequent data analysis.

Although all test samples survived the modified 4x life test there were clear winners with respect to friction torque and wear. The MoS_2-based bonded film coated samples exhibited the best overall low friction behavior while the polyamide-imide samples had the least amount of wear among all bushing systems tested. Ultimately, the team selected the phosphate-like binder MoS_2-based bonded film / stainless steel bushing system for flight usage as minimizing the friction torque in the pivots was deemed more important than minimizing pivot wear during the mission.

The bushing test series has provided valuable friction and wear data on a variety of candidate bushing materials and lubricants enabling the MSL Mobility Team to make critical design decisions about flight pivots on the vehicle. This data should also prove valuable for future Mars Surface Systems considering the use of bushings in highly loaded pivots.

Acknowledgements

The research described in this paper was carried out at the Jet Propulsion Laboratory, California Institute of Technology, under a contract with the National Aeronautics and Space Administration.

The author would like to thank the following individuals and their respective teams for their contributions to this bushing test effort:

Donald Striebing, NASA Glenn Research Center:	Phase One Bushing Testing
Dr. Christopher DellaCorte, NASA Glenn Research Center:	Phase One Bushing Testing
Dr. Phillip Abel, NASA Glenn Research Center:	Phase One Bushing Testing
Ray Andres, Jet Propulsion Laboratory:	Test Fixture CAD Design Support
Dr. Jeffrey Lince, Aerospace Corp:	Sample Wear Analysis
Christopher Voorhees, Jet Propulsion Laboratory:	MSL Rover Mechanical Sys. Engineer
Jaime Waydo, Jet Propulsion Laboratory:	MSL Mobility Mechanical Team Lead

References

1. Striebing, Donald, “MSL Mobility Risk Reduction Bushing Test Series” (August 2006)
2. Waydo, Jaime "Dither Analysis Code." *Matlab Script*, (September 2005).
3. Young, W. *Roark’s Formulas for Stress and Strain 6th Ed*. Dallas, McGraw Hill, Inc., ©1989, p. 650.
4. Lince, Jeffrey, "SEM of MSL Lube Test Results", PowerPoint Presentation (November 2006)
5. Lince, Jeffrey, “SEM of MSL Lube Test Results”, PowerPoint Presentation (August 2006)

Space Shuttle Orbiter Atlantis Liquid Oxygen Pre-Valve Detent Roller Cracking Investigation

Elizabeth Holleman*, David Eddleman*, Rebecca Jacobs** and James Richard*

Abstract

During routine inspections of the Space Shuttle's Main Propulsion System Liquid Oxygen (LO_2) pre-valve, the mechanism provided to maintain the valve in the open position was found cracked. The mechanism is a Vespel roller held against the valve visor by a stack of Belleville springs. The roller has been found cracked 3 times. All three instances were in the same valve in the same location. There are 6 pre-valves on each orbiter, and only one has exhibited this problem. Every-flight inspections were instituted and the rollers were found to be cracked after only one flight. Engineers at Marshall Space Flight Center, Johnson Space Center, and Kennedy Space Center worked together to determine a solution. There were several possible contributors to the failure: a misaligned visor, an out-of-specification edge with a sharp radius, an out-of-specification tolerance stack up of a Belleville spring stack that caused un-predicted loads on the Vespel SP-21 roller, and a dimple machined into the side of the roller to indicate LO_2 compatibility that created a stress riser. The detent assembly was removed and replaced with parts that were on the low side of the tolerance stack up to eliminate the potential for high loads on the detent roller. After one flight, the roller was inspected and showed fewer signs of wear and no cracks.

Introduction

NASA's Space Shuttle is propelled into orbit by two solid rocket boosters and three Space Shuttle Main Engines (SSMEs). The SSMEs are liquid rocket engines that use liquid oxygen and liquid hydrogen as propellant. The propellant is stored in the non-reusable external tank. During loading, the propellants flow through the orbiter by way of the fill and drain system on the Main Propulsion System. The propellants are loaded in this manner in order to cool down the various Main Propulsion System fluid components and to chill the engines. This prevents gas ingestion by the engines during ignition.

The Main Propulsion System contains various sub-systems including the feed system. The feed system allows flow of oxidizer and propellant from the external tank to the three SSME's. After the feed system manifold, there are three pre-valves that are used for isolation of the propellant supply from the SSME's. These pre-valves are used to prevent catastrophic failures of the oxidizer turbo pump during nominal engine shutdown as well as during a contingency situation when engine isolation is necessary. Because of these important tasks, the pre-valves are inspected and tested routinely.

Valve Function

Each Space Shuttle Main Engine has two 30.5-cm (12-inch) diameter propellant isolation valves. One valve is in the liquid hydrogen system and the other in the liquid oxygen (LO_2) system. They are referred to as pre-valves and are located in the Main Propulsion System. The pre-valves are used during all phases of the shuttle operation: fill and drain of the external tank, ascent, and in contingency situations. The primary purpose of the pre-valves is to stop the flow of propellant to the SSME's in the case of an engine failure or shutdown. The restriction of flow reduces the likelihood of an uncontained fire in the aft compartment or engine. The LO_2 pre-valves also serve a critical purpose during Main Engine Cut Off (MECO). During MECO, helium is injected from the SSME pogo accumulator into the area upstream of the high-pressure oxidizer turbo pump (HPOT). This maintains the proper pressure for shutdown of the HPOT and allows for safe engine shutdown. The pre-valves close, providing the sealing force to maintain

* NASA Marshall Space Flight Center, Huntsville, AL
** Jacobs Engineering Science & Technical Services Group, Huntsville, AL

the pressure and limit the volume that must be pressurized. The valves also allow the recirculation pumps to operate to chill the engines prior to launch. In order to prevent overpressure of the feedlines, the valve contains a reverse flow relief valve and a visor liftoff mechanism.

The pre-valves are pneumatically actuated, bi-stable, two-position valves. The valve has a half-moon-shaped inconel visor that seals against a Kel-F seat in the closed position. A photo of the valve between the open and closed positions is shown in Figure 1. To open the valve, helium is supplied to an actuator that rotates the visor out of the propellant flow path. When the valve opens, two Belleville spring-loaded mechanisms hold a small roller in detent grooves on each side of the visor to ensure the visor remains in the fully open position. These detent mechanisms serve as a mechanical latch to hold the valve in the open position to prevent an unwanted closure of the valve during engine operation. Because the valve is bi-stable, the detent mechanisms add redundancy to the valve. Helium is again supplied to the opposite side of the valve actuator piston to close the valve.

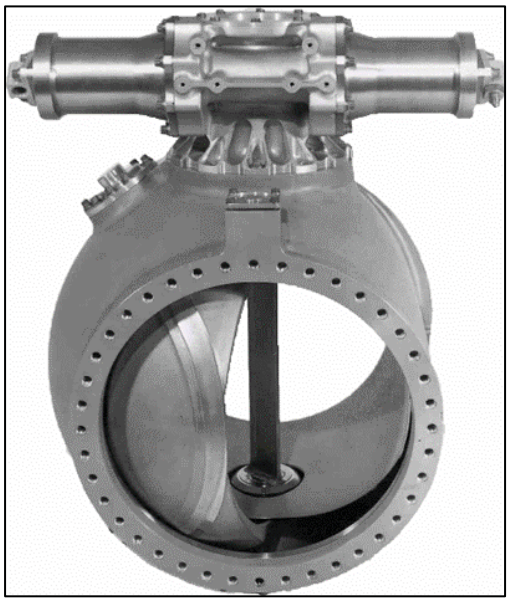

Figure 1: Space Shuttle Main Propulsion System Pre-Valve

Pre-valve Detent Mechanism Description

The detent mechanisms are composed of several piece parts as shown in the cross sectional and exploded views in Figures 2 and 3. The assembly contains a roller, pin, and follower that allow the mechanism to translate across the visor. The assembly also contains a stack of Belleville springs and spacers. The springs allow for vertical movement of the roller. The spacers protect the springs from rubbing on one another and allow the springs to invert.

The detent roller is manufactured from LO_2/LH_2 compatible Vespel SP-21. As the valve opens, the part of the visor known as the ramp comes into contact with the roller compressing the Belleville spring stack in the detent mechanism. The roller travels along the ramp to the detent groove, shown in Figure 4. Figure 5 shows the valve in the open position with the roller locked in the detent groove. Rotation of the visor itself is controlled by mechanical stops in the actuator that do not allow the visor to rotate more than 90 degrees. The stop also prevents the roller from rolling through the groove and out the other side. As the roller moves up the ramp, the follower also moves up. This upward motion compresses the Belleville spring stack. As the stack is compressed, the spacers slide within the detent cap guiding the entire stack's motion. They also keep the four Bellevilles from contacting each other as each is compressed so that they can move beyond the point where they invert. The top spacer contacts a lip on the cap and transmits the force of stack deflection through the cap and into the seven bolts holding the mechanism

within the valve body. The cap retains a static spring energized seal in the valve body that prevents propellant leakage into the aft compartment of the Orbiter. When the valve is commanded closed, the actuation force generated overcomes the force generated by the roller in the groove and compresses the spring stack until the roller is forced out of the detent groove. The roller then rolls down the visor ramp until the two parts are no longer in contact with each other. In the closed position, the detent Belleville's are only compressed to their installation height and the roller and follower hang inside the valve. The follower has a large land that contacts the retainer to hold it in place. The retainer serves multiple purposes: it prevents the follower and spring stack from falling into the valve and ensures the spring stack is compressed to the installation height before coming into contact with the visor, the retainer is keyed within the cap to prevent the mechanism from being installed in a manner where the roller and detent groove would not line up, and the retainer prevents the follower from pivoting or rotating as the roller moves up the visor ramp.

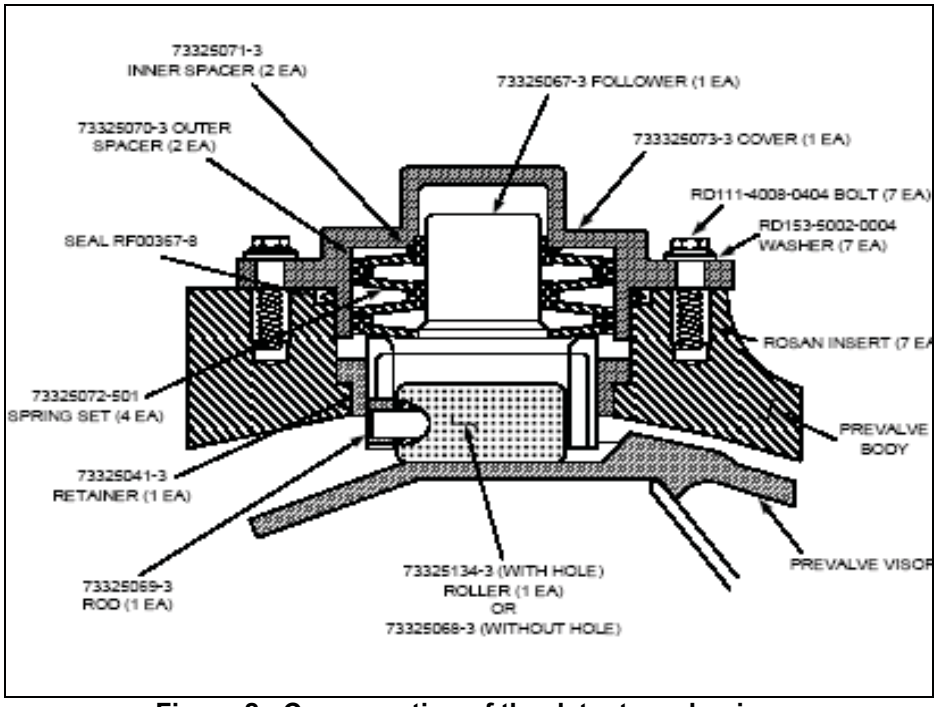

Figure 2: Cross-section of the detent mechanism

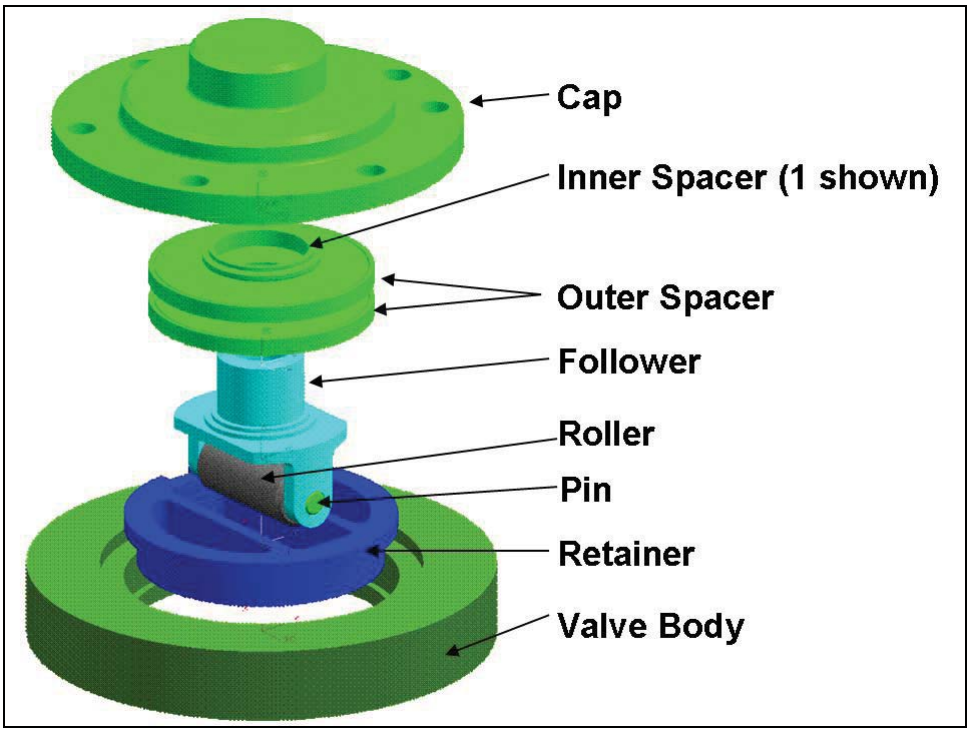

Figure 3: Exploded view of the different detent mechanism's piece parts

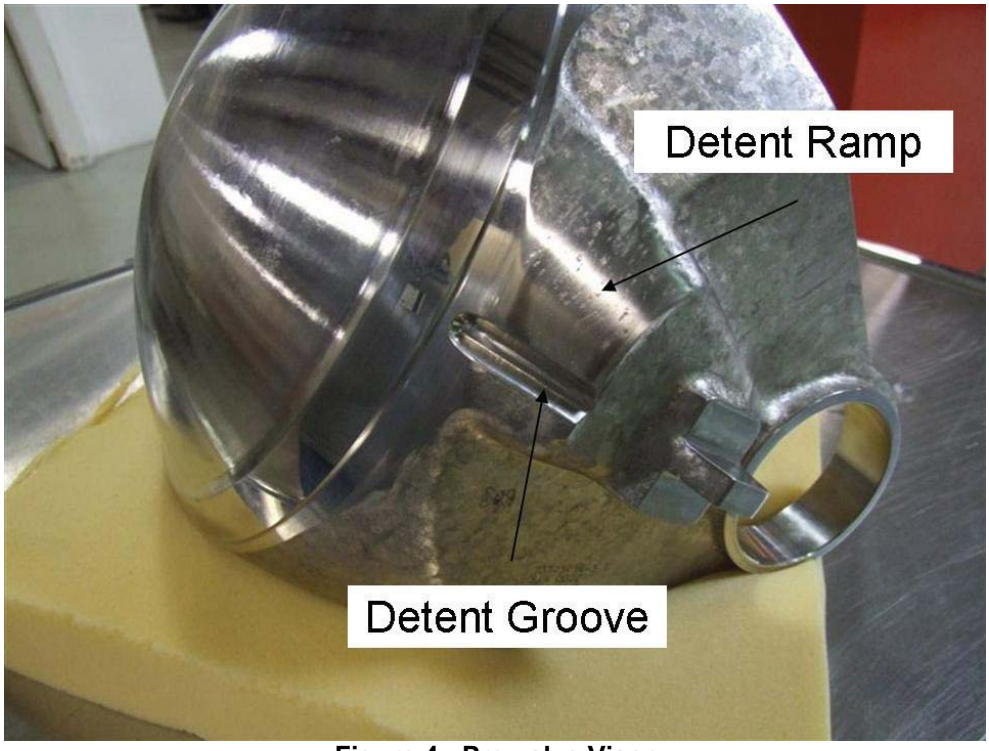

Figure 4: Pre-valve Visor

Figure 5: Roller locked in the detent grove when the valve is in the open position

Detent Mechanism Inspections

During an inspection of OV-104 (Atlantis) after the vehicle's second flight, one of the detent rollers in the engine 3 LO_2 pre-valve was found to have a crack through the full thickness and down one third the length of the part. The root cause of the crack was not found and the crack was dismissed as a one-time occurrence. However, as part of the forward plan, the requirement to inspect each roller during every vehicle's Orbiter Maintenance Down Period (OMDP) was instituted. During every OMDP, all six LO_2 and LH_2 detent mechanisms are removed from the pre-valves and inspected for wear or damage. Each roller typically shows a washboard pattern around its circumference that is considered nominal wear. This pattern is due to the large visor swinging and contacting the motionless roller. Because the surface of the visor is relatively rough and the visor moves at a fast rate, it is suspected that the roller does not roll smoothly across the visor. The slipping of the roller may contribute to the "wash board" wear marks that are typically seen around the roller.

As the Belleville spring is compressed, the roller is forced against the retainer that results in wear on the roller. Also, there are typically black indications on the retainer where this contact takes place. The black marks indicate deposits of Vespel material were transferred from the roller surface to the retainer.

Some rollers within the fleet are specially machined to have a smaller diameter in specific locations. The purpose of this process is to reduce the effect of rough or high spots on that specific valve's visor. During inspections after the initial flights of the OV-103 and OV-104, several rollers in the LH_2 and LO_2 systems were found with rough gouges at specific distances along their lengths. Borescope and visual inspections concluded these instances of damage were due to wear associated with the high spots on each visor. Two rollers showing this type of damage are shown in Figure 6. Examples of specially machined rollers with gaps to avoid a high spot on a discrepant visor are shown in Figure 7.

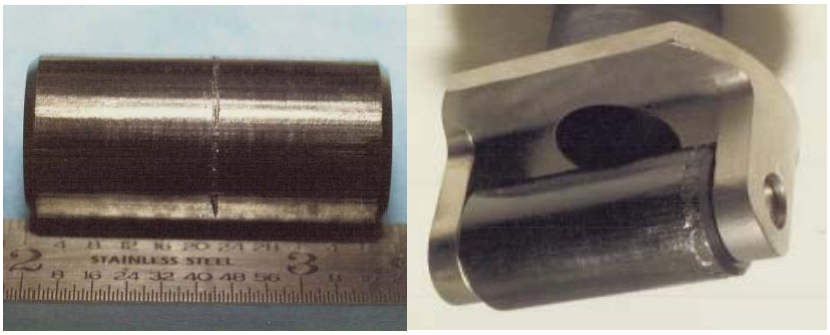

Figure 6: Rollers Exhibiting Wear due to High or Rough Spots on the Visor

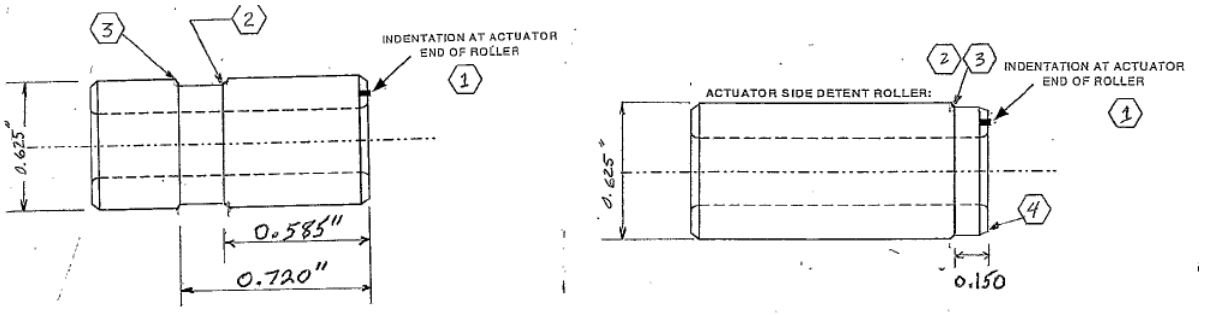

Figure 7: Drawings showing how these rollers are machined to avoid discrepant areas on valve visors

In addition to roller wear, the retainers also show signs of wear due to contact from the side of the follower. Deposits of the retainer material have been found on the pin and follower, which further supports the theory that the retainer is being damaged by these components. The cap also shows signs of wear due to the sliding contact of the four spring spacers. Example of nominal wear associated with spacer travel in the cap can be seen in Figure 8. All parts of the assembly are inspected thoroughly and replaced if the wear is considered significant. Minor wear to metal parts may be treated with Chem-film which is an acceptable practice for Shuttle LO_2 and LH_2 systems.

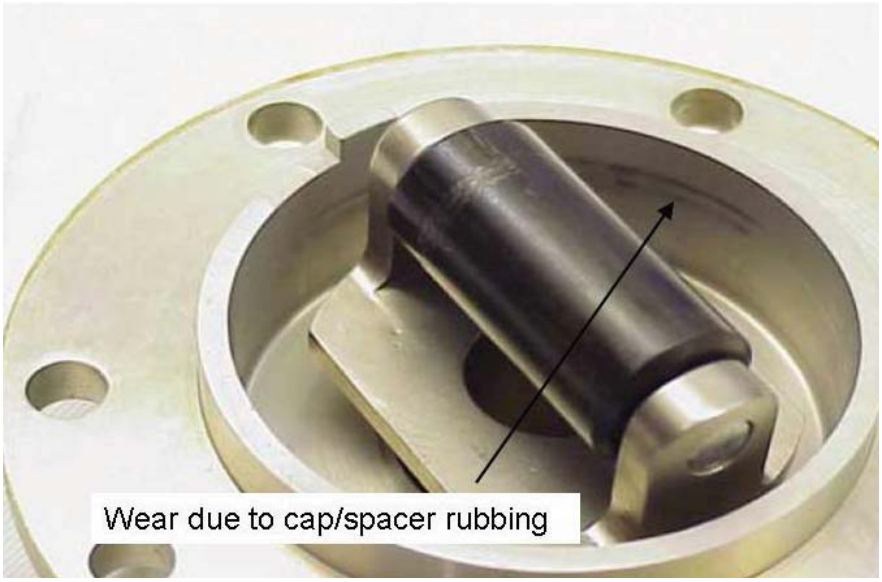

Figure 8: Cap showing signs of nominal wear due to spacer rubbing

Cracked Roller Anomaly

To date, three cracked rollers have been found through inspection. All 3 rollers were in the OV-104 Engine 3 LO_2 pre-valve. The first cracked roller was found after the second flight of OV-104, which led to the inspections discussed above. During OMDP for OV-104 after Flight 26, the second cracked roller was discovered. Following this investigation, every-flight inspections were instituted for the specific Engine 3 LO_2 pre-valve. During these inspections, the third cracked roller was discovered. Unlike the prior two cracked rollers, this roller cracked after only one flight. This raised concerns that a cracked roller that remains in service may degrade further and cause a serious failure in the LO_2 system.

A cracked roller may liberate debris. This debris should be captured by the pre-valve screen, which is a 1000-micron screen downstream of the pre-valve to prevent contamination from entering the engine.

Another failure mode is that if the roller completely fails and the metal follower comes in contact with the pre-valve visor, an ignition source would be created in the highly volatile LO_2 environment.

After the second failure was discovered, two likely causes were identified: roller material LO_2 compatibility testing marks, and detent groove leading edge sharpness. Before a soft good or non-metallic material is used in Space Shuttle LO_2 systems, each batch of the material must be compatibility tested. The Vespel SP21 used for the roller requires this testing. To ensure that rollers that aren't batch tested are not installed in the vehicle, a small dimple is machined into the end of the roller to indicate that the material successfully completed the required testing. The depth and diameter of the dimple are drawing controlled. The mark is to be no more than 0.76-mm (0.030-inch) deep and 1.57 mm (0.062 inch) in diameter. It was noted that the crack observed on the second and third cracked rollers initiated at the dimple and propagated through the thickness of the roller. The dimple was identified as a stress riser and a contributor to the cracked rollers. However, it was also noted that the first cracked roller did not have a dimple, so there is likely an additional cause.

Testing was performed to verify that a roller with a dimple has reduced fracture toughness. However, during this testing, the loads required to crack a roller were less than the estimated loads imparted by the Belleville spring stack in a nominal assembly. This information prompted further investigation after the third roller was found cracked. The original intent of the testing was only to prove that the dimple did affect the fracture toughness of the roller. The testing was performed at ambient conditions. The load required to crack a dimple-less roller was twice that of the load required to crack a roller with a dimple.

Molds of the visor detent groove were made so that measurements of the key dimensions of the visor could be taken. It was determined that the radius of the lip of the leading edge of the detent groove was sharper for this particular valve visor than drawings for the part allowed. The edge radius underwent a grinding and polishing process with the valve installed on the vehicle. Prior to machining, the radius was found to vary between 0.13 to 0.51 mm (0.005 to 0.020 inch) at various points along the length of the detent groove. The drawing requirement for this radius was 0.38 to 0.76 mm (0.015 to 0.030 inch). After the procedure, the sharpest dimension found along the length of the detent leading edge was 0.48 mm (0.019 inch). The polishing process was performed between the second and third rollers.

It was also noted from the mold impressions that the one end (labeled as "5" in Figure 9) of the leading edge was slightly higher than the other. This resulted in an unparallelism between the roller and visor interface. This unparallelism resulted in one side of the leading edge being approximately 0.64 mm (0.025 inch) higher than the other. This meant that one end, the horseshoe shaped end, compressed the detent roller more than the open end. All three cracks initiated on the end corresponding to the higher compression.

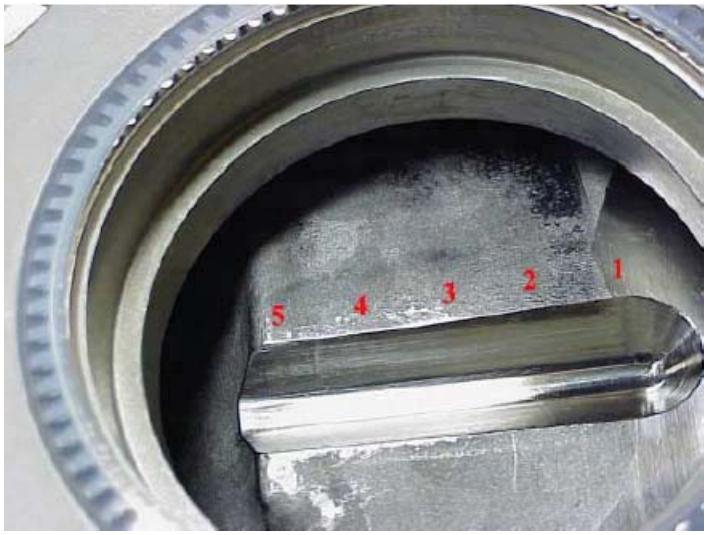

Figure 9: Pre-valve Visor Detent Groove

Rationale to fly after finding the second cracked roller was based primarily on the conclusion that the sharp leading edge of the detent groove was the root cause of the cracking. However, after the detent groove leading edge was returned to print, the third roller cracked after only one flight. The second and third cracked rollers can be seen in Figure 10. In each case, the crack was observed to run through the LO_2 compatibility testing mark and completely through the thickness of the roller. This can be seen in Figure 11.

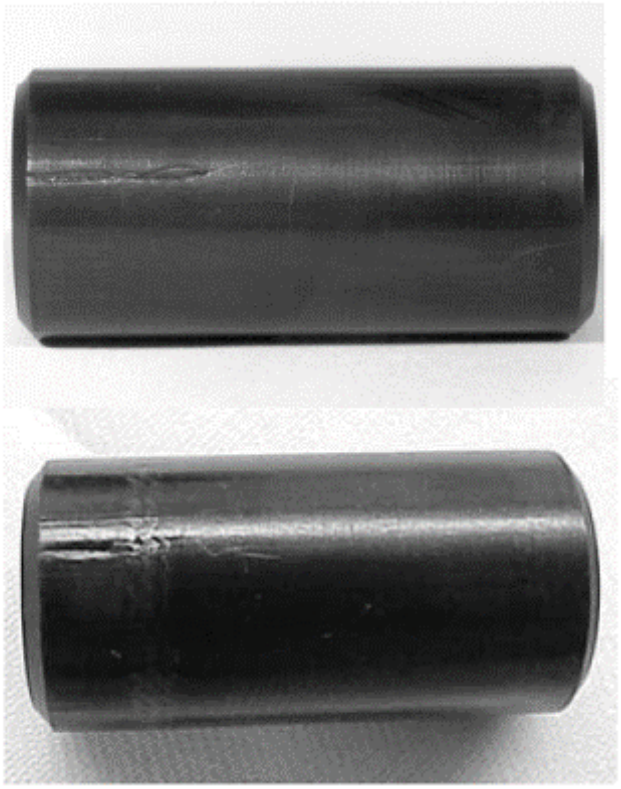

Figure 10: The second and third cracked rollers

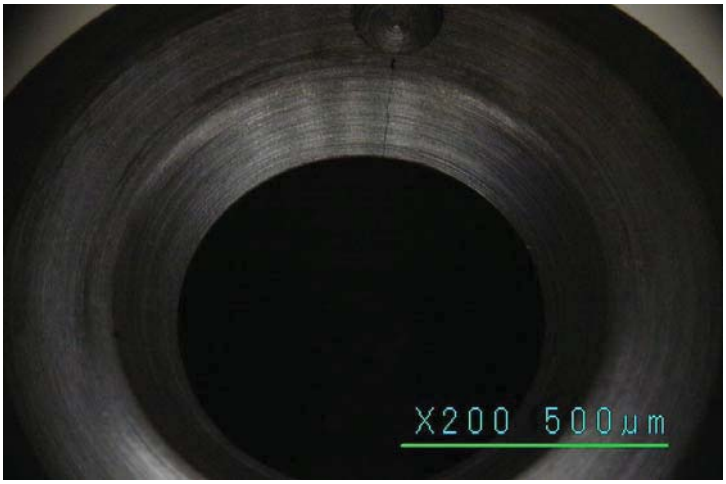

Figure 11: Crack can be seen through the compatibility testing mark and from the inner to outer diameters

During further examination of all available data it was noted that the visor to valve body height, recorded during the visor mold impression and grinding work, was out of family. This information kicked off a tolerance stack up analysis. The third cracked roller kicked-off an effort for a more in-depth investigation of alternate causes. Because the first two causes that were examined, the dimple and the sharp edge, did not preclude another cracked roller, it was necessary to look for a less obvious cause. Because the third failure was after only one flight, resources and attention not previously available were given to the problem.

The out-of-specification measurement of the visor height prompted the tolerance stack-up investigation. The measured distance of the visor from the valve body was used as a basis for a tolerance stack-up analysis. Actual measurements of the installed detent mechanism components were used, including a force-deflection curve of the Belleville spring stack set-up. The stack up of the individual components was subtracted from the visor height to determine if interference was possible. Interference would result in the spring stack reaching its solid height and imparting unexpected high loads on the roller. It was determined that combinations of nominal piece parts tolerances could result in deflections that caused the Belleville spring stack to go flat and introduce the high loads onto the roller. An illustration of the mechanism and the measurements used in the analysis are shown in Figure 12. As a solution, piece parts were carefully selected to produce an acceptable assembly on the low side of the tolerance band. This should preclude the spring stack from reaching a solid deflection height. Further mitigation was to machine an angle in the retainer surface that contacts the follower. The surface was angled to 2 degrees based on the marks left by the roller on the retainer. These marks indicated the angle at which the roller was moving when in contact with the visor. The modified retainer allows additional movement of the follower and prevents binding at the follower-retainer interface. This reduction in binding also reduces the load being applied to roller.

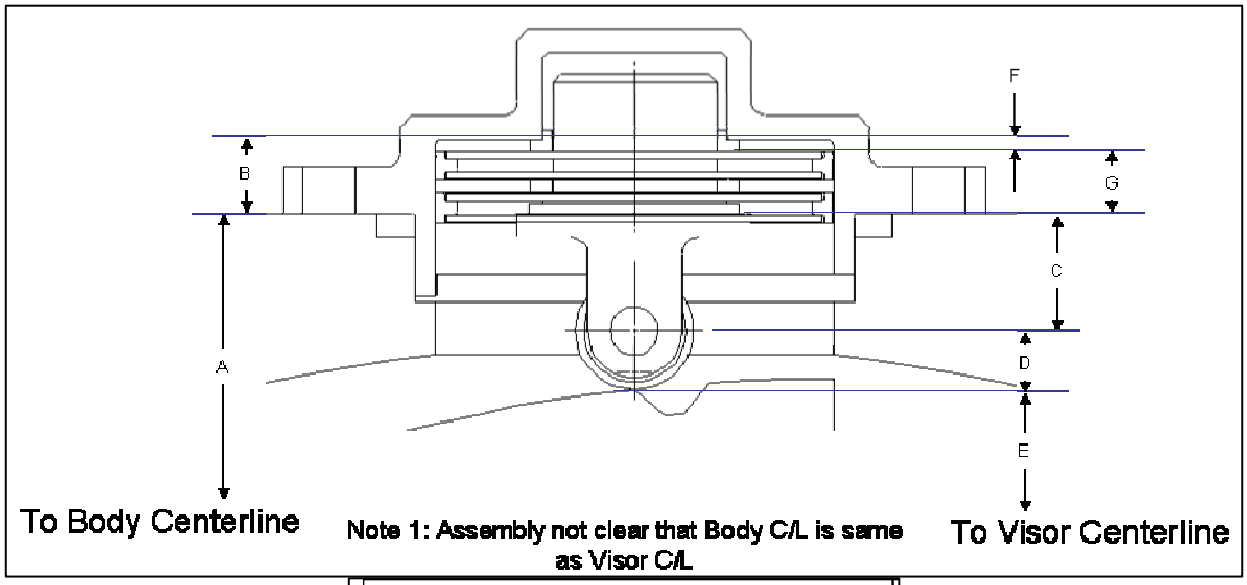

A	Valve center to housing
B	Cover height
C	Follower height from center pin to spring seat
D	Roller radius (pin/roller clearance stackup neglected)
E	Valve center to visor surface.
F	Inner spacer thickness
G	Spring stack height

Figure 12: Detent Mechanism Tolerance Stackup

Measuring the EHD Film Thickness in a Rotating Ball Bearing

Peter Ward*, Alan Leveille* and Peter Frantz*

Abstract

This paper presents two independent ways to directly measure the change in axial deflection of a bearing that is proportional to the magnitude of the total elastohydrodynamic (EHD) film developed. The first uses multiple capacitance displacement gages as a direct measurement of axial displacement and the second method uses the change in operating preload force to calculate the axial change in the test fixture and bearing stack. Convergence of the results from two independent techniques adds confidence to the experimental process. Either method can provide accurate EHD film thickness over extended time for a complete bearing under varying load, speed and lubrication conditions. Additionally, the methods are equally applicable to non-metallic materials, such as Si_3N_4 balls, which preclude the use of other techniques. The method has some advantages to the practicing engineer over the classical ball on a flat quartz plate because the full range of bearing design parameters and kinematic interactions are operating.

The EHD film thicknesses of two oils and one grease were measured in an operating 304 sized angular contact bearing for up to 600 hours of running time at 6000 rpm. EHD film thickness was determined by simultaneously measuring the resultant displacement and axial force change of the outer rings due to collapse of the EHD film when the bearing pair was brought from full speed to rest. Because each measurement of axial displacement was completed within 2 seconds, the results are not affected by a contribution due to thermal expansion. We compared a common synthetic hydrocarbon base oil (Pennzane) with a common mineral oil (Coray). We found the synthetic oil film thickness to be approximately one half that of the mineral oil. We also compared film thickness with both large and small amounts of grease. We found that the large grease amount produced a prolonged run-in transient film that was thicker than the base oil steady state film. However, with a smaller amount of grease, the thickness fell to a value that was comparable to the base oil. Initial assessment indicates that the degree of lubricant starvation is greater than can be accounted for with conventional EHD theory.

Introduction

Ball bearings in numerous aerospace mechanisms are lubricated with a single charge of grease or oil that is expected to last on the order of 10 years. Development and maintenance of an elastohydrodynamic (EHD) film that is sufficient to prevent wear is dependent upon application conditions, bearing design and lubricant properties. As demands on lubricant performance grow, lubricant conditions are pushed towards a deeply starved regime where conventional models of EHD film thickness break down [1]. Therefore, our experimental and theoretical tools for demonstrating lubricant performance for a given application are becoming increasingly compromised. For this reason, we devised an experimental approach to measure EHD film thickness of an operating pair of bearings with two objectives. The first is to directly measure the film thickness in applications of immediate relevance to specific flight requirements to ensure an adequate film is present. The second is to evaluate the validity of modern lubricant starvation models and to adapt them for use in design of aerospace applications. This presentation is intended to be an introduction and demonstration of the experimental technique.

The experimental procedure presented here provides an accurate measure of the time dependent EHD film thickness behavior. The magnitude of the EHD film in a bearing is proportional to the change in the axial stick-out (end play) of the bearing between a condition of running at speed with an EHD film and a condition of zero RPM with no EHD film. This change in end play was experimentally determined simultaneously with two independent techniques. The first was to measure it directly using air-gap

* The Aerospace Corporation, El Segundo, CA

capacitance displacement gages. The second way was to deduce it by combining the measured spring rate of the test rig in series with the calculated spring rate of the two bearings and then calculating what the axial change in deflection had to be to account for a measured axial force change between running with an EHD film and zero RPM with zero EHD film. The concurrence of these two methods provides a way of validating that the test set-up is correct for any given test. The measurement of axial change is similar in principle to the method of Tyler, et al [2]. However, our approach introduces a nearly isothermal measurement that eliminates the very significant effect of temperature on the measured change in axial stickout. To illustrate the importance of temperature, for steel parts and a 15-degree operating contact angle, a 1-degree F uncertainty in temperature across the bearing results in a measured stickout change of 34 micro-inches for the 304 size bearing reported herein. This uncertainty is much larger than the actual EHD film thickness.

Several other techniques for measuring film thickness in an operating rolling contact bearing have been described in the literature. Measurements of acoustic emission have been used to record the noise created by asperity contacts between the balls and races [3]. This technique is well suited for in-situ monitoring of real bearing applications, but does not provide a direct quantitative measure of the film thickness and loses resolution when the film thickness grows beyond 3 times the composite surface roughness. The electrical capacitance and resistance across the bearing has been used to infer the EHD film thickness [4,5]. However, the inferred film thickness is often dependent on uncertain estimates of several properties, such as the oil volume outside the contact, the size and shape of the contact, and the dielectric properties of the material between the surfaces. Ultrasonic reflection [6] is a promising new technique, but it is challenging to produce sufficient resolution under the relevant speed conditions. Furthermore, it measures only the film between the ball and outer race and not the inner race, which is often more deeply starved.

Analytical Method

As the film between the ball and races grows, the inner ring is forced to deflect with respect to the outer ring, resulting in a change in stick-out. To analyze the geometric situation, the increased film thickness is modeled as an increase in the overall ball diameter. Figure 1 shows the change in inner ring position caused by the hypothetical increase in the ball diameter. Figures 1A and 1B each show the cross section of an outer ring, ball, and inner ring, from top to bottom. Figure 1A represents the bearing with no lubricant film between the ball and race, such as would occur when the bearing is at rest. Figure 1B

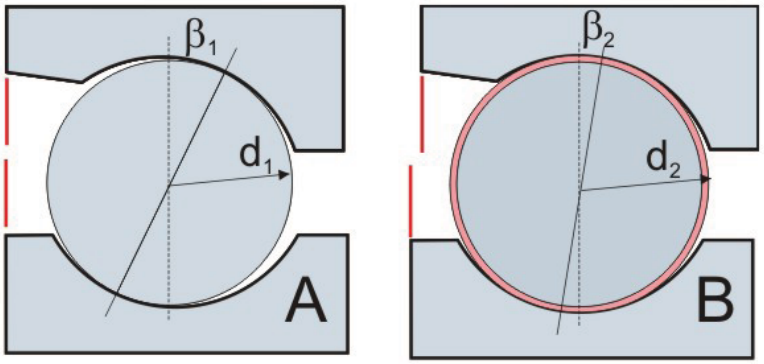

Figure 1. Cross section of a bearing raceway/ball contact at rest (A) and with a hypothetical lubricant film surrounding the ball (B).

shows the high-speed bearing, with the appearance of a lubricant film as a ring surrounding the ball. This film is shown with uniform thickness around the ball only for the purpose of illustration. The inner ring deflects to the left and the contact angle is reduced. The inner ring deflection is equal to one half of the change in end play of the bearing resulting from a change in the effective diameter of the ball. Additional deflection due to elastic deformation of the balls and races has also been accounted in our model. Details of the technique and results of our film thickness measurements are described below.

The end play of the bearing shown in Figure 1A (P_{E1}) is related to the ball diameter (d_1) by the following relationship:

$$P_{E1} = 2B_1 d_1 \sin \beta_1 \qquad \text{Eq (1)}$$

Where B_1 is the total curvature for the bearing in Figure 1A, given by:

$$B_1 = \frac{r_o}{d_1} + \frac{r_i}{d_1} - 1 \qquad \text{Eq (2)}$$

Where r_o is the inner ring radius and r_i is the inner ring radius.

Similar relationships may be written for the bearing shown in Figure 1B, with the subscript 2 substituted for 1. For each experimental data point, the change in end play ($\Delta P_E = P_{E1} - P_{E2}$) is measured with the techniques described below. The full-speed contact angle β_2 is measured by observing the ratio of the shaft rotational frequency to the ball group rotational frequency. The total film thickness, the sum of the inner and outer ring EHD films, is given by $d_2 - d_1$. Solving from equation 3, the total film thickness is given by:

$$d_2 - d_1 = \frac{2B_1 d_1 \sin \beta_1 - \Delta P_E}{2B_2 \sin \beta_2} - d_1 \qquad \text{Eq (3)}$$

Although this technique provides a quantitative measure of the sum of the inner and outer film thicknesses, it gives no information that allows one to discern how much of that sum is due to each interface. An approximate ratio can be obtained through the application of conventional EHD film thickness analytical methods [7]. This approach was used here to demonstrate that the film thickness at the inner ring is approximately 40% of the total, and the film thickness at the outer ring is the remaining 60%. Therefore, in our final analysis will treat the inner ring film thickness as being approximately 40% of the total film thickness.

Experimental Method

A pair of 304 sized bearings is mounted in a face-to-face (DF) configuration inside a steel housing, as shown in Figure 2. A single pair of hybrid bearings, with CRU20 rings, Si3N4 balls and a phenolic cage, was used for all experiments shown here. The preload force is both applied and measured using a compliant, ring-shaped load cell compressed between the lower bearing and the cartridge. A spacer separates the outer ring of the lower bearing from the load cell. To simplify alignment, the load cell bears on the housing through a ball-in-cone arrangement. Preload is set by screwing the upper and lower housing halves together. The upper end of the shaft is attached to a high-speed precision spindle that rotates the inner rings. The entire assembly hangs from the motor spindle by a connection to the shaft. The housing and outer rings are prevented from rotating by a lever arm (not shown) that bears on a second load cell to measure bearing drag torque.

In this arrangement, the outer ring of the upper bearing is stationary with respect to the housing, while the outer ring of the lower bearing translates axially through a distance equal to the sum of the two bearing displacements. Since the motion of each outer ring is equal to half of the change in end play, the total measured axial translation of the outer ring of the lower bearing (the sum of both bearings) is equal to the total change in end play of each bearing, ΔP_E. The bearing test cartridge is instrumented with sensors to detect displacement of the outer ring and changes in the operating preload. These sensors provide the change in end play that is used to determine film thickness with the “load change method” and the “air gap displacement method” described below.

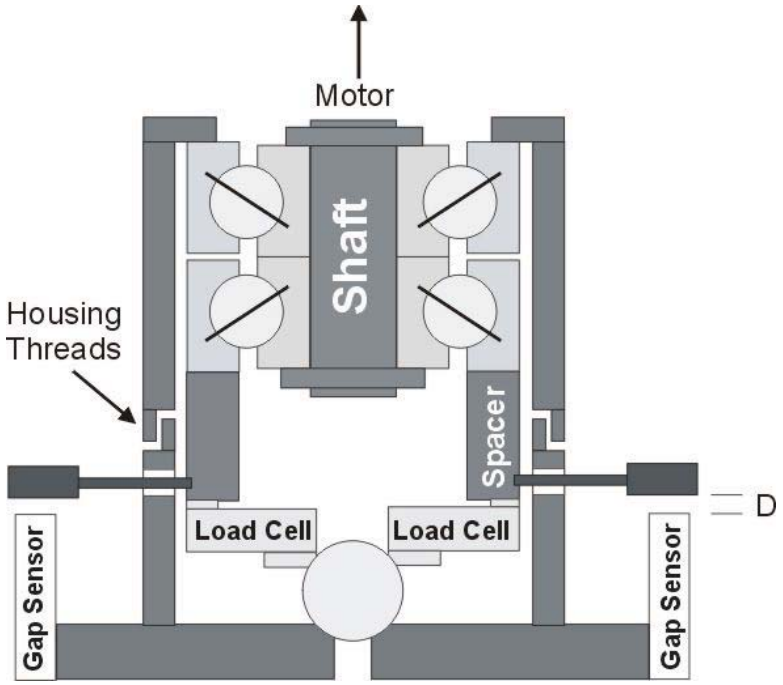

Figure 1. Schematic of the bearing test facility, not shown to scale.

Load change method

The first method to detect the change in end play uses the change in bearing preload from the load cell shown in Figure 2. The displacement of the outer ring is equal to the measured change in load times the yield rate of the bearing cartridge system, as shown in equation 4:

$$\Delta P_E = \Delta T \times Y_{system} \qquad \text{Eq (4)}$$

Where $\Delta T = T_2 - T_1$ is the measured axial thrust load change in lbs, and Y_{system} is the sum of contributions to the axial yield rate from the two test bearings and the test fixture in μin/lb. The yield rate of the bearing pair was determined using computational bearing analysis tools (DYBA). The bearing pair yield rate takes into account the change in bearing deflection due to elastic deformation at the Hertzian contact. The yield rate of the system was determined through experimental calibration by directly measuring the displacement for a given force.

The signal from this load cell is collected by a data acquisition system in real time during the bearing test. To avoid uncertainties in the outer ring position due to thermal fluctuations, the film thickness measurements reported here were determined from the nearly instantaneous change in end play when the bearing rapidly decelerated from full speed to rest. When the full speed and zero speed data points are collected nearly coincidentally in time, there is no period in which the temperatures can drift to cause thermal changes in the end play. An example of a test data collection sequence is shown in Figure 3. The data stream nearest to the top of this chart shows axial force measured by the load cell. Each of the three disturbances seen in this data are stop/start cycles during which the bearing deflection was measured. The full speed thrust load (T_2) was chosen as the data point immediately before stopping the bearing, and the zero speed load (T_1) was chosen as the data point immediately after the bearing came to rest. During each restart, we observe an overshoot transient due to slumping of the lubricant at rest and the subsequent redistribution after start-up. The difference between these two values is taken as the change in axial load (ΔT) to be used in equation 4. One drawback to this technique is that each time the bearing is stopped, the lubricant distribution is reset. This will tend to prolong the run-in period, and may cause the measured film thicknesses for a given amount of running time to appear thicker than they would if the bearing had no interruption of use.

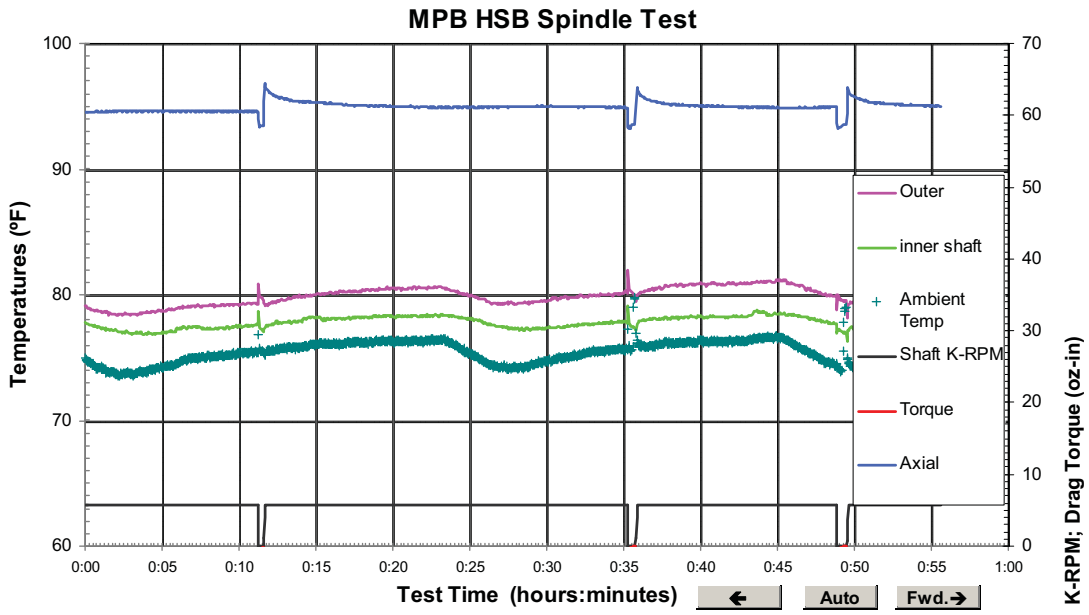

Figure 3. An example of raw data. The top data stream shows the axial load that is used to determine bearing deflections. The three data streams bundled near the center are, from top to bottom, temperatures of the outer ring, inner ring, and laboratory ambient.

Air gap displacement change method

The total axial deflection of the outer ring is directly measured as the deflection of reference paddles ($\Delta D = D_2 - D_1$) connected to the spacers that move with the outer rings, as shown in Figure 2. The axial position of these paddles is monitored with non-contact proximity (air gap) sensors. To eliminate uncertainties due to run-out of the bearing system, the response from a pair of paddles mounted on opposite sides is averaged to produce the total change in axial position. To convert this total change in axial position into a change in the bearing end play for use in equation 3, one must first correct for the displacement due to yield rate of the bearing pair.

To determine the contribution due to the yield rate of the bearing pair, let:

h_1 = axial deflection of a single row at thrust load T_1
h_2 = axial deflection of a single row at thrust load T_2
f_1 = change in stick-out of a single row due to the EHD film at zero speed = 0
f_2 = change in stick-out of a single row due to the EHD film at full speed

The axial positions given by the air gap sensor may be written as:

$$D_2 = 2(-h_2 + f_2) \qquad \text{Eq (5a)}$$
$$D_1 = 2(-h_1 + f_1) \qquad \text{Eq (5b)}$$

Or:

$$\Delta D = D_2 - D_1 = -2h_2 + 2h_1 + 2f_2 \qquad \text{Eq (6)}$$

So that:

$$2f_2 = \Delta D + 2(h_2 - h_1) \qquad \text{Eq (7)}$$

The quantity $2f_2$ is then taken as the change in end play (ΔP_E) to be used in equation 3. The quantity (h_2-h_1) is equal to the product of the measured change in thrust load and the yield rate of a single bearing. As mentioned above, this yield rate is determined using computational bearing analysis tools (DYBA). Since

this quantity adds to the capacitance measurement distances, the resulting EHD is larger than if this correction were not used.

Results and Discussion

Coray vs. Pennzane Oil

When reviewing the results shown below, bear in mind that these film thickness results apply only to this specific set of bearing geometry, materials and operational conditions. Each experiment shown here was performed with the same pair of 304 sized angular contact bearings operating at 6000 rpm.

The first experiments described here were designed to determine the time scales for run-in, and the final absolute film thicknesses, of two base oils that have been commonly used in aerospace applications. In each case, approximately 20 mg of the base oil, formulated with TCP, was added with a clean syringe to each row. This quantity was sufficient to show a meniscus at each ball/race interface at 10X. The bearings were then operated at 6000 rpm. At periodic intervals during the run-in, bearing operation was halted to measure the film thickness. At each interruption, film thickness was recorded and the speed was returned to 6000 rpm.

Results of these experiments are shown in Figure 4, where the open symbols represent Coray and the filled symbols represent Pennzane. In both cases, the triangles represent data collected with the load cell and the circles represent data collected with the displacement sensors. First of all, we find excellent agreement between the two independent techniques for measuring deflection of the rings. Second, we

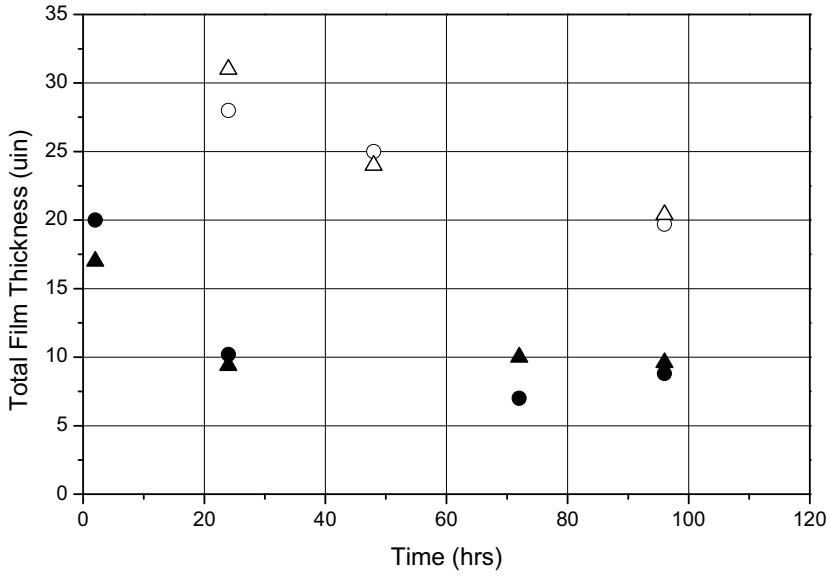

Figure 4. Total Film thickness (in microinches) as a function of cumulative time operating at 6000 rpm with neat base oils formulated with TCP. Open symbols represent Coray and filled symbols represent Pennzane. Triangles are the results from the load cell and circles are the results from the displacement sensors.

find that the run in of Pennzane was nearly complete after only 24 hours, while the Coray took significantly longer. Third, after 96 hours of cumulative use, the film thickness of Coray was more than twice that of the Pennzane. More significantly, the total film thickness for Pennzane at the contact between the ball and inner ring was very small. Using the Hamrock-Dowson expression [7] to determine the partitioning of the film between the inner and outer races, we find that 40% of the film is at the inner ring and 60% is at the outer. This implies that the inner ring film thickness is approximately 3.6 μin after

only 24 hours of operation. Since the composite surface roughness for the test articles is approximately 2.0 μin, the nominal operating condition provides a film that is under 3 times the composite roughness.

The fully flooded total film thickness (the sum of the inner and outer) predicted by the Hamrock-Dowson expression [7] is 132 μin for Pennzane. With the conventional Coy-Zaretsky starvation reduction factors [8,9], this prediction falls to approximately 77 μin for Pennzane. Our measurements show ~9 μin total film thickness after 24 hours. It is evident that our films are much more deeply starved than predicted by the Coy-Zaretsky analysis. The primary reason for this discrepancy is that the Coy-Zaretsky approach takes into account kinematic starvation, where resupply of the EHD contact is limited by rapid ball passes, but neglects deeper starvation due to a restricted amount of lubricant in the vicinity of the contact. In fact, the experiments used to validate the Coy-Zaretsky approach were performed an oil-air mist of lubricant provided to the contact [9]. Developing the ability to make quantitative estimates of this steady state film thickness with restricted lubricant supply is the subject of ongoing investigation.

Rheolube Grease Results

For the next set of experiments reported here, the bearing was cleaned and a single charge of 1.1 g Rheolube grease per row (Pennzane oil with a thickener, obtained from Nye Lubricants) was distributed throughout the ball complement. The bearing was then operated at 6000 rpm, and operation was interrupted sporadically to measure film thickness as described above. The symbols shown in Figure 5 represent the film thickness as measured by capacitance proximity sensors (circles) and load cell (triangles). The first data point was collected after the initial lubricant run-in disturbances were suppressed after 22 hours. The average value for the total film thickness from the two techniques was 19 μin. After this point, the film thickness fell to less than 17 min after 98 hours, but appeared to rise slightly to 18 μin after 365 hours.

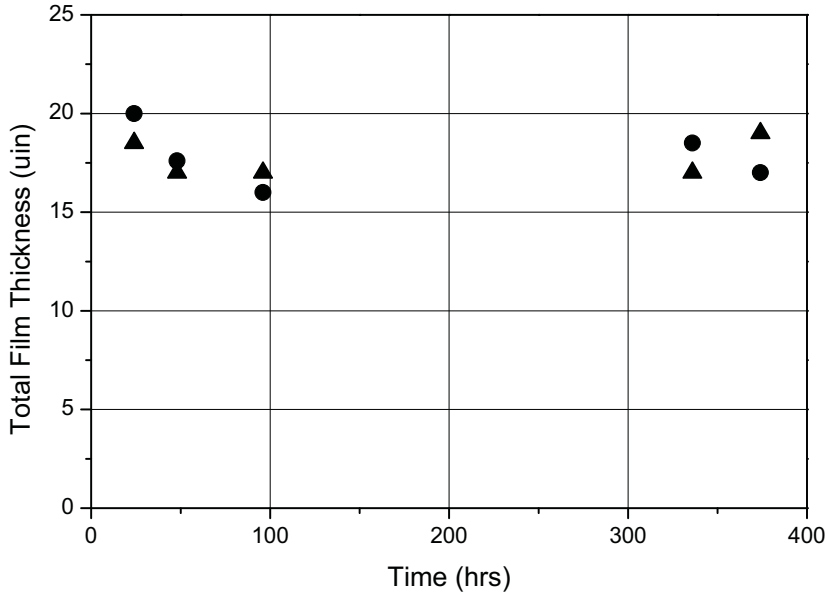

Figure 5. Total Film thickness (in microinches) as a function of cumulative time operating at 6000 rpm with a grease pack of 1.1 g Rheolube. Triangles are the results from the load cell and circles are the results from the displacement sensors.

The observation of a long-term grease film that is much thicker than the oil film contradicts many of the observations reported in the literature. Others have found that the response with grease is initially much greater during run-in, but that it falls to the oil film thickness after the run-in is complete and then it falls

further as the supply of oil from the thickener is reduced. For reasons explained below, we surmise that this indicates that our lubricant has not fully run in after 400 hours.

In the final set of experiments reported here, a thin film of Rheolube grease (0.14 gm per row) was applied to the bearing components before it was again operated at 6000 rpm. These results are shown in Figure 6. We found that the film began with a thickness that was comparable to the apparent steady state condition with the full grease pack (~19 μin). However, the film thickness was observed to fall continuously over the next 500 hours to approximately 9 μin. The final data points suggest that the rate of decline was reducing at this point, but it is unclear whether the thickness would have continued to fall below 9 μin with extended operation.

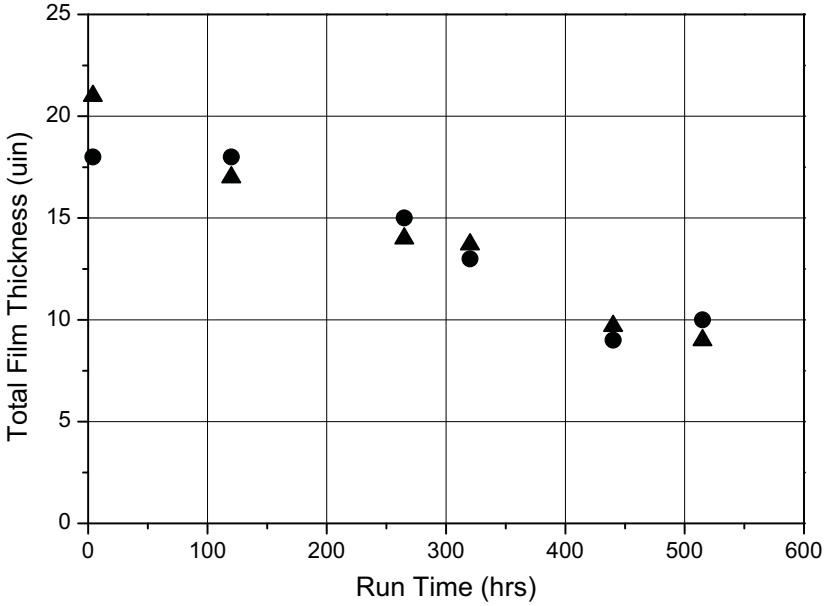

Figure 6. Total Film thickness (in microinches) as a function of cumulative time operating at 6000 rpm with a grease pack of 0.14 g Rheolube. Triangles are the results from the load cell and circles are the results from the displacement sensors.

The continued maintenance of a nearly 20 μin film thickness in Figure 5 was likely due to some prolonged retention of the grease thickener in the EHD contact. Figure 6 shows that the total film thickness will fall to 9 μin if starvation is driven further by restricting lubricant resupply. Figure 4 shows that if the film is resupplied only with neat oil, then the thickness will also fall to approximately 9 μin. We conclude that the robust film of Figure 5 must be due to some enduring intermittent resupply of grease to the contact rather than just oil. We surmise that a thin film of grease persists on the balls outside the running band, providing fresh grease to the contact when the ball spin axis is disturbed. This represents a transient condition that would likely diminish with continued operation. This run-in transient may have been artificially prolonged by a lack of disturbances to the bearing during our controlled testing. Therefore, Figure 6 suggests that the film thickness shown in Figure 5 would eventually fall to below 10 μin after prolonged use in a typical bearing application.

Conclusion

We have demonstrated a technique to measure the total EHD film thickness in an operating angular contact bearing. Excellent correspondence between the two independent methods of measuring outer ring deflection provides confidence in this measure. Our procedure for measuring the instantaneous

change in outer ring position provides excellent independence from thermally induced changes in outer ring position. We conclude that this technique is suitable for the investigation of film starvation in grease lubricated angular contact bearings.

Our initial investigation into film thickness with lubricants of immediate relevance to aerospace applications shows that the steady state Coray oil film was approximately twice that of the Pennzane oil film. Furthermore, the total Pennzane film thickness (9 μin) implies that the upper limit to the film thickness of the inner ring was 3.6 μin. This is less than three times the composite surface roughness (3 x 2 μin = 6 μin). This is also much less than the value predicted using conventional starvation analytical methods. Since the starvation analysis based upon surface tension driven resupply allows for an arbitrarily small film under certain conditions [1, 10], we will continue to pursue quantitative analysis using these techniques. However, further testing will be required to establish the oil film thickness in the vicinity of the contact (h_{oil}) before these methods can be used to produce a quantitative prediction.

Experiments with a large amount of Rheolube grease (1.1 g per row) show general agreement with other comparisons of grease and oil film thicknesses in the literature. We found that the film thickness was approximately equal to the flooded oil film thickness (before run-in), where the literature generally shows a typical grease to be slightly thicker before run-in. In contrast to the literature, however, we found that the grease film thickness did not fall appreciably during the nearly 400 hour test. We surmise that this is due to benign operating conditions that did not stimulate regular changes in ball spin axis. With prolonged periods of ball tracking, the depletion of grease from the ball surface was delayed, providing an intermittent supply of oil and thickener to the contact. This produced an extended run-in transient with a nearly 20 μin EHD film.

Experiments with a small amount of grease (0.14 g per row) show the results of a run-in that is more likely to represent the conditions of a real application. With regular disturbances in speed and/or load experienced during an actual application, the high yield stress of the grease thickener would cause channeling to the sides of the ball path on the races and more rapid depletion of thickener from the ball surface. This would approach the situation that was artificially created with the reduced initial charge of grease in this experiment. We found that the EHD film thickness fell over approximately 500 hours to approximately the same level as the oil film thickness. This also contradicts many of the results shown in the literature (for ball-on-plate interferometric film thickness instruments), which have shown a grease film thickness that is significantly reduced from the oil film thickness. However, it is possible that the film thickness in these experiments would continue to fall with continued testing.

Acknowledgements

This work was supported by The Aerospace Corporation's Independent Research and Development Program funded by the Space and Missile Systems Center (SMC) of the USAF under contract number FA8802-04-C-0001.

References

1. Cann, P.M. and Lubrecht, A.A. "An Analysis of the Mechanisms of Grease Lubrication in Rolling Element Bearings" *Lubrication Science,* 11 (1999), 227-242
2. Tyler, J.C., Carper, H.J., and Ku, P.M. "EHD Film Thickness Behavior in DMA Bearings. Part I – Experimental and Computational Techniques" *ASLE Transactions*, 22(3) (1977), 201-212
3. Miettinen, J., Andersson, P., and Wikstrom, V. "Analysis of Grease Lubrication Using Acoustic Emission Measurement" *I. Mech. E., J. Engr. Tribology,* 215 (2000)
4. Qi, G.-P. "Development and Application of the Instruments for Rolling Bearing EHL Oil Film Thickness Measurement" *Modeliing, Measurement, and Control A: General Physics and Electronics,* 73(3) (2000), 40-46
5. Zheng, W., Zhang, Z, Sun, S. "The New Development of Measuring EHL Oil Film Thickness for Thrust Bearing" *Proc. 17th IEEE Instrumentation and Measurement Technology*, vol. 3 1409-1413, IEEE, Piscataway, NJ.

6. Zhang, J., Drinkwater, B.W., and Dwyer-Joyce, R.S. “Acoustic Measurement of Lubricant Film Thickness in Ball Bearings” *J. Acoustic. Soc. Am.* 119(2) (2006), 863-871
7. Hamrock, B.J. and Dowson, D. “Isothermal Elasohydrodynamic Lubrication of point contacts, Part IV, Starvation Results” *ASME J. Lubr. Technol.* 99 (1977), 15-23
8. Chiu, Y.P. “An Analysis and Prediction of Lubricant Film Starvation in Rolling Contact Systems” *ASLE Trans.* 17 (1974), 22-35
9. Coy, J.J., and Zaretsky “Some Limitations in Applying Classical EHD Film Thickness Formulas to a High-Speed Bearing” *ASME J. Lubr. Technol.* 103 (1981), 295-301
10. Cann, P.M., Damiens, B., and Lubrecht, A.A. “The Transition between Fully Flooded and Starved Regimes in EHL” *Tribology International* 37 (2004), 859-864

Scanning System Development and Associated Bearing Cage Instability Issue

Manfred Schmid* and Christian Hehr*

Abstract

The Scan equipment used to control the MicroWave Radiometer Imager (MWRI) of the polar orbiting FY3 meteorological satellite was developed and delivered to the customer by Astrium Satellites GmbH. The instrument detects and monitors meteorological and biosphere environmental anomalies.

The key elements of the design and the most important design requirements and design features are described hereunder.

Special attention is paid to the bearing cage anomaly observed on the Scan Compensation Mechanism during the test campaign and to the subsequent root cause investigation performed.

Introduction

The scanning equipment consists of a Scan Drive Mechanism (SDM) rotating the instrument package, of a physically independent Scan Compensation Mechanism (SCM) used to eliminate disturbance moments induced by the SDM and of a closed loop Scan Control Electronics (SCE) controlling and synchronising the two mechanisms.

The heavy MWRI instrument package mounted on top of the Scan Drive Mechanism requests conical antenna scanning. This requirement leads to a continuously rotating mechanism of high scan rate stability.

One EQM and two FM sets of scanning equipment were developed, qualified and delivered to the customer.

During the mechanism test campaign a randomly occurring bearing noise was observed in the SCM. Apart from the mechanism design, the paper explains the way up to identification and elimination of the bearing noise issue under the given technical and programmatic constraints and provides the lessons learnt from this experience.

Key Equipment Design and Performance Requirements

The mass of the instrument package mounted on top of the SDM is 60 kg at an instrument Moment of Inertia of 2.7 kg-m^2. The instrument has to be accelerated within 180 s to the nominal spin rate.

The nominal spin rate is 1.7 s/rev. In order to achieve the required radiometer performance, the spin rate shall stay stable within an error bandwidth of ±0.34 ms compared to the nominal value. In order to achieve this stability, closed loop control is implemented.

For compensation of the momentum induced by the SDM into the S/C, a Scan Compensation Mechanism is provided. The SCM is physically independent from the SDM and it is designed as a separate mechanical unit mounted in line with the SDM rotation axis to the instrument structure. Both units, the SCM and the SDM are controlled by the digital controller implemented in the FPGA of the Scan Control Electronics (SCE).

The SCM rotation rate is directly synchronised to the SDM scan rate via the controller. The SDM scan rate is multiplied by a factor of 16, which leads to a rotation speed on the Scan Compensation Mechanism of about 565 rpm.

* EADS Astrium GmbH Satellites, Friedrichshafen, Germany

The chosen SCM speed ratio is the result of a trade-off between bearing life margin and flywheel inertia at minimum resulting flywheel mass (and at the given maximum allowable Flywheel diameter of 400 mm).

The equipment life is 3 years in orbit; this yields nominally 890 million revs on the SCM over life without margin. The operational temperature for the mechanisms is -30 to +50 deg C.

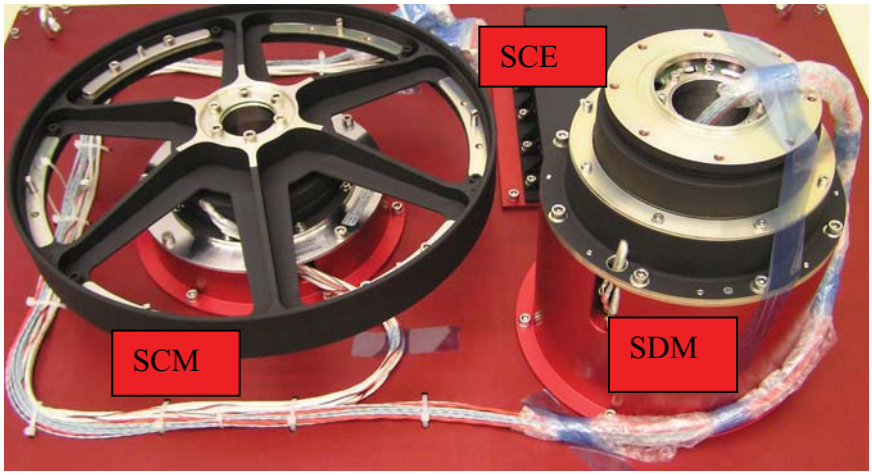

Figure 1. Scan Drive Equipment mounted to the Transportation Jig.

Scan Drive Mechanism Design

The SDM consists of a drive module using a set of inclined ball bearings, of a redundant brushless DC Motor and of a redundant optical encoder for closed loop velocity control. On the rear end of the drive Module, a slipring unit for power and signal transfer from/to the rotating Radiometer Instrument package is attached. The Harness is guided through the hollow drive shaft to the slipring rotor and from there via the slipring brushes to the slipring stator.

The I/F to the rotating instrument mounted on top of the mechanism is formed by a launch off-load device. The launch off-load device consists of axially pre-loaded flexible metallic bellows and of an accurately shaped conical Interface. The combination of both elements provides instrument alignment accuracy and torsion stiffness during mission as well. During launch the conical I/F is lifted off from the mechanism I/F, so to de-couple the instrument load path from the mechanism. After release of the Instrument HRMs on S/C side, the instrument is pulled by the preloaded SDM bellows back into the conical I/F in order to allow transfer of the drive torque from the SDM to the instrument at accurate alignment of the instrument rotation axes.

The Rotor shaft is mounted via two pairs of hard preloaded angular contact ball bearings in back to back arrangement into the SDM housing. The bearings are manufactured from Stainless Steel 1.4125 (440 C), the cages are manufactured from Phenolic Resin, vacuum impregnated with oil.

The motor is of the brushless DC type with completely cold redundant independent Stators. Its maximum operation torque is 2.3 Nm.

The redundant optical Encoders provide absolute position data with 16-bit resolution. Its output data are used for motor commutation on the one hand and for high accuracy motor velocity control on the other.

The Slipring is composed of 19 solid gold tracks and redundant gold alloy brushes to comply with the expected 3 years orbit life corresponding to about 55 million revs.

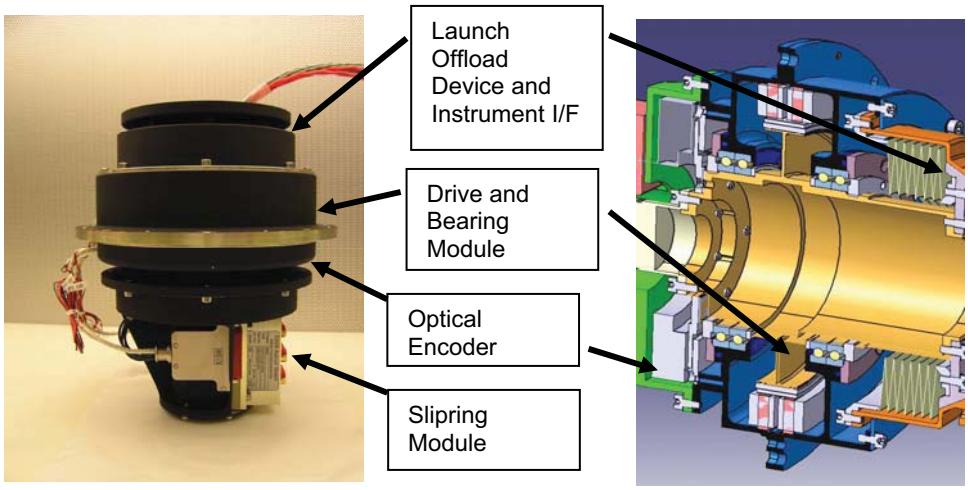

Figure 2. SDM Design

Scan Compensation Mechanism (SCM) Design

The function of the SCM is to compensate for the momentum induced by the rotating instrument into the S/C. The SCM consists of a drive module using a brushless DC Motor with redundant motor stators. The SCM motor is similar to the SDM, however it is optimised for the higher operation speed. Its maximum operation torque is 0.9 Nm. For rotation velocity feedback 3 Hall Sensors are included in each motor stator. To the motor output shaft a flywheel unit is attached. Trim masses for fine-tuning of static imbalance are mounted to the Flywheel.

Concerning the bearing configuration it has to be noted that the bearings and its lubrication concept were kept identical to the SDM in order to gain synergy by similarity during the mechanism development and bearing procurement process.

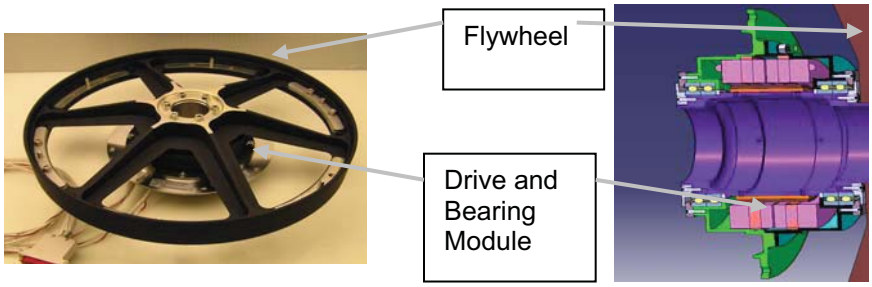

Figure 3. SCM Design

Scan Control Electronics

The Scan Control Electronics (SCE) is built up as a completely cold redundant unit, each supporting the main respectively redundant motor windings of each mechanism and receiving feedback from the redundant high-resolution encoders respectively from the Hall sensors. The controller is implemented into the FPGA.

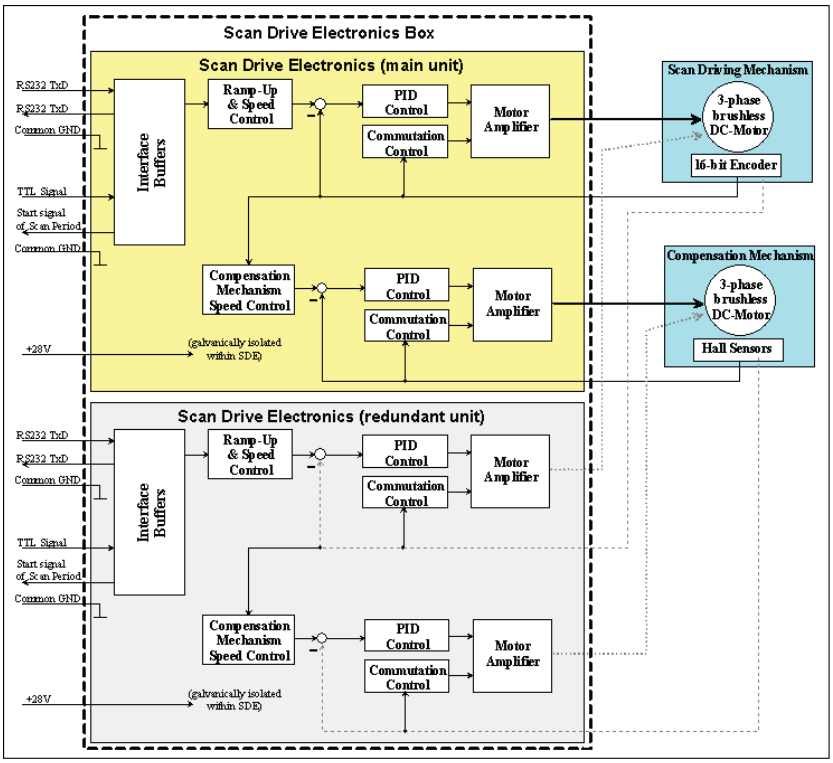

Figure 4. Scan Control Electronics Block Diagram

Mechanism Performance Test Summary

Apart from the standard verification approach applied to space mechanisms, two main critical functional performance data had to be verified. One of them was the rotation period of 1.7 s/rev at a stability of ±0.34 millisecond; the other one was the maximum residual momentum of <0.1 Nms induced into the S/C by the Scan equipment during start-up and operation.
Figure 5 shows the equipment performance test setup. In Figure 6 the typical scan rate deviation from the nominal value over a time of 2000 seconds is shown, while in
Figure **7** the residual torque profile over time is depicted. The scan rate deviation was measured by reading out the high-resolution encoder signal; the residual momentum was measured via a Kistler torque test device.

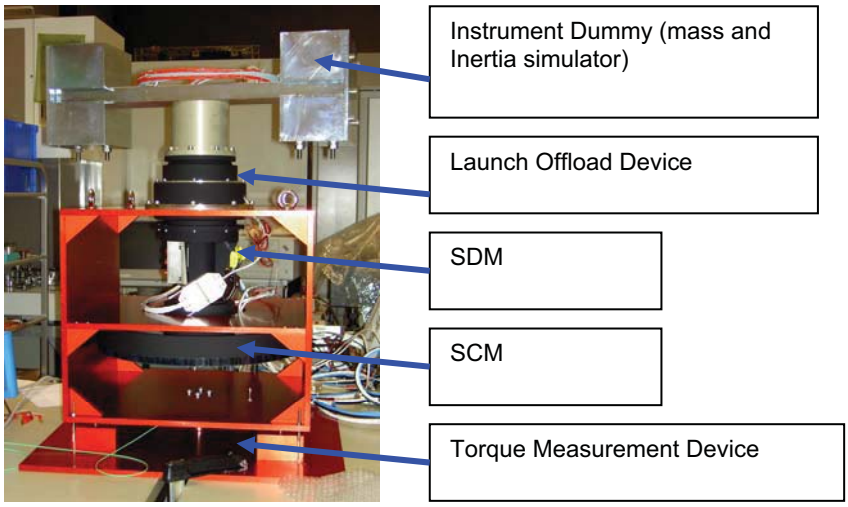

Figure 5. Functional Performance Test Set-up

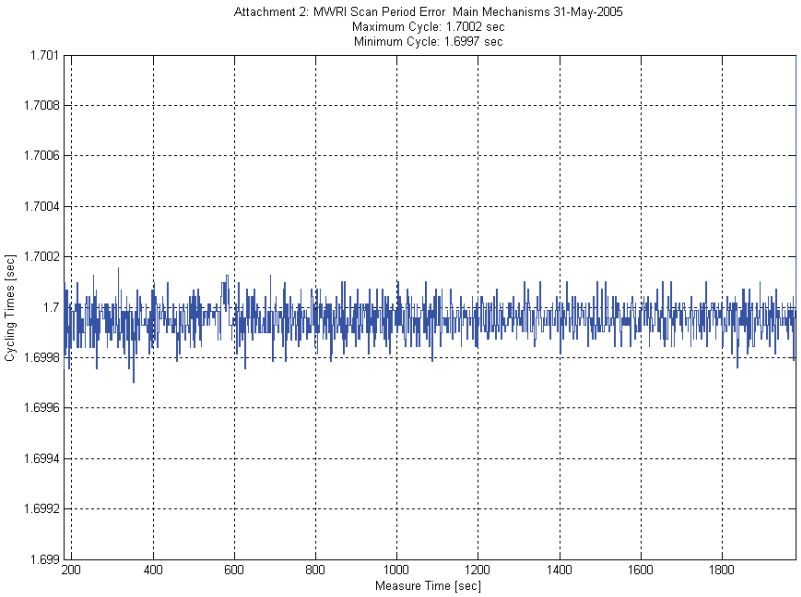

Figure 6. Typical deviation from nominal Scan Rate over time

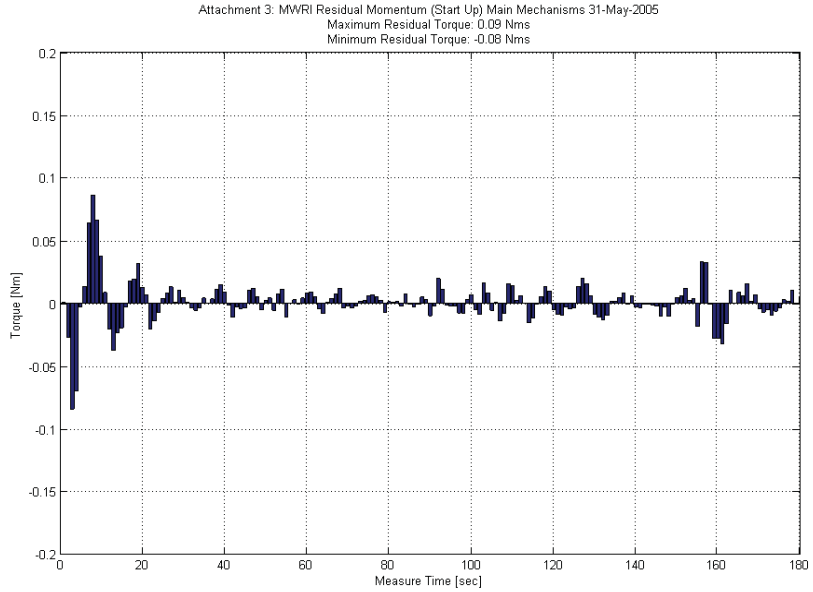

Figure 7. Typical induced torque profile during instrument start-up (180 seconds)

Bearing Unit Characteristics

Both, the Drive Mechanism rotating at slow angular velocity and the Scan Compensation Mechanism rotating at higher velocity, make use of an identical bearing configuration. The only major difference between the SCM bearing and the SDM bearing is defined by the higher bearing pre-load applied to the SDM bearing as a consequence of the higher operational forces acting to the SDM due to a potential later instrument CoG shift out of the nominal rotation axis.

By design, TiC-coated balls were preferred, however due to procurement issues originated by the transfer of the TiC coating process from Europe to the US, the availability of TiC-coated balls was limited at the time of bearing procurement. The finally delivered TiC-coated balls were mounted into the bearings by the

bearing supplier; however, scratches of unknown origin were identified during bearing inspection on the balls. This led to the implementation of the back-up bearing design using steel balls and to a subsequent change of the lubrication system. In the following table (Table 1) the bearing characteristics are listed.

Table 1: Bearing Characteristics

Bearing Characteristics	SDM Bearing	Differences for SCM
Bearing Type	Thin Ring	
Arrangement	Back to Back	
Material	440 C	
Cage Material	Phenolic Resin	
Ball material	TiC-coated steel balls (was changed later to steel only)	
Vacuum impregnated	Z 25 (was changed later to MAP grease and Nye oil)	
Cage guidance	Inner Race riding	
Number of Bearings	2 pairs, back to back	
Outer Diameter	98.425 mm	
Inner Diameter	77.788 mm	
Height of Bearing Pair	15.874 mm	
Ball diameter	4.762 mm	
Number of balls	42	42 (original number, reduced later)
Contact angle	27 deg	
Preload	750 N	400 N
Max Contact Stress	1200 MPa	1000 Mpa
Axial Stiffness	250 N/µm	330 N/µm
Radial Stiffness	450 N/µm	550 N/µm
Angular Stiffness	330 Nm/mrad	410 Nm/mrad
Running Torque	<0.08 Nm	<0.04 Nm
Calculated Life	>1.18E+10 revs	>18.6E+8 revs
Rotation velocity	35.3 revs /min	564.7 revs/min

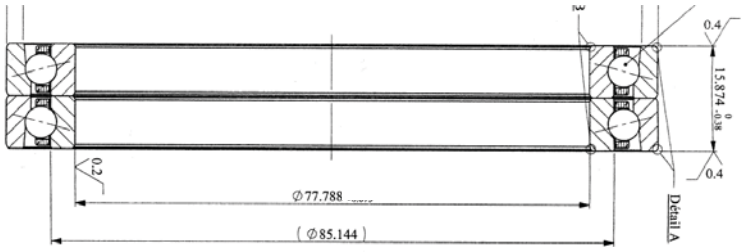

Figure 8: Bearing Dimensions

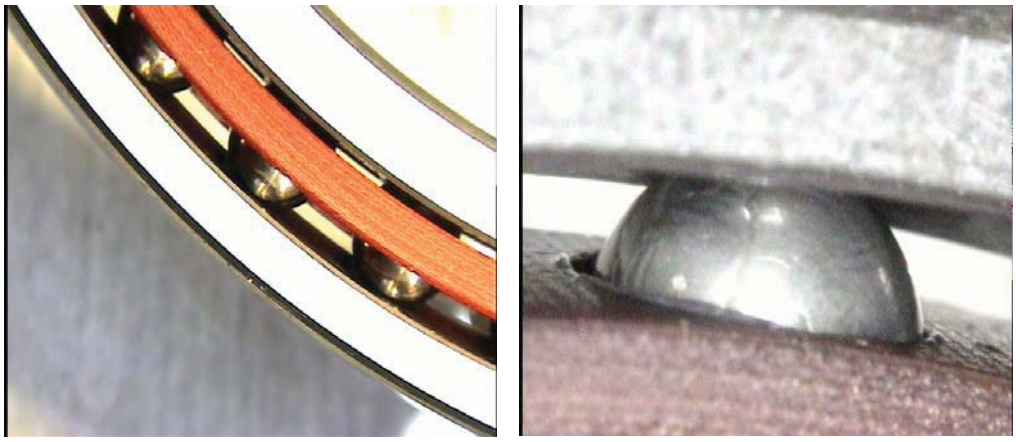

Figure 9. SCM Bearing Details

Observed Bearing Noise Issue on the SCM

In order to gain design and procurement synergy (considering the long lead times of ball bearings) within the extremely tight development schedule of 10 month for the EQM and of 12 month for the first FM equipment, an identical bearing concept was chosen for both mechanisms. It was confirmed by analysis, that at the given rotation speed of about 565 rpm on the SCM (performing momentum compensation) compared to 35 rpm on the SDM (supporting the MWRI instrument), the bearing life margin at the given load conditions was still very good.

Dynamic cage instability effects at the comparably low maximum rotation speed of about 9.5 revs/s were not expected. This latter assumption was supported by references where similar bearings had been used in Helicopter Subsystems at much higher speed.

After integration of the EQM equipment, functional testing was started. After some hours of perfect operation a sharp scratching noise was observed, obviously coming from the bearing unit of the fast running Scan Compensation Mechanism. The good mechanism performance was not affected by the phenomenon; the performance values were stable and as good as before.

The noise was not reproducible and it occurred only from time to time. After start up periods of noise free operation were observed, followed by periods of sharp randomly occurring noise. During mechanism speed up to the nominal velocity, the issue was typically observed at rotation velocities above 500 revs / minute, while during deceleration the effect was observed down to about 100 rev/min.

Consequently the mechanism was dismantled and all bearing seats and bearing Interfaces were checked again in order to identify any in-correct integration, tolerance or cleanliness issues and to verify the lubrication and cage condition. All tolerances were found as expected and no misalignment, debris, bad lubrication, bearing degradation or faulty integration could be detected.

The mechanism was re-integrated an operated again. All friction values were as expected, the operation was smooth. However, after some hours the noise came back. Again it was found that the issue did not jeopardise in any way the mechanism performance or power consumption, however the remaining general lifetime concern was quite severe.

During one subsequent performance test, a quite hard noise anomaly was detected, which suddenly disappeared. From this time onwards, the phenomenon was never detected any more throughout all the

qualification test campaigns, neither after vibration, nor during hot or cold operation. The unit operated perfectly.

Therefore the origin of the observed temporary anomaly could not be clearly identified at this stage on the EQM unit. Consequently the H/W was delivered to the customer for system testing activities according to the contract and still within the required lead time of 10 month.

Three month after delivery, an alert was received from the customer, who had observed again noise in the mechanism.

After receiving the mechanism back on site, the origin of the anomaly could be investigated in detail. At that time the FM1 mechanism was already integrated and functionally tested without any issue. However after an extended storage time of some days prior to environmental acceptance testing, also on FM1 the noise issue could be observed, however in a less severe manner than on the EQM. Therefore it was clear from now that a systematic effect was occurring.

Investigations and Results

Due to the missing characterisation possibility of all potentially influencing parameters in the specific application, a comprehensive empiric investigation was started in order to identify the major drivers for the anomaly.

By design, the SCM integration concept was kept simple. This design feature was identified as a key advantage during all following H/W investigations, since it was possible to dismantle and re-integrate the mechanism at least once a day for check of function and identification of the success of a corrective measure performed.

Basically four different causes for the anomaly were considered:

1) Bearing mounting conditions (in the mechanism)
2) Bearing internal design and load conditions
3) Cage design
4) Lubrication concept

The most important modifications performed on mechanism and bearing level are listed in the following table (Table 2) and the observed effects on the noise anomaly are described:

Table 2: Modifications performed on the EQM Mechanism

Potentially Influencing Parameter	Modification	Observed Effect on noise reduction	Comment
1) Bearing mounting conditions			
Potential Bearing integration / tolerance issue	Dismantling of mechanism and detailed inspection	No improvement possibility	All bearing seats and mounting interfaces were in nominal condition
Potential alignment issue due to two pairs of ball bearings in back to back arrangement.	Dismounting of one bearing pair, operation with only one pair of bearings	No improvement observed	to avoid static over-determination
2) Bearing internal design			
Too low bearing preload	Increase of pre-load compared to the nominal value	No improvement observed	

Potentially Influencing Parameter	Modification	Observed Effect on noise reduction	Comment
Too high bearing preload	decrease of pre-load to about 300 N	Cage noise was eliminated during ambient pre-testing, however this was not confirmed after vibration. It was observed after vibration that the bearing outer rings tended to rotate in the bearing seat w.r.t. each other at reduced bearing preload	After Vibration test at reduced pre-load, bearing noise was observed again.
Ball diameter variation out of nominal range with the effect of "slippage" of individual balls	New balls used	No improvement possibility	The ball diameter variations were in the nominal range. A new set of bearing balls was mounted, no noise reduction observed
Degradation of races due to potentially wrong ball to race contact line	Inspection / oil filtration	No improvement possibility	The races were inspected at supplier premises by microscope and were found to be all nominal
Degradation of ball surfaces	Inspection	No improvement possibility	The surface conditions of the balls were nominal
Potential inner / outer race circularity out of tolerance	measurement of race circularity	No improvement possibility	The circularity tolerances were measured. The values were within the specified toerance.
3) Cage design			
Too weak cages (large cage diameter at low cross section)	Manufacturing of stiffer cages with higher cross section	The noise production became worse after implementation of stiffer cages	The stiffer cages did not solve the issue. The observed noise became even worse. The original cage cross section was maintained
Cage guidance. The cage design and cage tolerances were reconsidered and different inner and outer race riding cages were alternatively manufactured.	Change of cage design from inner to outer ring riding configuration, Change of cage tolerances.	No improvement observed	Nominally the bearing cages were inner ring riding, they were changed to an outer ring-riding configuration. Since a positive effect on the bearing behavior was not identified, the inner riding configuration was maintained as the baseline.
Number of Cage pockets	The even number of pocket cages (42) was changed to an odd number of pockets (39)	No improvement observed	According to theory high velocity bearings gain cage stability if an odd number of balls is used. The number of 39 was maintained throughout the tests though it did not yield any improvement w.r.t. observed cage behavior.
4) Lubrication			
Lack of lubricant	Re-lubrication of the bearing	Noise disappears for some hours only, no long term improvement observed	Fomblin Z-25, Vacuum impregnated cages

Potentially Influencing Parameter	Modification	Observed Effect on noise reduction	Comment
Lack of lubricant	Extended non-operation time (storage time)	Noise issue was more severe after extended mechanism storage time (some days)	
Type of Lubricant	Change from Z-25 to Nye oil and MAP grease	No improvement observed	However: General improvement of lubrication performance over life could be achieved by the changed lubrication concept in combination with steel balls. Potential chemical degradation of Z 25 in combination with the steel balls and steel races could be avoided.

While the above measures 1) and 4) of Table 2 could be performed on Astrium site, the measures 2) and 3) directly related to the bearing configuration, had to be implemented by the bearing supplier but verified on mechanism level. It was found that this process was extremely time consuming and inefficient since it was very difficult to intervene regularly into the supplier standard manufacturing process for implementing any new parameter modification. Furthermore the bearing supplier himself was depending on lower tier suppliers (e.g. for cage manufacturing) so additional delays were resulting as a consequence.

Therefore it was decided to perform all necessary further bearing investigations and modifications directly at Astrium Satellites within the mechanism team. This approach allowed complete in-house control of the further investigation process without any un-necessary schedule delay. For this purpose all required bearing dismantling and re-integration tools were manufactured and the bearing dismantling and mounting process was defined in order to allow complete handling and control of all necessary further bearing modifications, independent from the bearing supplier. After dismantling the EQM bearings and cages on Astrium site, all parts were inspected and no degradation or abnormal condition of parts or lubricant was observed.

After implementation and check of the above measures it was quite clear that the anomaly was generated by the bearing cages as a consequence of occasionally occurring cage instability effects at the given rotation speed. However the mechanism of action causing the instability effects with subsequent noise production was not really understood.

Only three findings influencing the noise production remained:

The first important observation was that under low bearing pre-load the outer bearing races of a bearing pair tended to slightly rotate w.r.t. each other. This led to the suspicion that during operation unexpected forces produced by the cage are acting to the outer race.

The second observation was that at increase of cage stiffness (increase of cage cross section) the noise effect got worse.

In addition it was observed, that after an extended storage time (e.g. weekend) the noise issue was more severe than under continuous rotation. This was also in line with the fact that after delivery of the EQM to the customer (long storage time resulting from transportation, unpacking, start-up activities) the noise issue was observed again.

All three above observations lead to the conclusion that un-expected forces in the bearing were acting with the result of subsequent noise production.

The observation made during the first EQM tests namely that after occurrence of a sudden hard noise in the bearing the noise issue disappeared completely for all remaining test campaigns, could now be

explained by a forced rotation of an outer bearing ring of a bearing pair as a consequence of a transient jamming force produced by the cage. After rotation of the bearing ring to its new position, the cage stability might have been improved. This theory would also comply to the fact that for a stiffer cage the noise issue got worse (higher forces produced by the cage).

The key question was now to find the origin and influencing parameters for the transient forces obviously produced by the cage with the consequence of generating the observed bearing noise. The only possible explanation had to be searched in the cage configuration itself.

A special tool was manufactured to allow inspection of the cage circularity and the EQM cage dimensions were found to be within the “as designed” tolerances. Also the pocket dimensions and clearance to the inner race was in tolerance (chosen such that at cold operation the shrinking cage could not jam on the inner race due to different thermal expansion between race and cage).

The conclusion drawn from all the previous investigations was that the bearing cages might be deflected or pushed out of their nominal position from time to time thus generating high local friction forces and subsequent bearing noise. After relaxation of the individual force peak, and nominal stable cage rotation, the noise was not observed for a certain time. This theory was supported by the fact that the noise issue could be deleted for a certain time after bearing re-lubrication leading to lower friction and consequently also to lower built up cage forces.

As a consequence, a method had to be identified allowing to avoid the generation of stresses between bearing cage and balls or to damp the dynamic motion of the cage in a way suitable to avoid noise generation. As a result a quite un-conventional idea was realized. Three bearing balls of each bearing were dismounted from the positions 120 deg apart, i.e. three of the 39 cage pockets were left without a ball. This measure was performed after finding a positive Hertzian stress margin for a 36-ball configuration.

The effect was significant. The noise issue was not observed any longer and even during temperature test at qualification temperatures the bearing run smoothly and completely nominal. Also during a subsequent life test lasting for 4 months at nominal speed (corresponding to 100 million bearing revs), no further noise issue was observed.

Though the effect was not completely understood, it could be concluded that the bearing issue could be solved by changing the dynamic behavior of the bearing cage. This was achieved by taking out dedicated balls from three positions of the cage pockets. Figure 10 illustrates schematically the measures taken. The baseline Cage Configuration using 39 Ball pockets in an un-symmetric configuration with uneven pocket spacing was maintained, however 3 balls were taken out of this configuration (every 13th ball) to come to the final 36-ball configuration.

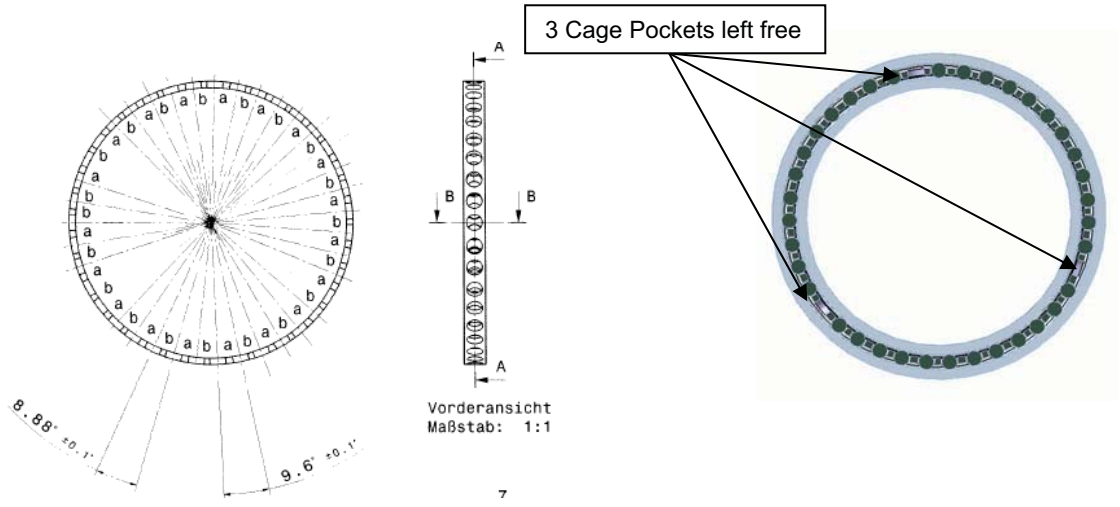

Figure 10: Bearing cage configuration and final bearing configuration using 36 balls only

As a consequence the identified measure was also introduced into the FM mechanism however here the observed noise issue was still observed in a reduced form. This led to the conclusion that the positive effect obviously caused by the reduction of balls in the EQM mechanism was compensated by another effect present in the FM bearings.

The remaining suspicion was, that the cage configuration as used in the EQM bearings was different from the FM cage configuration. This theory was fed by the fact that EQM and FM cages were manufactured from different batches of phenolic resin.

Since the existence of the cage instability issue was obviously also related to the environmental conditions e.g. to the mechanism storage time, time of operation, hot/cold operation and humidity, the theory was supported, that the poor geometric stability of the Phenolic Resin cages was one of the potential root causes for the noise issue.

Phenolic Resin is known to be quite sensitive to manufacturing processes, storage conditions and production batch and the resulting quality of a bearing cage is even depending on the location of the used material within the manufactured piece of raw material.

A non-circular shape of the bearing cage might have caused a “Hula Hoop” effect at the given rotation velocity resulting in abnormal forces between cage and balls with subsequent noise production.

Though at supplier premises the actual cage dimensions were checked on a 3D measurement machine, the confidence in these measurements was quite low, since the weak thin walled cages were expected to deflect under the contact load of the mechanical measurement device.

The FM1 mechanism disassembled and the bearings were completely stripped on Astrium Site. The measuring gauge already available from the EQM bearing inspection process was used to perform proper measurement of circularity and diameter of the cages in steps of 1/100 mm on all FM bearing cages.

It was found that the cages used in the FM mechanism were out of tolerance by up to 0.3 mm in diameter, compared to the EQM cages that were of good circularity.

As a consequence the selection of cages for the FM mechanism was taking place in order to identify the cages of maximum diameter conformity. These selected cages were then locally overworked by hand in order to generate a good circular shape.

After vacuum re-impregnation, the re-worked cages were integrated into the bearings again and the subsequent mechanism test at ambient conditions yielded prefect results. The noise issue on the FM1 was completely eliminated at the operational temperature extremes. Only at low survival temperature, which was -8 deg below worst-case operation temperature, a slight noise production was still observed. This was probably caused by cage dimensions changing with temperature from the circular shape at ambient conditions to any non-circular asymmetric shape at low temperature extremes in combination with the higher viscosity of the lubricant under this condition.

This finding supported the theory of the high influence of non-perfectly shaped cages at the given bearing size and rotation speed.

Since the thermal deflection over temperature is reproducible, the noise effect disappeared again completely after heating up the bearing from the survival temperature to the low operational temperature and from there up to ambient.

By using the identified 36-ball configuration supported by selection and optimisation of the available spare cages for good circularity, noise free performance over the whole required temperature range could be realized also on the both FM mechanisms.

Potential Causes for the Observed Instability Effects

Though a final conclusion on the root cause for the observed cage instability effect could not be drawn and the influencing effects could not be quantified or proven by an analytical model so far, the observations made on the H/W supports at least the following assumptions:

The cage instability is mainly caused by the dynamic forces resulting from a non-circular shape of the Phenolic resin cages (potentially also influenced by local density differences in the material).

A good oil film between the balls and the cage helps to avoid cage instability.

A weaker (more flexible) cage yields better dynamic stability than a more rigid gage does. In case instability occurs, the rigid cage is expected to produce higher transient forces between balls and cage pockets than a weaker (more flexible) cage does.

Taking out three balls of the bearing in a way as described above contributed to cage stability. This effect is potentially caused by a reduction of the lateral cage run-out or by reduction of dynamic cage forces produced by transient non-linear ball to ball and ball to race contacts. However the observed effect cannot be completely explained and proven without having established a very detailed dynamic bearing model that would have to be correlated with H/W test results.

Technical Conclusions and Lessons Learnt

Do not trust information gained from “similarity” of bearings. Bearing behavior is defined by a variety of parameters (size, material, cage dimension and tolerances, cage guidance, ball to cage clearance, ball dimensions, pre-load, mounting environment, environmental conditions, lubrication, life, operation velocity, operation profile, etc.) and no application is identical to another one. Check carefully these conditions before believing in “similarity”.

Thin ring bearings of the given size (diameter in the 100-mm range) and cage dimensions, operated at elevated speed (above the 500-rpm range) and at the given boundary lubrication conditions seem to be sensitive to cage instability effects, especially if the cage is not perfectly shaped.

Improper (non-circular) cage shape can be expected especially if Phenolic Resin cages are used, since here the potentially in-homogenous local material characteristics tend to cause un-symmetric internal stress levels after manufacturing and at exposure to temperature extremes. Also local density variations in the material might contribute to resulting eccentric forces produced at high-speed operation.

In applications requiring bearings of elevated rotation speed and at comparably large dimension, the use of Phenolic Resin cages is not recommended by the above reasons. Substitutes shall be considered at the beginning of the design process (e.g. Vespel, PEEK or similar).

Though the effect was not completely understood, it was found that residual dynamic effects due to cage un-symmetry were damped out and mitigated after reducing the number of bearing balls from 39 to 36 by leaving every 13^{th} cage pocket free. Using only bearing cages with an odd number of balls (39) unsymmetrical spaced, did not cause any improvement compared to an even ball number of 42.

In order to reduce the project risk, advantage should be taken from a simple mechanism design principle allowing easy dismantling of the mechanism in case of bearing issues. This implies that e.g. bearing press fits should be avoided if possible in order to support an easy and safe bearing integration and dismantling process.

Programmatic Conclusions and Lessons Learned

The observation was made that bearing suppliers produce very good standard bearing quality in view of dimensions of races and balls. Therefore a preferred option to mitigate technical and programmatic risks is to procure standard high quality bearings from experienced bearing suppliers, if no specifically designed

bearings are definitively required for the application. The lead times for standard off the shelf bearings are often very short compared to specifically designed space bearings.

Even if a bearing supplier offers dedicated space bearings, the main production process will normally focus towards manufacturing for industrial or military application. Therefore the support in case of bearing issues observed after bearing delivery is often limited and the implementation of any necessary changes might cause significant implications within the supplier standard manufacturing process.

In addition, the mechanism developer should be able to dismantle and re-integrate the procured bearings on site for later inspection, lubrication, pre-load or cage modification according to in-house procedures in order to mitigate the remaining technical and schedule risk.

By following the process as described below, extreme advantages were already gained in follow on projects w.r.t. schedule, technical risk and costs: The procured standard bearings are dismantled after delivery by the mechanism developer. The cages are designed according to the needs and produced from the material best suited for the application. The bearings are then adjusted to the requested bearing preload by grinding the race shoulders to the required dimension and lubrication is performed according to the needs. Then the bearings are integrated on site and inspection as well as early life test under representative worst case conditions is performed.

High speed bearings should be tested in any case in a representative bearing test set up at worst case operational conditions before implementing it into the space mechanism design. This becomes possible within the normal (tight) development time frame, if the procurement approach as described above is realized.

Launch Lock Mechanism Design Fault Tree Use and Coatings Study

Daniel Villa* and Gustavo Toledo*

Abstract

Characteristics of a design process of a launch lock (LL) mechanism are described. This process began with generation of data that proved a previous design would not perform its function reliably. The re-design was then accomplished through the use of fault tree analysis, which helped make a better connection between requirements and actual failure scenarios. FEA modeling techniques for proper stiffness verification through testing are explored. Proto-type testing revealed that coatings at a volatile spherical joint interface became the primary area of concern as multiple configurations failed. Boron Carbide, bare AM355 to Ti6Al4V with Braycote 600EF, Tiodize, Diamond-like nano-carbon (DLN), and improperly configured coatings of MoS_2 and TiCN were all shown to have unacceptable particle generation. TiCN and MoS_2 doped with SbO_3 and Au were shown to meet cleanliness requirements once coating parameters were properly controlled.

Introduction

Launch lock (LL) mechanisms are critical to mission success because they release payloads or unlock other deployable mechanisms such as gimbals or solar panels. Failure of these mechanisms often causes complete mission failure. Release and retention mechanisms in just the category of pyro-pin pullers have had 84 failures over 23 years of space mission applications. Investigation has revealed that 35 of these failures were caused by lack of understanding on the part of the personnel in charge of assuring the devices would work. Twenty-four were caused by poor design practice and incorrect use of the hardware and twenty-three were attributed to manufacturer's errors [1].

When an original LL device failed laboratory evaluation, considerable attention and oversight were given to the reliability and performance requirements of a replacement design. It was required that a fault tree be used to analytically demonstrate a mechanism reliability greater than 0.999. The analytical approach was necessary because reliabilities of these magnitudes require hundreds and even thousands of tests. For example, to demonstrate 0.999 with a 50% upper confidence limit requires 700 tests with no failures occurring [13]. Even after such testing, the reliability is strictly based on the testing methodology. The problem with demonstrating reliability analytically is that it can lead to considerable effort to get the "correct" reliability that may have little practical value. Its usefulness is found in the effort to understand reliability through a fault tree.

The traditional success criterion for system development is demonstrating requirements have been met through a qualification process. The problem with this approach is that it often leads the design to not be subjected to scrutiny beyond the designer's understanding of the requirements. This understanding often misses how a mechanism is going to fail. An enhanced approach is to include a requirement that designers think about failure modes through creating a fault tree early in the process. The fault tree could greatly aid in avoiding much more costly changes when hardware has been made, give a foundation for systematically developing the qualification process, and give a means of centralizing communication of failure modes for a mechanism.

Proto-type testing revealed that the major issue for the redesign effort was the spherical interface between the LL unit and the separation element. A spherical interface was chosen to permit an adjustable design that could meet an unknown tolerance stack-up without any required match machining operations. This interface turned out to damage surface coatings under random vibration due to its nearly under-constrained condition.

* Sandia National Laboratories, Albuquerque, NM

The resulting surface coating evaluations produced a robust solution but do not serve well as a strict scientific study. Due to schedule constraints, multiple variables were not controlled and recorded as thoroughly as desired. As a result, coatings which failed the testing shown here should not be discarded for other applications because conformity to important factors like surface preparation before coating application were not sufficiently controlled.

Previous Design Background

The investigation presented here started with the final qualification of a prior, virtually complete design. Upon receipt of three flight units, several problems immediately came up that were due to mechanism interference and jamming. After these problems were resolved and parts were prepared for testing, a question arose regarding performance under required preloading. A light pre-load was applied to the latching mechanism and it would not release. The mechanism was required to operate from a high output paraffin actuator (HOP) producing less than 222N of activation force. The design was altered to accommodate slim-line piezo-electric load cells to determine how much activation force was being applied by the HOP. It was found that even with a slight mechanism pre-load of much less than the required 4448N, over 1779N of activation force was required to actuate it. Upon actuation, the unit exerted an audible shock. It became clear that the problem was that the pre-load was transmitted perpendicularly into the mechanism such that a roller had to be rammed up a ramp (Figure 1). A solution to balance the undesired moment exerted by the pre-load and a sloped ramp to make pre-load application tend to open the mechanism were implemented and successful releases were achieved. This design change, however, now had a tendency of making the mechanism pop open spontaneously under static loading. This new problem resulted in the discarding of the prior design due the possible critical mission failure that could result in an accidental LL release.

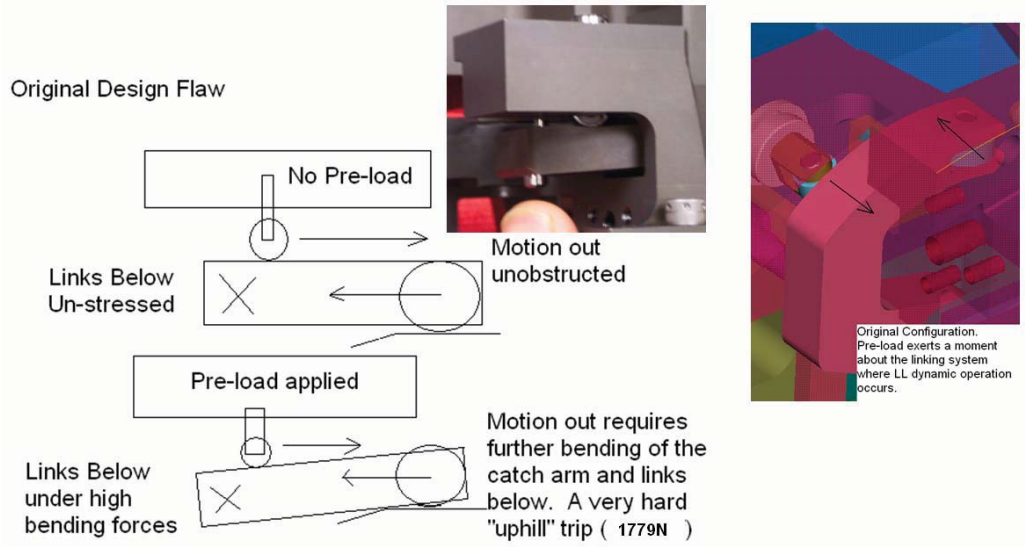

Figure 1. Original LL design problem

Design and development of the original unit did not focus on understanding failure modes. Requirements were considered but a positive method of meeting the requirement was formulated and was not critically analyzed from a mechanism functionality perspective. For example, the accepted demonstration of the device being 0.999 reliable was that the HOP's had a manufacturer's reliability of 0.97. Since the release was redundant with separate actuators, the reliability was therefore 1 – (1-0.97)*(1-0.97) = 0.9991. No analysis into the failure modes of the actual mechanism was done. Even the use of the manufacturer's 0.97 reliability number was applied incorrectly since the HOP was allowed to misalign by more than the operational requirement of 3 degrees due to the mechanism's clearances. With the original design's failure, the second design was conducted with a large amount of oversight developed to make sure the next design would work.

Several important lessons were learned from this design failure and were applied to the mechanism re-design. These are not new lessons for most experienced mechanisms engineers, but show how fault tree analysis could have helped avoid the problems encountered.

1. Avoid creating mechanisms with pre-load that transmits into the mechanism outside of its local plane of operation. Such forces will inhibit operation of the mechanism. Tolerance stack-up of multiple parts becomes a serious factor in loads transmission.
2. Redundancy of operation for a LL type mechanism must be applied with caution. Adding mechanical mechanism type redundancy only introduces complexity and gives another way for the mechanism to release. Two requirements must be met. 1) The unit will never open unless commanded (mechanical redundancy often hurts this) 2) The unit will always open if commanded to (mechanical redundancy sometimes helps this if complexity does not cause problems). Dual launch locks on a single deployed structure obviously should be avoided since such a design would require two releases for successful deployment.
3. The attempt to balance out the forces and implementation of a ramp were examples of trying to fix an unstable system by introduction of unstable equilibrium. High sensitivity to being in a correct locking state and correct placement of the balancing force elements were the variables in unstable equilibrium. A correctly reset unit could not be visually verified because the mechanism links were covered. A design should never be implemented which has such sensitivities. Reset type designs must easily be confirmed to be correctly configured.
4. Avoid mechanisms that push through a pre-load. Pre-load release should usually initiate the mechanism operation instead of mechanism operation initiating pre-load release.

Many other problems for the original design were identified.

1. Pre-load was considered as an afterthought. The design was sold on a low shock consideration that assumed that the pre-load release would be gradual. Overcoming friction was sudden and high shocks resulted.
2. The required pre-load could not even be achieved without doing damage to the mechanism, which was not observed in analysis because gaps were assumed to be zero.
3. Stiffness of the joint was evaluated as six linear spring constants that were derived from a linear model. The modeling assumed entire sections of surfaces were welded. The joint stiffness is actually a function of the pre-load and contact patch sizes that develop because of the geometry to joint size ratios present. This analysis completely neglected off diagonal terms of a generalized stiffness matrix.
4. Looseness of the mechanism was not evaluated. One HOP could misalign more than the required 3 degrees.
5. The separation element (Figure 2) was a square peg in a square hole intended to provide a 6d.o.f constraint. A good fit could not be achieved with this design. The peg tended to jam into the pocket. If it did not jam, it tended to wobble which leads to non-linear stiffness at low load levels.
6. Pre-load was applied through the main body of the entire design. The pre-loading tended to wear and damage irreplaceable interfaces.
7. The release interface was Ti6Al4V to Ti6Al4V with only Tiodize as a protective coating. The Tiodize tended to rub off. Probability of cold welding can be greatly reduced by using non-similar materials, hard coatings, and lubrication.

Design Development Using a Fault Tree

Assuring reliability has several stages. It starts with a robust design that is built to the correct requirements, continues with a qualification process that must envelope requirements, and must be followed by correct integration, which does not introduce unknown damage or an un-qualified configuration before the mission commences. Difficulties can often arise due to the lack of passing common knowledge of previous experts on to new personnel who do not know what is important and who may be under pressure to finish the job. A way to minimize this problem and to establish a common frame-work for methodically eliminating failure is to make a fault tree the central controlling entity of a design. Explicit connections of failure mode numbers to analysis, detailed drawings, procedures, and

derived requirements can serve to guide designers back to how they could cause failure. This centralized use of a fault tree was utilized in the LL re-design. The idea was originally driven by oversight requesting a strong analytical evaluation of the reliability of the device but the resulting fault tree analysis was found to be very beneficial to assist in orienting one's mind to eliminate critical failure modes. This process easily incorporates standard activities such as stress margin assessments and test plan creation. The specifics of general fault tree analysis are not discussed in this paper. Some good resources on this topic are contained in the references [13, 14].

Launch Lock Design and Qualification Process

The design functionality of the re-designed LL device is illustrated in Figure 2. It constrains a gimbal at a single location. The design has a spherical interface that allows the main housing to slide in a plane in order to meet an unknown tolerance stack-up without having to do any match machining. This requires lapping of the spherical parts to get a smooth fit. Release is accomplished via a low shock non-explosive actuator (NEA) 9131 [2].

The fault tree was created early in the design process based on 'brainstorming' sessions within the design team. Fifty-one mechanical events were identified, which were sources of either complete or partial mission failure (Figure 3). Fault tree events were then noted in drawings for critical dimensions and testing activities so that each part can be referenced to the fault tree (Figure 4). The fault tree work also lead to the development of mechanism-specific testing that went beyond a standard qualification process.

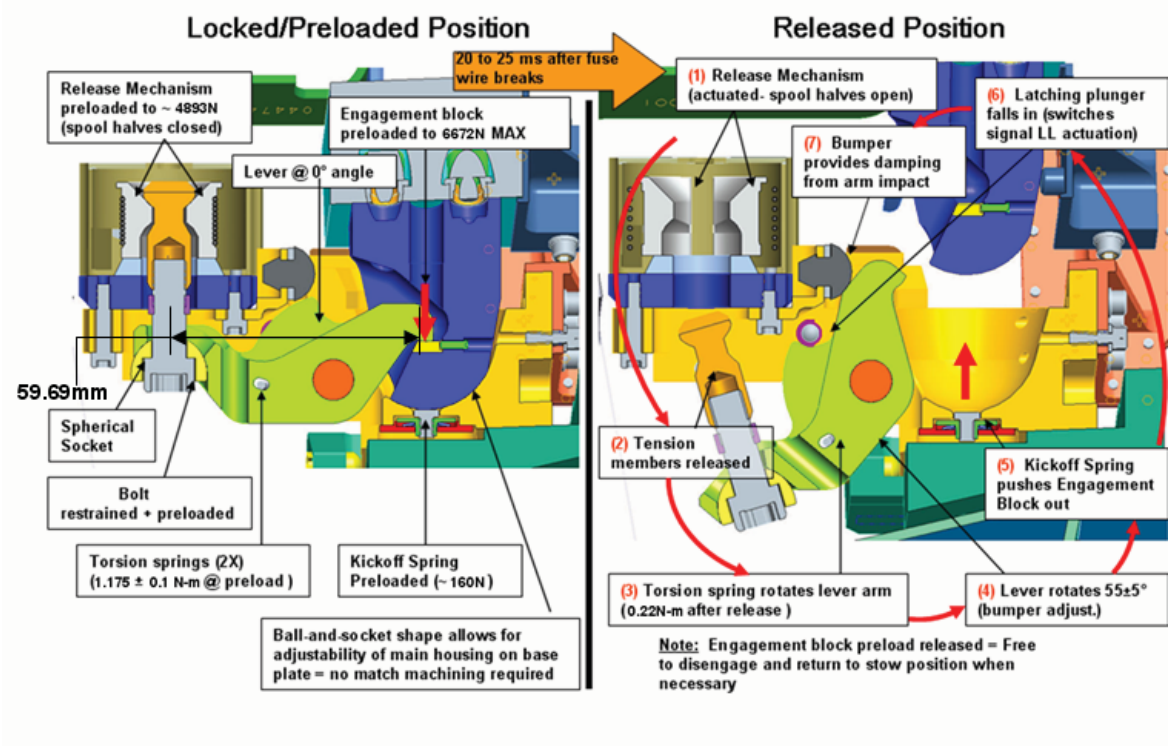

Figure 2. LL operation

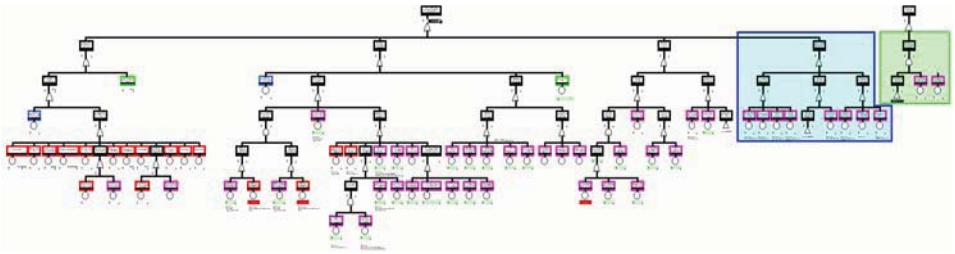

Figure 3. LL fault tree with 51 mechanical events

Stiffness and Pre-load

Since the LL constrains the gimbaled system at a single location, the overall stiffness of the system has a strong dependence on mechanism stiffness. Assessment of stiffness and pre-load are therefore critical to device performance. In the previous design, this was recognized but compliance with requirements was not correctly verified. The original design stiffness was quantified through a finite element analysis (FEA) that assumed that entire interfaces were rigidly joined. This was discovered to be a poor assumption for the pre-load and joint to length ratios present for the design. The stiffness was placed into the system level model as six springs with rigid connections between multiple interface points (Figure 5).

In the re-design effort, careful consideration of failure modes lead this incorrect model to be replaced with a mandate to experimentally measure the stiffness for the new design and to then use this data to tune a geometrically accurate FEA model via three springs at the spherical interface. This first order assessment of dynamic performance was considered sufficient since the 1st mode of the LL is much higher than the system level modes of interest. A test setup that allowed general force application to the separation element was designed (Figure 6). Monitoring of displacements was accomplished via LVDT's.

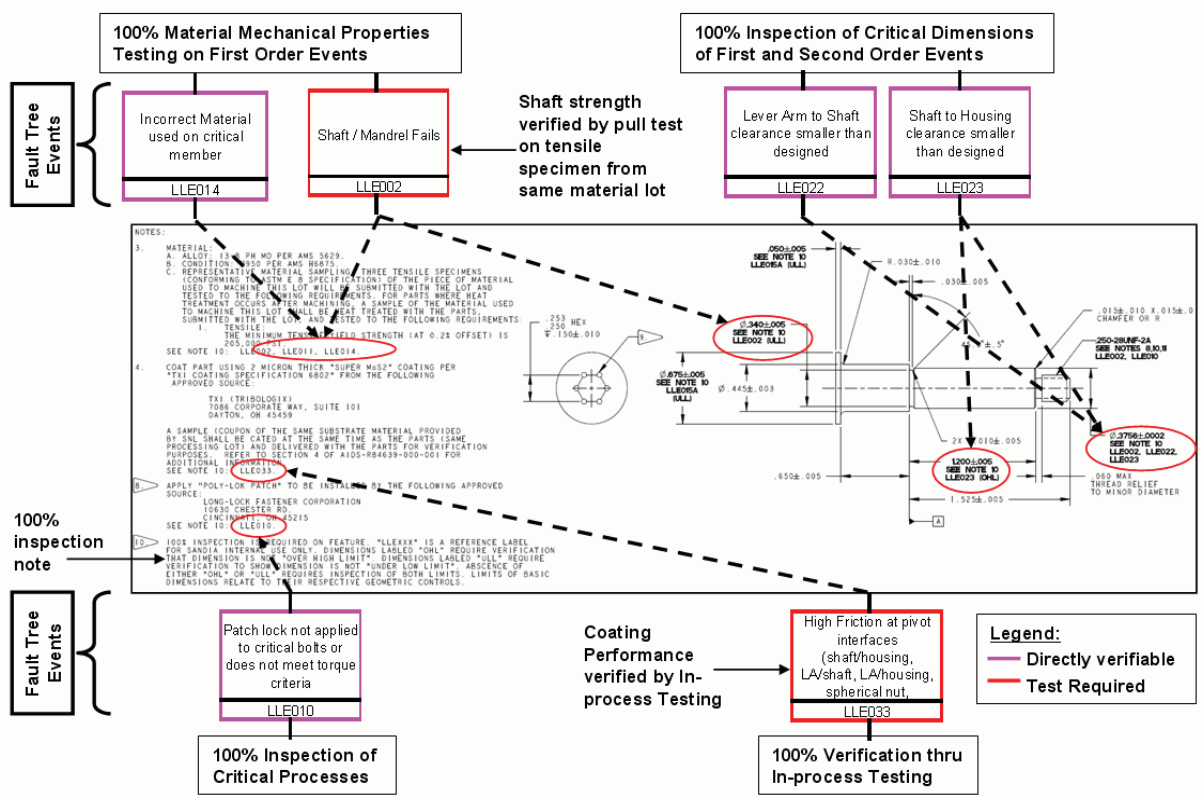

Figure 4. Drawing package connection to failure events

Stiffness was evaluated experimentally as a 3X3 matrix (translations only with rotations free) about the center of rotation of the LL spherical joint. This experimental assessment was compared to the same

entity calculated from modeling results. The resulting stiffness correlation achieved accuracy of 4 and 2% in the two directions that were critical to system level dynamics. The system level dynamics were considerably different after this process had been completed. The first mode had dropped by 6% and considerable changes in mode shapes and position had occurred. Load levels changed by up to 20% as a result of the changes.

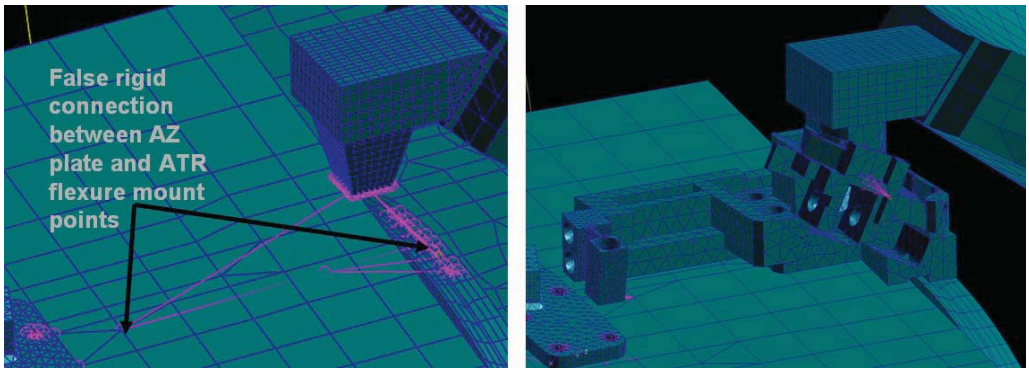

Figure 5. Original modeling (L) New modeling with experimental verification (R)

It is clear from these results that good modeling practice for single point constraint mechanisms should include detailed modeling as opposed to the six spring approach that was originally used. Use of a geometrically correct finite element analysis model, which has been verified experimentally, minimizes the possibility of oversimplified or incorrect modeling. In cases where the coupling is not accurately modeled as first order, even more advanced techniques such as frequency response function techniques could be implemented to evaluate joint characteristics [3-5]. These techniques could clearly benefit future system level modeling efforts but would require extensive development and validation to be used.

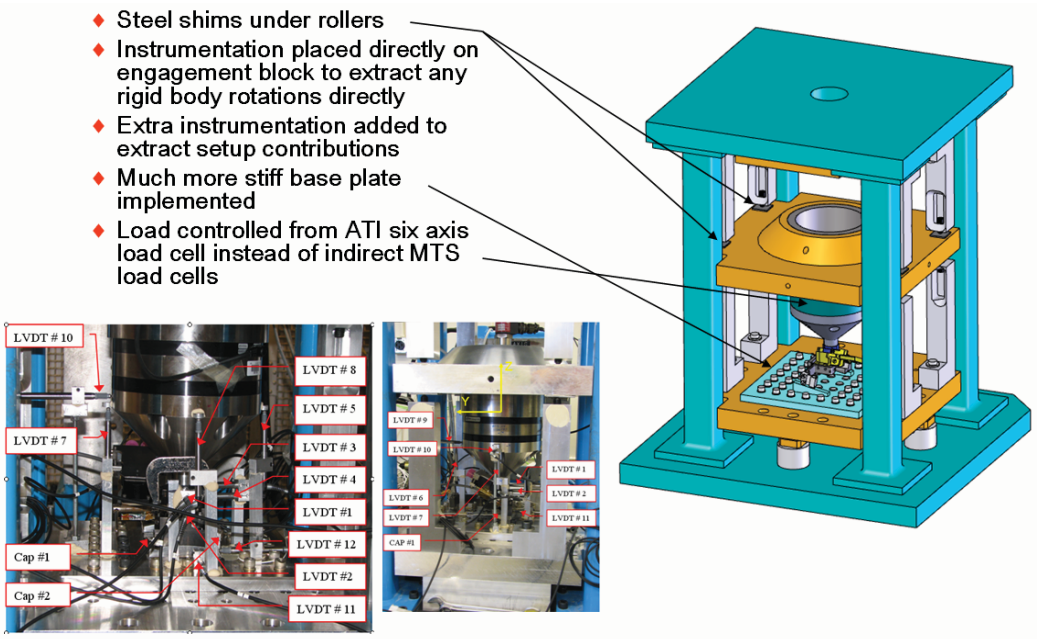

Figure 6. Stiffness setup and required improvements

The fault tree analysis reminded the design team of the importance of pre-load. The pre-load of the LL affects stiffness considerably. Use of a strain gauge rather than relying on torque was therefore required. Prior satellite hardware programs had used strain gauges and found that on occasions, the gauges sometimes did not work correctly when pre-load was applied. This lead to the need to be able to verify

strain gauge functionality on demand and to keep track of how much torque should be applied. In addition to these requirements, pre-load data showing variations under random vibration, design limit load (DLL) application, thermal cycling, and time were collected to assure that pre-load would not go out of the qualified range of 4448N to 6672N during the required duration of mechanism performance. A target pre-load of 5693N was formulated based on the recorded data.

Margin Assessment

The fault tree approach required the assignment of a probability of failure for each structural element. Positive margin assessment was therefore made at nominal and worst case geometry models. Since the LL is an adjustable system, the geometry of the model was put into a "worst case" configuration as judged by the author; who considered the development of moments due to DLL loading. Both high and low pre-load bounds were also applied from 4448N to 6672N since having lower level pre-loads could result in lower contact and clamping forces causing stresses to re-distribute to other mechanism components. The difference in Von-Mises stress between the two models was considered to be a 1-σ variation with respect to possible deviations from the modeled stress assuming a Gaussian distribution. This assumption gave a means of quantifying a probability of failure. For several parts, the difference from worst case to nominal in stress was not negligible.

This process was an example of allowing reliability numbers that do not add value to drive considerable effort. Carrying out this process was very tedious. The interpretation of actual worst case conditions is a very difficult problem that can be conflicting for different load cases. For example, a thicker member may be best for structural loading but may cause problems for thermal loading. It is also very hard to interpret stress differentials between mating parts because interface meshes were not exactly the same, requiring manual inspection during post-processing. In addition, contact conditions sometimes varied significantly. Development of simplification for this process or assigning 0% probability of failure for parts with positive margin in worst case conditions is recommended due to the tediousness and small real value of these efforts.

Assembly and In-Process Testing

One hundred percent inspection data was used to build the three flight units based on which parts were closest to nominal. The entire process of assembly was carefully controlled by a procedure that included all the necessary critical verifications that tie back to the fault tree. In the later stages of assembly, thorough characterization of each unit was carried out through a process that was dubbed "in process testing." This testing involved careful measurement of the mechanism drag under various configurations including a single torsional spring case. It quickly revealed that flight 1 and 2 easily met the required operational torque to friction torque ratio of 3 but that flight 3 did not. This task was highly valuable in understanding the mechanism and its performance.

Coatings Issues

The failure mode that was hardest to obtain satisfactory results for was the spherical interface from the LL main housing to separation element (Figure 2). The spherical interface was accepted because open rotational d.o.f's did not cause significant changes to the system level 1st mode and because it allowed the separation element to enter the pocket with an arbitrary orientation. This reasoning did not consider the resultant interface. The moment arm of the LL sphere is 15.82mm and the moment arm of the gimbal is 596.9 mm (Figure 7). This thirty-eight-fold amplification makes sliding at the interface due to the gimbal dynamic deformation inevitable even for very high friction and the highest pre-loads sustainable. The best alternative to attempting to prevent sliding is therefore to allowing the sliding to occur while attempting to minimize wear. This is opposite to a "no-movement-no-wear" approach like those presented for recent studies for rough diamond like nano-carbon (DLN) surfaces [6].

Configurations were not controlled to the degree necessary for exact sample-to-sample comparison and are very specific to the test setup used for vibration testing. Cleanliness, surface preparation, coating application methods, and lubricant application methods were not well documented except for the final TiCN-MoS_2 case. The only precisely controlled variables were pre-load (5693N) and test setup configuration. The random vibration (RV) environment generated was for a downsized test setup that replicates the exit angle of the flight unit but is smaller by a scale factor of 2.5 (Figure 8). The fixture was

designed such that root mean square force of a mass attached to the top is equivalent to that of the acceleration spectral density (ASD) required. The similarity of the test setup to the flight unit with respect to joint slipping was limited due to scaling effects. Later evaluations of the fixture indicated that RV levels at the top of the fixture were actually much higher than predicted for the flight interface and that, from this perspective, the test set up provides a conservative test case. In addition, testing was conducted at qualification levels +6dB above the required ASD on three orthogonal axes for three minutes each (Figure 9). Thermal vacuum testing was conducted with the unit oriented so that the weight of the separation element was free to fall. This 2-N weight was considered a lower bound for the force the gimbal would be able to exert if any adhesion occurred.

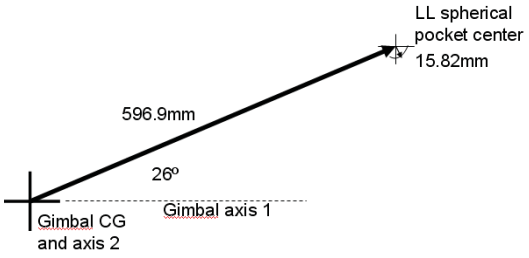

Figure 7. Gimbal configuration

The proto-type unit had 2 microns of Boron Carbide (B_4C) coating applied to both the separation element and main housing. B_4C is an extremely hard (micro hardness 4700 kg/mm square) ceramic film with a nano-crystalline structure applied via physical vapor deposition (PVD) [7]. It was initially chosen based on the requirement for a “good hard coating”. Given the limited initial requirements of good adhesion to Titanium and applicable temperature range, no specific control of the application process was required of the vendor and no adherence measurements were made before testing. No lubrication was placed between the opposing surfaces. When the elements were separated after vibration testing, a powder had formed between the two parts and extensive delaminating of the coating was visible (
Figure 10). No adhesion force significant to the application was observed between the parts. Energy dispersive spectrometry (EDS) analysis and scanning electronic microscope (SEM) images of the coating indicated that pockets of argon gas had been trapped in the coating layers during PVD application leading to poor wear properties (Figure 11). The coating was immediately rejected as unacceptable due to contamination potential and the fear that the delaminating could leave exposed clean, bare Ti to Ti in a launch sequence leading to cold welding. This also resulted in a search for a new, more appropriate coating for the hardware.

Due to scheduling constraints, a quick solution was desired. The separation element material was changed to passivated stainless steel AM-355 that was the least reactive alternative per MIL-STD-889B that also met strength requirements. A flight-like proto-type unit was re-lapped and DLN was applied on both elements and Braycote 600EF applied between them. This test failed because significant pre-load was not applied (Figure 12). A bare AM-355 to Ti6Al4V test was also run in hope a high friction interface would remain static and not create particulate (Figure 12). Separation occurred after the thermal vacuum cycles but significant fretting corrosion had taken place (Figure 12).

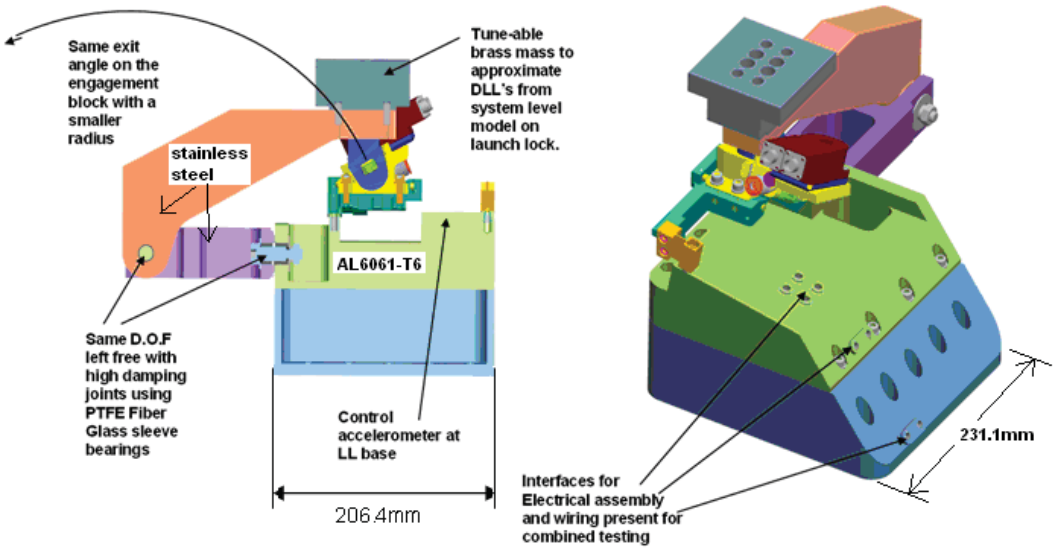

Figure 8. Random vibration test setup.

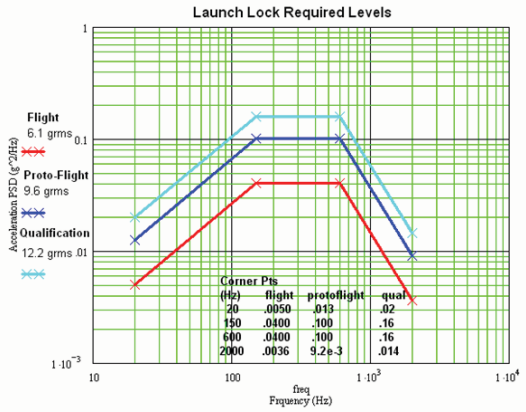

Figure 9. ASD applied at base of LL (Figure 8)

Figure 10. Damage of B_4C observed due to qualification level testing

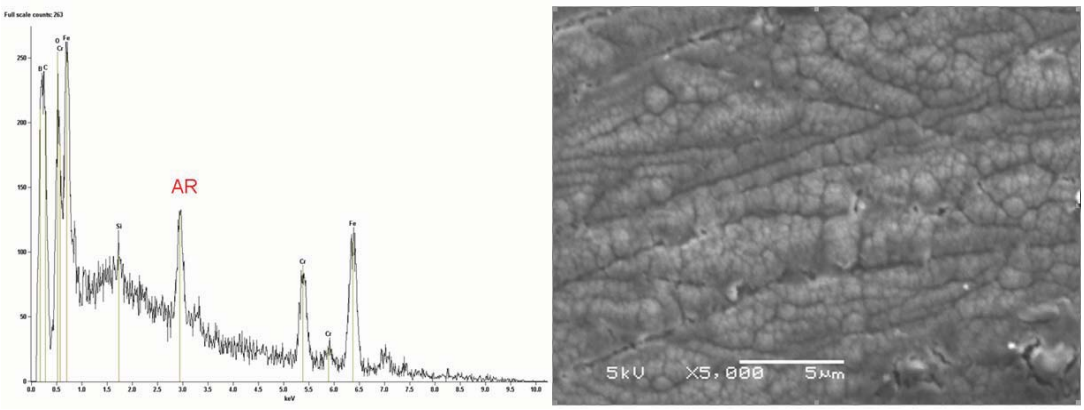

Figure 11. EDS analysis and SEM images of B_4C coating with argon gas bubbles

A case with only Braycote 600EF between the surfaces was also run but too much was applied without any dilution. It was learned afterward that Braycote must be applied in diluted form using the standard removal solvent. After doing application studies it was found that Braycote is very difficult to uniformly apply in diluted form. After RV and T-vac testing significant chemical reaction had occurred between the annealed Ti6Al4V and the Braycote (Figure 14). Reactions of these types are described in [8, 9]. This is the only case that did not separate at low temperature. The Braycote became very viscous and acted as a sealant, creating a suction cup-like phenomena. When room temperature had been reached, the elements had separated at an unobserved time. Another run with Tiodize and MoS_2 doped with SbO_3 and Au revealed Tiodize did not have good enough wear properties to survive the required environment (Figure 13).

Figure 12. Right: DLN coating failure due to lack of pre-load. Left: Bare metal case

Figure 13 L: Braycote to Ti6Al4V interface R: Tiodize and MoS_2 after RV and T-vac Testing

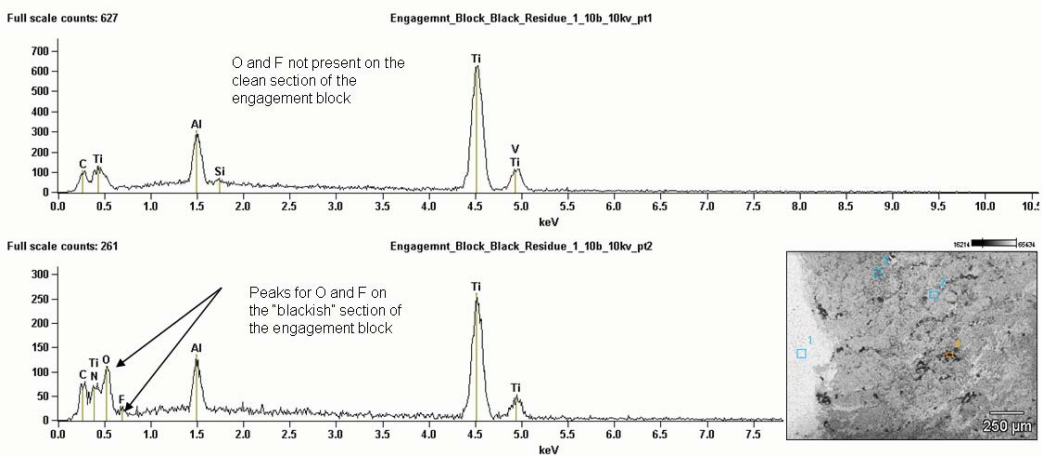

Figure 14. Separation element Braycote EDS analysis

A new coating dubbed "chameleon coating" utilizing MoS_2 and graphite was investigated but not tested due to its lack of flight history [10]. The friction data collected for this coating was promising and indicated excellent friction characteristics in wet and dry conditions. This may be an ideal coating for similar future applications where a complete testing process can be applied to guarantee flight performance.

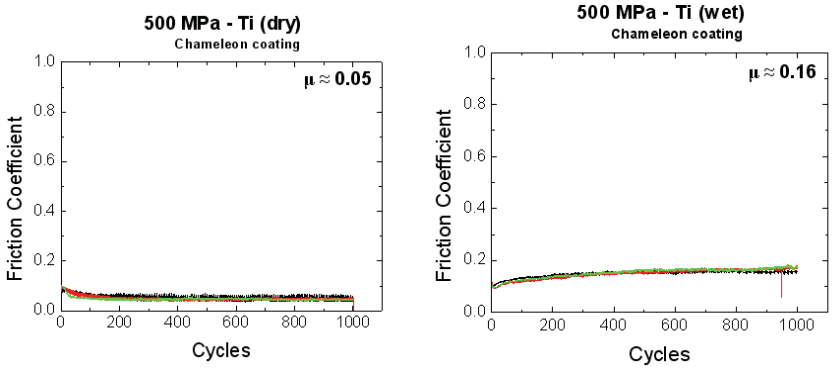

Figure 15. Chameleon coating friction characteristics

After further investigation, a final working interface was found. The initial attempt at this interface was to deposit one and a half microns of TiCN via PVD on the Ti6Al4V housing and one micron of MoS_2 via PVD doped with SbO_3 and Au to make the MoS_2 environment tolerant [11, 12] on the separation element. This first attempt initially had two failed regions (Figure 16). A second attempt at this approach included development of a specification for cleaning and preparation before coatings were applied. This process comprises an automated aqueous detergent ultrasonic cleaning, an in-situ cleaning and coating cycle within a chamber having capabilities of controlled atmospheres and sub atmospheric pressures and a post deposition tribo-finishing. This combination survived a total of 45 minutes of flight, proto-flight, and qualification levels. The toughness of TiCN with proper surface preparation on both elements coupled with the high lubricity of MoS_2 allowed the sliding interface to survive four times longer than required for testing and flight. A similar combination called "Starvic" by Platit [15] is claimed to have some flight history on space applications. Work concerning TiCN's low adhesion properties is contained in reference [16]. All of the cases are listed in Table 1.

It was found that coating thickness is very important. Four micron MoS_2 has considerably higher residual stresses and significant delamination for only 3 minutes of flight levels occurs. Scratch testing revealed this weakness (Figure 17). The 1.0 to 1.5 microns of MoS_2 is the confirmed working thickness.

Table 1. Coating cases evaluated

Cases Evaluated	Comments	Testing Applied (3 axes)	Result
B4C to B4C	Coating configuration not well controlled	9 minutes Flight followed by 9 minutes qual, elements seperated without T-Vac and then placed in T-Vac and released at low temperature of -70C	Coating failure Powder observed at the interface. Argon gas bubbles observed in post-mortem
Bare Ti6AL4V on AM-355	Attempted to create a static interface	9 minutes qual levels followed by T-vac	Fretting Corrosion and oxidation of AM-355
Bare Ti6AL4V on Ti6AL4V with Braycote EF	Braycote improperly applied studies showed uniform braycote application difficult	9 minutes Flight followed by 9 minutes qual, elements seperated without T-Vac	Considerable chemical reaction between titanium and braycote observed.
DLN to DLN with Braycote 600EF	Pre-load not correctly applied leading to failure.	9 minutes Flight followed by 9 minutes qual, elements seperated without T-Vac	Large sections of the DLN came off
MoS2 with SbO3 and Au to Tiodize	Units pre-loaded to 6672N (1500lbf)	9 minutes flight levels followed by 9 minutes qualification levels	Tiodize rubbed off and a single chunk of titanium came off and was not accounted for.
MoS2 with SbO3 and Au to TiCN 1st try	Units pre-loaded to 6672N (1500lbf)	9 minutes flight followed by 9 minutes Qualification	Unit survives the flight in pristine condition. Qualification levels lead to two chunks of titanium coming off and staying lodged on the seperation element
MoS2 with SbO3 and Au to TiCN 2nd try	Units pre-loaded to several values	One Unit with 3 minutes flight levels lbf pre-load, 9 minutes proto-flight levels 5693N, 9 min proto 4448N, and 9 min proto 6672N, 9 minutes qual levels. Second unit 9 minutes qual. T-vac applied and parts successfully released	**Both units did not have any loose material after testing.**
*T-vac = -45C to 61C 3-4 thermal cycles, flight proto-flight, and qual levels defined in Figure 9, Standard pre-load 5693N			

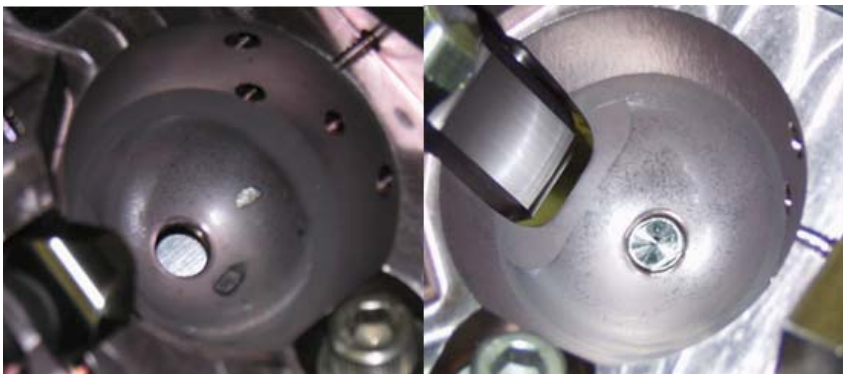

Figure 16 L: First TiCN-MoS_2 try. R: Successful TiCN-MoS_2 qual testing

The use of single point spherical interfaces with a moment arm ratio of the system described is successfully protected in this application by 1.5 to 2 microns of TiCN and 1.0 to 1.5 microns of MoS_2 doped with SbO_3 and Au with proper surface preparation of both elements. This combination represents a highly robust solution that survives significant wear due to slipping under long duration RV environments. It was learned that recalibration of coating equipment should be required using sample specimens. Samples should always be included in every coating application run with flight hardware, should always have a region masked and coating thickness measured, and EDS analysis, scratch testing, and SEM should be applied immediately after application to verify compliance.

Conclusion

The fault tree method proposed is a valuable tool for carrying out the entire design process as opposed to an uncontrolled original design effort. Applying this method to the LL re-design produced a very robust solution to the failed LL design with very thorough qualification process. Methods for measuring stiffness of the unit were successfully implemented and controlled. It was found that verified FEA methods are important for single point restraint devices and that six spring representations are not adequate for accurate modeling. The proposed fault tree process, if used correctly, is highly beneficial. However, it can

become over-burdensome if difficult assessments, such as the margin assessment mentioned earlier, are required. It is recommended that this process become a standard practice for critical mechanism applications. Many other methods for careful thinking could be proposed but it is extremely important that the mechanism community standardize methods for doing good design and clearly communicate this information to new personnel.

Through this fault tree driven design process, the major design issue that arose concerned finding a coating/lubricant combination that would not create debris under RV conditions. It was found that it is better under the single point spherical socket conditions described to allow slipping to occur freely over a smooth hard coating with very low friction rather than trying to constrain the interface completely. A robust solution was produced using TiCN and MoS_2 doped with SbO_3 and Au. This solution is strongly dependent on applying the correct coating thickness. It is recommended that future applications carefully weigh the no-match-machining benefit of a single point spherical interface constraining a significant inertia against use of a high friction flat or conical interface which will have fewer wear and coating issues [6].

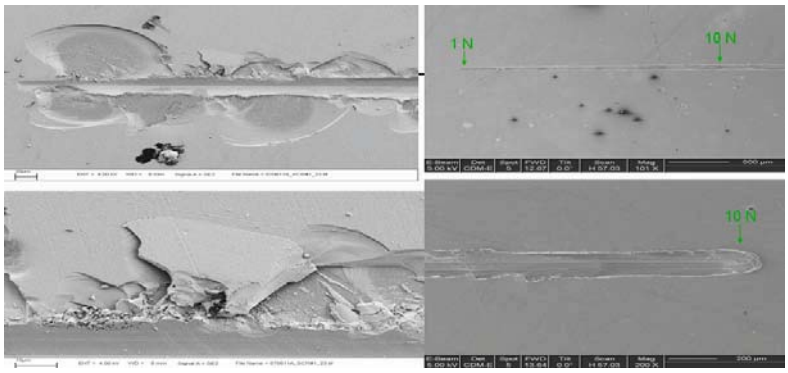

Figure 17. SEM Images of 4 micron thick (L) and 1.5 micron thick MoS_2 after scratch testing

Acknowledgments

This work was an extensive process executed by several people who played key roles and deserve acknowledgement. The design effort was aided by Roger Sirois, Prasad Somuri, Scott Nicolaysen, Chris Sorensen, Elmer Collins, Steven Moya, and Mark Vaughn. Testing and qualification were aided by Nathaniel Roberts, Paul Larkin, Brendan Rogillio, and Rand Garfield. Stiffness validation was led by Vit Babuska who was aided by Troy Skousen, and James Freymiller. Detailing support was lead by Wilbur Martin. Many others also helped with this work to a lesser degree than those mentioned.

References

1. Wilbur Shapiro, Frank Murray, Roy Howarth, and Robert Fusaro, “Space Mechanisms Lessons Learned Study,” NASA, 1995 http://www.grc.nasa.gov/WWW/spacemech/lessonscover.html
2. NEA electronics corporate home page: http://www.neaelectronics.com/
3. Ren, Y; Beards, C. F., “Identification of joint properties of a structure using FRF data,” Journal of Sound and Vibration; 7 Sept. 1995; vol 185, no. 5 p.845-66
4. Yang, TC; Fan, SH; Lin, CS; “Joint stiffness identification using FRF measurements” Computers and Structures; Nov. 2003; v.81, no.28-29, p.2549-2556.
5. Lee, U; Cho, JY ; Cho, CD, “Spectral FEM-based dynamic characterization of structural joints: Theory and experiment,” Key Engineering Materials; 2006; v.326-328, pt.1-2, p. 1629-1632.
6. Santos, LV; Trava-Airoldi, VJ; Corat, EJ; Nogueira, J; Leite, NF; “DLC cold welding prevention films on a Ti6Al4V alloy for space applications.” Surface & Coatings Technology; 24 Jan. 2006; vol.200, no.8, p2587-93
7. Boron Carbide “Diamond Black” Bodycote information flyer: http://mcna.bodycote.com/index.asp?sid=process&content=process.asp?ID=253

8. Herrera-Fierro, P.; Jones, W.R.; and Pepper, S.V.: “Interfacial Chemistry of a Perfluoropolyether Lubricant Studied by X-ray Photoelectron Spectroscopy and Temperature Desorption Spectroscopy.” J. Vac. Sci. and Technol. A, vol. 11, 1993, p. 354
9. Kasai, P.H.: “Perfluoropolyethers: Intramolecular Disproportionation,” Macromolecules, 25, pp. 6791–6799, (1992).
10. Zabinski, J S; Bultman, JE; Sanders, JH; Hu, JJ: “Multi-environment lubrication performance and lubrication mechanism of $MoS_2/Sb_2O_3/C$ composite films”: Tribology Letters; August 2006; v.23, no.2, p.155-163.
11. Prasad, S; Zabinski, J: “Super Slippery Solids”: Nature;vol 387; June 19th, 1997;p 761-763;
12. Zabinski, JS; Donley, MS; Walck, SD; Schneider, TR; Mcdevitt, NT: “Effects of dopants on the chemistry and tribology of sputter-deposited MoS_2 films”: Tribology Transactions; Oct 1995; v.38, no.4, p. 894-904.
13. Stamatis, DH, “Failure Mode and Effect Analysis: FMEA from Theory to Execution,” American Society for Quality, Quality Press, Milwaukee 53203, 2003
14. Fault Tree Handbook, NUREG-0492, U. S. Nuclear Regulatory Commission, January 1981
15. Platit website http://www.platit.com/
16. J Fontaine, 'Ultra-high Vacuum Friction Experiments to Simulate Material Transfer and Wear of the Platinum Proof Mass Used in the GRADIO Accelerometer'; Proc 10th ESMATS, ESA SP-524, September 2003.

Lessons Learned Designing a Spherical Satellite Release Mechanism

Ryan Hevner*

Abstract

A low-cost mechanism, part of the CAPE ICU payload, was designed to contain and deploy two spherical satellites from the Shuttle in December 2006. Overall the system successfully placed the satellites into orbit but encountered an anomaly. This flight anomaly and subsequent investigation revealed several key design issues. This paper discusses the lessons learned from the inaugural mission.

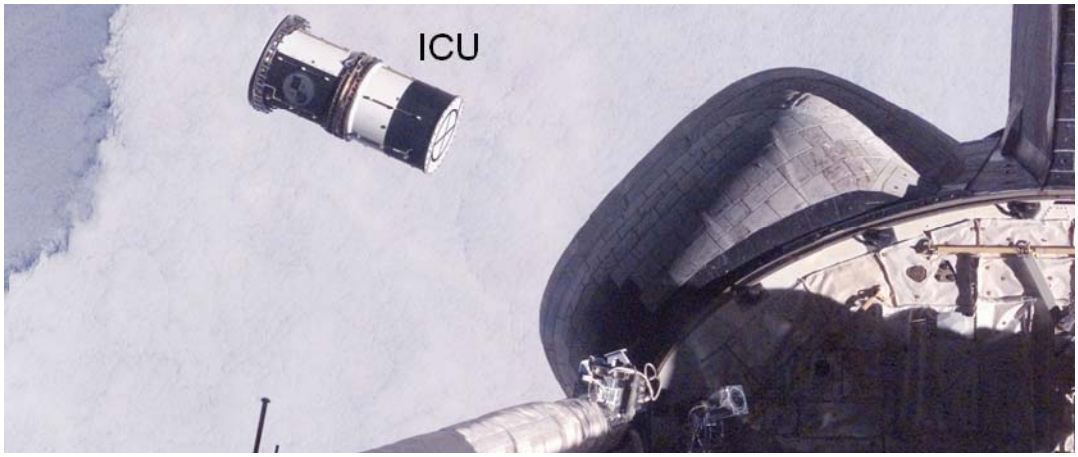

Figure 1. Ejection of ICU from CAPE aboard STS-116

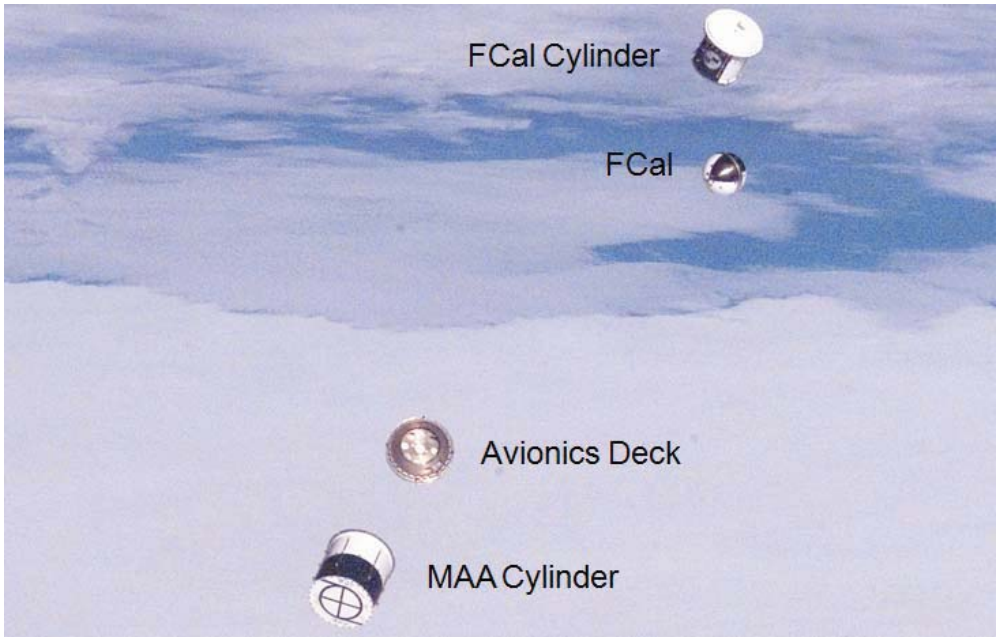

Figure 2. Separation of ICU, Releasing the Satellites

* Planetary Systems Corporation, Silver Spring, MD

Introduction

The goal of this project was to design a release mechanism for two spherical satellites. The mechanism was to fly on a risk reduction mission to verify the design and operation of the system for a future, more ambitious mission. Because of the need to maintain a constant drag coefficient under any orientation, the satellites had no external appendages or hard points for contact. The spheres and their release systems had to be enclosed within the Canister for All Payload Ejections (CAPE). CAPE is an aluminum cylinder 0.56 m ID x 1.3 m long. The Space Test Program-H2-Atmospheric Neutral Density Experiment Risk Reduction Mission (STP-H2-ANDE RR) flew aboard Space Shuttle mission STS-116.

The Naval Research Laboratory designed satellites were Mock ANDE Active (MAA) and Fence Calibration (FCal). MAA was 0.48 m in diameter and 52 kg. FCal was 0.44 m in diameter and 63 kg. MAA was desired to have a spin rate of 1-10 rpm upon orbit insertion. Each satellite was enclosed in its own cylinder. The cylinders were joined together by two Motorized Lightband separation systems (MLBs). When the MLBs separated, the satellites were simultaneously pushed out of the cylinders by compression springs. The name given to everything contained within the CAPE that separated from the Shuttle was the Internal Cargo Unit (ICU). At the end of one of the cylinders was a larger Lightband, CAPE Separation System (CSS) (see Figures 1-5).

The ICU was ejected from the CAPE by means of the CSS, a 0.59-m diameter NEA-actuated Lightband separation system. Approximately 40 seconds later, two diameter 0.50-m MLBs, ICU Separation Systems (ISS), were to simultaneously separate at the center of the ICU. The lower haves of each Lightband with the motor mechanism were attached to the central Avionics Deck. The upper half of each Lightband was attached to the open end of each cylinder. Upon separation, each satellite ejected from the cylinders through the center of the upper ring.

ICU Design

The ICU consisted of five separable elements, the FCal Cylinder/ICU Lid, FCal, Avionics Deck, MAA and MAA Cylinder. The structural components had the following masses, FCal Cylinder 38.1 kg, Avionics Deck 18.5 kg, MAA Cylinder 13.4 kg resulting in a combined ICU mass of 185 kg. Roller Guides on the outside of the cylinders ensured proper ejection from the CAPE. Conical pedestals held Viton o-rings. These o-rings compressed the satellites at + and – 45 deg latitude. The o-rings preloaded the satellites to minimize vibration during the launch environment. 6 Delrin sleeves ran axially along the inside of each cylinder to prevent marring of the satellites. Compression springs with Delrin guides were placed at + & - 36-40 deg latitude to aide in ejecting the satellites from the cylinders and overcoming any possible o-ring to satellite stiction. The upper portion of the spring guide held a radial ball bearing that contacted the satellite. Each satellite had two 10-mm diameter countersinks at 15 deg latitude nearest the Avionics Deck. The Avionics Deck Pedestals held accepting 90° conical tipped snubbers meant to engage the satellite countersinks. One snubber contained a magnet to activate an inhibit keeping the satellites turned off until ejection. The second snubber on each satellite acted as a back-up to prevent rotation of the satellite during launch incase the o-ring compression was insufficient. MAA contained a third snubber at its Delrin equator. This served as a temporary hinge point to impart rotation on MAA during its ejection from the cylinder. The entire structure of the ICU was 6061-T6 aluminum alloy. MAA had 6061-T6 hemispheres with a Delrin equator. Its surface comprised of alternating black anodized and gold irirdited quadrants. FCal had brass hemispheres with an aluminum equator. Its surface comprised of alternating nickel plating and white paint (Figure 6).

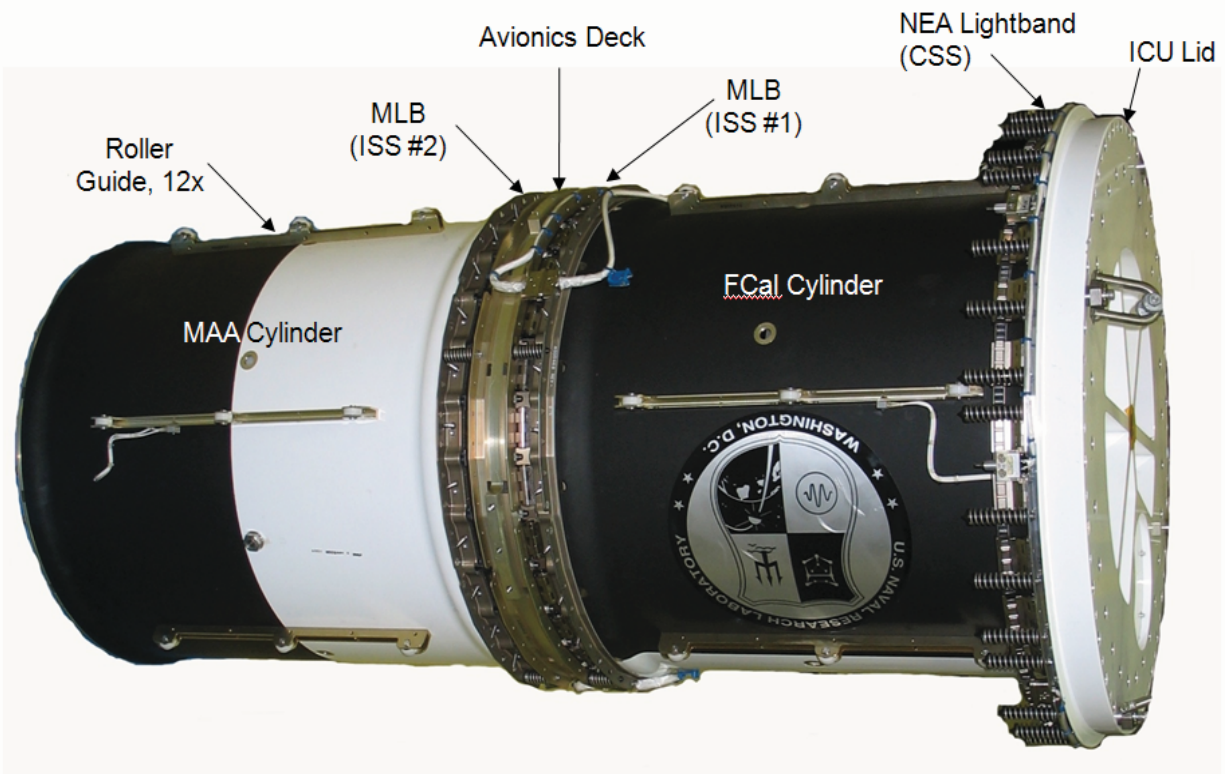

Figure 3. Internal Cargo Unit (ICU)

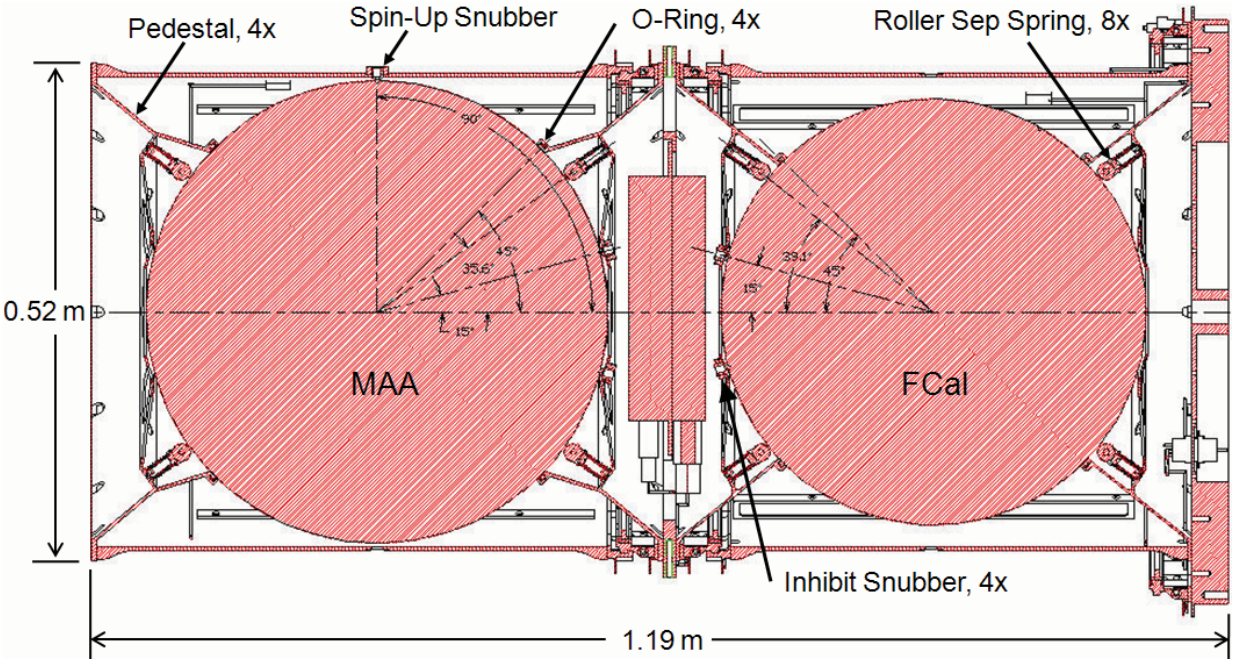

Figure 4. ICU Section, Stowed

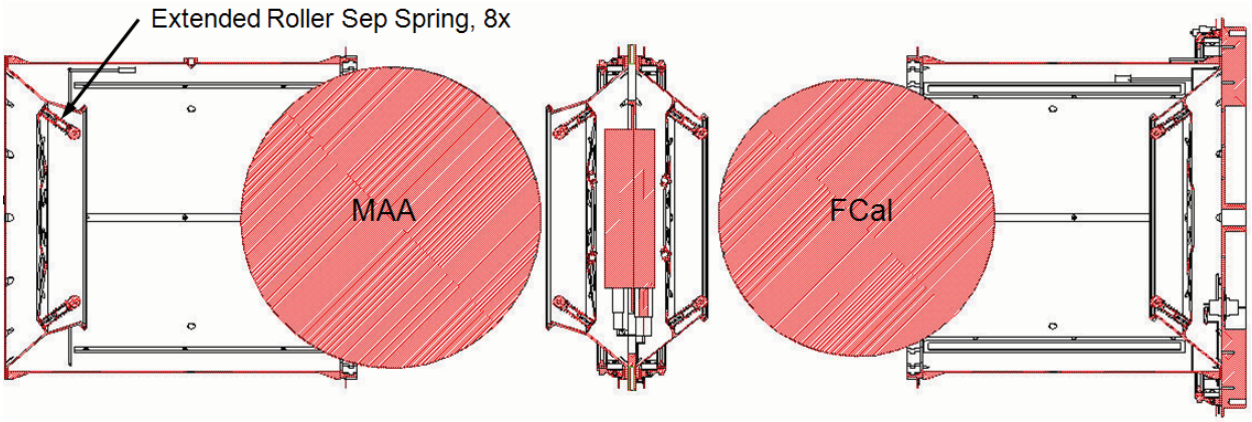

Figure 5. ICU Section, Deployed

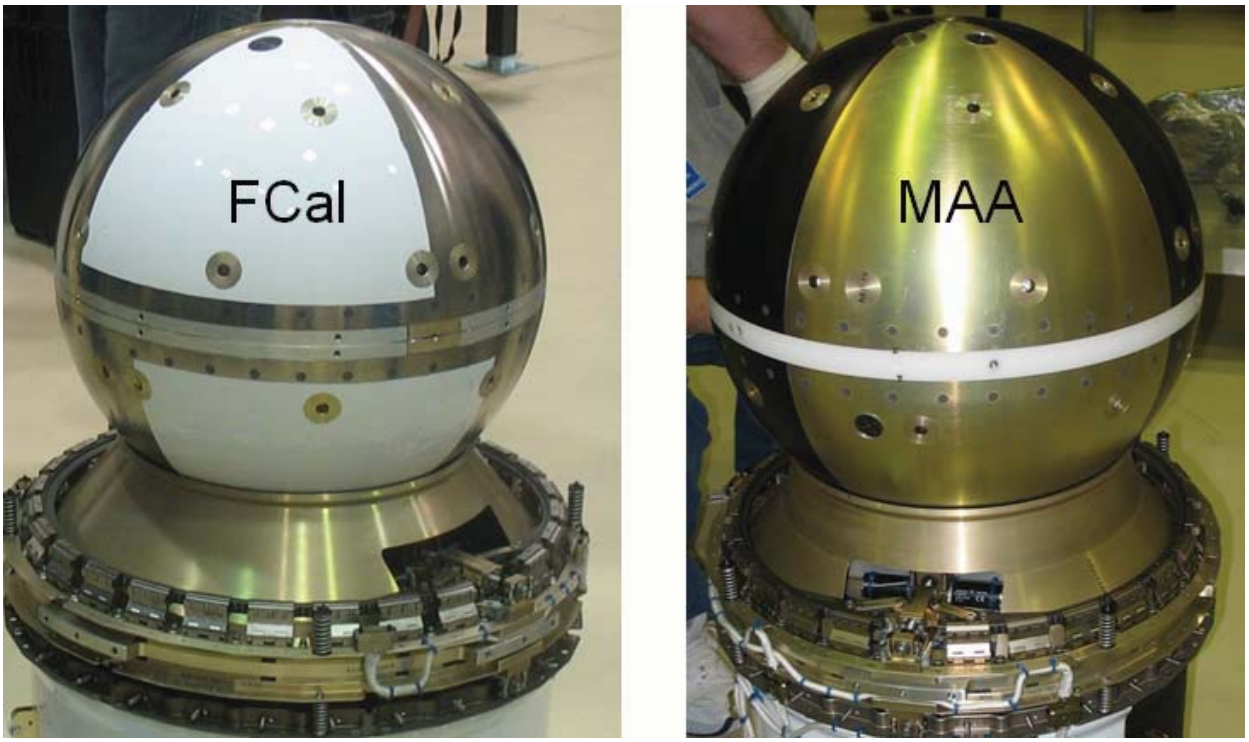

Figure 6. FCal and MAA Satellites Resting on the Avionics Deck

The Designed Separation Event

The ICU was designed to separate from the CAPE by means of actuating the NEA operated CSS Lightband. 32 compression springs on the CSS eject the ICU at a velocity of 0.52 m/s from the Shuttle. After 40 seconds, the timer in the Avionics Deck sends a signal to simultaneously separate ISS #1 and ISS #2, releasing the satellites from their respective cylinder (Figure 7).

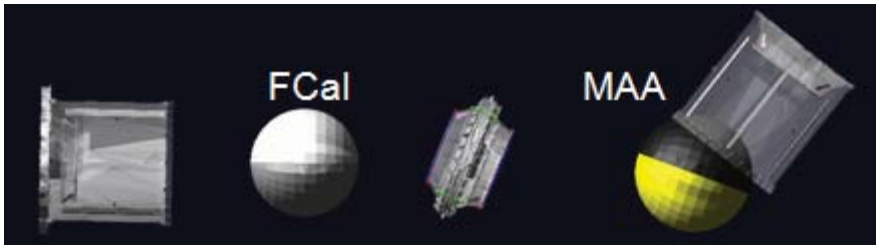

Figure 7. Anticipated ICU Separation Event

Flight Anomaly

By all accounts the ICU separated nominally from the CAPE. Video taken from the Shuttle shows the ICU ejecting smoothly with no observable rotation. Velocity appeared normal. See Figure 1.

The ISS separation event had an anomaly. The satellites did not simultaneously eject from their respective cylinders as expected. FCal separated from its cylinder. Its ejection rate was as expected except when the equator reached the end of the cylinder it temporarily “stopped” for a few seconds and then slowly continued out of the cylinder. The MAA did not come out of its cylinder. Instead of all bodies ejecting simultaneously away from the central Avionics Deck, the Avionics Deck “stuck” to the cylinder for a few seconds before slowly tumbling away. The Avionics Deck showed a noticeable rotation rate of 10-15 deg/sec while the MAA Cylinder had no observable rotation. MAA was not seen to eject for the entire 20 minutes that Shuttle video tracked the MAA Cylinder. Ground operations confirmed that MAA did finally eject approximately 1 hour after ISS separation (Figure 8).

Figure 8. Actual On-Orbit ICU Separation Event

Flight Anomaly Investigation

Closer look at the flight video showed slight shadow movement of ISS #2 (MAA Lightband) one frame before ISS #1 movement was noticed. The theory was that when ISS #1 separated it pushed the Avionics Deck back against the MAA Cylinder causing the halves of ISS #2 to temporarily contact. Eventually it was believed that one of the roller separation springs on the Avionics Deck re-contacted MAA. This imparted a torque on the Avionics Deck, but since the spring force's line of action bisects the center of MAA, the MAA/Cylinder received very little torque. This explains why the Avionics Deck spun-up and the MAA Cylinder did not.

Several ideas were also speculated in the days immediately following. Perhaps the MAA jammed on the spin-up snubber during ejection. MAA may have seized against the Avionics Deck snubbers when it attempted to rotate out. The o-ring stiction may have been so high that the springs could not overcome the force. The Lightband separation systems may not have separated cleanly.

Using dynamic simulation software, Matthew Eby of The Aerospace Corporation was able to model many variations of the separation event. This included simultaneous ISS separation and staggers of varying delay. He also adjusted the o-ring preload. In the end, the analysis confirmed the initial assumptions that ISS #2 separated 0.01 to 0.02 second before ISS #1. The halves of ISS #2 temporarily re-contacted and a roller separation spring re-contacted MAA, imparting the observed rotation on the Avionics Deck.

Since FCal ejected quickly it received far less scrutiny in the post flight investigation, however its anomaly is just as important to understand. FCal contained two antennas secured in a groove around its equator. These were to deploy several seconds after the magnetic inhibit was removed and the satellite ejected. These wires were noticed during assembly to slightly bulge out past the spherical surface near their root and initial bend into the groove. Also, the upper rings of the ISS Lightbands attached to the ends of the cylinders. The socket head cap screws used to attach them were secured with lock-wire. Great care was taken to keep the lock-wire close to the ring and out of FCal's deployment path and staked to remain in place. It can only be assumed that one or a combination of the following occurred. First, FCal may have come off the inhibit during flight, causing FCal to power on and release the antennae. This scenario is unlikely since two snubbers penetrate the surface of the satellite. Second, the antennae could have broken free or come loose, bulging out of the groove. The antennae could then have temporarily snagged on the lock wire of the upper ring. Lastly, a section of lock wire may have broke and stuck out into the deployment path of FCal, forcing it to bend out of the way as FCal passed by.

History Leading to the Anomaly

Late in the design phase of the ICU it was determined that the ICU Lid lacked the required stiffness to prevent the ICU from contacting CAPE's inner wall during launch. The designers lacked the necessary software to maximize the part's specific stiffness. Thus as time was critical and the mass margin was high a design was made to simply "throw mass at the problem" to increase stiffness of the ICU Lid. The impact of this change to other aspects of the design was not fully understood until later in the test phase.

The unique design of the ICU makes it nearly impossible to test the flight separation event. The only possibility was to test on a KC-135 "vomit comet". However the logistics and safety concerns of deploying and then restraining five separate bodies with a combined mass of 185 kg on a plane make it a difficult task. The program budget and schedule also did not allow for this. At the time, detailed dynamic analysis software was not available to the ICU designers. Therefore, an inexpensive 2D separation test was designed to simulate the flight event as closely as possible. The test consisted of 2D steel mock-ups of the 5 separable ICU components mounted on near frictionless planar air bearings (Figure 9). The masses

were fine tuned to match the expected flight masses. The test fixture itself worked well, allowing for verification and measurement of the separation velocities and satellite rotation rates. The spin-up snubber was present in the fixture; however the Avionics Deck snubbers were not present due to an oversight in the fixture design. Also, a simple means of implementing compressed o-rings could not be determined and thus they were also left out of the test.

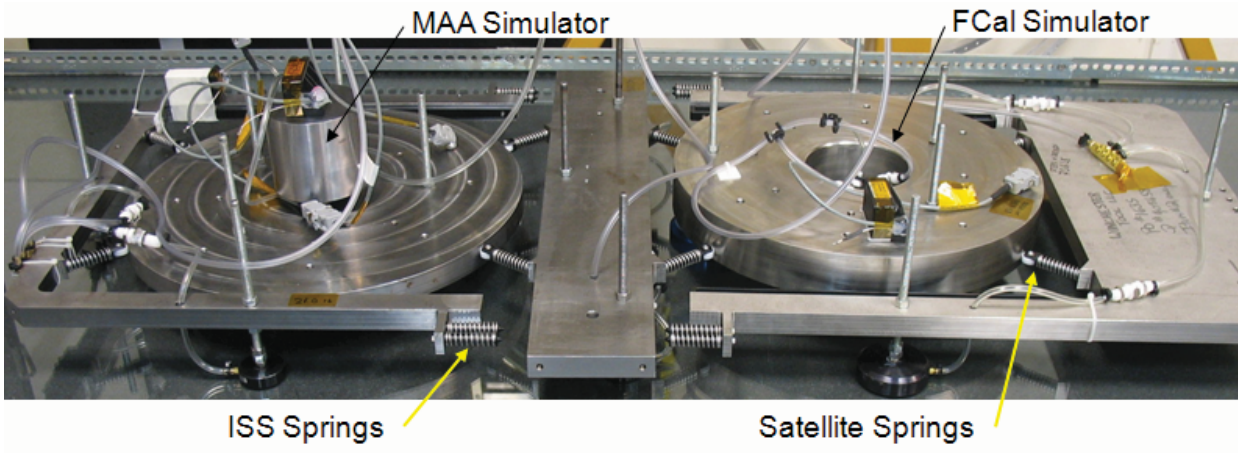

Figure 9. ICU 2D Separation Test Fixture

The 2-D separation test revealed that the separation velocities were too high. An imposed design requirement was that all components must separate from the Shuttle with a net velocity of 0.3 m/s. Energy had to be removed from the separation event to reduce the velocity of the MAA Cylinder. The required amount of energy removal was further impacted by the earlier decision to hastily increase the mass of the ICU Lid, effectively reducing the ICU separation velocity from the shuttle. It was deemed essential that the initial separating force from the springs remain the same to ensure proper operation of the Lightbands and overcome any possible stiction in the o-rings. It was thus decided to reduce the travel of all the compression springs from 20 mm to 5 mm. The final configuration consisted of 4 roller springs per satellite and 4 regular springs per ISS. The fully compressed force of each spring was 88 N.

The springs were modified and the test was re-run. Separation rates were within limits for all scenarios: simultaneous ISS separation, ISS #1 first and ISS #2 first. However, the test revealed a risk of the Avionics Deck re-contacting a satellite during staggered separations. It was deemed that tip-off of the Avionics Deck could not be controlled well enough to guarantee clearance. Thus it was decided that a simultaneous ISS separation was the best scenario for achieving proper separation of all 5 components.

Delayed ISS Separations

Because so much effort was put forth into meeting velocity and safety mission requirements no one fully considered the possible adverse effects of a near simultaneous separation. Care was taken to adjust the two Lightbands such that they separated as closely as possible. Repeatable separations within 0.01 second were achieved in ambient testing and the consensus off all involved parties was that this was “good enough”. The concept of re-collision was never considered. Table 1 shows data from the ambient testing to fine-tune the ISS separation times. It can be seen from the testing that a difference of 0.02 second was a distinct possibility as the post flight analysis presumes happened.

Table 1. ISS Separation Timing

	[sec]	
Trial	ISS #1	ISS # 2
1	0.896	0.896
2	0.896	0.904
3	0.904	0.896
4	0.904	0.896
5	0.904	0.896
6	0.904	0.912
7	0.904	0.904
8	0.896	0.896
Average	0.901	0.900
Std Dev	0.004	0.006
3*Std Dev	0.012	0.018

Temperature was also a significant contributor to the flight anomaly. Based on initial on-orbit data taken from the satellites, it is believed the ICU was -25 °C or colder at separation. Although not out the theoretical flight limits this was significantly colder than realistically expected. ISS motion was first noticed from the Shuttle video 42 to 43 seconds after ICU ejection from CAPE. This means the ISS Lightbands took approximately 2x to 3x times longer to separate than at room-temperature. The avionics timer was verified through ground testing. None of its components are believed to be temperature sensitive. Assuming the avionics timer worked properly, the suspect component is the Lightband itself. The mechanism that initiates separation in the Lightband consists of worm gears, brush motors, ball bearings, and a ball screw all lubricated with NYETORR 5200 vacuum grease. At this low temperature the viscosity of the grease increases substantially and thus increases the torque load on the motor. Testing performed on several Lightbands at similarly cold temperatures has shown that an increase in separation time from 0.9 sec to 3 seconds is entirely possible. This rise in torque and separation time further increases the standard deviation and probability of a delay between the ISS separations relative to ambient delays.

Preloading the Satellites

The use of Viton o-rings to preload the satellites resulted in several unknown affects to the separation event. Viton was chosen because it has low outgassing properties and is readily available. However, the limiting factor of standard Viton is that its rated minimum temperature is typically only -23°C. The o-rings may have been below this temperature when the ICU actually separated. No testing was performed on the o-rings at this temperature so it is unknown what their stiffness or condition was at separation and how that may have impacted the separation event. At the time no data was available on the percentage of stored energy in a compressed o-ring that imparts kinetic energy upon instantaneous compression release. It was believed low, but at the time unknown. As mentioned earlier, the 2D separation test fixture did not accommodate o-rings.

Since the flight, testing has been performed to determine the energy ratio of Viton as a function of temperature. A 380-mm diameter Lightband separation system was separated on a 5 degree-of-freedom air bearing fixture to obtain a baseline velocity. A 7-mm thick, 180-mm OD o-ring was then placed inside the Lightband and compressed to a known preload and distance. The Lightband was again separated and velocity measured. The change in kinetic energy due to the o-ring could then be calculated. The results can be seen in Figure 10.

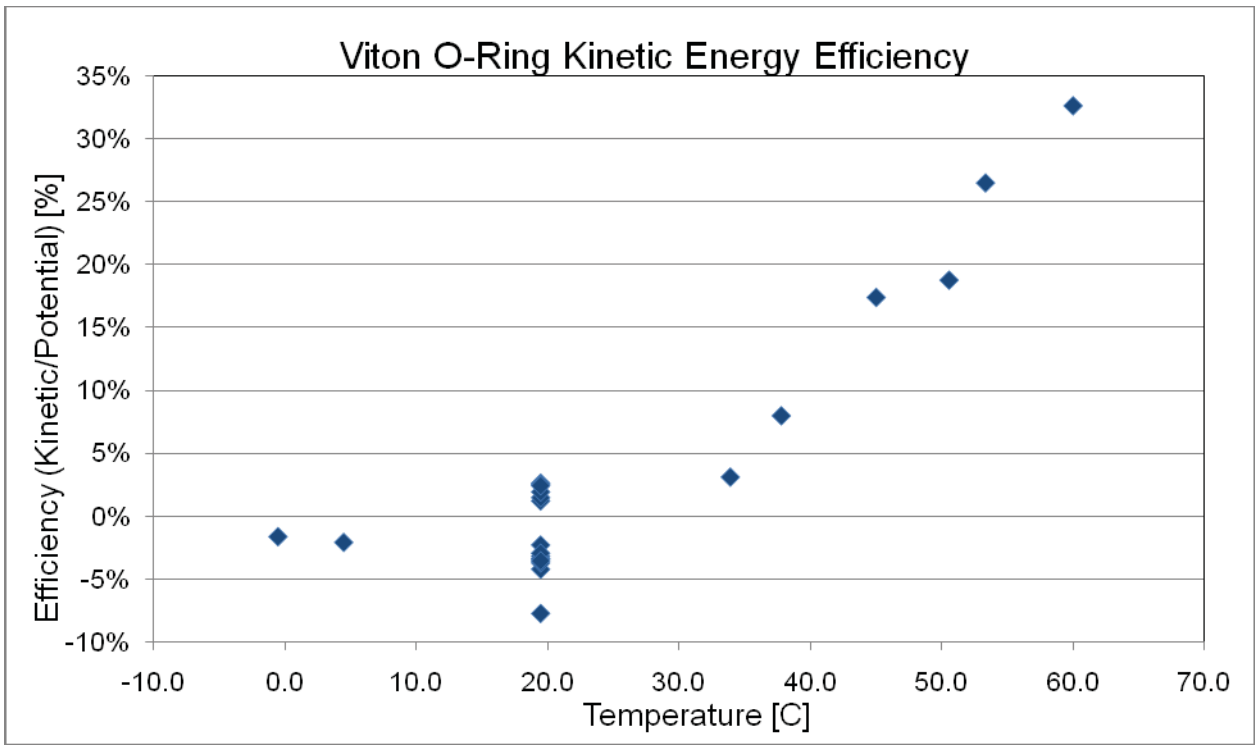

Figure 10. Ratio of Imparted Kinetic Energy to Stored Compression Energy in a Viton O-Ring

Several trials at various compressions were performed at room temperature, while only a few trials were performed hot and cold. This explains the scatter at room temperature and very little scatter elsewhere. However, from the data it is apparent that the energy efficiency of the o-ring increases with temperature. It was actually negative for some tests. The assumption is stiction between the Viton and aluminum rings decreased velocity. The test set-up and fixture limited the minimum achievable o-ring temperature to 0°C. It is still unknown how the o-ring would react at -25°C. If it follows the same trend however, it is likely that the preloaded o-rings had little effect on the separation event.

The other question that remained was the exact preload on the satellites at separation. Strain gages were bonded to the inside cylinder walls, transforming them into load cells. To keep them away from the satellites the strain gages were placed approximately 13 cm from the ends of the cylinders. These were calibrated by loading mock-up plates that simulated the interface of the satellites to the pedestals. Schedule and budget restraints prevented testing to correlate preload with respect to temperature. It also prevented the monitoring of preload over time to correlate creep in the o-rings and create a model to predict preload vs. time. The only data available was during a trial satellite installation where the satellites remained in the ICU for a few hours (Figure 11).

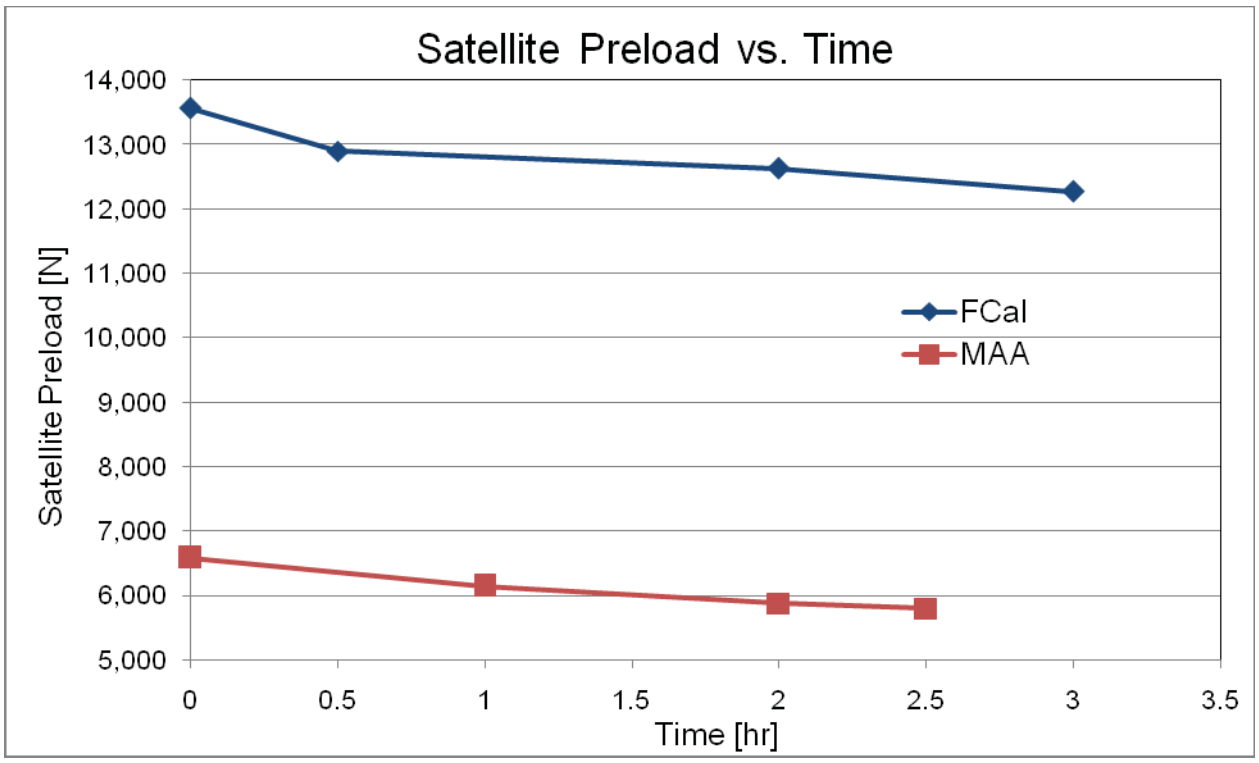

Figure 11. Decrease in Satellite Preload as a Result of O-Ring Creep

This short timeframe makes it difficult to predict whether the preload would continue dropping or eventually approach some asymptote.

The indicated preload readings were also subject to some skepticism due to the extremely low strain in the cylinders. Given the cylinders were 490 mm in diameter and 2.9-mm thick, the strain was on the order of 2E-5 to 4E-5. The indicator could measure this strain. The problem arose in bolting components together. Small variations in flatness often created localized stress increases that significantly changed the indicated preload. For instance, simply bolting the ICU Lid to the FCal Cylinder changed the indicated reading on FCal by 17,000 N. Because of this, care was taken to calibrate the load cells with everything fastened as in flight. However, the addition of preload shims could easily change the local flatness. With it being that sensitive, the preload on the satellites has a large tolerance. An improvement would be to put the strain gages on the outside of the cylinders so that they can be placed in the middle, as far away as possible from any localized interface stresses. Also, the flatness of all adjoining planes should be held as tight as reasonably possible.

Consideration was given to using something stiffer than Viton to contact and preload the satellites that would be non-marring. A Delrin strip was considered however this was too stiff. Since the shims can only be manufactured to 0.25-mm thick, replacing one shim would result in a preload change of several thousand newtons. The cylinder walls cannot be made much thinner without affecting the overall stiffness of the ICU. An o-ring appears to be the best option. A consideration should be made to investigate the performance of either low-temperature Viton or Butyl rubber (IIR) for this application given.

Impediments to Proper Satellite Ejection

The ability to ensure full compression of the roller separation springs inside the Pedestals was difficult. Since they were on the inside of the Pedestals they were hard to inspect when the ICU was fully assembled. Fine tuning of the spring's compression was performed with the Pedestals simply pushed against the satellites on a table. Additional compression due to o-ring preload had to be analytically accounted for. It is unacceptable to bottom out the springs and risk damage to their Delrin guide components so some tolerance had to be added to prevent this. This tolerance, along with the possible variations in o-ring compression due to satellite preload is a significant percentage of the overall spring travel. This means the exact force and energy imparted by these springs in flight was unknown and likely lower than desired. This may have additionally contributed to the satellite ejection anomaly. Moving the springs outside the pedestals and more accurately predicting the o-ring compression would improve the accuracy of this spring compression.

The spin-up snubber used to impart rotation on MAA may have contributed to MAA not ejecting. During all 2D testing the snubber performed flawlessly. Post flight dynamic analysis of the separation event revealed that as MAA ejects its countersink rides up on the snubber, temporarily pushing the satellite against the opposite side of the cylinder. During normal ejection this is fine. As the Avionics Deck quickly separates from the MAA Cylinder, the roller separation springs are long enough to overcome the temporary rubbing of the satellite against the cylinder. However, the combination of the Avionics Deck not immediately releasing and the possible shortened spring travel may have combined to stop MAA on the snubber.

The implementation of the conical snubbers used as satellite inhibits and to prevent rotation unnecessarily complicated the integration process and separation event. The snubbers could not be seen during installation of the satellites onto the Avionics Deck. Thus, alignment marks were devised to ensure the snubbers were concentric to their accepting countersinks. However, even with these marks it was difficult to confirm the exact position of the snubbers. If not perfectly aligned they may have gouged the surface of the satellite as the o-ring was compressed during preloading. They also may have prevented MAA from properly rotating out of the cylinder during ejection. Since they are located on the Avionics Deck, as the sphere attempts to rotate out of the cylinder, the snubbers may have been in the way, temporarily jamming the satellite. Ideally these snubbers would be removed. Testing should be performed to verify that the sphere will not move during random vibration. It is expected that a sphere with its center of mass in the geometric center and proper preload during launch will not rotate during vibration.

Conclusion

Overall, the ICU was a great success and served its purpose as a risk reduction mission to test the separation system of spherical satellites for future missions. It proved its functionality as a low cost means of placing two spherical satellites into orbit. The ICU ejected smoothly from CAPE by means of the NEA Lightband and Roller Guides. The containment and ejection system for the spheres proved feasible. The main issue was the oversight of assuming a perfectly simultaneous separation. This however can be corrected by purposely staggering the ISS separations by several seconds. The inclusion of penetrating snubbers on the satellites complicated the separation event. Other means of imparting rotation to the satellite should be considered, including self spin-up after ejection. With the improved simulation software now at the disposal of the designers, the separation event can be accurately modeled to minimize the risk of re-contact and ensure proper satellite ejection. It will also enable the designer to account for many different scenarios.

The 2D separation test proved to be of limited benefit in predicting the flight event. The limitations of the fixture produced results that cannot be assumed realistic. Developing a detailed simulation model in software is a better allocation of resources.

A result of this mission and subsequent investigation is that it is crucial to test a mechanism throughout the extremes of the flight environment. Assuming the system would perform at flight extremes as it did under room temperature conditions was a significant oversight. The ability to predict the satellite preload and understand the effects of a compressed elastomer on the separation event at various temperatures is essential to create accurate simulation models.

Lessons Learned

The following is a summary of the lessons learned during the design, test, integration and flight of the ICU. These lessons will be applied to the follow-on ANDE mission.

- Stagger the satellite ejections. This reduces the degrees of freedom and interaction possibilities by decreasing the number of separating bodies from 5 to 3 for each event. It is also impossible to get a truly simultaneous separation of both Lightbands.
- Tighten the flatness and alignment tolerances on all mating surfaces. This will improve the accuracy of satellite preload determination. Flatness of 0.025mm may be necessary.
- Remove the penetrating conical snubbers from the satellites. They needlessly complicate the separation event.
- Perform tests to confidently predict the preload creep on the satellites over several months.
- Ensure the material properties, specifically stored energy, of an elastomeric o-ring are fully understood across the entire temperature range.
- Increase the velocity of the ICU from the CAPE. This increases the energy available to impart on the satellite ejection event.
- Make both satellites out of aluminum to minimize any thermal induced preload changes.
- Reduce the risk of snagging by eliminating lock wire near the path of satellites.
- Painting scheme and alignment marks are valuable when viewing and analyzing on-orbit video.

References

1. Eby, Matthew A. / The Aerospace Corporation. “ICU Dynamic Simulation.” 22 April 2007.
2. Ritterhouse, Scott R. and Johnnie P. Engelhardt. Payload Deployment System with an Internal Cargo Unit. U.S. Patent 6,776,375. August 17th 2004.
3. Holemans, Walter. Reusable, Separable, Structural Connector Assembly. U.S. Patent 6,227,493. May 8th 2001. U.S. Patent 6,343,770. February 5th 2002. U.S. Patent 6,390,416. May 21st 2002.

Wear Life Testing of a Mission Critical Separation Interface

Jonathan P. Wood* and Joseph de la Fuente*

Abstract

This paper covers the wear life validation testing performed for a mission critical separation interface. The test was performed for the purpose of risk reduction, to demonstrate wear life margin prior to performing official qualification testing. The following is an overview of the mechanism, the design rationale of the test equipment and method, the test results, and the lessons learned. In addition to the specifics of the test, the implications of the test data on the design of launch lock mechanisms are discussed.

Introduction

The LLA (Launch Lock Assembly) is the mechanism used to restrain and deploy a large Payload Wing during its launch and mission sequence. The two halves of the LLA are mated by a preloading element in order to stow the payload wing for launch, as shown in Figure 1. These two halves separate by releasing the preload. This necessitates a separable joint within the LLA, capable of withstanding axial and shear loading. This joint, referred to as a shear tie, is subjected to significant wear under loads during launch. After launch, the joint must separate, in order for the payload wing to function. As such, the LLA shear ties represent a mission critical interface.

Due to the large mass and relatively small surface area of the payload wing, the bulk of wear that occurs during launch is due to the coupled loads between the launch vehicle and spacecraft. This creates a relatively large displacement rocking motion between the male and female shear ties at low frequencies (~20 Hz). This shear tie geometry and wear mode do not fit comfortably within heritage shear tie designs, so a unique test was devised to simulate the expected wear that would occur during ground test and launch.

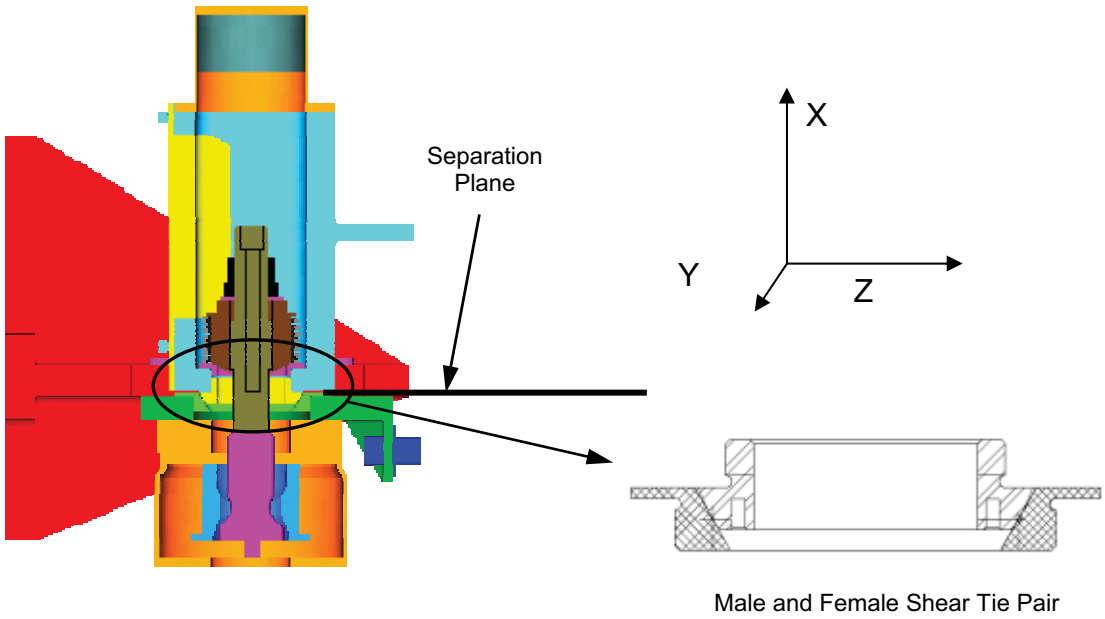

Figure 1. LLA cross-section showing shear tie interface

* Lockheed Martin Space Systems Company, Sunnyvale CA

Discussion of Heritage Data

Flight heritage is often considered to be the highest level of design validation. Although this is a reasonable statement, care must be taken in using heritage designs. The use of shear ties in launch locks is a good example of this. Although the LLA shear ties are similar in overall geometry to heritage shear ties (sphere-in-cone contact geometry), the spherical radius, cone half angle, and overall size deviate from heritage designs. In addition, the wear environment for this shear tie differs from heritage environments. Similarly, the coating used on the these shear ties (Tiodize type 2 over-coated with Tiolube 460), has significant heritage as a solid lubricant for space environments, but had not been used on previous Lockheed Martin shear tie designs. It was chosen for the LLA because it performed well when subjected to large-displacement wear under heavy loads in the material selection test described below.

The failure mode for shear ties is coating wear-through followed by galling, cold-welding, or adhesion of the base metal. In order to qualify a shear tie design by similarity, several requirements should be met. First, the same coating and substrate must be used in both applications. Second, the shear tie geometry should have the same overall configuration with a contact stress level that is enveloped by the heritage design. Finally, the wear environment for the new design or application must be enveloped by the wear environment for the heritage design.

Although the LLA shear ties are officially qualified during spacecraft level vibration and acoustic tests, the application was considered to deviate from heritage enough to justify a development level risk-reduction wear life test. Design changes resulting from a qualification test failure (especially at the spacecraft level), have heavy cost and schedule impacts, which can often be prevented during the design phase by performing appropriate development testing.

Flight-Like Wear Testing Background

The wear life of a shear tie is sensitive its subjected wear mode, as has been shown in past testing. This conclusion was drawn because of the difference between the results of two prior tests. The first test was a material/coating selection test. During this test, test specimens with shear tie contact geometry were loaded into an Instron machine and cycled axially (see Figure 2). Relative motion was achieved by varying the load on the shear ties – as load increases, the contact angle causes hoop deformations which allow axial motion. A fretting distance of approximately 0.6 mm (per cycle) was achieved. A number of shear tie material and coating combinations were tested using this method to evaluate the relative performance of each coating. Tiodize type 2 over-coated with Tiolube 460 was the highest performing shear tie coating in this test. The second highest performing coating is referred to as coating B. The life test data is shown in Table 1. As shown in the table, the wear life of the Tiodize coating was significantly longer and much more consistent under this wear mode than coating B.

Table 1. Material selection life test results

Specimens	Max Load	Failure
Coating	*kN*	*cycles*
Coating B	35.6	10250
Coating B	35.6	6250
Tiodize/Tiolube	35.6	15250
Tiodize/Tiolube	35.6	15250
Tiodize/Tiolube	35.6	14250

At the time the material selection was coming to a close, issues with shear tie coatings for another program required that a risk-reduction flight-like validation test be performed. The material selection test had been designed to compare the performance of a number of shear tie material/coating combinations, not to simulate launch. Because shear tie wear during ground test and launch is driven by random inputs (such as acoustic loads), comparing the wear life observed during the material selection test to the actual wear environment could not be done with a sufficiently high level of confidence. It was determined that a test should be designed that simulated the flight wear environment as closely as possible. Because the application for these shear ties involved high-frequency rocking motions between the shear ties (due to

acoustic energy), a random-vibration test was performed that re-created the primary rocking wear mode. Results from this test, (with respect to the cumulated fretting distance) are shown in Table 2. Coating B consistently outperformed the Tiodize coating, which showed much higher wear levels, and localized freckles of galling. Figure 3 shows a photograph of a galled shear tie test specimen.

The discrepancy between test results was surprising because the material selection test had applied the same contact stress level to the parts as the random-vibration test, and the maximum fretting distance applied during each cycle was similar between the two tests (0.6 mm for the material selection test, 0.7 mm for the random-vibration test). The fretting distance at which galling occurred was also different between the two tests (7000 mm for the Tiodize coating in the material selection test, ~5000 mm for the random-vibration test.) The coatings from both tests were cross-sectioned, and parameters such as coating thickness and coating consistency were in-family with both batches of parts.

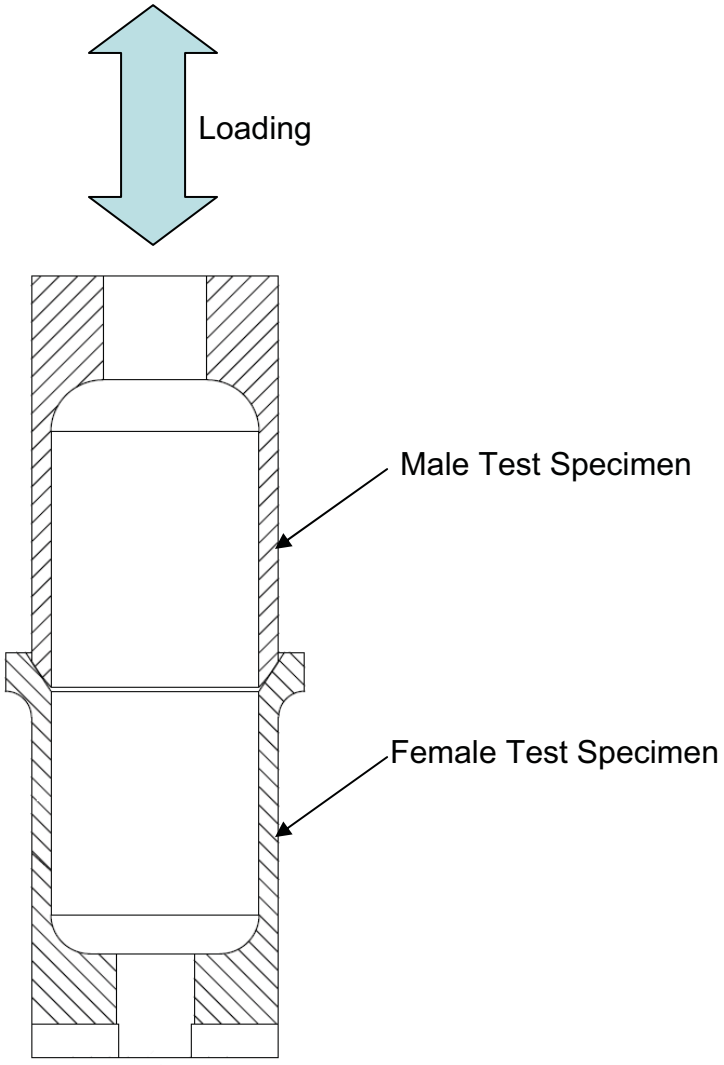

Figure 2. Schematic showing material selection test configuration

Table 2. Random-vibration wear test results

Coating	Relative Wear
Coating B	Low - Moderate
Coating B	Low
Coating B	Low - Moderate
Coating B	Low
Tiodize/Tiolube 460	Moderate-High
Tiodize/Tiolube 460	Moderate
Tiodize/Tiolube 460	Moderate
Tiodize/Tiolube 460	High - Galling
Tiodize/Tiolube 460	Moderate-High
Tiodize/Tiolube 460	Moderate
Tiodize/Tiolube 460	High - Galling
Tiodize/Tiolube 460	Moderate

By looking at the differences between the two tests, the following conclusions were drawn. First, it is important to re-create the same wear mode during a wear test – simply applying the same bulk fretting distance under the same contact stress may not provide the same result. Second, the actual geometry of the mating parts (not just the contact stress), seems to influence test results. The shear tie specimens from the material selection test had a larger overall diameter, larger spherical radius, and shallower contact angle than the random-vibration test specimens. (The geometry for the material selection test coupons was based on a new shear tie design).

Figure 3. Photograph showing galled test specimen (unacceptable wear pattern)

Although the contact stress level was the same for both tests, this contact stress level was achieved by applying a higher preload during the material selection test. Due to the higher preload, and the different contact geometry, the normal load distribution around the contact line was higher for the material selection test coupons. In addition, the material selection test was performed quasi-statically, and the random-vibration test applied fretting motions at roughly 80 Hertz. Based on these conclusions, the following guidelines are proposed.

Flight-Like Wear Test Guidelines

1. Shear tie wear testing should employ the same wear mode as the flight application.
2. Shear tie wear testing should occur under the same contact stress level, and with the same normal load distribution around the contact line.
3. It is recommended that test specimens employ the same contact geometry as the flight design (Same spherical radius and contact angle, at the very least).
4. Although the frequency that wear cycles occur is considered to be less important than other parameters, it is good to get as close as possible to the flight wear cycle frequency.

Payload Wing Shear Tie Wear Environment

Due to the large mass and relatively small surface area of the Payload Wing, the bulk of wear that occurs during launch is due to the coupled loads between the launch vehicle and spacecraft. This results in a wear mode characterized by relatively large shear tie displacements (rocking about the instant-center of the spherical surface) at a relatively low frequency (~20 Hz). Shear tie rocking angles are found by performing Finite Element Analysis of the next-higher-assembly. Although the coatings used for shear tie wear surfaces often provide low-friction surfaces, the interface cannot be accurately modeled as a frictionless ball joint. Unlike a frictionless ball joint, when a torque is applied to a shear tie joint, it will not begin to slip until friction is overcome. Conversely, the joint cannot be modeled as a rigid joint, because once slip occurs, the stiffness of the joint drops significantly. However, it is this blend of characteristics that does allow for some bounding assumptions.

Rather than attempting to determine the exact rotation angle that would occur (which would be highly sensitive to the friction coefficient of the coating), the problem was bounded by finding the maximum possible rotation angle and the maximum available overturning moment. The maximum possible rotation angle was found by modeling the shear tie as a frictionless joint, and the maximum available overturning moment was found by modeling the shear tie as a rigid joint. In this case, design load factors were used to ensure test conservatism. One factor that is important in creating a truly flight-like wear test is the random nature of shear tie loads. Because the forcing function that drives the motions of the shear ties is random, the maximum fretting distance is not achieved during the entire launch sequence. Typically, the rocking angle that occurs throughout a launch event will follow a bell-curve. The test was designed with this in mind – 1, 2, and 3-sigma rocking angles were applied with a corresponding number of cycles to match the expected statistical distribution.

For the rigid case, the maximum (3-sigma) moments are:

- M_x: 623 N-m (5866 in-lb)
- M_y: 333 N-m (2949 in-lb)
- M_z: 787 N-m (6966 in-lb)

For the zero rotational stiffness case, the maximum (3-sigma) rotations are:

- θ_x: 0.51 deg
- θ_y: 0.26 deg
- θ_z: 1.75 deg

Note that the coordinate system used above places the centerline of the shear ties along the X axis, per Figure 1.

The resultant of the rocking angles, (θ_y & θ_z), gives a total rocking angle of 1.77 degrees. Due to the arrangement of the shear ties, rotation about the shear tie centerline, (θ_x) to the extent shown above is not possible. Actual θ_x rotations are small in comparison to θ_y & θ_z.
Based on this data, 1, 2, and 3-sigma loads, displacements, and cycles were defined for the wear test. These test requirements are shown in Table 3.

Table 3. Wear Test Moments and Rocking Angles

Case	Overturning Moment N-m (in-lb)	Rocking Angle deg	Cycles	Frequency [Hz]
3 σ	855 (7565)	1.77	3	1.5
2 σ	570 (5043)	1.18	32	5
1 σ	285 (2522)	0.59	145	5

Test Description

In order to correctly envelope the flight wear environment, the following criteria were met in the design of the wear test:

1. Requirement: Shear tie wear testing shall employ the same wear mode as the flight application
   Compliance: The test simulates the dominant wear mode, which is rocking about the instant-center of the spherical wear surface.

2. Requirement: Shear tie wear testing shall occur under the same contact stress level, and with the same normal load distribution around the contact line.
   Compliance: Shear Tie Testing was performed using a flight-like LLA assembly, which was preloaded to the flight preload using the flight preloading procedure.

3. Requirement: The test specimens must have the same contact geometry as the flight design
   Compliance: Shear tie test articles were built to flight drawings & standards.

4. Although the frequency that wear cycles occur is considered to be less important than other parameters, it is good to get as close as possible to the flight wear cycle frequency. The flight wear mode occurs at a low frequency (~20 Hz). Testing was performed at a low frequency, and was limited by the capability of the Instron machine to main control at high displacements. (Failure to maintain position control would result in damage to the test article). A cycling frequency of 5 Hz was achieved for 1σ & 2σ tests, and 3σ tests were limited to 1.5 Hz due to the larger stroke.

Test Conservatism
The level of test conservatism applied during a wear test should be carefully considered. In the case of shear ties, there is often a higher level of uncertainty associated with wear predictions than a typical wear prediction. In addition, solid lubricant coatings are prone to lot-to-lot variations, which demand either a larger sample size, or a higher level of conservatism. In the case of this test, there was a high level of confidence that the shear ties would survive the test, so a high level of conservatism was used. Conservatism was maintained by several factors. First, design load factors were used to define the wear environment. These design loads were, on average, about 100% higher than coupled-loads analysis predictions. In addition, friction was ignored in determining the shear tie rocking angles. Finally, the number of 1-sigma cycles was doubled to account for any wear that could occur during acoustic ground tests, which resulted in the 145 cycles shown in Table 3.

Pass-Fail Criteria
The following pass/fail criteria were used for the test:
1. Successful deployment/separation of the shear tie interface after being subjected to all three load cycling cases, while utilizing only the “static” kickoff force provided by the LLA assembly (slow release of preload).

2. Acceptable wear patterns are observed on shear ties. Acceptable wear is defined as wear showing a galled area of less than 6.45 mm^2. The acceptable galling area is calculated by finding the area of a perfectly welded joint that would prevent separation, and dividing by three (Safety factor of three against failure to self-separate).

Test article

Although the entire LLA assembly was used as a test article for this test, only the wearing parts were considered test specimens. All of the wearing parts were made from Ti-6Al-4V, Solution Treated and Aged, coated with Tiodize type 2, and over-coated with Tiolube 460. The test specimens were fabricated to flight drawings and standards. A total of 3 sets of the wearing parts were tested. Three test specimen pairs were used to provide a reasonable idea of the variations in coating performance that might occur in a given lot. After each wear test regimen was completed, the wearing parts were inspected and replaced with the next set. Shear Tie specimens were preloaded to 28.9 kN ± 222 N (6500 lb ± 50 lb), which corresponds to a maximum Hertzian contact stress of 665 MPa (96.4 ksi).

Test Overview

Figure 4 shows a diagram of the test setup. A photograph of the test setup is shown in Figure 5. The primary wear mode for the LLA is a rocking mode about the shear tie center of rotation. This rocking mode occurs in two axes, so the resultant displacement was applied in one rotation axis. There is a third rotation mode on the flight article, a rotation about the central axis of the shear ties. This mode is small in magnitude, and was not enveloped by this test.

The spacecraft side of the test article was mounted to a base plate, which was mounted to the ram of a servohydraulic Instron machine. The “payload-wing” side of the test article (the bolt-catcher bracket), was grounded to the Instron load cell by a linkage that was connected to a steel block mounted to the bolt catcher bracket. As the base plate moved up and down, the shear ties were forced to rotate, introducing the desired wear mode.

Rocking motions were measured using two extensometers, one in line with the clevis, and another placed 6.35 cm inboard of the clevis. The purpose here was to provide a measurement of the rotation angle that would be somewhat independent of the deflections in the test fixture. The actual rocking angle applied during each test was found using the extensometer data, using the formula below.

$$\theta = \tan^{-1}\left(\frac{d_1 - d_2}{R}\right)$$

Where d_1 and d_2 are the extensometer displacements, R is the distance between the extensometers, and θ is the rotation angle.

Uncontrolled rotations were monitored using an autocollimator, which was set up to stare at a mirror flat mounted to the clevis mount (Figure 4). The rotations measured by this autocollimator were not recorded during testing – the purpose for this measurement was to monitor these rotations and verify that they were not affecting the shear tie wear during the test. The autocollimator readings were monitored during testing by personnel who were instructed to halt the test if more than 5000 μrad (0.3 degree) of rotation was observed in the non-controlled axis.

The test was conducted in three phases. The first phase, or “LLA Stiffness Characterization” phase, was performed to verify that the load limits set for each run would not be tripped during testing. The second phase was the actual wear test, and the third phase was the separation test.

Phase 1 Test

During phase 1, the Instron was controlled using its built-in position transducer. This was done as a safety measure, since the extensometers have a tendency to slip at higher frequencies. The loading cases for the test are shown in Table 3. Each test run was controlled using displacement control, with load limits set per Table 3. Prior to testing, the range of motion for the test article was measured at ±5.1 mm. In order to protect the test article from damage, displacement limits were set at ±4.4 mm. Phase 1

tests were performed at a drive frequency of 0.1 Hz. Two cycles were performed for each test run. During cycling, the preload in the preload rod was monitored, and the peak preload value was recorded. The autocollimator measurements were also monitored. For the autocollimator reading, some drift was acceptable, provided it was not cyclic in nature.

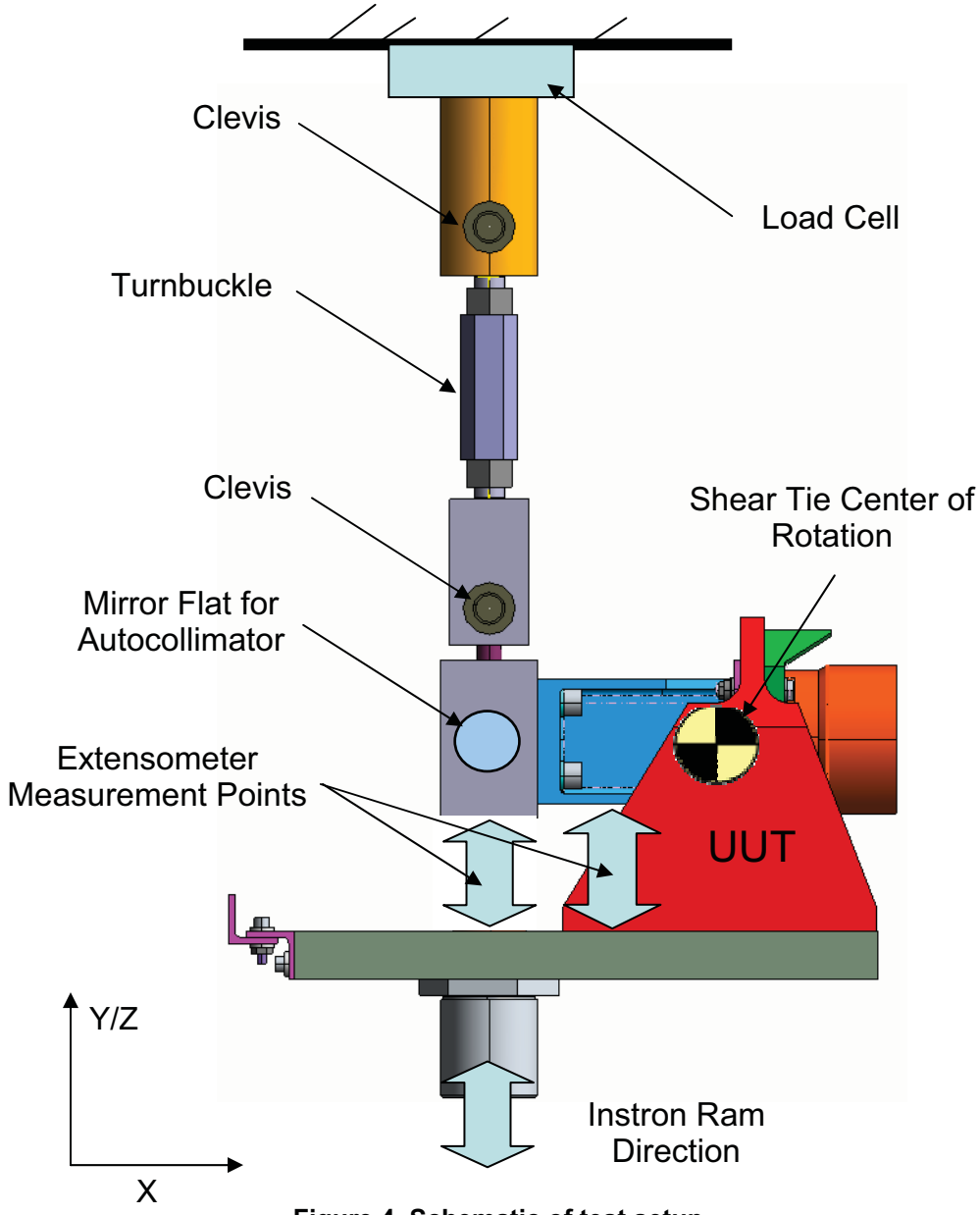

Figure 4. Schematic of test setup

Phase 2 Test

Phase 2 tests were performed using the same basic procedure as phase 1, but at higher frequencies, and with cycle counts corresponding to Table 3. The 1σ test run was performed first, followed by the 2σ run and the 3σ run. During pre-test trials, it had been found that the displacement limits were tripped if the drive frequency was increased too suddenly. For this reason, each test run was started at 0.5 Hz and ramped up to the final drive frequency. During this test, the autocollimator was monitored to verify that uncontrolled displacements were not inputting a significant level of additional wear.

Figure 5. Photograph of test setup

Phase 3 Test

After each specimen pair was subjected to all 1σ, 2σ, and 3σ test runs, a separation test was performed. The separation test fixture is shown in Figure 6. A cradle, which rides along a linear bearing, was used to support the bolt catcher bracket and clevis mount during separation. The function of this cradle is to limit rotation about the axis during the release of the preload. Unrestrained motion during this step may break any cold-welds that may have occurred, which could prevent the detection of shear tie failure.

During each separation test, the cradle was first installed on the base plate. Then, the ball-tipped screws were adjusted to contact the LLA. Next, the preload nut was unscrewed slowly, while monitoring preload. If a popping noise was heard, (which indicates the breaking of a cold-weld), the load when this occurred was recorded. Once the preload was removed, the shear ties were inspected and photographed.

Test Results

Anomalies and Failures

Some anomalies did occur during testing. The first anomaly was caused by excessive slop in the linkage between the Instron machine load cell and the bolt catcher bracket. The excessive slop was due to the clearance in the pinned joint between the test fixture turnbuckle and the Instron load cell. This affected the first set of specimens during the 1-sigma wear test by reducing the overall amplitude of wear cycles throughout the test. This problem was fixed before proceeding to the 2-sigma wear test by replacing the "standard" pin block on the load cell with a pin block that could be preloaded with a jam large jam nut. While testing the first set of specimens, it was also observed that the extensometers have a tendency to slip on their mounting posts during the 5 Hz tests. Grooves were filed into the extensometer mounting posts to mitigate this problem, but it continued to occur during testing of the second and third pairs of specimens during 5 Hz tests. This anomaly is considered to be of minimal impact, because the low frequency characterization tests provide accurate data to determine the actual rotation amplitude that

occurred during each test. Issues with the Instron controller caused two to three extra cycles to be applied to the second and third specimen sets.

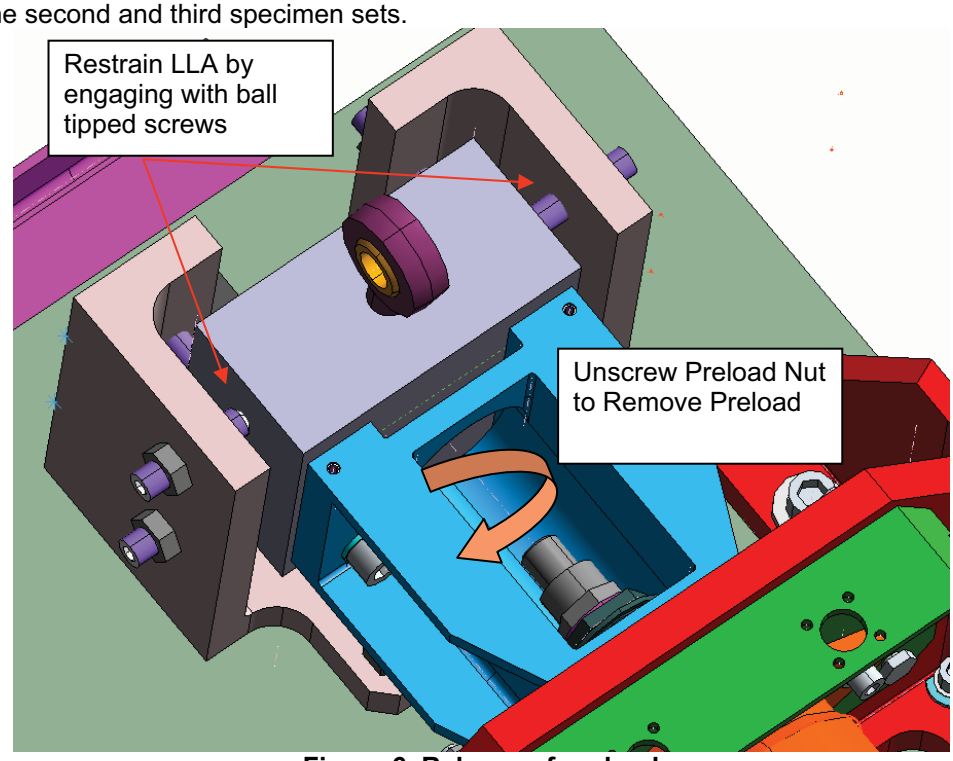

Figure 6. Release of preload

Results Summary

No galling or failure to self-separate occurred during testing. Photographs of a representative shear tie pair are shown in Figure 7 & Figure 8. The level of shear tie wear was acceptable. The wear on the shear tie specimens is very directional, as expected, and shows a layer of burnished-in MoS_2 (Tiolube 460) that is just beginning to flake away from the anodize layer. Inspection under a microscope shows that although the Tiolube layer is very thin, it is mostly intact. Comparison of this level of wear to the sequential wear patterns observed during life testing of this coating indicate that the coating has most of its wear life remaining.

Figure 7. S/N 006 male shear tie, showing acceptable wear pattern

Figure 8. S/N 006 female shear tie, showing acceptable wear pattern

A representative set of load/deflection curves is shown in Figures 9 -11. It is interesting to note that each curve shows a distinct Dahl slope, which represents a portion of rotation that is characterized by elastic deformation of the contact surface (due to shear stress) rather than sliding. The first 0.3 to 0.5 degree of displacement in each cycle was due to elastic shear. Once the torque to overcome friction is reached, the joint begins to slip, and the slope of the curve levels out.

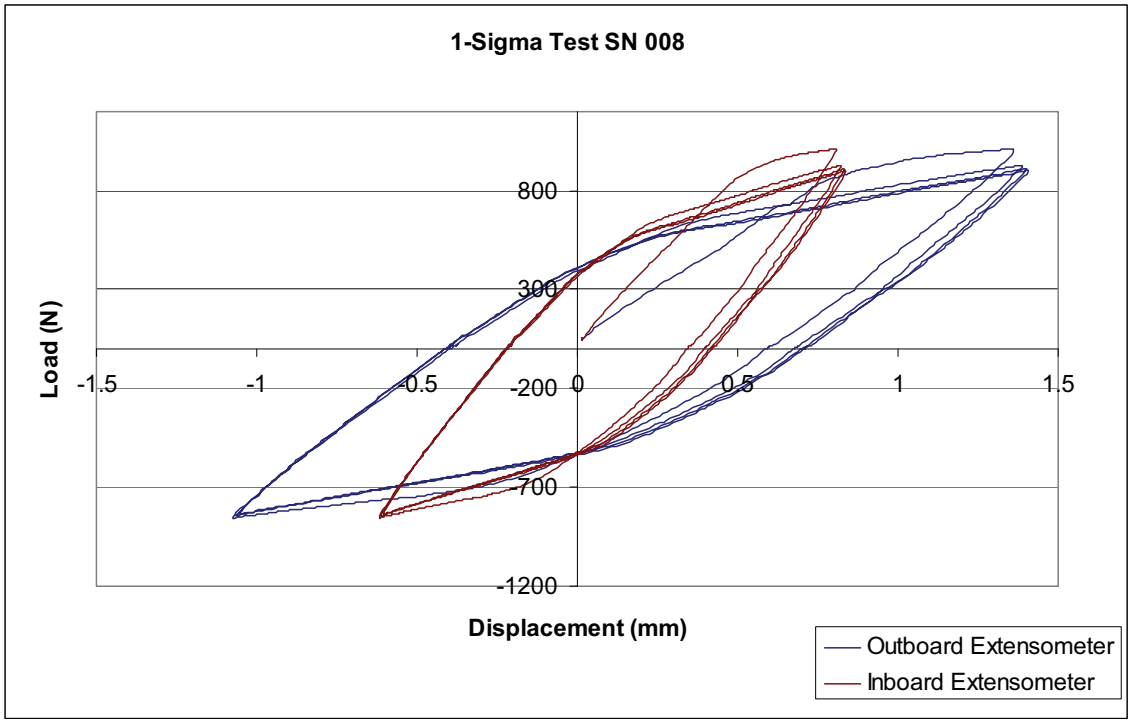

Figure 9. 1-sigma load/deflection curve

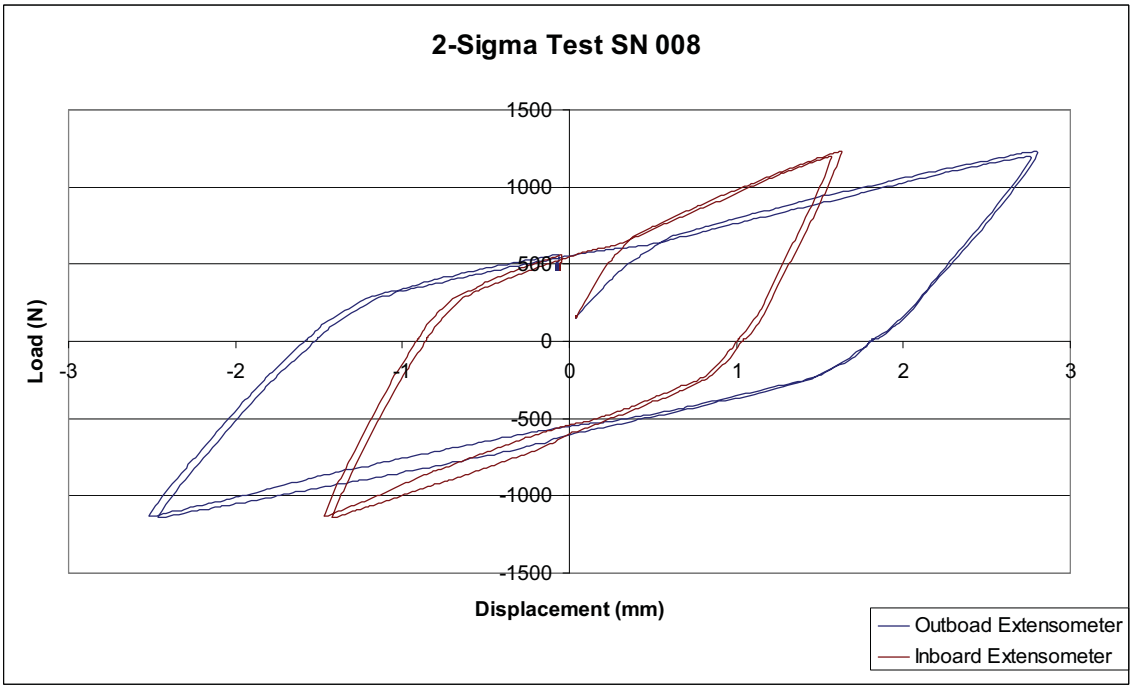

Figure 10. 2-sigma load/deflection curve

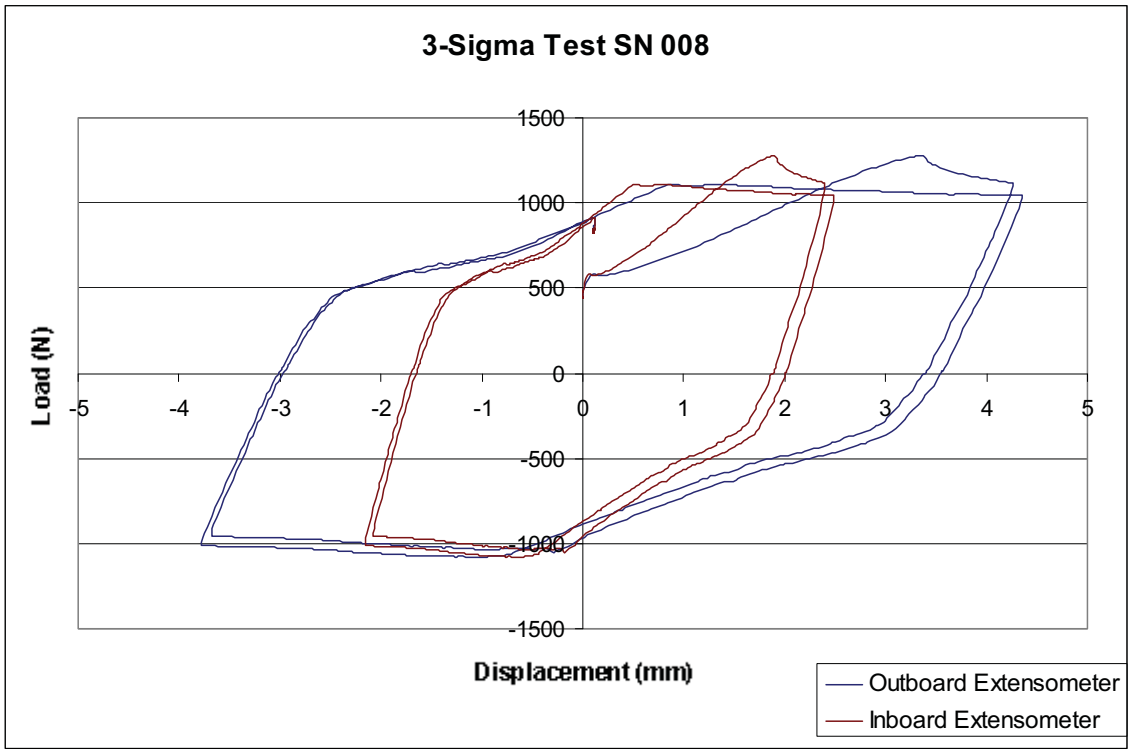

Figure 11. 3-sigma load/deflection curve

The rocking angle that occurred during each test was calculated, and is compared to the desired value in Table 4. Note that the 1-sigma test level for serial number 007 was about half the desired test level, as discussed in the anomalies and failures section. The friction coefficient was calculated from the load at which slip occurred during each test. The friction coefficient ranged from 0.03 to 0.08.

Table 4. Actual displacements during testing

Test	Serial No	Displacement			Angle		
		Measured	Desired	Difference	Measured	Desired	Difference
1-Sigma	006	0.049	0.059	17%	0.48	0.59	19%
	007	0.029	0.059	51%	0.29	0.59	51%
	008	0.049	0.059	17%	0.47	0.59	20%
2-Sigma	006	0.104	0.110	5%	1.05	1.18	11%
	007	0.104	0.110	5%	1.08	1.18	8%
	008	0.105	0.110	5%	1.03	1.18	13%
3-Sigma	006	0.157	0.165	5%	1.60	1.77	10%
	007	0.160	0.165	3%	1.83	1.77	-3%
	008	0.160	0.165	3%	1.60	1.77	10%

Conclusions

The LLA shear tie design is capable of surviving wear due to ground test and launch with acceptable wear patterns, which indicates positive life margin. After being subjected to an enveloping wear environment during risk-reduction testing, shear tie specimens showed wear patterns indicative of early wear stages. Displacements during the test (with one exception, as noted in Table 4) were within 17% of the desired value, and angular displacements were within 20% of the desired value. The reduction in measured displacements compared to “controlled” displacements occurred due to elastic compliance in the Instron machine and test fixture. The test levels were conservative to begin with (more than 2X predicted displacements), so it is considered that the test, as run, properly envelopes the wear expected during ground test and launch. The wear levels observed on all three shear tie pairs were similar, which indicates that the performance of the Tiodize/Tiolube 460 coating was consistent for the lot of parts that were tested. Because between 0.3 and 0.5 degree of displacement was shown to occur with negligible slip, any displacements that do occur during acoustic testing will have a negligible contribution to the overall wear of the shear ties. This demonstrates that the doubling of the number of 1-sigma cycles envelopes acoustic testing.

Test Telemetry

The results of this test serve to indicate the importance of taking the correct telemetry during wear testing. Good telemetry should isolate the measurement from test fixture deflections, providing a direct measurement of the desired data. By providing good telemetry, this test did more than just verify the wear life of the test specimens, it provided useful insights into the functioning of the shear tie interface that were used to verify assumptions about the wear environment, and determine the friction coefficient of the coating under flight-like conditions. In addition, the contribution of test fixture displacement to the overall displacement of the Instron machine was characterized.

Lessons Learned

This test provided some key insights on testing wear surfaces. Analyzing test data in real time allows one to catch issues that could compromise or invalidate test data and results. For example, a cursory examination of the test data between the one and two-sigma tests of the first shear tie pair caught the excessive test fixture slop early on in the test. The fact that test fixture displacement accounted for up to 20% of the desired rotation had little impact on the test result because of the high level of conservatism built into the test. If the level of conservatism had been lower, however, this could have been a significant problem. Test fixture displacements could have easily been characterized by examining data from the phase 1 tests, and used to scale up the Instron displacement, which would have ensured that the desired rocking angles were achieved.

Acknowledgements

The authors would like to thank the following people for their contributions to this test: Ed Boesiger, Luke Bunselmeyer, Stu Loewenthal, Mike Popyack, Kurien Thomas, Don Shaffer, and Charles Whipple.

Circular Hall Transducer for Accurate Contactless Angular Position Sensing

Laurent Sache*, Serge Reymond**, Pavel Kejik**, Mikael Sjöholm*, Daniel Bommottet*, Volker Gass*, Lionel Gaillard+ and Radjan S. Popovic**

Abstract

Demands for robust, reliable and accurate angular position sensing of space mechanism are increasing steadily. As a consequence, contactless sensors providing an alternative to triblogical drawbacks of the current sliding potentiometers represent a key factor for the development of future space applications. In the framework of the ESTEC activity [1] covering the selection of an angular position sensor (APS) based on MEMS technology and in collaboration with the EPFL-LMIS [2], RUAG is currently carrying out the qualification of a new contactless angular position sensor based on the Hall Effect. Providing the angle without need of a complex algorithm, it offers a more reliable, lighter, less sensitive to vibrations and cost effective sensing solution.

Introduction

Current rotary sensors are either potentiometers or encoders. Be it in the case where those systems are placed on the outside or on the inside of the satellite bus, the environmental conditions are typically very harsh.

Potentiometers cover low accuracy application in a range down to 0.4°. They have the advantage of simplicity, size, ease of implementation and low cost. Rotor and stator (track) typically have to be installed independently but this process is not extremely sensitive with regards to the relative alignment of brushes to track. The electrical interface is typically a 0 - 5V analogue one. On the other hand potentiometer reliability suffers from the sliding contact of a metallic brush on a plastic film with implemented conductive materials (carbon, etc). Various combinations of materials with and without lubrication have been applied but sufficient reliability could not be proven so far specifically for long time application like telecom (12 to 15 years). An alternative to such simple device would be the most demanding application.

Encoders are typically used when high resolution and reliability is required but suffer from their complexity of the mechanical integration and the electrical interface. Encoders have a higher mass and in case of high exposure to radiation they have to be additionally shielded by a metallic housing that adds weight. The electrical interface is digital (serial or parallel) and thus more complex to handle compared to the one of a potentiometer. Additionally encoders are expensive and normally come along with long lead times.

The ideal replacement of a potentiometer and/or encoder would be a sensor that combines both positive characteristics:
From the potentiometer:
- simple electrical interface
- simple mechanical interface (low sensitivity to misalignment)
- radiation resistance
- small and low weight
- low cost

From the encoder:
- high resolution

* RUAG Aerospace, Nyon, Switzerland

** Ecole Polytechnique Fédérale de Lausanne (EPFL), Lausanne, Switzerland

+ European Space Research and Technology Centre (ESTEC), Noordwijk, The Netherlands

The proposed angular position sensor is a magnetostatic encoder based on the Hall Effect. Commercial contactless angular sensors are composed of a two-axis sensitive Hall structure combined with rotating permanent magnets [3]. Most of these technologies provide a two-component analog output, which requires a digital signal processor to calculate the angular position of the permanent magnet (traditionally by the use of CORDIC algorithms [4]). The use of a Digital Signal Processor (DSP) increases the complexity of the surrounding electronics and limits the reliability of the sensor in harsh environment conditions. In this context, the new contactless magnetic sensor proposed here [5], based on a circular sensitive structure, provides the angle without need of a complex algorithm.

The full sensor consists of a passive magnets configuration providing a magnetic field and a sensing element located in the plane of the field. This second element is composed of an encapsulated monolithic silicon chip that detects the direction of the magnetic field. The sensing element being aligned with the magnetic rotation axis, this sensor is dedicated to plain shaft application where the magnetic element can be fixed on the rotating shaft and the sensing element can be held by the housing of the structure. A simple sketch of the working principle is presented thereafter:

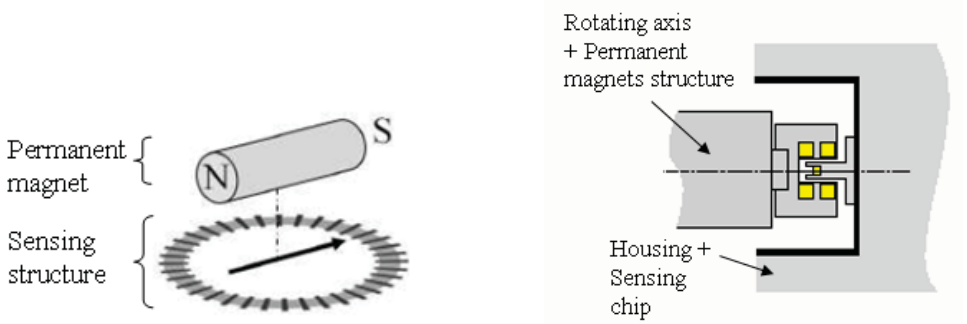

Figure 1. Schematic of the sensor principle (left) and sensor design (right)

This paper describes the sensor and presents the space qualification campaigns that are foreseen in the beginning of 2008.

The first section presents the sensing principle and its associated structure. The subsequent electronic includes in the chip to perform the basic measurement sequence along with the output information treatment is also outlined. A second chapter introduces the magnetic configuration offering the best combination between field homogeneity and sensor accuracy.

The development and the qualification of the sensor arise at two levels and in two steps:

- A first test campaign occurs at the sensor level and is presented in the third chapter. At this level, the electronic layout of the chip is not fully compliant with space standards, as no protection are implemented within the electronic layout with regards to radiation. This first level is a technology level and its main objective is to qualify through a test campaign the whole sensor composed of the rotating element and the sensing element inserted within a Chip On Board (CoB) package. This activity is performed within the framework of an ESA Technology Research Program (TRP) activity [1].

- A second test campaign occurs at chip level and is presented in the fourth section. At this level, the chip is encapsulated within a CERamic Dual In-line Package (CERDIP) and its layout incorporates radiation hardening techniques issue from the radiation test of the first test campaign. Those tests are undertaken at wafer and chip level according to European standards defined for monolithic chip space qualification.

Sensing structure

The sensor consists of a sensing structure, on-chip biasing, signal conditioning circuits and readout interface. The sensing element is an n-doped ring with N contacts equally distributed on the ring surface. Through switches each contact can be connected to the current source, to the ground or to the voltage amplifier. Many different connection combinations give information about the magnetic field. Here we present first a simple measurement sequence, with its associated sensitivity and zero-field offset, and a second sequence with a more efficient offset cancelling.

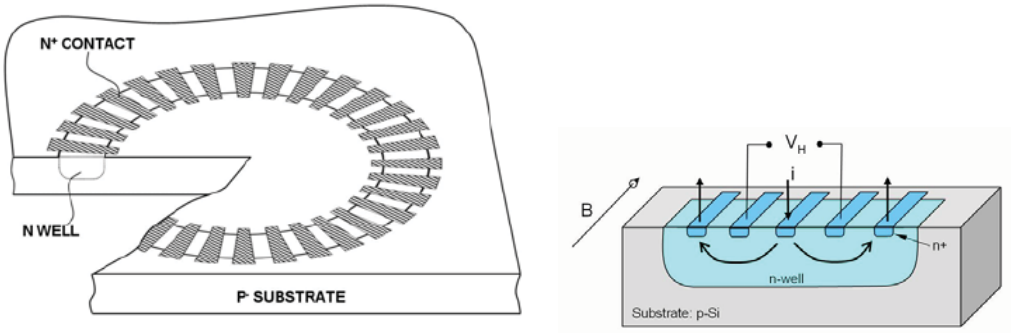

Figure 2. Integrated Hall structure and detail of a 5 Contacts Vertical Hall (5CVH) element

Sensing principle and basic measurement sequence

The measurement sequence is based on a 5 **C**ontacts **V**ertical **H**all element (5CVH) [6] that are composed by 5 in-line contacts. The current is injected through the outer contacts and collected in the middle one. The potential difference between the two remaining contacts (The Hall Voltage V_H) is proportional to one component of the in-plane magnetic field:

$$V_H \ \alpha \ B\cos(\alpha) \qquad (1)$$

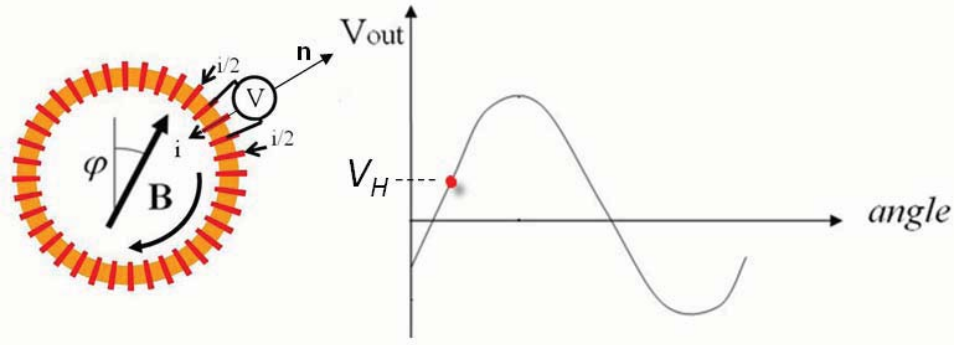

Figure 3. One step of the acquisition of the Hall voltage of one 5CVH.

At a time t, a series of 5 neighbor contacts are connected in such way to form a 5CVH. On a perfect device, the output voltage is proportional to $B\cos(\alpha)$, where α is the angle between **n** (a unitary vector normal to the middle contacts of the 5CVH) and **B**. At each clock time, the 5CVH element is shifted by one contact, and the Hall voltage becomes $B\cos(\alpha+2\pi/n)$. Over a full turn, the Hall voltage exhibits a sine function, with its amplitude proportional to the in-plane field and its phase equal to the field direction. The information about the field direction is contained in the first harmonic over the full turn period.

In a real structure, because of the imperfections (in the material and in the manufacturing process), the Hall voltage is superposed to an offset voltage. The key point is that the one-by-one shift of the 5CVH allows to compensate this offset. This can be easily understood by modeling the Hall ring by a circular array of non-identical resistors (see Figure 4). We can see that the contribution of the i^{th} resistor is cancelled. If a static defect induces an excess of voltage at the output at time *t*, the same defect causes an opposite voltage at time *t+1*. In this ohmic model, the dc offset, i.e. the sum over one full turn is zero.

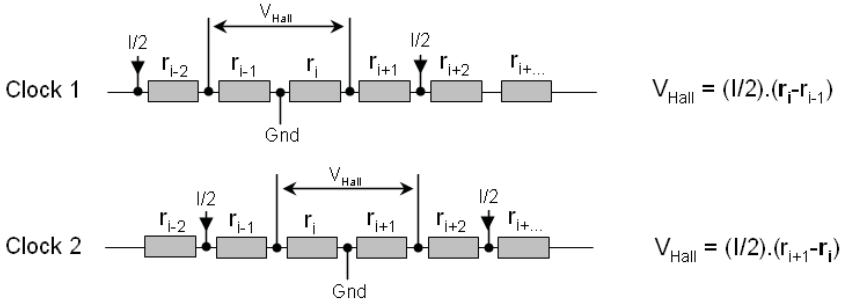

Figure 4. Resistor array model.

Zero field offset

The previous basic measurement sequence does not fully suppress the zero field offset. Even if the dc offset vanishes, a circular array of resistors, randomly distributed, create a non-zero first harmonic. In real devices, additional non-linear effects contribute to increase the offset. The most important one is the junction field effect, which, by squeezing the channel according to the applied voltage causes a dynamic modification of the conductive channel. Combined with the static imperfections, it prevents the full resistance cancellation. As a result, the sum of voltages over one cycle is not zero and degrades the accuracy of the sensor.

Another measurement sequence for suppression of the zero field offset

Depending on the application, another sequence can be implemented for cancelling the offset. A proposed special sequence called “subspinning” can cancels the output voltage; sum over a period much shorter that the full cycle. The aim is to suppress the residual first harmonic of the randomly distributed defects. A particular subspinning sequence is given thereafter on Figure 5.

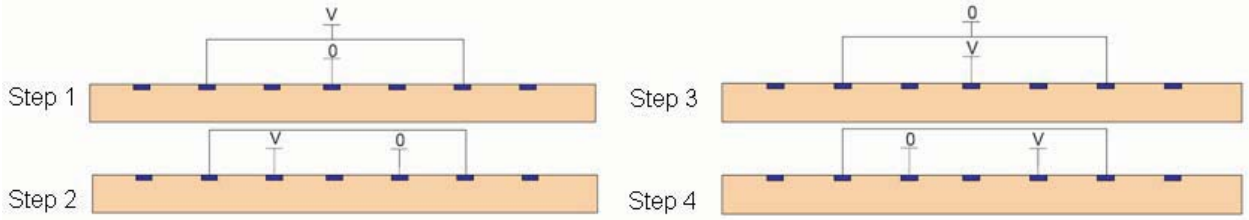

Figure 5. Subspinning sequence for the suppression of the zero offset.

The basic element is also a 5CVH, but the two extreme contacts are shorted and connected to a single current source, in order to make a four terminals device. At each position of the 5CVH, the four connections are circularly permuted, as for usual spinning current method. For a perfect array of resistors the sum over these 4 steps vanishes. As a consequence, the first harmonic is strongly reduced and the offset suppression factor is strongly reduced. Numerical simulations show that the subspinning sequence also suppresses the offset due to junction field effect.

Signal processing and Implementation

The selected technology for the sensor realization is a conventional CMOS 0.35-µm high-voltage technology. The supply voltage is 3.3 V. The sensing part is composed of an n-well ring with 64 n-doped contacts. The ring is formed by a deep n-well layer with about 6 µm of depth. The ring outer diameter is 50 µm. The ring width, contact number, size and shape were determined by optimizing the sensitivity using finite element calculations. A logic circuit ensures the correct switching sequence. The four-phase

subspinning sequence presented above is implemented for the readout of the 5C segments, resulting in 256 (4 x 64) measurement steps per full measurement sequence.

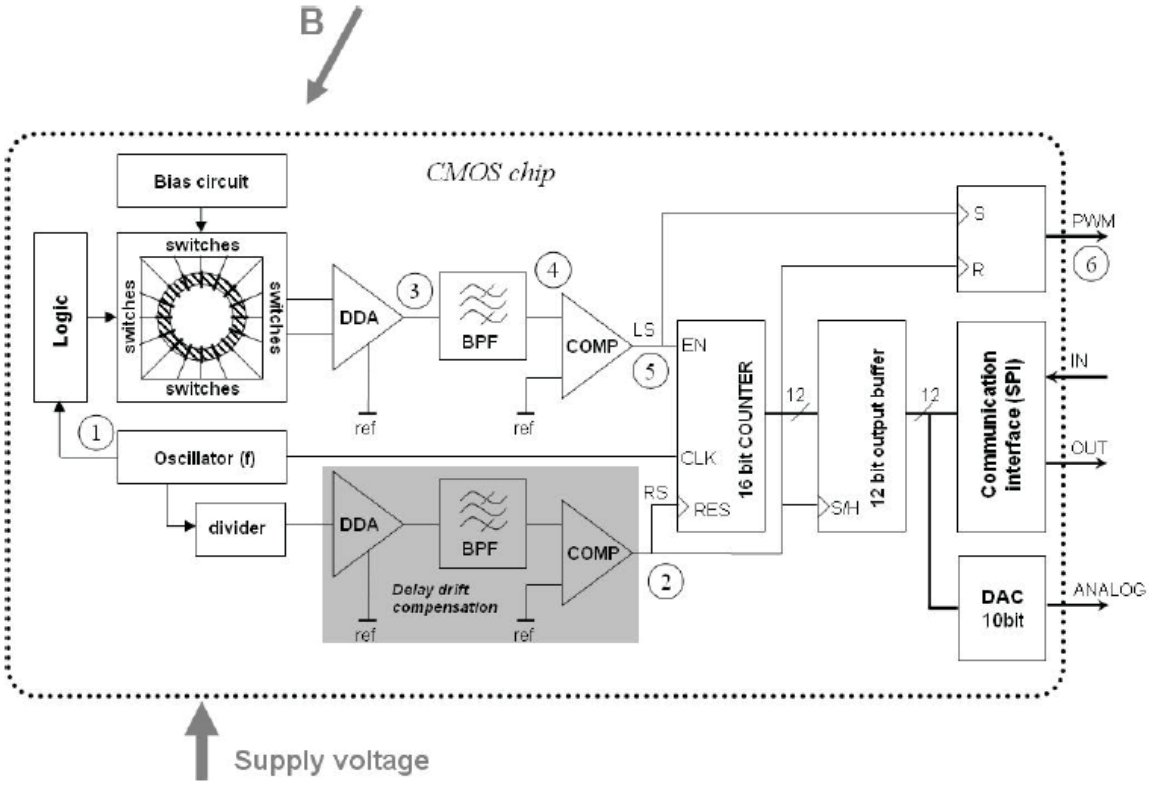

Figure 6. Block diagram of the APS

The measuring principle is based on the phase measurement between the detected signal **(5)** and the reference signal **(2)**. Switches realized by NMOS transmission gates connect the sensing structure to the bias circuit or Differential Difference Amplifier (DDA). The bias current generated in the bias circuit is derived from a bandgap cell. Oscillator, Logic and Divider blocks are realized by digital standard cells available from the foundry. The DDA, Band-Pass Filter (BPF) and Comparator (COMP) are optimized for low-noise, wide temperature range. The output signal is available in three different forms: Pulse Width Modulation (PWM), Serial Peripheral Interface (SPI) and analog output with 10 bits of resolution. Figure 7 shows the main signal waveforms in block diagram. The waveforms are cross-referenced by numbering.

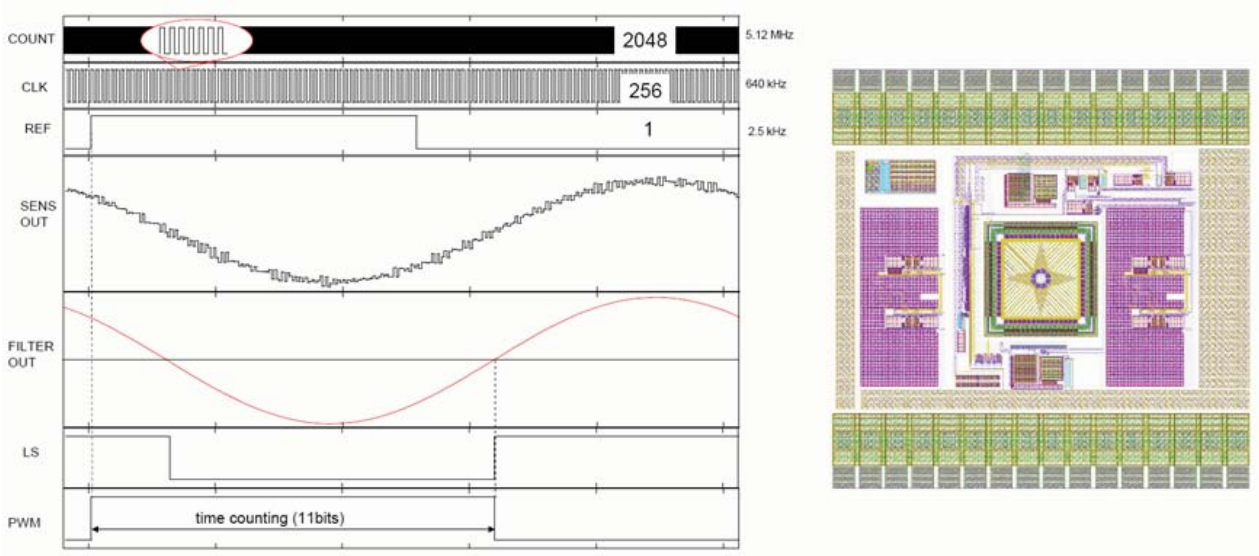

Figure 7. Main signal waveforms (frequency of the clock and reference signal are given for information) and view of the silicon layout.

The Hall voltage coming from the structure **(3)** is sensed and amplified by a differential difference amplifier (DDA) and buffered. The amplification gain is fixed so, that the amplified signal swing is about half of the full supply voltage range (3.3 V). The signal is further filtered through a 4th order band-pass switched capacitor (SC) filter, in order to suppress any high frequency parasitic signals induced by the Hall elements and offsets and 1/f noise caused by the DDA. The choice of the SC filter is due to its excellent stability of the filtering frequency and input-to-output phase shift over temperature. The signal is further filtered through a passive RC low-pass filter with cutoff frequency much higher (at least 10 x cycle frequency) in order to filter the ripple form of the signal coming from the SC filter. The filtered 1st harmonic useful signal (waveform **(4)** in Figure 7) is further transformed into a square wave signal through a comparator (waveform **(5)** in Figure 7). Thereby, the phase of the measured square wave signal can be compared with the reference signal in a logic phase detector circuit COMP **(6)**. In this way, the analog signal is converted to PWM digital form. Such a signal can be further easily converted to a digital word using a counter. Digitalized signal is read via an SPI interface, or converted to the analog form through a DAC. In order to minimize the influence of the phase drift in temperature caused by the electronics on the measured phase, the reference signal is treated in the same way as the detected signal. In other words, the reference signal with adequate magnitude and signal level is fed through a duplicated analog path composed of DDA, SC filter and COMP. In this way both signals are exposed to the same delay drift and the differential drift is minimized.

The sensor conditioning circuit is realized with a bandgap circuit in order to be insensitive to the supply voltage variations and well control the temperature drift of the bias current for the sensing part (Hall element). Since the sensing part is biased with relatively low current to keep the nonlinearity effect low, the drop voltage over the sensing part does not overreach the working range of an N type MOS transistor. Therefore, the sensing part is connected to the conditioning circuit and signal processing circuit via transmission gates composed only by NMOS transistor with optimized size. This allows minimizing the charge injection feed through from a digital driving part to the signal processing path. Chip size is of about 1.9 x 1.9 mm2. The system has 32 bonding pads with a pitch of 120 µm. The sensing part is centered with respect to the chip outlines (see Figure 7). Supply pads of the digital and analog part are split into two parts; in order to isolate the analog part from the digital part and prevent the clock feed-through.

Magnetic source

Requirements

The permanent magnet assembly must generate the magnetic field sensed by the detector. The field direction follows the rotation of the mechanism. This rotating element is composed of a mechanical structure that holds together the permanent magnet(s) in the desired configuration. Some of the main parameters of the magnetic source are listed thereafter.

- The magnetic field must lies within the chip plane. A small tilt is not an issue since a small and constant perpendicular component does not affects the angle reading.
- The magnetic field intensity must be large as an important field at the sensor position has two positive effects:
  - It increases the signal over noise ratio, which allows reducing the sensor bias current. This one limiting the power consumption and reducing the non linearity within the sensitive region that is the main cause of offsets.
  - It decreases the errors due to parasite external fields.
- The magnetic field must be homogeneous within the whole volume where the sensor is expected to move. This homogeneity is linked to the radius of homogeneity (HR) defined as the smallest distance from the center where the projection of the magnetic field in the sensor plan rotates by 0.05° (see Figure 8). HR varies with the distance along the z axis. The revolution of the function HR(z) around the z-axis defines the homogeneity volume.

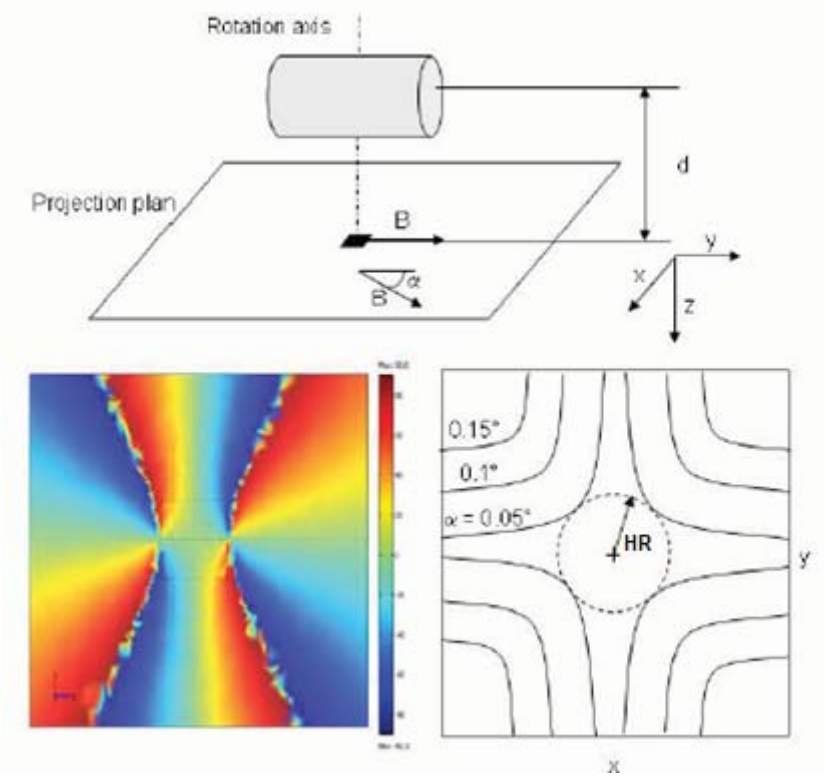

Figure 8. Definition of the homogeneity radius

- The stray field distance, depending on application, must be limited to reduce the field leaking out of the sensor region. A magnetic material (with high permeability) located inside the stray field region modifies the magnetic field distribution everywhere and thus might cause angular errors. In addition a small stray field offers a better compatibility with other nearby devices.
- The magnetic direction must be reproducible within the whole -60° to +90°C temperature range. Small changes in the field intensity does not directly affects the sensed angle, but in a real magnetic block, some region are usually close to demagnetization (corners, edges), and problem may arises when temperature induces a non uniform demagnetization. Therefore a magnet with

the smallest temperature coefficient is preferred. Similarly, radiations that can induce demagnetization must be limited.

Magnet material

The field intensity requirement imposes the use of rare earth magnets (meaning that one of the components is a lanthanide). The common compounds are NdFeB or SmCo. In general, NdFeB have a higher residual field (from 1 to 1.4 T instead of 0.8 to 1.1 T for SmCo) but this advantage is largely degraded by the other characteristics. First, SmCo has a smallest temperature coefficient (the reversible magnetism in SmCo decreases by 0.04 %/°C, which is about 10 times less than in NdFeB), higher Cure temperature and higher irreversible point (around 300°C for SmCo against 100°C for NdFeB), and therefore is less prone to irreversible loss of magnetism. As mentioned above, these effects are unwanted because a non-uniform demagnetization may lead to a change in the field orientation. Second, SmCo withstand radiation 2 to 40 times better than NdFeB. Finally, even though SmCo material is brittle and fragile, it is more resistant to corrosion and has a high resistance to oxidation. SmCo with the highest grade (corresponding to a higher coercively) are favorable to further improve the long-term stability. Among the highest grades, grade 28 is usually commercially available and is therefore a suitable material. The compound composition is Sm2Co17 and the blocks are fabricated by sintering. Its characteristics are listed in Table 1.

Table 1. Properties of SmCo28

Residual field (T)	Coercive field (kA/m)	Temp. coeff (%/°C)	Max working temp (°C)	Curie Temp. (°C)	Density (g/cm3)
1.03	760	0.04	300	800	8.3

Single magnet configuration

For production and magnetization simplicity the magnet assembly must consist of simple basic blocks (parallelepiped, cylinders, etc), with the magnetic moment orients and aligned with one edge.

For illustration, we show the performances obtained with a simple parallelepiped block (20 x 20 x 10 mm (x-y-z), magnetized along the x-axis). Figure 9 shows the field intensity and the HR as a function of the distance z from the magnet surface.

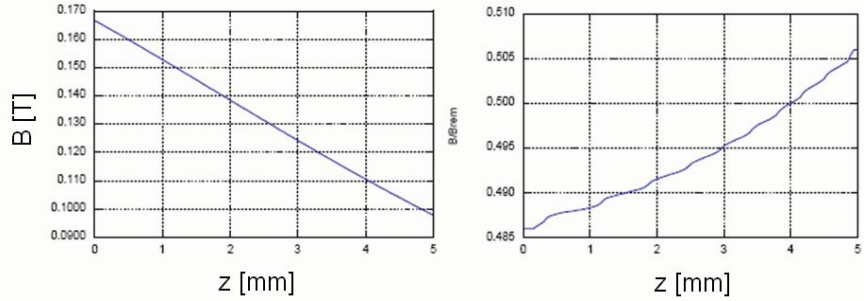

Figure 9. Field intensity (left) and homogeneity radius of a 20 x 20 x10 mm single block magnet

At 2 mm from the above single magnet surface (reasonable position of the sensor), the field intensity is around 140 mT and the homogeneity radius is 0.5 mm. These values comply with the homogeneity and intensity requirements. But the stray field distance is relatively large: 85 mm. Better performances in more compact configuration can be achieved with more complex magnet configurations.

Complex magnet configuration

The main idea is to constructively superpose the field from different magnet at the sensor location and destructively superpose at the outside. An arrangement known to allow this is the “Halbach” array [7]. Cylindrical Halbach array produce an intense field in a limited region and have a small stray distance because the total magnetic moment is zero. For the desired high accuracy, one suitable configuration consists in a Halbach crown made of 8 cubes, as shown in Figure 10. With fewer blocks, some volume is lost and with more blocks, the elementary cube is too small and the field intensity decreases (it is roughly proportional to the cube volume) [RD5]. A stack of two such crowns improves the field homogeneity and gives some displacement freedom along the z-axis (rotation axis). A comparison between the field

intensity and the homogeneity radius of a double-crown and a single-crown configuration is presented in Figure 11.

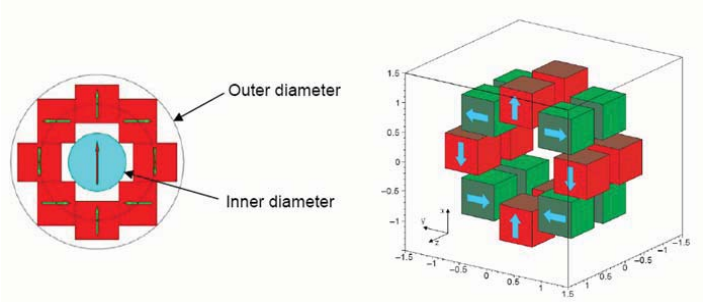

Figure 10. Left: Halbach crown made of 8 cubes in close contact. Right: Double crown configuration.

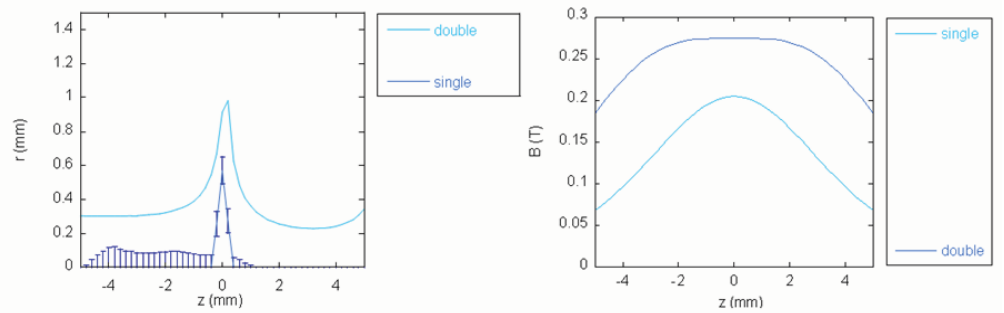

Figure 11. Comparison between a double and a single crown magnets configuration in terms of homogeneity radius and field intensity.

Table 2. Magnet assembly (dimensions in mm).

Outer diameter	Inner diameter	Height (along z)	Cube side	Cube pitch	Cube center radius
19	7.7	9.7	4	0.7	6.7

The angular homogeneity produced by the assembly with the parameters defined in Table 2 in the centre plane (z = 0) is shown in Figure 12. The homogeneity radius is close to 1 mm. Effect of displacements, errors in cube positioning, sizes and imperfection in the magnetization show that a displacement of the order of 0.1 mm affects the homogeneity radius by an amount of the same magnitude. The field intensity produced by the magnet assembly is around 270 mT. This relatively high value allows limiting the sensor bias current and thus decreasing the offsets. The stray field distance is 22 mm, i.e. about 10 mm out of the external diameter. The value is well below the values obtained for non-zero magnetic moment assemblies (like a single block solution).

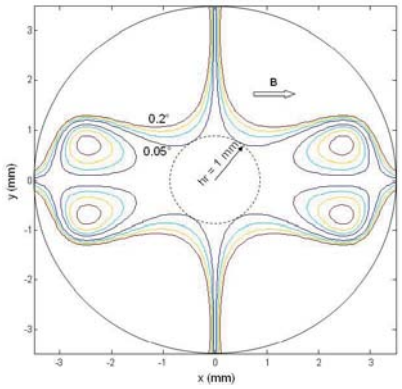

Figure 12. Angular homogeneity in the magnet center plane (z = 0) for a double-crown configuration.

Technology qualification campaign

Setup

The whole APS sensor is tested during the technology qualification campaign. The final test configuration dedicated to the tests is illustrated on Figure 13. The rotating element is mounted on a shaft guided trough a bearing system and drive by a precision actuator. An optical encoder, offering a high accuracy, is mounted on the actuator and represents the reference sensor. A decoupling between the APS and the driving system allow keeping the same configuration in a thermal vacuum (TV) chamber where a vacuum feedtrough is inserted between both systems.

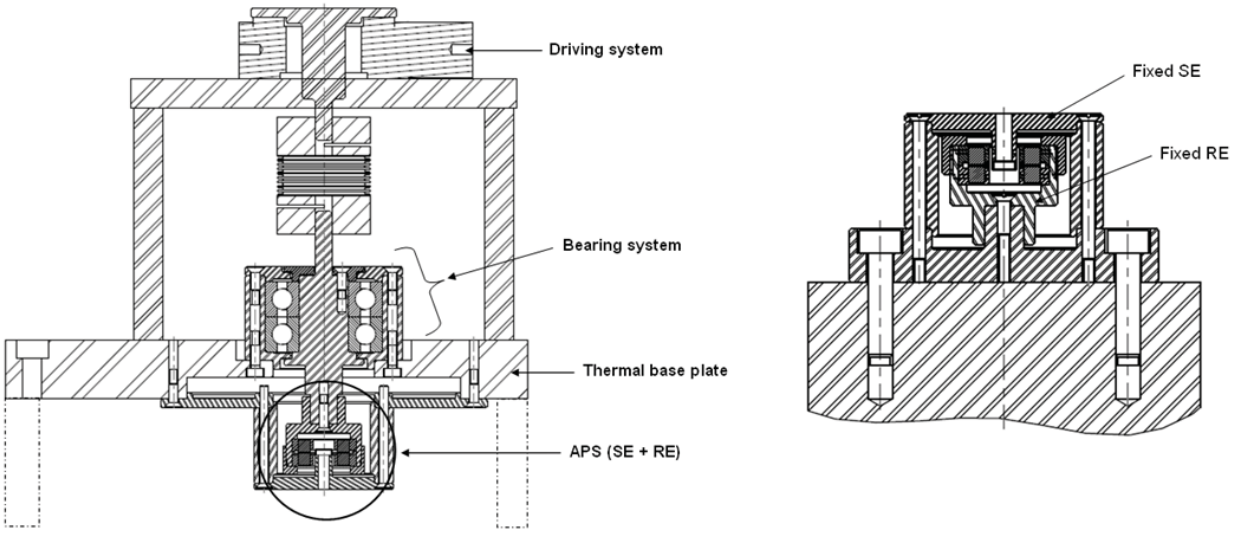

Figure 13. Left: APS functional and TV test setup. Right: APS setup for vibration, shock and radiation tests.

The technology qualification tests start at the reception of the Multiple Process Wafer run (MPW) with the plan detail thereafter. Standards procedure related to the test are also listed.

Packaging of the chip and package tests

- Visual inspection [ECSS 20500]
- Bond strength [MIL-STD-883]
- Die shear [MIL-STD-883]
- Encapsulation
- Dimension check: The outline dimension and envelope of both rotating element and sensing element are inspected according to the interface drawing.
- Weight: The weight of the unit, including the flying leads shall be less than 100g according to the sensor specifications.

Performance functional tests

- Range: The unit should be able to rotate without any limitation. 2 complete rotations are performed in both directions.
- Absolute measurement: The objective of this test is to verify that the sensor is not only an incremental sensor and that the angular position of the magnetic field can be recovered even after a shut-down of the power-supply.
- Accuracy: Following the sensor specification, the accuracy of the APS should be closed to 0.05°. The noise level gives a good representation of the minimum accuracy that can be reached by the sensor. However, this noise level depends on the electronic placed back along the sensor, in particular the RC filter used to convert the PWM output into an analog signal. The bit accuracy of the digital signal is most appropriate illustrate the real accuracy of the sensor. The noise of the analog output is also monitored for comparison. An angular accuracy of 0.05° corresponds to an analog voltage noise of Vcc/7200, i.e. less than 460 μV. This corresponds to a digital output on 13 bits, i.e. three bits of noise on the 16 bits channel.

- Resolution: The minimum incremental motion of the driving stage used to rotate the functional setup is defined to 0.004°. With such a resolution, the resolution of the APS can be investigated.
- Repeatability
- Drift parameters: Leakage current at several level of the chip layout, bandgap voltage are some of the drift parameters which can be influenced by radiation, EMC and temperature range and which are monitored.

The objective of the functional tests is to verify the specifications under environmental constrains describes in the next sections. These functional tests are repeated at reception of the chip, after the radiation test, after the vibration and shock campaign, after the EMC test and after the lifetime test.

Radiation test

The test is performed at the Proton Irradiation Facility of the Paul Scherrer Institute (PSI) in Villigen (Switzerland). Total Dose Irradiation (TID according to ESCC 22900) test and Single Event Effect (SEE according to ESCC 25100) test is performed. During the test, the sensing element is protected by a minimum of 4 mm Aluminum inner wall (sketch on Figure 13) that allows estimating the total dose for a worst-case 15-year radiation lifetime of a geo-stationary telecom satellite. The parameters of the radiation tests are the following:

- Proton Energies6 MeV
- Total dose: 300 krads
- Maximum flux: 100 rad/h

During the irradiation, the sensing element is facing a static permanent magnet, which allows for the monitoring of drift parameters of the sensor such as the leakage current that is monitored at several level of the block diagram or several parity bits that allow for the SEE detection. The output of this radiation test validates the hardening of the design that is implemented in the second chip layout.

Vibration and shock tests

The test sequence comports Sine vibration test, random vibration test and shock test. These tests are performed on the three axes of the sensor. The vibration tests are made at room temperature, in air and the unit is neither powered nor rotating. The APS setup (including the dummy shaft) is mounted on a dedicated test support fixed on the shaker for the vibration tests (Figure 13). The setup is first tested without the APS in order to identify frequencies related to the tooling itself. Vibration and shock loads are summarized in Table 3:

Table 3. Vibration and shock loads

Vibration	Test Axis	Input Frequency (Hz)	Amplitude	Duration
A) Sine Vibration	All 3 axis	20 – 50	25 mm peak (or max shaker limit)	2 oct/min +/- 10% (minimum duration 2 min)
		50 – 100	20 g	2 oct/min +/- 10% (minimum duration 2 min)
Sine vibration sweep rate:		2 octaves/minute (+/- 10%)		
Sine vibration duration:		2 minutes/axis (minimum) (+/- 10%)		
B) Random Vibration	All 3 axis	20 –100	+5 dB/oct	150 seconds
		100 – 500	0.5 g^2/Hz	150 seconds
		500 - 2000	-5 dB/oct	150 seconds
		Overall level :	20 g_{rms}	
Random vibration duration:		2.5 minutes/axis (+/- 10%)		
C) Shock	All 3 axis	500	100 g	-
		5000	1500 g	-
		10000	1500 g	-

Thermal vacuum test

The APS is installed in a thermal vacuum chamber with its rotation axis vertically mounted. The sensing element and its packaging is fixed on a thermal base plate inside the chamber in order to control the temperature of the APS mounting flange by conduction. The anodized support acts as a frame surrounding the APS in order to promote radiative exchanges. The APS is thermally cycled in vacuum (< 10^{-5} Pa) according to Figure 14.

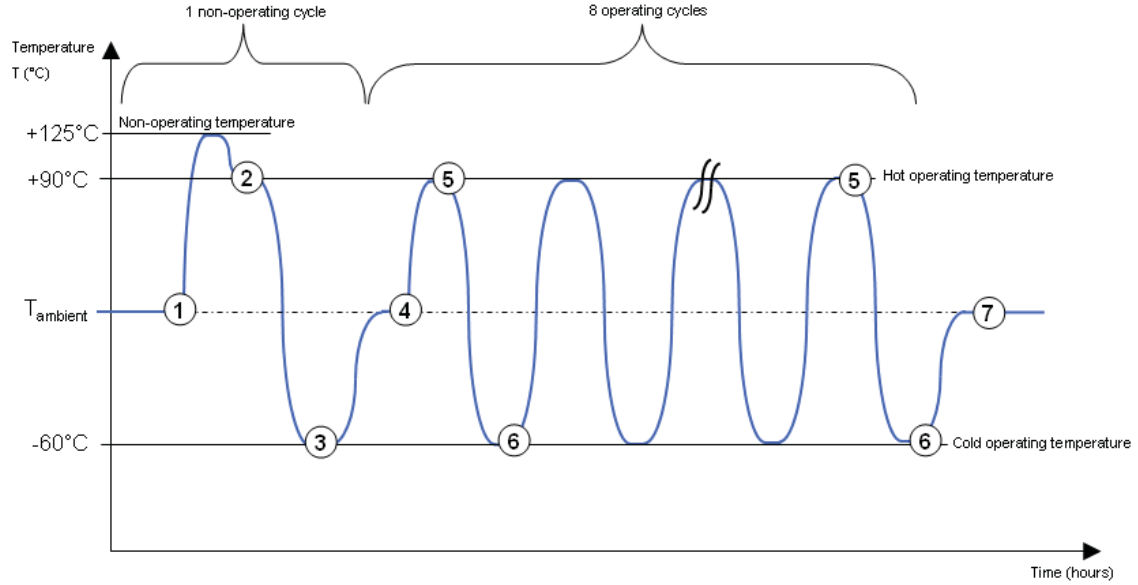

Figure 14. Thermal cycles performed on the APS.

The following operations occur during the thermal vacuum test:

- ① Thermal balance and non-operating cycle.
- ② Hot non-operational performance functional test.
- ③ Cold non-operational performance functional test.
- ④ Performance functional test at ambient temperature. Power switch on.
- ⑤ Hot operational performance functional tests (at 1 and 8th operating cycle)
- ⑥ Cold operational performance functional tests (at 1 and 8th operating cycle)
- ⑦ Performance functional test at ambient temperature. Power and rotation switched off.

The following parameters are monitored continuously during the operating cycles of the APS:

- Temperature of the various thermal probes
- Digital Output
- Analog Output
- Bandgap Voltage
- Driving torque (drag torque of the APS)
- Pressure

EMC test

Electromagnetic compatibility is the ability of electrical equipment to work satisfactorily in its electromagnetic environment without affecting this environment in an inadmissible way. The electromagnetic compatibility of the APS is verified by means of tests performed at frequency range between 10 kHz and 18 GHz in an anechoic room. The tests consist in the measurement of the radiated and the conducted disturbance immunity of the sensor (susceptibility) and to its emissivity in accordance with standard ECSS-E-10-03A.

Lifetime test

The APS sensor is thermally cycled in vacuum (< 10^{-5} mbar) between cold and hot operating temperatures (-60°C/+90°C). As the sensor includes micro-electronic parts, the number of thermal cycles (100) is adapted to such electronics systems.

Chip qualification campaign

In parallel of the previous TRP activity, a complete qualification of the chip itself, in accordance with space standards for the qualification of monolithic chip, is undertaken. Tests foreseen in this chip qualification activity can be divided in three steps:

- The production control tests which occur at the manufacturer level
- The screening tests
- The qualification tests

Production control tests

The wafer lot acceptance tests occur at the manufacturer level: The manufacturing of the wafers is monitor and PVM data are recorded during the whole process. The final lot is inspected through scanning electron microscope.

Then, in-process controls occur at the packaging level: After a pre-encapsulation visual inspection, bond strength and die shear tests are implemented. After the chip encapsulation, a dimension check of each packaged chip is performed.

Screening tests

These tests are performed on all the components. Screening tests consist mainly to reject faulty chips though hard electrical and temperature testing. During those tests, the drift parameters of the chip are monitored and compare to failure criteria. The following tests are foreseen:

- The serialized chips are subjected to a high temperature stabilisation bake (24h at 150°C) to determine the effect of storage at elevated temperatures without electrical stress applied. Drift parameters are monitored and control during the entire test.
- The chips are then be subjected to several burn-in tests at 125°C (reverse bias and power burn-in) in order to eliminating marginal devices, those with inherent defects which cause time and stress dependent failures. Drift parameters are monitored and control during the entire test.
- A measure of the drift parameters at ambient temperature is then foreseen and allow for the lot qualification.
- Before a final visual inspection of each chip, test of the quality of the package sealing are foreseen as well as evaluation of the ability of the terminations of the package for solderability.

Qualification tests

The parameters of these tests are the same as presented in the technology qualification campaign. These tests are performed on a minimum of 45 chips. 3 subgroups are constituted and follow respectively:

- Mechanical tests (15 chips): Vibration, shock, constant acceleration and seal tests followed by a visual inspection are foreseen in this subgroup. Drift parameters are measured along the tests.
- Environmental tests (15 chips): Thermal shock, moisture resistance and seal tests followed by a visual inspection are foreseen in this subgroup. Drift parameters are measured along the tests.
- Endurance tests (15 chips): Lifetime and seal tests followed by a visual inspection are foreseen in this subgroup. Drift parameters are measured along the tests.

Conclusion

The absolute angular position sensor presented here offers several advantages over common conventional potentiometer for space applications; based on a contactless technology, it offers a high reliability for long-term lifetime missions. Combining a Hall ring sensitive structure and control electronics with modern CMOS technologies, it gives the possibility to manufacture miniature accurate sensors. With this technique, the angular position can be obtained by a simple phase detection method, increasing the reliability of the whole system for harsh space environments.

The device has already been tested in ambient condition [8] and the results fulfill the expected performance of the sensor gathered in Table 4. The technology qualification of the sensor has just started and will be followed by the qualification of the chip itself. The reliability against vibration and shock loads is not considered as an issue for a sensor with such dimensions. Thanks to both radiation tests, one within the TRP activity before the other during the chip qualification campaign. The reliability of the chip against radiations (TID and SEE), allows for a progression margin and to a complete validation of the layout radiation hardness. Last point, but not least, is to verify the stability of the high accuracy of the sensor along the whole temperature range (define actually to -60°C to +90°C) and, with regards to the results, to propose an upgraded range of functional temperatures to increase the space applications panel covered by this contactless angular position sensor.

Table 4. Functional performances of the APS sensor

Specifications	Value
Operational lifetime	> 10.10^6 (theoretically ∞)
Orbit lifetime	> 15 years
Storage lifetime	5 years
Weight	< 100g (magnetic configuration depending)
Mechanical range	360° continuous
Measurement type	Absolute
Speed of rotation	< 1 RPM
Accuracy	≤ 0.05°
Resolution	< 0.01 °
Repeatability	< 0.01 °
Stability	< 1 ppm/°C

References

1. "Angular Position Sensor based on MEMS Technology", ESTEC/Contract No. 20404/06/NL/CP.
2. http://lmis3.epfl.ch/
3. Law L. "Angular Position Sensing with 2-axis Hall ICs", *Sensors* (http://www.sensorsmag.com), March 2003.
4. Volder J. E. "The CORDIC Trigonometric Computing Technique", IRE transactions on ElectronicComputers, vol. EC-8, no. 3, 1959, 330-334.
5. Popovic R. S. "Hall Sensor and Method of Operating a Hall Sensor", Patent number EP1679524 A1, 12.07.2006.
6. Popovic R. S. "*Hall Effect Devices*", Adam Hilger (IOP – Institute of Physics Publishing), 2nd edition, 2004, pp. 261-264.
7. Raich H. "*Design and Construction of a Dipolar Halbach Array with a Homogeneous Field from Identical Bar Magnets: NMR Mandhalas*", Concepts in Magnetic Resonance Part B (Magnetic Resonance Engineering), Vol. 23B, 2004, pp. 16-25.
8. Reymond S., "True 2D CMOS integrated Hall sensor", IEEE sensors 2007.

Electrically Powered Separation Nuts

Barney Little*

Abstract

Traditionally, over the past 50 years, space mechanisms have been powered by pyrotechniques (pyro). Pyro-powered mechanisms provide the greatest power-to-weight ratio of all types of mechanisms. Hi-Shear Technology Corporation, a major supplier of pyro-powered devices, has developed two new electrically powered separation devices, a separation nut and a cable release device.

Advantages of Electrically Powered Separation Devices
Hi-Shear's electrically powered separation devices have advantages over pyro-powered devices, some of which are:

1.) Resettable
Hi-Shear's electrically powered separation devices are resettable for up 25 times (tested 50 times) with out disassembly or refurbishment.

2.) No Pyro
Hi-Shear's electrically powered separation devices have no pyro, which provides the following advantages:
- No special explosive handling or storage.
- No stray voltage or bridgewire resistance tests required.
- May be installed at any time on the vehicle assembly line.
- No special access covers required for electrical tests.
- No pyro shock.

3.) No Out-gassing
Hi-Shear's design does not depend on elastromeric seals to prevent liquid or gaseous emissions.

4.) Ultra-Low Shock
Hi-Shear's electrically powered separation nut produces only 1% of the shock energy of a pyro separation nut. The release of bolt preload, which is the greatest contributor to shock, is slowly performed through a helix. Pyro shock has been eliminated since there is no pyro.

5.) Easy Usable Power
Hi-Shear's electrically powered separation nut uses only 15 watts at 28 VDC of power and does not require special firing circuits.

The Hi-Shear electrically powered separation devices provide reliable separation systems using mature release technology.

Introduction

Hi-Shear has been designing and producing separation nuts since 1964. All of these separation nuts use the same basic bolt release system. Figure 1 shows the functioning of the basic bolt release system.

Figure 1a shows the bolt release system in the pre-actuation condition. Three or four threaded segments are held radially together by a load ring or collar. The segments are seated on a base keyseat that prevents the segments from rotating during bolt torquing. The seating plane between the segments and the base keyseat is at a slight angle to provide outward radial loading during bolt loading and post

* Hi-Shear Technology Corporation, Torrance, CA

actuation. An extractor provides force to help extract the bolt and hold the segments in a release position after actuation. The bolt is torqued to a preload value that provides an outward radial load on the segments that are restricted by the load ring or collar.

Figure 1b shows the bolt release system during actuation. The load ring or collar is moved up by gas pressure or spring. The threaded segments that are no longer restricted by the load ring or collar move out, releasing the bolt. The bolt is extracted by a combination of force from the extractor and the preload. With some applications, an external spring loaded extractor may be required for a positive complete extraction.

This basic bolt release system, used in all of Hi-Shear's separation nuts, provides a forty-year pedigree to the new electrically powered devices.

Shock Produced by Separation Nuts

The shock produced by Hi-Shear separation nuts is due to several different factors. Not all of these factors are present in all designs.

Pyro Shock
Pyro shock is produced by the rapid burning of the pyrotechnic in the initiator with its associated rapid pressure increase. In pyro actuated separation nuts, pyro shock provides approximately 10 percent of the shock output. In electrically powered separation nuts, there are no initiators and therefore, no pyro shock.

Bolt Strain Energy Release
This shock is produced by the rapid release of the preloaded bolt strain. In the standard pyro-actuated separation nut, this shock accounts for approximately 60 percent of the shock output. This shock is greatly reduced in Hi-Shear's Ultra Low Shock Pyro and Electrically Powered separation nuts by the slow release of the strain energy.

Mechanical Impact
Mechanical impact shock is produced by the collision of parts in the nut during actuation. This shock accounts for approximately 30 percent of the shock output in standard pyro-actuated separation nuts. The electrically powered nut's release is slow, therefore low impact collision of internal parts.

Figure 2 shows the shock output of the electrically powered separation nut. The electrically powered separation nut shock energy output is only 1% of the standard pyro-actuated nut.

Hi-Shear's Electrically Powered Separation Nut

The electrically powered separation nut in the fastened position without the bolt torqued is shown in Figure 3. The reset tool is used only at the time of installation and is removed after the bolt is torqued to the preload value. The leads come from the release motor that requires 28 VDC at 15 watts to actuate the nut. The installation tool is temporarily holding the spring-loaded locking ring in place. *W*hen the bolt is torqued, the radial force on segments holds the locking ring in place and then the installation tool is removed.

Figures 4 and 5 show the cam release assembly. In the locked position, the cam ring is forcing the rollers through the slots in the outer helical ramp into the pockets in the inner helical ramp. When the cam ring is allowed to rotate counter clockwise by the motor, the radial force on the rollers rotates the cam ring, releasing the rollers from the pockets in the inner helical ramp. This allows the inner helical ramp to screw down in the outer helical ramp, releasing the strain load on the bolt as shown in Figure 6. With the bolt load released, the radial force on the segments is removed and the wave spring lifts the locking ring off of the segments. The segments are driven outward, releasing the bolt. A bolt extractor is required to reliably separate the bolt from the nut.

Lessons Learned

The original separation nut design used a DC brush motor. The DC motor drove the cam ring through a worm gear drive. The motor drew a lot of power and took a long time to actuate the nut. The cam ring was modified to be driven by the nut preload and a simple catch is used to release the cam ring.

Conclusion

Non-pyro electrically actuated separation nuts provide the following advantages over pyro-actuated nuts:

- Resettable
- No LAT required
- No out-gassing
- Ultra low shock
- No special explosive handling or storage

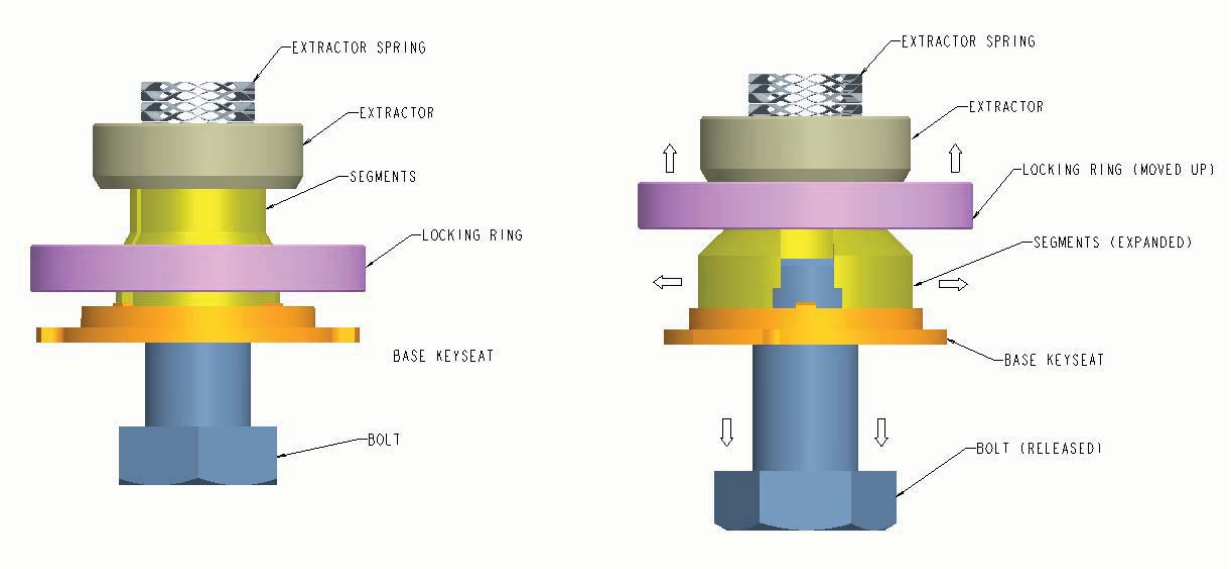

Figure 1a. Before Actuation **Figure 1b. After Actuation**

Figure 1. Hi-Shear's basic bolt release system

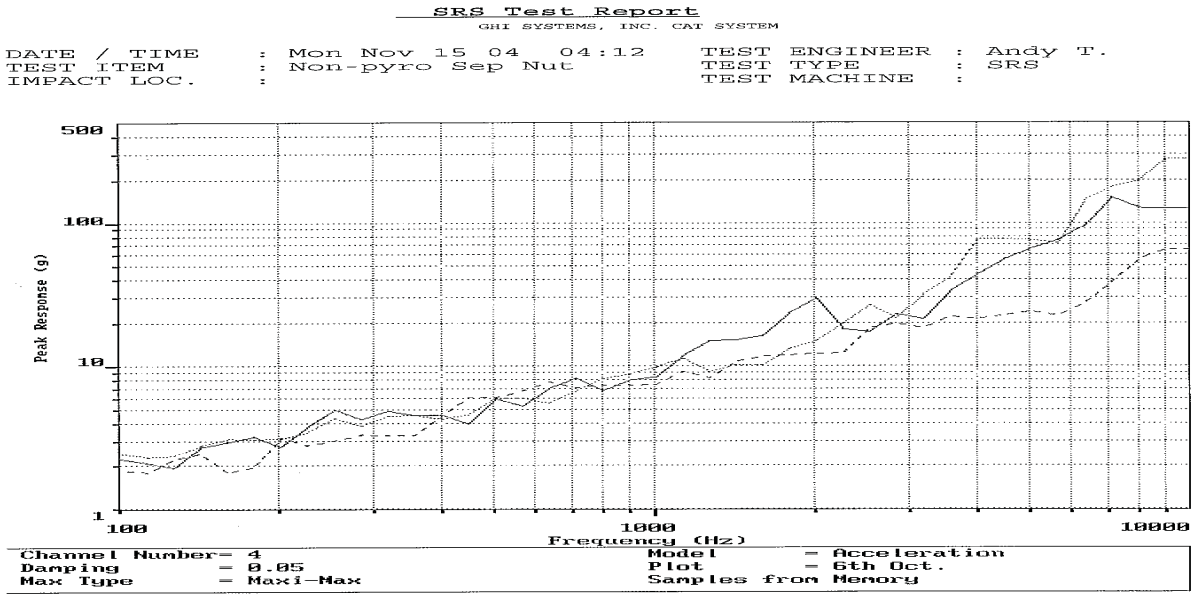

Figure 2. Bolt Release Shock Output

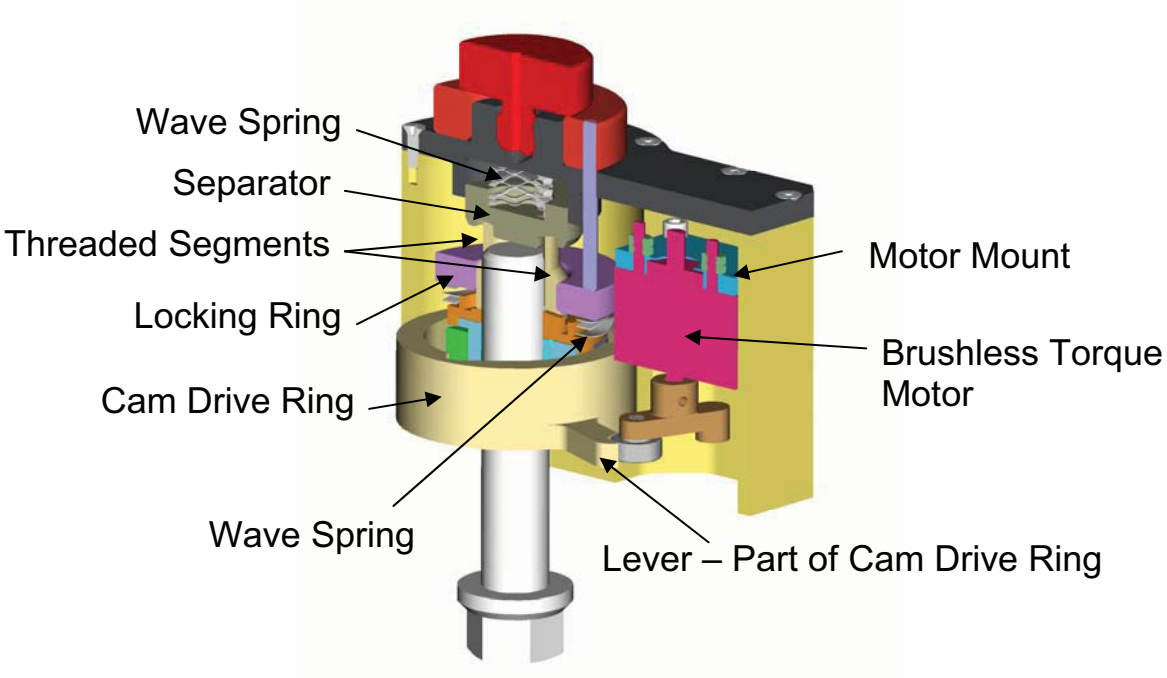

Figure 3. SN9700 Series Cross Sectional View "Fastened Position"

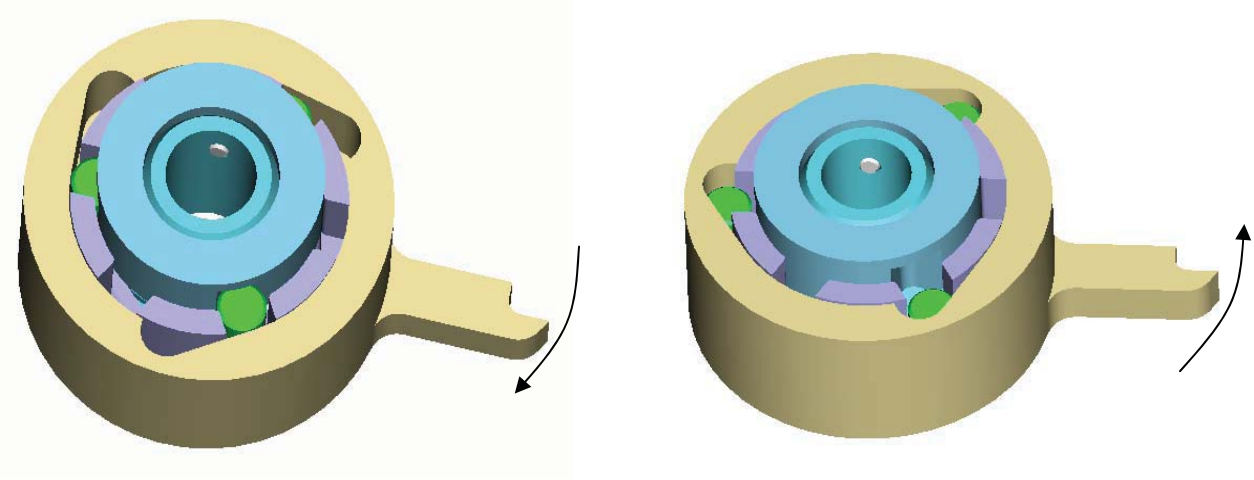

Figure 4. Cam Assembly Release Mechanism

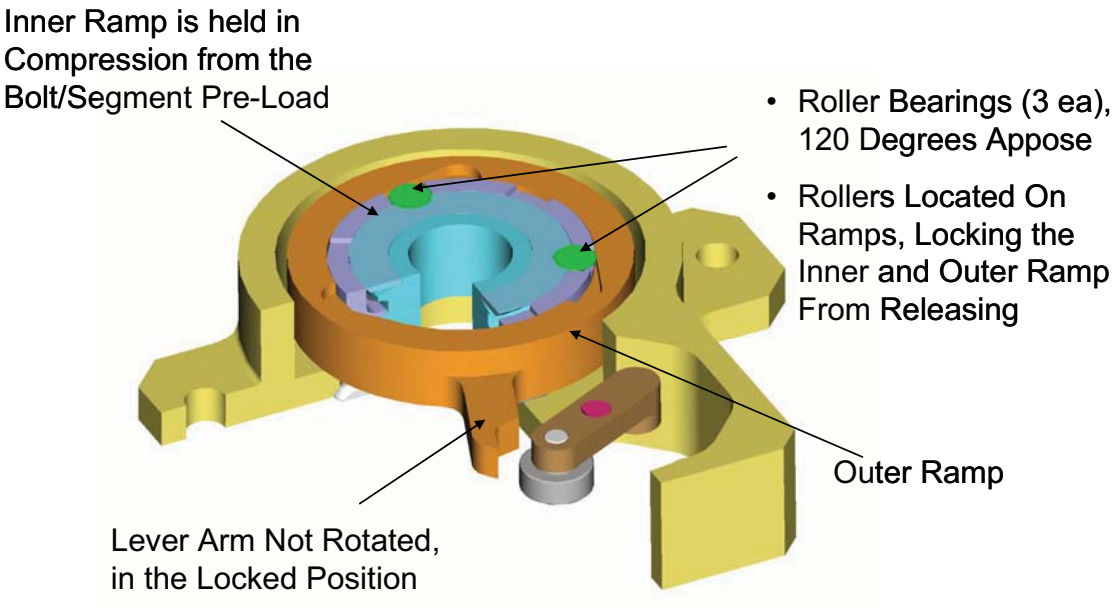

Figure 5. Cam Assembly in the Locked Position

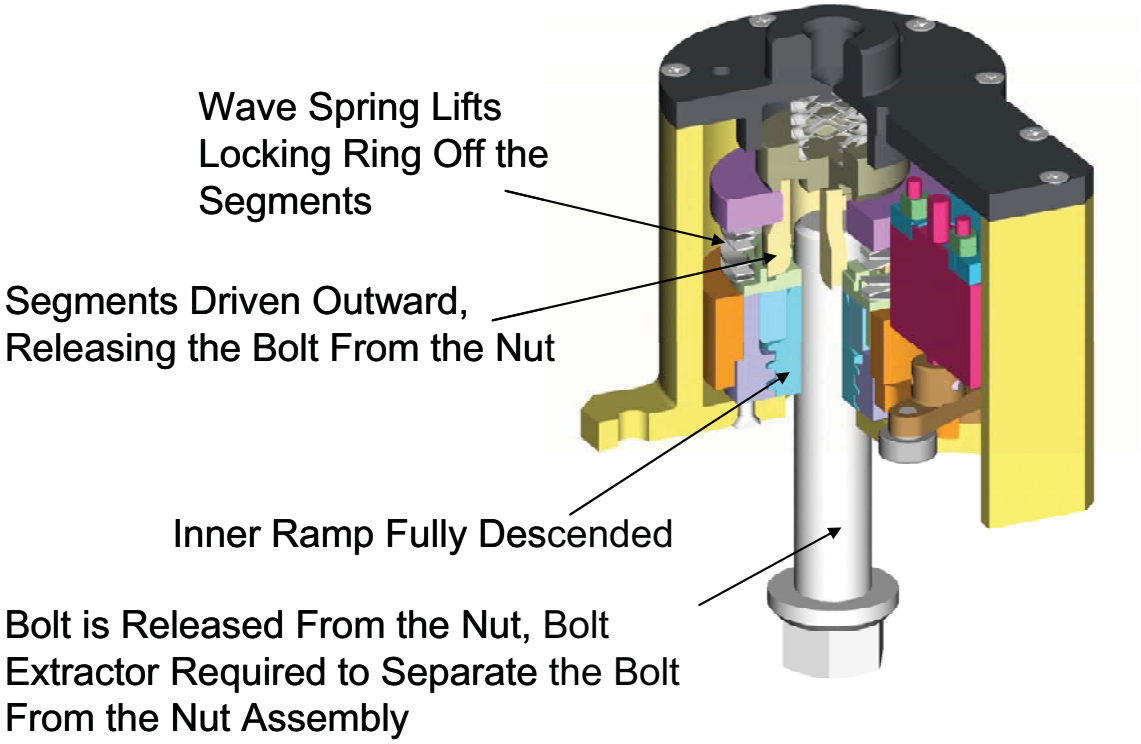

Figure 6. Cross Section SN9700 in the Actuated Position

A Radiation-Hardened, High-Resolution Optical Encoder for Use in Aerospace Applications

Pat Kreckie*

Abstract

Advances in aerospace applications have created a demand for the development of higher precision, higher accuracy, radiation-hardened encoders. Historically, encoder products have proved somewhat deficient due to precision, accuracy, weight, and alignment concerns. MicroE Systems' Mercury II aerospace encoder design provides the precision and accuracy required by these applications while also addressing radiation, weight, and alignment concerns. The encoder is a grating-based, reflective, interferometric encoder consisting of three major components: a scale, a readhead, and processing electronics. The system is a kit design that is easily configured and forgiving of misalignments. Its large tolerance of tilts and translations during setup and operation, make this design ideal for aerospace requirements. The system is small in footprint and weight and requires minimal power for operation. The ability to attach multiple readheads to one processing electronics unit, as well as its alignment tolerances, makes it versatile enough to meet the most demanding applications.

Background

An optical encoder is a device that uses optical sensing of some sort to determine the position of a surface with respect to the system's sensor head. Typical systems consist of a scale, a sensor head(s), and processing electronics (Figure 1). Encoder systems may be linear or rotary, reflective or transmissive, kit or packaged, incremental or absolute.

MicroE Systems' Mercury II encoders are grating-based interferometric encoders. Light from a source within the sensor head is incident on the scale. The scale attaches to the surface being monitored. The scale is a glass substrate containing a periodic grating structure. The incident light reflects and diffracts from the grating. The diffracted beam re-enters the sensor head and forms interference fringes on a detector array. The processing electronics calculate the interference fringe pattern's spatial phase from the detector array signals. Scale movement (surface movement) results in fringe pattern movement across the detector array. The processing electronics re-analyze the resulting fringe pattern and produce a system output corresponding to the surface's new position.

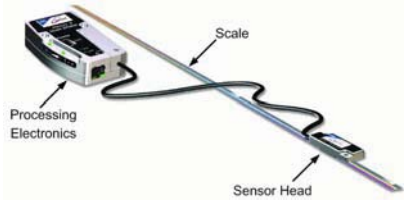

Figure 1. Encoder Components

* MicroE Systems, Natick, MA

Optical Design. The optical system (Figure 2) consists of multiple light sources, a window, a scale, and a detector. Single-mode vertical cavity surface emitting lasers (VCSEL) are the system's light sources. Each VCSEL emits 850nm diverging beams with excellent spatial and spectral coherence. In this design, four VCSELs are used – primary and redundant VCSELs for the Main signals and primary and redundant VCSELs for the Index signals. Although VCSEL lifetimes are excellent, the redundant set further improves the reliability of the system. VCSELs offer many advantages over other laser sources including excellent mode stability, low current draw, and very long lifetime. The vertical cavity design allows for emissions from the surface of the die, simplifying its mounting, eliminating the need for additional beam directing optics and facilitating an extremely small system footprint.

Scale Design – Main Track. The Main and Index VCSELs illuminate the Main Track and Index Track sections of the scale, respectively. Each VCSEL generates a diverging beam that passes through a window (not shown) and exits the sensor head.

The scale's Main Track section is an optical chrome-on-glass grating with a 20-µm period. The incident Main VCSEL beam reflects and diffracts into multiple overlapped beams from this scale region (Figure 3).

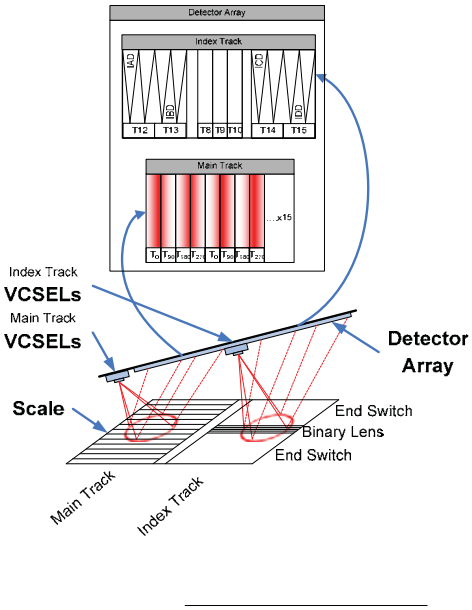

Figure 2. Optical System Layout

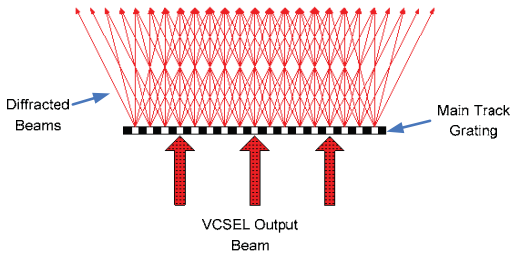

Figure 3. Main Track Diffracted Beams

These beams reenter the sensor and illuminate a four-channel Main Track detector array. Since multiple coherent beams overlap on the detector, interference fringes form on the Main Track array (Figure 2) according to the well-known Talbot effect. This effect, when illuminating with a point source, governs the shape, period and contrast of the fringes. [1]

Due to the grating's square-wave design with a duty cycle of roughly 50-50, the even diffracted orders are suppressed and the fifth and higher orders are relatively weak leaving the zero, first and third orders as dominant. The Gaussian distribution of the VCSEL beam further reduces the power of the higher orders at the detector; so the interference fringes formed at the detector are primarily generated by the interference of orders 0, 1 and 3. The detector is situated in a Talbot plane where the grating is "self imaged"; so, given the limited set of orders contributing to the interference, the fringes consist mainly of the fundamental with the third harmonic.

As the scale moves, the diffracted orders shift either up or down by various amounts depending on the order of each particular diffracted beam. This phase shifting causes the interference fringes to move across the array resulting in a modulated current from the detector. Given fringes that are well defined by the physics of the Talbot effect, the resulting signal modulation is predictable and controllable.

Scale Design – Index Track. The Index Track section of the scale contains three regions: two (2) end switches and a binary lens (Figure 2). The end switches are highly reflective regions used in the continuous automatic gain control of the VCSELs' output energies during operation. The binary lens region is the index mark for the system. The binary lens creates a focused line of light on the detector as the index VCSEL beam sweeps across this region. This index pulse defines the "home" position of the system. Because the binary lens is a physical reference on the scale, it is highly repeatable.

Detector Design – Main Track. The detector is a silicon photodiode with excellent response at the 850 nm wavelength of operation. The die has two separate arrays: one for sensing the main encoder position signals (Main Track) and one for detecting the index pulse (Index Track) (Figure 2). The main detector region is an interleaved array of 120 cells grouped together to generate four output signals T0, T90, T180 and T270. One optical fringe spans four of the cells, with each of those cells feeding one of the four output channels with a spatially phased modulated current.

There are 30 detector quads and 30 fringes across the length of the main array (Figure 2). The detector samples the sinusoidal optical fringe pattern every 90°: 0°, 90°, 180°, 270°. By grouping the photodiodes in an interleaved fashion, each signal is the averaged sum over 30 periods across the entire fringe pattern. These four signals are amplified and differenced to create the analog sine and cosine signals, which are subsequently digitized and interpolated.

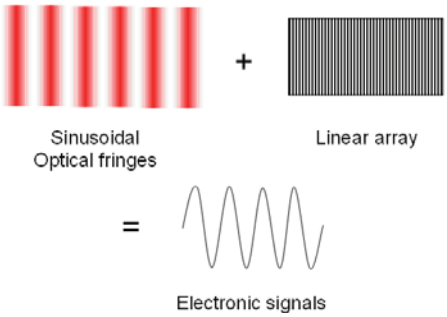

Unlike conventional encoders, small sensor-to-grating gap changes do not have a detrimental or unpredictable impact on the fringe quality. Therefore, the detector and electronics can be designed with foreknowledge of the fringe characteristics, and tuned for the very best response and filtering. In particular, the main detector array cells have been designed to filter out the third harmonic in the interference fringe pattern. These active cells are arranged in a zigzag pattern (Figure 4).

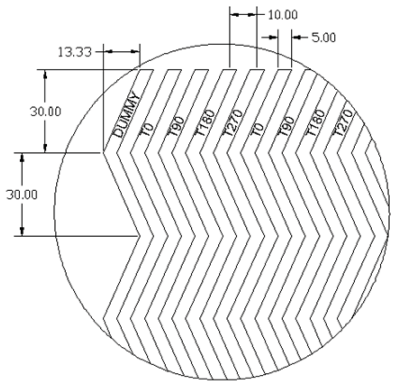

Figure 4. Main track array (dimensions in microns)

The zigzag shape causes the cells to cut across the fringes over a prescribed distance, washing out the third harmonic to generate high fidelity sinusoids, thereby ensuring very high encoder accuracy. With optical harmonic distortion minimized, only electrical offset, electrical gain mismatch, and electrical distortion remain as the primary sources of error.

Detector Design – Index Track. The detector's Index Track is separated into three (3) regions: two (2) end switches and one (1) index region (Figure 2).

As the Index VCSEL beam sweeps across the scale's end switch regions, the beam uniformly reflects onto the Index region of the detector. The detector's end switch regions sample the beam's energy and perform automatic gain adjustments to the detector's signal amplifiers and a current adjustment to the corresponding VCSEL.

As the Index VCSEL beam sweeps across the scale's binary lens, the resultant line of focused light is incident on the detector's index region. The index region consists of 3 cells arranged in a linear array. As the grating moves, the focused line of light sweeps across this three-cell array generating three analog pulses. Comparator circuitry generates a very robust *index window* (IW) digital pulse, roughly one main track cycle wide. The IW is subsequently gated with the interpolator output to yield a one-LSB wide index pulse.

Mechanical Design and Alignment Tolerances. The encoder system accommodates multiple angular and translational motions. Conventional encoders based on geometric optics typically require the alignment between the sensor head and the scale remain within very tight tolerances. In contrast, the interferometric approach employed in the aerospace encoder system permits both a large operating gap between sensor and scale and a very generous operational alignment envelope.

By using a diverging beam from a VCSEL light source, the encoder sensor head can tip and tilt with respect to the scale, while still directing sufficient energy to the grating that diffracts and reflects back to the sensing array in the head. The diffracted beams overlap throughout a large distance along the optical z-axis to form interference fringes that are sensed by the array anywhere within that region. Because the system does not have an intermediate optic between the scale and the detector, the optical fringes do not distort throughout the alignment tolerance range (Figure 5).

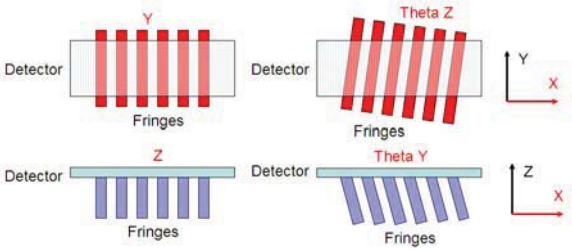

Figure 5. Sensed interference fringes

These key features differentiate the Aerospace Encoder from other options. The very forgiving initial alignment conditions and the large tolerance of tilts and translations along axes other than the measurement axis during encoder operation, make this design ideal for aerospace requirements. Table 1 outlines the alignment tolerances of the Aerospace Encoder. The values reported in the table are based on reduction in analog signal amplitude only and represent a conservative range.

Table 1. Alignment Tolerances

Axis	Mercury II Aerospace
Y	± 300 µm
Z	± 200 µm
Theta Z	± 2°

For ultimate stability through temperature, the sensor mounts with either screws or adhesive along the y-axis in line with the VCSEL and detector, thereby minimizing drifts due to thermal expansion.

Electrical Design. The electronics design is based upon the second generation of MicroE's Mercury incremental encoder. All of the analog signal processing is performed in a mixed mode ASIC, while the digital processing occurs in an FGPA. A/D converters provide the interface between the analog signals and the digital signal processing. The signal processing is ratiometric, making it insensitive to common mode changes, and the processing algorithms utilized are either not affected by single event upsets (SEU) or quickly recover from upsets without permanent change. For more information, see the Upset Effects section.

Analog Signal Processing. All analog signal processing is performed in a mixed mode ASIC. There are 4 signals generated from the multi-element, interleaved, main track photodetector array (0°, 90°, 180°, and 270°). Transimpedance amplifiers convert these currents to voltages. The 0° and 180° signals are subtracted and amplified to form differential, high-level sine signals while the 90° and 270° signals are subtracted and amplified to form differential, high-level cosine signals. The signals from one photodetector section combine with the corresponding signals in the other. The high signal to noise ratio obtainable in the design provides high-speed operation and still interpolates to 14 bits (1.22 nm). This high signal-to-noise ratio also allows for a low noise encoder.

The combined sine and cosine signals are applied to a dual, high speed, A/D converter, located in the sensor head. Three index signals generated from the detector array form the index window used to identify a home position. The Transimpedance amplifiers convert the index currents to voltages in the ASIC. These signals are processed to form two complementary, high-level signals, which, in turn are applied to the inputs of a comparator. The comparator output is the index window. Additional processing occurs during the digital signal processing.

The ASIC also contains the laser drivers. These are controllable current sources, with built-in over-current protection for the VCSELs and circuitry for selecting either the primary or the redundant VCSELs.

Digital Signal Processing—All digital signal processing is performed in the FPGA. The serial outputs from the two A/D converters in each sensor head are applied to the FPGA through RS-422 receivers. This FPGA applies gain, offset, and phase correction, interpolates the signals from each of the sensor heads to 14 bits (1.22 nm), counts fringes, defines the home position from the index window, formats the output signals and provides timing signals.

Cyclic Error—For gain, offset, and phase (GOP) correction, the system uses a patented GOP correction algorithm that iteratively reduces gain, offset, and phase errors by sensing the respective GOP errors and adding correction coefficients to the sine and cosine signals.

Once the correction factors are fully reduced, they are fixed so that the encoder position is repeatable, as shown in Figure 6 and Figure 7.

The Lissajous is a graphical depiction of sine versus cosine. Lissajous roundness is used to measure cyclic error along with encoder position verses reference. Note that a change in the vector length of the Lissajous does not result in a position change.

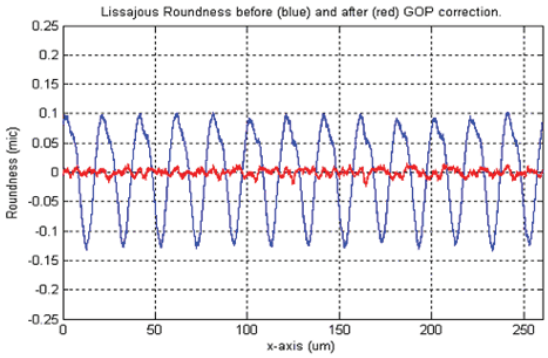

Figure 6. Typical MII Lissajous roundness cyclic error correction

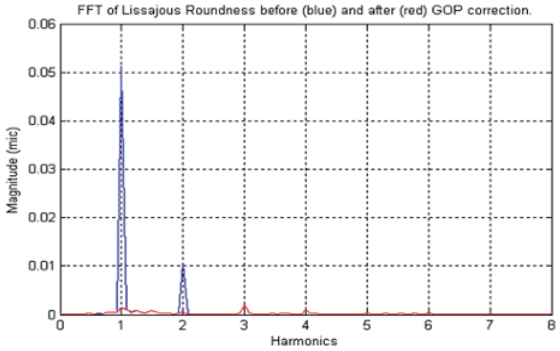

Figure 7. Typical MII Lissajous FTT cyclic error correction

A/D conversion and interpolation—To ensure proper fringe counting, the A/D conversion and interpolation rate is considerably high. The highly effective calibration/correction algorithm developed by MicroE provides extremely high accuracy (see the Accuracy Section below).

To take advantage of the algorithm at any time, enable the Calibration mode and pass over 40 fringes. The digital processing also provides an accessible troubleshooting mode. Parameters such as signal amplitude, laser current, and signal speed are exportable.

To maintain a constant input signal level to the A/D converters, an automatic gain control (AGC) loop varies the VCSEL current. This loop uses the vector magnitude of the main track as the control. If the required magnitude cannot be obtained (to within a predetermined percent of the target amplitude), the circuit will switch to the redundant VCSEL.

Operation of the index circuitry allows measurement of the index VCSEL power at all times except at the index. This measurement determines whether to select the back-up VCSEL. Due to the large operating signal range of the index circuitry, it is not necessary to use AGC. The fringe counting and index circuitry are robust (see the Fringe Counting section below).

Formatting the output signals is performed within the FPGA. A low voltage differential signal (LVDS) driver/receiver translates the input and output signals from the device. Internal timing synchronizes to a 68 MHz oscillator.

Upset Effects. As previously mentioned, the circuitry and algorithms in the design are either not effected by upsets or quickly recover from upsets with no permanent change. All digital circuitry uses integrated circuits fabricated using radiation-hard processing and all critical registers use triple redundant voting logic to eliminating SEU concerns. Thus, it is only necessary to consider the following three effects on the analog signals: fringe interpolation, fringe counting, and index homing.

Fringe Interpolation. MicroE utilizes an interpolation method that is absolute in nature. It is essentially an arctan method of interpolation. Therefore, if the sine or cosine signal is disturbed, the interpolated value will become incorrect (as it will for any encoder, incremental or absolute), but will recover with the correct position word by the next interrogation as long as the encoder has not moved beyond one optical fringe; i.e., one analog signal cycle.

Fringe Counting. The algorithm utilized for fringe counting only allows the count to change when the sine transitions from the fourth to first quadrant (increase count) or the first to fourth quadrant (decrease count) and ignores the all other quadrant changes. In order to miss a count, the disturbance would have to be larger than the peak amplitude of the normal signal, effectively eliminating one of the quadrants. Radiation analysis indicates that the amplitude of the upset signals is more than an order of magnitude lower than this.

Index Homing. The index circuit uses the index window to determine which fringe is *home*. The algorithm that determines this *home* position requires that the index window be a minimum of one-half fringe wide. Under normal rate conditions, this is a minimum of 100 µs. Since any upset signal will decay with a time constant of 1.7 µs (due to the system bandwidth), it is not possible for an upset to be present for 100 µs.

Accuracy. The Aerospace sensor has several improvements over older encoder models. In particular, the detector is larger for better averaging and robustness and the array pattern modified for better signal filtering as mentioned earlier; these all contribute to enhance intrafringe accuracy.

Note the Aerospace Encoder's enhanced harmonic suppression and the low error of 18-nm peak—a dramatic reduction of approximately 4x down from the typical 70 – 80 nm peak error of previous models. In addition to these short-range accuracy improvements, the Aerospace Encoder's long-range (interfringe) accuracy improved due to the larger sampling area and a shorter optical path length between the grating and the sensor head.

Radiation—MicroE uses radiation-hardened integrated circuits for the encoder electronics. Due to the inherent radiation hardness of GaAs, radiation environments do not present a problem for the VCSELs in the encoder. Data shows that the primary effect of high dose radiation on VCSELs is a moderate reduction in output power. The encoder design accommodates these levels of changes. The VCSEL driver design utilizes AGC to maintain a constant output power further mitigating the effects of radiation.

Conclusions

The Mercury II Aerospace Encoder provides many advantages over standard encoders:

- Small, low-mass sensor with ultra low Z-height fits in compact motion systems
- Superior resolution and accuracy - resolutions up to 1.22nm (linear), 268M CPR (rotary); interpolation accuracy of ≤ 30 nm mean, std. dev. 4 nm (linear glass scales); up to ± 1 µm (linear glass scales up to 130-mm long)
- High-speed operation - up to 2.5m/s at 0.1-µm resolution
- Versatility - one sensor works, linear or rotary glass scales
- Broad sensor alignment tolerances, built-in red/yellow/green setup LEDs, and pushbutton setup make sensor, index and limit setup fast and eliminate ancillary setup instruments
- Large alignment tolerances
- Large range of thermal performance
- Proven solid history as reliable and dependable
- Robustness features include all differential digital outputs, all digital signals from the sensor, and double-shielded cabling for superior EMI/RFI immunity; scale contamination resistance insures encoder operation even with fingerprints, oil, dust and other forms of contamination

References

[1] Emil Wolf, Editor, Progress in Optics, Volume XXVII North Holland, Publisher, 1989

A Novel Grabbing/Latching Mechanism Without Moving Parts

Brian W. Gore* and Gary F. Hawkins*

Abstract

A preliminary design concept and prototype hardware have been developed for a grabbing/latching mechanism that uses no moving parts. The mechanism uses an innovative material named a Machine Augmented Composite (MAC), or MACterial, in a female configuration to accept a male bar or rod with almost imperceptible resistive force. However, when a reversing force is applied to disengage the bar/rod, it is virtually impossible to remove it due to the increasingly applied holding force. In other words, the higher the removal force applied, the higher the clamping force to resist it. The theory and physics behind this and other MACterial concepts are presented herein, as well as several potential applications that have been defined; surely there are many other applications only limited by one's imagination.

Introduction – or, How Does it Work?

A "machine" is defined in the Merriam-Webster dictionary as

> **Machine** *n*, An instrument (as a lever) designed to … modify the application of force, power, or energy.

The Aerospace Corporation's Dr. Gary Hawkins has developed a material dubbed a Machine Augmented Composite, or MACterial, which uses tiny machines, or flexures, embedded within a softer matrix material to give the composite unique properties. For example, when one applies a compressive force to a sample of MACterial, the sample deflects as if it is in shear. Conversely, if one applies a shear force, the material can either compress or elongate, depending on the direction of the shear force applied. Figure 1 illustrates a simple 4-bar linkage machine used in a typical MACterial and its resulting stress/strain response.

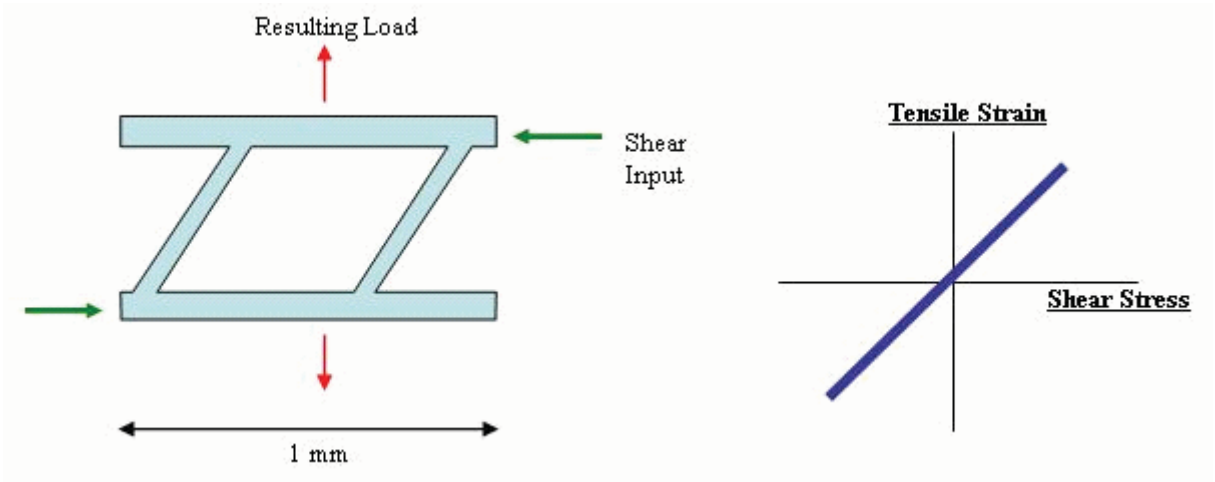

Figure 1. Example Of A Machine To Be Placed Into Composite Material

When a series of these machines, placed in a row or in a 2-dimensional array as in Figure 2, are embedded into a matrix material such as silicone, graphite epoxy, or any other suitable material (see Figure 3), the material takes on the properties of the machine when subjected to external loads.

* The Aerospace Corporation, El Segundo, CA

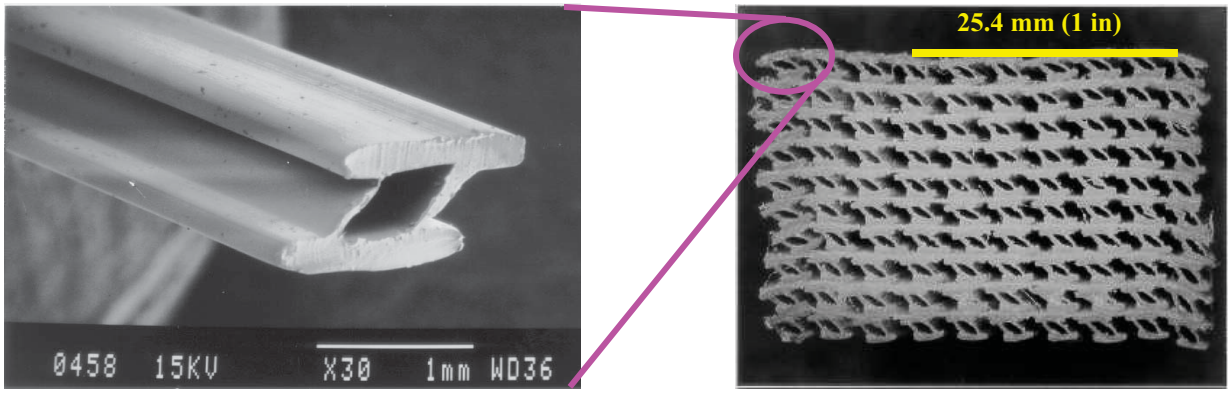

Figure 2. Extruded Nylon Simple Machine (Left); 100 Machines In 2-D Arrangement Before Matrix Infiltration

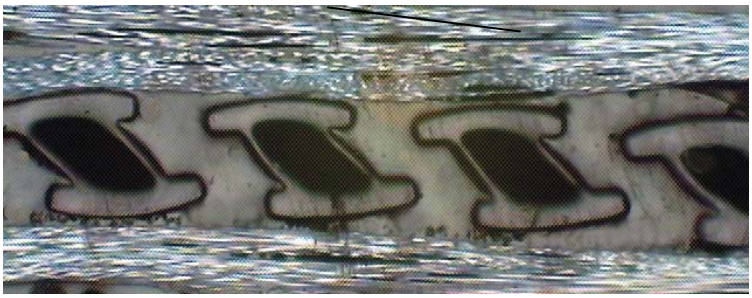

Figure 3. One Ply Of Machines Inside Matrix Material

With a bulk material made up of many little embedded machines, or even a material made up of a few number of larger ones, one can construct a combination of material and mechanism to accomplish interesting tasks. Figure 4 shows a simple example of a one-layer MAC and an engaged slider bar that can be measured for push-in or pull-out forces. In this example, pushing the slider bar to the left is considered the "easy" direction, and pulling it to the right is considered the "hard" direction, since that is the direction with the tendency of the MAC to grab or latch onto the slider bar, much like the common "Chinese finger puzzles" in which the harder one pulls, the more tightly the subject is constrained.

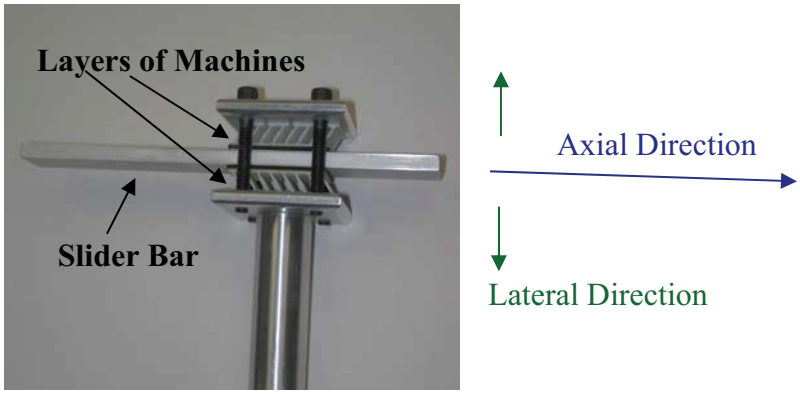

Figure 4. Grabbing Mechanism Prototype, With Slider Bar Engaged

Theory – or, Why Does It Work?

It is all about friction. The explanation starts with the classical friction equation,

$$f = \mu * N, \quad (1)$$

where f is the force required to break static friction and generate motion. A typical plot of this relationship is shown in Figure 5a, in which several values of μ are shown.

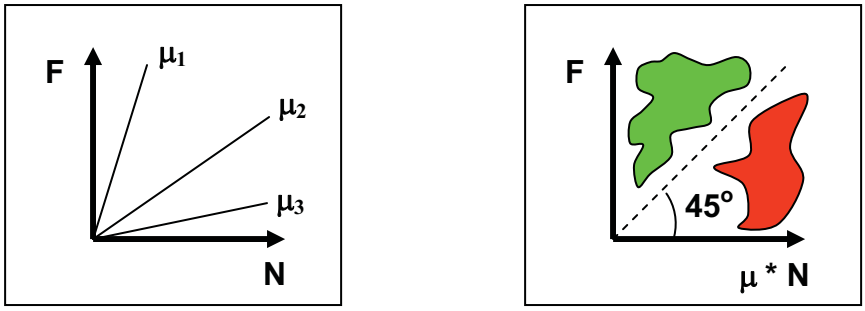

(a) (b)

Figure 5. Classical Friction Relationships

In Figure 5b, F is plotted against the quantity μ * N, so one can see that if F is above the dotted equality line (in the green zone), motion will occur, and vice-versa for the red zone below the equality line. Normally this relationship is true for the classical block-on-an-inclined-plane example, but this application, with the schematic shown in Figure 6, is a bit different.

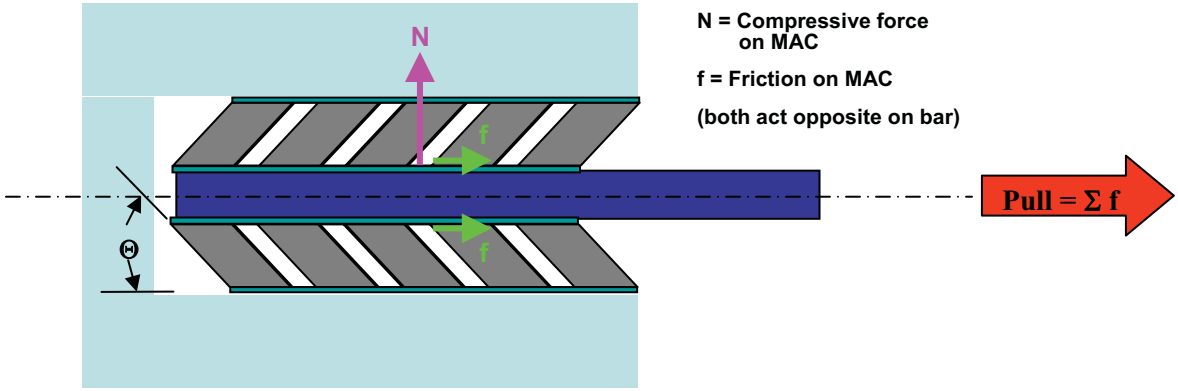

Figure 6. Schematic Of Grabbing Mechanism Prototype, With Slider Bar Engaged

We can also break down the schematic into a more simplified model of what is occurring, as illustrated in Figure 7.

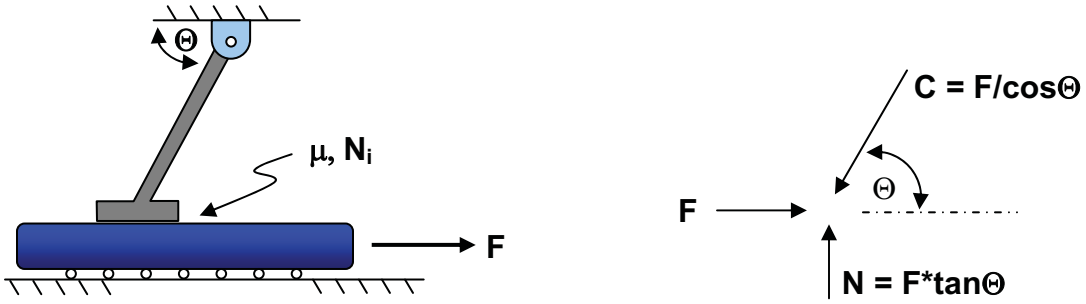

Figure 7. Force Model for Bar Retraction Case

Assuming there is a small compressive preload, N_i, between the gray MAC member(s) and the bar, and if one begins to pull the bar out of the device (to the right, as in Figure 6), friction between the bar and the MAC member creates a compressive force, C, in the MAC members which, in turn, increases the Normal force, N, between the MAC member and the bar. It is now clear that, unlike the classical example, N is a function of F such that

$$N = N_i + \{F * \tan(\Theta)\} \quad (2)$$

The next logical question is, under what conditions will the bar seize and not be able to be pulled out of the device as in Figure 6? By substituting Equation (2) into Equation (1) and rearranging terms, an expression for f, the required force to overcome friction in this system, can be determined.

$$f = \mu N_i / \{1 - \mu * \tan(\Theta)\} \quad (3)$$

One can see that for the classical example, or when $\Theta=0^o$, the denominator goes to 1 and the familiar equation, $f = \mu N$, exists. This is because there is no component to cause compression in the MAC member. Also interestingly, when $\Theta=90^o$, the denominator goes to $-\infty$, and thus f goes to zero. This is because the MAC members are at their bottom-dead-center position, and any movement of the bar will tend to bend, or raise, the MAC member up off of the bar with decreasing normal force. But for the seizing condition, the additional factor – compared to the classical equation – in Equation (3) plays a part. If this "Slide Factor," S, is defined as

$$S = 1 / \{1 - \mu * \tan(\Theta)\}, \quad (4)$$

then S can be plotted for various values of μ and Θ, as shown in Figure 8.

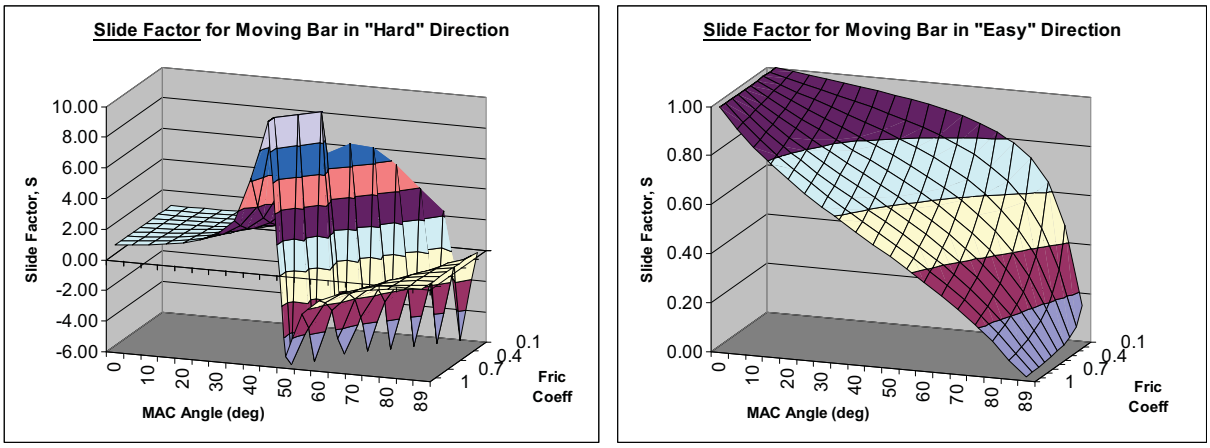

Figure 8. Threshold Values for Seizing for Various Friction and MAC Angle Values

This is a useful format to determine when the bar will be seized and when it will be free to slide. As long as S is positive, it means that a realistic value of f (force required to break free) DOES exist to give the bar the capability of breaking free from static friction; it does become more difficult as S approaches ∞. This describes the green region in Figure 5b. After the discontinuity, for higher values of μ and Θ, S values flip their sign and become negative. What this means is that the only way to break free is to apply a negative f, which means pushing it in the opposite direction.

For the opposite case of pushing the bar in the reverse, or "easy" direction, the same essential theory holds true, except Equation (2) contains a negative sign since the friction resulting from the applied force F tends to reduce the normal, or compressive, force between the MAC and the bar. That also flips the sign in Equation (3), and results in the S-values plotted on the right in Figure 8. By the same discussion above, since ALL of the S-values for reasonable MAC angles and friction coefficient are positive (and ≤ 1), it is proven that it is always easy (f is always $< \mu * N$) to push the bar into the device as in Figure 6.

Some Results – or, DOES it Work?

Several prototypes in various stages of this application were constructed in The Aerospace Corporation's Space Materials Laboratory (SML), and experiments were compared to theoretical analyses. The first study used laboratory instrumentation to compare the axial and transverse deflections of the small nylon machines with and without a matrix material surrounding them. Figure 9 illustrates that, much like traditional composites, the matrix material has very little effect on the behavior of the bulk material.

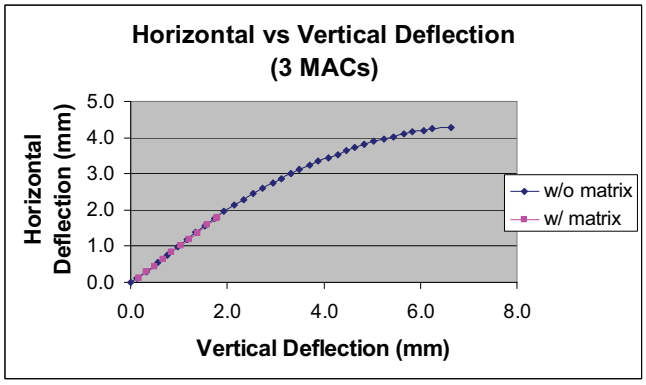

Figure 9. Matrix Material Has Little Effect On Bulk Behavior

The next investigative study compared similar results as above for different geometric configurations of the machines. Samples were constructed with 45-, 60-, and 75-degree machines in them, and the same horizontal-vs.-vertical deflection tests were run. It was shown, as in Figure 10, that the "grabbing" efficiency can easily be affected by the design of the machines. For both the 60- and 75-degree machines, there is more than a one-to-one effect between shear and axial displacement, indicating very desirable potential applications that can exploit this mechanical advantage.

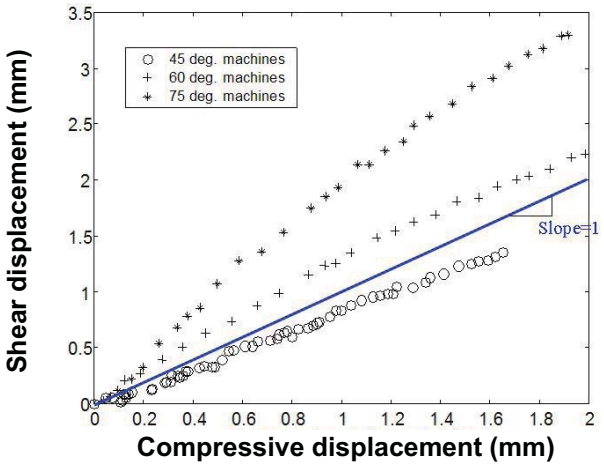

Figure 10. Geometric Effects Of Different Angled Machines

In addition, a similar laboratory experiment was constructed to measure the transfer of force from a compressive direction to a transverse direction, using MACterials. Figure 11 depicts the experimental setup, and Figure 12 displays the force relationship data. One can see that the force relationship in Figure 12 is very similar to the displacement relationship in Figure 10 for the same MAC design, with the 45-degree machines producing a relationship slope in both cases of slightly less than one.

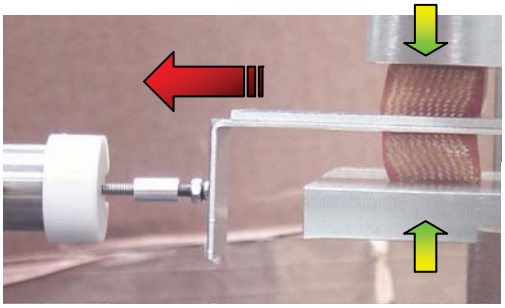

Figure 11. Measuring The Relationship Between Compressive And Shear Forces

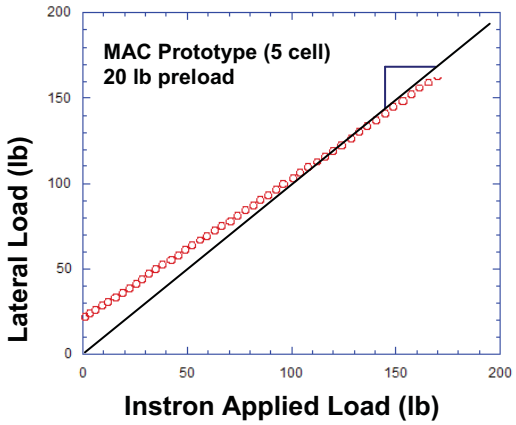

Figure 12. Effect Of Instron Applied Load On The Lateral Load Caused By MAC Movement

Next, getting back to the type of MAC device discussed in the theory section, Figure 13 shows axial and lateral force measurements that were made using this setup while sliding the bar in the "easy" and "hard" directions.

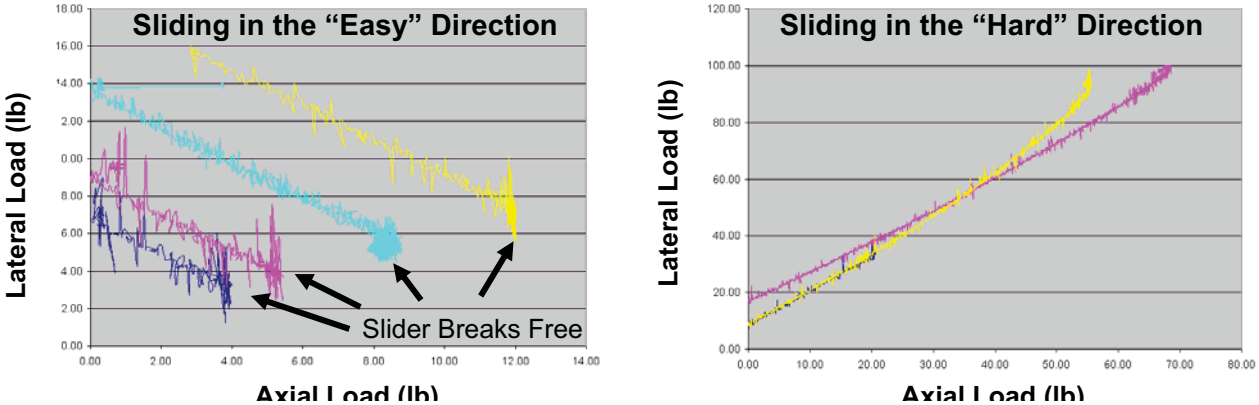

Figure 13. Experimental Data From Insertion/Retraction Test

When sliding in the easy direction, the data in the plots moves from the upper/left direction, where axial load applied to the bar is zero, and the finite values of lateral load are the initial compressive preload, N_i. As axial load is applied and increased, moving to the right, the lateral – or pinching – force gets reduced until the slider bar breaks free. Conversely, when sliding in the hard direction, the data starts out in the lower/left corner with no axial load applied, but with a finite lateral preload, N_i. As retraction force is increased the lateral, or pinching, load moves upward with an increasing slope as the resultant lateral load seizes it.

Data from these measurements can also be shown to be well correlated with ABAQUS finite element analyses, from which a sample finite element model (FEM) is shown in Figure 14.

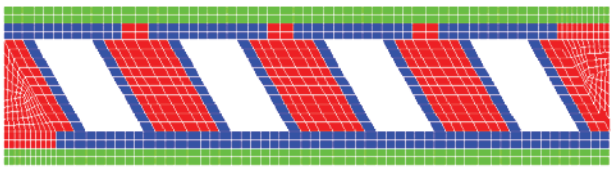

Figure 14. Sample Abaqus Finite Element Model

Using a FEM for a sample with a 60° MAC angle, Figure 15 shows one case of measured and experimental data, and how well they typically agree. Having a well-correlated FEM is very important and convenient so as to not have to make many different variations of hardware prototypes for testing.

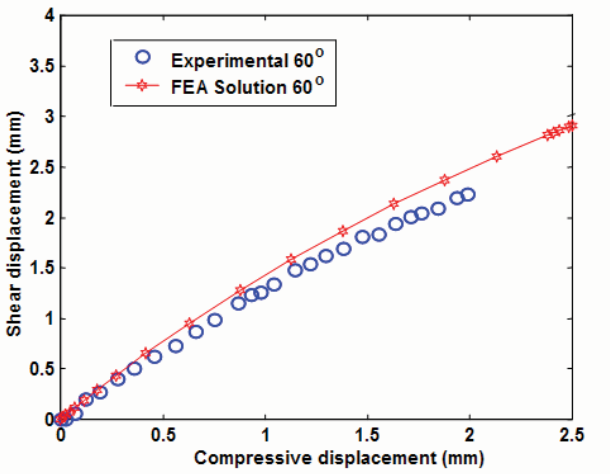

Figure 15. Correlation Between Analysis And Experiment For MAC Displacement

So far, this paper has discussed the static behavior of MACs, but there has also been a significant amount of effort expended to study the dynamic response of these MACterials. Specimens can be designed to drastically alter the behavior of impacting bodies, redirecting energy and stresses in ways that cannot be achieved with standard materials. For example, the use of a material that modifies forces may provide new methods for energy control in vehicles that can minimize impact damage to people or property. Also being explored is this material's potential use in ballistic applications, such as bulletproof vests and armor. For more information on the dynamic behavior of MACs, see Reference 2.

Conclusion – or, Can it Work FOR YOU?

Machine Augmented Composites have been developed in the Space Materials Laboratory (SML) at The Aerospace Corporation and have been shown to have the potential of achieving fascinating results. With the ability to change the direction of force, displacement, shock, or rotation, or act as a one-way retention mechanism without moving parts, MACs could provide unique and innovative solutions to a wide variety of problems. By presenting the work done by SML, perhaps it will resonate with one or more members of the space mechanisms community to solve a particular issue which has eluded a more conventional solution.

Alternatively, devices utilizing this concept, perhaps even in conjunction with current device technology could be newly developed and used by the industry. Being able to design from the start using MACs could lead to more efficient designs and better performance, with lower risk. An increased robustness as a result of a lack of moving parts, pyrotechnics, or other weaknesses in contemporary mechanical assemblies is a driving factor and a worthwhile goal.

There are varied space-related static applications that have been identified thus far for which this concept could be useful. Some examples include release devices, end-of-travel retention devices, electronic board clamps, or zero-insertion force electrical connector interfaces. Besides being useful for static applications, dynamic studies have also led to other investigations, both theoretical and practical, in widely varying areas such as hard-stop load re-distribution, shock attenuation, even sporting goods and body armor protection. Other space (or non-space) related applications are only limited to the engineer's imagination.

Acknowledgements – or, Who Did the Work?

The authors wish to acknowledge The Aerospace Corporation's Independent Research & Development Program, whose support made this development work, as well as its continued refinement, possible. Michael O'Brien and Tony Tang created the ABAQUS models and ran the drop tower tests, and Rafael Zaldivar, Juliet Schurr, Dhruv Patel, and James Yamasaki were instrumental in constructing the experiments, performing the laboratory measurements, and collecting data.

References

1. Hawkins, G. F., O'Brien, M. J., Tang, C.-Y., Von Bremen, H. F., Theoretical And Finite-Element Modeling Of The Z-Macs, Aerospace Technical Report ATR-2003(8810)-3, September 30, 2003.
2. Tang, C.-Y., O'Brien, M. J., Hawkins, G.F., "Embedding Simple Machines to Add Novel Dynamic Functions to Composites," Journal of Materials, March 2005.
3. Zaldivar, R. J., O'Brien, M. J., Schurr, J. N., Yamasaki, J. T., Hawkins, G. F., The Load-Load Characteristics Of Z-Shaped Machines, Aerospace Technical Report ATR-2003(8810)-2, September 10, 2003.
4. Zaldivar, R. J., Yamasaki, J. T., Schurr, J. N., Hawkins, G. F., The Fabrication And Mechanical Behavior Of Z-Shaped Machine-Augmented Composites, Aerospace Technical Report ATR-2002(8810)-1, March 5, 2002.

Docking System Mechanism Utilized on Orbital Express Program

Scott Christiansen* and Troy Nilson*

Abstract

Autonomous docking operations are a critical aspect of unmanned satellite servicing missions. Tender spacecraft must be able to approach the client spacecraft, maneuver into position, and then attach to facilitate the transfer of fuel, power, replacement parts, etc.

The philosophical approach to the docking system design is intimately linked to the overall servicing mission. The docking system functionality must be compatible with the maneuvering capabilities of both of the spacecraft involved. This paper describes significant features and functionality of the docking system that was eventually chosen for the Orbital Express (OE) mission. Key analysis efforts, which included extensive dynamic modeling, are also described. Zero-g simulation tests were performed to validate the dynamic analyses.

The docking system was flown and operated on the Orbital Express mission. The system performed as intended and has contributed to demonstrating the feasibility of autonomous docking and un-docking of independent spacecraft.

Introduction

Once on orbit, typical spacecraft have limited lives. The harsh environment and lack of access make any type of external support or maintenance nearly impossible. Anything from simply running out of fuel to failure of a significant component can end the life of an otherwise useful spacecraft. If some type of servicing capability were possible, flight operators could potentially get more out of their flight systems.

While limited servicing capability has been available through the Space Transportation System, or Shuttle, high cost has limited its use to very expensive systems within the Shuttle's orbital reach, notably the Hubble Space Telescope. Over the past decade there has been a push to develop the capability of autonomous servicing of orbiting spacecraft. The intent is to create autonomous, un-manned, tender spacecraft that might provide services such as spare propellant, or new or replacement parts to already orbiting client spacecraft.

Several practical needs can be met through autonomous servicing

- Extension of the life of spacecraft due to propellant replenishment
- Replacement of components that are obsolete or have failed
- Capture and move spacecraft to more effective orbit
- Recovery of a spacecraft with a failed deployment by assisting deployment
- Examination of a spacecraft to determine cause of failure

The company began working on a docking mechanism concept and prototype docking system on an Air Force Research Laboratory (AFRL) Small Business Innovative Research (SBIR) program in 1999. As the docking mechanism design matured, the Orbital Express program was developing requirements for docking hardware. These eventually converged and our docking system was chosen for the flight demonstration.

* SpaceDev, Louisville, Colorado

Docking Mechanism Evolution

Initial Prototype Docking Mechanism

Beginning in 1999, SRC undertook a design effort to develop autonomous soft docking. The project began with a Phase I SBIR grant from AFRL, who provided bounding conditions to the problem that included an estimated spacecraft size and mass (a cylinder, 50-cm OD x 130-cm L, 50 kg) and a requirement to dock two small microsat spacecraft and transfer fluid and/or electrical data between them. Yet, definition of the various needs that might arise when servicing obsolete or exhausted spacecraft had to be formulated. A key challenge became one of both establishing concept requirements as well as designing to address those requirements.

Evaluation of existing designs revealed a myriad of related technology. Most available technology related to extra-vehicular activity (EVA) interfaces, robotic boom end-effector configurations, or impact docking mechanisms. Much of this technology, by nature, required manned intervention. Most of these systems were primarily intended for large spacecraft and impact docking applications, and were not well suited for the more precise requirements of autonomous soft docking and alignment of fluid and electrical couplings. A critical component in identifying design requirements involved defining the eventual use and application of the intended mechanical docking system. Further research did not yield any definitive mission scenarios, but did present general ideas regarding potential applications. Two mission scenarios were conceived:

> Client (on-orbit spacecraft needing service) / microsat (spacecraft servicing the client): A microsat could be launched on an as-needed basis to directly service an orbiting client. This would provide very specific refurbishment based on the individual needs of the client. Response time would include arranging a specific launch for the re-supply microsat.
>
> Various client satellites and a microsat base station (both on-orbit): The client calls on the microsat base as needed. This could provide faster service, but would be limited to common, more generic types of refurbishment or repair.

In either of these scenarios, the tender would need to approach the client, match velocity and orientation, establish initial mechanical contact, pull together to rigidize, establish electrical contact, and finally, the pair must fly together as a single unit while docked.

Prototype Trade Studies

In parallel with organizing general mission requirements, the design team looked at many different methods of joining, grappling, and aligning. Four techniques that seemed reasonable with respect to a plausible flight control approach were traded in more detail:

1. “Harpoon”
2. A telescoping probe
3. Impact docking with a large conical guide
4. “Claw-type” linkages interfacing with a trefoil

The harpoon configuration, in which a probe is launched at a target, latches on, and is reeled back into guide features, seemed unpredictable and presented complications concerning the alignment of fluid and electrical couplings. A telescoping probe, where a telescoping pole extends to the mating spacecraft, engages a target feature, and retracts to join the two, turned into a complicated multi-mechanism apparatus not well suited for the direction and vision taking form. Impact docking was eliminated as an option because soft docking seemed safer for the two spacecraft and better suited to precisely align fluid and electrical couplings and prevent potential damage of components.

After extensive evaluation, SRC selected a three arm grapple design (Figure 1). The design would consist of two main subassemblies: an active mechanism and a passive structure. The active mechanism would consist of a motor driven lead screw that would actuate three individual linkages. The linkages would engage the passive structure, whose geometry would allow it to be constrained by the linkages. Further retraction of the linkages would seat the passive structure into a three point kinematic mount,

establishing a rigid interface. Release of the structure would be achieved by reversing these steps, with separation velocity provided by the spring loaded kinematic mounts. Construction on the prototype developed under the Phase I SBIR was completed in the early part of 2000. Figure 2 shows a picture of the completed design.

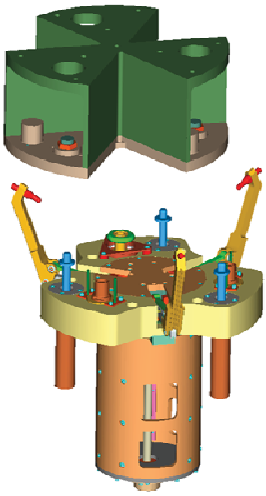

Figure 1: SRC grappling concept

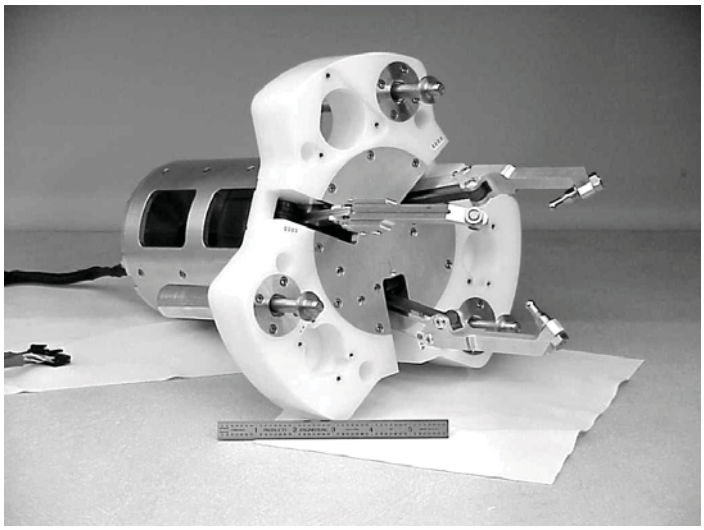

Figure 2: SRC prototype

Prototype Testing

Beginning in early 2000, SRC began extensive testing on the prototype hardware in order to evaluate its effectiveness and limitations. The test program included two significant components:

- In-house off-load testing: An off-load fixture was designed and manufactured to assist in understanding various dynamics of docking as well as to prove system ability to dock and transfer cryogenic fluids (LN2).
- Micro-gravity flight: A test plan was developed and executed to test the prototype in a micro-gravity environment.

Counter Balanced Off-load Testing

In order to gain a general understanding of the docking system dynamics, a test was constructed using a simulated inertia mass and cable/pulley system. Figure 3 shows the system with the prototype mounted in the lower left hand corner. The passive side was mounted to an adjustable tip/tilt fixture allowing tests to be performed in various misalignment configurations. Adjustment of the cable attachment point (universal joint) and offload weights provided an approximation of a zero-g environment. During development, more than 200 mechanical mate/de-mate cycles were successfully completed.

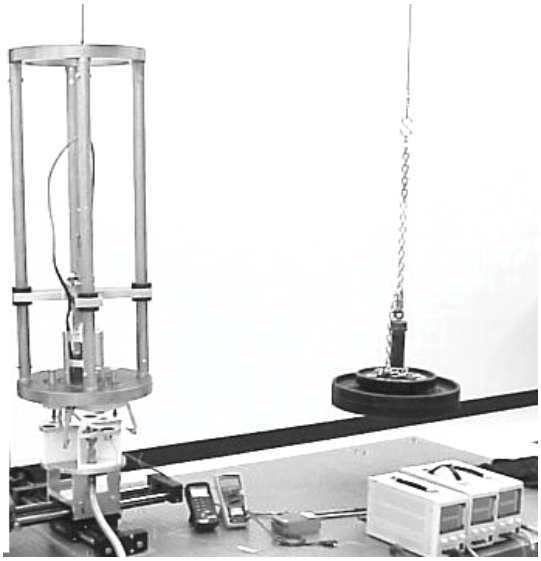

Figure 3: Off-load setup

Figure 4: Micro-g flight

Micro-gravity Testing

The second component of testing included a flight on NASA's modified KC-135 aircraft flown from Ellington Field near Johnson Spaceflight Center (JSC), Houston (Figure 4). The experiments focused on the grappling and capture events that could be accomplished within the 25-second micro-g window each parabola. The experiment was designed to have two separate, free-floating simulators that represent the relative mass and inertia of a client and a servicing satellite (approximately 2:1, client to servicing). The active and passive halves of the prototypes were each mounted to their respective mass/inertia simulator. With JSC crew assistance, the two halves were positioned within capture range. The active docking mechanism was immediately powered in an attempt to demonstrate "zero" gravity docking. Because of the limited time in micro-gravity, consecutive phases of the docking sequence were performed throughout a series of parabolas. Despite these limitations, the micro-gravity tests proved instrumental in demonstrating the mechanism behavior. The basic functionality of the docking system was demonstrated. Observations of dynamic behavior during the test led to improvements of the design prior to the next prototype build.

Development of 2nd Prototype and Orbital Express Flight Design

The OE program was intended to develop an industry-wide standard architecture to perform cost effective autonomous satellite servicing. To demonstrate the technology, OE planned to use two spacecraft: the client vehicle, referred to as NEXTSat, and the servicing vehicle, referred to as ASTRO. An illustration of the OE vehicles is shown in Figure 5. The demonstration mission launched both vehicles together and performed a series of mating and servicing operations on-orbit.

Orbital Express and the Phase II SBIR

A major criterion for autonomous docking success is the reliability of the capture system. SRC already had developed and tested a functional prototype, and the capture requirements were well suited to the SRC design. OE was still in the proposal stage and the design of the mechanical docking system (MDS) [this was the second generation prototype/engineering unit] was proceeding under AFRL funding. It therefore became necessary to balance the design objectives of OE within the practical limits of the SBIR scope. At the onset of the MDS design effort, SRC worked closely with Boeing, who was providing much of the initial insight into the technical requirements.

Figure 5: Orbital Express vehicles, conceptual drawings

Significant Changes from Initial Prototype

Mechanism Capture Capability

During the initial prototype design, a clear definition regarding the capture capability envelope did not exist. In light of the emerging requirements, the prototype capability was not sufficient to meet the requirements of the OE program. Therefore, the capture capability would need to increase in order to accommodate the precision of the guidance and navigation controls. The required capture capability would be achieved from scaling up the design, with minimum impact to the overall mechanism configuration. In short, the mechanism size and stroke were increased to create a much larger "capture zone".

Mechanism Structural Capacity

The initial prototype had also been developed for use with a microsat, and its structural capability was not suited for large vehicle payloads. Thought was given to refining the load paths in order to handle the increased strength and stiffness requirements. The drive train also needed to be enhanced in order to achieve the necessary mated interface stiffness. As a starting point, it was decided that the capacity would be designed to accommodate the largest operational vehicle payloads encompassed in the scope of the OE program.

Mechanical Docking System (MDS)

From a functional standpoint, the design that emerged looked very much like a scaled-up version of the original hardware. The design had nearly doubled with respect to the prototype. However, the design had not only grown in size, but had matured in complexity to accommodate its enhanced capabilities, both internally and externally. Figure 6 displays the second generation prototype hardware, officially designated MDS. The requirements that encompassed the design effort are displayed in Table 1.

MDS Testing

In-house Development Testing

SRC completed in-house testing of the MDS design that contributed additional information for the parallel effort of the OE flight unit design. In house testing included stiffness characterization, off-load testing, and mated interface load. All tests performed proved the MDS unit design accomplished the main goals of the program.

Computer Simulation

Latch arm stiffness measurement was one of the several tasks undertaken on the MDS hardware. The lateral and radial stiffness of the linkage assemblies had been measured in both the deployed and captured position. By considering these measured stiffness values together with analysis of dynamic

simulation results, higher fidelity results and conclusions were produced. Dynamic Analysis and Design System (DADS) software was used to model the capture and retraction features of the MDS. The model included complete mass properties of two satellites, a zero gravity environment, and contacting features of the MDS.

In excess of 400 cases were simulated to explore performance issues using a uniform distribution of initial condition parameters. The analysis concluded that the mechanism was always capable of positive captures given reasonable limits of relative initial test conditions.

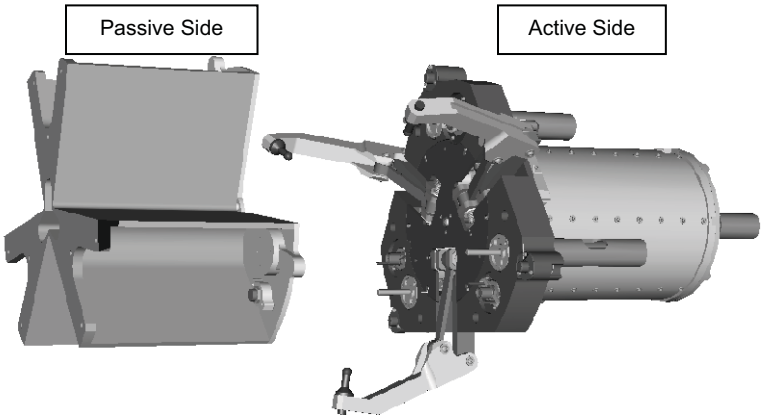

Figure 6: MDS, second generation prototype

Table 1: MDS Phase II Design Requirements

Parameter	Value
Axial Capture Distance:	15 cm
Angular Capture Misalignment Tolerance Pitch/Yaw Roll	 ±5 degrees ±5 degrees
Lateral Misalignment Tolerance:	±5 cm
Linear Contact Velocity Tolerance:	3 cm/s
Preload:	11250 N
Capture Time:	< 10 s
Capture and Latch Time:	< 240 s
Interface Outer Diameter:	< 46 cm
Active Side Mass:	< 23 kg
Passive Side Mass	< 11.5 kg

6 Degree of Freedom (6 DOF) Tests

The main goals of these tests were to correlate/verify the dynamics analysis model and to demonstrate functionality and performance of the hardware in a flight-like environment. 6-DOF testing was performed with the test equipment as shown in Figure 7. The test simulated full, relative six degrees of freedom with the actual hardware in the loop. During testing the active half of the hardware was mounted to a moveable platform supported by six hydraulic actuators. The passive half was mounted above the active half at a fixed location with a force/moment sensor in the load path. Software commanded the six legs to

start the test at a user-specified set of relative initial conditions between the active and passive halves. Once the test was started, software simulated the complete relative dynamics of the two vehicles due to the real contact between the active and passive halves during the capture sequence. The test results were then compared to the dynamic model simulation predictions. Comparison of the test data confirmed the model accurately depicted the capture dynamics. The information gained from the MDS tests was critical to the flight design effort.

Figure 7: 6-DOF testing facilities at MSFC

Docking System Mechanism Description

Following are more detailed descriptions of some of the significant features of the docking mechanism final design as it was flown on the Orbital Express program.

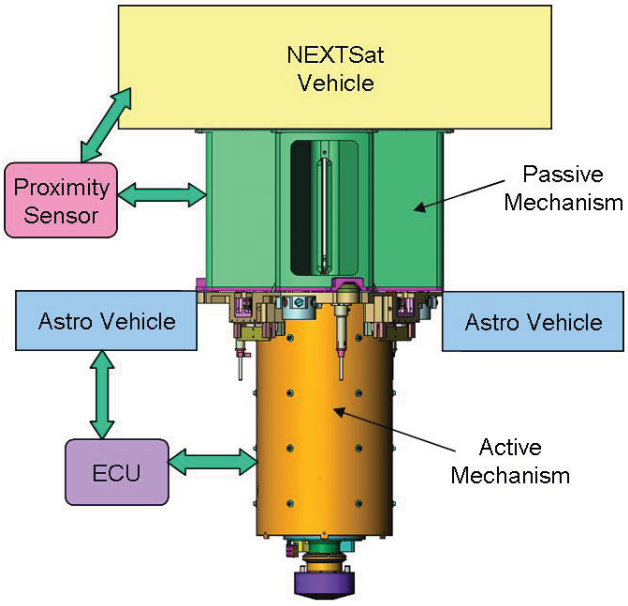

Figure 8: Docking system major components and schematic layout, as configured for Orbital Express

Orbital Express Capture System (OECS)

The capture system consists of an active side and a passive side. The active side contains the grappling arms and the drive system; this side would normally be part of the supply spacecraft. The passive side provides capture features and a sensor to indicate proper engagement of the grappling arms; this side would normally be a part of the client spacecraft. Figure 8 shows a general schematic of the system configuration.

Capture Sequence

To understand the OECS unit, a description of its functionality is necessary. Figure 9 displays the typical steps involved in a capture operation.

1. The linkages of the active mechanism begin in a deployed (open) state. The passive structure is held in a station keeping envelope within the capture capability of the active mechanism.

2. Upon receipt of command, the motor begins to actuate a ball screw which translates an internal piston along the length of the active mechanism canister. The piston moves three separate four-bar linkages that make up the grappling linkages. The linkages then move downward over a roller feature. The camming action of the roller causes the linkages to constrict, engaging the passive structure. The wedge shaped architecture of the passive structure guides the tips of the linkages into center grooves. Capture is achieved as the passive structure is constrained within the bounds of the linkages.

3. As the linkage tips move down along the grooves, they engage a shelf feature, allowing the active and passive structures to be drawn together. As retraction proceeds, alignment occurs in stages. Continued motion of the linkages causes the interface plate of the passive structure to contact push-off rod struts that act as a three point alignment mount on the active mechanism. The alignment features each consist of a spring loaded pin with conical ends that seat into tapered cups on the passive structure. These features provide a gross alignment. With further retraction, additional features align the electrical couplers within their allowable tolerance.

4. At the final stages of retraction, the passive structure becomes fully constrained by a final set of cup/cone features. Rigidization then occurs as the motor applies the necessary preload to provide the required interface stiffness.

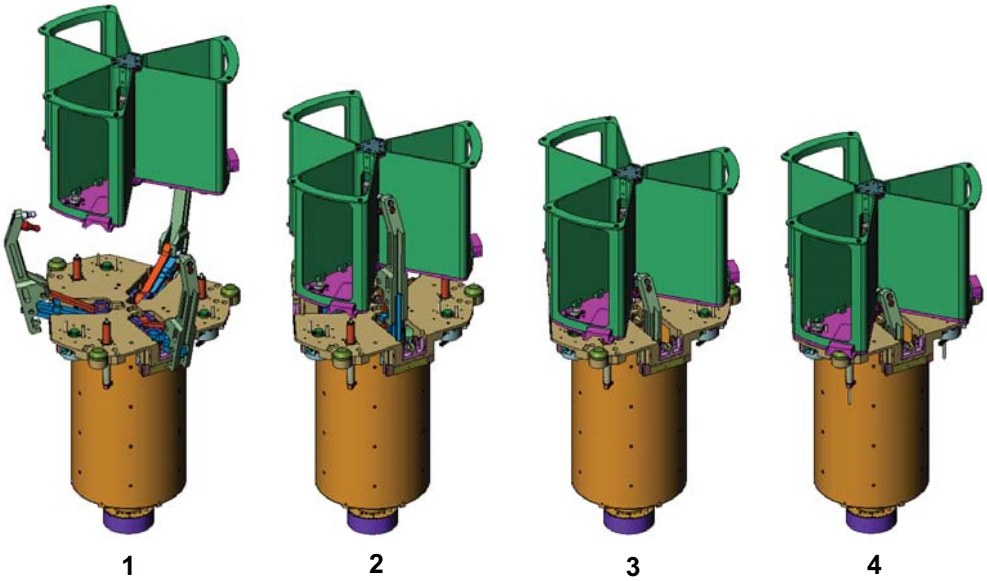

Figure 9: Orbital Express Capture Mechanism Capture Sequence

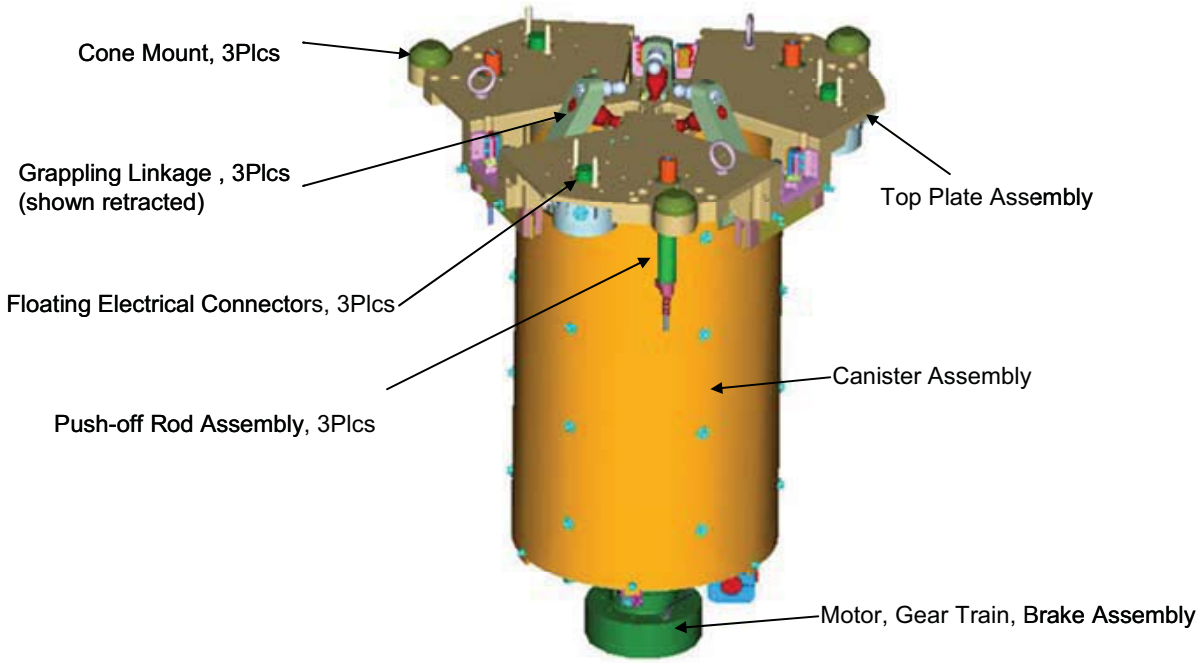

Figure 10: Active mechanism cross-section

Active Mechanism

The Active mechanism is composed of a top plate assembly to which the canister assembly is attached (Figure 10). Within the canister assembly is a drive train consisting of a motor, ball screw, and radial/thrust bearings which transfer load into the housing. All three linkages are fixed to a piston, which is connected to a ball screw via a ball screw nut. The linkages consist of one upper grappling linkage and two lower linkages which make up a four bar connection. Mounted to the canister is a reaction roller that guides the linkages through deployment. Alignment occurs via two separate features: push-off rods, and alignment pins. The three push-off rods are spring loaded features that seat into alignment cups on the passive end to provide gross alignment. The cone mounts are hard mounted features that also seat into cup features on the passive side. This geometry provides a statically determinate final position after mate.

Passive Damping

The need for passive damping was identified during simulation and prototype testing. Concerns had been raised regarding difficulties that could arise during capture; specifically, the passive half impacting the push-off mount and rebounding. While it was agreed that the passive side would need to be held within a station keeping envelope during capture, a non-zero relative velocity would likely exist between the two spacecraft. This could result in slight amounts of contact between the two faces of the active and passive halves, making it difficult to maintain the passive structure in the required envelope. Also of great concern was unintentional impact involving even larger than nominal velocity deltas, and the possibility of damage to the mechanism.

Another motivation to introducing damping involved oscillations occurring during the capture event. Testing of the prototype in a micro-g environment exhibited a tendency for the passive structure to oscillate within the constraints of the linkage tips and the push-off mounts. Computer simulations performed by Boeing confirmed this behavior. In order to address this issue, a spring damper system was added to the push-off struts on the active mechanism. Figure 11 depicts a cross section view of the push-off mounts with the spring damper system.

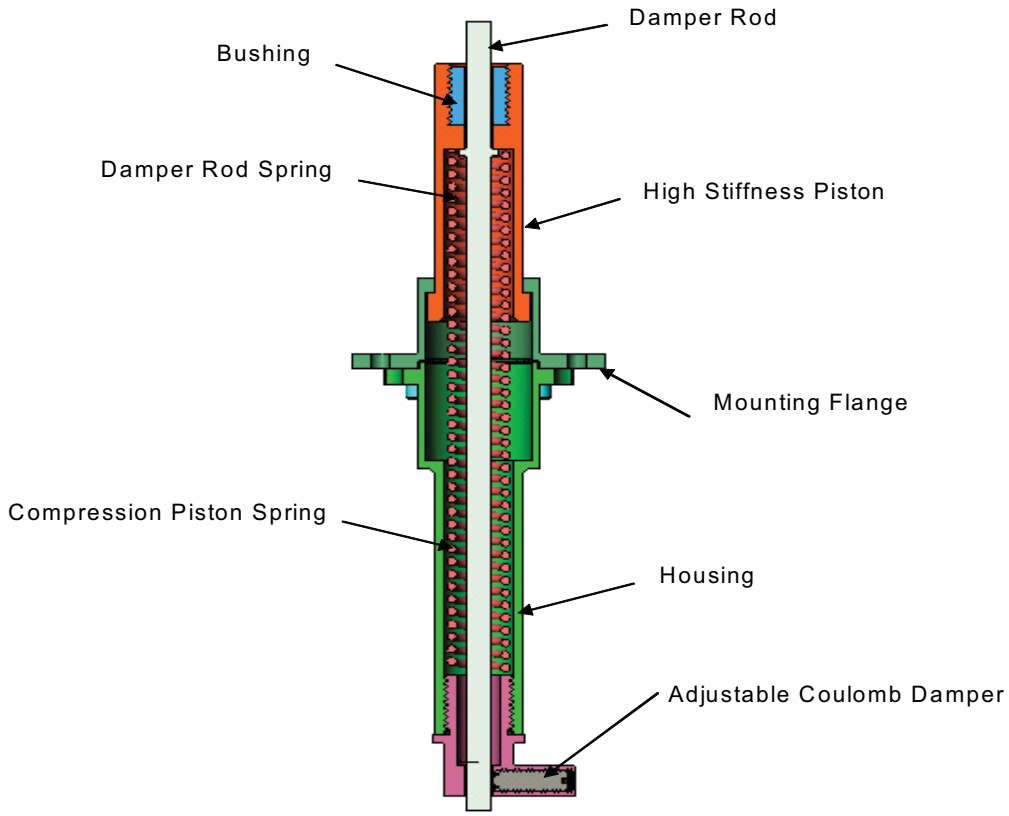

Figure 11: Push-off rod cross-section

Torque Sensing Mechanism

Running the motor/actuator until proper preload is achieved was accomplished using a torque sensing mechanism (Figure 12). To apply a preload in the mated position, a specific torque from the motor is required. The torque sensing mechanism is adjusted to activate limit switches at the set torque needed for proper preload. Once the limit switches are activated, the motor is commanded to stop. In the stop mode, the motor/actuator applies a brake holding the preload developed.

Passive Assembly

The passive assembly (Figure 13) is a three wedge shaped trefoil. The faces of each wedge terminate at a center groove that runs along its length. The passive interface consists of an interface plate that is mounted to the three trefoils. Part of this geometry includes retention lips, or shelves, which provide the linkage with a positive feature to grapple. The interface also includes kinematic cup features which help to align the structure and institute preload. The OE program required a sensor to confirm that capture had been successfully accomplished (Figure 9, step 2). Light Emitting diodes (LED's) located on the passive assembly detect when the active assembly arms are in the captured position (Figure 14)

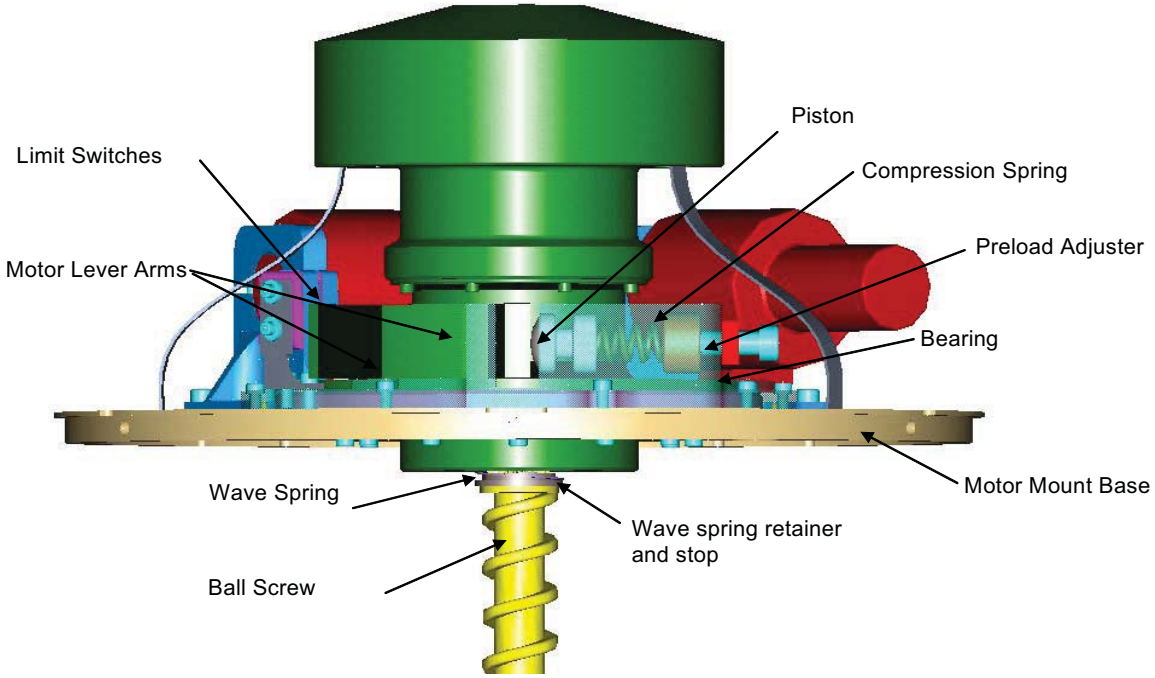

Figure 12: Torque sensing mechanism

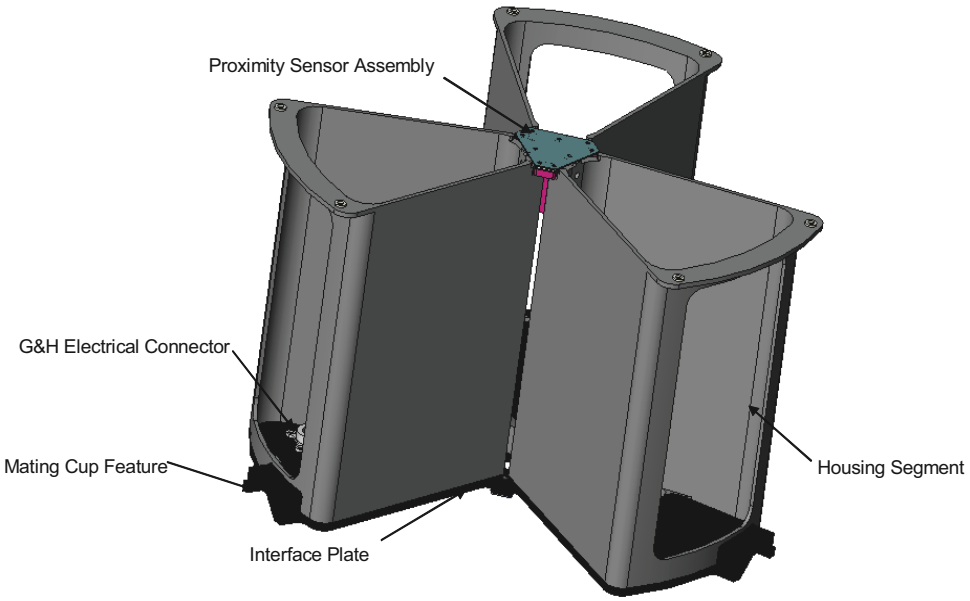

Figure 13: Passive assembly

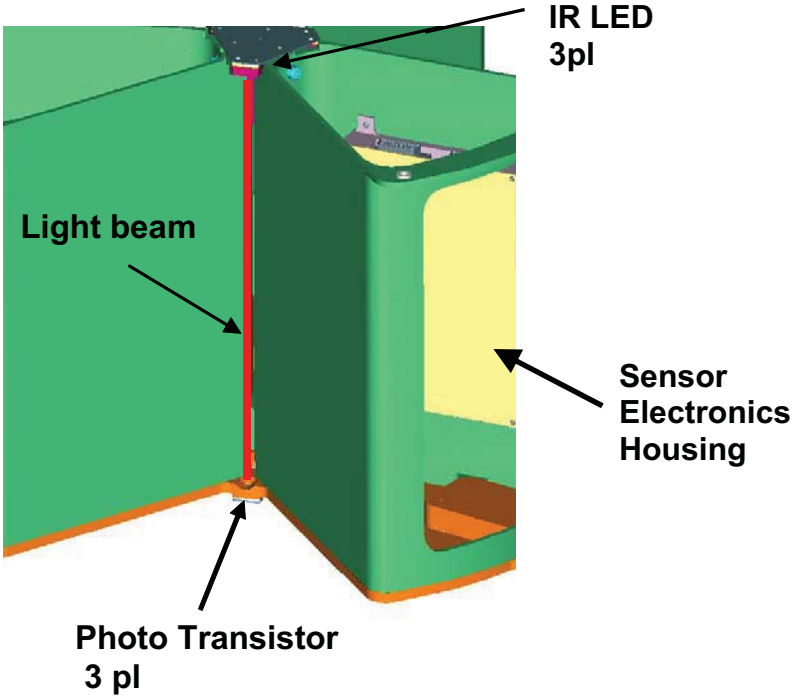

Figure 14: Proximity sensor detail

OECS Flight Unit Testing

Acceptance Testing

Based on the experience gained with the two prototypes, SRC developed and performed comprehensive acceptance test program. In-house testing included many of the same elements that were present in the prototype and MDS testing: mate and de-mate verification, stiffness characterization, and off-load testing. In addition, thermal, thermal vacuum, and vibration testing were performed.

Computer Simulation

Dynamic models were updated to include all modifications incorporated after development. Significant load cases were analyzed to verify that mechanism performance met the Orbital Express requirements. The same software and methodology were used as for the development unit design effort.

6 DOF Testing

The final phase of qualification and flight testing included 6-DOF testing similar to that which was performed on the MDS. Although the MDS and OECS mechanism features important for capture and alignment are almost identical, small changes were made to the design based on the results of 6 DOF testing of the MDS. Furthermore, the manufacturing fidelity of the OECS qualification components was flight-identical, unlike the MDS which was of engineering development unit quality. For these two main reasons, a second 6-DOF test of the qualification unit was performed. The goal was to once again confirm that the dynamic modeling accurately depicted the dynamics encountered during capture and alignment.

Orbital Express Mission

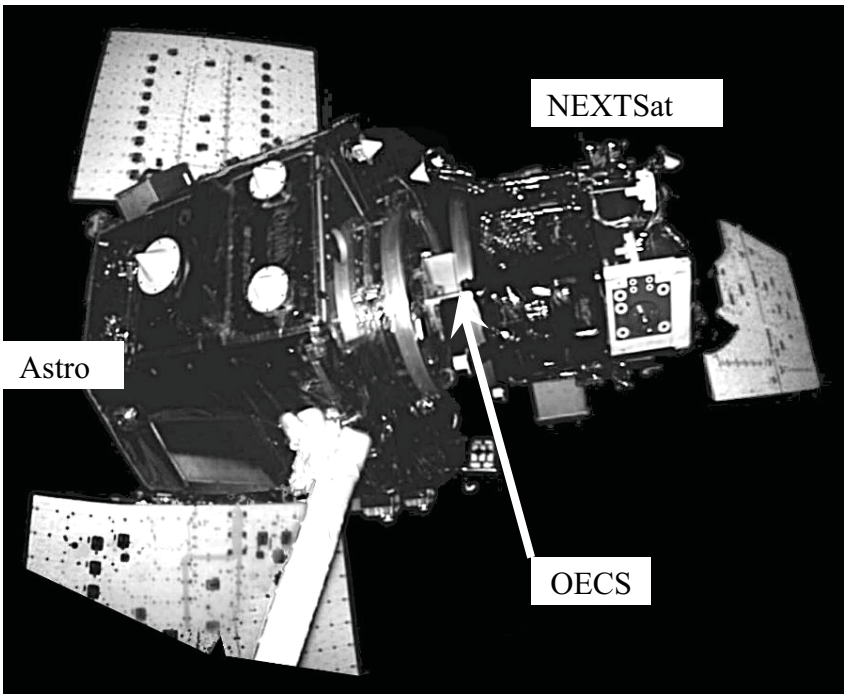

Figure 15: Astro and NEXTSat mated by OECS during flight

For the Orbital Express mission, the two spacecraft were launched attached together with an adapter coupling ring. The OECS docking mechanism was engaged in a unique, preloaded condition for launch, but was not the primary load path for support of launch loads for NEXTSat. After system checkout and stabilization, the robotic arm was used to attach the two spacecraft together. Prior to free flight operations, the robotic arm was used as a safety measure to keep the two spacecraft connected while the adapter coupling ring was released and jettisoned. The first docking operation was performed by moving the spacecraft with the robotic arm (the two spacecraft were already de-mated and were held together by the arm) and operating the OECS docking mechanism. This operation was successfully performed and confirmed that further docking operations could be performed. After proving out a "captured" docking operation several distinct free flying docking operations were performed. In each case the separation of the spacecraft, the proximity flying, and the subsequent re-docking were performed autonomously by the two spacecraft without ground control intervention.

While docked, key refurbishment operations were performed:

- The electrical connections were utilized for direct communication and electrical power transfer between the spacecraft.
- The fluid connector was engaged and transfer of propellant was successfully performed.
- The robotic arm was utilized to install an electronics box on a mating port on the NEXTSat spacecraft.

Overall, all mission goals were successfully completed. The two spacecraft have since been decommissioned.

Conclusions

The OECS flight mechanism performed as expected and has supported demonstration of the effectiveness of the soft docking approach enabled by the design. The blending of technology and vision yielded a simple and effective concept. Through a series of design trades and system testing, the application of minimal mechanisms, and the use of common proven technology (i.e. motors, lead screws, and linkages), a highly functional design resulted. What began, during the primary phase, as a well developed concept quickly evolved into a commercially viable product.

References

1. Shane Stamm and Pejmun Motaghedi, “Orbital Express Capture System: concept to reality,” SPIE Conference, May 2004.

2. DARPA website http://www.darpa.mil/orbitalexpress/

Ultra Light Self-Motorized Mechanism for Deployment of Light Weight Spacecraft Appendages

C. Boesch[*], C. Pereira *, R. John **, T. Schmidt **, K. Seifart **, H. Sparr **, J. M. Lautier [+], T. Pyttel[++]

Abstract

A mechanism to deploy satellite reflector antennas was developed to provide a rotation angle of up to 90 degrees. The energy necessary for deployment is stored within curved tape springs, which are buckled and thereafter folded into stowed position. The release at the hold down points and stored energy of the buckled tapes triggers the deployment.

New characteristics with respect to similar mechanisms are a complete guidance without friction combined with a high pointing stability (0.01° half cone). No additional latching elements are needed.

The presented hinge integrates several functions (deployment motorization, guidance, latching and pointing stability) in a compact design weighing less than 0.6 kg (1.3 lb). This paper reports the development process from concept to finished product including material characterization, simulation, verification approach and lessons learned. The design of The Ultra Light Mechanism for Advanced Antenna Systems (ULMAAS) is not exclusively intended for deployment of reflector antennas. The concept is scaleable for different appendages, e.g., solar generators or masts.

Introduction

The Ultra Light Mechanism for Advanced Antenna Systems (ULMAAS) focuses on a new generation of lightweight reflector antennas requiring compact and accurate deployment systems with no motorization and high pointing stability. An ultra light reflector of Astrium [1] was selected as reference application. This allowed specifying requirements more precisely and establishing a representative test program.

The development started with a survey covering comparable deployable mechanisms of the last 40 years. A simple design emerged from this survey and a patent application covering its unique features was submitted. The concept aimed for a device with low mass, high reliability and high pointing accuracy. A major characteristic is its completely frictionless deployment.

The next steps were the trade-off on materials and geometry, simulations, and functional testing. Verification of the mechanism performance was done using a dummy antenna in a qualification process that includes multiple deployments after thermal cycling in order to gauge repeatability of deployment kinematics and reliability of end position.

Requirement Specifications

A performance specification was written with the help of Astrium in Toulouse and other antenna manufacturers in order to guide the development of the mechanism. The specification was a general catalog of requirements not specifically tied to a particular design. Some of the key parameters and requirements are listed below:

- Antenna payload with 2.2-m (7.5-ft) diameter and a mass density of 2.2 kg/m^2 shall be deployed
- Mass should not exceed 0.5 kg (1.1 lb) including interfaces to the spacecraft and deployable appendage

[*] RUAG Aerospace, Wallisellen, Switzerland
[**] HTS GmbH, Coswig, Germany
[+] ESA-ESTEC, Noordwijk, The Netherlands
[++] University of Applied Sciences, Friedberg, Germany

Proceedings of the 39th Aerospace Mechanisms Symposium, NASA Marshall Space Flight Center, May 7-9, 2008.

- Occupied volume in the folded configuration should not exceed 140 x 200 x 80 mm^3 (0.1 ft^3)

The main performance parameters are:

- Deployed stiffness should exceed 2 Hz
- Position accuracy at end of life should be better than 0.01° half cone
- Deployment repeatability should exceed 0.005° half cone
- Latching shock on the payload should not exceed 100 N·m (75 ft·lbf)

The performance environment included the sine loading (15 to 20 g) and random vibration of a typical launcher for these antennas (12 g_{RMS} in-plane / 20 g_{RMS} out of plane) as well as a qualification temperature range between -90°C and +90°C (survival) with a deployment range of -40°C to +70°C. Consideration of a storage period of five years in the folded configuration without loss of deployment torque required accelerated creep testing.

Material and Geometry Trade-Offs

A key point of the development was defining a baseline conceptual design. The survey of state of the art devices revealed advantages and disadvantages of existing technical solutions. A typical representative of a compact mechanism is the elastic collapsible hinge (ECH) such as the Maeva [2] hinge depicted in Figure 1.

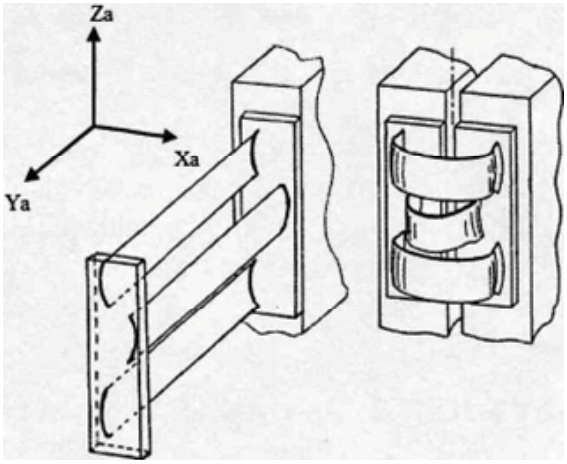

Figure 1. Maeva hinge

At first sight the advantage of the hinge concept is its simplicity, but appearances are deceiving and the overall behavior is complex and requires an extensive investigation of curved tape spring elements, which are cornerstones of the design. A short outline of the main characteristic of these elements follows.

Tape Spring Characteristics

We know tape springs from steel measuring tapes that utilize the snap-in effect to achieve a straight and stable cylindrical shape. Curved tape springs provide a self-latching function. Fundamental studies of design and performance of these elements were carried out by Pellegrino and Steffen [2] [3] at the University of Cambridge. The schematic bending behavior is illustrated in Figure 2.

The tape springs are stiff until they buckle under a bending moment. In the buckling zone, the affected cross section is flattened. The peak value is higher for bending against the tape spring curvature (opposite sense) than for equal sense bending. The steady state moments are almost equal in both directions

The challenge in using an ECH design is building a high deformable hinge with sufficient deployment torque and end stiffness. This was solved by using curved spring elements of different length. The longer

spring bent in an S-shape, in both equal and opposite senses, can be accommodated below the shorter one resulting in a compact folded hinge with high torque capability.

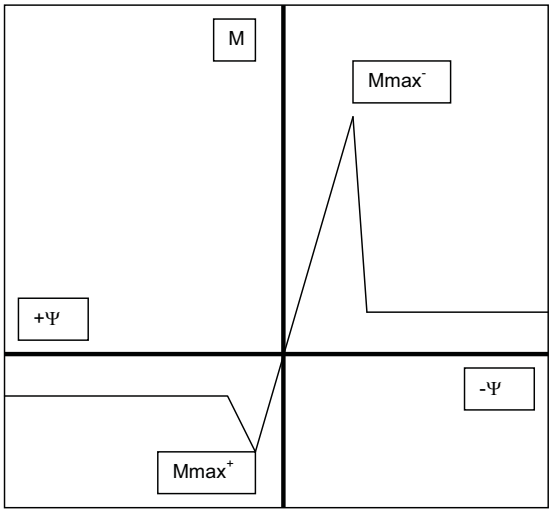

Figure 2. Typical moment vs. angle graph for curved tape springs

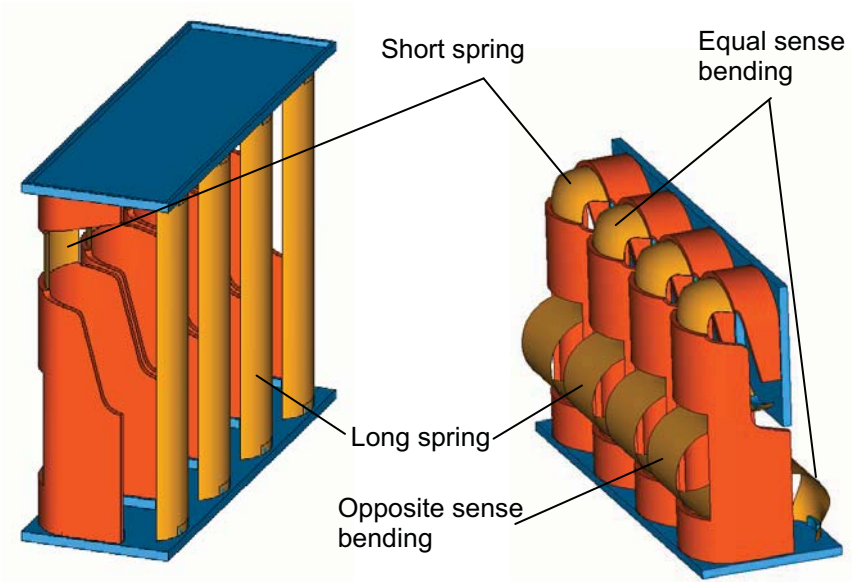

Figure 3. Baseline concept in deployed and folded state

Design

The design of the ULMAAS incorporates four pairs of tape springs in a row, each with the curvature facing inwards as shown in Figure 4. The rectangular arrangement maximizes torsion stiffness.

The major parameters for motorization and stiffness of the hinge are the free length of the spring, the curvature and the width of the tape springs, and their thickness. The shorter spring (Spring B) can be seen as a pivot for the mechanism. The distance between the springs controls the bending stiffness of the deployed hinge. The different length of the spring elements is compensated by four support bodies.

The support components provide large cut-outs with sufficient clearance for the flattened long tape springs (Spring A) in their bent configuration.

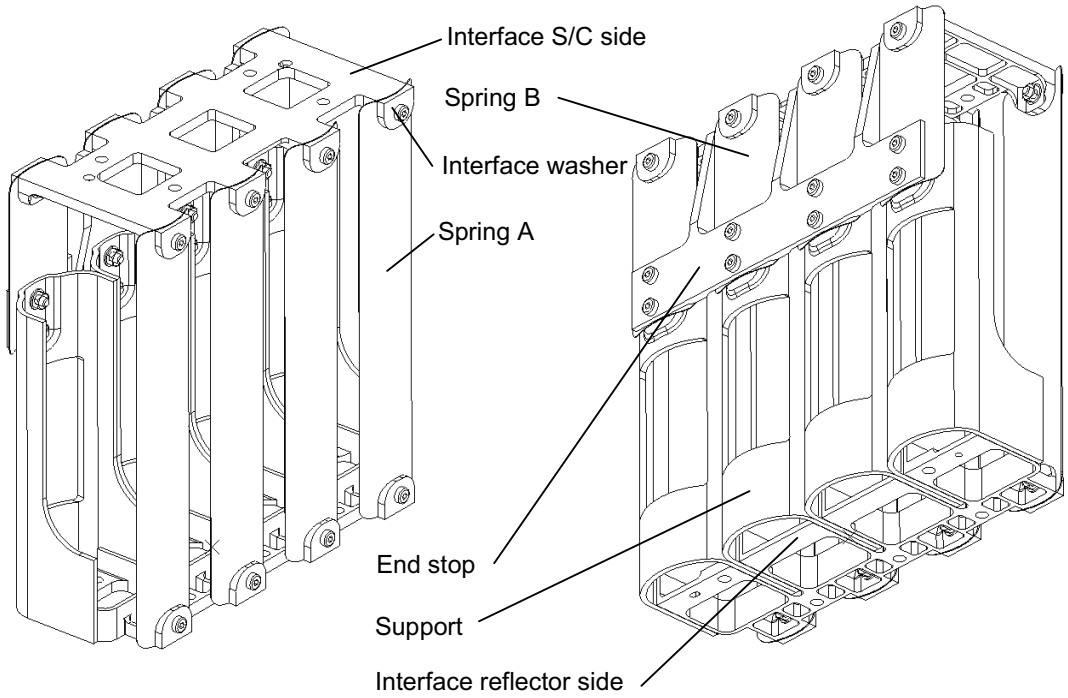

Figure 4. ULMAAS Design

Tape springs are connected to metallic fittings by adhesive bonding and an additional screw connection. The bond minimizes stresses around the bolting hole while the bolt connection with curved washers reduces peeling loads on the adhesive. On the backside of the small spring, an end stop limits travel of the hinge during deployment after reaching the straight configuration (back buckling). It does not have effect on the alignment precision of the hinge.

A material trade-off for the springs included metallic and fiber reinforced materials, stiff materials with a high elastic deformation ability. Achieving a high pointing stability over a wide range of temperatures meant that the ratio of thermal conductivity to coefficient of thermal expansion was a main driver in the selection process. The decision to use carbon fiber reinforced plastic (CFRP) is based on the high thermal stability of this family of materials.

After selecting CFRP as the material of choice, a direct comparison of several carbon fibers was made in a search for a good balance between high stiffness and high elastic strain. The selected fiber is a Toray T800 carbon fiber with a 295 GPa (43000 ksi) tensile modulus and an elongation of 1.9%. The matrix system has been selected to meet stringent thermal stability and outgassing requirements. Bryte EX-1515, a cyanate ester system with considerable space heritage, was selected.

Spring Design

The performance of the hinge in terms of stiffness, torque and the general ability to bend is determined by the design of the spring elements. The total thickness has to be in the range of 0.3 to 0.45 mm, corresponding to laminates with three to four plies. The availability of thinner prepreg material is deemed advantageous in the lay-up design of the spring elements as it allows greater tailoring of the composite.

A principle relation between the bending radius of the tape spring ***r*** and the curvature radius ***R*** of the spring cross section was derived by Pellegrino [3]. The factor connecting these radii is derived from stiffness parameters of the specific lay-up. Equation (1) is used to assess the bending radii of the lay-up.

$$r = \sqrt{\frac{D_{11}^*}{D_{22}^*}} \cdot R \qquad \text{with } [D^*] = [D] - [B]\,[A]^{-1}[B] \tag{1}$$

[A], [B], [D] are the non-zero quadrants of the laminate compliance matrix. D_{11}^* and D_{22}^* are the diagonal terms of the matrix [D*]. *R* is the curvature of the tape spring and *r* the resulting bending radius.

The bending radius is important because it allows a design that fits in the desired envelope of the hinge. With the approximate bending radius and the knowledge that the tape spring will nearly flatten in the cross direction, the peak strain can also be assessed.

The calculation considers only one single tape spring but the pair of springs will influence each other during folding. The actual behavior is also driven by edge effects, material and manufacturing imperfections that cannot be predicted properly.

Based on the performed analyses, the following lay-up combinations were selected for further investigation:

- [0,+45,-45,90] and [0,-45,+45,90]
- [0,+60,-60] and [0,-60,+60]
- [0,+45,-45] and [0,-45,+45]
- [90,+45,-45,0] and [90,-45,+45,0]

Analysis

The activities in the field of simulation and calculation were intended as a support of the design and to establish a verification approach to correlate and predict test results thus allowing scale-up of ULMAAS to meet specific end user requirements. Analysis was broadly based and included stress/strain, stiffness, buckling, deployment torque and thermal deflection predictions

Stiffness

Natural frequencies of the coupled system hinge and antenna were determined in finite element (FEM) calculations using I-DEAS software (see Figure 5a). The calculated frequencies showed good agreement with those derived from test data later on. The lowest natural frequency was 3.2 Hz and represents the torsion stiffness. The frequency in the folding direction (bending mode) is nearly the same (3.4 Hz).

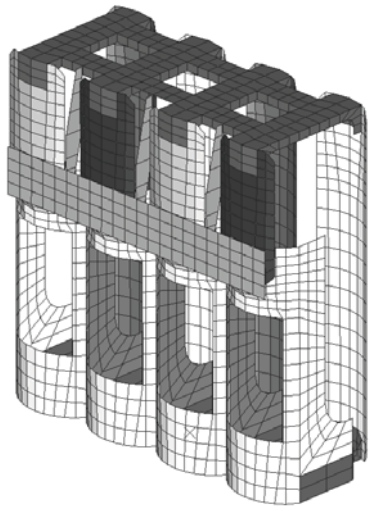

Figure 5a. I-DEAS Simulation model

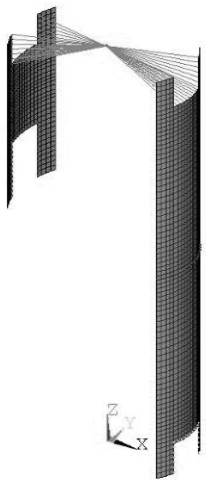

Figure 5b. ANSYS Simulation model

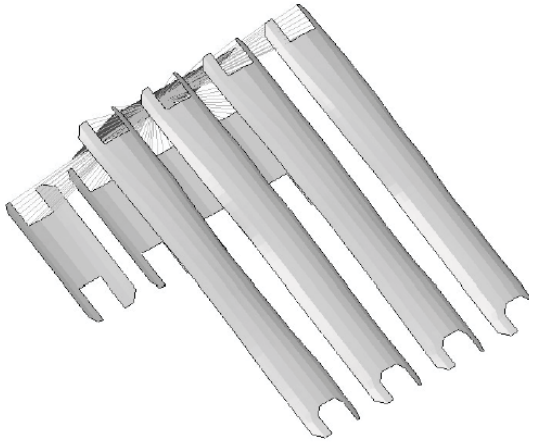

Figure 5c. Simulation model PamCrash

Influences to the global stiffness of ULMAAS were assessed parametrically on simplified models with variation of free length of the springs, spring curvature as well as the size and shape of the fixation area. The change of the length of one spring will affect the general bent shape, stiffness, buckling strength and both motorization torque and end of deployment shock.

Deployment Torque Analysis

The folding and deployment of ULMAAS is a geometrically non-linear problem. The anisotropic material properties of the composite make the FE calculation very complex. Convergence is sensitive both to the material properties and the mesh. The corresponding motorization torque of the hinge was calculated with an implicit code for a single pair (Figure 5b) of spring elements and with an explicit code for the whole hinge (Figure 5c). In both cases, elastic instability points occur. In this regard, the calculation using ANSYS software (Figure 5b) was very challenging.

The hinge model has a large rotational stiffness that is obtained by the chosen geometry of springs as cylindrical sectors and the relative large distance between the spring rows. To come into regions of large bending rotations along with small changes for the rotational moment at the antenna side, one has to overcome a snap-through-instability of the longer spring. In order to match real behavior observed in single spring models, the simulation used an arbitrary disturbance by applying a local displacement to the center of the long spring (Spring A in Figure 4) at the beginning of the movement. In real tests, a pre-flattening of the springs has to be done to ensure folding without damage to the tape so that essentially the same disturbance as required for the mathematical models is necessary.

Most interesting in the simulation is the transition of the long spring behavior starting from an almost symmetrical deformation state (three bending zones) to the final S-shape (two bending zones). It can be seen that the moment versus deployment angle curve in Figure 6 reaches a minimum, which can be identified as a snapping through between two qualitatively distinct deformation states (elastic instability).

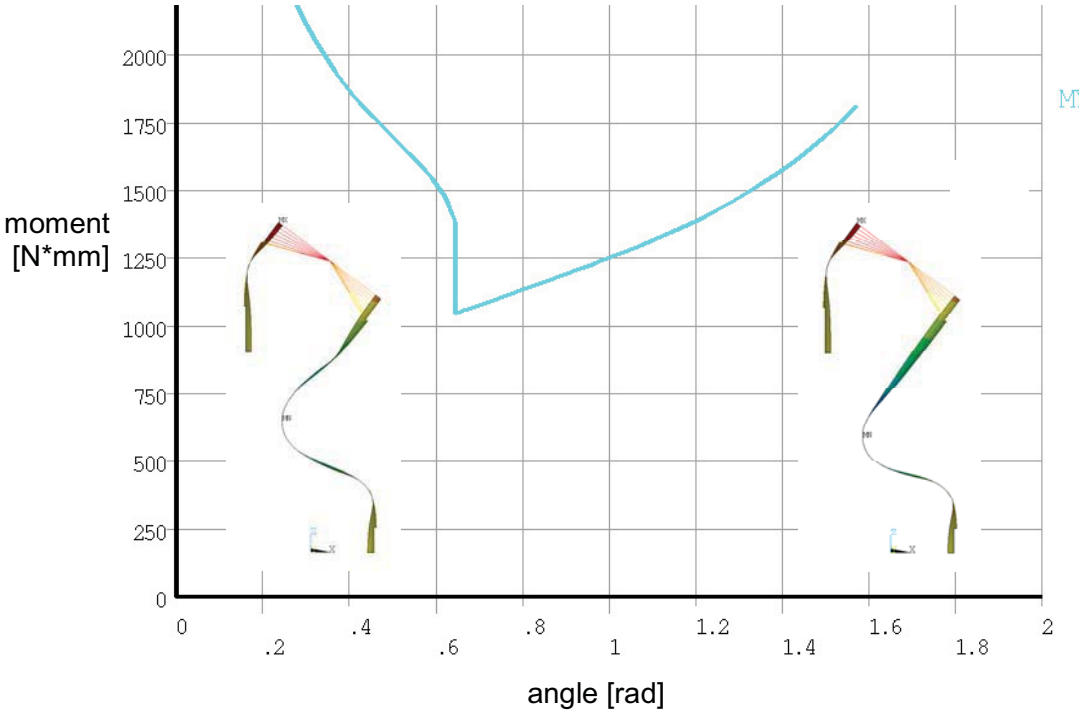

Figure 6. ANSYS simulation – moment vs. angle

The moment versus angle relationship could be determined during the unfolding process. To do so, all auxiliary forces or displacements were removed. But the unfolding analysis did not fully converge to the straight position. Furthermore the implicit code was very sensitive to material stiffness properties.
A simulation with PamCrash (Figure 5c), which is an explicit solver, was more stable to model variations and allowed introduction of anisotropic material properties. The effects of coupling in the stiffness matrix for the anisotropic material were clearly visible in the out of plane behavior of the springs seen in Figure 7. The disadvantage one has to face using the explicit code is the rather long solution time (days rather than hours), which limits iterations and variations in the parameters of the model.

Both simulation and test showed that end of deployment shocks are quite high. A reduction of torque cannot be achieved without reducing the deployed stiffness and although certain margin exists in this regard (3.4 Hz vs. a 2 Hz requirement) it was decided to implement a damping system.

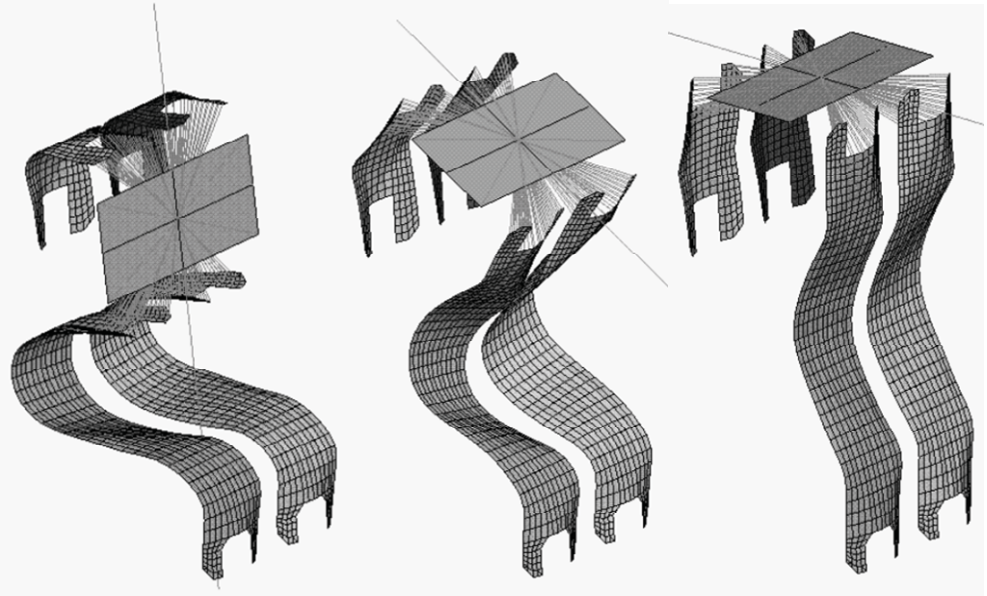

Figure 7. PamCrash simulations – hinge deployment

Thermal Investigations
The objective was to predict thermo-mechanical behavior of the hinge. Using the existing FEM, an orbit simulation with the I-DEAS TMG module was performed. Previous calculations revealed that even with low CTE materials an additional thermal insulation is necessary to meet the stringent requirement of pointing accuracy. A multi-layer insulation (MLI) was included in the simulation where a geosynchronous orbit was simulated. The results (Figure 8) showed a moderate temperature gradient within the hinge. Hot and cold spots appeared at the interface points. Temperature extremes were in the range of -60°C to +20°C and corresponding deflections are moderate and stay within the pointing budget of the mechanism.

Material Testing

The material testing was performed in order to obtain property values and re-run the analysis with them. Tests were performed in the two orthogonal directions. The tests of the CFRP material covered included following measurements:

- Density was measured to obtain the exact mass of the model in the simulation.
- Glass transition temperature
- Thickness allows assessing the manufacturing quality. Furthermore, the bending radius depends on the thickness.

- Fiber, matrix and void fraction reveal a lot about the manufacturing quality but are not really necessary for the analysis because strain/stress tests were also performed.
- Young's modulus, maximum strain and ultimate stress in tension and compression at reference temperature, minimum and maximum temperatures.
- Coefficient of thermal expansion (CTE) tests are very important as one of the most stringent requirements refer to pointing stability, which is driven mostly by the thermal characteristics of the material.
- Long-term stress relaxation to assess the change of deployment torque over time due to storage of the hinge in folded configuration for a long period of time.
- Moisture pick-up
- Thermal conductivity

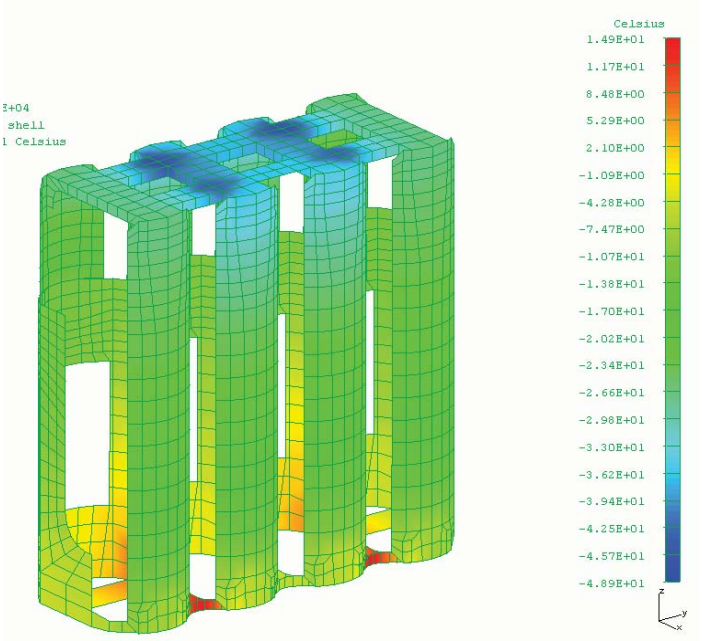

Figure 8. Thermo mechanical simulation – Thermal Gradients

Figure 9 shows the test machine used for the test and the failure mode in compression of a sample.

Figure 9. Test set-up and destroyed compression sample

For the long-term creep test, a pair of short tape springs were glued to fittings and then bent and mounted to a test jig as in Figure 10. Accelerated testing at 60°C was performed in parallel to room temperature tests.

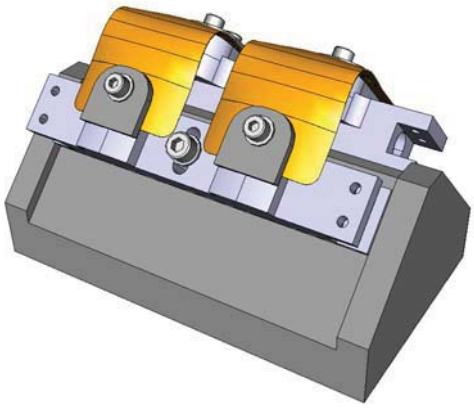

Figure 10. Test Jig for creep test
Bread Board and Performance Testing

Bread Board Testing
Basic investigations in terms of CFRP bendability, handling and component interface were performed with a full-scale breadboard model as shown in Figure 11. The observations made were used to enhance the design of the hinge and identify weak points.

Figure 11. Full-scale breadboard model

Several deployments were performed with the test gadget and an inertia dummy attached to observe the unbuckling and latching of the springs. The breadboard made it easy to exchange the tape springs. This allowed replacing tape springs quickly and made it possible to test different lay-ups. The different lay-ups were assessed qualitatively regarding their robustness against defects. Figure 12 shows a side and a top view of the test gadget with a dummy inertia attached.

Performance Testing: Motorization
The laminates are by their very nature asymmetric. To compensate for coupling effects, they were mounted pair-wise in the test gadget. The test gadget has the same dimensions as the hinge except for the width, which had been halved. The test rig is depicted in Figure 13. The measurement determined the angle-moment relationship of the hinge and thus the motorization of the ECH. The test was performed by applying equal torque to both interfaces. The resultant angle was measured from 90° to approximately 5°.

Smaller angle a higher torque than the test rig could withstand, so the peak moments close to 0° could not be determined during these tests.

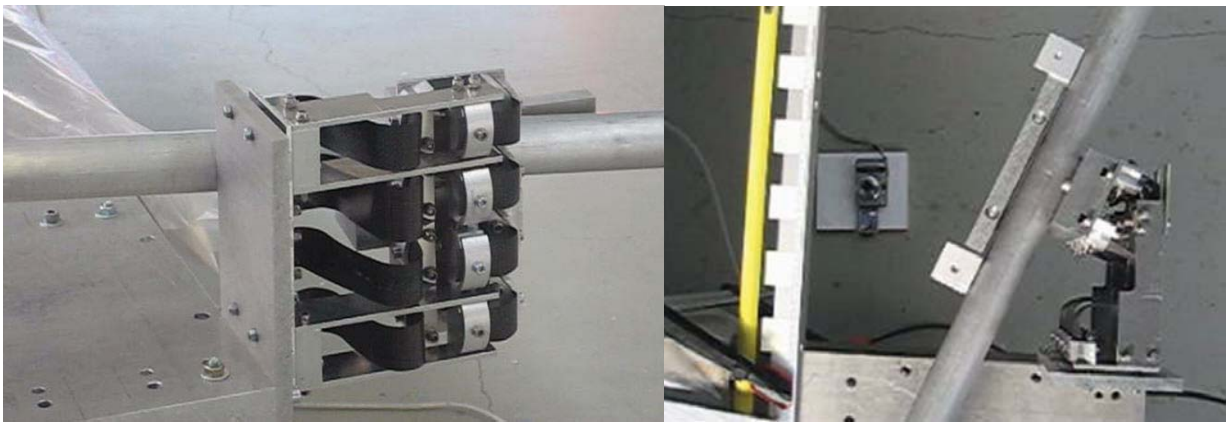

Figure 12. ECH and dummy inertia

Figure 13. Test rig during static tests

Figure 14 shows the results from 5° to 90° for different lay-ups. It shows that the motorization depends mostly on the laminate thickness. In contrast to this, the spring behavior is driven mostly by the lay-up identifiable in the graph between 15° and 40° where the buckling shape of the long tape spring changes. Furthermore, the test revealed the robustness and sensitivity to bending of the specimens. Therefore, the selection of appropriate lay-up was not only based on the numerical data but also on the observations recorded.

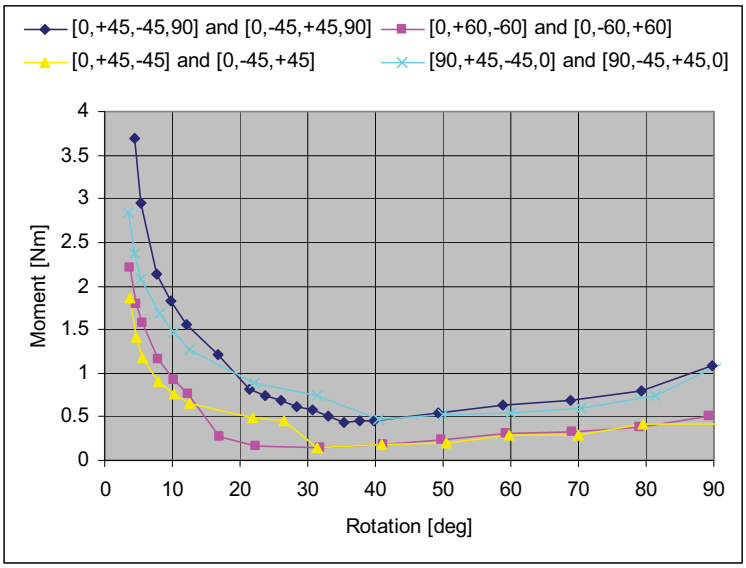

Figure 14. Quasi static moment vs. angle

Performance Testing: Stiffness

The stiffness and the dynamic test required a different test jig. The test facility used a jig to mount the hinge, a dumbbell shaped dummy inertia to simulate the spacecraft appendage, a video camera to record the dynamic behavior of the hinge during deployment and laser interferometers to monitor the static deflection under a given load and the pointing accuracy after every deployment. Under the mounting plate, hinge force transducers measured the latching shock. The set-up is shown in Figure 15.

To determine the bending stiffness of the hinge, weights were attached at both ends of the dummy inertia. This led to a pure bending moment about the hinge axis. The distortion due to the applied load was monitored by laser interferometers pointing on a target fixed to the hinge.

As the displacement is very small, it was assumed that the distance from interferometer to target is constant at all time. A detailed view of the apparatus is given in Figure 16.

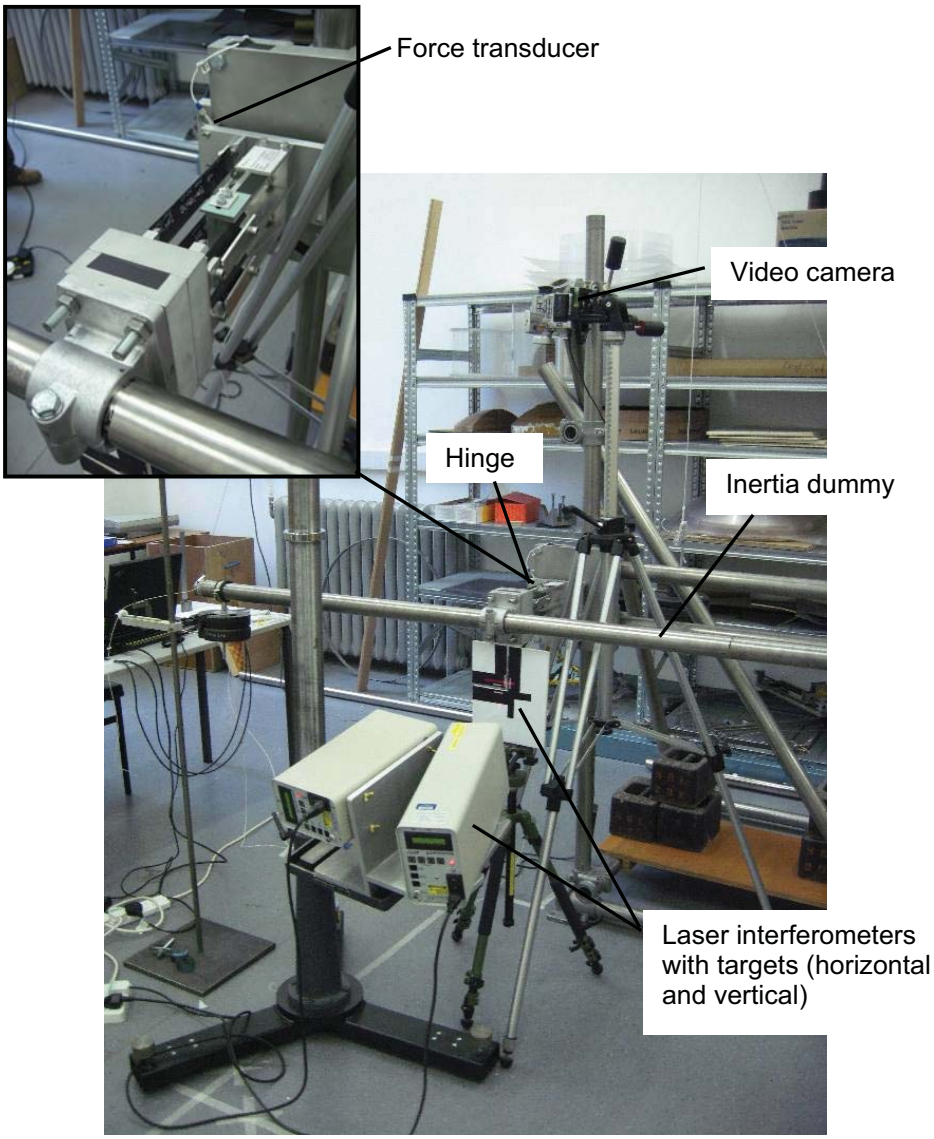

Figure 15. Test setup for stiffness and dynamic test

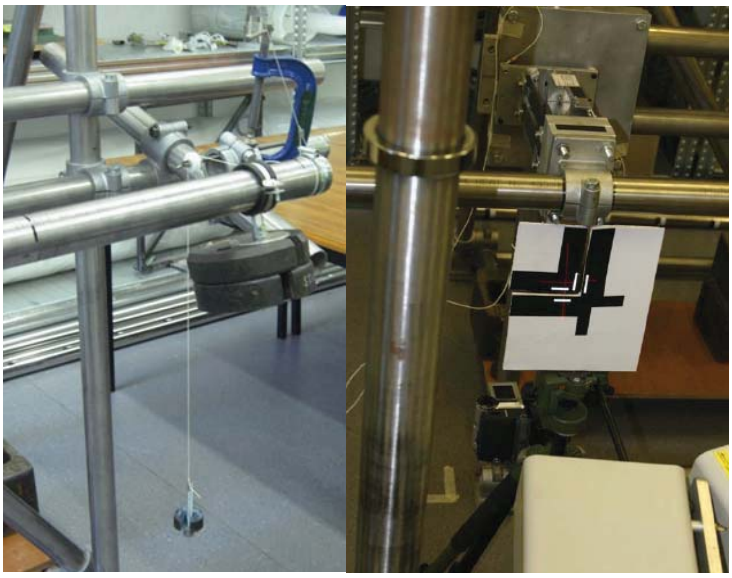

Figure 16. Test setup for stiffness measurement

Figure 17 shows that the deployed stiffness is mostly driven by geometric parameters (curvature, tape spring width, but not thickness) rather than by the lay-up. Except for the thickness, all tested items had identical dimensions. The lay-up is decisive for the motorization torque but not for the deployed stiffness.

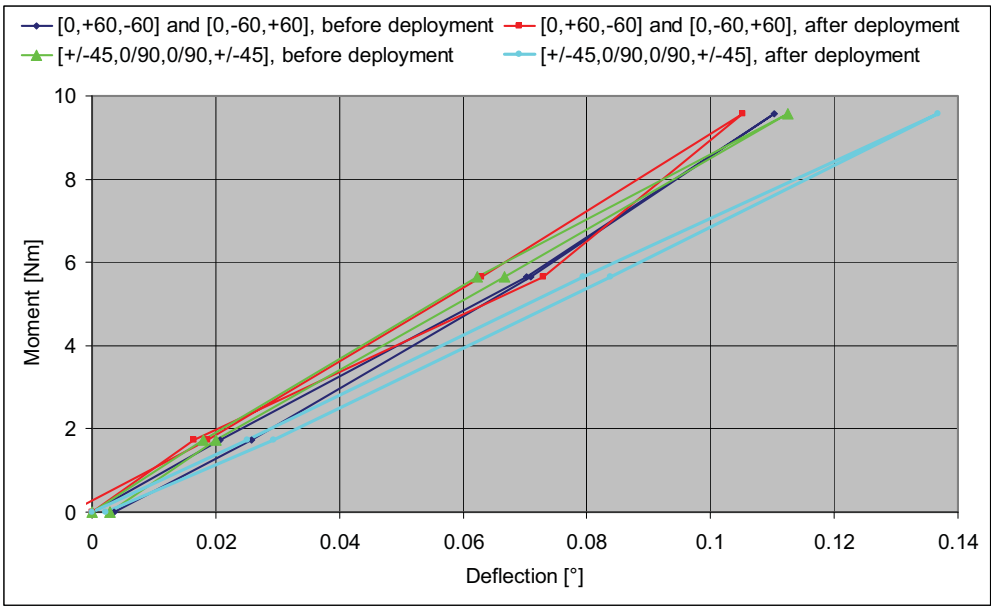

Figure 17. Stiffness of the hinge

Performance Testing: Dynamic and Latching Shock

The setup proved to be difficult, as the non-symmetric lay-ups tend to deform sideward when bent and the clearance to the side walls of the rig had to be adjusted carefully. The force recording, which is depicted in Figure 18, showed that most of the travel of the appendage was accelerated with low spring torque, which corresponds to the quasi static measurements. A notable first peak can be interpreted as the huge stiffness increase of the tape springs close to zero degree deflection. A second peak, which was higher and in negative direction resulting from overtravel, is the one to be regarded by the maximum

shock criteria of the performance specification. The decay of the vibration and the periods of the amplitudes allow an assessment of structural damping (15-20%) and natural frequency (3.85Hz).

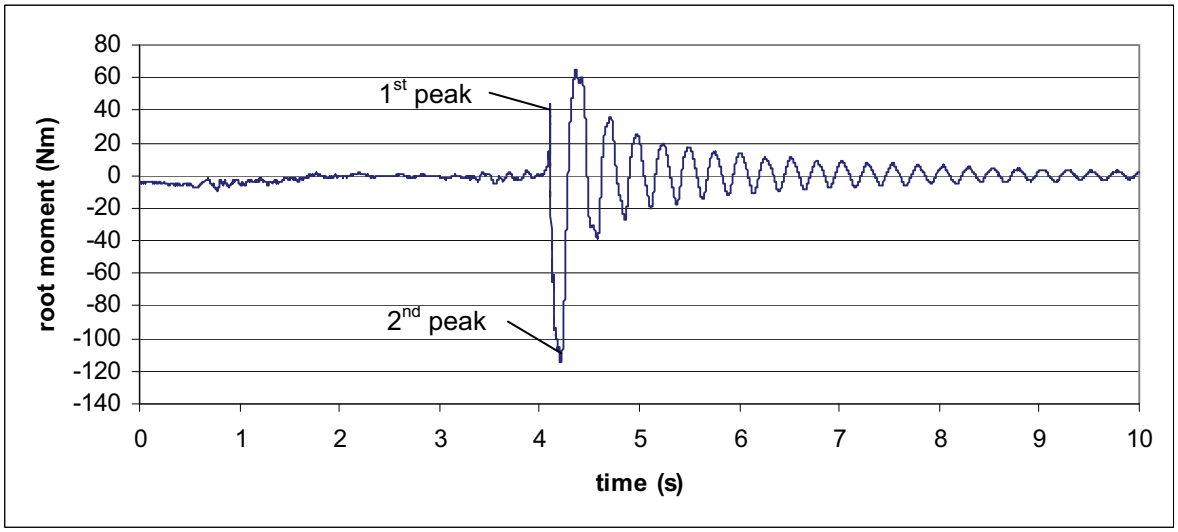

Figure 18. Dynamic moment vs. time

The final lay-up design is based on to the best variant in sample testing either [0, 60,-60] or its mirrored variant [0,-60, 60]. The thickness of the composite is approximately 0.33 mm. The support parts that are bridging the different length of the springs are made from the same laminate with a thickness of 2.5 mm.

Conclusions

The final design of ULMAAS, a light weight self-motorized deployment mechanism, was achieved through iterative analysis and testing. The first analytical predictions led to a design with a very high deployment torque, which then had to be mitigated. Use of dedicated tests showed that the lay-up of the composite could be fine-tuned to reduce this torque without a substantial reduction in deployed stiffness. The analysis approach shows that prediction of characteristics is possible even for complex non-linear problems but in this case it goes hand in hand with testing, as the traditional approach of validating an analysis with a test will not work.

References

1. Nicolas Elie, Alain Lacombe, Stéphane Baril, *Ultra-light reflectors: A high performance and industrial concept for commercial telecom antennas*, EADS SPACE Transportation
2. Sicre[1], Givois[2], Emerit[2], *Application of "Maeva" Hinge to Myriade Microsatellites Deployments Needs*, CNES[1], Metravib[2]
3. Pellegrino S., et al, *IUTAM-IASS Symposium on Deployable Structures: Theory and Applications*, Drodrecht: Kluwer Academic Publishers, 2000
4. Pellegrino, Yee, *Foldable Composite Structures*, University of Cambridge, UK, 2003

Development of the Aquarius Antenna Deployment Mechanisms and Spring/Damper Actuator

Joel A Johnson*

Abstract

The Aquarius Instrument's large radar reflector dish needed to be stowed for launch, and then deployed on-orbit. The Deployment Subsystem consisted of a cantilevered boom structure and two single-axis hinge mechanisms to accurately deploy and position the reflector dish relative to the radar feed horns. The cantilevered design demanded high stiffness and accuracy from the deployment mechanism at the root of the boom. A preload-generating end-of-travel latch was also required. To largely eliminate the need for control systems, each deployment mechanism was actuated by a passive spring motor with viscous-fluid damping. Tough requirements and adaptation of a heritage actuator to the new application resulted in numerous challenges. Fabrication, assembly, and testing encountered additional problems, though ultimately the system was demonstrated very successfully. This paper revisits the development to highlight which design concepts worked and the many important lessons learned.

Introduction

Aquarius Project

Aquarius is the primary, NASA-funded instrument aboard SAC-D, a service platform designed, built, and operated by the Argentinean Comision Nacional De Actividades Espaciales (CONAE). Launched in 2010 with a 3-year earth-orbiting science mission, Aquarius's primary objective is to map sea-surface salinity to better understand the interactions between the global water cycle, ocean circulation, and climate (salinity affects seawater density, which governs ocean circulation). Aquarius's sensitive L-band radiometers measure ocean brightness temperature while a scatterometer corrects for ocean roughness effects. The channels share a 2.5 m x 2.8 m composite Reflector cantilevered from the Instrument Primary Structure.

The Reflector and support Boom must be folded to fit within the 3m fairing of a Delta II (Fig. 1). The Reflector pivots about a single-axis hinge-line between it and the Boom, performed by the Upper Deployment Mechanism (UDM). Similarly, the 2 m long Boom pivots at its root via the Lower Deployment Mechanism (LDM). Once stowed, the Reflector is restrained against the Primary Structure via two pyrotechnic Separation Nuts. Upon reaching orbit, deployment occurs in two stages to prevent the Reflector from dragging across the launch restraints (Fig 1). Staging is provided by a pyrotechnic Pin Puller at the LDM, which carries no launch loads. Initial separation of the Reflector is assisted by Kick-off Springs. At the end of its deployment, each Deployment Mechanism latches into final position.

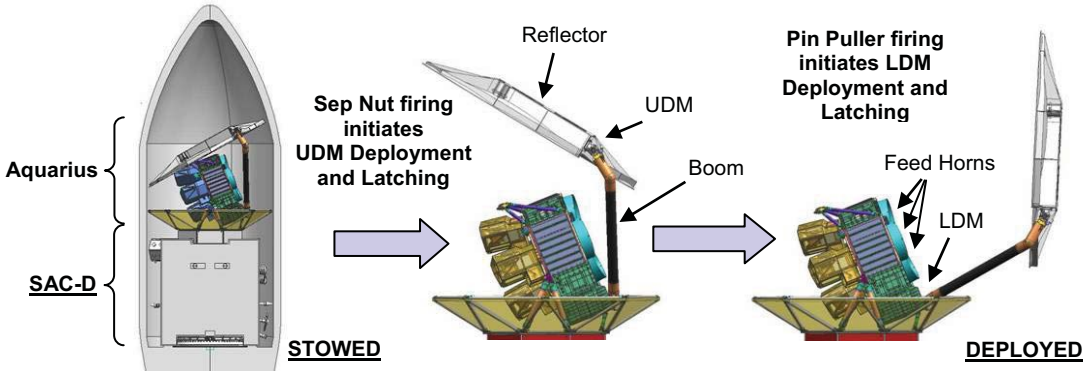

Figure 1. SAC-D Launch Configuration and Aquarius Deployment Sequence

* Jet Propulsion Laboratory, California Institute of Technology, Pasadena, CA

Proceedings of the 39th Aerospace Mechanisms Symposium, NASA Marshall Space Flight Center, May 7-9, 2008.

Together, the Deployment Mechanisms and the Boom comprise the Deployment Subsystem. The overall concept had been accepted at PDR, with actuator selection being an important aspect of the design. “Passive” constant-torque spring motors [1], rate-limited with viscous-fluid rotary dampers, had been chosen to eliminate the need for motor control electronics [2]. JPL’s Spring/Damper Actuator had heritage from Mariner, Viking, Galileo, NSCAT and other missions, but hadn’t been flown in over a decade [3].

The author was tasked with developing the Deployment Mechanisms from this post-PDR level, to overseeing delivery of a single protoflight Mechanism/Boom assembly. The work was carried out at the Jet Propulsion Laboratory, California Institute of Technology, under a contract with the National Aeronautics and Space Administration. The ensuing phases of Design, Fabrication, Assembly, and Test all came with their unique set of challenges, successes, failures, and lessons learned.

Design

Requirements

The requirements that significantly drove design were as follows [4]:

1. The 1st mode of the deployed Reflector shall be greater than 2 Hz (originally 3 Hz)
2. The Reflector I/F shall be positioned relative to the Primary Structure I/F in the nominal deployed location within the following tolerances: (Reflector pointing alignment)
    a. As-delivered: ± 0.1 degree, ± 0.25 mm
    b. Deployment repeatability: ± 0.05 degree, ± 1 mm
    c. Mechanical jitter: ± 0.005 degree, ± 0.25 mm
3. Temperature requirements: (Protoflight/design temps)
    a. UDM Bearings: -75/+45°C Op, -95/+25°C NonOp
    b. Damper: -5/+45°C Op, -50/+60°C NonOp

Requirements 1 and 2c meant that the deployed system needed to be extremely rigid. The rotational inertia of the deployed Boom/UDM/Reflector about the LDM was approximately 200 kg*m^2. An LDM rotational stiffness of about 340,000 N*m/rad (allocation) would be necessary to meet the original 3 Hz requirement. At the same time, the system was tightly mass constrained. This presented a significant challenge, taking months of iteration and optimization to try to develop an acceptable Hinge/Latch design. When it started looking like it might not be possible, the Project relaxed the requirement to 2 Hz with surprisingly little resistance. *The lesson learned was that before spending too much time trying to meet a requirement, find out how rigid (!) it is.*

Lower/Upper Deployment Mechanisms

Each Deployment Mechanism was comprised of the Hinge (Axle/Clevis/Bearings), the Latch, the Spring/Damper Actuator, the Cable Spool, and Telemetry Switches (Fig. 2). The LDM also included a Pin Puller for staging.

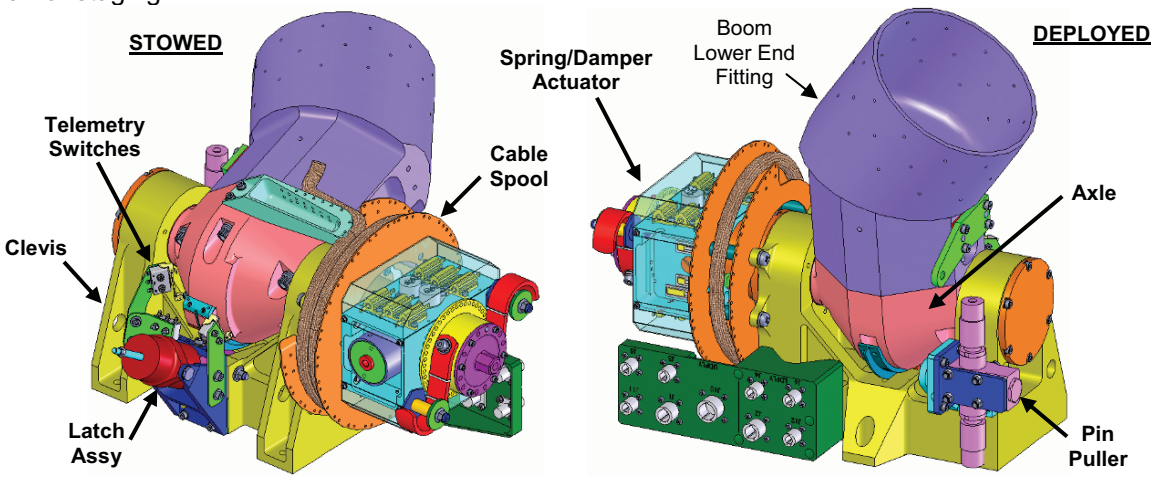

Figure 2. Lower Deployment Mechanism (LDM)

Hinge

The Hinge consisted of an Axle supported on bearings mounted in a structure called the Clevis (Fig. 3). The Spring/Damper deployed the Axle approximately 60 degrees where it hit a Hardstop and a Latch engaged. The force couple between the Bearings and the Hardstop/Latch resisted motion in the deployment direction. Ultimately, the system performance was driven by the stiffness of the structural connection between these two elements, as well as the coupling of this stiffness to the mating structures.

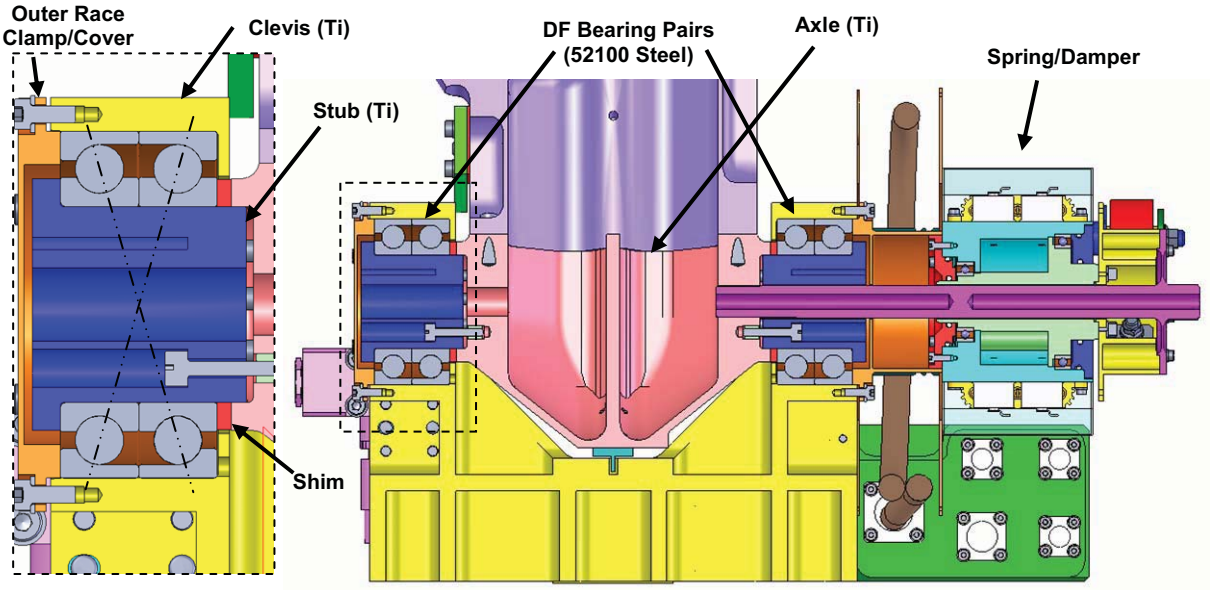

Figure 3. Hinge

The PDR design consisted of a hinge-line created by two angular contact bearings preloaded across the entire mechanism. It had been noted that thermal differentials within the Hinge would make it difficult to maintain the bearing preload, and it was recommended at PDR to switch to a back-to-back duplexed (DB) pair at one end, and a floating radial bearing at the other. Unfortunately, due to the stiffness and pointing requirements, it became impractical to implement a bearing that floated axially. Instead, duplex pairs were installed at each end. To minimize the over-constraints, face-to-face (DF) pairs were used, and a careful procedure of axial shimming was implemented. Temperature effects also had to be carefully considered.

The use of duplex pairs meant the necessary stiffness and load capacity could be achieved in a bearing with nearly half the OD, which would be necessary to keep from doubling the drag. As a result, the Hinge was reduced by about 40% in all three dimensions. However, the Hardstop/Latch was maintained at as great a distance from the hinge-line as practical, since latched stiffness would increase as roughly the square of this distance. Effectively tying all these elements together became crucial for high stiffness, resulting in a very compact design. As such, both the Hardstop and the Latch were made as integral with the Hinge as possible to reduce the structural inefficiencies associated with mechanical interfaces.

The philosophy of minimizing interfaces was used throughout the design. This became especially important when it came to how the Hinge was to be assembled. Parting the Clevis for Axle installation would have resulted in a massive, heavily bolted seam, as well as registration features and special fabrication steps for bearing alignment. Parting the bearing housings would introduce the same issues, as well as uneven bearing support. Instead, the Axle was parted in such a way as to have negligible effect on Hinge stiffness, with none of the other complications (Fig. 3). Radial load on the Stub results in a shear that is carried through the Stub's press fit with the Axle, and a moment that is supported by the toe-heel reaction from the axial Bearing clamping. It also turned out that the clamping could be athermalized through simple selection of fastener length. The Stub Axle design, though initially viewed as unconventional, was very successful in the end.

The system design was further optimized through careful consideration of load paths. This resulted in the somewhat "organic" shape of the Axle and how it "flowed" into the Boom. The lower Boom End Fitting contributes significantly to the stiffness of the Axle and was developed integrally.

A slight exception was that a three-point semi-kinematic interface was implemented between the LDM and the Primary Structure to minimize the potential distortions from bolt-up, because it provided the easiest adjustment if ever required, and because it happened to offer the most direct load path into the Primary Structure at the time. While isolating the Hinge from the mounting interface in this fashion had its benefits, it should be noted that it also had the potentially negative effect of "putting up blinders" to design options that spanned the interface. In hindsight, though the semi-kinematic interface mitigated several *potential* problems, the existing problem of stiffness possibly could have been remedied more quickly and more efficiently had the Primary Structure been modified to help impart stiffness to the Hinge (like was done between the Axle and Boom Fitting). *A lesson learned was to not stop engineering upon reaching an interface. To the extent possible, approaching an interface design from both sides may offer better solutions.*

The inertia supported by the UDM was only about one-tenth of the LDM's, dramatically reducing the stiffness needed to meet the frequency requirement. However, to minimize the number of drawings, parts, test configurations, and spares, it was decided to keep the two Mechanisms as similar as possible. Therefore, the UDM was nearly identical to the LDM, except its deployment angle was shifted by about 20 degrees and it was mass-optimized by thinning most cross-sectional areas of the Axle and Clevis.

Bearings

Every aspect of the Mechanism design encountered complications, and the Bearings were no exception. The initial bearing selection was influenced by the availability of some size 107 spindle bearings left over from another project that would expedite an early brassboard model. To maintain alignment, zero-clearance shaft and housing fits were needed to keep the Hinge axis from permanently shifting under the high radial loads experienced during launch and deployment. At the same time, the Hinge had a very large temperature range because thermal control would be considered only as a last resort. The titanium hardware and the 52100 steel bearings therefore faced a large CTE mismatch problem. Consideration also had to be given to the radial temperature gradient, which strongly affects preload in a DF bearing [5]. Further adding to the challenge, schedule didn't allow for custom-toleranced bearings, nor fabricating the hardware to match the bearings that were available, resulting in an increased tolerance stack-up. Lastly, the bearings would be lubricated with a light grease-plate of Castrol Braycote 601EF, both for simplicity and schedule. At the lower limit of Braycote's recommended temperature range, the high lubricant viscosity would be the dominant source of drag. Lubricant drag calculation had the largest uncertainty, requiring additional conservatism.

Bearing analysis software [6] was used to evaluate the wide range of worst-case scenarios. Maintaining a line-to-line fit at one temperature extreme would result in excessive interference at the other, leading to unacceptably high ball stresses. Therefore, some amount of clearance had to be accepted. Further complication then derived from the software's race clamping inputs. Axial clamp force and coefficient of friction determined if the bearing race was constrained radially by the axial clamping. This effected bearing preload as a function of temperature, depending on whether the race could slip and therefore behave as steel, or if the race was constrained and forced to have a CTE closer to that of the titanium it was clamped between. Given the unreliable nature of the inputs (and somewhat questionable accuracy of the calculated effect), clamping was assumed to always work to the detriment of the system. The final result was that bearing preload and stiffness rapidly dropped off at each end of the temperature range. After many iterations and lots of fine tuning, ID and OD fits were established that just barely maintained the necessary preload at the temperature extremes, without excessive drag elsewhere. While the worst-case analysis was extremely conservative, it was seen as prudent to balance the uncertainty associated with significantly modifying the ground-in preload of duplexed bearing pairs through heavy interference fits (over 25 μm on a 62-mm diameter). The bearings were baselined with a "medium preload" for minimum drag, but with so much hinging on them (!) stiffness testing was planned, and "heavy preload" models were procured just in case additional stiffness was needed. *The lesson learned was that bearings are complicated items with long lead times, and should be one of the first elements designed.*

Latch

The Latch proposed at PDR was a hasp design like that used on Magellan, NSCAT, and MER. As the Hinge was being designed, this type of latch was abandoned in favor of a wedging pawl latch (Fig. 4), based on ability to create preload, stiffness, capture range, and form factor. The Pawl began engaging one degree before the Axle reached the Hardstop, eliminating the potential for rebounding and helping to "drive it home". The Latch Depressor was implemented so that the work of "cocking" the Latch was done in the stowing process, and wouldn't impede deployment. This also simplified analyses and reduced test cases. The Pawl was actuated by a redundant pair of nested helical compression springs, through a simple linkage. The linkage was near its knuckle point in the stowed position, to minimize force and drag on the Latch Depressor, with a snubber to prevent linkage over-center. By the same linkage, the torque applied to the Pawl increased to a maximum at the nominal latched position. A very detailed analysis was performed to calculate the preload force between the Axle and Hardstop generated by the Latch (Fig. 5), which was needed for maximum stiffness. The design resulted in only a 13% preload variability over a large (0.5 mm) range of capture. The Hardstop and Latch Strikeplates could be shimmed for adjustment of the Axle's deployed position, and to center the Latch in the middle of its capture range. The design also had to account for disengaging the Latch after a test, requiring tooling to be developed at the same time.

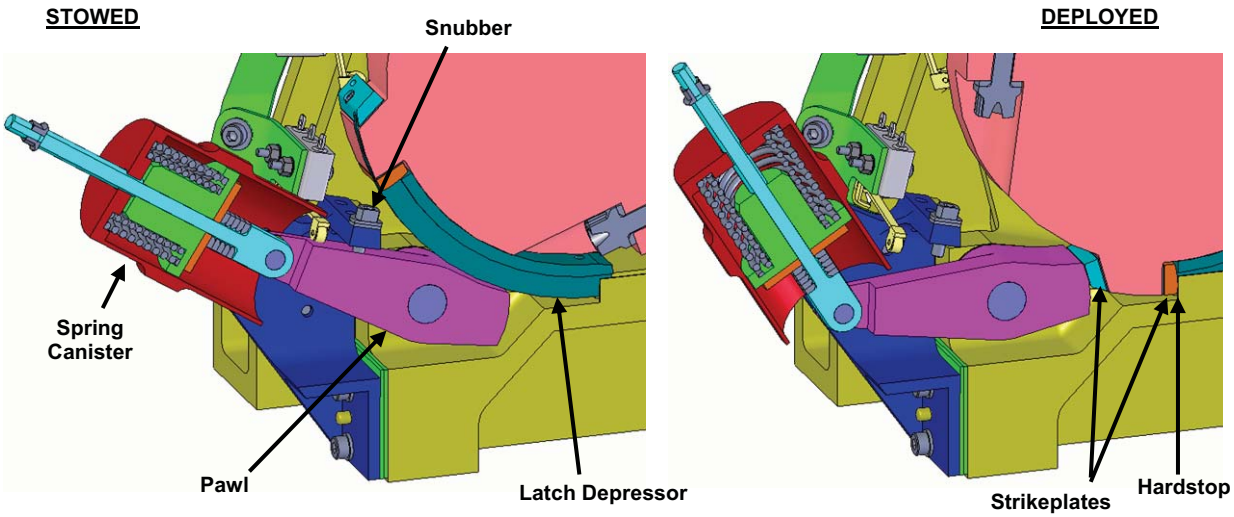

Figure 4. Latch

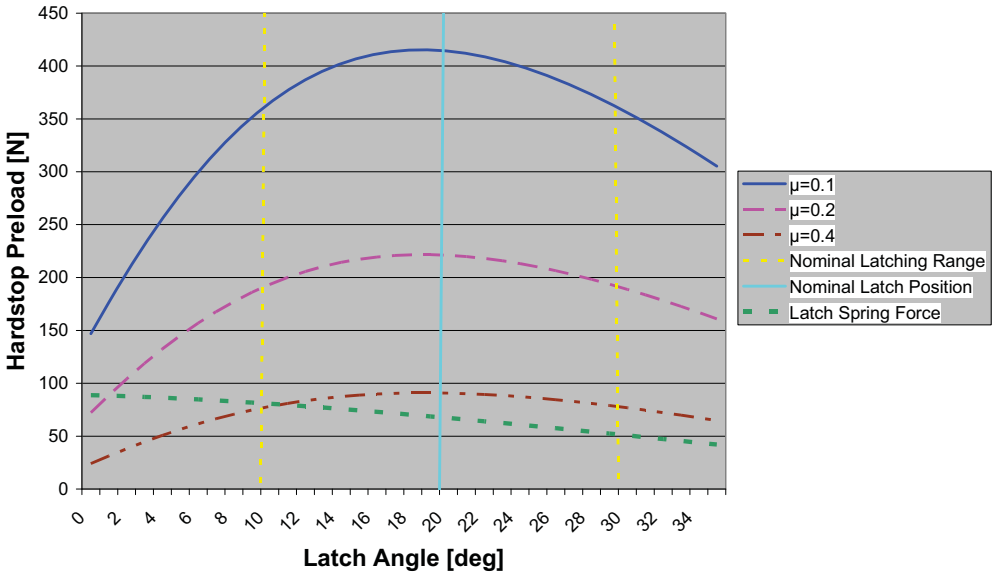

Figure 5. Hardstop Preload due to Latch, for various coefficients of friction

Spring/Damper Actuator

Implementing the heritage Spring/Damper also proved to be considerably more complex than initially planned. The first obstacle was thermal control. Viscosity of the Damper's silicone working fluid was strongly dependent on temperature. After much petitioning, it was finally agreed that the narrow operational temperature band should be actively controlled by the Instrument, while the survival limits could be maintained with mechanical thermostats. Given the high criticality of the Dampers, both redundant heater circuits and redundant thermostats were required. Power resistors were chosen as heaters due to their robustness and simplicity. Finding adequate surface area to mount all the thermal control hardware dramatically altered the exterior of the Actuator from the heritage configuration (Fig. 6).

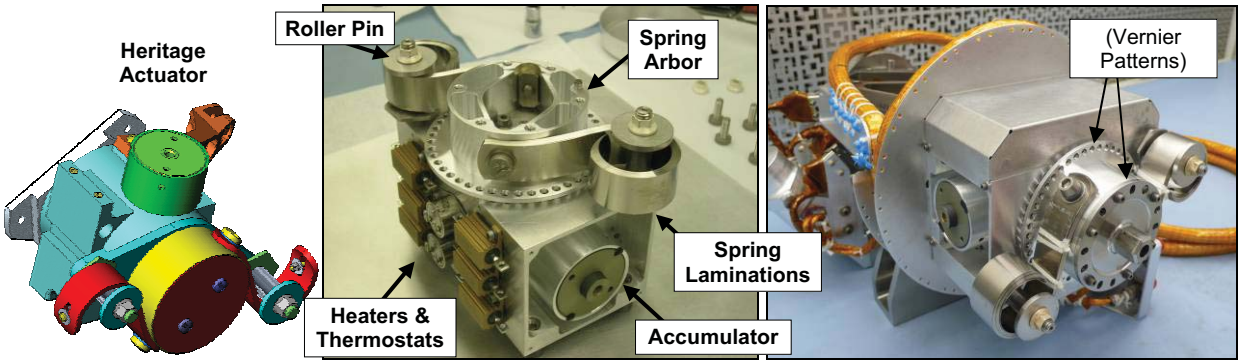

Figure 6. Heritage vs. Aquarius Spring/Damper Actuator

Because the Spring/Damper had flight heritage, there was extreme resistance to making any changes. The fluid dynamics within the Damper were considered especially sacred, mainly because there weren't any of the original developers around. This caused problems because design elements such as bearing fits and spring sizings were not scrutinized adequately, as would be found at assembly. Additional weaknesses and design inconsistencies were perceived, but were not allowed to be addressed. Other elements deemed inconsequential to the damping function, such as direction of rotation, o-ring seals, bearing clamps, structural mounting, and output couplings were modified to facilitate assembly and tailored to the Aquarius implementation. Also, the heritage belleville springs used to generate fluid pressure within the Accumulator were no longer available. Substitutes were found that happened to result in a more constant fluid pressure and were a better material choice. A lubricating PTFE coating on the constant-torque Spring Laminations of the Spring Motor was no longer available, either. Qualifying an acceptable substitute would take time, and application of the coating would complicate the fabrication process. After reasonable investigation, the coating was assessed to be ineffective at solving the spring buckling problem for which it had been implemented, and was eliminated from the design.

The Spring/Damper had to be slightly decoupled from the Axle, so that during launch the dynamic motions of the Boom would not be transmitted and result in extremely high loads. A torsionally-compliant Driveshaft (Fig. 7) was designed, which meant the deploying Reflector could behave more like a pendulum. This was aggravated by the Damper having two damping regimes: low damping initially to accommodate kick-off and stimulate first-motion, transitioning into higher damping to slow the deployment and minimize end-of-travel impact. This transition had the potential to incite deployment oscillations. ADAMS software was used to model the deployment dynamics and tune the Driveshaft. This model was later used as a basis for developing the complicated Gravity Off-Load Fixture (GOLF) that would be used to support the Antenna during instrument-level ground deployments.

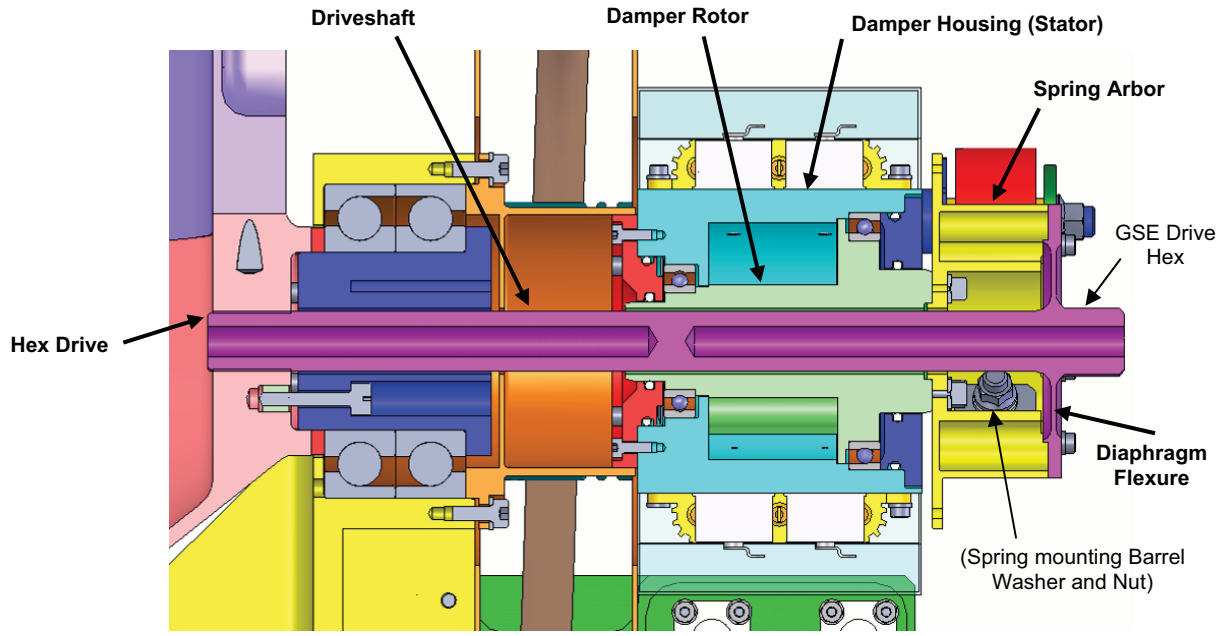

Figure 7. Spring/Damper Driveshaft

The two damping regimes in fact came in very handy. The Spring/Damper had a full stroke of about 100 degrees, while each Mechanism only deployed about 60 degrees. By biasing the deployment more within one damping regime or the other, the total deployment time and behavior could be tuned. To facilitate this adjustment, the Driveshaft was designed with a vernier rotational indexing pattern between the Axle's hex drive and the Damper Arbor's 22.5-degree bolt pattern (Figs. 6,7). The resulting 7.5-degree increment (3*22.5 – 60 = 7.5) allowed the room-temperature deployment time to be systematically adjusted from about 10 s to over a minute in ~10-s steps. This was finer resolution than practical for a splined shaft, and much easier to fabricate. The Driveshaft was also designed to account for misalignment between the Spring/Damper and the Axle. The diaphragm flexure accommodated up to 0.5 mm lateral / 0.2 degree angular error with very little side load, while the potential for handling damage from over-travel was eliminated by the shaft snubbing against the Damper Rotor.

A vernier pattern was also used for locking the Spring/Damper in nearly any rotational position. A pin inserted between holes in the Spring Arbor and Damper Housing (Fig. 6) provided 1 degree position increments, essential when aligning the Driveshaft and during assembly and testing operations.

Figuring out how to assemble the Spring Motor was its own R&D effort. The trouble was how to uncoil the unwieldy and incredibly stiff Spring Stack in order to install the bolt that mounted the Stack to the Spring Arbor. The solution was to assemble the Stack over a spreader bar that held the coil open and allowed the bolt to be installed. Both Stacks were mounted to the Arbor, and then hooked over the Roller Pins. With a big hand tool, the Arbor was then cranked into position and attached to the Rotor. This system worked, but resisting the torque of the Springs while trying to align the Arbor and drop it onto the shear pins in the Rotor was tricky, and could result in damage to the interface. Later, a much easier and safer procedure was developed where the Arbor/Spring assy and Rotor were mated first, the Springs were retracted with a special tool, and then the Roller Pins were installed. *The lesson learned was that assembly considerations and tooling design are just as important as the hardware design.*

Telemetry

The Deployment Mechanisms were equipped with microswitches that provided telemetry about the stowed/not stowed, not deployed/deployed, and not latched/latched states (Fig. 8). Like the Latch, these Switches were implemented such that they were depressed in the stowed state. The Stowed and Deployed Switch Actuating Levers rode on cams and toggled within 1 degree of the Axle stowed and

deployed positions. The Axle had no stop in the stowed direction, so the use of cams allowed Axle over-travel without damage to the Switches. The cams also mitigated the potential of the deployment being stopped by a misaligned Switch [2].

Since the Switches were considered ancillary, they were not given appropriate design attention early on. This resulted in less-than-ideal placement from mounting, functional, and cabling standpoints. Their relative proximity to the Pin Puller also raised concerns about shock sensitivity. A ceramic button in the Switch had a record of failing due to pyroshock. Live firings were performed to measure the shock levels across a breadboard Hinge, resulting in a program to qualify the Switches to 6000 g's. While the Switches themselves passed, the standard two-bolt mounting system failed to keep them from shifting. They had to be adhesively bonded to Brackets, with the Bracket then given an adjustable interface to the hardware. *The lesson learned was that testing will uncover problems that were never imagined.*

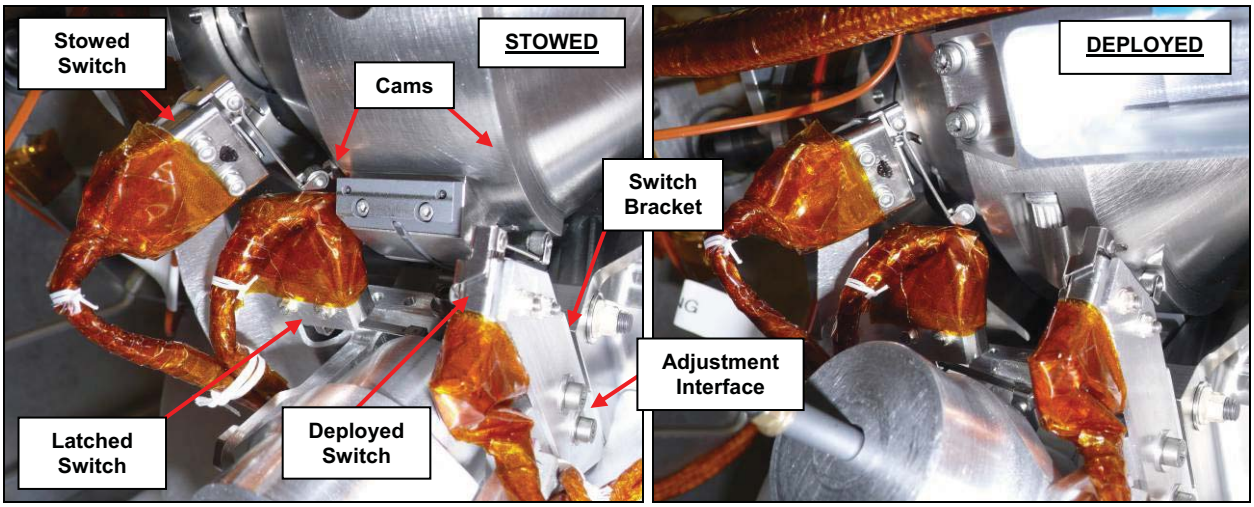

Figure 8. Telemetry Switches

Cable Spool

Electrical cabling to the Reflector and UDM had to pass across the hinge-lines. This was accommodated by a flexing section of round cable held within the Cable Spool (Fig. 9). The section was wrapped snuggly around the Spool for launch, and unwrapped as the mechanism deployed. The fixed ends of the Cable were rigidly attached to the Clevis and Axle via Brackets, so cable motion was controlled and repeatable. This was done with lacing cord for "simplicity" of adjustment, but was actually rather tedious to implement.

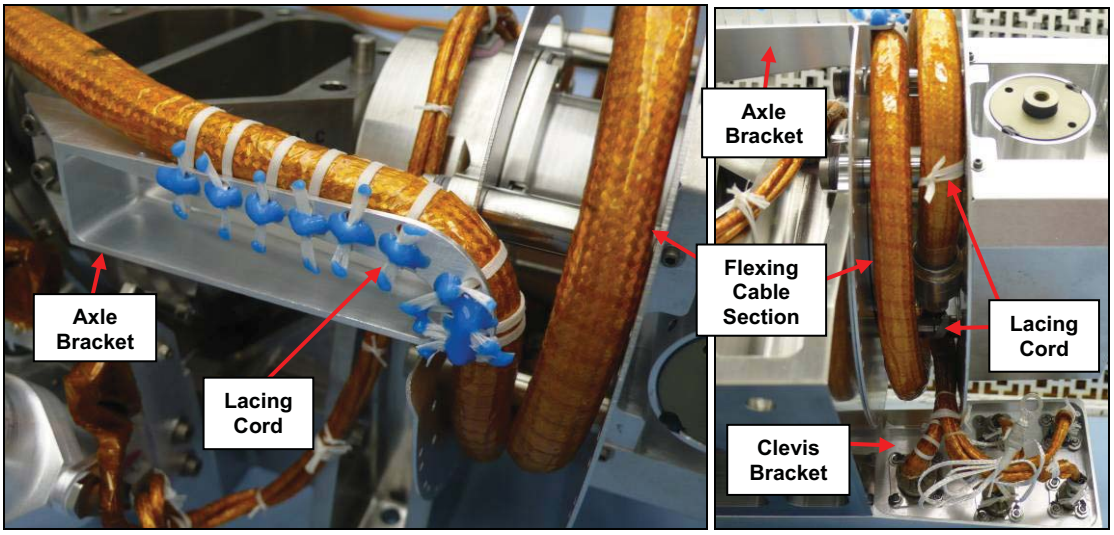

Figure 9. Cable Spool

Pin Puller

Implementation of JPL's standard Pin Puller turned into another development process, since there were no guidelines or requirements on appropriate mounting techniques, clearances, tolerances, etc. The only verbal direction was to mount the Pin Puller so that no side-loads were put on the Pin, requiring adjustable interfaces for Pin alignment. The Pin was rated for loading in double shear, but there was no definition of how that condition was to be created. With a standard tongue-and-clevis arrangement (Fig. 2), and the clearances needed between each, appreciable four-point bending was introduced. The device had to stage deployment of the LDM, without restraining the dynamic motions of the Boom during launch. FEM analysis predicted the amplitude of Boom motion, and the hole in the Tongue was oversized accordingly. This would lead to an impact load against the Pin after Reflector separation, but the driving load case actually resulted from the UDM deployment hitting its Hardstop. While the Inconel Pin was extremely strong, the materials preferred for the Tongue and Clevis all showed significant yielding from the bearing stresses. This yielding added to the bending moment (now in three-point bending) and side loads put on the Pin, and there was concern that the yielded material could get extruded into the joint and cause binding. Despite its load rating, the Pin Puller had to be analyzed. Predictions of the material extrusion were also made, and chamfers were put on the edges of the holes to accommodate it.

Thermal Blanketing

The Mechanisms were to be blanketed with Multi-layer Insulation (MLI). Initially, this was envisioned as a flexing "boot" around the entire Hinge. However, the complexities of designing a dynamic, flexing blanket that would not interfere with the deployment were daunting. The unfavorable testing and validation process won out over the thermal concerns of solar trapping in the unblanketed cavities, and the concept was dismissed in favor of independent, static blanketing and surface treatments of the Axle, Clevis, and Damper.

Fabrication/Procurement

An LDM brassboard unit was built in aluminum to validate Latch design, assess manufacturability and fabrication tolerances, validate the assembly process, validate the stiffness model (though testing never took place), and was used to measure pyroshock levels on the electronic parts due to the Pin Puller. The brassboard came together quickly and wound up being extremely useful, in that it clearly pointed the way though several design crossroads and helped alleviate some lingering design concerns. Stereo-lithography models were also made as cable and blanket mockups. By going to the effort to make them fully articulating, they wound up becoming invaluable for all sorts of unexpected purposes such as verifying interfaces and assembly procedures, developing microswitch locations, testing the Cable Spool, and simply as a visual aid for conveying information. *The lesson learned was to prototype early and often.*

In contrast, obtaining the flight hardware proved to be quite difficult. Vendors were late. Parts were dropped on the floor, or scrapped on the last machining operation. One shop was even broken into and had its computers stolen. A large percentage of fabricated parts arrived out of spec and had to be fixed or remade. A number of discrepancies slipped through the inspection process and were not discovered until assembly. Parts were also "lost in the system", only to show up days after the replacements arrived. Worst of all, acceptable parts were destroyed through careless handling and during simple operations such as installing alignment pins. While everyone agreed that such a large number of problems was atypical, there was little solace in the appreciation of just how right Murphy had been. Assessing the impact of all the problems, and determining the proper courses of action became a second full-time job. *The lesson learned was to only use vendors with a demonstrated history, and even then to take an active role in every step of the process, i.e., via site visits, meeting with the machinists, routine status updates with pictures, personal shepherding of the items through processing, etc.*

Bearing procurement was nearly as frustrating. Between initial investigation and placing the actual order, lead time doubled and became unworkable. As a result, a frantic search for suitable off-the-shelf bearings was launched. This was complicated by the need for proper certs, but eventually IBSCO and Jamaica Bearings Co were able to locate and deliver the required items (or acceptable substitutes) from warehoused stock. The Damper bearings would not be identical to the heritage ones, but analysis indicated they would suffice (fortunately, one of the changes implemented in the new design also resulted

in reducing the bearing loads). The bearings would all require cleaning and lubrication in-house, but this just provided more "opportunities for learning". *The lesson learned was simply, order bearings early!*

Obtaining the Damper fluid took equal patience and luck. While readily available, it could only be purchased in 55-gallon drums, shipped from Europe. Needing only a quart of two different viscosities, this was difficult to justify. One liter samples were free, but certs were out of the question. Samples were requested anyway, under a plan to certify the material in-house through chemical analysis and viscosity testing. As fortune would have it, the samples arrived with lot codes. A quick call to a different department at the manufacturer was all it took to obtain the certs corresponding to those lot codes. *Lesson learned: sometimes it's better to be lucky than good.*

Assembly

The Spring/Dampers were the first items assembled. At this time, a number of design problems were encountered. The heritage wave spring that preloaded the bearings did not fit in the heritage bore. When a suitable off-the-shelf replacement could not be identified, the heritage wave spring was "filed to fit". Its preload force would be reduced, but such was the lesser of many evils. Even worse, the outer bearing race it was preloading should have had a sliding slip fit to the housing, yet when machined correctly per the heritage drawings, there was substantial interference. The only solution was to re-machine the Damper Housing. Adding insult to injury, the Heater Resistors had been modeled mirror-image, resulting in a reversed bolt pattern. While mounting the Resistors upside-down was considered, the proper solution was to disassemble the Damper yet again for re-machining. There were also repeated problems with pinched o-rings, though luckily all were immediately obvious from the incomplete seating of the parts. This had historically been a problem, and unfortunately wasn't solved despite paying special attention to the design of the o-ring glands. Subsequently, the Dampers underwent a helium sniff test to check for leaks prior to filling. *The lesson learned was that heritage designs need to be completely analyzed and understood, or else they may surprise you. Also, always dry-fit assemblies to discover problems early, and recognize that o-rings can be finicky.*

As mentioned earlier, installing the deployment Spring Lamination Stack was tricky due to the bolting of the Stack to the Spring Arbor. This was made more difficult by having to thread the bolt into the stationary barrel nut, during which operation the hard Springs wore on the fully-threaded bolt causing damage and generating debris. In addition, the Hi-Torq recess of the heritage fastener continually stripped. Drilling out the threads to make a barrel *washer* allowed the bolt to remain stationary, and a standard, locking nut to be installed from the back (Fig. 7). The bolt was also changed to one with a grip and hex wrenching, making assembly a snap. *Here, the lesson learned was that tricky assembly procedures should be practiced ahead of time.*

As with the heritage devices, the Spring Motor developed a heritage problem. As the actuator deployed, each spring lamination coiled at a slightly different rate than the one next to it due to the difference in rolling diameter. This required the laminations to slide over each other. The inner laminations were also heavily pinched against the Roller Pin due to the force of all the laminations above. The resulting interlaminar sliding friction and the Roller Pin drag generated enough resistance to the coiling of the inner laminations that they would instead "bunch up" ahead of the Roller Pin in a runaway buckling fashion (Fig. 10). This was the case for nearly the inner third of the laminations, at which point the force from those above was low enough to allow the necessary slippage. The earlier decision to not lubricate the Springs increased the problem, and a few spare (coated) Springs from Galileo were used in the innermost two positions. This helped, but didn't solve the problem completely (which is probably why it had been deemed ineffective). The Vespel SP-3 (MoS_2) Roller Pin Sleeves were wet lubricated with Braycote, and the OD of the Sleeves was increased to give greater mechanical advantage over the rolling friction (though this wasn't implemented), each with further improvement. The ultimate solution wound up being the heritage solution, which was to band the laminations together with lacing cord. While not graceful, this was the only approach that offered any sense of reliability. *The lesson learned was that while heritage should be appropriately scrutinized, don't be <u>too</u> eager to change a design.*

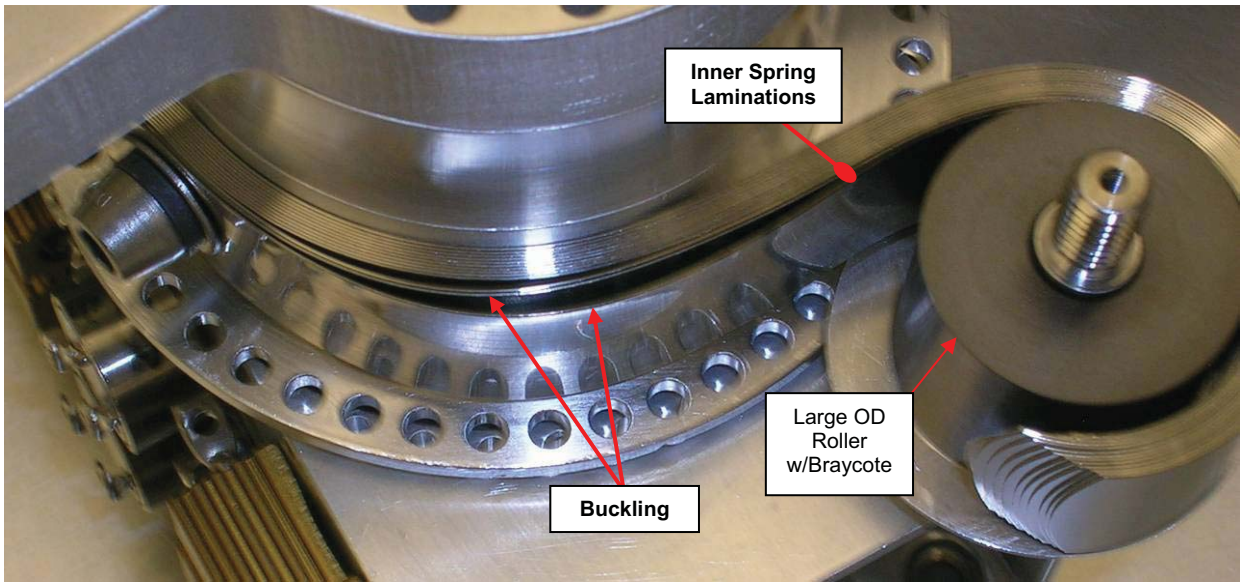

Figure 10. Actuator Spring Buckling

Reconstructing the system used to fill the Dampers was again another big task. Filling was done under vacuum, with a gas-actuated “syringe”. The fluid was first outgassed, then drained into the piston of the syringe and injected into the Damper. Everything was heated to expedite the process, since the fluid was extremely viscous. Learning the idiosyncrasies of the system took practice, and some redesign was required to get it working properly. One unexpected difficulty was simply finding a location for the bell jar. Intentionally heating and outgassing silicone oil was not something folks wanted anywhere near their clean rooms. Instead, a clean tent had to be built. The first usage was filling heritage actuators to characterize how fluid viscosity affected deployment rate. As the viscosity was increased, the damper began having erratic behavior, similar to that reported by Stewart, Powers, and Lyons [7]. It was suspected that the fluid was cavitating, or the damper was not filled completely. Having not anticipated such a problem, the fill volume had never been precisely characterized, nor the empty damper weighed for comparison. Disassembly might destroy the evidence. The damper was x-rayed, but the energy required to penetrate the thick aluminum housing left the fluid nearly transparent. However, by standing the damper on end for a while, and then flipping it on its side and taking a series of x-ray images, a very faint line was seen to slowly move (Fig. 11). Since no free movement was possible in a full damper, the line was assumed to be the surface boundary of the fluid where the meniscus was tangent to the view. This discovery led to the realization that the heritage filling pressure was far too low, and that the fluid heating was inadequate. These issues were remedied, and there were no further filling anomalies.

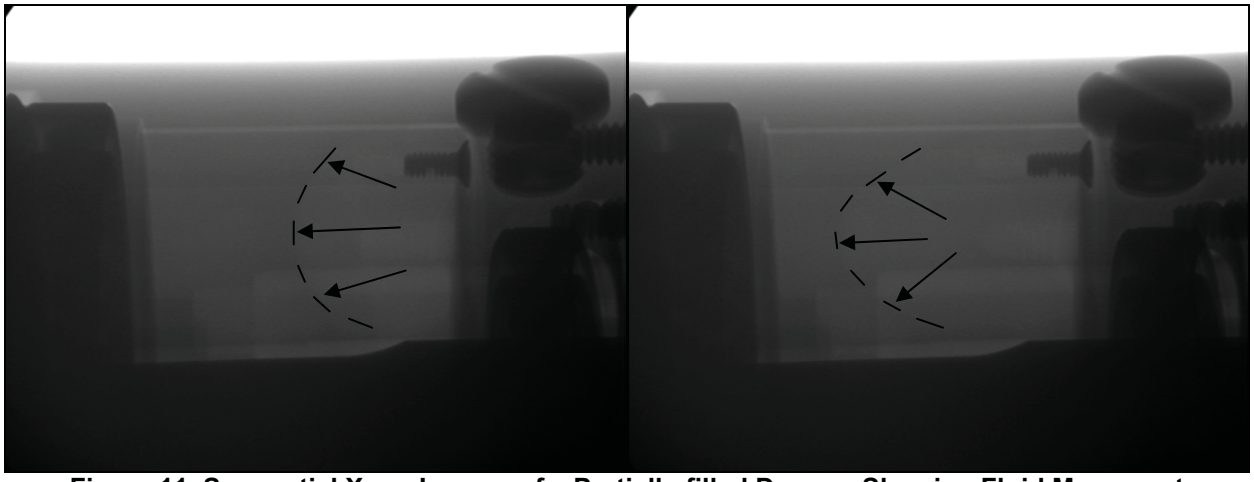

Figure 11. Sequential X-ray Images of a Partially-filled Damper Showing Fluid Movement

Assembling the Hinges and Latches went relatively smoothly, once all the known dimensional discrepancies had been corrected. Special tools were made for pressing in the Bearings and Stub Axles, so that no load was applied across the balls. Fortunately, disassembly had also been considered in the design phase. This came in very handy when one of the Stub Axles was installed improperly and needed to be removed. Simple design features allowed what could have been a real catastrophe to be only a minor inconvenience. *Lesson reinforced: always consider disassembly, especially for items with press fits.*

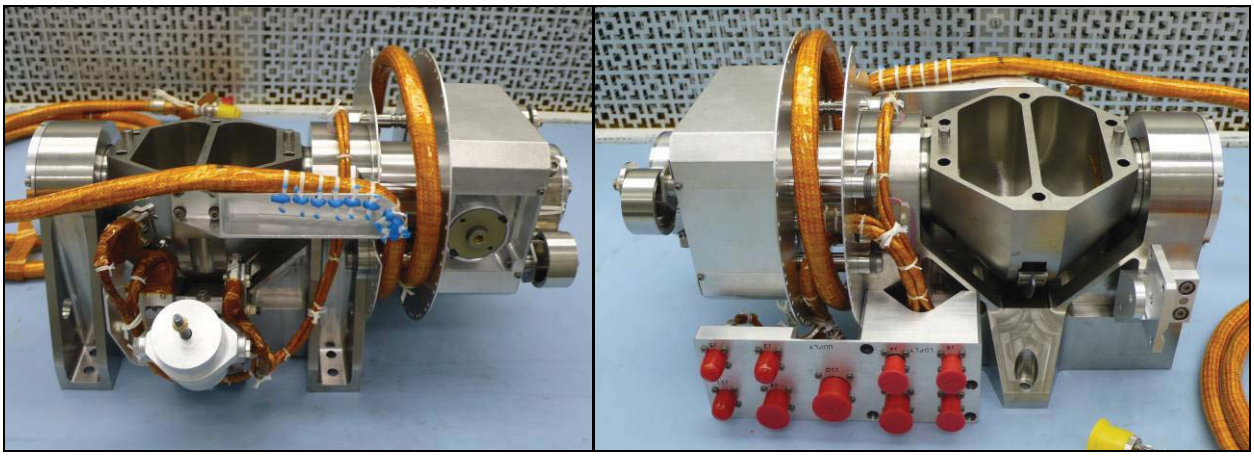

Figure 12. Assembled LDM

Boom

To meet alignment requirements, the Boom was bonded using the flight LDM and UDM as fixturing. After functionally verifying the Mechanisms, they were mounted to a jig that represented the deployed Primary Structure and Reflector interfaces, and the Boom was assembled between. All piece-part fabrication tolerances were thereby taken up in the bondlines, and the end-to-end alignment was as good as the jig.

Testing

Temp/Atm Deployment and Stiffness Testing

The start of mechanism testing turned out to be a real eye-opening experience. The objectives of the first Temp/Atm Deployment Test were to functionally demonstrate deployment and latching of the Mechanisms at temperature, and to satisfy thermal cycling requirements. Stiffness Testing was then designed to apply a moment to the Hinge, at temperature, and measure the resulting rotational deflection. The Clevis was mounted to a rotation stage having a horizontal axis, and a large weight was cantilevered off the Axle to apply the moment (Fig. 13). The resulting deflection was measured by linear variable displacement transformers (LVDT's). Slowly rotating the stage through 360 degrees resulted in one complete load cycle and a mapping of the hinge stiffness.

Regrettably, test preparations were neglected due to all the fabrication and assembly issues. In the panic to catch up, the test engineer took many shortcuts and wound up making many mistakes. In the end, far more time and resources were spent fixing the resulting problems than if testing had been delayed to allow for proper preparation. Without going into all the gory and embarrassing details, the following list highlights a number of lessons learned. *The most important lesson of all was that test development requires the same level of attention, scrutiny, review, and verification as the hardware to be tested.*

- *Be sure all test requirements are well established and communicated to all supporting parties*
- *Verify the complete test setup prior to testing. That means functionality, mechanical interfaces, electrical cabling, thermal control, and especially the data acquisition system are all thoroughly demonstrated under environmental conditions*
- *When designing GSE to interface with flight hardware, simply duplicate the flight interface rather than try to re-engineer it from scratch*
- *It's better to have two simple test fixtures than one complicated one*
- *Make accurate predictions of the expected test performance*

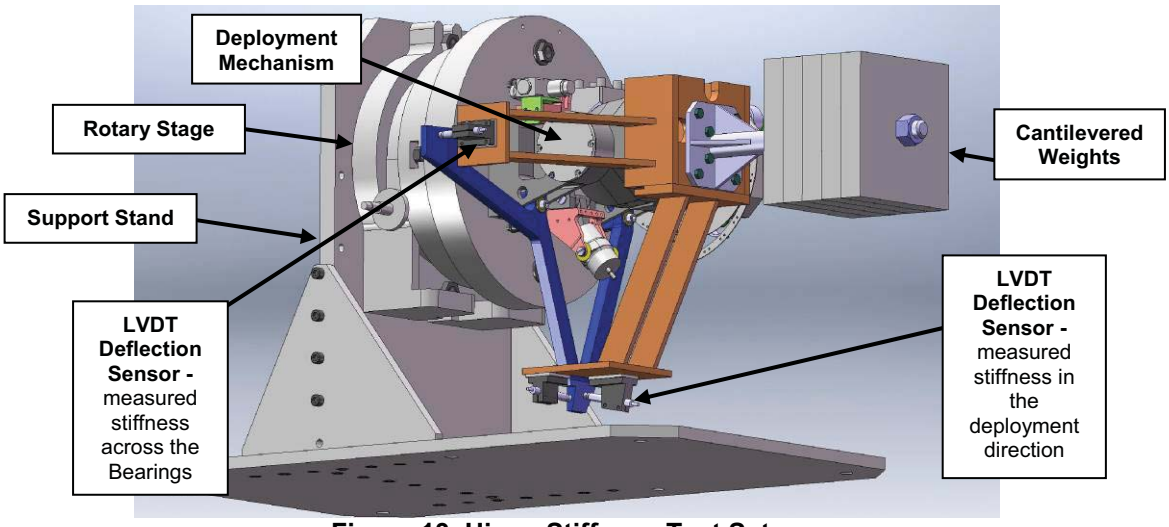

Figure 13. Hinge Stiffness Test Setup

The only hardware issue of any significance wasn't uncovered until well after testing. When the test report was delivered, it was discovered that the post-test deployment time of each Mechanism was roughly 30% longer than the pre-test deployment time. The Mechanisms had undergone enough rework since the testing that studying the hardware would yield little insight. Even worse, the associated data files couldn't be located. After subsequent testing to rule out some possibilities, the leading suspect was increased bending resistance of the Cable in the Spool due to the thermal cycling. The investigation into this anomaly is ongoing, including life-testing of the actuators. *The lesson learned is that even if a test seems successful, review the data immediately and make sure to back it up.*

Mockup Inertia Margin Testing

The objective of Mockup Inertia Testing was to verify and characterize the Mechanisms under flight-like conditions, and to demonstrate actuator margins. Each Mechanism was bolted to the wall of the lab, and an insulated thermal chamber was built around it (Fig. 14). An inertia mockup representing the mass and stiffness properties of the flight deployable was attached to the Axle. Deployment was horizontal, and gravity offloading was provided by a cable that pivoted about a point on the axis of rotation. The Axle was held in the stowed position by an electromagnet. For the UDM, the separation Kick-off Springs were also represented. Axle position was recorded with an encoder, Telemetry Switches were monitored, and the final deployed and latched position was measured for repeatability with a dial indicator.

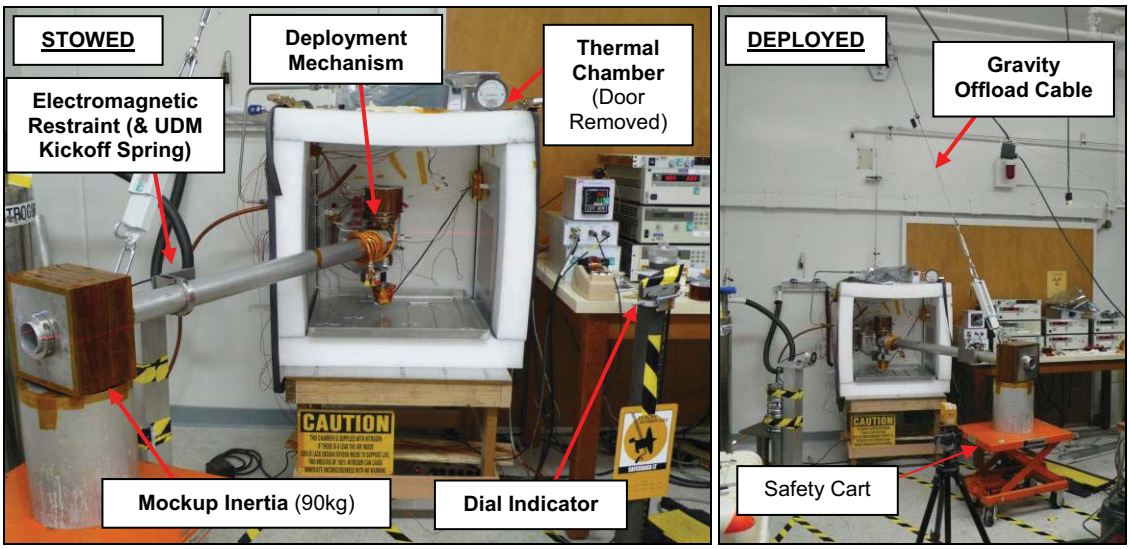

Figure 14. Mockup Inertia Margin Test Setup

With spring-driven actuators, demonstrating torque margin was more complicated than just turning down a power supply. The Spring Motor produced torque from two stacks of spring laminations. One stack was decoupled to reduce the torque output by half. Successful deployment under the worse-case-drag conditions therefore demonstrated at least 100% margin. The Latch was similarly handicapped by removing one of the redundant springs, and 100% margin was demonstrated in a maximum deployment velocity scenario.

With a new test engineer, and having learned a lot from the previous testing, things went much more smoothly, but not perfectly. The biggest issues were with the data acquisition system, which still had a number of bugs and other problems. There was also a lot to learn about constructing a thermal chamber. While thermal regulation with heaters and LN_2 was fairly straightforward, preventing condensation was not. Water molecules are extremely mobile, and even positive pressure along with purge rates over 15 volume exchanges per hour didn't eliminate frosting of the hardware. Also, directing GN_2 into an LN_2 stream can result in snow as the moisture in the GN_2 freezes.

Conclusions

The Aquarius Deployment Mechanisms enabled the radar Reflector to be stowed for launch and deployed on-orbit. While the Mechanisms were relatively simple latching hinges, the challenging requirements demanded extreme scrutiny of every design detail. Use of a heritage Spring/Damper Actuator faced the dilemma of trying to maintain heritage while simultaneously having to adapt to the new implementation. Unending fabrication, procurement, and assembly issues caused test preparations to be neglected, which in turn led to terrible testing difficulties. Despite all the challenges and setbacks, the Deployment Mechanisms ultimately exceeded all of their performance requirements. Many important lessons were learned in the process, as described throughout the paper.

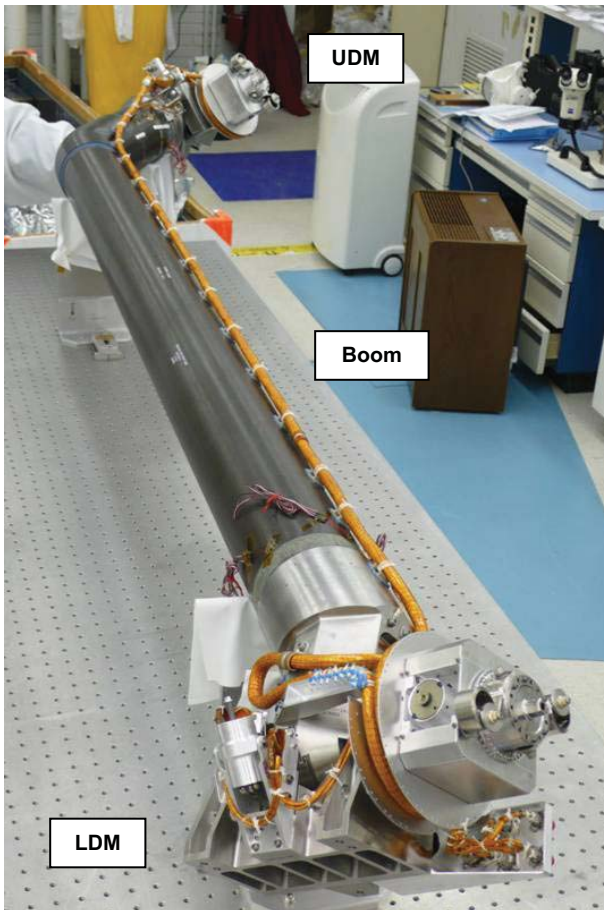

Figure 15. Final Deployment Boom Assembly

References

1. John R. McGuire and Joseph A. Yura, "Advances in the Analysis and Design of Constant-Torque Springs", *30th Aerospace Mechanisms Symposium, May 1996, pp. 205-220*
2. Robert L. Fusaro, "NASA Space Mechanisms Handbook", *NASA-GRC, NASA/TP—1999-206988, July 1999, pp. 145-152 (damper), pp. 94-95 (telemetry switch)*
3. Jack D. Harper, "Viscous Rotary Vane Actuator/Damper", *10th Aerospace Mechanisms Symposium, April 1976, pp. 198-207*
4. "L4 Aquarius Mechanisms Subsystem Requirements, Initial Release", *JPL Document D-35155*
5. Alexander H. Slocum, "Precision Machine Design", *Society of Manufacturing Engineers, Dearborn MI, Jan 1992, pp. 464-468, 539-543*
6. Alan R. Leveille, "Bearings Analysis Program Version 10 C", *Licensed by The Aerospace Corporation, El Segundo CA*
7. Alphonso Stewart, Charles Powers, and Ron Lyons, "Improvements for Rotary Viscous Dampers used in Spacecraft Deployment Mechanisms", *32nd Aerospace Mechanisms Symposium, May 1998*

Deflection Analysis of the Space Shuttle External Tank Door Drive Mechanism

Michael A. Tosto[*], Bo C. Trieu[**], Brent A. Evernden[+], Drew J. Hope,
Kenneth A. Wong and Robert E. Lindberg

Abstract

Upon observing an abnormal closure of the Space Shuttle's External Tank Doors (ETD), a dynamic model was created in MSC/ADAMS to conduct deflection analyses of the Door Drive Mechanism (DDM). For a similar analysis, the traditional approach would be to construct a full finite element model of the mechanism. The purpose of this paper is to describe an alternative approach that models the flexibility of the DDM using a lumped parameter approximation to capture the compliance of individual parts within the drive linkage. This approach allows for rapid construction of a dynamic model in a time-critical setting, while still retaining the appropriate equivalent stiffness of each linkage component. As a validation of these equivalent stiffnesses, finite element analysis (FEA) was used to iteratively update the model towards convergence. Following this analysis, deflections recovered from the dynamic model can be used to calculate stress and classify each component's deformation as either elastic or plastic. Based on the modeling assumptions used in this analysis and the maximum input forcing condition, two components in the DDM show a factor of safety less than or equal to 0.5. However, to accurately evaluate the induced stresses, additional mechanism rigging information would be necessary to characterize the input forcing conditions. This information would also allow for the classification of stresses as either elastic or plastic.

External Tank Door Background

The ETD cover openings in the Orbiter's underside, which are access regions for the umbilical and structural connections between the External Tank (ET) and Orbiter. The ETD sits at the aft underside of the Orbiter, and is prominently visible in its open configuration in Figure 1.

After jettisoning the ET during ascent, these doors are closed while on orbit and remain closed throughout the duration of flight and descent, until they are opened after landing for inspection. Proper door closure is critical to avoid excessive aero-heating during descent through the Earth's atmosphere. Thermal analysis has shown that if the doors are not fully closed and aligned with surrounding TPS tiles within 3.8 mm (0.15 in), a safe descent would be questionable [1].

The three main ETD subsystems are the Centerline Latches (CL), Door Drive Mechanism (DDM), and Uplatch Mechanism (UM). The CL locks the doors in their open configuration while the ET is connected to the Orbiter and throughout the ascent stage. With the ET jettisoned, and while in orbit, the DDM is commanded to move both doors from their open to closed configuration. Finally the UM, which has three hooks, is activated to latch the doors in their closed configuration and compresses the thermal and pressure seals for proper closure. Figure 2 shows a close-up of the starboard-side door with the DDM and the three hooks of the UM highlighted.

[*] National Institute of Aerospace/University of Virginia, Hampton, VA
[**] NASA Langley Research Center, Hampton, VA
[+] NASA Johnson Space Center, Houston, TX

Figure 1. OV-103, *Discovery*, Before STS-114

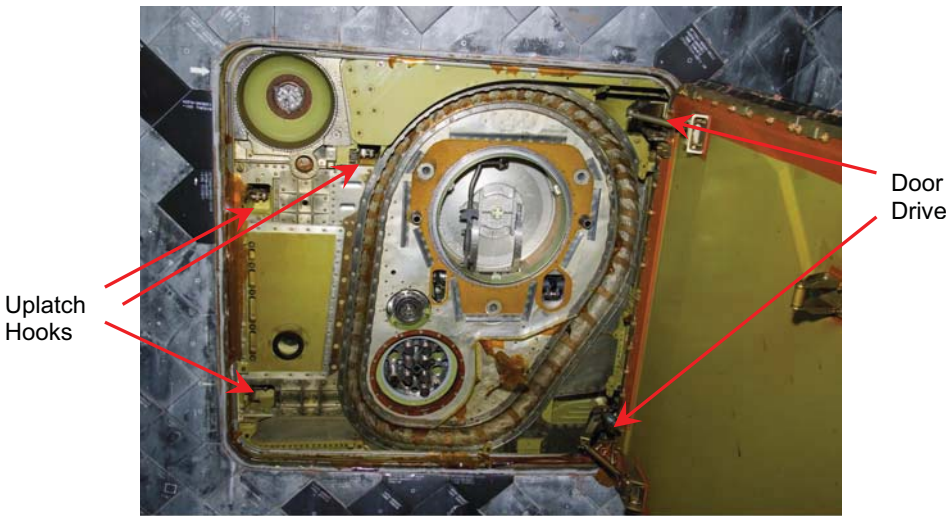

Figure 2. Close-Up of ETD Showing Uplatch Hooks and Door Drive

A Pro/E CAD model of the port-side ETD including the DDM and UM in its closed and latched configuration is shown in Figure 3. Actuators are not shown.

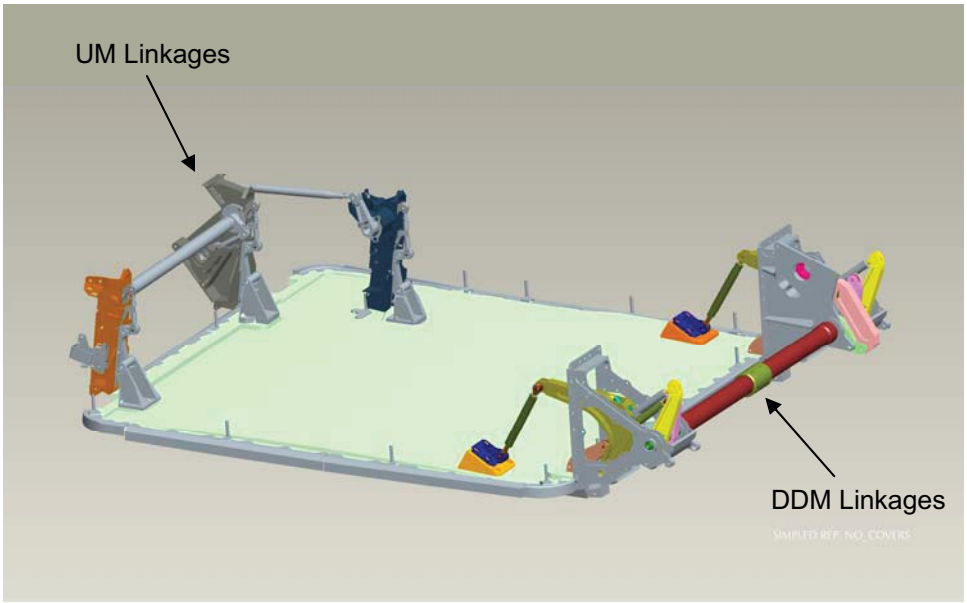

Figure 3. Port Side ET Door Configuration including DDM & UM

Analysis Approach

During the Space Shuttle mission STS-118 of August 2007, ground telemetry data indicated that the ETD did not fully complete their travel before the uplatches were commanded to engage. Because the DDM actuator has a fail-safe brake that engages when no power is applied, the mechanism is constrained at its input link as the door is forced to close. This constraint at the input link effectively creates deflection in the DDM linkages during uplatch operation and will therefore induce an associated stress.

FEA is frequently used to calculate stress for such loading conditions. Within this approach, a single analysis will describe the static loading of a given mechanism configuration. Additionally, the analyst must create a mesh of the entire mechanism, and then re-mesh for each configuration of interest. This process can be both labor intensive and time consuming, and most importantly, the mechanism dynamics are lost in such quasi-static analysis.

In this paper an alternative modeling approach is proposed for use in the multi-body dynamics software MSC/ADAMS. This approach utilizes lumped parameter approximations to model the compliance of individual parts within a mechanism. To represent each flexible part, single degree of freedom linear springs were introduced for links in tension and compression, while torsional springs at the base of rigid cranks were used for links in bending. With the door drive input crank fixed, the door was then forced to close, thereby simulating the conditions seen by the actual mechanism. To validate the representative equivalent stiffnesses, each was iteratively updated until convergence using the ratio of FEA stresses calculated based on spring deflection and spring force.

Modeling

Simulation to Obtain Deflections

Normal operation requires that two sets of indicators, at the uplatch hooks and in the door drive actuator, are both observed during door closure before running the uplatches. However, during the STS-118 mission only the first set of these indications was initially obtained. Therefore the door was within the

capture envelope of the UM (51 mm or 2 in from complete closure), but had not fully reached its intended latching location. Because the DDM's actuator brake is on during uplatch operation, the proposed analytical approach is used to find the induced deflections in the DDM linkages due to this unusually long uplatch stroke. Based on these deflections, or alternatively the associated spring forces, linkage stresses can be computed. For elastic deformations, cycling the ETD's DDM and UM mechanism will return the door to its final closed configuration with respect to the Shuttle as expected. If plastic deformations have occurred then the door may form gaps or a step with respect to the Shuttle.

The Pro/E model of the DDM shown in Figure 3 had been previously constructed at JSC and LaRC, and was used as a starting point for subsequent analysis. This model was imported into ADAMS, with the appropriate piece-parts merged into functional moving parts. As shown in Figure 4, the door rods within ADAMS are a simplified geometric representation of the actual linkage. For the purpose of the mechanism analyses, we chose to represent these links as rod elements with revolute joints at each end.

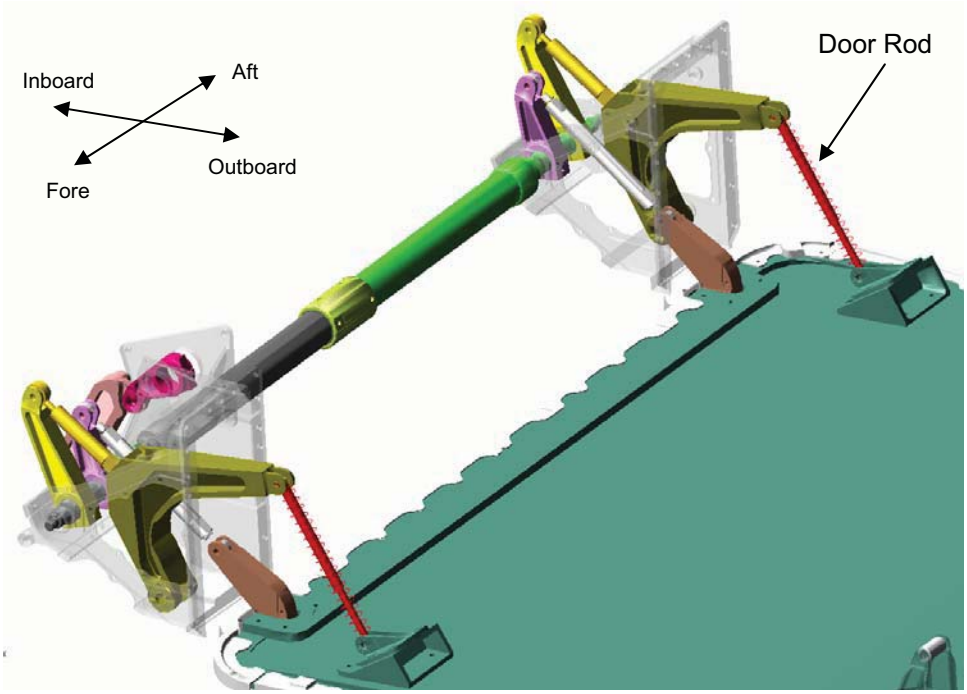

Figure 4. ETD Door Drive Mechanism

For deflection analyses, the linkages of the DDM are represented in ADAMS as spring or compliant members, while the door and shuttle frame are considered rigid. Figure 5 shows each part of the linkage and its spring equivalence depending on loading: linear springs are used for tension or compression and torsional springs (at the base of a rigid crank) for bending. For the "follower 1" part, both compression and bending loads exist, thus both linear and torsional springs are used respectively.

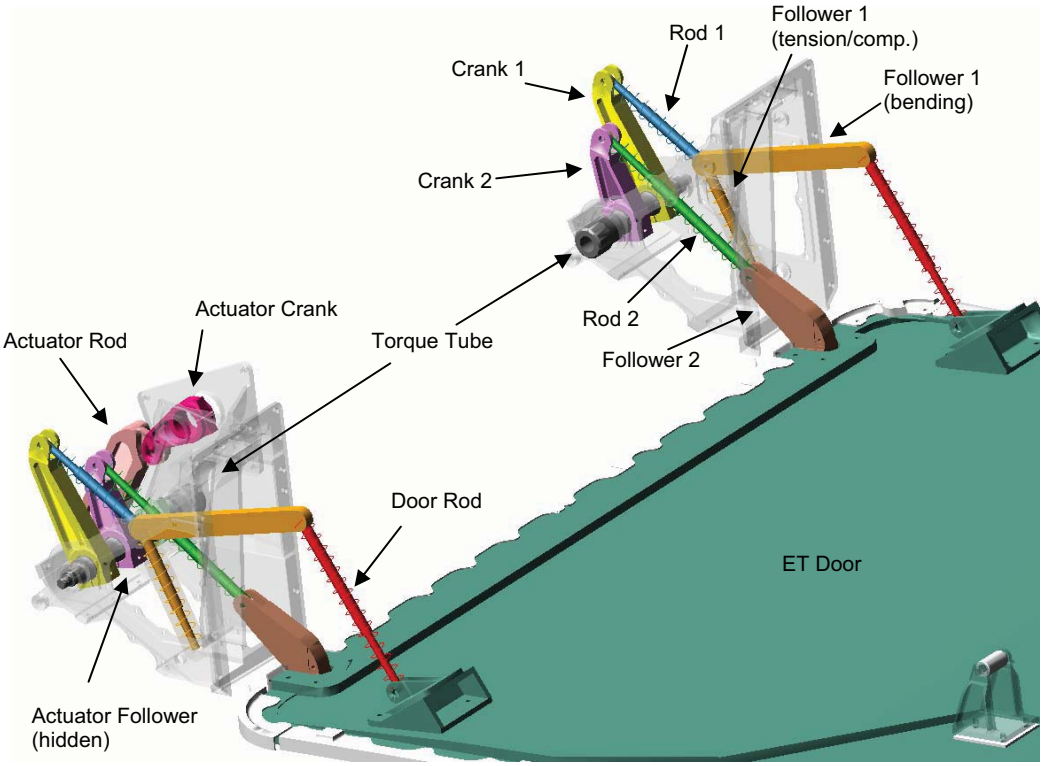

Figure 5. Spring/Compliant Representation of the DDM

To find initial equivalent stiffnesses for use in this lumped parameter model, a representative cross section of each part was taken near its midpoint and used to find values of cross sectional area (A) for linear springs and area moment of inertia (I) for torsional springs. Linear stiffness was found using equation (1) for a rod under axial load [2], and torsional stiffness was found using equation (2) for a cantilever beam with end load, assuming small deflections.

$$k_{eq} = \frac{EA}{l} \qquad \left[\frac{\mathrm{N}}{\mathrm{mm}}\right] \tag{1}$$

$$k_{eq} = l^2\left(\frac{3EI}{l^3}\right)\left(\frac{\pi}{180}\right) \qquad \left[\frac{\mathrm{N\cdot mm}}{\mathrm{deg}}\right] \tag{2}$$

To run the dynamic simulation, the actuator crank is fixed (motor brake is on) while the opposing edge of the door is forced to move in the closing direction 25.4 mm (1 in). According to the door's rigging specifications, actuation of the DDM must leave the door between 25.4 mm (1 in) and 44.45 mm (1.75 in) of the fully closed and latched configuration under gravity [3]. Therefore, if the door were to stop short at 50.8 mm (2 in), then the maximum amount of additional displacement would be 25.4 mm, if the door were rigged to its minimum sag of 25.4 mm. Figure 6 shows this requirement, as presented in the ETD installation and rigging procedure [3].

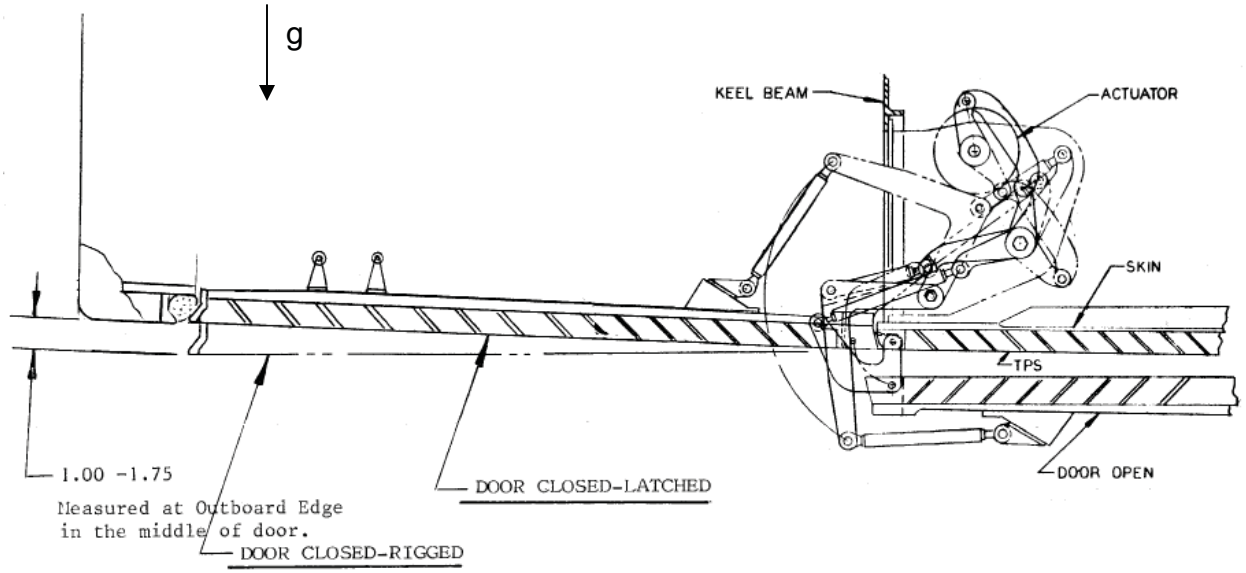

Figure 6. Port-side Door Looking FWD, Door Sag Specification

Iteration of Stiffness Approximations

If FEA is used to find stress in each component based on the results of dynamic simulation, this corresponds to a switch from a lumped parameter model in MSC/ADAMS to a distributed model in MSC/NASTRAN. While the resulting deflections and forces are analytic within ADAMS, where force and displacement for each link obey Hooke's law for a given equivalent stiffness, stresses computed in FEA using boundary conditions (BCs) based on these displacements and forces will be different unless the equivalent stiffness is the same in both models. In a linear static analysis, stress is proportional to force; therefore the ratio of stresses in these two load cases is equal to the ratio of applied force respectively. Equation (3) shows this relationship, where the subscript "disp" signifies an FEA model with displacement BCs, and "force" signifies an FEA model with force BCs. Similarly, subscripts "f" and "ds" indicate FEA and dynamic simulation respectively. After running an initial dynamic simulation and calculating the associated stresses, k_f is the only unknown in equation (3).

$$\frac{\sigma_{disp}}{\sigma_{force}} = \frac{F_{disp}}{F_{force}} = \frac{F_f}{F_{ds}} = \frac{k_f x_{ds}}{k_{ds} x_{ds}} \tag{3}$$

An iterative process is employed to ensure that the equivalent stiffnesses k_f and k_{ds} are in fact the same. By updating the value of k_{ds}, the stress ratio shown in equation (3) can be manipulated. When this ratio becomes equal to one, k_{ds} is therefore equal to the unchanged value of k_f. After an initial set of deflections and forces is obtained from the ADAMS model, these results are used as the input to a NASTRAN model of each flexible component. Using the stress ratio described above, a new equivalent stiffness for each link is computed according to equation (4). This result is then used to update the ADAMS model, thereby completing the loop of a process that can be repeated until convergence.

$$k_f = \left(\frac{\sigma_{disp}}{\sigma_{force}}\right) k_{ds} \quad \Rightarrow \quad k_{ds}[i+1] = \left(\frac{\sigma_{disp,i}}{\sigma_{force,i}}\right) k_i[i] \tag{4}$$

Results

Deflections

Table 1 shows the deflection of each part in the linkage from the initial iteration of ADAMS simulation. These deflections are used to compute the stress in each linkage member to classify it as either elastic or plastic deformation.

Table 1. Deflections in the DDM for 25.4 mm (1 in) at Door Edge

Linear Deflections		
Location	**Part**	**(mm)**
Aft Hinge	Follower 1	5.67E-02
	Rod 1	-3.05E-02
	Rod 2	5.74E-02
	Door Rod	-1.74E-01
Fore Hinge	Follower 1	4.80E-02
	Rod 1	-2.57E-02
	Rod 2	1.08E-01
	Door Rod	-1.48E-01
Actuator	Actuator Rod	-2.23E-01

(positive = tension, negative = compression)

Angular Deflections		
Location	**Part**	**(deg)**
Aft Hinge	Follower 1	1.63E+00
	Crank 1	3.09E-01
	Crank 2	-2.54E-01
Fore Hinge	Follower 1	1.38E+00
	Crank 1	2.59E-01
	Crank 2	-4.76E-01
Actuator	Actuator Crank	-2.00E-01
	Actuator Follower	3.15E-01
Torque Tube	Tube	-2.64E-01

(positive = fore [right hand rule])

Convergence of Equivalent Stiffness

Using the previously outlined process, stress ratios were calculated at iteration 0 and compared to the predicted stress ratio, calculated as a stiffness ratio. To find this stiffness ratio, the manually calculated approximate stiffness was used in place of k_{ds}, and a stiffness found directly from a finite element model (by applying a representative load of 4448 N (1000 lbf) and extracting the displacement) was used in place of k_f. These values are shown in the columns marked “K ratio [0]” in Table 2 and Table 3. Stress ratio values after one iteration, which should approach 1, are shown in the columns marked “σ ratio [1]”.

Table 2. Convergence of Stress Ratios, Links Axially Loaded

Location	Part	K ratio[0]	σ ratio[0]	σ ratio[1]
Aft Hinge	Follower 1		1.016	1.011
	Rod 1	0.619	0.636	1.004
	Rod 2	0.829	0.835	0.997
	Door Rod	0.829	0.832	1.009
Fore Hinge	Follower 1		1.065	1.013
	Rod 1	0.619	0.632	1.002
	Rod 2	0.829	0.833	0.994
	Door Rod	0.829	0.831	1.001
Actuator	Rod		1.271	0.996

Table 3. Convergence of Stress Ratios, Links Loaded in Bending

Location	Part	K ratio[0]	σ ratio[0]	σ ratio[1]
Aft Hinge	Follower 1	1.701	1.806	1.061
	Crank 1	1.418	1.650	0.999
	Crank 2	1.491	1.624	1.005
Fore Hinge	Follower 1	1.701	1.793	1.062
	Crank 1	1.418	1.660	1.000
	Crank 2	1.491	1.630	1.007
Actuator	Crank	1.577	1.585	1.010
	Follower	1.549	1.415	1.062

Using these results, equivalent stiffnesses can be evaluated for convergence based on stress ratios. If the stress ratio is equal to 1 then the stiffness values used in ADAMS are equal to the equivalent stiffness of the part's finite element model. Therefore, a stress ratio error can be computed by subtracting 1 from all ratio values. As this stress ratio error approaches zero, the actual ratio will approach 1. Figure 7 and Figure 8 show the initial stress ratio error values at iteration 0, and the updated stress ratio error values after one iteration. Note that error values greater than 0 signify a part whose stiffness will be increased in the next iteration, while error values less than zero signify a part whose stiffness will be decreased in the next iteration.

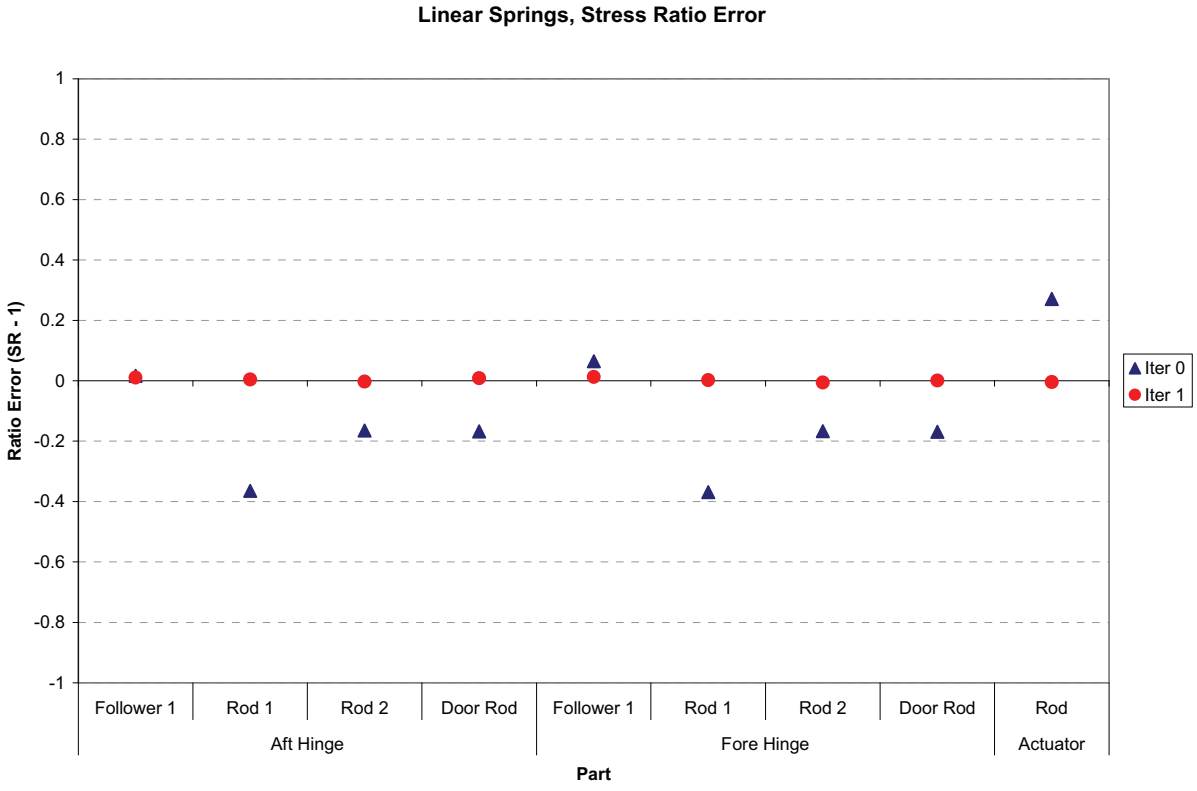

Figure 7. Stress Ratio in Parts Represented by Linear Springs

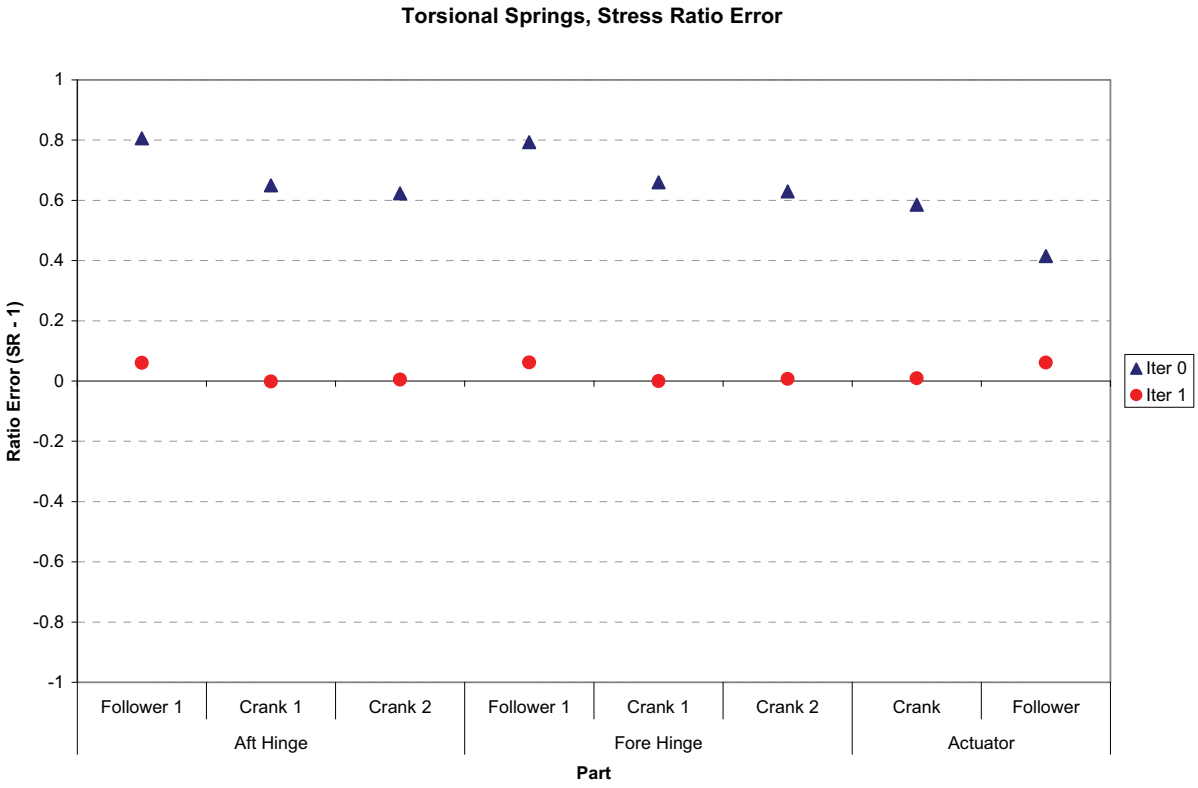

Figure 8. Stress Ratio in Parts Represented by Torsional Springs

Stress Analysis

The stress results for each component after one iteration (used to find the "σ ratio[1]" values in Table 2 and Table 3) are shown below in Table 4 and Table 5. These values represent the predicted stress induced by a 25.4 mm (1 in) forced movement of the door's outboard edge, with the DDM actuator crank fixed. To calculate factor of safety (FS) values, an allowable stress of 703 MPa (102 ksi) was used based on A286 stainless steel [4].

Table 4. Stress Results After 1 Iteration, Parts in Bending

					Displacement LBC		Force LBC			
Location	**Part**	**Deflection (deg)**	**M (N·m)**	**F (N)**	**FEA σ (MPa)**	**FS**	**FEA σ (MPa)**	**FS**	**σ ratio[i]**	**σ ratio[i-1]**
Aft Hinge	Follower 1	1.85E+00	2.34E+04	1.01E+05	1.44E+03	0.49	1.36E+03	0.52	1.061	1.806
	Crank 1	3.83E-01	2.27E+03	1.56E+04	5.12E+02	1.37	5.12E+02	1.37	0.999	1.650
	Crank 2	-3.15E-01	-2.38E+03	-2.45E+04	5.38E+02	1.31	5.36E+02	1.31	1.005	1.624
Fore Hinge	Follower 1	1.52E+00	1.92E+04	8.32E+04	1.19E+03	0.59	1.12E+03	0.63	1.062	1.793
	Crank 1	3.11E-01	1.84E+03	1.26E+04	4.16E+02	1.69	4.16E+02	1.69	1.000	1.660
	Crank 2	-5.87E-01	-4.43E+03	-4.56E+04	1.00E+03	0.70	9.93E+02	0.71	1.007	1.630
Actuator	Crank	-2.48E-01	-1.80E+03	-2.47E+04	6.52E+02	1.08	6.46E+02	1.09	1.010	1.585
	Follower	3.91E-01	2.71E+03	3.35E+04	9.51E+02	0.74	8.96E+02	0.78	1.062	1.415

Table 5. Stress Results After 1 Iteration, Parts in Tension/Compression

				Displacement LBC		Force LBC			
Location	**Part**	**Deflection (mm)**	**F (N)**	**FEA σ (psi)**	**FS**	**FEA σ (psi)**	**FS**	**σ ratio[i]**	**σ ratio[i-1]**
Aft Hinge	Follower 1	1.10E-01	8.42E+04	2.58E+02	2.73	2.55E+02	2.76	1.011	1.016
	Rod 1	-9.77E-02	-2.51E+04	3.48E+02	2.02	3.47E+02	2.03	1.004	0.636
	Rod 2	1.37E-01	3.41E+04	2.58E+02	2.73	2.59E+02	2.72	0.997	0.835
	Door Rod	-4.26E-01	-1.06E+05	8.07E+02	0.87	8.00E+02	0.88	1.009	0.832
Fore Hinge	Follower 1	9.00E-02	6.92E+04	2.12E+02	3.31	2.10E+02	3.36	1.013	1.065
	Rod 1	-7.99E-02	-2.06E+04	2.84E+02	2.48	2.83E+02	2.48	1.002	0.632
	Rod 2	2.55E-01	6.36E+04	4.78E+02	1.47	4.81E+02	1.46	0.994	0.833
	Door Rod	-3.50E-01	-8.72E+04	6.61E+02	1.06	6.60E+02	1.07	1.001	0.831
Actuator	Rod	-3.44E-01	-7.56E+04	1.73E+03	0.41	1.74E+03	0.40	0.996	1.271

Although these results do show some components with factors of safety less than one, this does not necessarily mean that closure of the ETD during STS-118 would have resulted in yield. Because the actual rigged door sag was not known at the time, this analysis did not produce a definitive prediction of additional stress induced in the door drive linkage. Because the minimum computed factor of safety for 25.4 mm (1 in) of door motion was 0.40, the door could be forced to move up to 10.16 mm (0.40 in) at its outboard edge before allowable stresses would be reached.

Conclusions

Through the use of MSC/ADAMS, a flexible multi-body dynamic simulation of the ETD DDM was quickly constructed and used to find linkage deflections. The advantage of this type of analysis is its relative simplicity compared to a full FEA model of the DDM, combined with preserved accuracy of mechanism kinematics. This simplicity allows for rapid construction of the model in addition to a reduction in computer computation time. Although complex geometry is reduced to lumped equivalent stiffnesses, the analyst has the ability to select each flexible degree of freedom that will be of primary interest and include it in the model. The stiffness used for each of these individual degrees of freedom may then be verified using FEA and iteratively updated as necessary.

The analysis shows that some components of the ETD have factors of safety less than one and may undergo plastic deformation. However, this is not conclusive because the forcing of the door is based on the worst case possible within rigging specifications. To complement the analyses described in this paper, actual rigging data from the Orbiter *Endeavour* taken before STS-118 could be used to reach a better estimate of stress in the DDM. Predicted stresses could then potentially be further confirmed through experimentation using a training mockup version of the DDM.

Acknowledgement

We would like to dedicate this paper to the memory of Marlon C. Batey. Marlon worked as an aerospace engineer in the Mechanical Systems Branch at NASA Langley Research Center over the past three years. Without his contributions to the team, the work described here would have been much more difficult. In addition to his diligence and motivation, it was always a pleasure to work with him. Marlon has been and will be greatly missed.

References

1. Don Picetti, Thermal Analysis and Test Results for ET Door Paint Striping, Boeing Orbiter Element, S063244, Daily PRCB Presentation
2. Rao, Singiresu S. Mechanical Vibrations, Fourth Edition, Pearson Prentice Hall, 2004
3. Brinkworth, D. “ET/Orbiter Umbilical Door Mechanism Installation and Rigging Procedure”, Space Division Rockwell International, Doc. No. ML0308-0058 rev. C, 1982
4. MatWeb Material Property Data, http://www.matweb.com/search/DataSheet.aspx?MatID=13246&ckck=1

Failure of the Trailing Umbilical System Disconnect Actuator on the International Space Station

Adam Gilmore[*], Chris Schmitt[**], Laura Merritt*, and VJ Bolton[**]

Abstract

In December of 2005, one of two trailing umbilical cables used on the International Space Station (ISS) Mobile Transporter (MT) was inadvertently severed by an internal cutter system designed to free a snagged cable or jammed reel while transporting hazardous payloads. The mechanism's intended means of actuation is electrical; however, troubleshooting revealed a mechanical actuation occurred. The investigation of the failed component revealed several lessons learned in developing hardware requirements, understanding and following the rationale behind the requirements throughout the design life cycle, understanding the impacts of gaps and tolerances in a mechanism, and the importance of identifying critical steps during assembly.

Introduction

On December 16, 2005, a power switch on the ISS was tripped by a short circuit. Video of the MT and Trailing Umbilical System (TUS) cable revealed the cable routed to Interface Umbilical Assembly (IUA) 2 on the nadir side of the MT had been inadvertently severed (see Figure 1). When the cable was severed the live wire tips contacted metal causing a short, leading to a tripped power switch. Commanded actuation requires three independent power switch closures to the TUS Disconnect Actuator (TDA), and telemetry analysis indicated no possible electrical cause. The only remaining cause of the severed cable was a mechanical failure of the TDA.

A team was formed to evaluate the failure, understand the impact of operating the MT with a single TUS cable in the near term, and implement the recovery plan based on an extensive failure investigation. This paper will describe the high level system, the lower level mechanism design and failure, the design and assembly errors, along with the implemented changes, and current operating configuration. As the investigation proceeded, it was clear that not only did the mechanism fail, but that the need for the mechanism was outdated for the current ISS requirements.

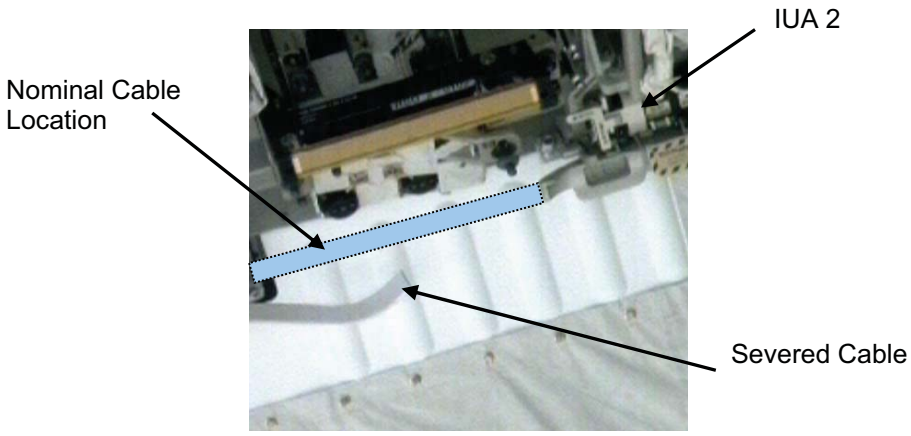

Figure 1. Severed TUS Cable on IUA 2

[*] NASA, Johnson Space Center, Houston, Texas
[**] Boeing, Houston, Texas

Hardware Description

System Description

The ISS MT moves along the Integrated Truss Segment rail, and in conjunction with the Mobile Base System (MBS) and Space Station Remote Manipulator System (SSRMS), are used to transport payloads. When the MT is latched down at a worksite, the Umbilical Mating Assembly (UMA) provides the necessary power to the MBS and SSRMS. The MBS, SSRMS, and other payloads will now be generically referred to as the MT payloads. The TUS cable provides both power and data at any point along the truss to the MT, but only data and video to payloads. Therefore, the MT payloads do not receive power between MT worksites. The capability to remotely free a stranded MT can be critical to the survivability of the payload and also provides a way to prevent a catastrophic hazard.

The TUS consists of two parallel cables, one on each side of the MT. Each cable in this redundant system is on a retractable reel stored within the S0 truss segment (see Figure 2). The Interface Umbilical Assembly (IUA) is the interaction point between the MT and the TUS. The MT also has two IUAs, one for each TUS cable. Contained within the IUA is the TDA which allows the crew or ground to remotely sever the TUS cable and free the MT in the case of a TUS reel jam or failure during translation. The ability to remotely cut the TUS cable was a feature added early in the ISS Program to prevent catastrophic hazards due to moving hazardous materials along the truss rails.

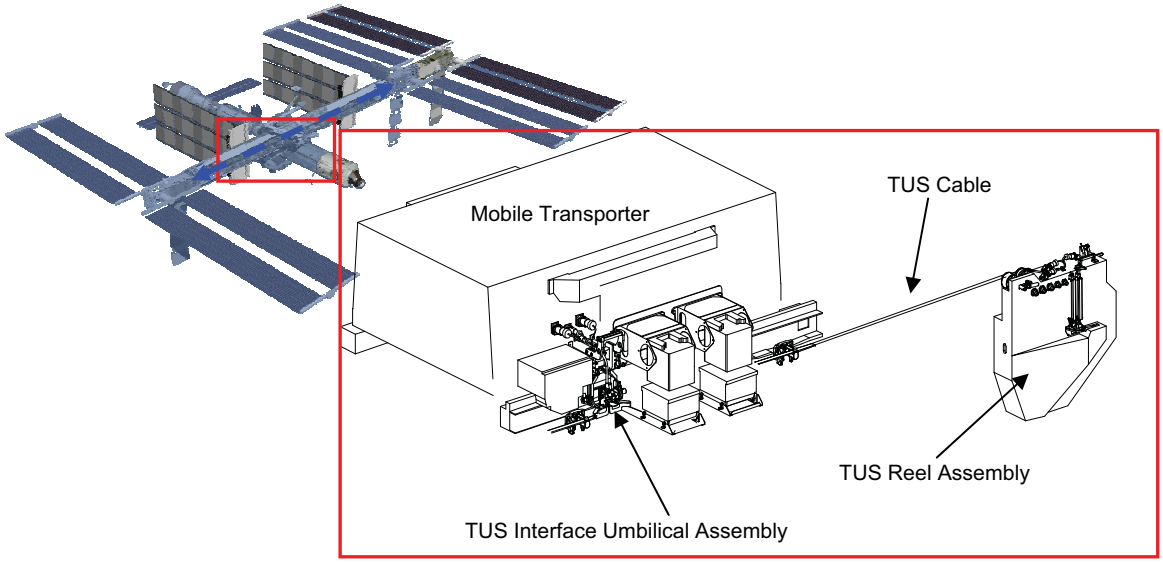

Figure 2. MT Schematic

TDA Mechanism

The TDA is a low shock, fast acting guillotine cable cutting mechanism. A cross section is shown in Figure 3, omitting the Release Plunger Compression Springs and the Restraining Wire that is wrapped around the Split Spool 15 times. The Primary Compression Springs load the T-plunger, which drives the blade that cuts the TUS cable (not shown). There is a compression spring under the Release Plunger, which pushes the Actuator Plunger into the Split Spool. The two halves of the Split Spool are held together with a Restraining Wire and connected to a fuse wire at the end (not shown). The fuse wire holds the restraining wire in place.

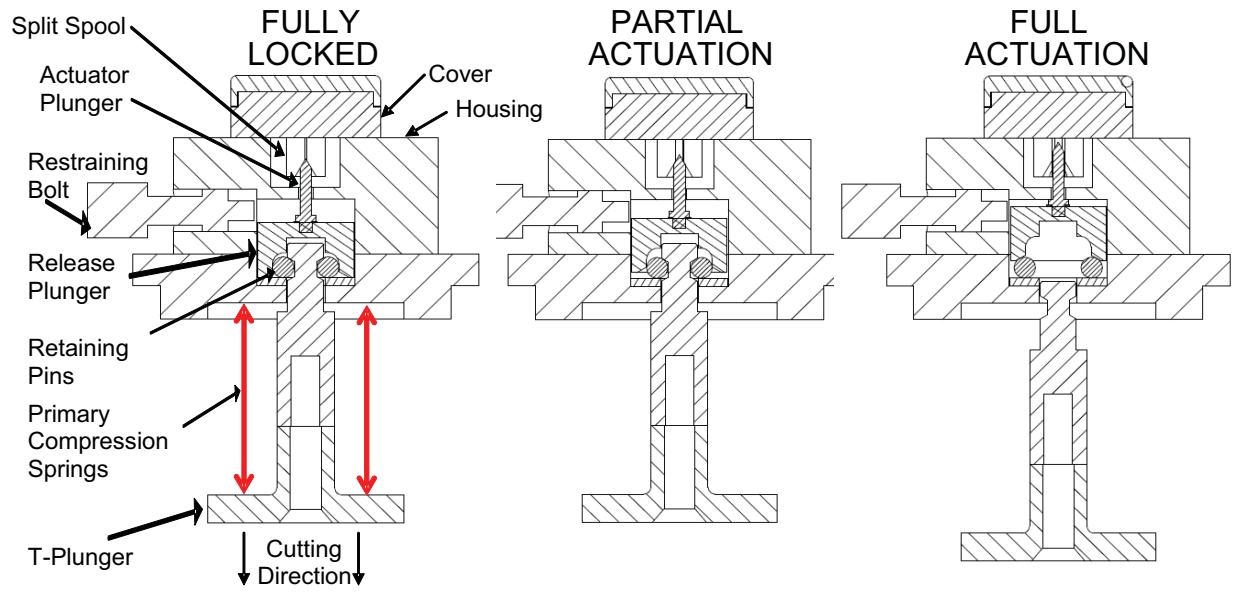

Figure 3. Actuation of the TUS Disconnect Actuator

TDA Actuation

To actuate the mechanism, current is passed through the fuse wire, causing it to weaken and break under load. The Restraining Wire is then free to uncoil; thus it quickly unwinds from the Split Spool (see Figure 4). With the Restraining Wire out of the load path, the spring under the Release Plunger pushes the Actuator Plunger, splitting the two halves of the Split Spool apart as the Actuator Plunger moves upwards. With the Release Plunger clear, the Retaining Pins are forced outward by the T-plunger. Without the Retaining Pins in the load path, the Primary Compression Springs are able to release their stored energy, pushing the T-plunger through the assembly, and driving the cutting blade into the TUS cable. See the actuation sequence in Figure 3.

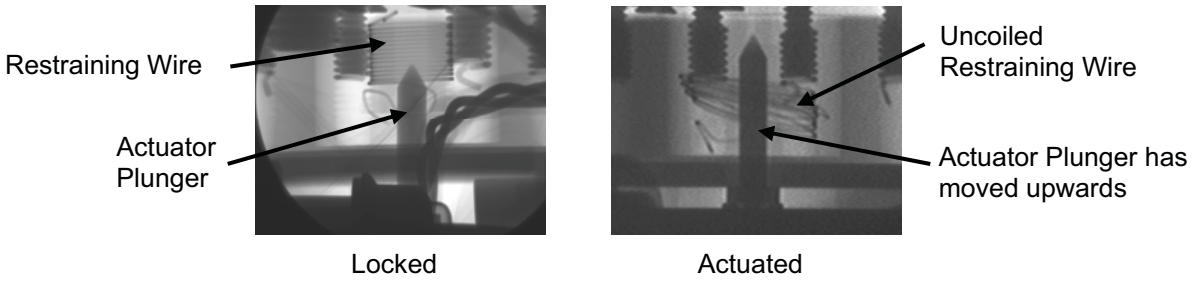

Figure 4. TDA X-Rays

Restraining Bolt

The Restraining Bolt is used to prevent inadvertent actuation during launch vibration. In Figure 3, the crew interface is on the left side of the Restraining Bolt, and the shaft to the right of the threads blocks the Release Plunger if the TDA is actuated inadvertently. By design, a small gap is intended between the fully engaged Restraining Bolt and the Release Plunger. This ensures that the Split Spool locks the mechanism and the Restraining Bolt is truly a redundant feature. During initial on-orbit activation, the Restraining Bolt is removed, which arms the TDA. The “Fully Locked” view of Figure 3 shows the TDA armed with the Restraining Bolt backed out from the launch position.

Failure Investigation

The first indication of the TDA failure was the tripping of a power switch. Telemetry analysis found no electrical faults, indicating a mechanical failure was the likely cause. Subsequent video review confirmed the cable was cleanly cut, and the full TDA actuation sequence had occurred. The remaining TDA mechanism failure modes were: Structural failure of the Restraining Wire, Split Spool, or T-plunger; tolerance stack-up effects; assembly or process errors; and orbital debris impact.

Structural Failure

Structural failure modes that were identified as a possible cause were compression yielding or creep of the Split Spool material (Torlon), fatigue or creep failure of the Restraining Wire, or yielding of the T-plunger assembly components. Failure due to fatigue or creep of the Restraining Wire was considered low likelihood because the load on the wire is constant with small magnitude thermal cycle loads that are evenly distributed. Fracture of the T-plunger was ruled out due to large cross sectional area and adequate strength margins for a nominal design. Under nominal design loading conditions the Torlon Split Spool also has adequate strength margins.

Design and Tolerance Assessment

An assessment of the design was performed to determine what effects the as-built hardware could have on the position of the components within the mechanism. The results of the assessment indicated that when the components were built to the nominal drawing dimensions a gap would exist between the Actuator Plunger and Split Spool. If the as-built components were biased to one side this could increase that gap. The TDA assembly drawing omits this gap (see Figure 5).

During assembly of the flight units, the top portion of the T-plunger is installed and the Release Plunger with Retaining Pins is compressed. Next, the Restraining Bolt is engaged to hold the Release Plunger in place and preclude release of the top portion of the T-plunger. The Primary Compression Springs are then mechanically compressed, and the bottom portion of the T-plunger is installed and fastened to the top portion with a single bolt. The final step installs the TDA Cover with Split Spool to the Housing. After reviewing the assembly process it was clear that any gap between the Actuator Plunger and Split Spool would go undetected during final assembly of the flight unit. That gap is maintained by the Restraining Bolt until the unit is activated on-orbit. During on-orbit activation the Restraining Bolt is removed and the Release Plunger would move to close the gap (see Figure 5).

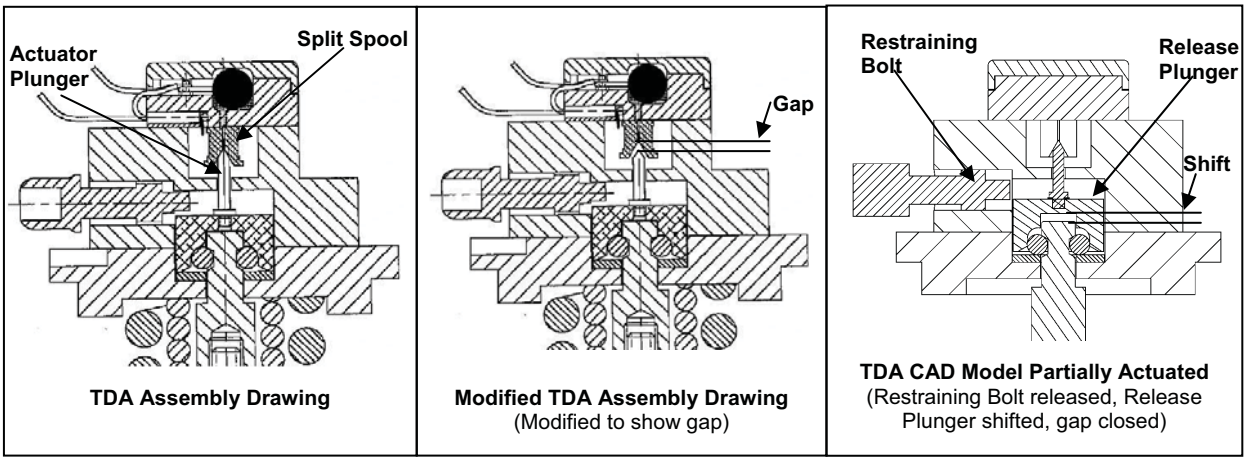

Figure 5. Gap Illustrations

This movement was confirmed on-orbit when the Restraining Bolt required higher than expected torque during removal due to the load being applied to the bolt from the Release Plunger. This was seen again when the Restraining Bolt would not re-engage during failure troubleshooting years later, since the Release Plunger had shifted and created interference. When the gap is closed, the TDA is placed into a partially actuated state that changes the load path within the mechanism. After the failed TDA was returned to the ground, a CAD model was created using the as-flown component dimensions. This model further illustrated the gap and clearly showed a discrepancy in the design assembly drawing.

Ground Investigation

Upon return of the failed TDA, disassembly and non-destructive evaluations were performed. The first was an x-ray of the TDA Housing and internal components to determine whether or not the Restraining Wire and Fuse Wire were still intact. In addition, a detailed survey was performed of the exterior of the TDA Housing and Cover. Since the TDA mechanism was actuated and disassembled from the IUA on-orbit, the T-plunger and spring dimensions and surfaces could also be inspected. The x-ray of the TDA Housing clearly showed the Restraining Wire and Fuse Wire were still intact and did not cause the failure. When the outer covering tape was removed from the top portion of the TDA Cover, a non-uniform gap nearly 1.02 mm (0.04 in) tall was found between the Cover and Housing, indicating an assembly error. This gap was also confirmed by a subsequent review of the x-ray. The markings on the removed tape were consistent with a gap that had been present from initial Cover installation.

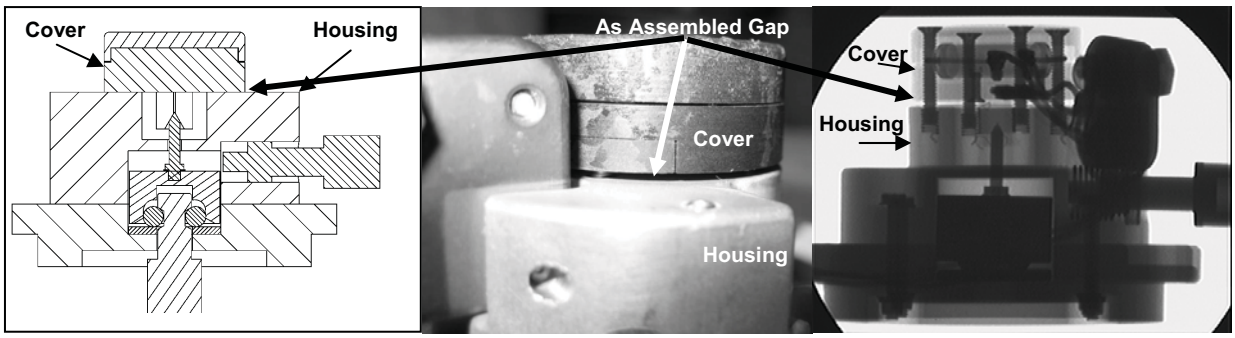

Figure 6. Failed TDA External View (tape removed) & X-Ray

Upon inspection of the T-plunger, yielding was found where it contacted the Retaining Pins. Prior to obtaining the failed TDA, a series of ground tests were performed to support the planned on-orbit repair strategy. These tests included both a slow mechanical release of the Actuator Plunger and a near instantaneous release of the Actuator Plunger. Mechanical actuation was achieved by slowly backing out the fasteners that hold the Cover and Split Spool to the Housing, thus allowing the Release Plunger to shift and release the T-plunger. This test resulted in three findings that were significant to the failure investigation: 1) The T-plunger release required significantly less travel than expected (~0.965 mm (0.038 in) actual vs. ~4.75 mm (0.187 in) expected), 2) The edge of the T-plunger notch was mechanically yielded at the Release Pin interface, 3) The Split Spool was damaged at the Actuator Plunger interface. Post flight inspection of the failed TDA T-plunger indicated similar notch yielding at the Retaining Pin interface. The travel required to mechanically actuate the TDA was similar to the gap that was seen between the Cover and the Housing on the failed TDA. This indicates the TDA was very close to actuating when the Restraining Bolt was first removed on-orbit.

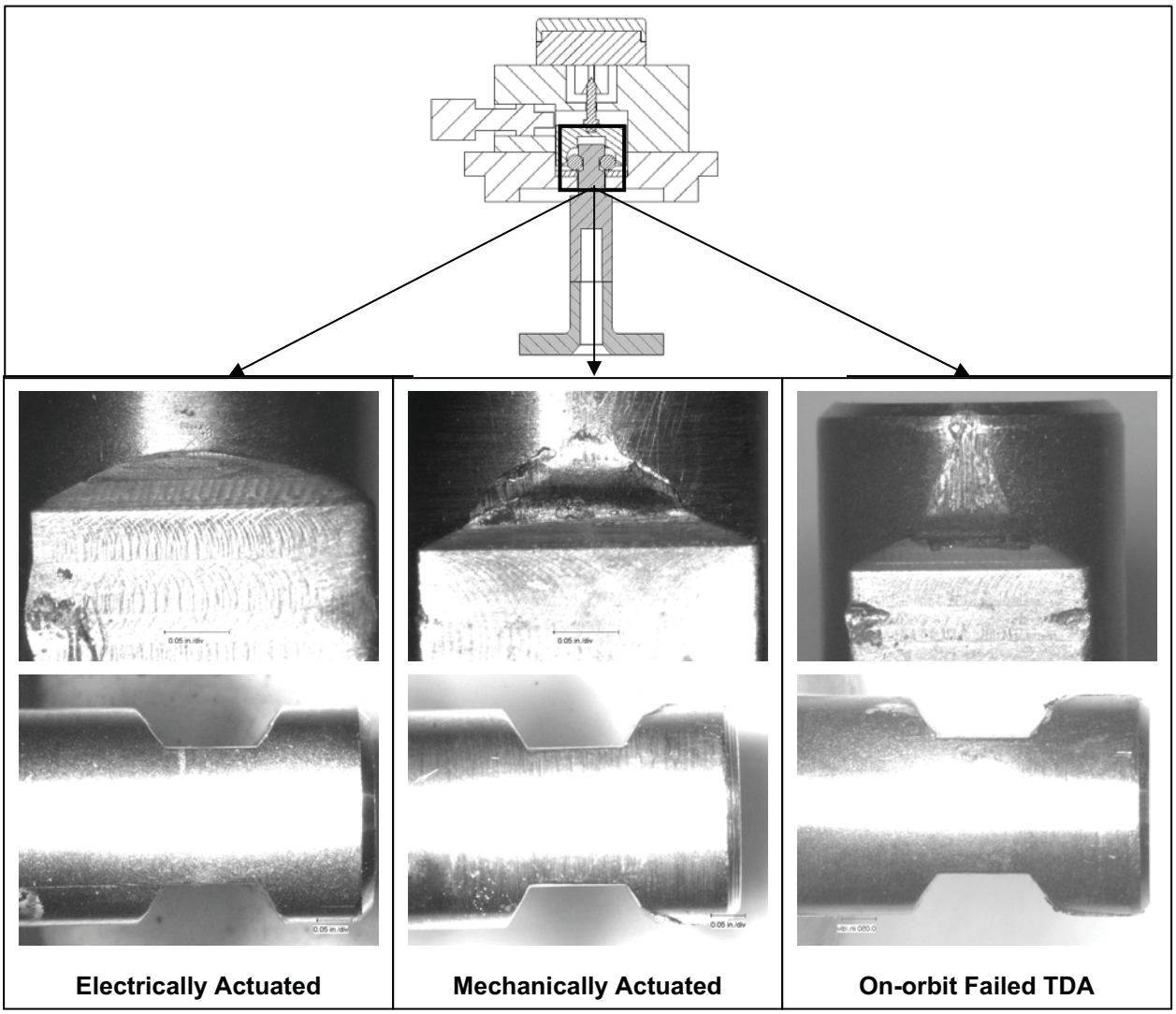

Figure 7. T-Plungers Post Actuation

The Split Spool and Restraining Wire were inspected via x-ray and visually after initial disassembly. The Restraining Wire was intact and did not allow the Split Spool to separate. The Split Spool was then separated by removing the Restraining Wire to allow a detailed inspection of the Split Spool halves. The inspection revealed the Release Plunger had compressively yielded the interior of the Split Spool. This finding was consistent with the damage seen during the mechanically actuated ground test. This damage is caused by an increased force transferred to the Actuator Plunger from the Primary Compression Springs during a slow release actuation. As the Release Plunger travels upward the Primary Compression Springs force the Restraining Pins outward. This outward force is then transmitted to the Release Plunger and subsequently to the Split Spool. When the TDA is electrically actuated the Split Spool is free to separate and thus does not compressively yield (see Figure 8).

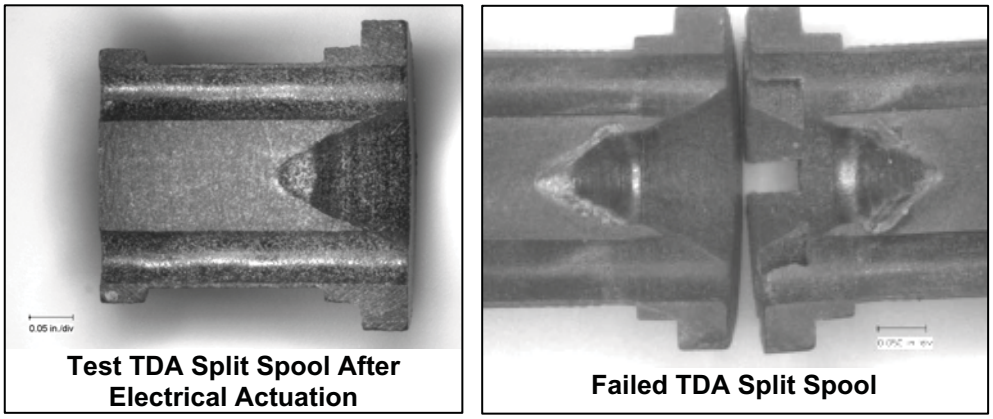

Figure 8. Split Spool Details

Review of our findings from the ground testing, analysis, disassembly, and inspection of the failed unit revealed the failure was caused by a combination of the as-built gap, the gap created during assembly, and overstress of the T-plunger and Split Spool. The gaps caused by design tolerances and an assembly error put the mechanism in a position that was near firing. This position put the T-plunger and Split Spool in a loading configuration that was not consistent with the validated design and exceeded their structural capability.

Implemented Repair

The ISS Program was tasked with developing a forward plan for the IUAs on-orbit and the remaining spare on the ground while maintaining MT capability for continued assembly. Consideration was required for both controlling hazardous transportations as well as the loss of power to payloads in a stranded MT case. The ISS Program no longer plans to transport hazardous cargo; and therefore, determined the TDA and cutting capability is not presently necessary. There is still the open issue of losing critical payloads in the MT stranded case, but that was being addressed by the ISS Program and not a requirement that the repair team had to solve.

In the weeks after the TUS 2 cable sever, the team was concerned with the possibility of a second TDA failure on IUA 1 leading to a TUS 1 cable sever. In early February 2006 during Russian Extravehicular Activity (EVA) 15, the TUS 1 cable was routed outside of the TDA to prevent it from being cut until a long term repair could be implemented. The configuration of the MT leading up to the removal of the failed system was the TUS 1 cable was severed (IUA 1 failed) and the TUS 2 cable was routed outside of the TDA. The team prepared a repair to regain full MT redundancy in one Shuttle Flight, STS-121 (ISS Mission ULF1.1), in July of 2006. One requirement was to fly a spare TUS Reel containing a fully intact cable with connectors. In addition, the blade blocker (see Figure 9) was designed and tested on the ground to be installed EVA onto IUA 1 to prevent the TDA from cutting the cable in the case it too mechanically failed. The repair allowed for IUA 1 to be fixed in place in one short EVA task.

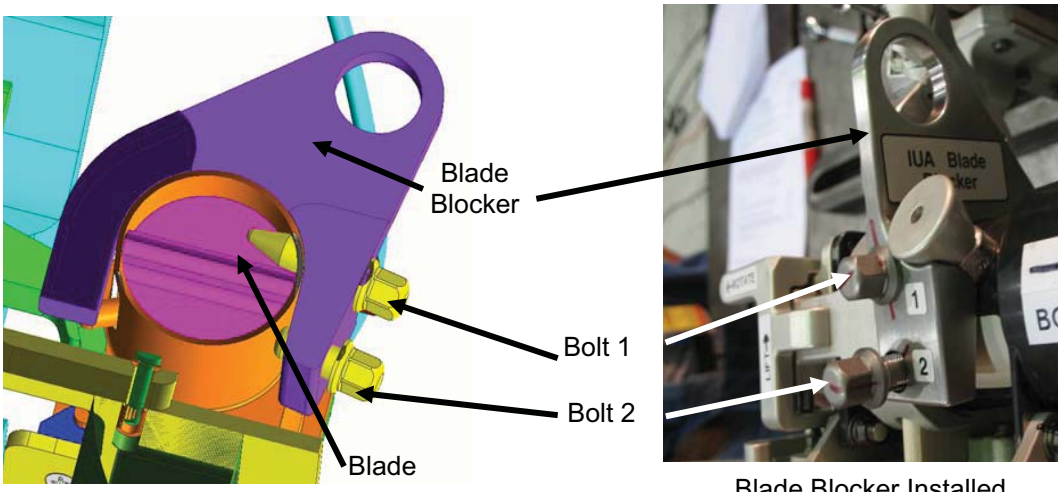

Cut Away Showing Bolt 1 Engaged

Blade Blocker Installed

Figure 9. Blade Blocker Details

Next was to address both the ground spare and the failed IUA 2 on-orbit. For the ground spare the TDA hardware was removed to prevent inadvertent actuation once in service. The IUA itself is still required for power conditioning, TUS cable to MT interface connections, and cable strain relief. This modified spare unit was installed in place of the failed IUA 2 during the STS-121/ ISS ULF1.1 mission. With the removal and replacement (R&R) of the TUS 2 Reel, installation of the blade blocker onto the IUA 1, and R&R of IUA 2 with the newly configured spare, the MT System was left with full redundancy at the end of the mission. In a subsequent decision, the ISS Mission Management Team decided the crew would disassemble the failed TDA on-orbit and only return that small portion to the ground for failure investigation. The failed IUA 2 was re-configured much like the spare unit during the mission and now serves as a fully operational IUA spare on-orbit without any ground re-processing required. Figure 10 illustrates the configuration of a newly configured IUA.

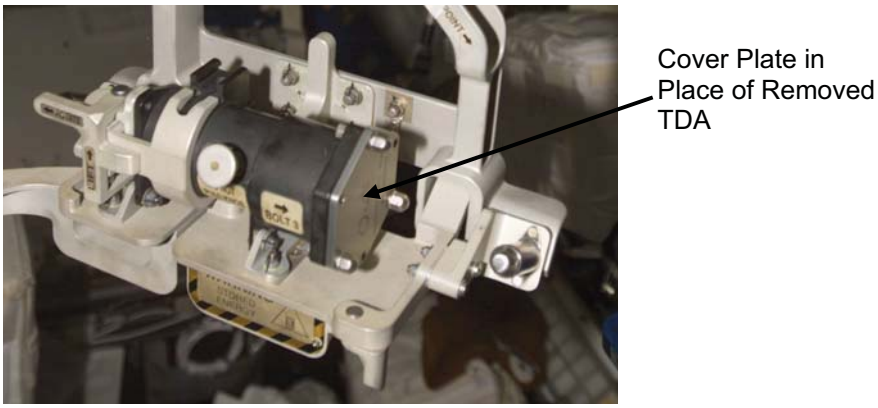

Figure 10. New IUA Configuration

Lessons Learned

During teardown of the failed unit, four opportunities for improvement were identified: The original requirement to remotely free a stranded MT was no longer valid, mechanism initial position could significantly change the load path, a critical inspection point was missed, and structural materials were not selected for robustness. The TDA remained in place after a major program change eliminated the risk it was meant to mitigate. Unfavorably stacked tolerances would create a load-changing gap. Installation requirements checked torques, but not seating between subassemblies. Finally, a polymer was selected for a compressive strength application. Explanations of each issue and our recommendations for correction are presented as mitigation for similar problems in other mechanisms.

Requirement Validity

In this case, the original requirement was based on a need to mitigate an explosive hazard with a short time to effect. The explosive hazard was created by moving hydrazine propellant tanks onboard the MT for re-supply. If a system failure prevented the MT from moving the tanks, fast recovery was critical. This drove the design process towards selecting a remotely activated device. The fast acting Split Spool mechanism in the TDA responds very quickly and was a good choice for those conditions. A different use environment with a longer time to effect may have changed the design direction.

Changes in requirements eliminated the need for external hydrazine tanks. When Russian derived propulsion systems were added, the external tanks of hydrazine were eliminated. Without the tanks, there was no longer an explosive hazard onboard the MT.

Removing the major hazard from the system changes the trade study variables, especially time to effect. In this case, without a need for instant response, an externally activated quick disconnect or motor driven mechanism may have been adequate. Failures of those mechanisms would not require the expense and difficulty of a shuttle mission to deliver a large, new, replacement part.

When the propulsion change was made, the risk posed by a system failure should have been reexamined more thoroughly. A near instant response method was no longer necessary, and slower acting alternatives to the TDA could have become viable options. A detailed reexamination of requirements after each major design change would screen for impacts such as this. A new trade study at that point may have changed the requirements for disconnection greatly. A different approach, like a quick disconnect, could mitigate the destructive aspects of a cable disconnection and reduce the severity of an actuator failure to the overall system.

Tolerances and Drawing

Cross sections of the TDA assembly drawing show a close fit between the Split Spool and the Actuator Plunger and a gap between the Restraining Bolt and Release Plunger. As-built assembly indicated a gap at the Split Spool and a closed gap at the Restraining Bolt to Release Plunger interface, as seen in Figure 5, leaving the TDA partially actuated and changing the load path.

Creating a gap between the Actuator Plunger and the Split Spool allows a partial actuation of the TDA when the Restraining Bolt is removed. The effect of creating that gap is movement of the Retaining Pins along the slope of the T-plunger, as shown in Figure 10. When this loading condition is created, the high force from the Primary Compression Springs is concentrated on a significantly smaller area within the TDA. The designed line contact reduces greatly as it approaches a point contact as shown in Figure 10. Any yielding at that point exacerbates the problem and further actuates the TDA.

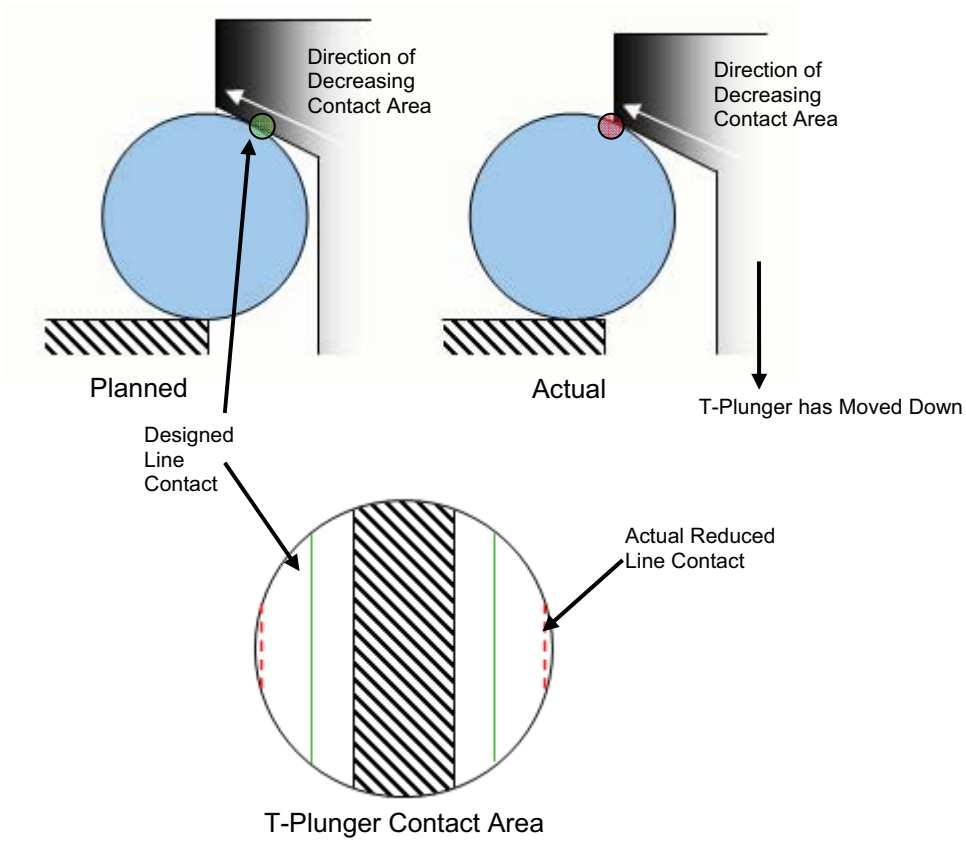

Figure 10. Change in Load Condition at Retaining Pin

A detailed design study and resting state review considering the impacts of spring forces would point out the possibility of these issues and their impact to loading within the mechanism. Defining critical dimensions for Split Spool and Actuator Plunger height to ensure the Restraining Pins would remain fully seated could prevent a gap and the associated high loading condition.

Mandatory Inspection Point Selection

During disassembly of the failed TDA, a significant 1.02 mm (0.04 in) gap was found between the Cover and the Housing. This additional gap exacerbated the design gap at the interface, worsened the partial actuation state, and increased the load concentration.

Cover installation drawings called out a torque requirement for the bolts used to attach the Cover, but did not require any dimensional inspection or verification that the two parts were in solid contact. As a result, if the bolts reached their minimum installation torque before the parts were fully seated, a new gap could be created between the Split Spool and the Actuator Plunger.

Adding a mandatory inspection of the gap between the Cover and the Housing would prevent creating a gap from incomplete seating between the parts. Required inspection for both fastener torque and seating should be considered whenever an interface is critical to the load path of your mechanism.

Heritage Design

Disassembly of the Cover portion of the TDA assembly revealed deformation and yielding of the Split Spool (see Figure 11). Torlon Split Spools of this type had been used previously in switches for power systems.

Figure 11. Split Spool Deformation

In other applications, Torlon was highly desirable because of its electrical insulating properties. For the TDA, electrical properties were irrelevant. Structure focused requirements for this portion of the TDA would have weighted strength as far more important than electrical resistance. Torlon would not be as robust as steel for this application. Since electrical resistance was irrelevant, a steel Split Spool would be a more desirable choice for a compressively loaded structural member.

Where mechanical and strength properties are the main requirement, they should be weighted more heavily than flight history or other concerns. If the Split Spool was never overloaded, polymer selection would not have been a problem. In this case, other issues led to structural members experiencing loads in excess of design loads and failed by yielding. Caution should be used whenever adapting heritage designs that were developed for other applications.

Conclusions

Evidence indicates the TDA was in a partially actuated state from the moment it was activated on orbit, thus fundamentally changing the load within the mechanism and creating an unforeseen failure mode. This investigation discovered several issues that should be mitigated in future designs: 1) Ensure that the requirements driving your mechanism design are still valid and are properly weighted in trade studies. 2) Verify that the as built components of the assembly will produce a mechanism that will function as intended both structurally and kinematically. 3) Inspect dimensions that control the kinematics and load path of the mechanism, checking both torque and seating of assemblies. 4) Lastly, focus material selection requirements on each specific application and exercise caution when reusing heritage design. A TDA with these issues corrected would not experience the failure seen on-orbit.

The Mars Climate Sounder In-Flight Positioning Anomaly

Bruno M. Jau* and David Kass*

Abstract

The paper discusses the Mars Climate Sounder (MCS) instrument's in-flight positioning errors and presents background material about it. A short overview of the instrument's science objectives and data acquisition techniques is provided. The brief mechanical description familiarizes the reader with the MCS instrument. Several key items of the flight qualification program, which had a rigorous joint drive test program but some limitations in overall system testing, are discussed. Implications this might have had for the flight anomaly, which began after several months of flawless space operation, are mentioned. The detection, interpretation, and instrument response to the errors is discussed. The anomaly prompted engineering reviews, renewed ground, and some in-flight testing. A summary of these events, including a timeline, is included. Several items of concern were uncovered during the anomaly investigation, the root cause, however, was never found. The instrument is now used with two operational constraints that work around the anomaly. It continues science gathering at an only slightly diminished pace that will yield approximately 90% of the originally intended science.

Introduction

The MCS instrument is one of six scientific instruments flying aboard the Mars Reconnaissance Orbiter (MRO) spacecraft, launched Aug. 12, 2005. The instrument's purpose is to acquire data about the Martian weather and climate. Science observations started Sept. 24, 2006. The duration of mapping operations is scheduled for two earth years but it is hoped that MCS can continue to acquire data for an additional two years. Current information about the MRO mission and this instrument can be found in JPL's [1] and the Planetary Society's [2, 3] web pages. A nearly identical instrument, performing surface science investigations around the Moon, will be launched onboard the Lunar Reconnaissance Orbiter Spacecraft in October of 2008.

On Dec. 11, 2006, about a day after a solar flare near Mars, the instrument's elevation drive started to miss its intended positioning by a few steps several times. The flight software reacts by automatically executing a saving routine after several positioning errors, stowing the instrument in a sun-safe position. Initial evaluations revealed no obvious cause; the position errors were random and happened a few minutes or many days apart. Up to now, over 200 positioning errors have occurred; all with the elevation drive. Scan image evaluations confirmed that most errors were four steps away from the commanded position. A tiger team was tasked to review all software, electronics, and mechanical aspects, to hopefully find the cause of the anomaly and to suggest remedies. This paper gives an account of the MCS in-flight anomaly and its investigations, provides technical background material about it, and lists possible causes. Lessons learned are included for future space instrument builders. The paper should also be of interest for the general public that likes to learn about the intricacy of space science.

Science Objectives and Data Acquisition Techniques

MCS is an infrared (IR) band radiometer, primarily performing atmospheric measurements by measuring the radiance profile versus altitude at the limb (or horizon). One minor component of the science objectives also involves measurements of the surface for thermal and radiative balance calculations [4]. The radiances are inverted via a retrieval process to obtain profiles of temperature, dust, clouds, and humidity versus altitude. The individual profiles are then combined in 4-dimensional "maps" (covering space and time for each measured quantity) to examine the weather and climate of Mars.

* Jet Propulsion Laboratory, California Institute of Technology, Pasadena, CA

The resulting data will be examined and compared to Martian atmospheric models, much like terrestrial meteorological data. This will provide an understanding of the atmospheric temperatures and winds as well as the ways in which the solar heating directly and indirectly forces them. It will also provide valuable knowledge of Martian climate changes from season to season.

The original plan also called for routine surface observations. This would have represented a small portion of the overall science (~10%) from the instrument. They were primarily for studying thermal and radiative changes of the seasonal polar caps to determine their influence on the weather and climate. The surface observations are also used for establishing the lowest 10 km of the atmospheric profiles. An anomaly-imposed operational restriction currently limits the view to only 10° below the limb, which yields limited, but useful measurements of the surface. Due to the curvature of the surface, this corresponds to an emission angle of 65°, which is useful for some surface science as well as to help constrain the lowest part of the atmospheric profiles.

Detector Configuration

For each of the nine channels (8 IR and 1 visible), the instrument has a 21 element detector array on the focal plane. These are oriented so that they provide a profile of the radiation from the surface to ~80 km when pointed at the limb. Each individual detector is 0.2° by 0.35°, with the narrow dimension providing 5 km vertical resolution on the limb to meet the desired vertical resolution for the profiles.

The radiance profile seen at the limb is a combination of two main factors. The first factor is the amount of emission/absorption; and whether it is opaque at the wavelength of the channel (in which case the detectors do not see all the way through the atmosphere). The second factor is the temperature of the atmosphere. Both tend to decrease with altitude (ignoring the special case of clouds). Combined, these changes tend to produce a radiance profile that stays constant until the atmosphere starts to become transparent, then decreases more or less exponentially (see Fig. 8 for an example profile).

Since the detector signals are not chopped, frequent calibration views of space and the blackbody (or solar) targets are necessary to provide a good calibration of the observations. On the other hand, time spent on calibration views (and the time spent moving between calibration views) is time when no science data is collected, leading to a desire to minimize the calibration observations.

Individual observations are performed with 2 second integration times, but are usually combined to improve the signal to noise in the most sensitive cases. When staring at the limb, the signal to noise and rapid change in signal with altitude allows shifts of as little as 5% of a detector's width to be noticed. The pointing accuracy requirement for the actuators is not that strict since other sources of pointing errors (in particular, spacecraft orientation) also interfere. However, since the pointing can be determined from the radiance profile, the pointing accuracy requirements on the actuator are looser than this.

Instrument Scanning Patterns

MCS slewing is driven by the observations needed to support the science goals of the instrument, including the calibration views. Both the azimuth and elevation actuators are used to achieve the necessary orientations, although the elevation actuator performs the majority of the slewing.

The scanning is described in detail in [4], but a few locations played a key role in understanding the anomaly. A graphical representation of the range and frequency of scanning is shown in Fig. 1. The first position is the stow position. This is with both actuators pointing at 0°. This is a sun safe position that is used when the instrument is powered off, since even a momentary exposure of the telescopes will destroy the focal plane. It is also used when the instrument is standing down from normal operations.

When the elevation is at 0°, the telescopes are staring at the built-in black body, one of three calibration views. The second calibration target, the solar target, is at an elevation of 37°. The standard MCS scan observes the blackbody about five times per hour and the solar target once an hour.

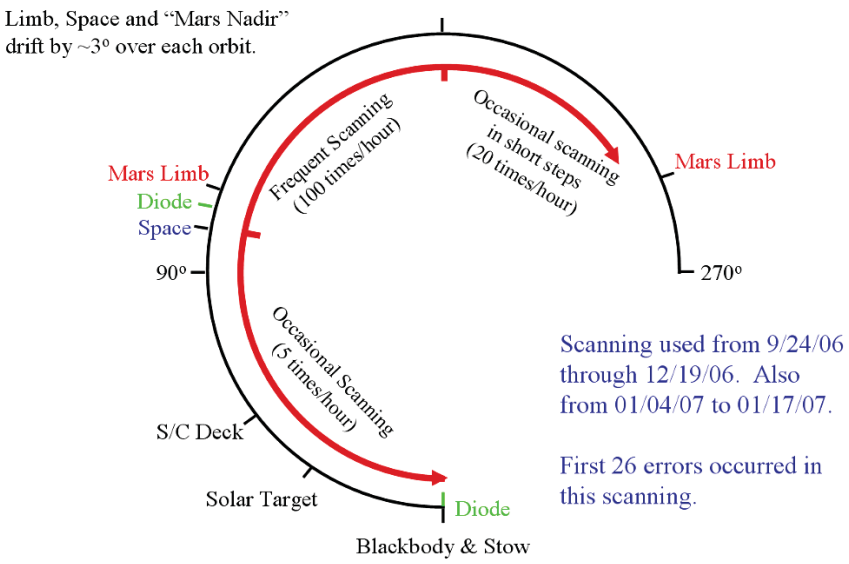

Figure 1: Range of Elevation Actuator Operation

Most of the time, MCS is pointed at the limb (or horizon) of Mars to acquire the key observations of the Martian atmosphere. The location of the limb varies by ~2° due to the elliptical nature of the MRO orbit, but is centered on the elevation actuator position of 111.2°. Tied to the limb location is the space view (the third calibration point). It is 8.4° above the limb (or a nominal elevation angle of 102.8°).

When the elevation actuator points between the limb and 250°, MCS is viewing the surface of Mars. In particular, at an angle of 180°, it is pointing in the nadir direction, the sub-spacecraft location.

Scanning is controlled by a series of tables (called SST—Scan Sequence Tables) that contain a list of commands, each indicating the slew and observation duration. These are executed serially by the flight software. The most common scanning is a 35-second cycle that points at nadir for 4 seconds, moves to point at the limb for 16 seconds, then points at space for another 4 seconds before repeating. This pattern was used to determine the lifetime requirement of 1.75M scan cycles.

A second regularly used pattern is the blackbody scan. This scan starts at the space view (usually at the end of a limb scan), moves to view the black body, returns to view space and finishes by slewing to nadir for the start of the next limb sequence.

The high-resolution camera (HiRISE instrument on MRO) placed requirements on MCS, limiting the MCS contribution to the spacecraft jitter that would interfere/blur the HiRISE images. In addition to the jitter requirements, a freeze command was implemented that would point MCS at a sun safe position on the limb during off-nadir HiRISE imaging.

Mechanical Description of the MCS Instrument

Key Design Requirements

The critical design requirements pertaining to the anomaly were:

- *Joint Life: The elevation drive shall survive 3.5M cycles:* This is double the nominal mission lifetime of 1.75M cycles to provide the appropriate margin (and to provide lifetime for an extended mission). This is a significant driver for the design of the transmission and the selection of the lubrication. Pennzane 2000 [5] was chosen as lubricant because of its excellent life characteristics. The life test of a joint proved that transmission and lube could survive the required cycles without much degradation (see [6] and "Qualification Testing" below). Due to scanning limitations imposed since the actuator anomaly, the actual scanning cycles for the primary mission will be significantly lower.

- *Pointing Accuracy: The drives must be able to position the instrument to within ±0.025 deg:* The step rate was chosen to be 0.1 degree; the positioning thus has to be within ¼ step, which is well within a stepper actuator's capabilities. During acceptance testing, all measured pointing accuracies were within ±0.015 deg for both drives over the entire range of motion. This level of accuracy is close to the pointing detection threshold of the detectors.

- *Redundant Position Sensing: The joint shall incorporate two redundant diodes as position sensors.* Diodes are incorporated in the joint drives at 0° and 105.7°. The diodes are regularly checked in-flight. Neither has ever malfunctioned.

- *Position Holding: The drives shall hold their position when power is removed:* The actuator's detent torque, providing 18 in-lb (2 Nm) of holding torque, served as launch lock and holds the joint's position during observations. No drifting has ever been detected during sensing.

Mechanical Construction

The following is a brief mechanical description of the instrument. A more detailed description of MCS can be found in publication [6]. The completed instrument is shown in Figure 2. As can be seen, the entire instrument is covered by thermal blankets.

Figure 2: The Completed MCS Instrument

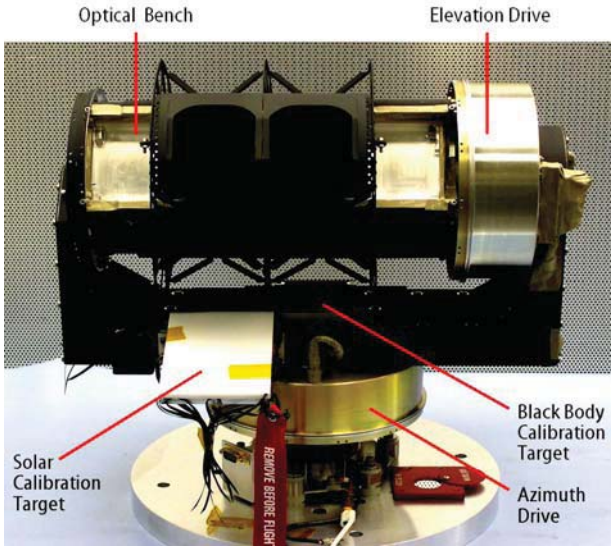

Figure 3: Instrument without Blankets

Figure 3 shows the instrument without its thermal blankets. It consists of an optical bench assembly, two rotational drives that provide azimuth and elevation scanning capabilities, and a yoke-like structure that serves as structural support for the upper part of the instrument. All motor control electronics resides on three individual electronics boards located inside the yoke structure.

The optical bench is a thin walled rectangular structure, containing two telescope assemblies. One of the telescope assemblies is depicted in Figure 4. The focal plane is at the inside surface of the hexagonal block at the upper right. A cross sectional view through the optical bench is shown in Figure 5: The incoming light passes through the baffle first. The beam is then relayed by a 3-mirror optical beam system before reaching the detector arrays at the focal plane. The telescope's control electronics is on two electronics boards, one attached to the top, the other to the bottom of the optical bench.

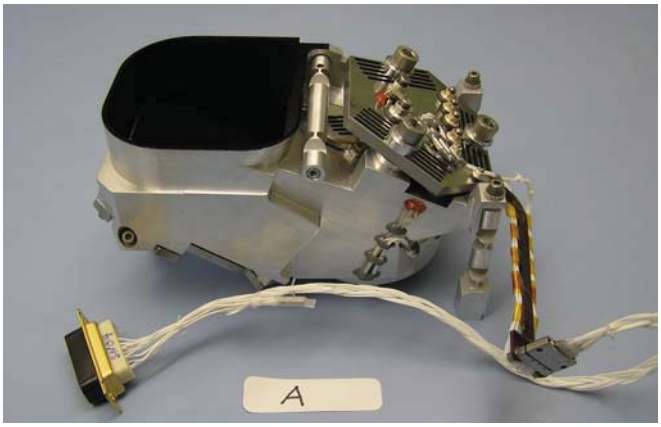

The solar calibration target is the bright plane that can be seen in Figure 3. It reflects indirect sunlight into the instrument. The black body calibration target is recessed in the yoke structure. The instrument can calibrate itself against the black body calibration target when the instrument is pointing straight down.

Figure 4: One of two Telescope Assemblies

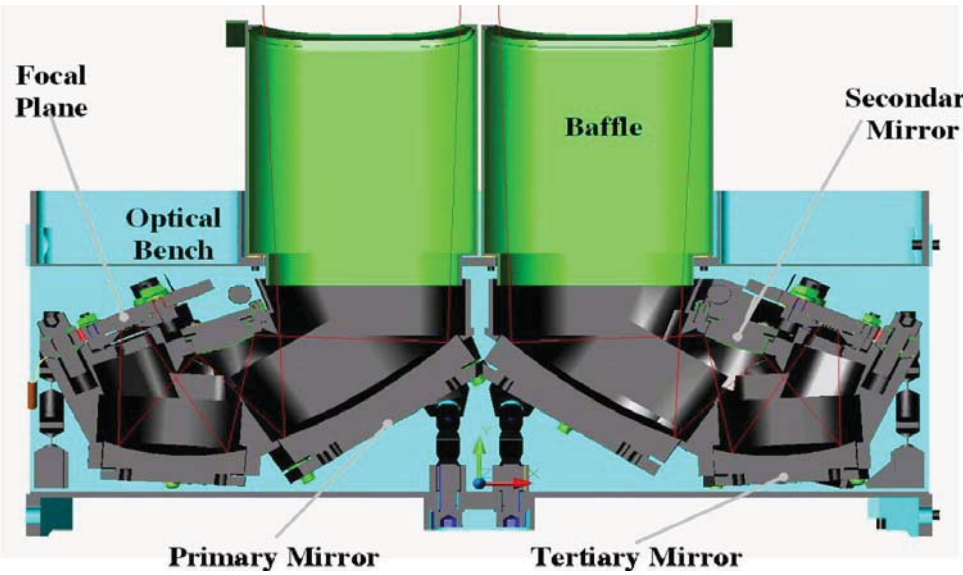

Figure 5: Cross Sectional view through the Optical Bench

Joint Drives

Both joint drives [7] combine an actuator and a twist cap section in a compact design. Their actuators are identical but the output bearing configurations are different: The azimuth joint has a hub extension so that its bearings could be spaced further apart; and it features dual duplex bearings. This enabled it to withstand the more severe launch loads at the base of the instrument. To further increase the bearing's load capacity, all output bearings feature full compliment ball bearings, thus eliminating the usual bearing retainer (see "Keystoning Effects" below). A final difference is that the azimuth joint has the bearings in a back-to-back configuration for stiffness, whereas the elevation joint has them aligned front-to-front, enabling compliance to the third bearing at the other side of the optical bench. Fig. 6 depicts the azimuth joint with its output bearings spaced further apart. An azimuth-type joint was used for the life test.

The motor is a brushless stepper motor, having a step angle of 30 degrees. It has redundant windings and detent capabilities. Its stall torque is 0.012 Nm. The transmission is comprised of a planetary gear stage, followed by a harmonic drive. The overall gear ratio is 297:1.

The twist cap chamber contains six printed circuit flex cables in a clock spring arrangement, enabling the electrical wiring to transition from the stationary to the rotating section. Each flex print has 14 electrical traces for a total of 78 power and signal traces and 6 grounding traces.

Position Sensing

There are two diode assemblies per joint, sensing the joint's position at 0° and at 105.7° degrees. The 0° position is used for re-initialization. The 105° position is between the limb and space views, and is crossed twice every 35 seconds.

A disk (near item 5 in Fig. 6) normally blocks the light path between the light emitting diode (LED) and the phototransistor. The disk has one slot, allowing diode light to pass through when the slot passes a sensor. The slot size had to be made quite large (approx. 1-1/2mm) for sufficient light from the diode to pass through. Therefore, the sensor is triggered for up to six steps during each diode passage.

During initialization, the 0-step is determined by scanning past the 0° diode first while recording all positions the diode is triggered, then computing the center position. By evaluating the diode and knowing which of the four motor phases corresponds to the computed center step, the controller can uniquely determine the joint's position. Subsequent position sensing only checks if the sensor is triggered when the software anticipates passing the previously determined center step of either diode. To save diode life, the diodes are only turned on when the system expects to pass one of the sensors.

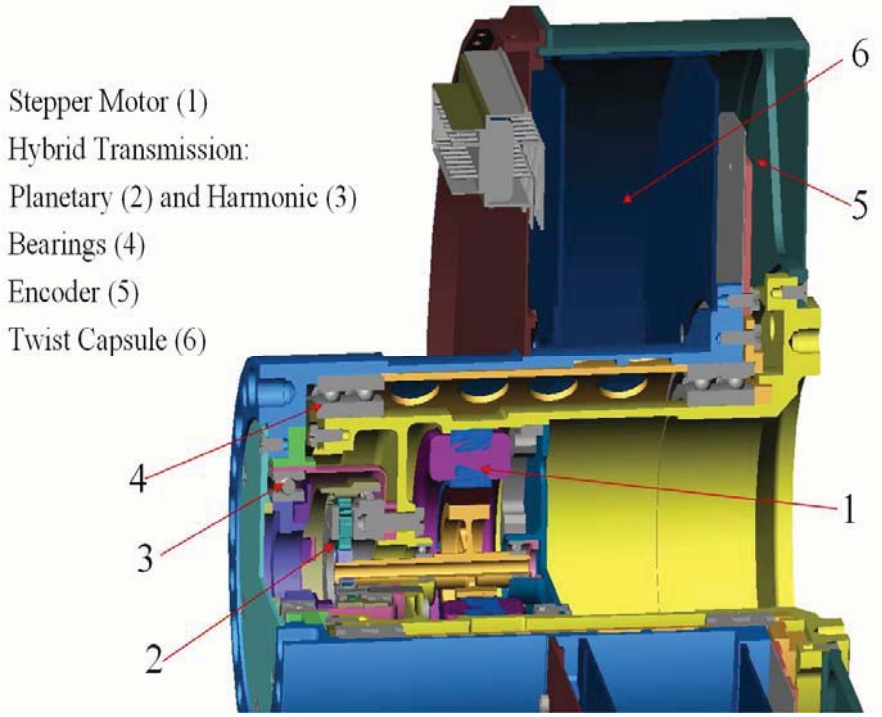

If the actual joint position does not correspond to the commanded position (due to whatever causes the anomaly), the position error has to be at least 3 steps away from the commanded position to be detected by this sensor system, having a 6 step diode trigger window. A sensed error reading is recorded but not reported immediately, thus complicating the error analysis (see "Error Discussion" below) Error cancellation is also possible if a subsequent error is in the opposite direction. However, if the flight software detects an error, it will reinitialize (see below), even if a subsequent error (hysteresis effect), should cancel it out.

Figure 6: The Azimuth Actuator/Twist Cap

Motor Control

Micro-stepping motor control was implemented to reduce motor vibrations that otherwise would propagate to other sections of the spacecraft, in particular to the highly sensitive HiRISE camera. The flight motor controller is a 4-phase micro-stepper controller: At low speeds, the motor driver ramps the currents in a quasi-sinusoidal fashion, rather than by discrete square waves. A complete sine wave advances the motor by four cardinal steps. Hence, an electrical cycle is comprised of 4 phases. At higher speeds, the current input per motor step switches to fewer discrete micro steps. The number of micro steps diminishes to two with increasingly shorter step duration when the motor approaches full speed.

For the error analyses, it is important to note that, if the energized motor functions as expected, it is in sync (or in-phase) with the motor controller at nominally zero position errors. Should the motor loose steps, its speed most likely will drop to zero or it will automatically re-synchronize to the controller at a multiple of four steps from the commanded position. Since most of the measured position errors were four step errors, it follows that the system stops one control sequence away from the commanded position. This does not explain, however, the few other position errors for which telemetry indicated another step difference from the expected position, even some confirmed position overshoots. A mechanical cause, producing substantial overshoots, is highly unlikely.

Qualification Testing

Common wisdom says: test what you fly, fly what you test. But reality is not that simple: A full instrument qualification program was undertaken for MCS, as is customary for flight hardware, including a separate life test for one drive joint. Both flight joints were independently acceptance tested as well. The purpose of this section is not to give a full account of the test program, but to highlight some limitations the test program faced, and the consequences this might have had for the anomaly and anomaly investigation.

- *Tests not done in zero-G*: this was universally considered as acceptable. The issues were that the life test had to be done with the joint axis aligned horizontally. Otherwise, the lube might have gravitated out of the bearings and the flex tapes would have sagged and rubbed against the twist cap walls.

- *Life test not done in vacuum:* This remained a contested item throughout the development with ever reoccurring questions at reviews, particularly concerning lube issues and heat dissipation. There were just simply not enough resources to do a full-simulated life test, lasting 18 months, in vacuum: Heat dissipation concerns could be settled by doing the necessary analytical work. The lube issues were partially resolved by scientific evidence, partially by pointing to similar devices that used the same lubricant and successfully operated in space.

- *Joint testing not done with a flight-like controller*: In today's short development cycles, there often is not enough time to develop long lead components in time for integrated testing: A duplicate flight-like controller was not available for the life test, nor was a flight-like controller ready in time for the qual/acceptance testing of the joint drives. For all joint stand-alone testing, an off the shelf, 2-phase pulse with modulated (PWM) stepper motor controller, emitting square wave signals, was used. The flight controller uses micro stepping instead.

It was determined only during integrated instrument testing that the motor produced substantially less torque than anticipated with the micro stepper controller. This jeopardized much of the previous qualification and acceptance testing. Re-testing was not possible on the integrated instrument and renewed joint stand-alone testing was impossible due to time constraints. In particular, the input waveform generated by the flight controller was insufficiently measured, analyzed, or understood.

To compensate for the reduced torque, an in-flight remedy was implemented, increasing the in-flight minimum temperature for the elevation actuator to 15°C. This keeps the viscosity of the actuator's lube lower, offsetting the decrease in torque with the micro stepper controller. Fortunately, enough heaters and additional heating power could be made available. What remained unsettled, however, was that the actual torque the motor produces with the micro stepper driver was not well known, nor was the effect of using different electrical motor inputs sufficiently well understood and evaluated.

One position error occurred during a routine aliveness test in spacecraft assembly and testing. It was unfortunately not detected until a review of the telemetry a few days later. A visual inspection of the instrument revealed no issues. The instrument performed as expected and all other telemetry was as expected. Due to limited resources and time, no further investigation was performed at that time, although instrument scanning was monitored for a repeat occurrence (none occurred prior to launch).

The obvious 'lesson learned' here is to allow enough time for adequate overall system testing and to have spare resources. The follow-on Diviner development proved that this is difficult. Schedule slips and late delivery of components again required substituting flight components with dissimilar engineering model (EM) components, causing the overall end-to-end system testing to be shortened as well.

Joint Drive Operational Parameters

Parameters		Life Test	Ground Test	Azimuth Drive	Elevation Drive
		MCS	MCS	MCS in Flight	MCS in Flight
Nr of load cycles required		3,500,000	N/A	350,000	3,500,000
Env. or Op. Tempearture	degC	-2, +3, RT, +60°C	-3	5 to15°C	15 to 25°C
Load Velocity	steps/sec	450	380	263	263
Load Acceleration	deg/sec²	25	25/42	25	42
Load Inertia	kgm²	0.1045	.12 to .14/.03	0.12 to 0.14	0.03
Voltage	V	28	28	32.5	32.5
Electrical Input		PWM	micro stepping	micro stepping	micro stepping
Environment		Nitrogen	air	vacuum	vacuum

Table 1: Life Test Joint vs. Space Operations

- *Differences between life test and space environment:* Table 1 lists the differences between the life test and the actual in-flight conditions for all MCS joint drives. In summary, the load inertia was close to the value for the azimuth joint, but the 3.5M load cycles reflect the life of the elevation drive. With the life tested joint surviving 3.5M cycles at a torque level equal to twice the value the elevation drive requires, and by using a square wave controller that produces much larger dynamic load spikes (hammering

effect), it can be stated that the life joint was over-tested. The testing validated the mechanism and flex cable's ability to function properly far beyond the full life requirement of this mission. Moreover, it demonstrated a capability that far surpasses previous NASA flight experiences with similar space flight mechanisms. During the entire life test, the drive stalled only once at 2.3M cycles at -2°C. The cause was increased viscosity of the lube because of a slight degradation of the lube due to aging. Cold testing was resumed at +3°C and finished without any further incidence.

Figure 7 shows a close up picture of the harmonic drive, taken after the life test: No mechanical wear could be detected at any mechanical parts, nor was there any graceful degradation evident, which would have expressed itself, for instance, by substantial increases in backlash. But the lube's color had changed from brown to black in the engagement zones between gear teeth and in the bearings. Chemical analyses, however, revealed that lube samples taken from inside the engagement zone had retained their lubricating capabilities. The joint thus maintains its full capabilities.

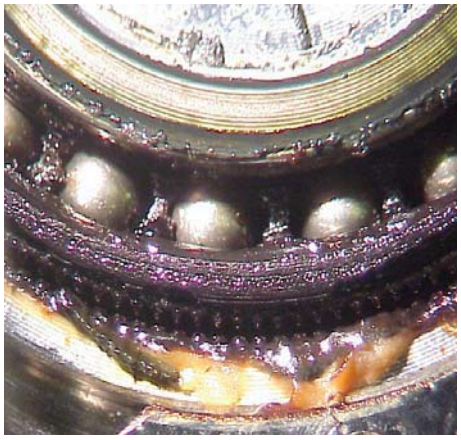

The overall conclusion based on life test results (for life test conditions), is that the joint demonstrated its capability to survive the required mission error free, pointing away from a mechanical cause for the anomaly: The life test joint is still being used on occasion today, proving its mechanical integrity and the lube's lubrication capabilities time and time again. It runs error free, provided it receives the proper electrical input signal and current.

Figure 7: Close up View of Mechanical Components after the Life Test

Keystoning Effects

During the assembly of Diviner's elevation joint, it was noticed when the partially assembled joint was rotated freely (actuator not attached yet), that the output bearings occasionally experienced some hard spots for no obvious reasons. The bearings ran smoothly again when part of the inner ring preload, applied by the bearing retainer (at arrow tip of item 4 in Fig. 5) was removed. Initially, a non-flat retainer surface was suspected that could have deformed the thin cross section bearings. But even after re-machining the retainer shoulders and checking flatness and perpendicularity of every shoulders of the bearing assembly (all within ±0.0003 in, 0.008 mm), hard spots could still be detected occasionally when the full retainer preload of approximately 120-lb (54-kg) axial load was applied. This resistance was somewhat position dependent and lasted over a short distance of up to 30 degrees, but could disappear and reappear at different locations.

Not finding another cause, the bearing supplier [8] was contacted. Their engineering department related that they had experienced similar behavior on other applications with full complement bearings as well. The phenomenon is called keystoning. Here is a somewhat personal explanation of this writer for what happens: If the balls are not rolling exactly on the same race diameter, which can happen with angular contact bearings, the rotational velocity of the balls inside the bearing are not exactly the same. Hence, with no retainer to separate the balls, they progress from contacting each other to pressing against each other in the high load zone. That causes sudden frictional forces between balls. This friction force is not sustained over a long distance because the external load on balls fluctuates (i.e. if the bearing's external load is applied radially, then the balls roll away from being under the high radial load zone). After the external load on a ball is removed, it is free to re-align itself in the race grooves and w.r.t. other balls. Thus, a friction load may or might not build up when balls enter the high load zone.

With a retainer present, a ball might temporarily push against the retainer's finger that engages between two balls. But since the retainer is much more compliant, it will not produce excessive friction forces in the high load zones. Thus, the retainer prevents keystoning from occurring. Lesson learned: avoid using full

complement bearings, especially for dithering motions that rotate the bearing just by just a few degrees, even if it means paying the mass penalty for going to a larger size bearing with a retainer.

For Diviner's elevation drive, the remedy was to reduce the pre-load the inner bearing retainer ring exerts. This was possible because this joint does not require the stiffness the azimuth joint needs. The Keystoning behavior noticed during the Diviner assembly was not noticed during the MCS assembly. However without objective evidence that it is not present on the MCS elevation actuator, it is impossible to say that the MCS actuator does not exhibit the same keystoning behavior.

Actuator Pointing Error Detection and Response

Instrument Position Error Detection and Response

Position errors occur when the MCS flight software (FSW) and the hardware disagree on the position of an actuator. The position of the actuators is checked when passing through either of the diode locations. Position errors only occur while slewing, but a mis-pointing caused by a position error will persist (with the same magnitude) until the actuator is re-initialized.

When the MCS FSW determines there is a position error, it sends an error message in the engineering telemetry. After reporting a position error, the FSW re-initializes both actuators, removing any pointing errors. While re-initializing the actuators, slewing is done at a very slow rate and errors are generally irrelevant since the FSW is searching for the diode. After a certain number of position errors, the instrument fault protection stows the instrument and waits for ground intervention.

The complexity is that the FSW does not report the error when it is detected; it is only reported at the end of an SST (sequence of slews). Thus, the actual pointing error occurred at some point before the last diode crossing in the SST. This also means that if the position error occurred early in a long and complex scan pattern, the instrument will be mis-pointed until the end of the SST.

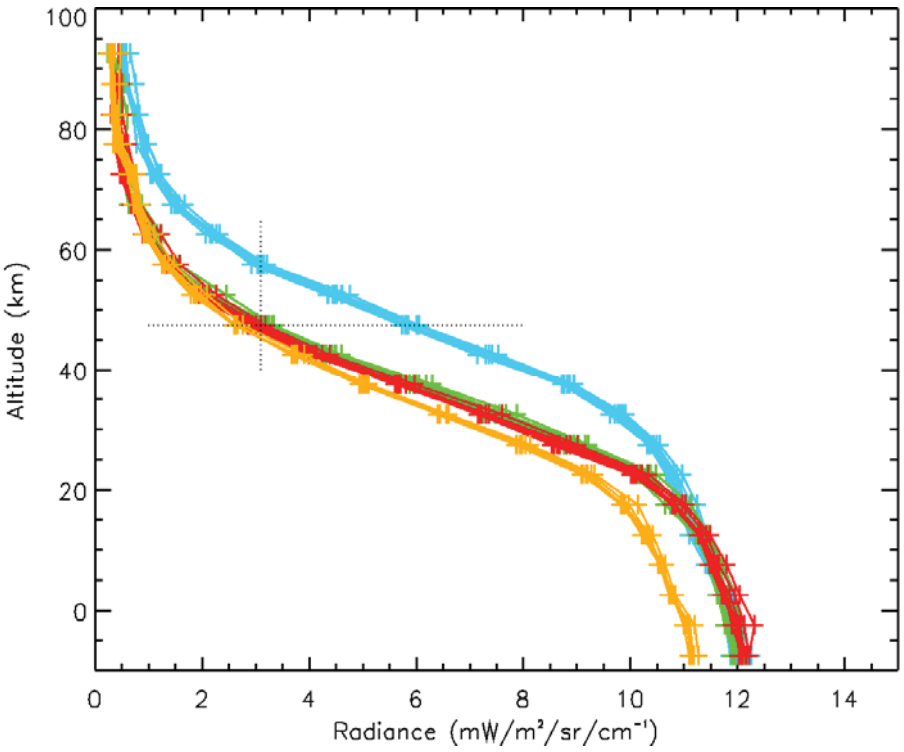

Limb Validation of Pointing

Without an absolute position encoder, it is not possible to determine the size of a particular error. However, the team has been able to use the instrument data to determine roughly how many steps the instrument is out of position by looking at the radiances when pointed at the limb. This is done by using channel A3 (core of the 15 micron band) and comparing the calibrated radiances of the limb views during the period around when the error is reported. We use limb view before the probable slewing error, while the error is in effect, and after the actuator has been re-synchronized.

Figure 8: Detection of Slew Errors at the Limb of Mars

Figure 8 shows an example analysis. For each observation, MCS acquires eight samples of the limb (thus the clusters of 8 lines). The actual detector values are the + symbols, placed on an altitude scale

based on spacecraft (S/C) pointing and assuming the pointing is correct. The red and green families are the two measurements before the error occurred. The light blue profiles are after the pointing error and the brown family is after the actuator was re-initialized. The most accurate determination is done where the radiance is changing the fastest with height. In this case, the 50 to 60 km region was used. It is obvious that the light blue family is mis-pointed. The dotted horizontal line indicates detectors that should be at the same altitude and have the same radiance. The vertical dotted line shows the actual family of detectors that have the same radiance, and are pointed at the same altitude. The two detectors between the actual and expected alignments indicate a pointing error of two detectors. Since each detector is approximately 0.2° tall (or 5 km on the limb), this is a pointing error with the actuator pointing 0.4° (equivalent to 4 steps).

This provides additional information on the timing of many position errors by indicating that the actuator was already mis-pointed while observing the limb, thus reducing the number of candidate scans for the error. The limb view radiances also sometimes (as in Fig. 8) provide knowledge of the magnitude and direction of the error. Based on experience, we have found that for small errors (< 1°), looking at the limb radiance provides a pointing accuracy of one actuator step (0.101°).

There are cases (especially over the poles) when the atmosphere is changing too fast with latitude and it is not possible to accurately measure the pointing error. The profiles are too different to determine which detectors are actually pointing at the same location. In many of these cases, it is still fairly obvious that the actuator is mis-pointed. There are also cases where there are no limb views during the scanning sequence before the error is fixed by re-initializing the actuator. In these cases, the size of the position error cannot be determined.

Actuator Anomaly Timeline

Initial Flight Errors

MCS started primary science phase operations on Sept. 24, 2006. After an initial flurry of scanning changes, routine operations settled in. On the evening of Dec. 11, 2006, MCS FSW detected a position error and re-initialized the actuators. Over the next 4 hours, three additional position errors occurred and caused the instrument fault protection to stow the instrument as designed. This occurred at ~5% of the tested life of the actuator.

Over the next two days, an analysis of the telemetry during the position errors showed no other signs of a problem. The initial study of the science observations by the team indicated that there were no large pointing errors in the data. The first four errors were very intermittent and all showed preconditioning by the black body viewing (see below). The last instrument ground commanding prior to the error (a routine health status check) had been 3 days before. The last change to the scanning had been 11 days before. All of the commanding was verified to be correct and not the cause of the position errors.

Initial Response and Diode System Testing

An initial fault tree was defined. The most likely candidate on the tree was the elevation 105°-diode system (since this diode had reported all four errors). The other early candidate was the occurrence of a solar particle event about a day before. Three initial actions were taken: Another health status check was performed (it was unchanged). Second, on Dec. 14, MCS fault protection was initialized with a count of 6 position errors (stow on the 7^{th} error) and scanning resumed. This was to see if the errors were transient. And if not, the scanning would hopefully provide additional information on the actuator health. After 7 hours of scanning, MCS FSW had detected 7 more position errors and again stowed the instrument. This scanning did show that the blackbody preconditioning (see below) was not required for an error to occur. It also indicated that errors could occur in sequences other than the limb scan.

In order to test that the problem was the 105°-diode system, a quick patch was developed to disable its use by the FSW. On Dec. 19, this was ready, installed, and scanning resumed with the position error counter set back to its default value of three. The expectation was that this would stop the FSW from reporting position errors, allowing the investigation to focus on the 105°-diode system while the instrument continued to collect science observations. If the position errors were due to a real mis-pointing

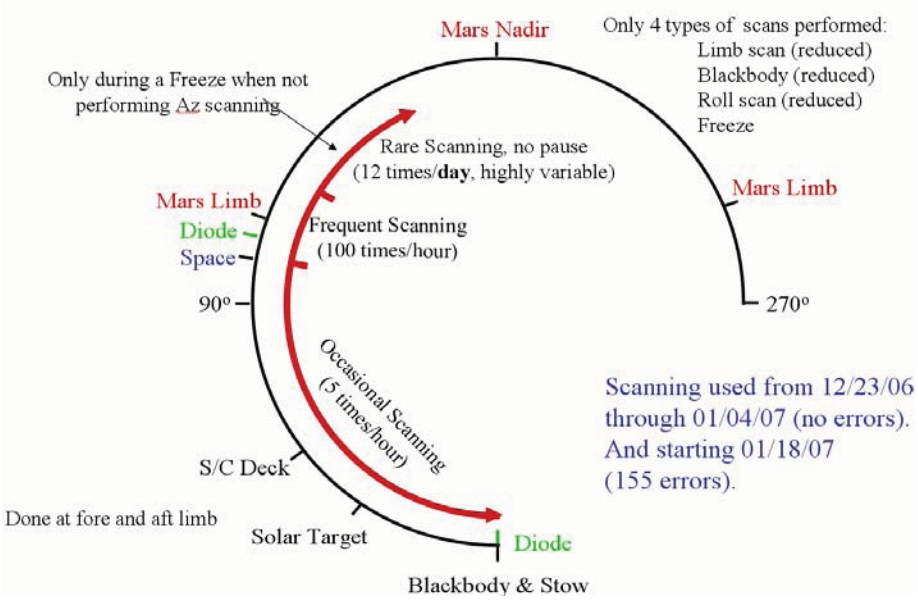

of the actuator, then they would soon be caught by the 0-diode and corrected by the re-initialization. After approximately 6 hours of scanning, 4 position errors had been detected by the 0-diode.

Initial Diagnosis Tree and Reduced Scanning

A "problem scan" diagnosis tree was developed to identify the slew or slews causing the errors. It was also designed to determine if there were operational workarounds for the position errors. The first step was to use a reduced set of scanning (Fig. 9) that only involved using a blackbody scan and a limb scan, both limited to 10° below the limb. For sun safety reasons, freeze commands were still allowed to cause occasional scanning up to 35° below the limb. This scan pattern was designed to rule out one of the three candidate scans. Additional steps were designed to differentiate between the other two scans.

Figure 9: Range of Reduced Scanning

The reduced scanning was started on Dec. 22; it ran over the holidays without producing any errors. The next steps of the tree were started on Jan. 2, but still failed to produce additional position errors. Concerned that the results of the steps in the diagnosis tree were misleading the full scanning pattern was tested on Jan. 4. This did not generate any position errors until the morning of Jan. 16.

Initial Ground Analysis

In the intervening time, a number of analyses and ground tests were performed. Testing involved using the MCS life-test actuator and the EM micro stepper controller to attempt to generate position errors. Unfortunately, this controller deviates from the flight controller in a number of ways, shedding some doubt about the meaningfulness of the test results. The initial effort focused on reduced bus voltages (showing a very sharp transition from scanning without errors to not scanning). Attempts to corrupt the scan control software to introduce position errors met with limited success. Failing to execute a slew step at high speed would produce a 4-step position error. Reviews of the software design indicated that short of very targeted and special corruption, there were no ways to mis-command the actuator. And if such corruption existed, position errors would occur on all scans longer than 16°. Reviews of the electronics revealed that much of the firmware and hardware was shared by the two actuators and none of the separate components had known intermittent failure modes. The mechanical review also revealed no obvious causes or mechanisms for generating position errors. During this time the detailed analysis necessary to detect small position errors on the limb was also developed.

Initial January Response and Frequency Study

The next step on the instrument was to repeat the tests from December to see if they made the errors (temporarily) disappear again. In doing this, an attempt was made to isolate the part of the process that had eliminated the errors. The first new scanning, on Jan. 17 involved overwriting parts of MCS random access memory (RAM) to eliminate any corruption. This did not eliminate position errors. A second step taken on Jan.18 was to return to the reduced scanning. Again, position errors occurred. In these two tests, the error frequency seemed to have increased from 1/hour of scanning to 2/hour, although the time between errors was still highly variable.

The next experiment was designed to better understand the error statistics and to obtain a larger population of errors to examine for trends and correlations. The previous testing had generated 33 errors. The fault protection counter was increased to 50 and reduced scanning was resumed. MCS scanned for almost 3 days before generating the 51 errors and stowing. For sun safety, the scanning was pointed at the aft limb instead of the standard forward limb. This also changed the thermal environment of the elevation actuator. The time between errors varied from 2 minutes to 13 hours. The average was 1/hour (2/hour if the 13 hour gap was not counted). There was a hint that the frequency was increasing slightly towards the end of the 3 days. This run also had the first occurrence of an error immediately following the re-initialization of the previous error.

Azimuth Scanning

Next, the investigation proceeded to attempt to isolate the error by performing extensive (and identical) scanning in azimuth to see if errors would occur. This would either implicate or exonerate the shared components. The plan for test #8 was to scan for one orbit in elevation as usual and then slew in azimuth using the same scan pattern for the next orbit. Due to the control limitations of the instrument, an occasional slew in elevation would occur during the azimuth orbits to respond to freeze commands.

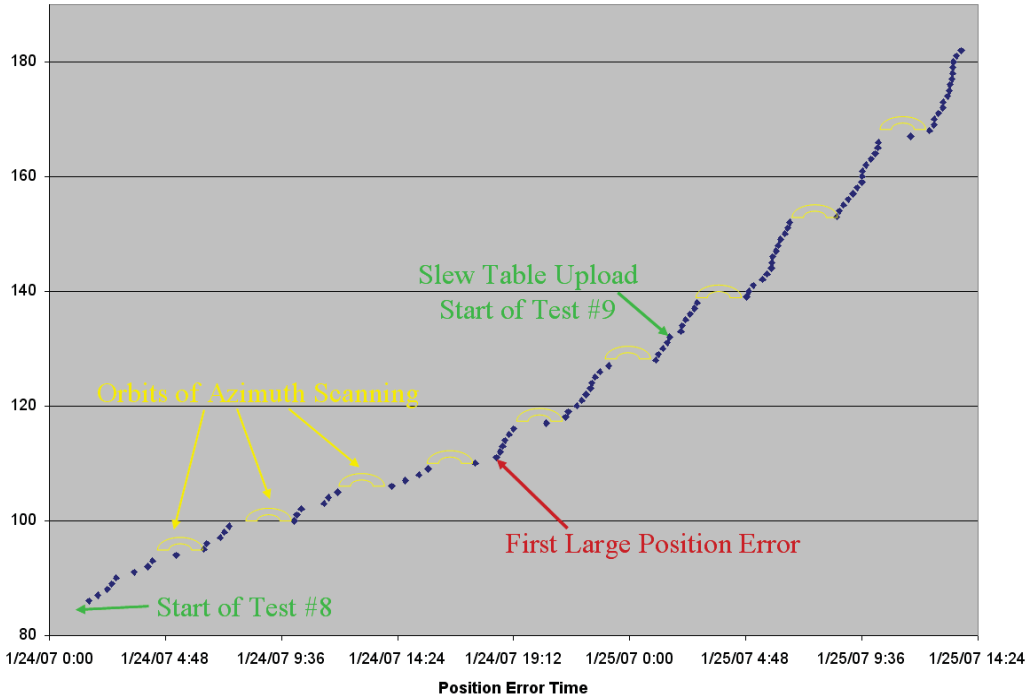

Figure 10: Error Rate in Late January Testing

The results are shown in Fig. 10, plotting the time of the error versus error number. The yellow crescents are the orbits with azimuth scanning. All of the errors during the azimuth orbits are associated with elevation scans. Part way through, it was decided to proceed with the next test (test #9) and remove the last difference between the two actuators by overwriting the elevation slew table with the azimuth table.

A number of features appeared in the test. First, there were no position errors during azimuth scanning. This implicates the drive electronics not shared by the actuators and the elevation actuator itself. During the analysis, it was discovered that on 5 occasions, a much larger error had occurred (they ranged from 2.6° to over 11°). All five errors were associated with slews going more than 10° below the limb. The direction of all the errors was consistent with either stalling on a slew or many 4-step small errors on the way to 35° below the limb (~145° in elevation space).

The other trend noticed during these tests (shown in Fig. 10) is an increase in the error frequency. And even more disconcerting, the rate of increase appears to accelerate. A careful analysis showed that the

major jump in error rate occurred when the first large position error occurred. Note that even at the most rapid, the average was still over 20 slews between errors.

One interpretation of the two tests (in addition to eliminating a large number of systems from the fault tree) was that the elevation actuator was rapidly degrading and would soon be inoperable. The final error rate was also significantly degrading the ability to perform good science observations. And the large pointing errors introduced a sun safety issue. This led to the formation of an anomaly tiger team. At this time, Starsys [7] was actively brought into the investigation.

Limb Staring and Ground Testing

It was not know if the progressive degradation was due to use or just due to aging. Given the fact that staring at the blackbody provided no science, it was decided to move once (Feb. 9) to stare at the limb and avoid using the elevation actuator until the anomaly investigation could perform a thorough analysis. The theory was that if the actuator were to remain jammed in that orientation, it provided the maximum science return (estimated to be about 70% of the planned science).

One series of key tests was a set of torque measurements and controller waveform sampling. These were performed with the EM controller with either the life test actuator or a test motor. Testing revealed that the micro stepper controller using the flight parameters generated significantly less torque than expected. This system no longer met (and did not come close to meeting) the design requirement of a factor of 2 for torque margin at the lower end of the 26 V to 36 V S/C voltage range. There were a number of other peculiarities in the power waveforms supplied to the actuator, mostly related to limitations of the motor controller processor.

Most of the torque reduction was traced to a miscommunication over the back-EMF (electromechanical force) constant to be used for the flight motor winding configuration. A new parameter was determined by analysis and then refined experimentally with the life test actuator. With an increased back-EMF constant, effectively supplying more current, the motor torques were still marginal, but at least now met design requirements at the nominal operating voltage of 32.5V.

In late March, MCS was power cycled due to an MRO safe mode entry. After the power cycle, MCS returned to limb staring. This removed corruption concerns and a number of other very unlikely items from the fault tree.

The in depth investigation determined there were no plausible catastrophic failures on the fault tree. The investigation also developed fixes for a number of the torque and slewing issues (although not all could be fixed, some were built into the way the MCS FSW controlled the motors). But the investigation was not able to point to a root cause, or even a plausible root cause.

Continued Flight Actuator Testing

It was decided to resume using the elevation actuator in late May, incorporating the changes in the motor control parameters to increase the instrument torque and clean up the waveform to the extent possible. The scanning was further reduced to only involve the blackbody (but only twice per hour), space views and the limb. The first four blackbodies were followed by a limb scan that had a position error, ending the test. Due to the simplicity of the scanning, the limb radiance analysis indicated all four errors appeared to be overshoots (the only other scenarios involve complex inaccuracies of the 105° diode system and scans ending exactly the “right” distance short).

The instrument returned to limb staring at this point. An evaluation of the fault tree in light of overshoots focused on actuator resonances (the only fault on both the overshoot and undershoot branches). The blackbody pre-conditioning of all errors (as opposed to January when errors were so frequent, many were occurring without the pre-conditioning) also led to considerations of slew length. The next test (on June 14) reduced the top speed of the actuators to avoid any resonance effects. The change to the top speed did not appear to have any effect; three errors occurred within 30 minutes and the instrument stowed.

Following the end of the previous test, scanning was resumed, but only between the limb and space (~8° total slew length). This was an attempt to see if eliminating the blackbody pre-conditioning improved the

performance. A first position error occurred after 30 minutes, followed by two more 4 hours later. No errors were seen after the third error. Short scans, while not immune to errors, seemed to have improved the performance by eliminating position errors. This scanning continued for the next week without errors.

On June 22 (after developing a new diagnosis tree), the 8° scanning was extended 20° above the limb. The goal was to see if scans that reached top speed failed. They did not fail and after running for 24 hours, it was decided to try the May 31 scanning to verify that position errors had not disappeared again. Unfortunately, 4 errors occurred within approximately two hours and the instrument was returned to scanning only between the limb and space. Again, there were no position errors in this range of scanning.

To try to pin down whether the errors were position dependent or slew length dependent, the scanning was modified on June 28 to add blackbody sequences, but to do the move to and from the blackbody in a series of 8° slews instead of one long slew. This was not successful with errors still occurring on the limb scan following the blackbody scans (although at about half the rate as earlier in June). This seemed to point to a position dependent error generating mechanism. The instrument was returned to a state where it was scanning between the limb and space, and the instrument remained free of errors.

Errors Disappear after Reduced Scanning

Over the July 4 week, one blackbody per day was added to the scanning. This was inserted due to keystoning concerns since an 8° slew does not move the balls of the output bearings by a full diameter; it was essentially just rocking them back and forth. This scanning had been performed for most of the previous two weeks and was expected to continue for at least another week over the holiday. The expectation was that one position error would be generated every day or two and if the frequency increased rapidly, instrument fault protection would cut in and stow the actuators.

No position errors occurred. This led to experimentations (over the next two weeks) where the timing and frequency of the blackbody calibrations was varied (reaching the original 5/hour rate). None generated position errors. It seemed that scanning over a limited range for an extended period with the updated motor control parameters (higher torque, cleaner waveform), had made scanning elsewhere less prone to errors. Or perhaps scanning over any region above the limb made scanning in that region less prone to errors. Yet, scanning in January seemed to have contributed to the increase in error frequency.

Resumption of Calibration Views

In late July, a spacecraft issue led to the actuator anomaly investigation going on hiatus until early October. During this time, scanning between limb and space with occasional blackbody scans (done in short 10° scans due to the spacecraft issue) was performed. Also, further EM testing revealed that the new motor controller parameters were causing the controller to current limit when the spacecraft bus voltage was at 32.5 V. The clipping distorted the current waveforms and had the potential to introduce a new source of position errors. This led to the design of a new set of motor controller parameters with slightly lower peak currents that did not clip on the life test actuator in the lab, but still had a slightly higher torque then the January tables and the cleaner waveform.

Starting in October, a set of steps was performed to return to more normal scanning with the new motor controller parameters. This was done gradually with several days between each change in configuration or slew profile. These steps included increasing the number of blackbody views back to 10 and adding in a view of the solar target. However, the elevation actuator was never allowed to go higher then 120°. Combined, the addition of these observations allowed the science channels to be fully calibrated.

Final Flight Testing—Returning Below the Limb

With full calibration restored, a new round of careful testing was started. Given that the errors seemed to be at least partly position dependent and could possibly be improved by repeated scanning, it was decided to slowly expand the scanning below the limb (>120°). During this process, the fault protection was set on a hair trigger to stow the instrument on the first error. This was the region where large errors had previously occurred. Since large errors seemed to be associated with increased error rates elsewhere, there was a desire to minimize the number that occurred.

The first steps was to return to reduced scanning, but eliminate all possibility of going more than 10° below the limb. This was accomplished by some very careful analysis to insure sun safety. No position errors occurred while scanning 10° below the limb over four days. Therefore, the next step was to expand the range to 20° below the limb. Within 20 minutes (and 30 limb scans), a position error occurred and instrument fault protection stowed the instrument. The error was determined to be a small (4-step) position error.

The next day, the scanning pattern was reduced to go only 10° below the limb. This was successful and no further position errors have occurred as of this paper.

Discussion of Errors and Error Statistics

MCS has experiences 203 position errors. The errors fall into 5 groups according to when they occurred (see above). The first error was prior to launch. The first flight family occurred in Dec. 2006, a second family in Jan. 2007, a third family in June 2007 and the final position error occurred in Oct. 2007.

All of the errors have been characterized to the extent possible, given the limited in-flight telemetry. Unfortunately, an extensive analysis of the instrument and spacecraft telemetry associated with the errors has been mostly unproductive, both on an individual basis and in statistical analyses.

One of the difficulties in the investigation is that the specific slew with the position error is almost never known. There is almost always at least a pair of suspect slews for any given position error. In some cases, there are many possible slews where the error could have occurred. And given the slew pairs are in opposite directions, in most cases, an undershoot on one slew or an overshoot on the other could be responsible for the identified error. The May and June diagnostic tests were set up to minimize this uncertainty. But without an absolute position indicator, not all of the uncertainty could be removed. However, there are a few significant points that the analysis did uncover.

Even though the errors families appear indistinguishable, various error-type subsets stand out:

- The five large errors (errors where pointing is off by more than 1 degree) all occurred in January. All of these large errors are known to have occurred at elevation angles > 120°. Since slewing operations were stopped in Jan. 2007, the instrument was only slewed past 120° for ~20 minutes in October.

- Most of the pointing errors that could be measured are 4-step errors. The preponderance of the 4-step errors is assumed to be due to the 4-phase nature of the MCS controller. At nominal speed, a four-step error could potentially be generated by an approximately 15 m-sec lasting signal disturbance. But there are at least four errors that are 2-step errors (and a small family that may be 5 or 6 step errors). One possible way of generating 2, 5 and 6 step errors is to have the error occur at the end of the slew.

- The time (or scanning) between individual errors is highly variable, ranging from 2 minutes (the first scanning after re-initializing) to over 13 hours in one case. Even within a given time frame, the time between errors is highly variable (for example, the 13-hour interval followed a 2-minute interval). While errors may have occurred on consecutive slews, they never occurred on more than 5% of the slews, and in most periods, the frequency is below 0.1%. The general error frequency increased during the December and January groups of errors. During the May/June diagnostic period, the error frequency decreased until the instrument reached an error free state using the current set of environmental constraints.

- No correlation of errors with any environmental condition has been found (at the resolution of the available data). In particular, there are no significant temperature fluctuations. The only possible exception is the spacecraft bus voltage: For most of the MRO orbit, the voltage is at 32.5 V, but it dips as low as 28 V during the eclipse (slowly dropping at eclipse and then returning to 32.5 V immediately afterwards). There are relatively few errors at low voltages (since the bus is at 32.5 V most of the time). At most, the probability of an error at 28 V is twice that above 32 V, but this might not be statistically significant. The life-test actuator (and the limited testing of the flight actuator), indicate there is a very abrupt transition between completely stalling (at 22.8 V) and running fine (at 22.9 V) with the micro stepper controller. Thus, any in-flight voltage fluctuation should not cause errors. Due to the rapid

increase in torque with applied voltage, this also indicates that there is probably ample torque margin when most errors occur.

- The errors appear to occur with any slew lengths. A rigorous exploration of slew length dependency was not undertaken (ambiguities between slew lengths and error rates makes the existing data difficult to interpret). Errors definitely occurred on both short slews and long slews (short slews are < 16° and do not reach top speed). Several of the four errors definitely occurred on slews of ~8°. It is possible that errors preferentially occur on long slews, but this probably only indicates that the error probability correlates with the distance covered.

- It appears that at least one error can be associated with a slew in each direction. Also, at least one error is an undershoot. There are four errors that (assuming the diodes can detect all combinations of a 4-step error) are overshoots. But without the exact knowledge when slew errors occurred, it is often not possible to determine the direction of slewing, nor whether the error was an overshoot or undershot.

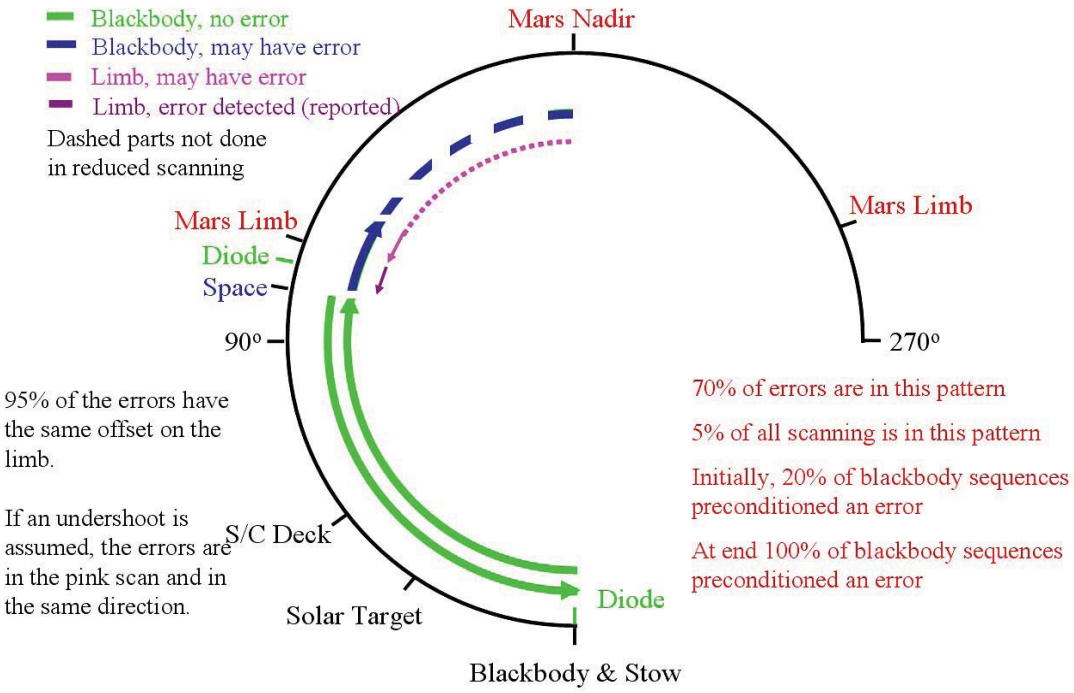

Figure 11: Blackbody then Limb Error Pattern

Error "Preconditioning"

One peculiar pattern reoccurs frequently as position error: Many of the position errors are in the limb scan sequence following a blackbody sequence. Figures 11 & 12 illustrate the pattern in two different ways. Due to crossing the diode in the blackbody sequence, and the fact that there is no error reported at the end of that SST, it follows that slewing to and from the black body (K and K^{-1} slews in Fig. 12), which are unique to the blackbody sequence, do not generate the errors. Therefore, the error (if it occurs) is in A, B or C. Slew B does not often occur (it is related to tracking the limb), thus, the error has to occur in either A or C. Slews A and C are a very often occurring pair, occurring ~20 times more frequently than the blackbody pair. Approximately 70% of the total errors occurred in the A-C pair immediately after a black body scan, even though this combined pattern occurs in only 5% of the total slewing. Equally interesting is that 95% of the cases where the pointing error is known, it has the same sign.

The cause of this preconditioning is not understood. Initially, 20% of the black body sequences preconditioned an error. When the errors were the most frequent, all black body sequences preconditioned a position error. Extensive analysis of the MCS software, electronics and mechanical assembly, has failed to point out any reason for such a preconditioning to occur.

Current Status and Conclusions

Currently the instrument is producing ~90% of the expected science (including all of the atmospheric science). Thus, it was decided to forego further experimentation with the flight instrument. It was determined that the next testing would significantly risk the current actuator performance and would be unlikely to shed any light on the cause or behavior of the anomaly. Instead, it was decided to run the instrument with some operational restrictions to gain as much science as possible through the end of the primary science phase (Dec. 2008). There are two operational restrictions: The first is to use the new SST tables developed during the investigation. The second is to limit scanning in elevation to no more than 10° below the limb. This has prevented further errors.

There is currently no identified root cause for the position errors. All conceived investigations with EM hardware, life test actuator, or in-flight evaluations have failed to shed further light on the issue. Likewise, design reviews and theoretical studies have been exhausted without identifying an obvious root cause.

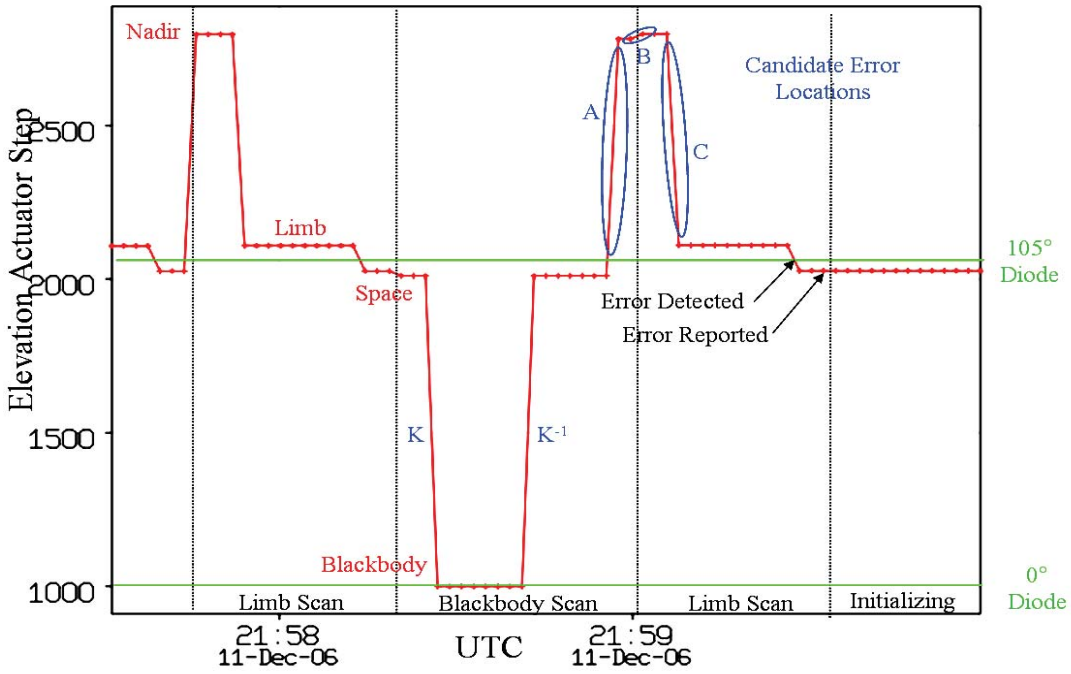

Figure 12: Slews Implicated in a Typical Position Error

While four potential root causes have not been completely eliminated, none appear to be the answer. None of them matches all observed or anticipated behavior of the hardware. All have major issues that would be sufficient to eliminate them from consideration.

It also should be noted that none of the potential error sources could explain the probable overshoots. It is very difficult to generate sufficient un-commanded movement in the motor to create a 4-step overshoot. While the motor controller could do so, the same software, firmware, and hardware are acting as motor controller for both actuators. Thus if it generates overshoots, it would do so for both actuators. Detailed independent reviews and extensive testing of the motor controller has not shown any propensity to generate overshoots.

The remaining potential root causes are:

- *Keystoning:* It has been demonstrated that keystoning produces position dependent behaviors. But it only occurs at the output bearings (where the available torque is high) and could be expected to affect

both actuators (as well as the life test actuator). Keystoning, if it manages to create position errors, would most likely produce large errors (stalling), not 4-step errors, and would never create overshoots.

- *Excessive Friction/Debris:* Excessive mechanical Impedance in transmission or driven load, specific to the flight elevation system, is a possibility. Its origin might be foreign particles/debris in the actuator, parts rubbing each other due to positional shifts, a somewhat loose thermal blanket, workmanship issues, etc. It could explain some positional dependence and subsequent disappearance of the errors with the higher current tables now in place. However, it is difficult to imagine how this failure mode could generate the short four-step nature of most errors, nor would it produce overshoots.

- *Drive Electronics Parts Intermittent Failures*: It is possible that the errors are due to a (partial) failure of an electronics part of the elevation motor driver. This might be due to the solar flare. But the motor driver is completely position insensitive. Besides, none of the known failure modes of any electronics part used has a history of intermittent behavior, nor would it self-correct over time.
- *Controller-Motor Interactions:* The errors could be caused by a subtle interplay between the waveforms generated by the motor controller software, the interpretation of them by the motor drive electronics and the momentum, motion, and normal phase lag of the rotor. Testing and reviews were unable to identify any specific categories of interactions (e.g. resonances) that might produce this behavior, but due to the complex and poorly modeled interfaces involved, there might be an interaction that was not noticed or did not exist with the test equipment, that is slightly dissimilar to the flight hardware. This type of phenomena might be expected to affect both actuators as well. This scenario has no obvious mechanism for generating position dependent errors either. It is also not obvious why it would suddenly appear after several months of perfect operations, get significantly worse, then disappear again.

References

[1] http://mars.jpl.nasa.gov/mro/

[2] http://www.planetary.org/programs/projects/mars_exploration/mars_climate_sounder/

[3] http://www.planetary.org/programs/projects/mars_climate_sounder/objectives.html

[4] McCleese, D. J., J. T. Schofield, F. W. Taylor, S. B. Calcutt, M. C. Foote, D. M. Kass, C. B. Leovy, D. A. Paige, P. L. Read, and R. W. Zurek (2007), Mars Climate Sounder: An investigation of thermal and water vapor structure, dust and condensate distributions in the atmosphere, and energy balance of theolar regions. J. Geophys. Res., 112, E05S06, doi:10.1029/2006JE002790.

[5] Pennzane is a product of Nye Lubricants Inc., Fairhaven, MA.

[6] Jau, B. M., "Mechanical Description of the Mars Climate Sounder Instrument." IEEE Aerospace Conference, Big Ski, Montana, March 1-8, 2008.

[7] The Joint Drives were supplied by Starsys Inc., Louisville, CO.

[8] Bearings supplied by Timken, Keene, NH.

Picture Credit

Figures 6 and 7: Courtesy of Starsys Inc.

Acknowledgement

The research described in this paper was carried out at the Jet Propulsion Laboratory, California Institute of Technology, under a contract with the National Aeronautics and Space Administration.

Icy Soil Acquisition Device for the 2007 Phoenix Mars Lander

Philip Chu[*], Jack Wilson[*], Kiel Davis[*], Lori Shiraishi[**] and Kevin Burke[**]

Abstract

The Icy Soil Acquisition Device is a first of its kind mechanism that is designed to acquire ice-bearing soil from the surface of the Martian polar region and transfer the samples to analytical instruments, playing a critical role in the potential discovery of existing water on Mars. The device incorporates a number of novel features that further the state of the art in spacecraft design for harsh environments, sample acquisition and handling, and high-speed low torque mechanism design.

Introduction

The Phoenix Mars Mission, currently en route to Mars, consists of a lander equipped with tools and analytical instruments designed to assess the history of water and the habitability potential of the Martian polar ice-bearing soil. Icy soil is believed to exist in these regions underneath a shallow layer of regolith. The Phoenix lander includes a scoop mounted on the end of a robotic arm that will be used to remove the layer of loose soil covering ice-bearing materials. Once these materials are encountered, an ice-sampling tool within the scoop will penetrate and acquire icy soil samples that will then be delivered to analytical instruments by the Robotic Arm to ascertain the existence of water ice. The scoop and ice sampling tool is known as the Icy Soil Acquisition Device (ISAD). The ISAD is a first of its kind mechanism that will support the Thermal Evolved Gas Analyzer (TEGA) and the Microscopy, Electrochemistry and Conductivity Analyzer (MECA) experiments with critical soil samples.

The ISAD has two main functions; bulk digging of loose soil and precision sampling of hard ice-bearing soils. It is partitioned into two main chambers. The front chamber is used as a scoop, and performs the function of removing bulk material. The rear chamber contains a high-speed cutting tool, which penetrates and acquires harder icy soil. The two main chambers are separated by a series of panels. These panels prevent bulk material from filling the rear chamber of the ISAD during digging of loose soil, and also allow acquired icy soil to be transferred to the front chamber using a series of Robotic Arm wrist movements. A funnel feature in the front chamber allows for precision delivery of loose and icy soil to analytical instrument inlet ports. The ISAD also has two blades, the first attached to the front of the scoop, and the second attached to the bottom of the scoop, which are utilized for scraping surface regolith and ice.

When acquiring icy soil, the ISAD is preloaded against the surface so that the cutting bit is retracted into the scoop. The drivetrain is energized, rotating the cutting bit at high speed. Spring preload on the cutting bit forces it into the soil. Icy soil is ballistically ejected from the surface, into the rear chamber of the ISAD, where it is captured. Several samples can be acquired, after which the icy soil is transferred to the front chamber of the scoop using a series of Robotic Arm wrist motions. The sample is then delivered to science instruments by the Robotic Arm.

The ISAD is a first generation mechanism to be qualified for space flight. There are many aspects of the design that are unique, and should be brought to the attention of the spacecraft mechanism community. Many of these features will likely be used on subsequent missions, and this paper will provide details on their design, and lessons learned. This paper will first discuss the highly constrained design space dictated by the fact that the mechanism was a very late addition to the payload of the Phoenix Mars Lander. It will then give an overview of the ISAD device and its operational usage. The paper will discuss details of the design that are critical for understanding the lessons learned, and the unique features of the mechanism. Solutions to the constrained design space and lessons learned during design, assembly and testing will be presented in detail.

---

[*] Honeybee Robotics Spacecraft Mechanisms Corporation, New York, NY

[**] Jet Propulsion Laboratory, Pasadena, CA

Proceedings of the 39th Aerospace Mechanisms Symposium, NASA Marshall Space Flight Center, May 7-9, 2008

Design Discussion

Driving Requirements

Prior to the ISAD, the planned method of acquiring ice-bearing soil samples used a set of passive blades mounted to the exterior of the Robotic Arm digging scoop. Once a layer of potentially icy soil was encountered, these blades would be dragged across the surface of the hard icy soil by the Robotic Arm to produce piles of loose material, which would then be acquired by the scoop and deposited at the instrument inlet ports. Several blade geometries were tested in dry analog material to determine the feasibility of the sample acquisition method. It was found that the method of scraping material and using the scoop to acquire it produced an insufficient amount of sample for the TEGA instrument within a reasonable amount of time. Due to potential sublimation loss of water ice, a faster, more productive method of sample acquisition was required. Honeybee Robotics Spacecraft Mechanisms Corporation was contracted by the Jet Propulsion Laboratory to provide an end-of-arm sample acquisition device that would produce at least an order of magnitude improvement on the passive scraping method, which had been generating on the order of tenths of cubic centimeters.

The ISAD was a late addition to the payload of the Phoenix Mars Lander. Most lander subsystems had already undergone their critical design reviews and were well into the fabrication, assembly and test phases by the time the ISAD was conceived. As a result, the ISAD had to comply with existing subsystems that had not been designed with an active end-of-arm sampling device in mind. This led to a number of requirements that tightly constrained the design space of the ISAD. These requirements, as well as a limited budget and rapid development schedule led to innovative design solutions and compromises.

One of the main drivers throughout the design process was the overall ISAD mass. The Robotic Arm was designed and analyzed to support a hollow scoop, with relatively light weight digging and scraping blades. The Robotic Arm's severe launch load environment required that the ISAD mass be limited to 0.75 kg in order to maintain sufficient strength margin.

The design of the ISAD was also limited by available resources of the lander electrical subsystem. There was one switched circuit available for an active device, limiting the device to one motor. A preset drive voltage of 24.6 to 29.3 VDC limited the speed of the motor to a narrow range of velocities. This voltage input was also unipolar, meaning that the ISAD would need to function unidirectionally. A restriction in the overall power available to the device resulted in a current limit of 1.0 Amp, causing a constraint on the available motor torque. Further constraining the amount of torque available for sampling was a requirement to start motion of the mechanism when preloaded against the ground with a torque margin of 1.0. Although an encoder was integral to the motor selected, there was no means of reading the encoder signal, resulting in an open loop device architecture, with no direct data feedback to tell if the device functioned properly. By reading the overall Robotic Arm subsystem power data, it could be determined that the device ran, however there would not be enough resolution in the data to calculate motor torque or speed. Due to limited budget and schedule resources, motor selection was limited to existing Jet Propulsion Laboratory flight spare stock from the Mars Exploration Rover project.

Productivity of the sampling device was also a key driver in the design process. The TEGA instrument requires at least 1 cm^3 of icy soil material at its inlet ports to capture enough sample to perform an analysis. To fulfill this requirement, multiple sampling placements of the ISAD can be performed, however sublimation loss of water ice places a constraint on the total duration of these groups of sampling occurrences.

During the conceptual stage, it was determined that vibration greatly improved the movement of icy soil over metallic surfaces at Mars ambient temperature and pressure. This resulted in a self-imposed requirement for the device to produce its own vibration to help fluidize particles and move them over internal transfer surfaces.

Several other requirements placed constraints on the geometry, function and material choices of the device, including operational and survival temperatures (-80 °C to +45 °C and -108 °C to +110 °C respectively), required interior volume for digging operations (300 cm^3), structural survival of digging loads during soil overburden removal, and surface coatings for thermal balance, durability and imaging.

Overview of Design

The ISAD is partitioned into two sections, a front and a rear chamber. The front chamber is used to collect bulk material acquired by scraping or digging, and transfer the soil overburden away from the main trench. Up to 310 cm^3 of loose material may be collected in the front chamber at a time. A Primary Blade is attached to the front of the scoop that helps break up weak soil. The front chamber can also be used for precision drop-off of bulk soil to science instruments located on the lander deck. A funnel feature shown in Figure 2 channels acquired material into an 18.2-mm wide slot, improving the accuracy of sample delivery. The funnel and scoop geometry were designed to maintain functionality at lander tilts of up to 16° with respect to the local surface normal. The ISAD scoop and funnel feature are separate components and are made of 7075-T73 aluminum with a hard coat clear anodize for abrasion and wear resistance. This coating on the interior surfaces also reduces glare when viewing acquired samples with the Robotic Arm Camera. A tungsten carbide secondary blade on the bottom side of the scoop provides a means of penetrating harder materials.

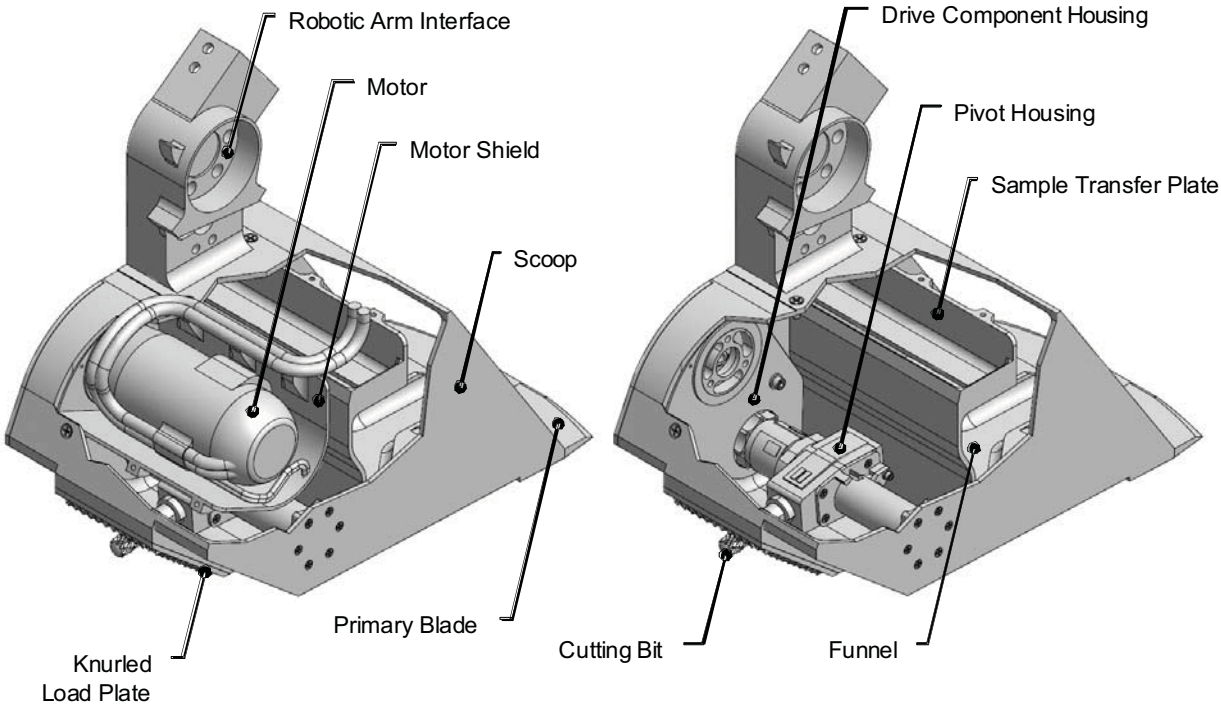

Figure 1. Cutaway of ISAD Showing Internal Components

The rear chamber of the ISAD contains a high-speed rasp cutting tool for penetrating the surface of hard icy soil, and acquiring the cuttings produced. Acquisition is accomplished by first preloading the ISAD scoop into the surface such that the spring-loaded cutting bit is forced into the scoop. A knurled contact plate grips into the icy soil preventing motion of the scoop and RA during rasp operations. The rasp cutting bit is then energized, resulting in rapid penetration of the surface, causing a plume of cuttings to ballistically enter the rear chamber of the scoop.

The tungsten carbide cutting bit is 6.35 mm in diameter and protrudes from the rear chamber through a 7.9-mm slot when the tool is in free space. The rasp cutting bit is mounted to a pivoting housing, which has a total stroke of 15°. Two hard stops prevent overtravel of this pivot housing. The “lower” hard stop limits the depth of penetration of the rasp cutting bit. The “upper” hard stop is positioned in order to allow the cutting bit to fully retract into the scoop. The pivot housing is spring loaded using a torsion spring. The torsion spring acts to force the cutting bit into the material, providing the necessary weight on bit of approximately 6 N for penetration of icy soil.

The rasp tool is driven by a brushed DC motor. The motor is powered by a current limited on-off circuit, which provides a maximum of 1.0 Amp, at 24.6 to 29.3 V. Accounting for frictional drag in the system, the actuator is able to produce 41 mNm of output torque at the rasp cutting bit and bit speeds of approximately 5300 RPM at room temperature. Torque is transferred from the motor shaft to the rasp cutting bit through a set of spur gears, and a pair of miter gears yielding an overall speed reduction of 1.25:1 from the motor to the bit. All gears are AGMA Q10, constructed of 15-5 PH stainless steel and age hardened to condition H1000. Figure 3 shows a cross section of a portion of the ISAD drivetrain. The cutting bit is supported on the upper end by a back to back angular duplex bearing pair while the lower end is supported by two shielded radial bearings. Another set of duplex angular bearings support the pivoting housing while three additional radial bearings support various drive train gears. All bearings are ABEC 7 and comprised of 440C stainless steel balls and races with phenolic retainers. All bearings and gears were grease plated with a solution containing 10 wt% Castrol Braycote® Micronic 600EF.

The device includes three resistive strip heaters that warm the mechanism to allowable operational temperatures. A 2.1-watt heater is attached to the motor, and two additional heaters, 2.7 watts and 1.6 watts are attached to the pivot housing. A temperature sensor on the motor provides ISAD temperature feedback. All components used to power the rasp cutting bit are thermally isolated from the main scoop body through the use of vespel as an insulating material. This minimizes heat transfer from the drivetrain components to the scoop sample transfer surfaces in an effort to reduce icy sample loss due to sublimation.

The cutting tool includes a set of features for producing vibration of the scoop surfaces. This vibration is essential for moving acquired sample from the rear chamber of the scoop to the front, and for improving the transfer efficiency from the front funnel to the instrument inlet ports. The vibration mechanism is only engaged when the rasp cutting bit is in its rest position against the “lower” hard stop. A cam feature attached to the rasp cutting bit engages a low-friction surface, which is grounded with respect to the scoop. As the rasp bit rotates at high speed, the cam feature causes the pivot housing to oscillate such that the spring loaded housing impacts the “lower” hard stop once per revolution, resulting in high frequency vibration.

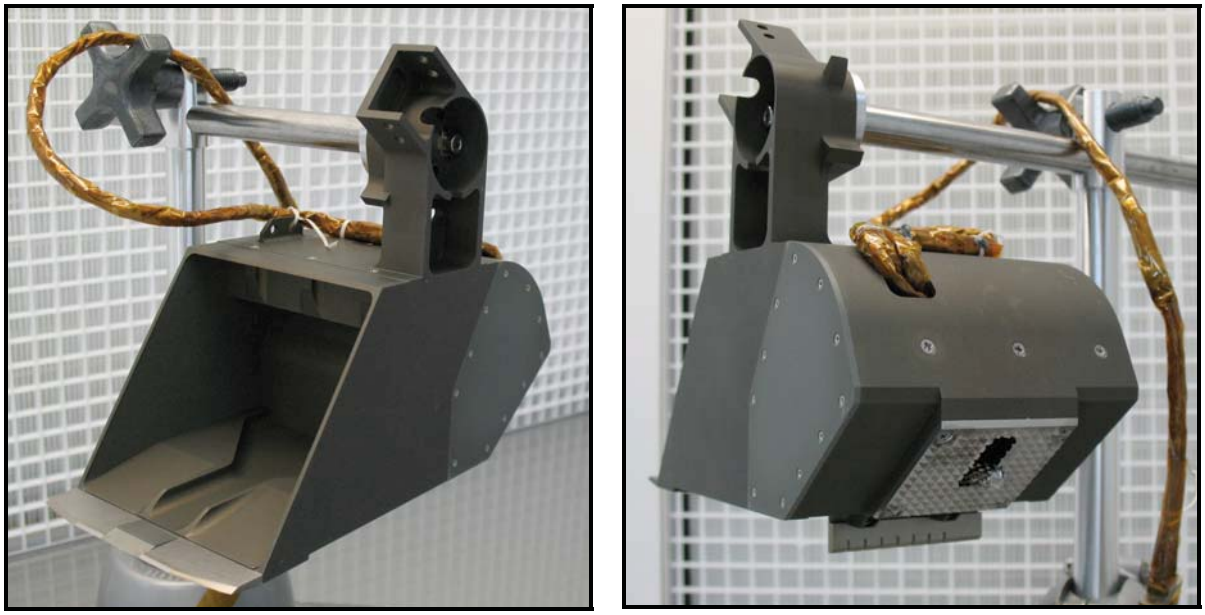

Figure 2. Icy Soil Acquisition Device Flight Unit on Assembly Fixture

The front and rear chambers of the scoop are separated by a sample transfer plate. During digging operations, this plate prevents the majority of scooped material from filling the rear chamber of the ISAD, which could result in jamming of the cutting tool. This plate also acts to move sample from the rear

chamber to the front chamber so that samples acquired using the rasp cutting tool can be dropped off to instruments in the same manner as bulk soil. The plate consists of a vertical and a horizontal shelf, with a slot in the horizontal shelf. This creates a labyrinth through which material can be transferred from rear to front by rotating the entire scoop about the Robotic Arm wrist axis. The sample transfer plate is made from 7075-T73 aluminum with a hard coat clear anodize for abrasion and wear resistance.

Once digging reveals hard icy soil, the secondary blade, located on the bottom of the scoop, may be used to prepare the surface for acquisition by the rasp tool, depending on the surface topography. This flat edged blade will scrape the icy soil to form a more uniform surface for placement of the ISAD. Once the surface has been prepared, the RA will place the ISAD such that the rasp tool is in contact with the target area. The RA will then preload the ISAD with a minimum preload of 40 N. The rasp cutting tool will then be energized for a period of approximately 30 to 60 seconds, resulting in acquisition of icy soil. The RA then relieves the preload on the ISAD and retracts it from the surface. Placement and acquisition can be repeated several times in different locations, depending on the amount of sample desired, and the spacecraft resources available. After all acquisition operations have been completed, the sample is transferred to the front of the scoop for imaging by the RAC, and drop-off to the analytical instruments. The transfer operation consists of a series of RA wrist motions to move the sample along a number of panels that divide the front and rear chambers of the scoop. During the transfer operation, the rasp cutting tool can be energized, inducing vibration to aid in the flow of particles.

Mechanism Design and Test Lessons Learned

High Speed Low Torque Seal Design

The Icy Soil Acquisition Device is a high speed, low torque sampling device. The Maxon REØ25 motor, coupled with a reduction ratio of 1.25 : 1, has a nominal output torque of 0.054 N•m (0.478 in•lb). In order to transfer the maximum possible amount of torque to the cutting bit, the frictional drag torque of the drivetrain needs to be minimized. Some sources of frictional drag in the mechanism's drivetrain include inefficiencies in spur and miter gear torque transfer, drag due to lubrication of bearings, and preloading of angular contact bearings. These effects can be minimized by tight tolerances and good assembly techniques, however the largest variability in a low torque mechanism's friction drag can come from the dust seal if not accounted for early in the design process.

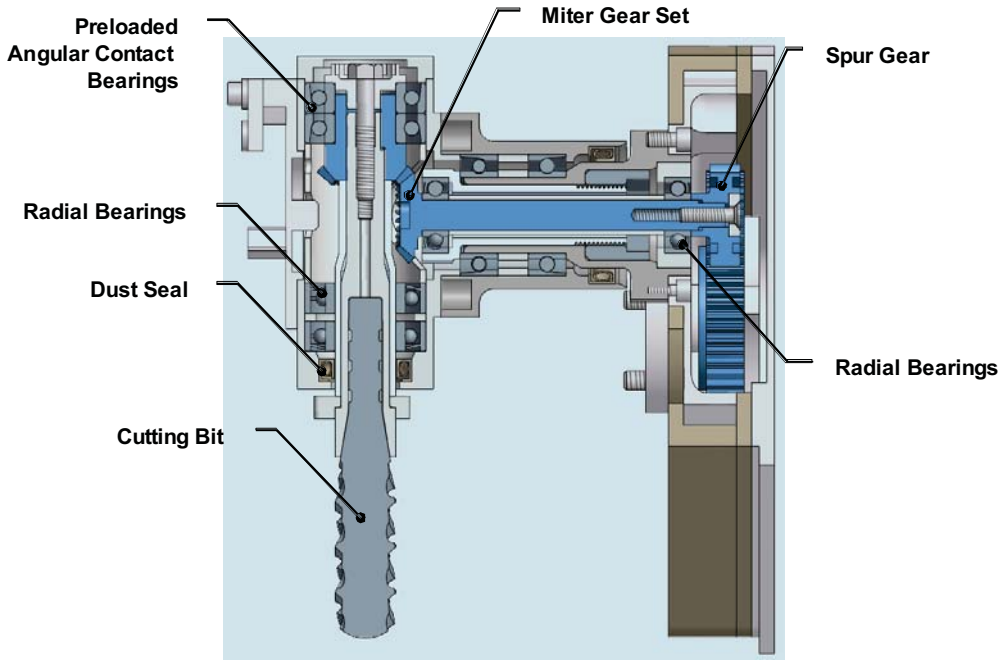

Figure 3. Drivetrain Cross Section Showing Dust Seal Location

As shown in Figure 3, the ISAD drivetrain utilizes a dust seal near the cutting bit to protect the critical internal components from dirt and dust migration. A custom canted coil spring energized seal was used for the dust seal, with Glass Filled Polytetrafluoroethylene Molybdenum Disulfide Reinforced (GFPM) polymer as the seal material, and 316 Stainless Steel as the backing and spring material. The shaft material on which the seal mates is 6Al-4V Titanium alloy.

When specifying a custom dust seal for a low torque application, it must be understood that manufacturers typically fabricate this type of seal to withstand high-pressure liquids and gases. As a result, spring energized seals are typically designed to be tight on the shaft, causing drag torques that can be a significant portion of the available torque when dealing with a mechanism such as the ISAD. With this effect in mind, the manufacturer was instructed to design the seal to a shaft diameter of 6.53 mm, when the actual shaft diameter was 6.34 mm. The difference was based on previous experience with high speed, low torque sealed mechanisms. When the seals were delivered, they were qualitatively determined to have an unacceptable amount of drag torque on the 6.34 mm Titanium shaft. This was expected, and material was removed from the shaft to reduce the frictional drag of the drivetrain. The required shaft diameter was determined by pressing the seal into the seal housing, and using hardened gage pins of varying size to find the optimal shaft size. By gently rotating the gage pin by hand, the technician could “feel” the difference in drag torque. This qualitative assessment of the drag torque resulted in the final diameter of the Titanium shaft being modified to 6.09 mm, a difference of 0.44 mm from what was originally specified to the manufacturer. This diameter produced the minimum amount of drag torque while maintaining a dust seal around the shaft. Subsequent testing performed on an identical seal revealed that the seal drag torque at room temperature on the 6.09-mm shaft was approximately 0.0035 N•m, while a 6.53-mm shaft would have produced a drag torque of about 0.018 N•m. After thermal dynamometer testing the Flight Model ISAD unit, the total drag torque of the mechanism was determined to be approximately 0.013 N•m at the low temperature operational extreme of -80 °C, and 0.007 N•m at room temperature (+20 °C). Had the manufacturer-recommended shaft diameter been used, the drivetrain drag torque would have increased by a factor of three at room temperature, leading to greatly reduced startup torque margin, and possible stalling of the mechanism at low temperatures.

When designing a custom spring seal for a high-speed low torque mechanism, it is difficult at best to determine the size of shaft, which will mate with a particular seal without having the seal in hand. Similarly, there is a large amount of risk associated with fixing the shaft diameter, and attempting to specify to the manufacturer the seal diameter to provide a dust seal while minimizing the amount of mechanism drag torque. The risk inherently lies with schedule and cost constraints, which were significant drivers in the development of the ISAD.

To minimize the impact on development schedule and project cost, the spring seal should be specified initially for a nominal shaft diameter. The shaft itself should be designed with the intention that material be removed once the spring seal, shaft and housing are in hand. This involves leaving enough material on the diameter of the shaft to allow for machining prior to final assembly of the mechanism. In this torque regime, it is critical that the shaft be matched to the actual seal press fit into the housing, as a slight variation in shaft diameter can make a substantial difference in the drag torque.

An additional observation related to the seal was noticeable change in frictional drag after exposing the mechanism to the high end of the required temperature range during thermal vacuum contamination control bakeout. While GFPM is rated for temperatures safely exceeding the +110 °C maximum that the ISAD was subjected to during thermal cycling, a noticeable difference in drag torque was observed after soaking for 8 hours at this temperature. Specifically, an additional 0.004 N•m of torque (approximately 10% of actuator output capability) was measured indirectly by considering the additional motor current to drive the mechanism under “no-load” conditions with the vibration feature disengaged. This observation was consistent for both the engineering and flight units. Initially it was not clear that this additional frictional drag was due to the GPFM seal. Since the change in drag did not warrant disassembly of the mechanism for inspection of this component, the seal could not be completely confirmed to be the root cause. However, all other possible scenarios were deemed highly unlikely .The seal hypothesis was supported by the fact that the drag slowly decreased to normal levels after several minutes of operation. Assuming the seal was the source of the additional drag, the reason for its change in behavior could be: (1) a slight tightening of the GFPM seal on the shaft due to pressure applied by the canted spring; (2) a change in the frictional properties of the GFPM-on-titanium material combination due to out gassing of

volatiles or (3) a combination of both effects. For mechanisms that are sensitive to slight increases in drag torque, it is recommended that mechanism designers experiment with these spring energized seals at the expected environmental conditions prior to finalization of the design.

Cam Actuated Vibration Mechanism Design

The ISAD includes a unique method of producing the vibration necessary for moving particles across sample transfer plates within the scoop. To the best of the authors' knowledge, this cam vibration mechanism is unlike any other flight-qualified device, and the design contains several important features that contribute to its successful operation. This type of mechanism can be utilized on future planetary sampling systems where vibration is required to aid the flow of particles.

The cam vibration mechanism utilizes a spring preloaded pivoting assembly to produce an impact force on the base of the ISAD scoop. Figure 4 shows the "Pivot Housing" in its rest state, with the mechanism un-powered. In this state, the "Cutting Bit" is in the fully extended position, and the pivot housing is fixed against the "Lower Hardstop". As the cutting bit rotates, the "Cam" gradually engages the "Bumper", raising the pivot housing off of the lower hardstop, against the direction of torsion spring preload. As the cam and cutting bit rotate further, a change in the cam geometry causes the cam to suddenly disengage from the bumper. This releases the preloaded pivot housing, allowing it to impact against the lower hardstop. This impact is directly coupled with the rotation speed of the cutting bit, and results in an approximately 90 Hz frequency. Both the cam and the bumper are individual components that can be changed out without affecting the design of surrounding hardware. This minimizes schedule risk, as cam and bumper design can proceed without delaying fabrication of mating hardware.

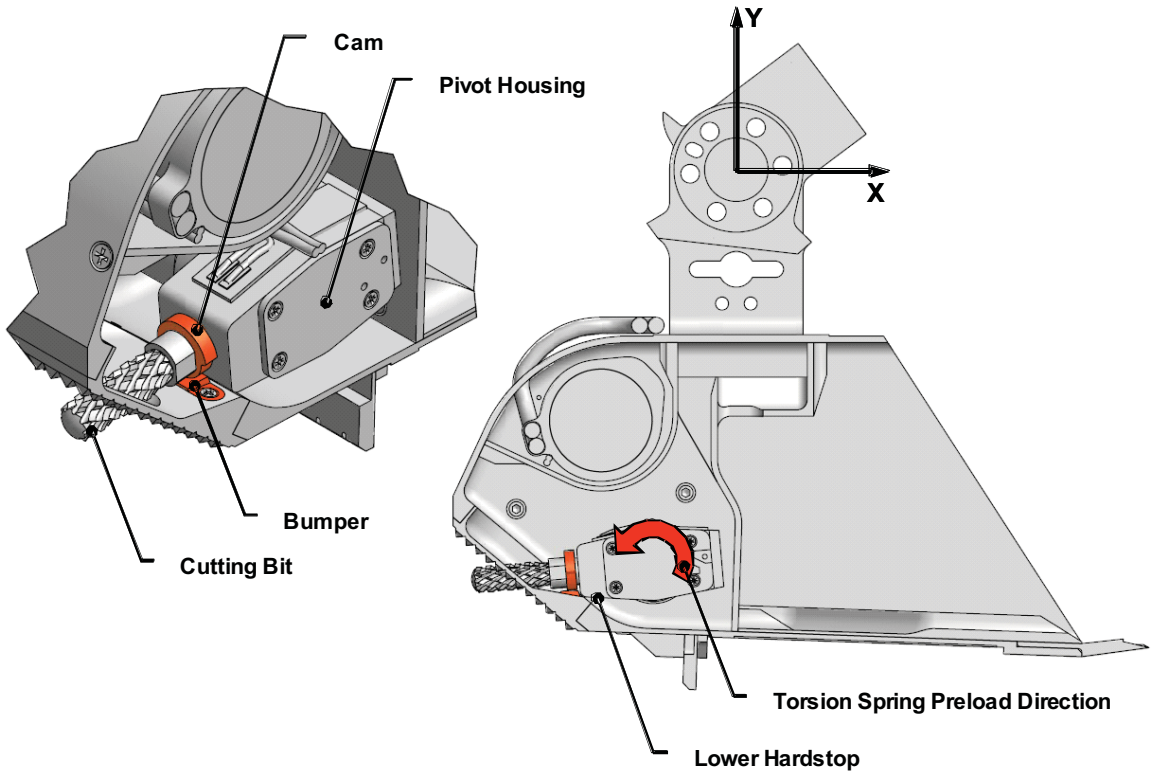

Figure 4. Cam Vibration Mechanism Section View

The primary challenge of a cam-actuated vibration mechanism is designing the interface between the cam and the bumper to function throughout the expected lifetime of the device. Gradual wear of the cam and bumper will ultimately degrade the ability to produce vibration. Material choices, cam and bumper geometry and surface treatments all contribute to the functionality of the mechanism as it nears the end of its required operational life. The cam vibration mechanism on the ISAD was required to function for a total

number of output revolutions of 383,000. Due to the unique nature of the device, a demonstration of two times life was required to prove flight worthiness.
The geometry of the cam was an important consideration in the design. Figure 5 shows the wear of an early prototype cam made from 17-4 PH Stainless Steel age hardened to condition H900 with no surface treatment. This cam interfaced with a bumper made from 50% cold worked Nitronic 60. These parts were designed for simplicity of fabrication in a short amount of time, and minimal consideration was given to the cam geometry. The wear shown in the images occurred after one hour of operation at 5300 RPM (approximately 318,000 output revolutions). These tests were performed in a vacuum chamber at Mars ambient conditions on a test fixture with similar geometry and rotational speed as the flight ISAD design. The vibration produced at the end of the test was insufficient to fluidize even dry particles. These images show the importance of geometry and material selection to the overall success of a cam-actuated vibration mechanism. The combination of 17-4 PH and Nitronic 60 is typically used to minimize galling and wear in sliding friction applications. In this application, the high speed and abrupt impact quickly deteriorated both materials.

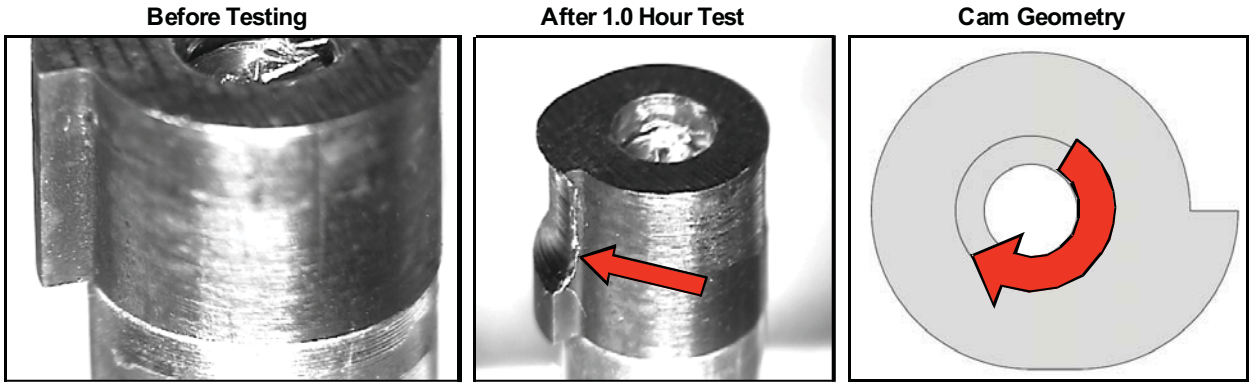

Figure 5. 17-4 PH Prototype Cam Wear and Geometry

As shown in Figure 5, the geometry of the prototype cam was not optimized to deliver a smooth transition between the minor diameter of the cam and the major diameter. The transition was abrupt, and occurred in the final quarter rotation of the cam. The flight cam design utilizes a cycloidal cam profile to gradually transition from the minor diameter to the major diameter through three quarters of a rotation. Cycloidal cam geometry is used in cam design where a sinusoidal acceleration profile is desired to minimize reaction loads. Equation 1 shows the desired cam acceleration profile. The displacement profile can be determined through integration and application of boundary conditions. The formula for the radius of the cycloidal cam profile is shown by Equation 2.

$$a = C \sin 2\pi \left(\frac{\theta}{T} \right) \qquad \text{Equation 1}$$

$$r = \left[r_{ROOT} + \left(\frac{h\theta}{T} \right) \right] - \left[\left(\frac{h}{2\pi} \right) \sin \left(\frac{2\pi\theta}{T} \right) \right] \qquad \text{Equation 2}$$

r = Cam radius , r_{ROOT} = Minor radius of cam, h = Distance between major and minor radius of cam
T = Period of cam

Age-hardened Vascomax C-300 Stainless Steel was chosen as the material for both the cam and the bumper due to its superior strength and hardness (52 Rockwell “C”). In addition, a low-friction electroless nickel coating from General Magnaplate (Magnaplate HMF) was used as a surface treatment on both the cam and bumper to reduce frictional effects, and improve surface hardness at the contact interface.

Figure 6 shows post-test images of a cam of identical geometry, material and surface treatment as the flight unit cam vibration mechanism. This cam, along with a flight-like bumper was tested in a Mars ambient environment to approximately 780,000 revolutions, two times the required life of the mechanism. The test was performed in several segments on a prototype ISAD with similar sample transfer plates and geometry as the flight ISAD. After each segment, a known mass of dry sample was placed in the rear chamber. Using the cam vibration mechanism, the material was transferred to the front of the scoop, where the mass was again measured. After a demonstration of two times the required life, the efficiency of sample transfer using the cam vibration mechanism did not show any signs of degradation, remaining at 90% or greater. As shown in Figure 6, there was minimal wear to the surface treatment at the end of the test, preserving the cycloidal geometry and the ability to produce vibration. The bumper showed similar minimal signs of wear. During the lifetime test, a witness plate was used to capture the material worn away by both cam and bumper. Comparing the measured mass of the worn material to the total calculated mass of the "ramp" portion of the cam, less than 10% of the ramp was worn away. This combination of material and geometry produced a cam vibration mechanism, which will continue to generate vibration well past the required operational life.

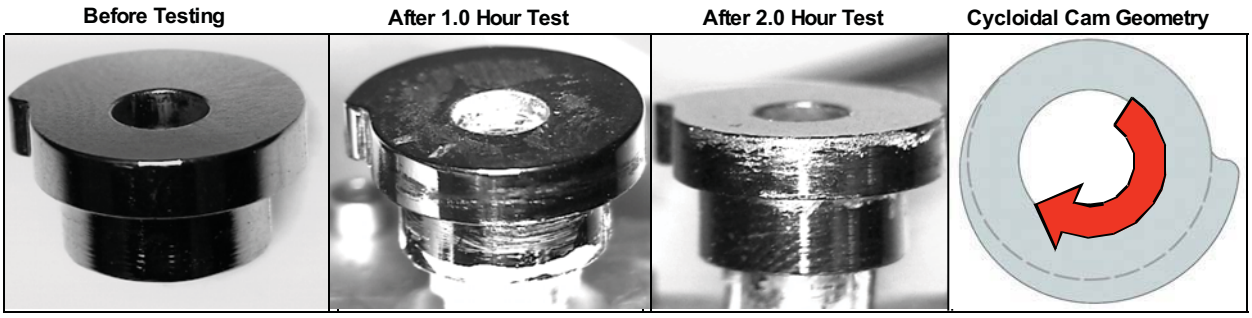

Figure 6. Cycloidal Cam Geometry

Small Form Factor Braze Joint for High Load Capacity

The cutting bit of the ISAD is a modified commercially available tungsten carbide rasp bit typically used in ceramic tile applications. A consumer rasp bit was selected due to budget and schedule risks associated with designing and testing custom cutting bits. A variety of bits were tested early in the design process, and a selection was made which provided the best sample production performance in dry analog material. For assembly purposes, a decision was made to vacuum furnace braze the cutting bit to a stainless steel shank to allow the use of threaded fasteners as a connection mechanism.

The ISAD cutting bit protrudes from the rear of the scoop when in the rest position. This results in exposure of the bit to potentially high loads during trench digging operations, and icy surface scraping operations with the secondary blade. As shown in Figure 4, during digging or scraping operations, the ISAD is translated in the "X" direction. To reduce the risk of damaging the bit and drivetrain during these sequences, the Pivot Housing is designed to retract automatically into the scoop if inadvertent loads are applied to the bit while digging or scraping. During these operations, loading of the ISAD is not limited to the X-Y plane. The Robotic Arm can impose lateral loads in the ISAD "Z" direction of up to 50 N. There is no retraction mechanism for the cutting bit to absorb loading in this direction, and although the lateral loads are small compared to those sustained by the structure in the X-Y plane, they are large enough to risk damaging the brazed connection of the cutting bit.

The ISAD cutting bit is only 6.35 mm (0.250 in) in diameter, due to limitations in the amount of torque available, and the desire to run at high speeds to increase sample acquisition productivity. This limited the selection of braze joint form factors to those that could be fabricated with the amount of material available on the cutting bit shaft. Due to the high speed nature of the design, minimizing shaft runout was desirable to reduce imbalance of the mechanism. The exposure to high lateral loads, and the brittle nature of tungsten carbide added further complexity to the design. A number of distinct features were incorporated into the braze joint design to minimize stresses in the connection while maintaining shaft runout between the cutting bit and stainless steel shank. These features can be applied to brazed connections for similar high speed, small form factor applications.

Figure 7 illustrates a prototype braze joint which was fabricated and load tested. Due to packaging constraints, it was necessary to reduce the diameter of the carbide bit to fit into the stainless steel shank. Three grooves in the bit provide for mounting of gold-nickel alloy wire to act as filler metal for the braze joint, but also decrease the overall strength of the tungsten carbide bit. The dimensions of these preform grooves is dependent on the amount of filler metal required to coat the surface of the braze joint. A loose radial clearance in this region between the bit shaft and the shank allows for braze filler metal to flow. The joint also includes an alignment feature near the base of the cutting bit teeth which controls shaft runout, but does not allow a sufficient gap for braze filler metal to reinforce the connection. Figure 8 shows the completed braze joint after having performed load testing. The joint was sectioned in order to view the internal braze penetration. Cracks at each of the three preform grooves are evident in the figure. Whether load testing, or the act of sectioning the joint was the cause for these cracks is unknown, however it is clear that the aspect ratio of depth to height of the preform grooves resulted in a high stress concentration at the base of these features, and failure of the brittle tungsten carbide shaft.

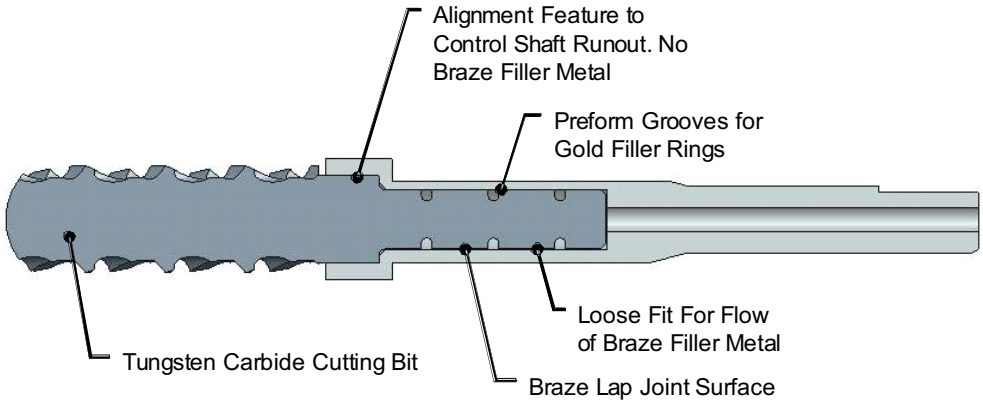

Figure 7. Prototype Cutting Bit Braze Joint Design

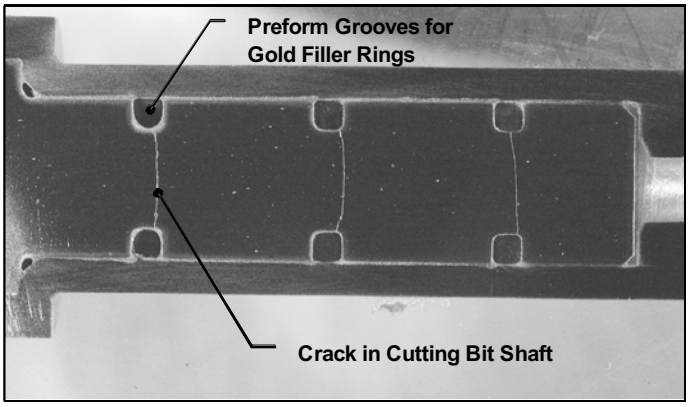

Figure 8. Prototype Cutting Bit Braze Joint Section Showing Cracks in Bit

The braze joint implemented on the flight ISAD unit utilizes the same cutting bit as the prototype design, but includes a number of improved geometric features for decreasing stress and controlling shaft runout. Figure 9 shows the final design of the braze joint. The material selected for the bit shank was 15-5 PH Stainless Steel. The material selected for the braze alloy was 82% gold and 18% nickel. Following the completion of the braze operation, the entire assembly was precipitation hardened to Condition H1000 to harden and strengthen the shank.

Compared to the prototype design, the aspect ratio of the preform grooves was changed to minimize stress concentrations at the base of the groove. Gold bands were used rather than gold rings, resulting in

shallower and wider grooves while maintaining the necessary volume of filler metal. This significantly reduces the stress concentration at the grooves. This design also incorporates a tapered transition between the outer diameter of the bit and the reduced diameter at the braze joint. This provides for ease of assembly while minimizing the stress concentration due to the change in geometry. To further strengthen the joint, a shallow recess in the tapered region allows braze filler metal to flow into the tapered region. To control runout of the bit, a tightly toleranced region at the base of the cutting bit allows the bit to maintain concentricity with the stainless steel shank during assembly and throughout the braze cycle.

These minor changes in geometry help to increase the load capacity of the brazed joint. The brazed joint survived a lateral load of 50 N applied at the tip of the cutting bit, with a proof load factor of 1.2. High-resolution X-Ray images of the joint confirmed that no cracks formed as a result of load testing, and that braze filler material penetrated all lap joint connections, including the tapered region. It should be noted that during the brazing process, the cutting bit was facing up with respect to gravity, demonstrating that capillary action alone allowed braze filler metal to flow into the tapered recess area, further strengthening the joint. Running the bit at its peak speed of approximately 5300 RPM and visually observing the runout confirmed that concentricity between the cutting bit and the shank had been maintained. Figure 10 shows the brazed assembly.

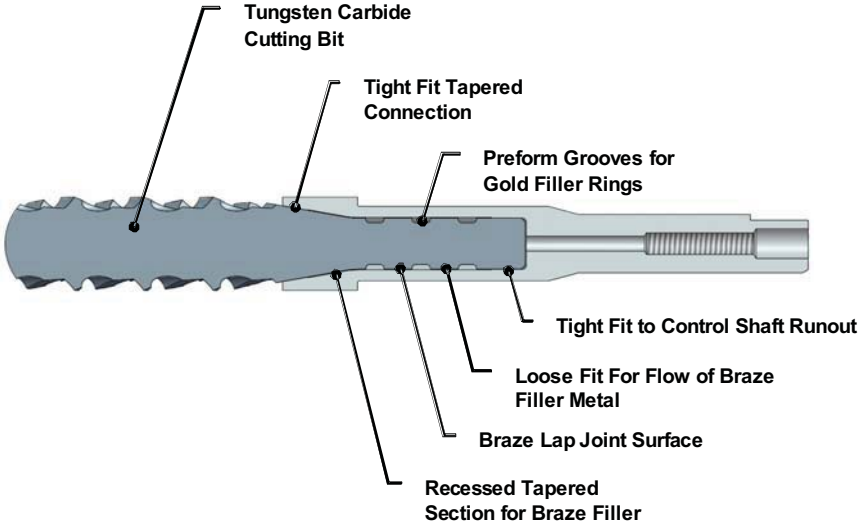

Figure 9. Flight ISAD Cutting Bit Design

When designing small form factor braze joints exposed to high load conditions and consisting of one or more brittle materials, it is important to minimize stress concentrations around geometry transitions, and to reinforce these transition areas with braze metal whenever possible. This braze joint is optimized for the geometry and material constraints imposed by the ISAD design. Had these factors, in addition to budget and schedule limitations not been present, the design may have taken a less involved approach, possibly utilizing a solid tungsten carbide shaft rather than a braze connection, or a less brittle material for the cutting bit.

Figure 10. Flight ISAD Braze Joint

Torsion Spring Design

During a sample acquisition operation the load plate on the ISAD is preloaded against the target by the RA, and the rasp bit retracts into the scoop body, applying a preload (or "weight-on-bit") to the soil. This weight-on-bit is produced by a torsion spring. In its free state the rasp cutting bit protrudes from the back of the ISAD scoop and is preloaded by the spring against an internal hard stop that provides 5.0 N of weight-on-bit at the bit tip. When loaded against a soil target the bit pivots into the back of the ISAD to a maximum deflection of 15° and applies 6.6 N of weight-on-bit at the bit tip. This weight-on-bit range was selected based on the ability of the bit to penetrate into frozen Mars soil analog targets to the full depth of the tool and to meet the actuator startup torque margin requirement. Generally, increasing the weight-on-bit of the rasp decreases torque margin but increases the ability to penetrate hard icy soils, so a compromise between the two was required.

The spring is made from 1.5-mm (0.059-in) diameter 17-7 PH stainless steel wire that has been age hardened, shot peened and passivated. The spring has 12 coils with an 11.1-mm (0.438-in) coil outer diameter. One leg of the spring is formed tangential to the coil and the other axially aligned with the coil. Since the spring assembly is directly in line with the soil particle transfer path, both the coil diameter and leg geometries were constrained in volume and shape so as to allow unhindered particle flow underneath the assembly. To reduce the potential for jamming by foreign debris, the spring coils were covered by a protective housing that was integral with the spring mount. The spring coil inner diameter is constrained by an aluminum arbor with a General Magnaplate TUFRAM wear resistant surface treatment.

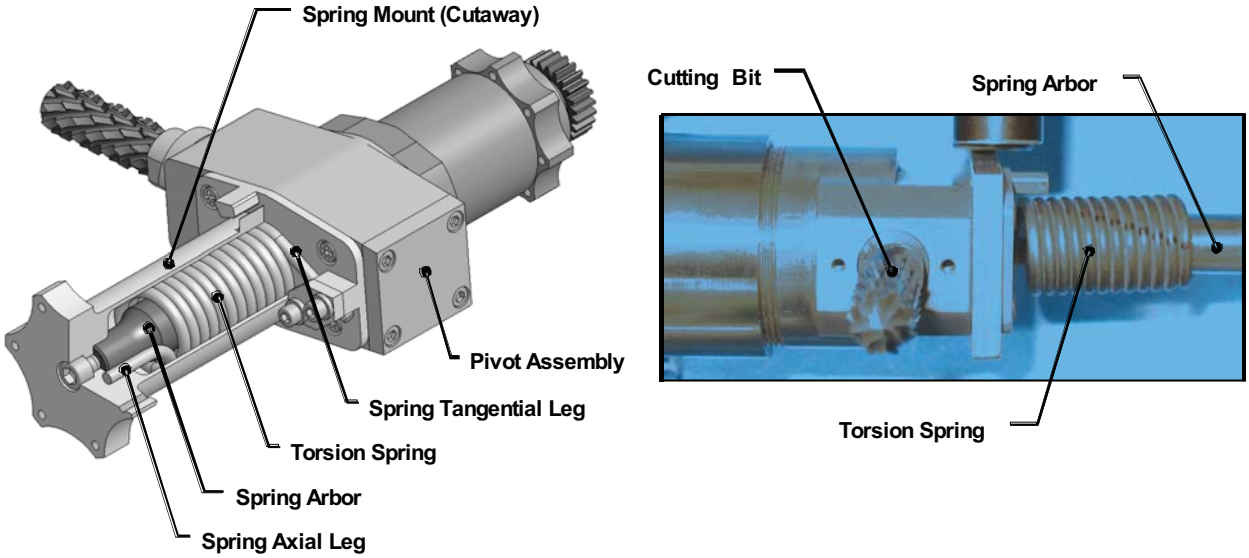

Figure 11. (Left) ISAD Pivot and Spring Assemblies; (Right) ISAD Spring Test Fixture

The spring was designed to produce a change in weight-on-bit over the 15° bit pivot stroke of 0.7 N. Such a narrow range of weight on bit was desired to maintain sample acquisition performance over the entire stroke of the cutting bit. The ISAD flight unit spring produces a change in weight-on-bit of 1.6 N over the 15° stroke, a difference of 0.9 N between the theoretical and actual values. This difference is a combined result of the spring manufacturing and integration processes. The spring rates of the springs provided by the manufacturer were slightly higher than that called out in the manufacture drawing (0.023 in-lb/° actual compared to 0.019 in-lb/° theoretical), which yields an increase of approximately 0.3 N over the stroke of the bit. The remaining 0.6-N difference between the actual and theoretical weight-on-bit values is attributed to friction in the spring assembly and the accuracy of the test method. Some of the springs also had non-linear torque versus deflection curves and there was some variability in both the slope and offset of this curve. In addition to spring rate differences, there were small variations in the axial leg geometries of the springs, such as leg straightness, the angle at which the leg protrudes from the coil, and the radius of the axial leg bend. The leg straightness and bend radius had an effect on the fit of the spring into the outer housing and the geometry of the assembled spring when wound up. As seen in Figure 11, when

wound up the coil tends to pivot about the axial leg anchor point and move out of alignment with the arbor. This misalignment can cause the spring to contact the arbor, housing or both, which increases friction in the assembly, resulting in a higher spring rate.

It was anticipated that there would be variability among the as-received springs. Therefore, five times as many springs were fabricated than were required in the delivered ISAD units. This provided the ability to choose the best springs out of the lot to be integrated into the ISAD units. The springs integrated into the ISAD units were selected based on having a minimal and constant spring rate and acceptable axial leg geometries. Since there is significant variability from spring to spring, each spring had to be "tuned" appropriately for each ISAD unit. To achieve a desired range in weight-on-bit from a particular spring, the mounting hole location in the spring mount for the spring's axial leg was determined following testing of that spring in a custom test fixture. As stated, the ISAD flight unit weight-on-bit range is 5.0 N to 6.6 N, which was measured at room temperature. Tests conducted with the mechanism soaked at -80°C yielded weight-on-bit values of 5.5 N to 8.2 N over the 15° stroke of the bit, an increase of 1.1 N over that measured at room temperature. This increase is attributed to added friction in the spring assembly at cold temperatures as well as a potential increase in the spring stiffness.

When considering a custom torsion spring to provide a narrow range of output torques at specific deflection angles, there are many sources of error between the theoretical design and the actual performance. If a torsion spring is required to operate within a precise performance range it is important that sufficient margin be accounted for in the design so that deviations in spring performance due to the manufacturing process, mounting method and assembly process do not adversely affect mechanism performance. For future mechanisms, it is recommended that the use of an axially aligned torsion spring leg be avoided when variability in performance is undesirable. An axially mounted leg is sensitive to both the spring mounting scheme and the assembly procedure. In the case of the ISAD, spring preload directly affected the actuator torque margin and bit productivity. A specific range was desired, but the spring was successfully implemented in the design by fabricating a relatively large batch of springs that could be selected from to find the best match for each unit and by waiting until the spring was selected before locating mounting holes for the axial leg.

Conclusion

The ISAD is a first of its kind device to be qualified for space flight. Many aspects of the design are unique, but can be applied to future spacecraft mechanisms. The highly constrained requirements space resulted in the use of a number of unconventional design features and methods, while schedule and budget restrictions played a large factor in many design decisions.

Designing a low torque mechanism while preventing debris migration from damaging sensitive drive components requires knowledge of the effects of the dust seal on the overall frictional drag of the mechanism. Depending on available torque margin, shafts that interface with dust seals may require modification to minimize seal drag. Seal behavior across the environmental range should also be characterized before design finalization.

A cam-actuated vibration mechanism is an effective means of inducing vibration to help fluidize both dry and ice-bearing soils and powders. The limitation on the overall life of the mechanism is the interaction between the cam and the bumper. Proper material, surface treatment and geometry selection is critical to extending the lifetime of the device.

Designing a small form factor braze joint for brittle material to sustain high load conditions involves careful consideration of the connection geometry. Materials such as tungsten carbide require gradual changes in geometry, and reinforcement with braze filler material to sustain high loads. Abrupt geometry transitions can result in failure of the joint when load is applied.

Use of torsion springs in a mechanism where a narrow range of output torque is required should be avoided. If space or packaging constraints dictate the use of a torsion spring, the spring should be designed using legs that exit the spring tangentially, rather than aligned with the spring axis. An axially aligned leg imposes a high degree of unpredictability on the output torque due to frictional effects

between the spring, the housing and the shaft. Significant torque margin should be applied to the spring design to account for these effects.

Acknowledgments

The authors would like to thank all of the ISAD program technicians, machinists, designers, engineers and managers at Honeybee Robotics and JPL for their commitment to developing this device. Specifically, the authors would like to thank Mark Balzer, Don Lewis, Don Noon and Greg Peters all of JPL for their time and technical insights.

This work was performed under a contract with Jet Propulsion Laboratory, California Institute of Technology, for the National Aeronautics and Space Administration. References herein to any specific commercial product, process or service by trade name, trademark, manufacturer, or otherwise does not constitute or imply its endorsement by the United States Government or the Jet Propulsion Laboratory.

Sample Manipulation System for Sample Analysis at Mars

Erik Mumm[*], Tom Kennedy[*], Lee Carlson[*] and Dustyn Roberts[*]

Abstract

The Sample Analysis at Mars (SAM) instrument will analyze Martian samples collected by the Mars Science Laboratory Rover with a suite of spectrometers. This paper discusses the driving requirements, design, and lessons learned in the development of the Sample Manipulation System (SMS) within SAM. The SMS stores and manipulates 74 sample cups to be used for solid sample pyrolysis experiments. Focus is given to the unique mechanism architecture developed to deliver a high packing density of sample cups in a reliable, fault tolerant manner while minimizing system mass and control complexity. Lessons learned are presented on contamination control, launch restraint mechanisms for fragile sample cups, and mechanism test data.

Introduction

The Mars Science Laboratory (MSL) currently scheduled for a Fall 2009 launch is NASA's next roving mission to Mars. The rover is equipped with several instruments designed to assess the habitability of Mars, both past and present. One of the instruments, Sample Analysis at Mars (SAM) provided by Goddard Space Flight Center consists of a Gas Chromatograph Mass Spectrometer, Quadropole Mass Spectrometer, and Tunable Laser Spectrometer. Both atmospheric and solid samples can be analyzed by SAM. SAM's Sample Manipulation System (SMS) stores and manipulates sample cups used for experiments involving solid samples.

The SMS is a first generation flight system. The SMS is responsible for controlled manipulation of the sample from SAM's sample inlet device to pyrolysis ovens, where samples are pyrolyzed and evolved gasses plumbed to the analytical suite. Seventy-four sample cups are populated in two polar arrays on the SMS carousel. Cups may be re-used in an extended mission scenario. Once inserted into the pyrolysis oven, the SMS applies a predetermined force to create a hermetic seal between the sample cup and the interior of the oven. The sensitivity of SAM's spectrometers require the SMS to be very clean so as not to contaminate Martian samples and produce false positives or mask sample signatures with known outgassers within the SMS.

This paper covers the design, test, and preliminary lessons learned during the development of the SMS. Concentration is centered on the overall design of the SMS that includes several mechanisms. Lessons learned from contamination control, and results from environmental testing are presented.

SMS Design

Driving Requirements

The purpose of the SMS is to store and manipulate sample cups used to analyze solid samples with SAM's instrument suite. The SMS, Figure 1**,** accepts solid sample from the MSL rover via SAM's Solid Sample Inlet Device into any of 74 sample cups and transports the selected sample cup to a pyrolysis oven. Once the SMS inserts the sample cup into the oven, it creates a seal force sufficient to provide a leak rate between the cup and the oven less than 1E-5 cc He/sec. The SMS must consume less than 6-Watts continuous and 18-Watts peak power.

The sample cups are separated into three categories: solid sample quartz cups (60), foil topped metal cups for wet chemistry experiments (10), and foil topped metal cups containing calibration sample (4). The SMS must position each cup within 0.71 mm true position at multiple interfaces including the solid

[*] Honeybee Robotics Spacecraft Mechanisms Corporation, New York, NY

Proceedings of the 39th Aerospace Mechanisms Symposium, NASA Marshall Space Flight Center, May7-9, 2008.

sample inlet device, foil puncture stations for the metal cups, and a pyrolysis oven on each row of the SMS Sample Carousel Disk.

To allow SAM to re-use sample cups in an extended mission scenario, the SMS must deliver up to 1350 Newtons with an accuracy of ±10% of the commanded seal force. A seal is created with the Pyrolysis Ovens via an annealed copper disk brazed to the sample cup and a titanium knife-edge on the oven. Each successive use of a sample cup requires a larger seal force.

Contamination control played a significant role in SMS development. The spectrometers aboard the SAM suite have the capability to detect molecules in the parts-per-billion range. Thus, the SMS must be extremely clean, free of particles, and exhibit a very low outgassing rate. The outgassing rate of the SMS was required to be less than 4.2E-14 g/cm^2/sec as measured by a Quartz Crystal Microbalance. This ultimately corresponded to a delta/delta frequency reading on a TQCM of 1 Hz/hour/hour during bake-out.

The SMS must move the sample from the inlet location and seal it in the pyrolysis oven in five minutes or less. This requirement is driven by the extreme contamination sensitivity. A given sample cup, once preconditioned in the pyrolysis oven, must not be exposed to the interior of the SMS for an extended time to prevent contaminating the measurement on the solid sample. Contamination concerns required the SMS to provide a vacuum seal to prevent contamination of the interior of the SMS during Assembly, Test, and Launch operations.

The SMS must be capable of recovering from an unexpected power loss. Feedback devices and a robust high level control architecture combined to provide full fault detection and correction capability.

High Level Architecture

The four main subsystems of the SMS are identified in Figure 1. Not shown is a contamination cover that fully encases the SMS within SAM. The SMS is not exposed to the exterior of SAM or the Rover, except when the Sample Inlet Tube (~ Ø4.3 mm) is open to deliver a sample.

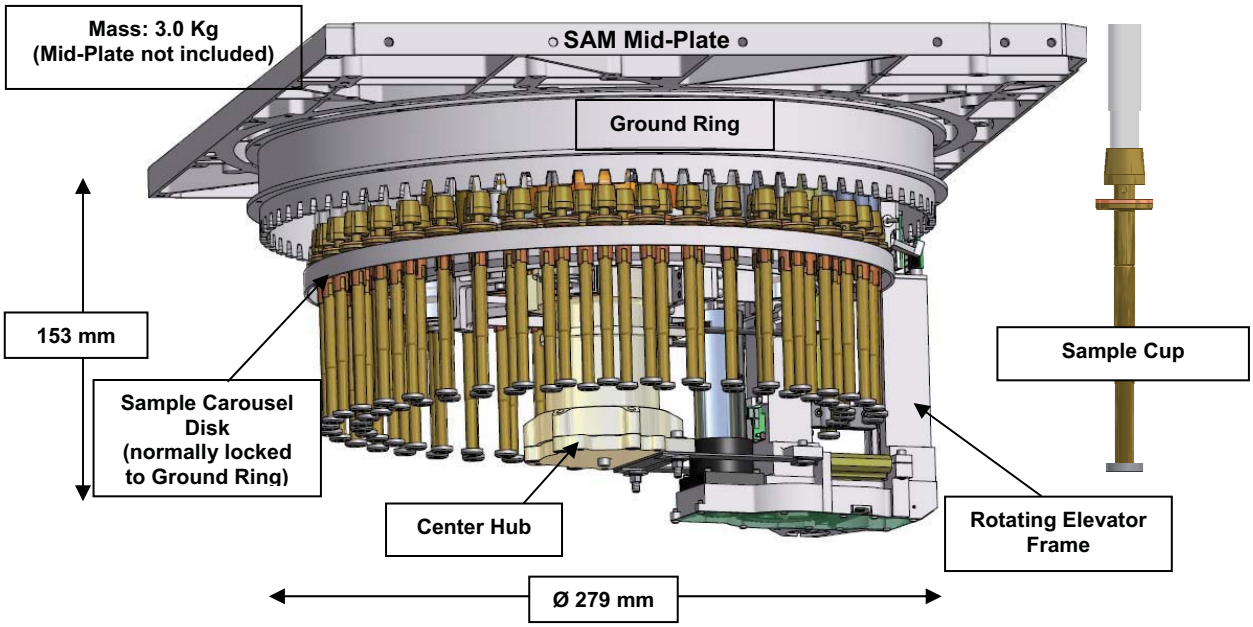

Figure 1 - SMS Main Subsystems

The SMS is an under-actuated 3 Degree-Of-Freedom robotic system. Two rotational degrees of freedom are provided by the Center Hub Actuator. A toggle mechanism on the Sample Carousel Disk either couples the Sample Carousel Disk to the Ground Ring or the Rotating Elevator Frame (REF). When the

Sample Carousel Disk is coupled to the REF, the Center Hub Actuator positions a given sample cup at an oven, inlet, or puncture station. When the Sample Carousel Disk is coupled to the Ground Ring, the REF rotates independently of the Sample Carousel Disk and positions the Elevator subassembly beneath a given sample cup. At that point, the Elevator actuator (3rd DOF) can raise and lower the sample cup to its interface. Figure 2 through Figure 4 demonstrate the sequence of operations involved in decoupling the Sample Carousel Disk from the Ground Ring and moving a cup via the Carousel actuator to another position.

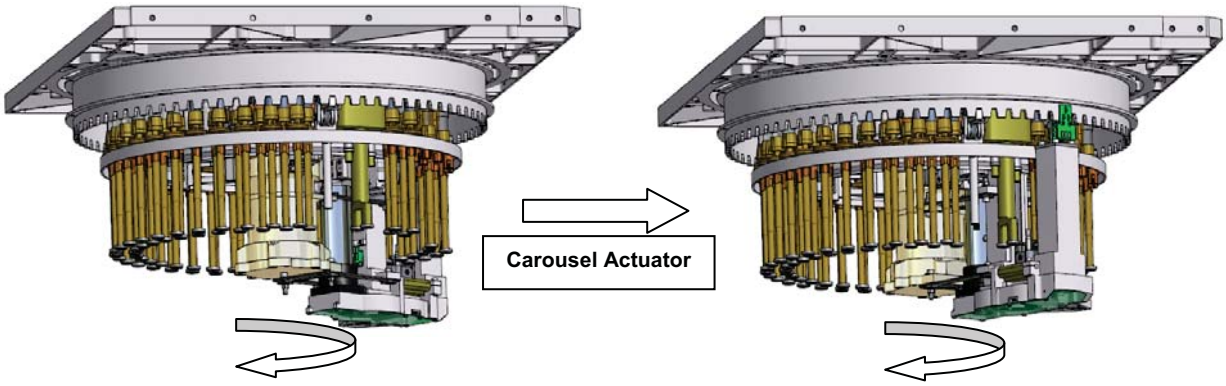

Figure 2 – Center Hub Actuator Moves Rotating Elevator Frame to Toggle Mechanism, Sample Carousel Disk is Stationary

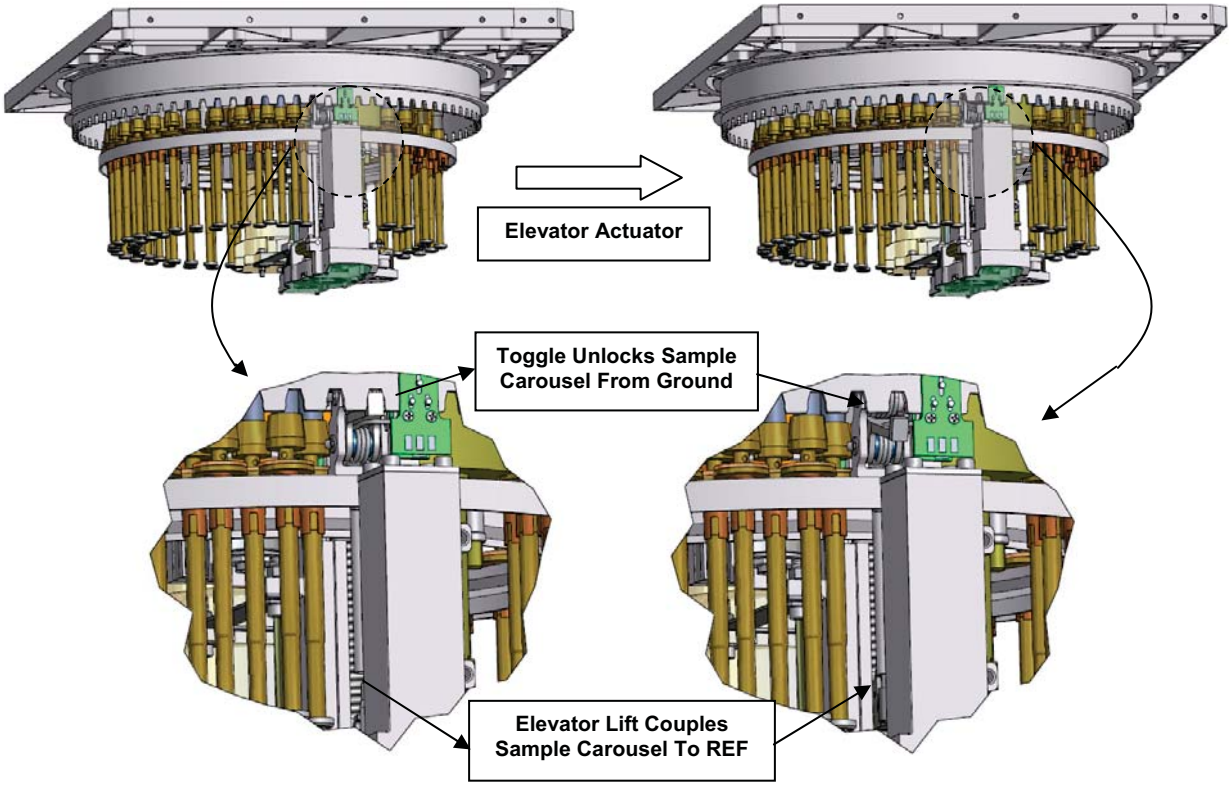

Figure 3 - Elevator Actuator Raises Lift to Unlock Toggle Mechanism from Ground Ring and Couple with Rotating Elevator Frame

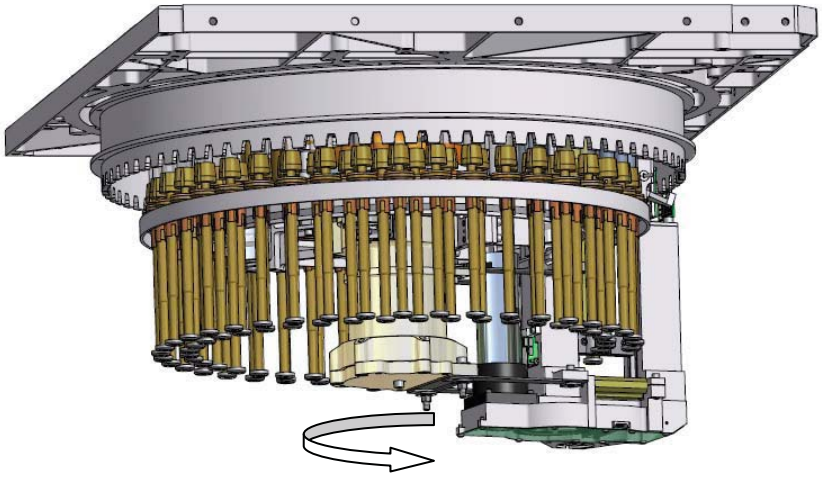

Figure 4 – Center Hub Actuator Moves Rotating Elevator Frame and Sample Carousel Disk to Position a Sample Cup

Center Hub Actuator

The center hub actuator is comprised of a hall commutated brushless dc motor, 25:1 planetary gearbox, and 100:1 cup style harmonic drive for an overall gear reduction of 2500:1 and 30000 counts per revolution, Figure 5. All components are grease-plated with Braycote 600 EF Micronic. The maximum speed at the output of the harmonic drive is 2 RPM. The maximum continuous torque output is 3.4 N-m. The Carousel Motor is current limited by the motor control board so as not to exceed output torque limits. Actual running torque of the Center Hub Actuator is only ~.05 N-m at the output of the 25:1 planetary stage. External loads are not significant during operation.

A duplexed pair of angular bearings in the face-to-face configuration is located near the harmonic drive output. A Conrad bearing is located at the interface of the cross-support arms to the center hub. The Center Hub bearings support approximately 70% of the system mass during launch and EDL, including the Sample Carousel Disk.

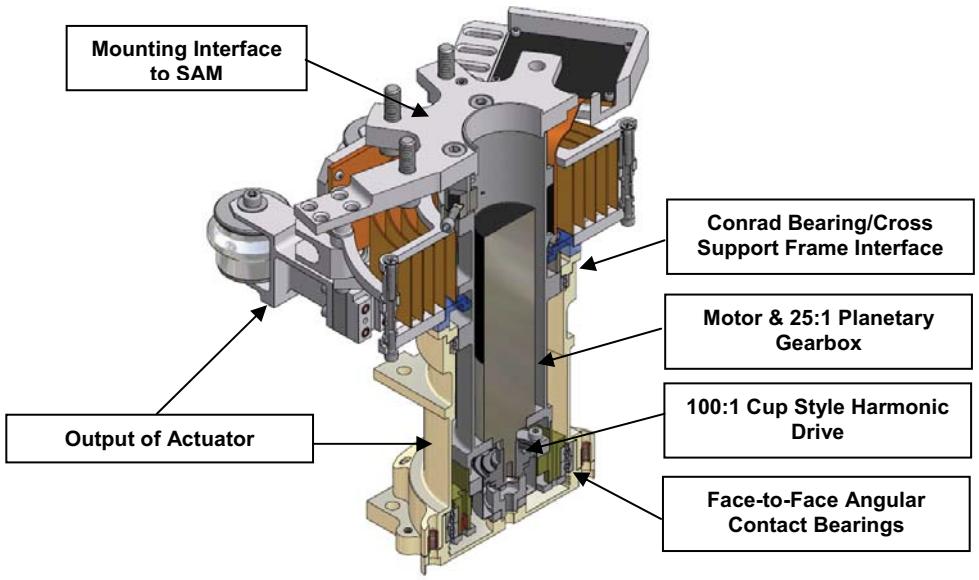

Figure 5 – Center Hub Actuator & Center Hub Assembly

The cross support arms support the Sample Carousel Disk via a set of 4 wheels rolling in a v-groove in the Sample Carousel Disk. Each Cross Support Arm wheel contains a set of preloaded angular pair bearings in the back-to-back configuration. The Cross Support Arm wheels roll in the Sample Carousel Disk groove when the Sample Carousel Disk is locked to the Ground Ring, Figure 3.

Due to the tight positioning requirements of the Sample Cups, the Sample Carousel Disk was required to be concentric with respect to the center hub axis of rotation. To accomplish this in the presence of significant manufacturing tolerance stack-up, the radial position of the cross support rollers was adjusted during assembly to ensure the Sample Carousel Disk was concentric to within 0.05 mm. Shims were independently precision ground to desired thicknesses at the assembly level, Figure 6.

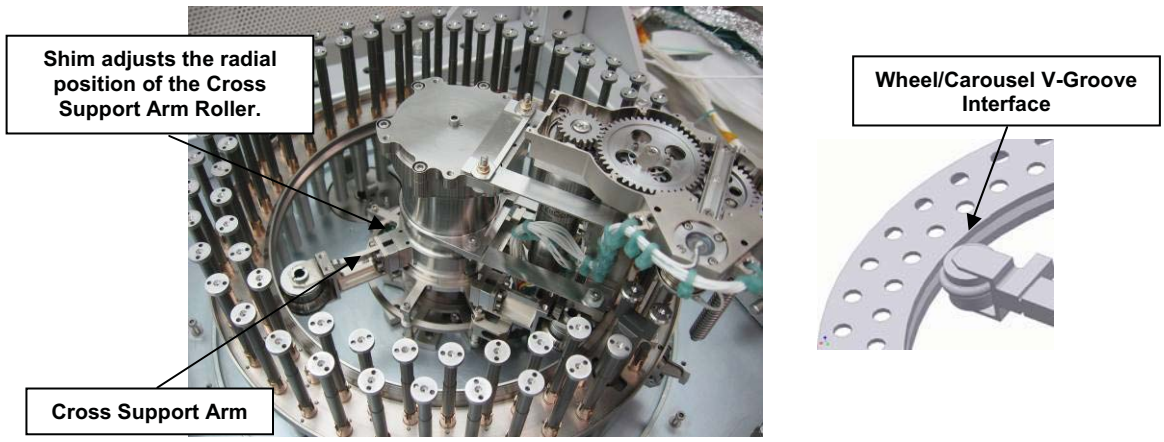

Figure 6 - Radial Adjustment Shim for Carousel Disk Concentricity

Using a single actuator to position both the Rotating Elevator Frame and the Sample Carousel Disk required more than 360° of rotation of the center hub. A twist capsule carries power and signals to the elevator actuator and feedback switches on the Rotating Elevator Frame. To prevent damage to the twist capsule in the event of actuator run-off, hard stops were implemented in the Center Hub. To allow for greater than 1 revolution of travel, an intermediate hard-stop ring travels between the ground and the output of the center hub, Figure 7. This design allows for 693 ° of rotation, hard stop to hard stop.

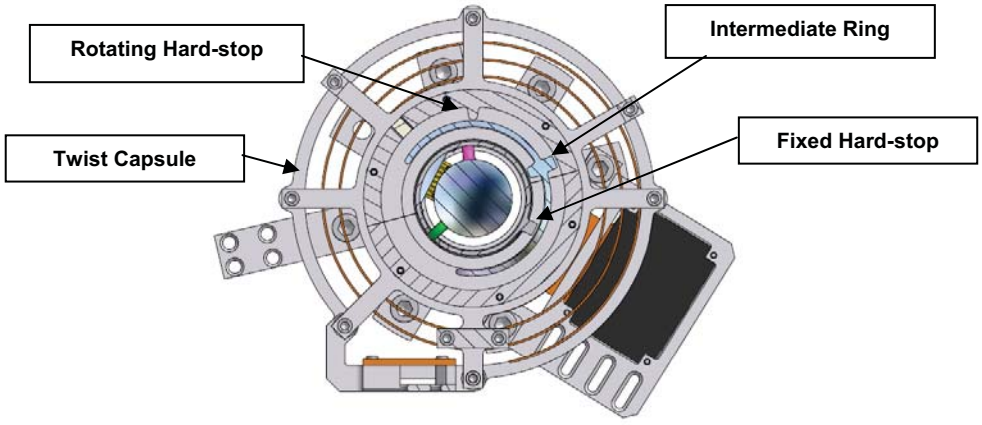

Figure 7 - Top Section View of Center Hub Twist Capsule and Hard-stops

Rotating Elevator Frame

The Rotating Elevator Frame consists of a linear actuator to raise and lower cups, a parallel spring flexure, and a launch lock for the elevator subassembly, Figure 8. The parallel spring flexure allows the

Elevator launch lock cleats to de-mate when there is no load applied to the elevator lift via a sample cup. This system allows for a re-usable launch lock mechanism and a reduction in structural mass required to deliver a seal force to a sample cup or the contamination seal. The 1350 Newtons that the elevator delivers is all reacted locally, Figure 9. The load path does not trace back through the center hub assembly, which would have required significantly more structural mass to accommodate.

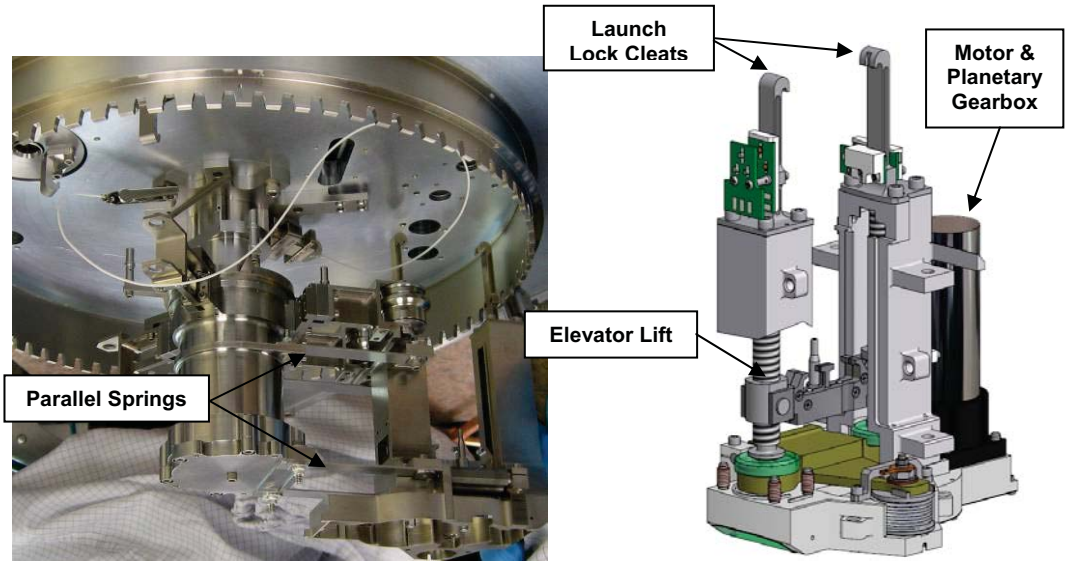

Figure 8 – Elevator Actuator & Rotating Elevator Frame

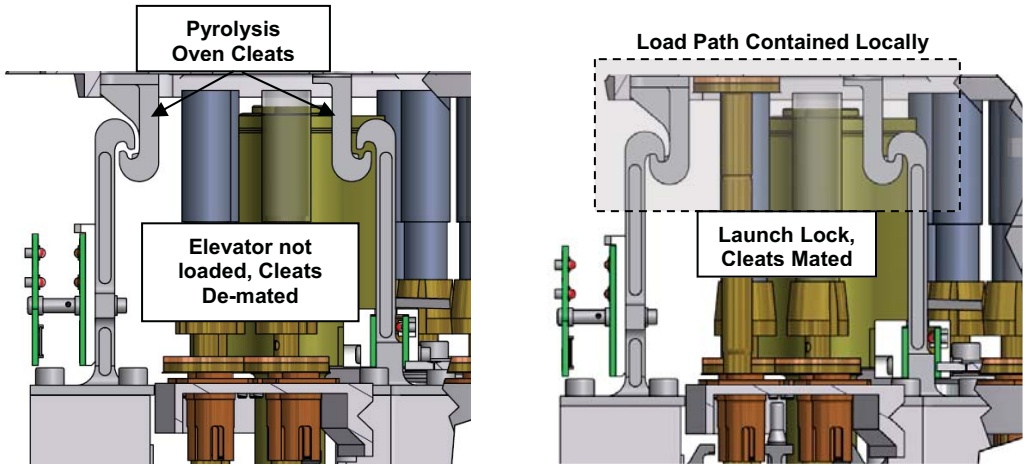

Figure 9 - Rotating Elevator Frame Launch/Seal Lock

Elevator Actuator

The linear actuator for the Elevator consists of a hall commutated brushless DC motor, 80:1 planetary gearbox, 2.4:1 spur gear arrangement, and a pair of 5/16-12 ACME lead screws, resulting in resolution of 1088 hall counts per millimeter. The two lead screws are mechanically coupled via Custom 455 H1000 Stainless Steel spur gearing in the bottom of the Elevator Assembly. The two lead screws are Nitronic 60, 50% Cold Worked Stainless Steel and the ACME nuts are 15-5PH H1025 Stainless Steel. The ACME screw is non-backdriveable for coefficient of friction > 0.09. A magnetic detent brake on the motor rotor is sufficient to hold the elevator preloaded in the event there is no friction in the leadscrew nut. The lead screws rotate in Nitronic 60, 20% Cold Worked Stainless Steel journal bearings and 440C needle roller thrust bearings. The screws, nuts, bearings and gears are grease plated with Braycote 600 EF Micronic. Reservoirs in the journal bearings and the root of the ACME screws were also packed with the same grease.

Elevator Seal Force

The elevator actuator is required to deliver 1350-N force to a sample cup to an accuracy of ±10% of the commanded force. The force delivered by the actuator must be commandable to allow for multiple uses of a single sample cup. An appropriately sized load cell could not be found that could withstand the temperature range (-55 to 110°C). A desire to reduce the burden on the control electronics and the added cost of development and qualification of a load cell led to an alternate solution custom tailored to the SMS design.

The load path for the seal force is transmitted through the lead screws and thrust bearings to a compliant flexure arm, Figure 10. The lead screws and lift assembly are allowed to translate along the axis of the applied load. A spherical shoulder on the bottom of each lead screw allows the flexure arm to rotate about its hinge axis without inducing moments in the spur gearing and the leadscrew/nut interface. Further, the lift assembly is pinned to each leadscrew nut to allow the lift to flex without inducing moments in the lead screws, thereby maximizing the efficiency of the screw/nut interface. At the end of the flexure arm is a spring-loaded electromechanical switch. With no load applied, the switch is an open circuit. Once a load is applied to the lift, the switch begins to close. Once the load reaches 450 Newtons, the switch closes. A short stroke wave spring provides the repeatable contact force for the switch assembly. Once the switch closes, the structure becomes a linear spring. The stiffness of the structure, in units of motor counts per Newton, is determined during mechanism calibration. Therefore, once the switch closes at a known force, all backlash in the load path and drivetrain has been eliminated. Commanding the motor to run a specific number of hall counts past the switch transition will result in the desired seal force applied to the sample cup. An integrated bellows assembly keeps the switch contact area free of particulate and Martian dust.

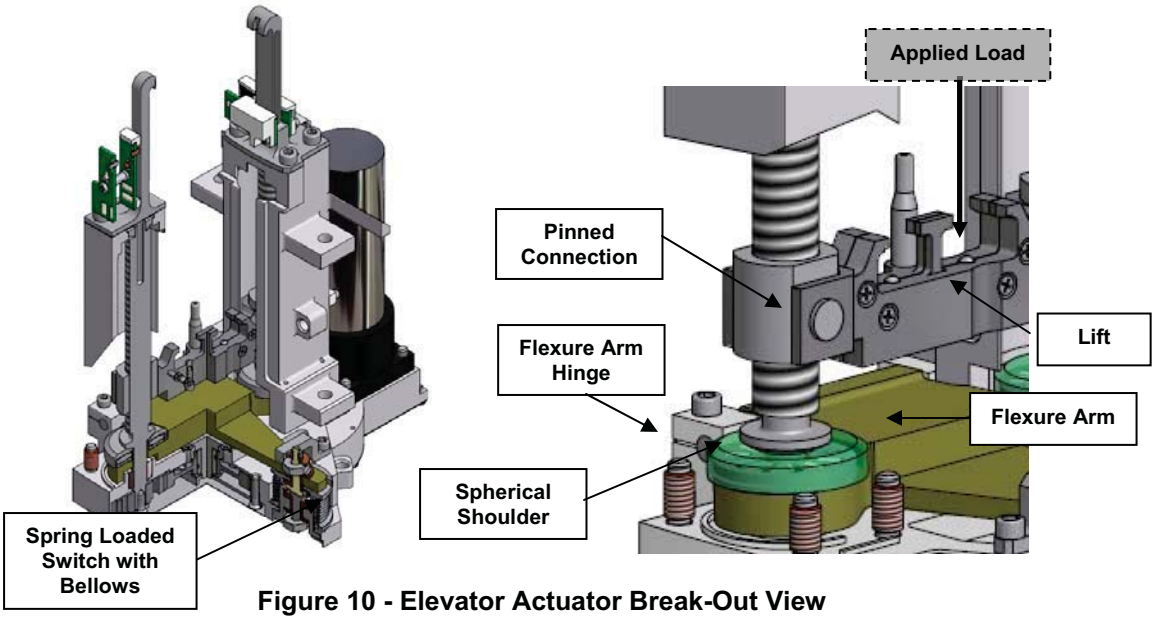

Figure 10 - Elevator Actuator Break-Out View

Incremental Encoder

Optical switches reside at the output of the Rotating Elevator Frame and consist of opposed LEDs and Phototransistors. A pair of LED/PT switches, together with the tooth profile on the Ground Ring act as a custom incremental encoder located at the output of the mechanism, Figure 11. The “region of alignment” indicates the REF is in a position where it is acceptable to actuate the toggle mechanism or raise and lower a cup. By integrating feedback to the output of the mechanism, motor hall counts can be compared to optical switch state transitions to detect faults by a prompt, safe, and recoverable means. Together with the hard-stops on the center hub, the SMS is capable of full recovery from an unexpected loss of power that would result in the loss of position information. The SMS may also operate should either the motor hall sensors or the optical switches fail. It is a redundant control scheme.

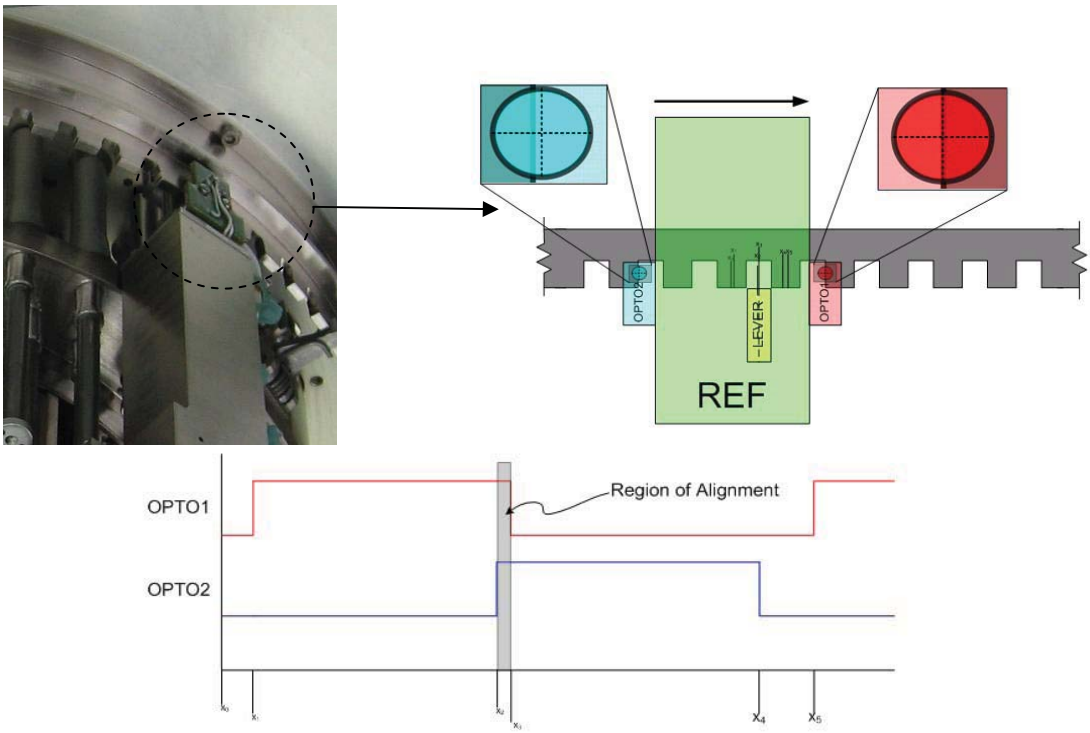

Figure 11 - REF Incremental Encoder

Sample Carousel Disk

The Sample Carousel Disk holds all 74 sample cups, the toggle mechanism, and the Vacuum Seal and excess sample container, Figure 12. There are 37 sample cups located on each row of the Sample Carousel Disk. The packing density of the Sample Carousel was maximized to provide as many clean cups as possible within the allotted volume. Each sample cup can interface with the puncture station, pyrolysis oven, and sample inlet on its respective row. Two rows of cups provides for redundancy in the event of a pyrolysis oven failure.

In the launch position, the vacuum seal is elevated at the solid sample inlet location. O-rings provide a vacuum tight seal to prevent the sample cups from being contaminated prior to arrival at Mars. Also integrated into the vacuum seal is a reservoir to collect excess sample flushed through the inlet tubes. When the vacuum seal is in place, the launch lock on the elevator assembly is active. Each sample cup is constrained to the Sample Carousel Disk by a cantilever spring detent release/restraint device. The sample cup restraint must hold the sample cups during launch and EDL activities and release when the cup is used for an experiment on Mars.

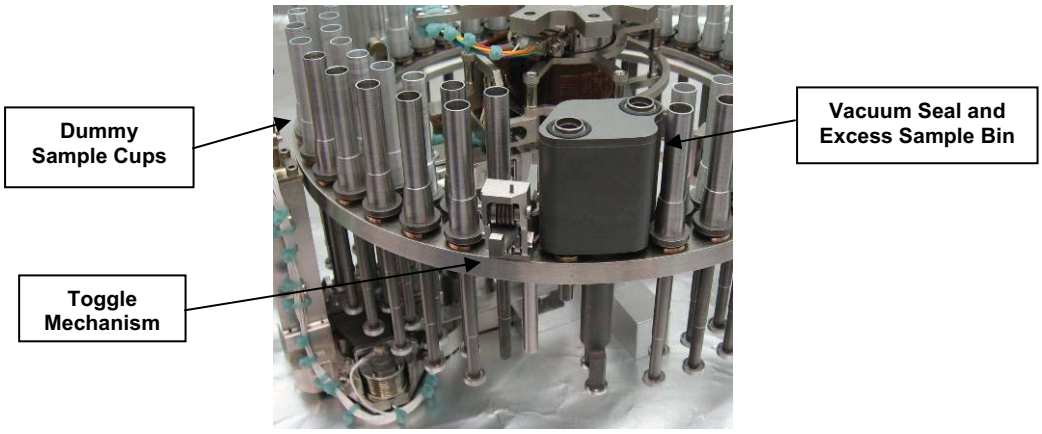

Figure 12 - Sample Carousel Disk

Test Results and Lessons Learned

The SMS Flight Model has recently completed its Flight Model Proto-flight test campaign. An Engineering Model was also subject to an extended proto-flight test program and 2X life test. Several lessons learned are reported here as a result.

Sample Cup Launch Restraint

The launch restraint for the sample cups required a redesign during Engineering Model Testing. The initial design utilized a canted coil spring to restrain each cup during launch and EDL events. A canted coil spring is often used in spring-loaded shaft seals to provide low friction mitigation against dust and debris on rotating shafts. The canted coil springs can also be used as a detent device for a shaft sliding through a cylinder. The initial design utilized an Inconel X-750 canted coil spring housed in a Nitronic 60 Stainless Steel bushing, Figure 13. The sample cup stem is Titanium 6AL-4V plated with a Canadize™ coating (Polymer infused Titanium Oxide) from General Magnaplate Corporation. A groove on the Titanium Sample Cup Stem allowed the spring to constrict and consequently provide a restraint for the sample cup. When the sample cup is used, the Elevator actuator would apply an axial force to the sample cup stem and cause the canted coil spring to “dilate”, thereby releasing the cup from its restraint.

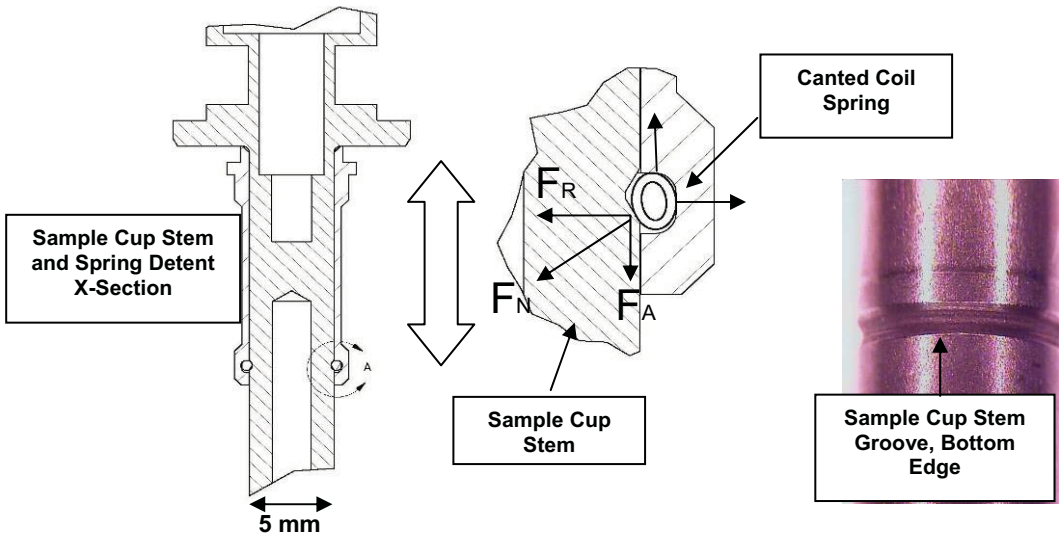

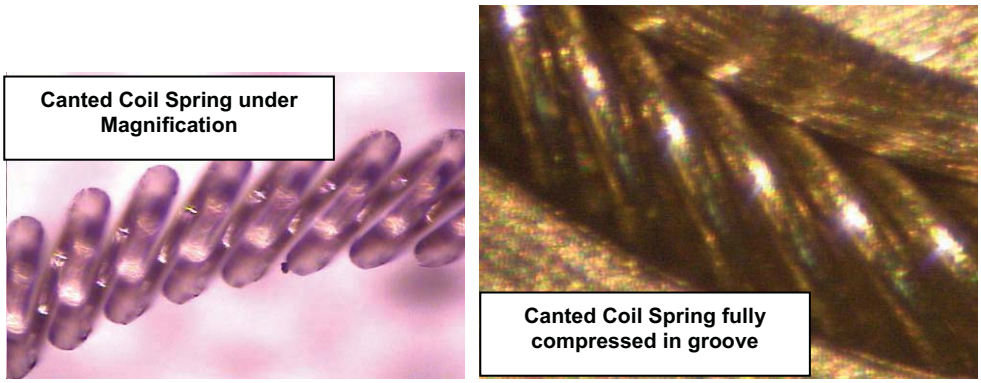

Figure 13 - Initial Sample Cup Restraint

There were several issues with this design. Initially the restraint force was not sufficient to hold the cups in place with sufficient margin during launch. The Sample Carousel Disk can see responses peaks as high as 130 Gs during random vibe. To address this issue, the bushing groove diameter was reduced to radially compress the spring more, resulting in a higher detent force. Once all the parts were precision cleaned in ultrasonic cleaners through multiple baths (3 IPA, 1 Simple Green, 1 Acetone), the coefficient of friction between the spring and the sample cup stem increased. The resulting spring deflection was also getting close to the solid "height" of the spring. Thus, the behavior of the restraint/release device behaved differently in the clean room than in the pre-cleaned state. Subsequent testing on the Engineering Model in the clean room showed signs of erratic behavior. It proved to be very difficult to pair springs with sample cups. Eventually a point was reached where the Carousel was fully populated with cups exhibiting "acceptable" performance.

The Engineering Unit was then subject to a vacuum bake-out at 90°C for 24 hours. Following the bake-out, the cup stems exhibited stick-slip behavior, which was not entirely unexpected given the performance in clean room bench testing. Most of the cup stems would only release after a much higher load was applied by the Elevator actuator than was previously necessary. Some did not release at all. It was determined that the combination of increased compression on the canted coil spring, precision cleaned components lacking surface lubricants (particularly after the vacuum bake-out), and a sharp corner on the bottom edge of the sample cup groove (Figure 13) resulted in high contact stresses at the spring/stem interface which caused the intermittent and unreliable behavior of the restraint/release device. Some cup stems were then modified with a radius on the bottom edge of the groove in the sample cup stem. Preliminary testing showed promise that eliminating the sharp corner on the groove and thereby reducing the contact stress at the interface would allow the cup stem to release in a predictable and reliable manner.

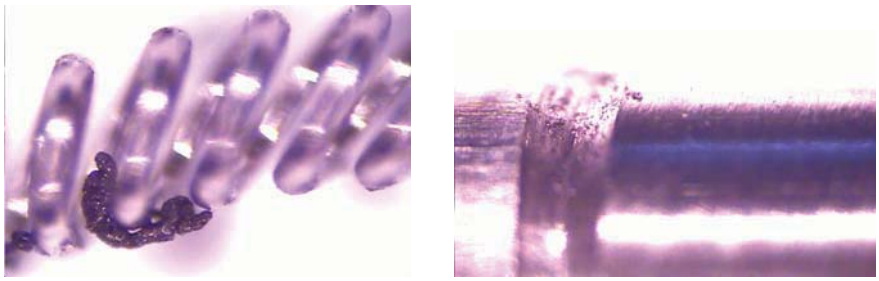

Figure 14 - Post Random Debris in Cup Stem Restraint Device

Six of the modified cup stems were then integrated into the sample carousel disk for vibration testing. The lateral X and Y tests were performed first, in which the in-axis was normal to the center axis of the sample cup. The Z-axis test aligned with the cup's major axis. On the full level random test, 5 of the 6 modified

cup stems released from their restraint. None of the remaining 68-cup stems released during the test. However, in post-test performance testing, the unmodified (sharp groove corner) cup stems did not release. Inspection identified the cause as significant debris generation due to the random vibration environment. The debris lodged in between the coils of the spring and seized the release mechanism entirely, Figure 14.

The design that worked in T/V testing did not pass Random Vibe and vice versa. The proposed solution was to add another spring to the top end of the sample cup bushing in an attempt to stabilize the cup stem and prevent it from rattling and generating debris in vibration. The compression of the spring was also reduced to keep contact stresses as low as possible. Several variations utilizing two springs were tried. A component level random vibration test was then performed based on the response seen on the Carousel Disk during the system test. There were no candidate solutions based on the two-spring concept as a result of the test. The springs were not sufficient to prevent the sample cup stem from rattling in the bushing and generating significant debris.

The final design eliminated the canted coil spring entirely, Figure 15. The springs were replaced by integrated cantilevered beams that snap into the same groove in the sample cup stems that the spring used. The cantilever beam bushing is Brush Wellman Alloy 25 Copper Beryllium in the TH-04 condition. The bushing was also electro-polished to reduce surface roughness and contact stresses. A much more repeatable and reliable restraint and release mechanism has been evident with this design. It does not allow the cup stem to rattle during random vibration and contact forces between the beams and the cup stem are easier to predict and control.

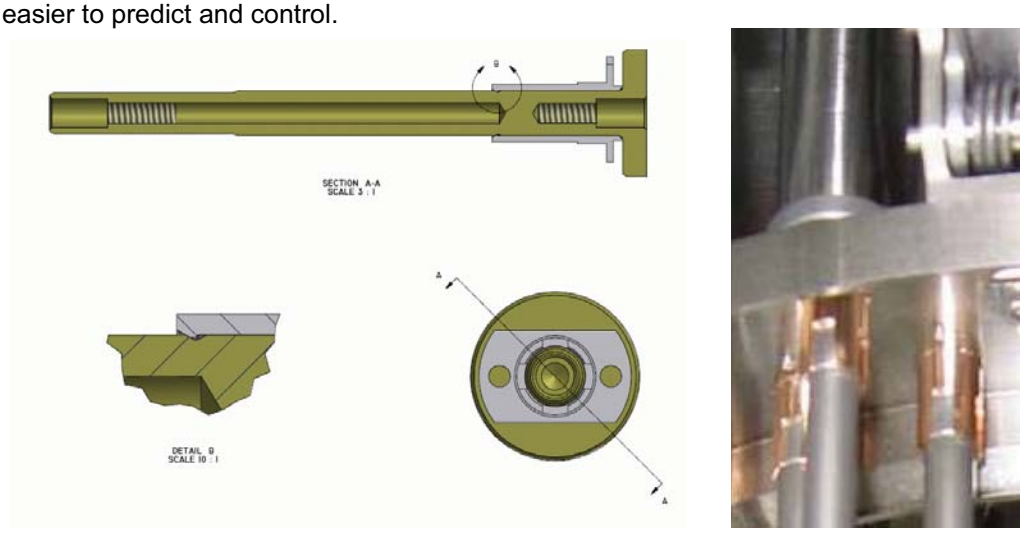

Figure 15 - Final Sample Cup Restraint Design

The major lessons learned from the sample cup restraint exercise are as follows.

1. Beware of lab test results that involve friction. Always precision clean parts to eliminate any oils or other lubricants that can collect in a lab environment. Precision cleaned parts behave differently than pre-cleaned parts.
2. Do not rely on components that are difficult to analyze and debug for a critical restraint application. The form factor of the canted coil spring and its release behavior made analytical predictions prone to large errors. The spring interaction with the cup stem was difficult to model and hidden from view.
3. If a canted coil spring is used to provide a detent for a component, ensure the vibration environment is well understood and excessive debris will not result. The canted coil spring can be a good solution for light detent applications if used in a conservative manner.
4. Be aware of the lap joint in the spring where the wire is welded. If not considered, the weld can also add to non-linearities/asymmetry at the interface between the two components. If high contact stresses exist, the weld may be problematic.

Contamination

Another lesson learned in the development of the SMS pertains to contamination. When designing an instrument with extremely stringent outgassing and contamination requirements, work with all third party suppliers early and often on the contamination front. Expensive bake-outs resulted because assembled components such as motors were manufactured without additional contamination control guidelines in place. Once components are assembled, the vent path for all outgassing molecules becomes long and tortuous. The SMS motors required a 6-week bake-out before they were acceptable to use. Eliminating excessive polymeric harness staking and connector potting can also drastically reduce bake-out time and cost. Integrate metallic features in parts to tie harnesses down to rather than staking with polymerics. Avoid thick layers of polymerics. The thicker the layer, the longer it takes to diffuse and the longer the bake-outs become. The science return of the mission would have been compromised had the bake-outs not been sufficient.

Optical Switches

Optical switch thresholds will change with temperature. Be mindful when using optical switches to zero position counters in mechanisms. If position counters are reset with an optical switch transition, ensure the behavior of that switch has been characterized through its temperature range, particularly if a fine aperture is not implemented. Testing on the LED/PT switches used in the SMS demonstrated a shift with temperature in the threshold voltage of the optical switch, Figure 16. The SMS implemented a differential switch scheme with the custom incremental encoder that cancelled out the temperature shift. Optical switches on the elevator mechanism did not require fine positioning that counter resets would affect.

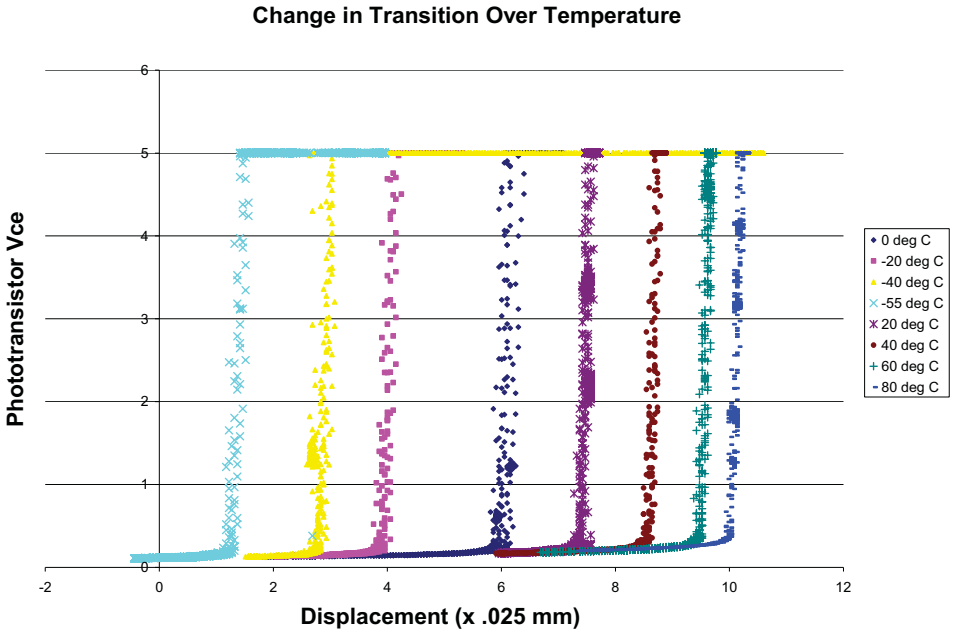

Figure 16 - Optical Switch Performance Vs Temperature

Seal Force Feedback

The performance of the Load Cell replacement in the Elevator Actuator mechanism was sufficient to satisfy SMS requirements. Paramount to the success of the design was a reliable switch closing force. So long as the force at which the switch closed remained consistent and was sufficient to remove any structural or electromechanical play in the load path and drive train, the stiffness of the structure can be utilized to apply a given force. Take care to tune the structural stiffness to the accuracy requirements and ensure the actuator feedback device has sufficient resolution to stay well within the required force accuracy, Figure 17. This is an effective method for applying a known force to a large number of distinct components of varying geometries.

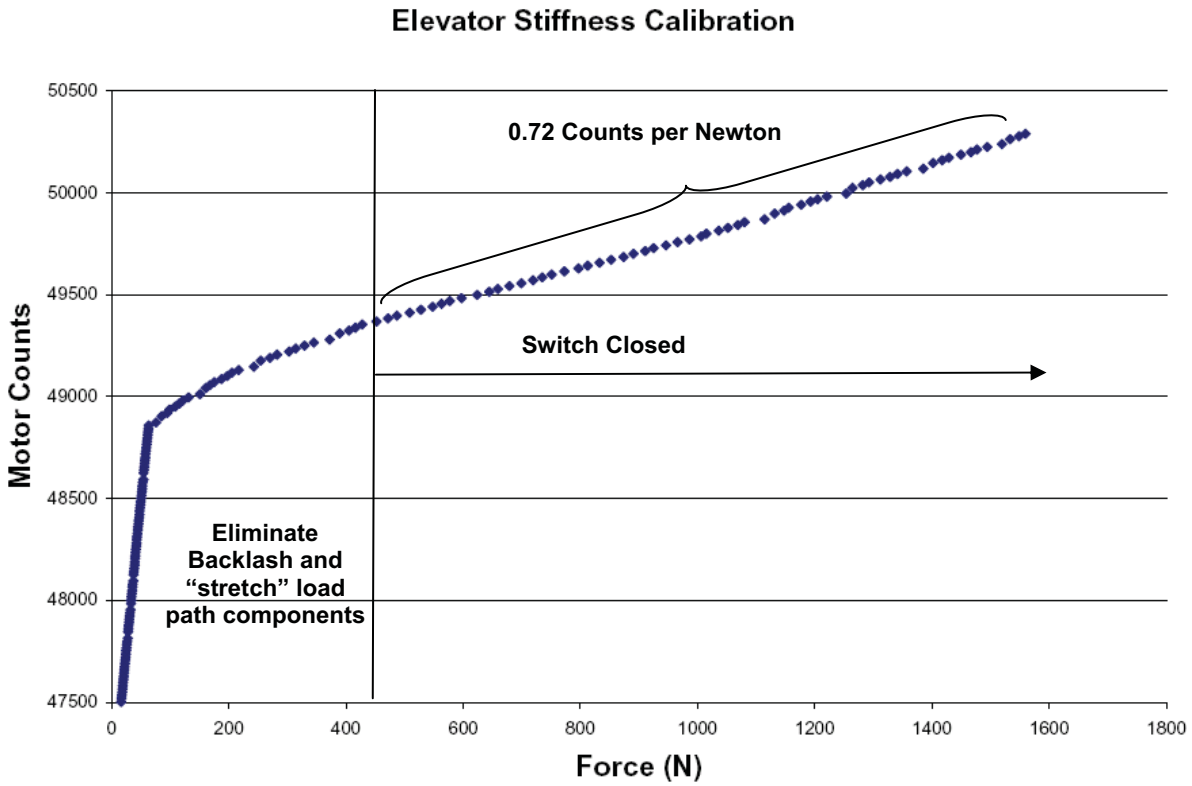

Figure 17 - Elevator Stiffness Calibration

General Test Data

Figure 18 plots the motor current versus time of the SMS during a complete Pyrolysis Experiment sequence. The sequence includes two sample cup seals, four Sample Carousel Disk re-orientations, and one vacuum seal/launch lock operation. Only the profile at -55C is shown. The SMS motor currents were approximately 30% less at the maximum operating qualification temperature (70° C).

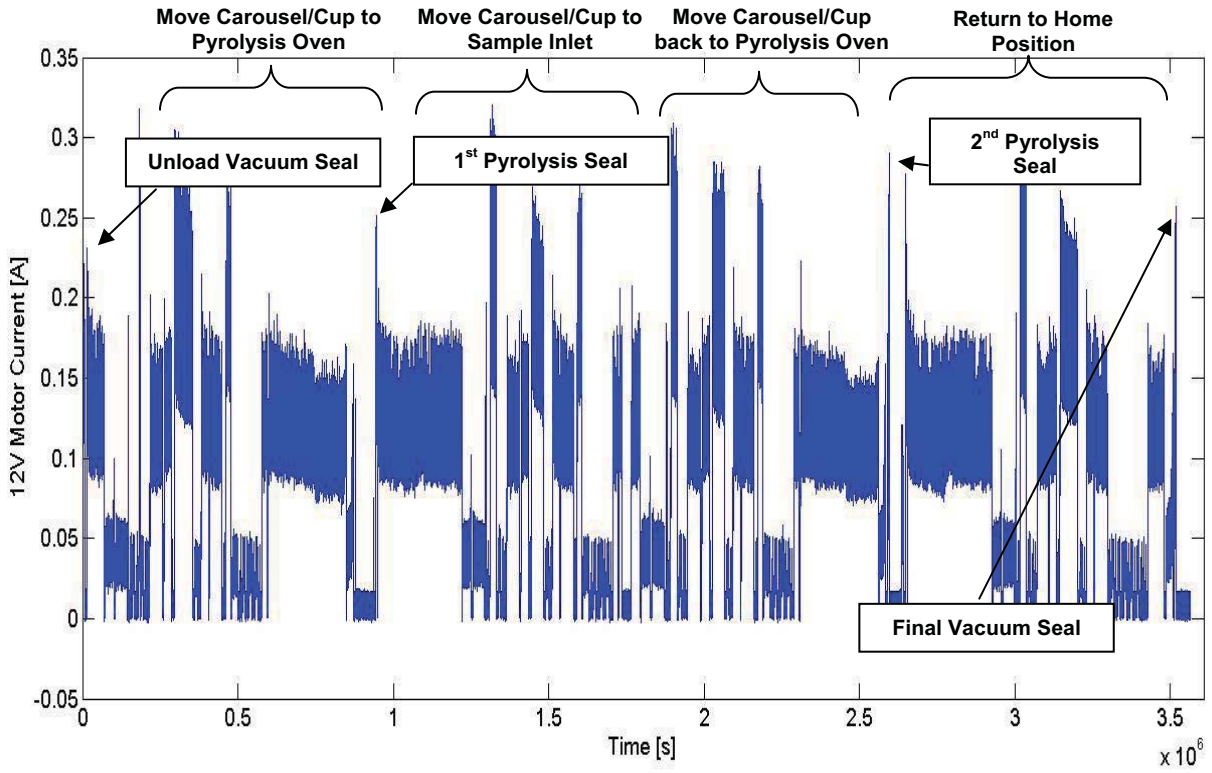

Figure 18 - Pyrolysis Experiment Current Profile

Conclusions

The Sample Manipulation System provided many challenges to the design team. Keys to designing mechanisms for very sensitive science experiments are to get involved with third party vendors as early as possible in the manufacturing stage. Assess the feasibility to bake-out sub-components prior to assembly. The problems encountered with using canted coil spring detents were a design oversight and should not be construed as a recommendation against using them for other applications. The debris generated inside the sample cup bushing demonstrated that another method for positive retention of the sample cup was necessary. The canted coil springs proved to be effective when used as a light detent device. Optical switches will drift with temperature. If a fine aperture is not implemented, the voltage threshold on the Phototransistor will occur at different degrees of LED obscuration. Lastly, the compliance of a structure can be an effective means of delivering a commandable force via an electromechanical actuator. All structural and drivetrain backlash must me eliminated prior to initiating the position move to a desired force. One means of doing so is implementing a repeatable spring-loaded switch to put the mechanism at a known point on the stiffness calibration curve.

Acknowledgments

The authors would like to thank all of the SMS program technicians, machinists, designers, engineers and managers at Honeybee Robotics and GSFC for their commitment and expertise. Specifically, the authors would like to thank Oren Sheinman and Rodger Farley of GSFC and Tom Myrick for their time and technical insights.

This work was performed under a contract with NASA Goddard Space Flight Center, Greenbelt, Maryland. References herein to any specific commercial product, process or service by trade name, trademark, manufacturer, or otherwise does not constitute or imply its endorsement by the United States Government or the Goddard Space Flight Center.

A System for Suspending and Vibration-Isolating a Large Spacecraft for Testing in Vacuum

David A. Kienholz*

Abstract

A system is described for suspending from above a 15,900-kg (35,000-lb) payload for ground testing in a vacuum chamber. The system provides very low suspension frequencies to isolate the payload from ambient vibration. It also includes active capability to maintain a very stable ride-height and attitude of the payload. Passive magnetic dampers are included to suppress pendulum-mode lateral oscillations. Designated as the Large Suspension / Isolation System (LSIS) the system is described in terms of its design, analysis, fabrication, and component-level testing.

Introduction

Spacecraft are often required to maintain a very accurate line-of-sight for a beam-pointing instrument. Doing so requires knowledge of the on-board disturbances, any external disturbances, and the dynamics of the spacecraft as they relate to the line-of-sight. Verifying the first and last of these in ground testing can be quite difficult because of the need to isolate the spacecraft from any external disturbances that would be only artifacts of the ground test environment. The present case was particularly challenging because of the shear size of the test article and the fact that the ground testing had to be done in vacuum. In response to this challenge, a unique vibration isolation system was developed.

The system design was derived from smaller versions developed originally under NASA sponsorship for simulating the free-floating boundary conditions of space in ground dynamic testing, such as modal surveys of very flexible spacecraft [1]. While a number of such systems have been built, including even one designed for operation in vacuum [2], none approached the capacity needed for the present application. The primary accomplishment of this development was demonstrating that the design was scalable to much larger sizes than built previously. In fact, experience reported here indicates that it can be scaled to even larger sizes.

Requirements and System Architecture

Figure 1 shows a simple schematic of the test articles and the suspension system. There are actually two separate test articles that must be held in accurate registration to each other during the test. The larger, designated Body C in the figure, was essentially two relatively rigid bodies connected by a trusswork. The smaller, called Body A/B, was initially separate but was, in some tests, connected by trusswork to Body A/B. The entire apparatus, payload and suspension devices, is inside a large vacuum chamber with the suspension devices mounted to a framework near the top of the chamber.

The defining characteristics of the development were (1) the schedule was very aggressive, and (2) very little information about the payload was available to the suspension system designers. No hard requirement was ever set for the vertical suspension frequency, usually a defining requirement. Early simulations indicated that a value of 0.50 Hz or lower would be adequate so this was taken as the allowable maximum. The ride height and orientation of the payloads had to be highly stable once they were "floated" on the suspension and the test began. Again, no hard quantitative requirements were set but predicted values of uplift force resolution given later and the resulting position resolution were accepted as adequate.

* CSA Engineering, Inc, Mountain View, CA

Figure 1 shows the payloads supported from above by a total of 14 suspension devices. The red objects are called active/passive (Type A) devices since they have the facility for real-time adjustment of their uplift force to maintain the payload ride height and attitude. The blue symbols are passive-only (Type P) devices, which have greater lifting capacity but have no real-time trim capability. The green symbols are passive dashpots, which damp the pendulum modes of the payload. The next two sections explain the design and fabrication of these hardware elements.

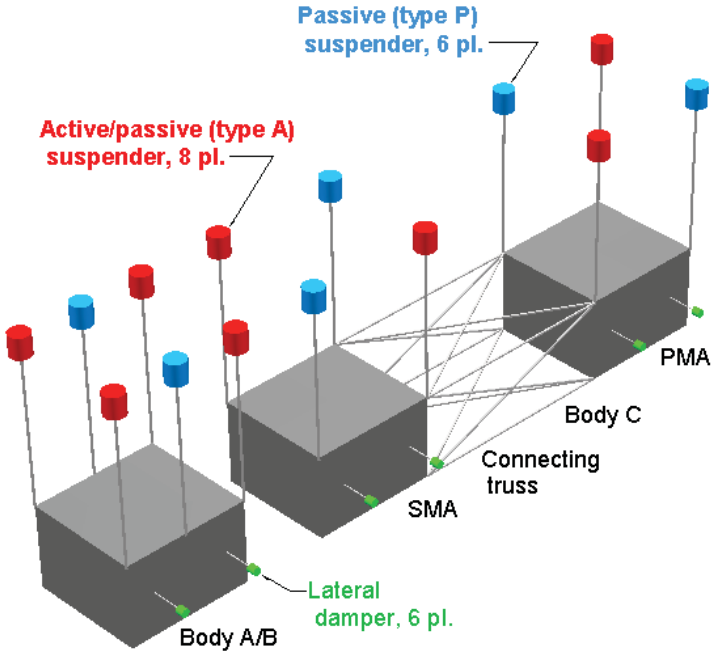

Figure 1 Schematic of the isolation system and payload.

Operating Principles

Figure 2 shows the operating principle of a Type A suspension device. The uplift force on the payload is provided by a special type of air spring composed of a frictionless piston moving inside a cylinder with the pressurized volume under the piston ported to a much larger external volume. The piston rod shown extending through the lower end of the cylinder is only for illustration. The real configuration is explained in the next section. Pressure in the external volume (and thus in the cylinder) is controlled by a precision mechanical regulator, which also provides make-up air.

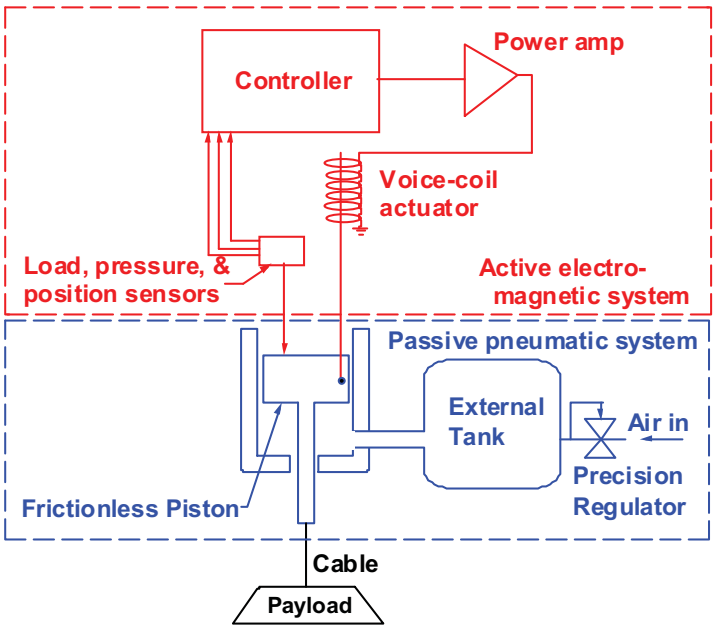

Figure 2 Operating principle of passive plus active suspension device.

In Type A devices, a voice coil actuator (actually several in parallel) act in parallel with the air spring to provide real-time fine trim of the uplift force. The primary feedback sensor is a high-resolution pressure transducer. It senses the very small, slow, random pressure variations that occur in the air spring. A central controller receives this information from all 14 devices. It then calculates the trim force required from the voice coils of each of the eight Type A devices in order to maintain the initial ride height and attitude. The controller then calculates the required actuator currents and sends digital commands to

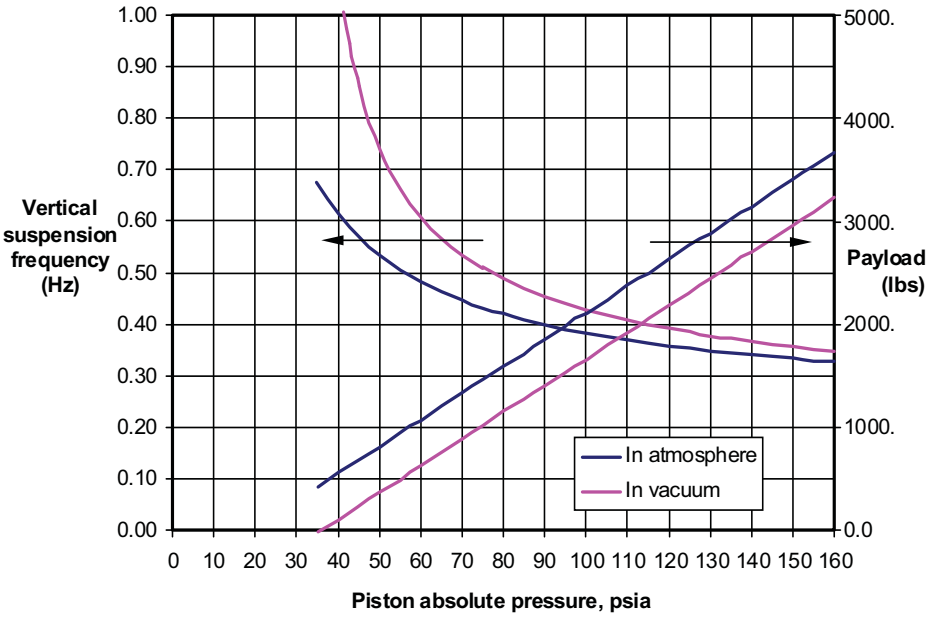

Figure 3 Calculated vertical suspension frequency and payload.

the power amplifiers driving the actuators. The update rate is slow enough that the controller is of the look-shoot-look-shoot type and is thus inherently stable.

The air spring using a frictionless piston behaves essentially as an ideal regulated air spring. Its stiffness is purely a function of the gas properties of air, the piston area, and the total pressurized volume. The relationship, derived from basic thermodynamics assuming linearity and isentropic compression and expansion, is $k = \gamma A^2 p_o/V_o$ where k is the stiffness, γ is the specific heat ratio of the gas (1.40 for air), A is the piston area, p_o is the mean absolute pressure and V_o is the mean volume. The dependence of stiffness on pressure means that the suspension frequency is essentially independent of payload mass[2]. Further, it means that an air spring can always be brought back to a zero sag condition under weight load by adjusting the mass of air in the cylinder. Implementation via a frictionless piston rather than a flexible air bag has the advantage that an air bag adds significant stiffness, which sets a lower limit to the suspension frequency. The suspension frequency of a piston air spring can be reduced without limit by increasing the external volume.

Figure 3 shows the calculated suspension frequency and payload for a payload suspended by a Type A device with 227-l (60-gallon) accumulators. There is some loss of payload capacity and increase in suspension frequency because of the vacuum itself. As will be shown, the moving element of the suspension devices is subject to vacuum force, which slightly decreases the payload capacity and increases the suspension frequency. The increase in frequency is also caused by flexible metal bellows seals needed for vacuum compatibility.

Design of Suspension Devices

Figure 4 shows two views of a simplified solid model of a Type A suspension device. Missing from the model is the “bell jar” vacuum housing that encloses the part of the mechanism above the baseplate. The housing recaptures all the exhaust air from the air bearings and pistons such that it can be routed via a tube out through the wall of the vacuum chamber. This and the bellows seals around the carriage rails that extend downwards through the baseplate are the essential features that make the devices operable in vacuum.

[2] This independence requires that the absolute pressure be at least several times the ambient pressure acting on the top of the piston.

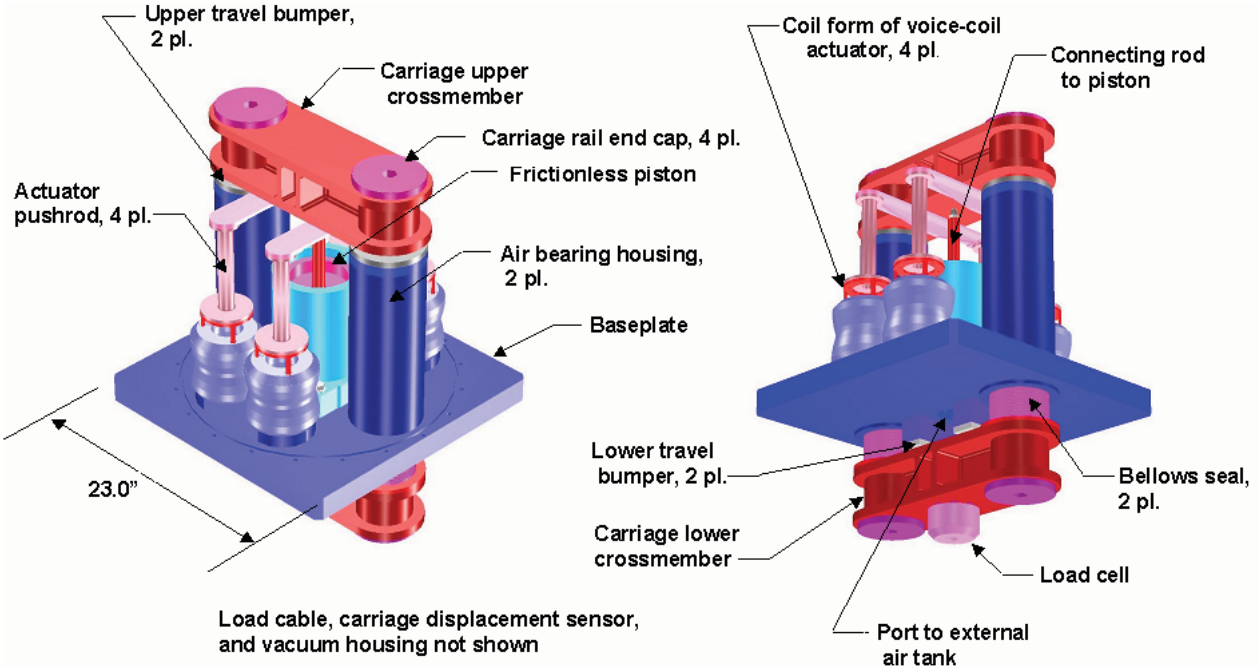

Figure 4 Conceptual design of suspension (type A with active augmentation).

The device consists of two main subassemblies: a moving carriage shown in shades of red and a fixed frame shown in shades of blue. The carriage moves vertically on four journal air bearings, two in each of the two cylindrical housings as shown. The carriage lifts the payload via a cable connected to its lower crossmember through a load cell as shown. In the present application, the load cells are used to monitor the force distribution among the devices when "parked", i.e. when the air springs are deflated and the carriages rest against their lower travel stops. Uplift force against the upper crossmember of the carriage is supplied by the frictionless air piston through a connecting rod. The piston is actually a combination of a journal air bearing and a piston. A very thin, stable air film is produced around the piston skirt such that it never actually touches the cylinder, thus eliminating all friction. A small amount of air leakage is allowed with make-up air being supplied by the precision pressure regulator supplying the external accumulator tank. As noted earlier, the carriage lower crossmember is sealed against the bottom side of the baseplate by two flexible metal bellows seals which surround the two carriage rails as shown. Type A devices use four voice coil actuators operating in parallel with the air piston. Type P devices do not have voice coil actuators but have dual air cylinders for increased lifting capacity. Both Type A and Type P devices include LVDT displacement transducers to sense the carriage position, high-resolution pressure transducers for monitoring piston pressure, and load cells for monitoring the load distribution.

Pistons are 146.0 mm (5.75 inches) in diameter for a bore area of 16,753 mm^2 (25.96 in^2). This produces a gross uplift force of 13,890 N (3115 lbf) at a gauge piston pressure of 8.28 bar (120 psig). Type A devices are nominally rated at 11,147 N (2500 lbf) in vacuum which accounts for the weight of the moving carriage and the vacuum force pulling down on the carriage (the interior of the bell jar housing is at atmospheric pressure). The Type P devices use two pistons of this size and are rated at 24,524 N (5500 lbf) in vacuum. Vertical stroke between the travel bumpers is 3.8 cm (1.50 in) for both types.

Voice coil actuators are driven by current-control analog power amplifiers using 16-bit digital commands. Force resolution of the active subsystem in a Type A device is approximately 0.36 N (0.08 lbf).

The magnetic pendulum dampers (Figure 1) are built from the magnet bodies of the voice coil actuators with the wire coil replaced by a solid copper annulus. A flexure suspension is used to allow the conductor to move axially in the magnet body while remaining concentric to it. Details are in the next section.

Figure 5 Suspension devices. Type A, augmented (left), Type P, passive only (right).

Figure 5 shows some of the delivered hardware. The Type A suspension device on the left is identified by its single piston and four voice coil actuators. The Type P on the right has dual pistons and no voice coils. The circular groove in the top side of the baseplates is for the O-ring that seals the bell jar flange to the baseplate. All air and electrical feedthroughs are located in the baseplate where the interfaces can be accurately machined. The devices are shown mounted on assembly and shipping stands. Figure 6 shows a bell jar being trial-fitted onto a Type A suspension device.

Figure 6 Trial-fitting of vacuum housing onto suspension device.

Figure 7 shows a Type A during assembly. The carriage is assembled into the frame initially without the bellows seals. After the plumbing, wiring, and various small subassemblies are added, the lower crossmember is removed, the seals are mounted into place, and the crossmember is reinstalled. This allows the carriage motion to be checked for friction before the bellows are added and also protects the bellows, which are somewhat fragile, from damage during most of the assembly process.

An example of the bellows seal is shown in Figure 8. It is formed bellows rather than edge-welded. While the latter type would have had the advantage of lower added stiffness, it would have been much more costly and would have had an unacceptably long delivery time. Since analysis had shown that the target suspension frequency could be met with formed bellows, that was the type used. The end flanges are machined with standard O-ring grooves as shown and then tungsten-inert gas welded to the formed bellows. The bellows are fabricated from 321 stainless steel because of its high ductility. The flanges are made from the same material for welding compatibility. Inside diameter of the bellows is 93.7 mm (3.69 in) and flange-to-flange length in the unstrained condition is 107.4 mm (4.23 in). Stiffness added by the bellows is about 2.90 N/mm (16.5 lbf/inch) per bellows.

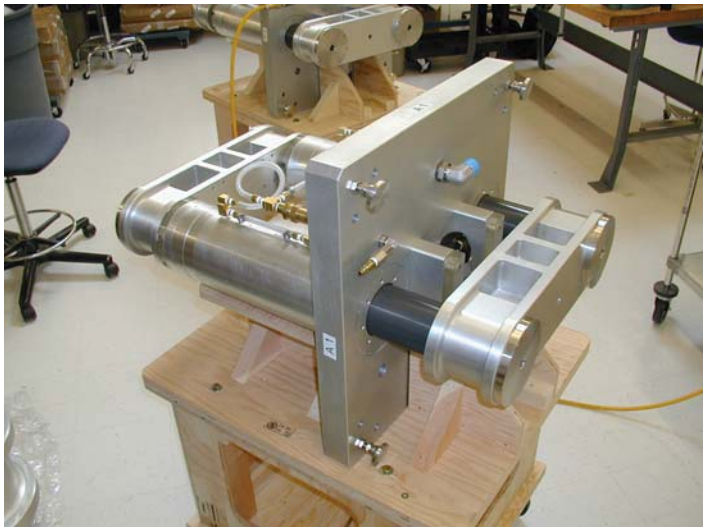

Figure 7 Partially assembled Type A device showing the carriage rails and lower crossmember. Bellows seals are installed later.

An important consideration for internally pressurized, formed bellows is lateral (inchworm) buckling. Because the critical buckling pressure is always proportional to axial stiffness divided by length, there is a certain stiffness that must be tolerated. As usual, this controlled the design since the critical pressure had to be at least 1 atm. Measured buckling pressure was found to be in good agreement with theoretical predictions.

Figure 8 Flexible metal bellows seal.

Figure 9 shows two views of the passive magnetic pendulum dampers. The body of each damper was mounted to a temporary stanchion fixed to the floor of the vacuum chamber. The moving element of the damper was then connected to the payload by a “stinger” having a flex joint at either end. The resemblance of the magnet bodies of the dampers to those of the voice coil actuator (Figure 5) is clear. While damping performance could have been improved by a custom design, the ad-hoc design based on the actuators was adequate so the ever-present schedule pressure dictated its use. Working stroke of the dampers was about 12.7 mm (0.5 inch). Overall length of the assembly as shown is 248.7 mm (9.79 in) and the envelope diameter is 279.4 mm (11.00 in). Weight is approximately 11.4 kg (25 lb) per damper.

Experience in modal testing has shown that pendulum modes have practically zero inherent damping. The basic reason is that the potential energy is stored in geometric stiffness rather than elastic stiffness of a material. Hence, there is no material loss factor to dissipate energy. While relatively simple compared to the suspension devices, the passive pendulum dampers were essential to the overall success of the suspension system.

Figure 9 Passive magnetic dampers for payload pendulum modes

Testing

The aggressive development schedule for LSIS left time for only the most essential tests prior to shipping the hardware. These were friction and proof load tests of the suspension devices and leak rate tests of the devices and their accumulator tanks. Dynamic tests were performed after the fact on a spare damper for engineering purposes. This section reports methods and results for these tests.

Friction tests of suspension devices.

Figure 11 shows the setup for friction tests. A custom test stand (the white structure in the figure) was designed and built for the purpose. It provided a mounting location for the device under test and a means of moving the carriage up and down through a small stroke while the air spring and accumulator tank were fully pressurized to their maximum expected operating pressure. Force applied to the carriage to produce the motion and resulting displacement were transduced and recorded. If friction was present, it would show up as a step in the force at the instant the carriage motion reversed direction. The amplitude of the step would be twice the friction force.

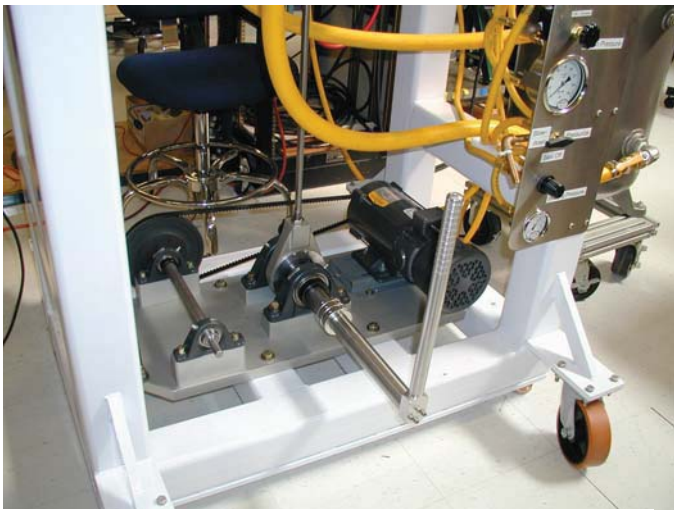

Figure 10 Actuation mechanism for friction tests of suspension devices.

Figure **10** shows a detail of the actuation device for moving the carriage. Initially a variable speed, DC electric motor was to be used to turn a crankshaft with a small, 1.27-

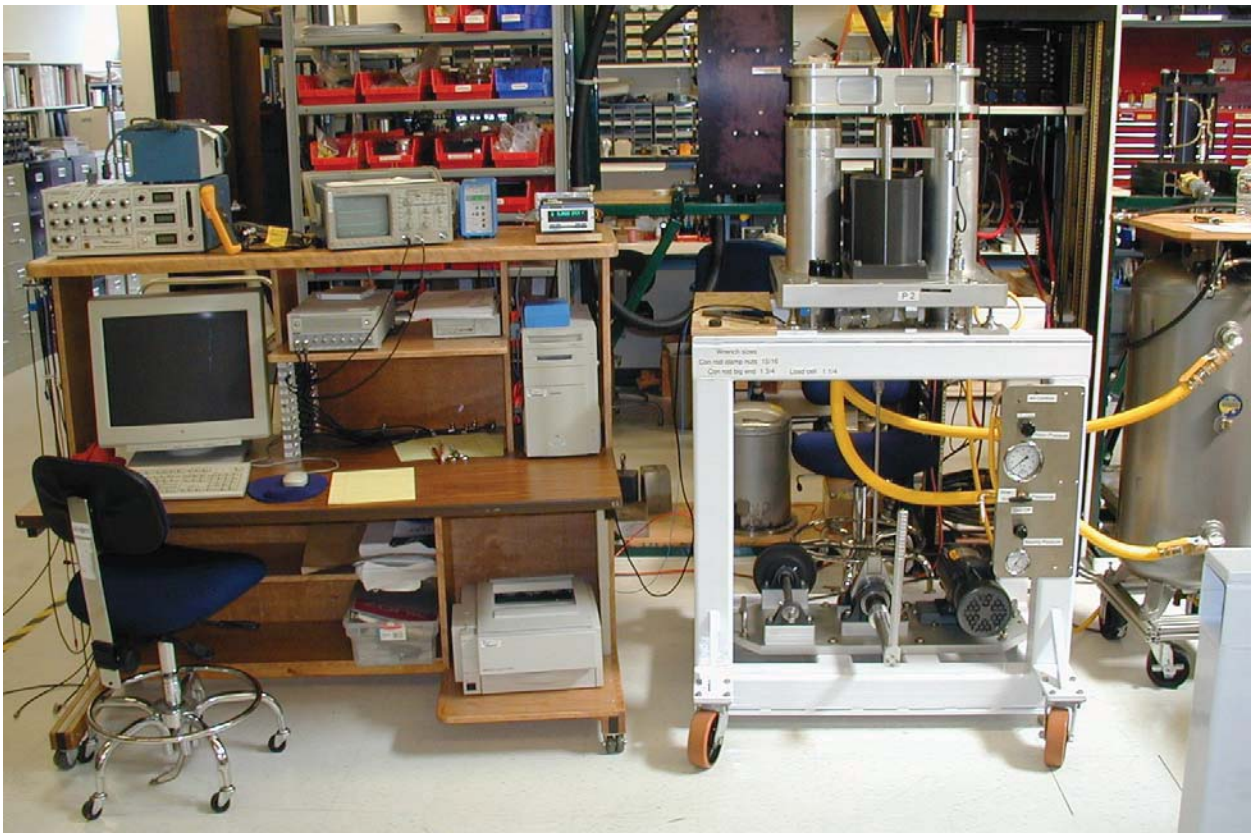

Figure 11 Test rig for measuring friction in suspension devices

mm (0.050-inch) stroke. The motor speed was reduced to about 120 RPM at the crank by a two-stage timing belt drive. However, in initial trials, it was found that the SCR motor controller would not control the speed smoothly as the crank passed TDC and BDC and the motor transitioned from driving to retarding the load. Large spikes in the motor torque occurred which would have obscured the small transients due to friction, had such been present. The solution was actually a simplification to the rig. A hand lever was fabricated and mounted directly on the crankshaft to replace the motor drive. With practice, it was possible to use the lever to rotate the crank back and forth through about 180 degrees with very smooth transitions in rotational direction. This was the system used for the actual tests although the DC motor and most of the belt drive are still present in the photographs.

Figure 12 and Figure 13 show typical results. Figure 13 is data obtained with a device operating correctly. The force trace, which has had its DC component removed, shows no sudden steps at the points where the displacement hits its extreme values and the direction of travel reverses. Figure 12 shows a case where there was friction. A step of about 5.3 N (1.2 lbf) occurs as the carriage reverses direction. This data was obtained in testing of a Type A device so the friction force (half the step amplitude) amounted to only about 0.019% of the average force. However, this exceeded the nominal specification for smaller devices of this type (<0.005%) so the offending part (the piston) was rejected. It was replaced with a spare unit that passed the test. Experience has shown that friction, if not due to some obvious rubbing of a visible moving part against a fixed part, is almost always due to the piston. Of the 22 pistons and cylinders fabricated, only one failed the friction test. This is actually a better yield that is typically obtained with smaller piston/cylinder sets. It appears that frictionless pistons are actually somewhat easier to build in larger sizes than in smaller.

The force transducer used for the tests was a piezoelectric, charge mode type with a charge amplifier having a time constant of about 10 seconds. The extremely large dynamic range of this measurement system allowed detection of force transients well under 1 N in the presence of DC forces of 25,000 N.

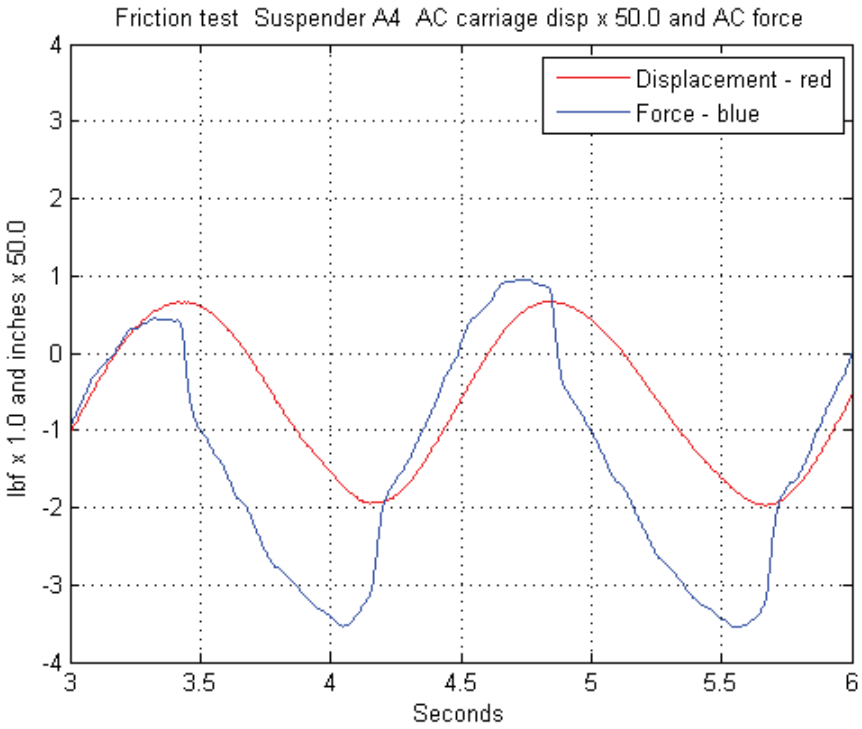

Figure 12 Test result for suspension device showing friction between piston and cylinder.

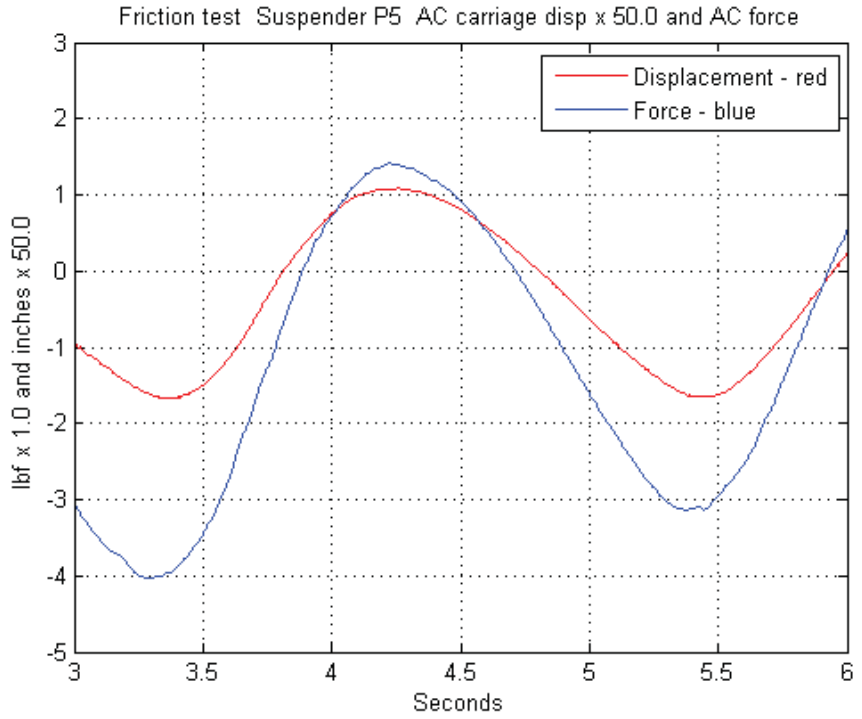

Figure 13 Typical test result for suspension device without friction

Leak rate tests

Because both the suspension devices and their accumulator tanks were to be used in a vacuum chamber, their leak rate was obviously of concern. The usual method of leak testing, developed for vacuum chambers, involves helium bagging the device, pumping the interior down to vacuum, and analyzing the gases pumped out to see how much helium is present. Because the suspension devices contain air at several different pressures with vacuum outside the device, this standard method would not have been representative of operating conditions.

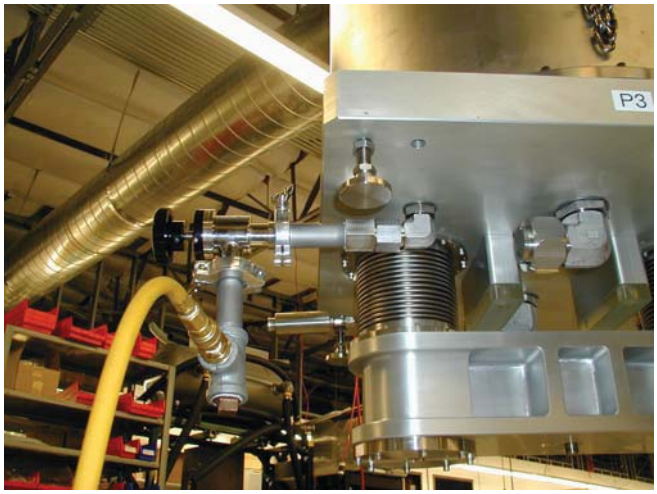

Figure 14 Low-leakage vacuum valve used in leak rate tests

Fortunately, the allowable leak rate was fairly generous, at least by the standards of the vacuum industry. The method used for the suspension devices was to pressurize the interior of the device to 1.01 bar (14.7 psi) above ambient, valve off the device with a low-leakage valve (Figure 14), and then record the interior pressure and temperature over several days. Mass loss from inside to outside was then calculated from the ideal gas law for air and compared to the allowable. The same method was used for the tanks except that they were pressurized to 3.45 bar (50 psig). Not surprisingly, it was found that sensing pressure alone was not adequate. Even with the device under test inside an insulated “doghouse”, pressure variation due to diurnal temperature variation was much larger than that due to leakage. Temperature compensation was essential to the method.

Pressure was measured using the same ultra-high-resolution quartz crystal pressure transducers used in the ride-height control of the actual system. They use the change in natural frequency of a quartz crystal due to pressure as the sensing mechanism. A built-in digital frequency counter allows a pressure resolution of a few parts per million. A built-in serial interface allows transmission of data to the recorder or controller without loss of accuracy. While quite slow by normal analog standards, their update rate was adequate for both the leak rate tests and the ride height controller. Temperature was measured by RTDs with signal conditioning that included A/D converters and serial interface to the recorder.

Figure **15** shows typical pressure and temperature time history data from leak testing of one of the accumulator tanks. Figure 16 shows the time history of air mass in the tank calculated from the measured temperature and pressure after subtracting the average value. Also shown in Figure 16 is a straight line whose slope represents the allowable leak rate. While the trace showing the measured mass loss is somewhat erratic, it is clear that the time-average leak rate is less than the specified maximum allowable. While some test articles failed the test initially and required some leak chasing and debugging, all eventually passed in time for delivery per the schedule.

While adequate for the purpose, the leak rate measurement method was slow and only practical because equipment was available to test more than one article at a time. It would not be practical for testing at the much smaller leak rates typically specified for vacuum chambers or for the bellows seals of the suspension devices. The latter were tested by standard helium mass spectrometer methods prior to assembly of the suspension devices.

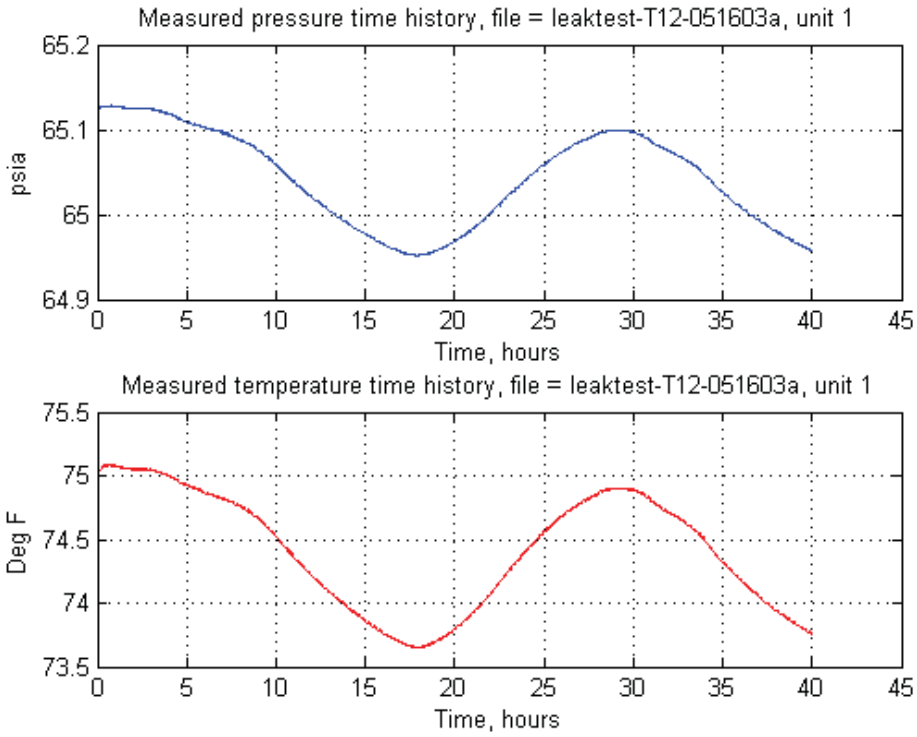

Figure 15 Pressure (top) and temperature (bottom) of air inside an accumulator tank during leak rate test.

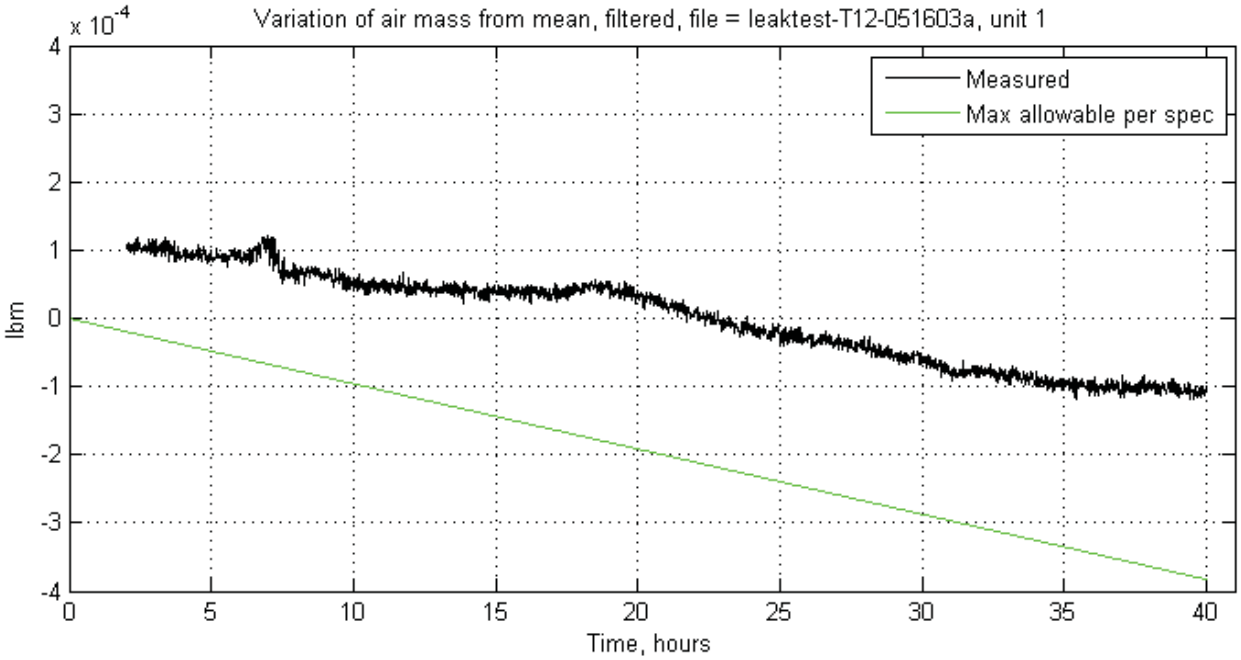

Figure 16 Leak rate calculated from measured pressure and temperature

Proof load tests of suspension devices

Each of the 14 devices was proof tested to twice its rated load capacity. A modified version of the friction test rig was used for this purpose. Shown in Figure **17**, it substituted a hydraulic cylinder for the crankshaft mechanism of the friction tester. Force was determined from the hydraulic pressure applied by a hand pump. The proof loads produced severe deflection of the elastomeric travel stops built into the suspension devices (Figure 4) but they all survived and returned to normal after the load was removed. No failures occurred during proof load tests.

Figure 17 Setup for proof load test of suspension device

Dynamic testing of dampers

One of the passive magnetic dashpots was tested to verify its damping properties. Figure 18 shows the test rig. The body of the damper containing the magnets and back iron (the shiny object in the photo) is mounted to a bulkhead in the center of the aluminum frame of the rig. The conductor is mounted on a carriage rail that forms part of the rig. The rail runs on two journal air bearings to eliminate any friction. One end of the rail (the right end in the photo) protrudes through the end bulkhead of the test rig frame. It is driven axially by an electrodynamic shaker working through a piezoelectric load cell. The other end of the carriage rail mounts an aluminum disk that serves as a target for a non-contact eddy current displacement sensor. The eddy current probe mounts to the left-end bulkhead of the test rig frame. The shaker is driven with a band-limited random current and the signals from the force and displacement sensors are input to a multi-channel digital Fourier analysis system. It computes a frequency response having carriage velocity as the input (denominator) quantity and force as the response (numerator) quantity. In the process, it removes from the force signal the portion that is due to the known inertia of the moving carriage. What remains is the drag force from the magnetic damper only. The result is a complex-valued function of frequency whose magnitude represents the damping force per unit of velocity (often called the dashpot constant, although it is anything but constant in this case). The phase of the complex function represents the phase of the damping force relative to the velocity.

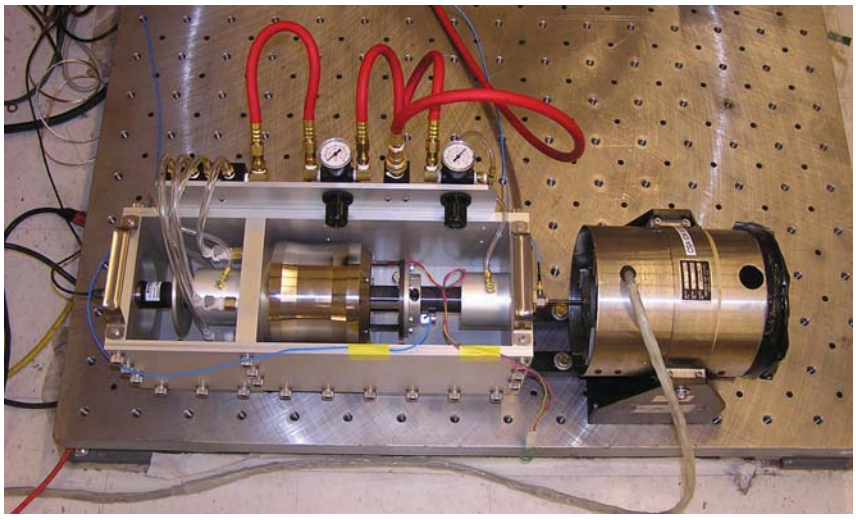

Figure 18 Test rig for measuring complex stiffness of magnetic dampers.

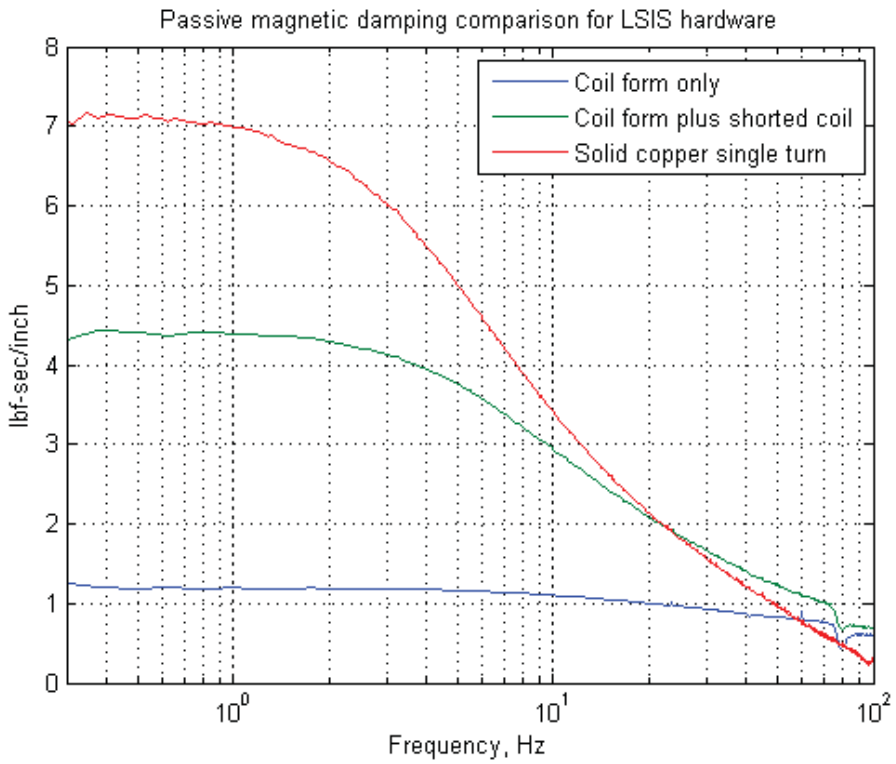

Figure 19 Measured force/velocity ratio for the magnetic damper

Figure 19 shows the magnitude of the measured frequency response function for three configurations of the conductor of the damper. The uppermost (red) curve is for the dampers as delivered and installed with the suspension system. These used a single, solid-copper annulus (also called a single shorted turn) as the conductor. The middle (green) curve is for a conductor formed from the same wire-wound coil used in the voice-coil actuators but with the wire ends shorted together. The blue curve is for the aluminum coil form (also called the bobbin) used in the voice-coil actuators but with no wire windings. Not surprisingly, the force/velocity ratio increases as the resistance in the induced current path is decreased, just as theory predicts.

The back iron assembly of the voice-coil actuator (identical to that of the damper) was of a design that produced relatively high inductance in the coil. For the actuator, this was not important since it is used essentially only at zero frequency. For the damper, it was expected that this would cause the induced currents in the damper conductor (which cause the damping force) to drop off with increasing frequency. This would be valuable for the present application since it would allow the magnetic dashpots to damp the very low frequency pendulum mode (less than 1 Hz) but then disappear at higher frequency so as not to transmit disturbing forces into the payload at higher frequencies. The red curve of Figure 19 shows that the design was quite successful. At frequencies over about 50 Hz where the resonances of the payload begin, the force/velocity ratio is reduced by about an order of magnitude from its DC value.

Conclusion

Figure 20 shows eight of the fourteen suspension devices mounted in a framework, ready to be suspended from the roof of the vacuum chamber. These are the eight that support the Body C of Figure 1. While schedule constraints did not allow systematic tests, informal measurements of the vertical frequency by the end user indicated that it was, in fact, 0.50 Hz as designed. Most important, the degree of vibration isolation provided was sufficient to allow the functional tests of the spacecraft to be performed without limitations from ambient disturbances. The LSIS did its job.

The primary conclusion from the development was that the very low stiffness pneumatic suspension devices are scalable. In fact, anecdotal evidence suggests that, at least up to the largest sizes built to date, obtaining the critical zero-friction behavior is actually easier in larger devices (piston bores over about 76.2 mm (3 inches)) than in smaller ones. A system is now in preliminary design that will use multiple devices with piston bores over 203.2 mm (8 inches) to float a payload of approximately 45,454 kg (100,000 lb) in vacuum.

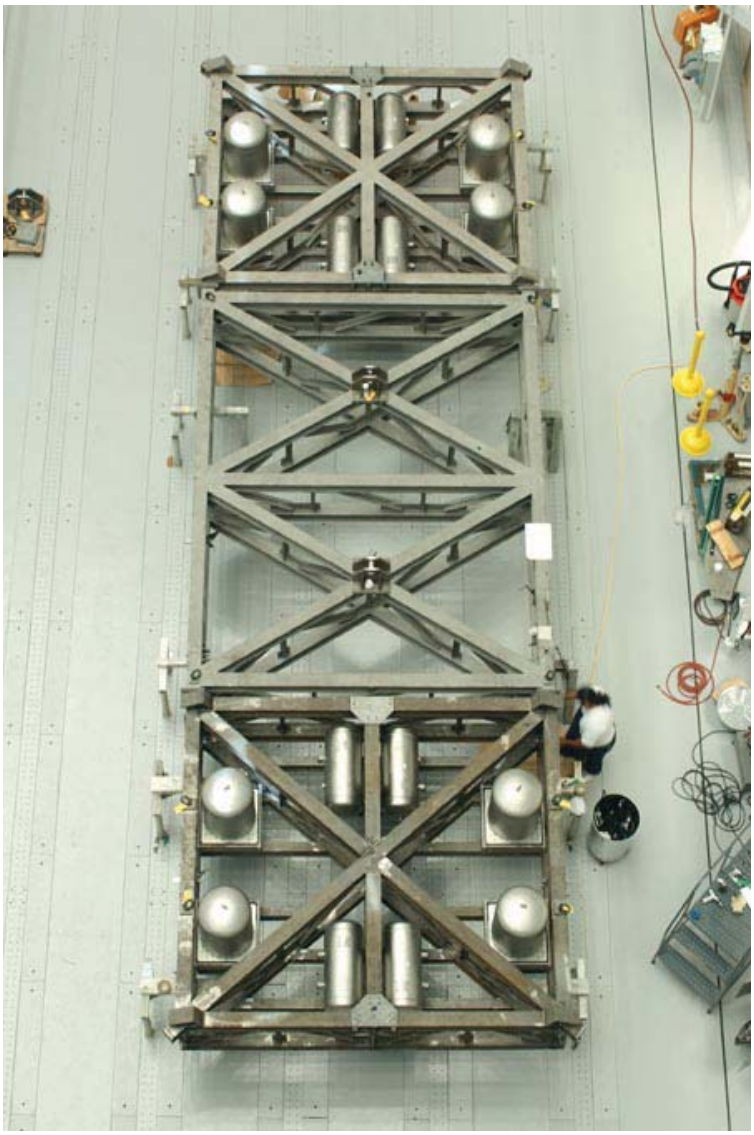

Figure 20 Eight suspension devices with accumulator tanks mounted in frame for supporting Body C. Size is evident from the person in the lower right of picture.

References

1. Kienholz, D.A. "Simulation of the Zero-Gravity Environment for Dynamic Testing of Structures," Proc. 19th IEST Space Simulation Conference, Oct 28-31, 1998, Baltimore, MD
2. Sillls,Jr.J.W., Voorhees,C.R. "Characterization and Application of Pneumatic Suspension Devices for Vibration Disturbance Testing," Proceedings of the 20th International Modal Analysis Conference, February, 2002.

Gas Strut Separation Alternative for Ares I

Brian Floyd* and James Owens

Abstract

This paper presents a design alternative and the rationale for a stage separation system based on Metering Adiabatic Gas Struts (MAG Struts) for the Ares 1 launch vehicle. The MAG Strut separation system was proposed as an alternative to the current Ares 1 separation system, which relies on small solid rocket motors to provide the main separation force. This paper will describe technical issues that were addressed during the trade study and present a conceptual design of the strut system that best resolved the issues. Needed development testing and programmatic considerations will be addressed as part of the paper.

Introduction

Gas struts show promise as an efficient way to provide the separation force for launch vehicle staging. Strut systems are currently in use on a number of vehicles, but so far all have been unmanned. Several factors make the MAG Strut system unique. The struts are entirely self-contained. They are themselves pressure vessels, which are pre-charged with gas prior to launch. They require no additional actuation, but simply act as springs when the physical connection between stages is severed. Due to the mass properties of the separating stages, this system provides excellent nozzle clearance during fly-out in off-nominal conditions. Consequently, safety and mission success objectives are enhanced. Since the struts are light weight relative to other separation systems capable of applying the same force, the separation timing can be adjusted to separate earlier during the assent trajectory, increasing payload lift capability. The proposed struts apply the separation force smoothly during release in order to minimize disturbance of the Upper Stage propellant and reduce the buckling loads applied to the upper stage aft skirt. The trade study also predicts significantly lower life-cycle-cost. Since the MAG Strut system is not in flight operation on any launch vehicle, development testing and system-qualification introduce some risk into the Ares program, which is a barrier to adopting the system.

Background

The Ares I launch vehicle will lift the Orion crew vehicle to low-earth orbit for manned missions to the International Space Station and to the moon. Ares I consists of two stages. The first stage is a modified Space Shuttle Solid Rocket Booster (SRB) with 5 solid motor segments instead of the 4 segments currently used for shuttle. The Ares I upper stage is a LOx / LH2 stage powered by a J-2X engine. The stages are connected by a cylindrical interstage and a conical frustum. The J-2X engine is housed in the compartment formed by the interstage and frustum.

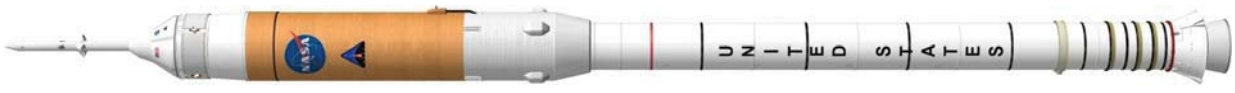

Figure 1 - Ares I

In the current flight trajectory baseline, the first stage ascent phase ends when the first stage reaches 178 kN of residual thrust. Eight Booster Deceleration Motors (BDMs) fire to push the first stage aft. Eight Ullage Settling Motors (USMs) thrust forward to maintain positive acceleration on the upper stage. Once

* NASA Marshall Space Flight Center, Huntsville, AL

the USMs and BDMs are ignited, a pyrotechnic joint at the forward end of the interstage initiates and the vehicle begins to separate. Figure 1 shows the Ares I configuration with the BDMs mounted on the interstage. In the most recent configuration, they are relocated to the aft skirt of the first stage. The J-2X nozzle exit plane is 7.1 meters aft of the separation plane. With the current arrangement separation system, it takes approximately 1.7 seconds for the nozzle to pass the forward end of the interstage.

Nozzle Clearance During Fly-Out Considerations

Many factors affect the amount of radial clearance between the engine nozzle and the interstage wall during the fly-out. The most significant factor contributing to clearance issues for BDM separation is asymmetric plume impingement force on the first stage that can occur if one motor fails to fire. Secondly, since the first stage has 178 kN of residual thrust at the time of separation, significant pitching and yawing loads may be imposed on the stack before separation and on the first stage after separation due to thrust vector pointing uncertainties. With one BDM out, a worst-on-worst analysis of the separation shows contact between the interstage and the engine nozzle during fly-out. Monte Carlo analysis of this scenario shows that nozzle clearance can only be demonstrated to a 2.5-sigma level.

The proposed MAG Strut system uses eight gas-charged struts mounted inside the interstage to force the two stages apart. The struts essentially act as alignment guides during separation. Figure 2 shows the relative position of the struts on the interstage to the USMs and the BDMs they will replace.

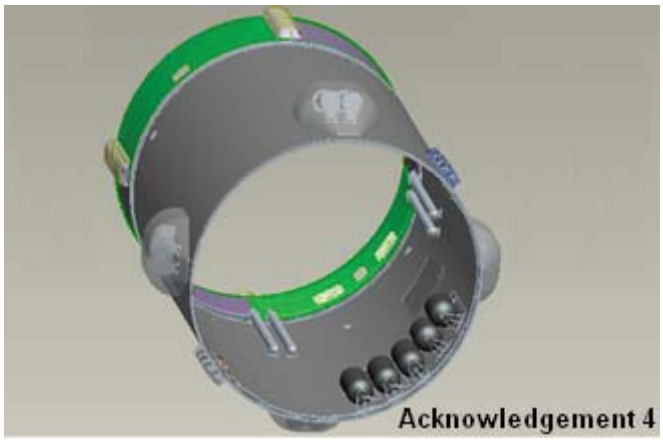

Figure 2 - Interstage showing BDMs and Struts

Although the struts extend above the separation plane, they provide superior clearance, even with one strut out. The primary reason for this superior performance is that the mass-moment-of-inertia of the Ares I upper stage/crew vehicle is approximately ½ that of the mass-moment-of-inertia of the expended first stage, while the distance from the upper stage/crew vehicle center-of-gravity to the J2 nozzle exit plane is approximately ½ the distance of the center-of-gravity of the first stage to the separation plane. Figure 3 shows the relative positions of the centers-of-gravity of the separated stages to the nozzle exit plane and first stage separation plane. With a strut system, any disturbance force, regardless of its origin, is compensated for by the struts, forcing the separated stages to rotate in the opposite directions. The rate-of-rotation, W, induced on the two bodies in always close to 2/1 with the upper stage/crew vehicle rotating at twice the rate of that of the first stage. The rate of rotation of each body is small with the gas strut system. Distance D3 is considerably larger than distance D4 so some of the disturbance force coming from the first stage results in translating the upper stage in the same direction the interstage is moving. This translation effect, though beneficial, is not as significant as the rotational compensation.

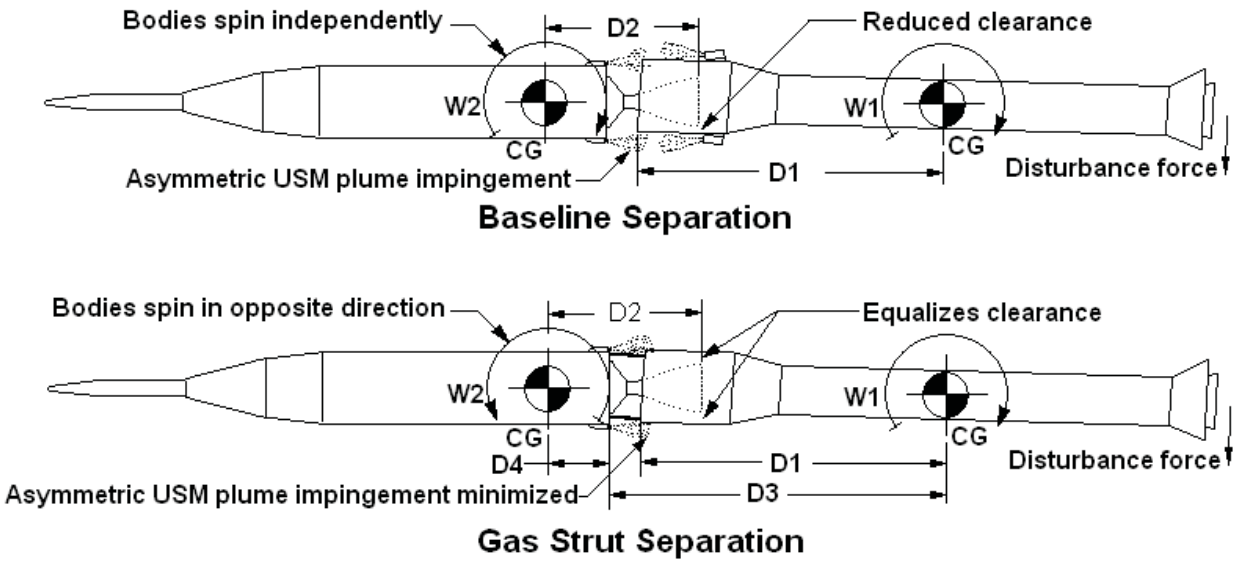

Figure 3 - Comparison of Gas Strut Separation and BDM Separation

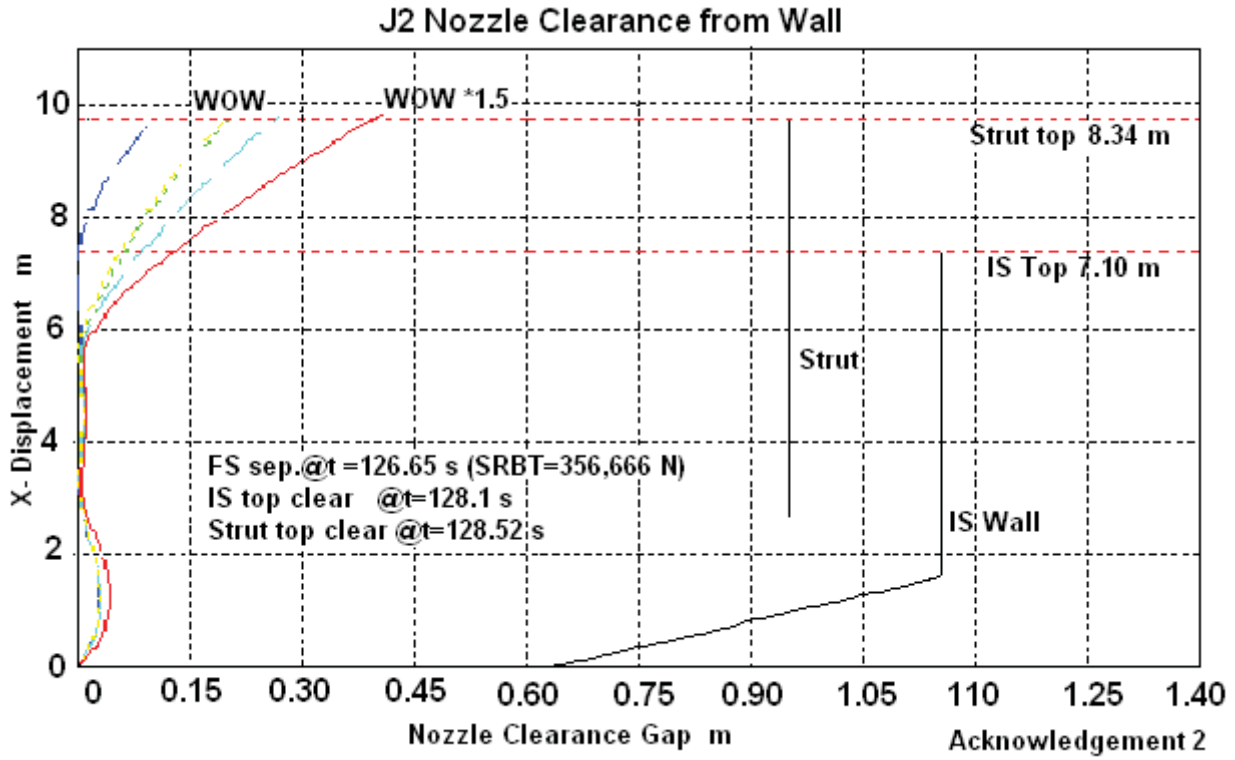

Figure 4 - Ares I Separation Clearance using Gas Strut System

Figure 4 shows the preliminary clearance results for the Ares I upper stage engine nozzle with one strut out. The WOW*1.5 curve represents a worst-on-worst assessment of the radial clearance with a margin of 50% added to account for unknowns in the analysis. Even in this conservative case, the nozzle clears the extended end of the strut by 45.7 cm. The dash lines represent WOW case clearances for different failed struts with different disturbance scenarios. Two seals must fail on the same strut to result in a 100%

pressure loss. Based on the analytical results, one strut failure cannot result in the loss of an Ares I mission due to nozzle contact. Consequently, the MAG Strut system is inherently two-fault tolerant.

Plume Heating on Upper Stage

At the Ares I System Definition Review, the vehicle was configured with BDMs mounted near the aft end of the interstage in four pods containing two motors each. The USMs were mounted on the upper stage aft skirt, also in four pods of two at the same angular positions around the cylinder. One problem with this configuration is the interaction of the USM and BDM plumes. Even though the nozzle exit planes were separated by over 4.5 meters axially, extreme heating was predicted in the upper stage engine compartment during separation because the BDM plumes deflect the USM plumes into the interior of the interstage. Also, debris generated by the separation pyrotechnics will likely be propelled into the engine compartment by the interacting plumes. The use of gas struts eliminates these debris and heating concerns. Relocating the BDMs to the first stage aft skirt would resolve this issue.

Payload-to-Orbit Benefits

Gas strut separation produces a significant increase in payload-to-orbit capability. This gain is a result of reduced aerodynamic drag, momentum transfer between the stages, and ascent trajectory optimization.

The interstage-mounted BDM pods are the largest protrusions from the nominal outer moldline (OML) of the vehicle. As such they account for a total of a 110 to 120 kilogram payload penalty due to aerodynamic drag. The proximity of the BDMs to transition from the conical to cylindrical is a major factor in the high drag. Locating the struts inside the interstage eliminates all aerodynamic drag effects.

For the baseline trajectory, the amount of residual first stage thrust at separation is limited by the capability of the BDMs. For an 8 BDM configuration with one motor out, separation must wait until first stage thrust drops to 178 kN. Because the struts have a better weight to performance ratio than BDMs, the trajectory can be optimized to improve performance. Figure 5 indicates the amount of payload that can be gained relative to the baseline flight profile. The steeper section of the curve indicates a significant payload improvement, but the strut system mass (including additional upper stage structural mass) begins to offset the benefit as residual thrust increases. Separation at 356 kN of residual first stage thrust is thought to be optimum for Ares I. This results in approximately 90-kg additional payload due to improved trajectory performance.

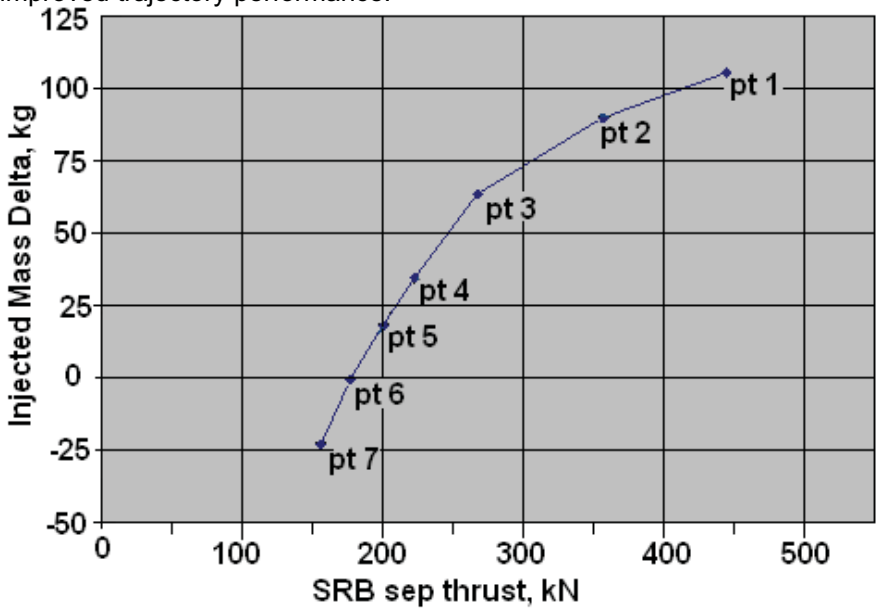

	Residual thrust (kN)	Payload gained (kg)
pt 1	445	105.8
pt 2	356	90.1
pt 3	267	63.9
pt 4	222	34.6
pt 5	200	18.3
pt 6	178*	0.0*
pt 7	156	-23.0

*Thrust used for baseline

Acknowledgement 1

Figure 5 - Payload Delta from Baseline vs. Separation Thrust

During separation with gas struts, the first stage thrust continues to act on the upper stage until the end of the stroke. Initial calculations show that this momentum transfer adds payload performance at a rate of 8.93 kilograms for every meter per second of ΔV. Preliminary strut designs result in an increase in upper stage ΔV of 3 to 3.7 meters per second. This amounts to 27 to 33 kilograms of additional payload. Figure 6 shows the relative velocity gained by the upper stage for a separation with 356 kN of residual thrust.

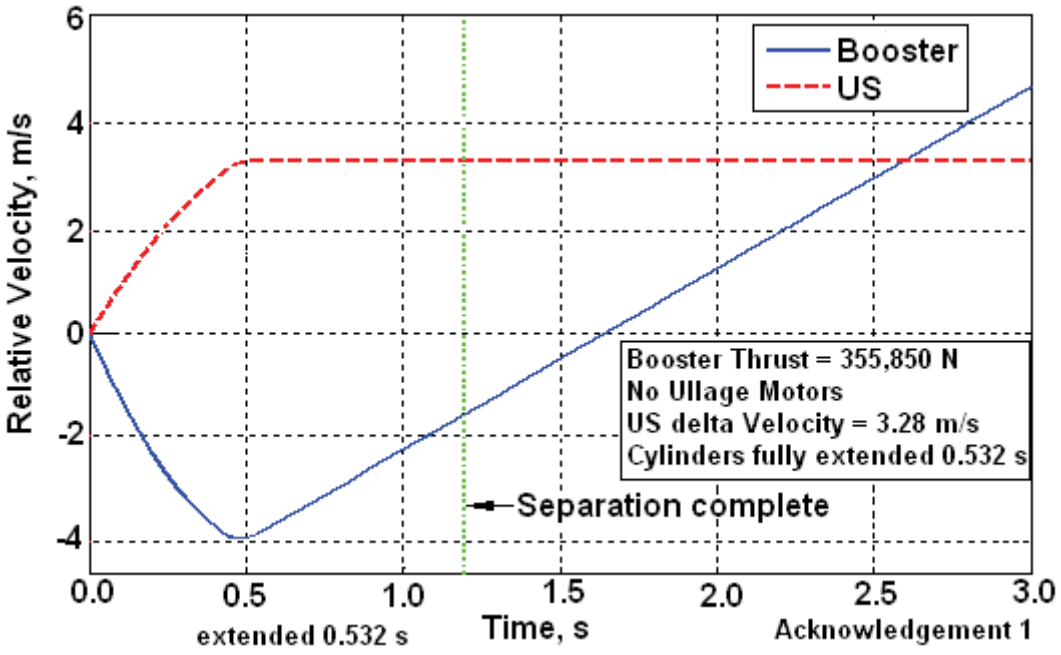

Figure 6 - Momentum Transfer Effects for a Separation at 356-kN SRB Thrust

The mass of the struts and upper stage fittings for a 356 kN thrust separation are about half that of a BDM system that separates at 178 kN of residual thrust; however, because more of the mass remains with the upper stage, no additional payload advantage from the change in system mass is realized.

Table 1 - Approximate Payload Benefit

Reduced Drag	110 kg
Earlier Separation	90 kg
Momentum Transfer	27 kg
Mass Delta Benefit	0 kg
Total Payload Benefit	227 kg

Cost Considerations

The projected unit cost for each BDM is approximately $200,000. There are many reasons for this high cost. One of the most risky processes of solid rocket motor manufacturing is the casting and curing of the solid rocket propellant. The process is very hazardous and requires extensive risk mitigation to prevent inadvertent propellant ignition. The risk mitigation techniques are well known, and accidents are now rare, but the process is expensive. Additionally, post-casting inspection sometimes reveals defects in the cast propellant. If a defect is found, most often the motor is discarded.

Per unit cost for gas struts should be significantly less than BDMs, since there is no hazardous material to procure and handle. Also each flight unit can be acceptance tested, so manufacturing will not require the strict process control necessary for solid motors. If a defect is discovered during the acceptance testing,

in most cases the strut could be saved by simply reworking or replacing the defective parts. In addition, since the struts are inert until they are pressurized, ground handling hazards are eliminated, making handling a low-cost operation.

Parametric cost modeling bases the estimated cost on weight and similarities to selected components for which cost are available. Since the struts are half the weight of BDMs, they would be half the cost assuming equal complexity. This is the only level of cost analysis that is possible given the maturity of the MAG Strut design. Actual per-unit cost would need to be reevaluated after developed units have been fabricated and the design finalized.

MAG Strut Design

The MAG Strut struts are designed to take advantage of the increase in payload to orbit by separating at 356-kN residual first stage thrust. To achieve this, a significant force is required. Consequently, the struts can place a substantial bending moment into the edge of the aft skirt, increasing the potential for buckling during ascent. Also, sudden release of the energy stored in the struts could result in a significant jerk to the upper stage, which could affect propellant quality and tank pressure. The MAG Strut design is proposed in order to counter these effects. During ascent, only a low pressure acts against the upper stage aft skirt. At separation, the force applied increases gradually, which minimizes potential for skirt buckling and mitigates concerns about sloshing induced in the propellant tanks.

The MAG Struts are designed with two chambers as shown in Figure 7. The low-pressure chamber is meant to provide the initial force requirement for separation. The initial force calculation for each strut would be as follows:

$$\left\{\left[\frac{(7.62\ cm^2)}{4}\right]*\pi\right\}*10{,}342\ kPa+\left\{\left[\frac{(17.78\ cm^2-7.62\ cm^2)}{4}\right]*\pi\right\}*1{,}034\ kPa=68{,}124\ N$$

With 8 struts, the force of 545 kN is more than sufficient to overcome a SRM residual thrust of 356 kN and the transient oscillatory force from the SRM, and therefore preventing re-contact of the two stages during separation. (See Figure 8 for a plot of the transient oscillatory thrust of the Ares 1 first stage.) The high-pressure chamber is intended to store the gas needed for the main part of the strut stroke. After 40 cm of stroke, this force reaches 1,495 kN. This force is capable of driving the first stage and upper stage apart with sufficient velocity margin to achieve separation with a residual first stage thrust of 356 kN.

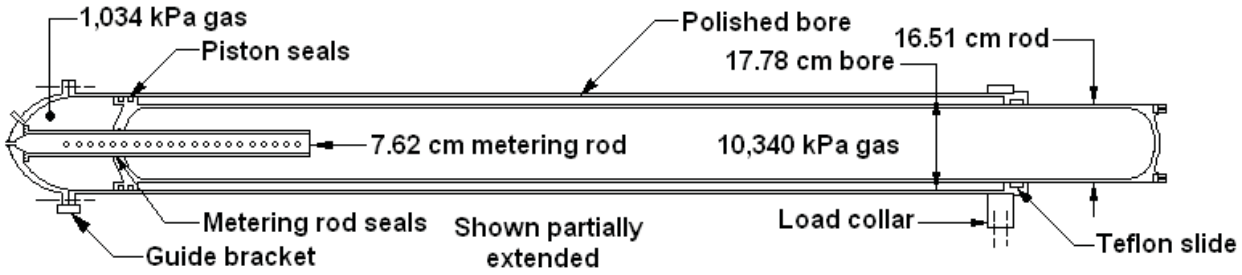

Figure 7 – Schematic of the Proposed MAG Strut Design

The metering rod has a pattern of holes that are exposed as the strut strokes, providing a gradual force buildup that will minimize impulse on the upper stage. Figure 9 shows a computer-aided design (CAD) rendering of the strut in the collapsed position. Figure 10 shows a CAD rendering of the strut in the extended position. Initially no holes are exposed. Once the strut has stroked 2.54 cm, 6 holes are exposed. Figure 11 shows the cumulative area for the exposed holes as a function of stroke. Every 2.5 cm of additional stroke exposes more holes to achieve the gradual force build-up. (The summation of

the total exposed hole-area for two different hole-sizes in shown at the bottom of the chart.) A large range of force profiles is possible with different hole-patterns. Holes larger than the “O” ring seal diameter would likely catch the seal, causing damage during stroking. A hole diameter of 3.96 mm would be the largest recommended hole size for a seal with a 4.83-mm diameter cross-section.

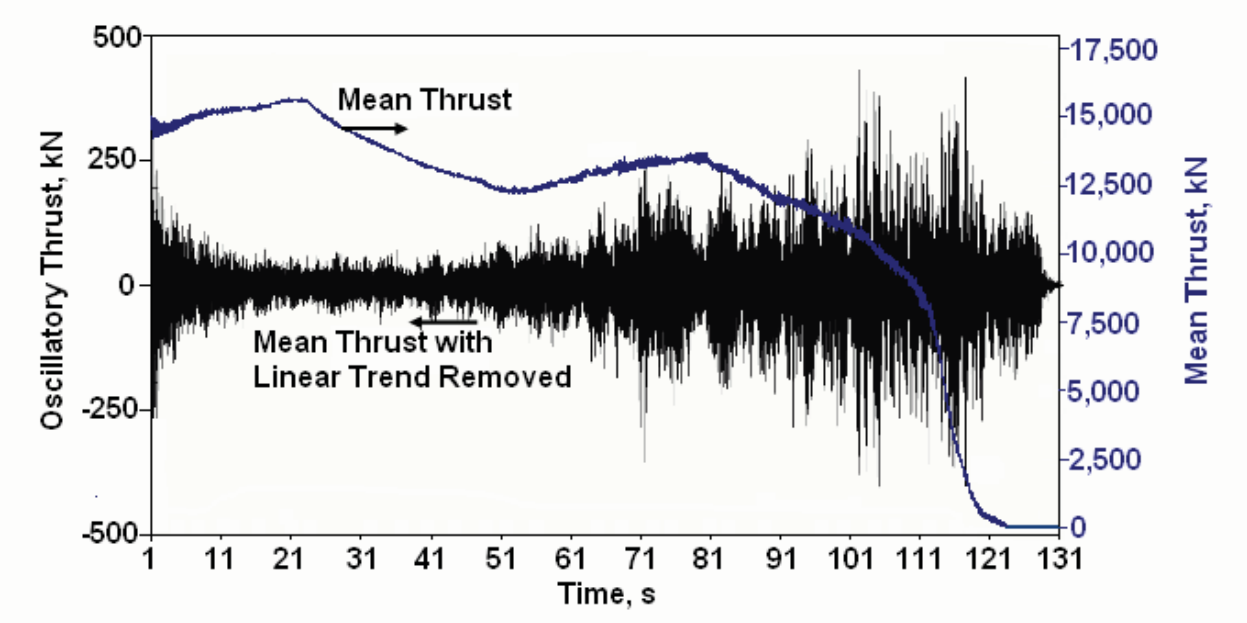

Figure 8 – Average Thrust and Oscillatory Thrust Test Data for 5 Segment SRM

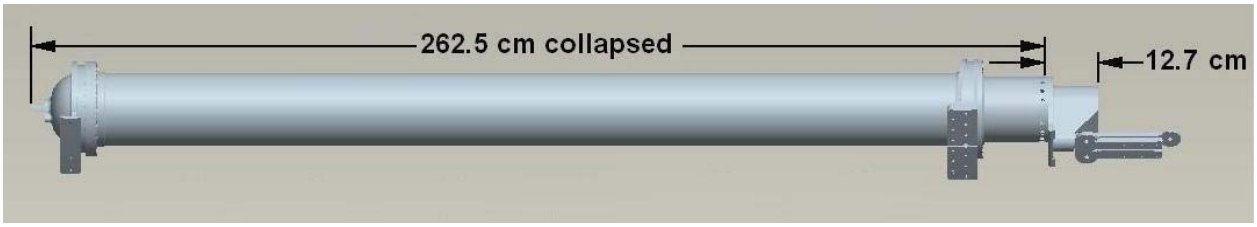

Figure 9 - Strut Rendering (Collapsed)

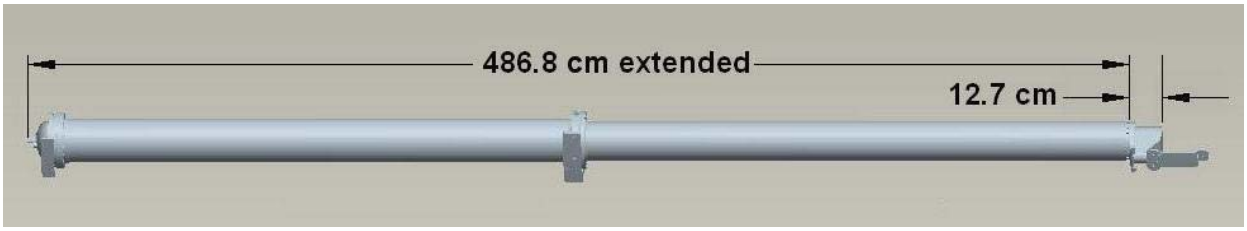

Figure 10 - Strut Rendering (Extended)

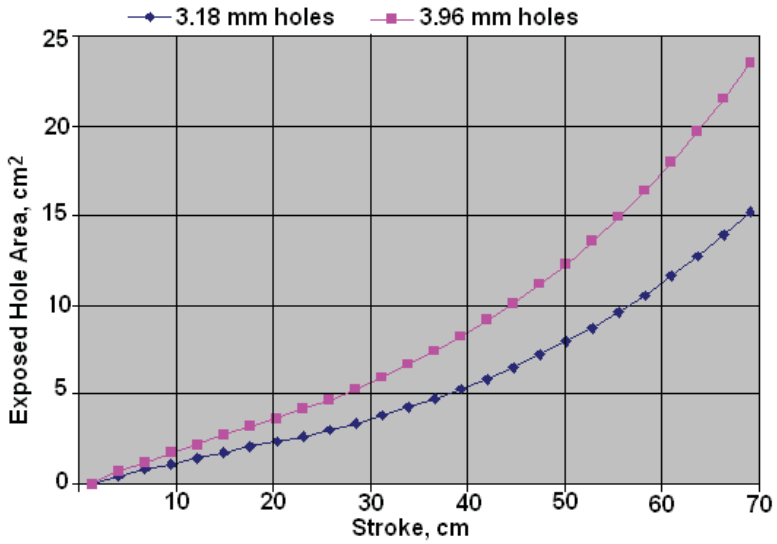

Figure 11 – Exposed Hole Area for Two Candidate Hole-Patterns

If the low pressure chamber is allowed to be at ambient pressure by providing a very small hole to the exterior of the strut, the strut can operate with only one pre-pressurized volume. This variation would make it possible to charge only one chamber prior to launch, eliminating some potential failure modes. A strut with a 9.208-cm diameter metering rod and with no pressure in the small chamber would provide slightly more initial separation force than the strut shown in Figure 7. This strut variant opens up the possibility of designing a hermetically sealed strut or other point design.

Since the desired thrust profile for the struts is based on requirements derived from a fluids analysis of the hydrogen tank pressure, having a strut capable of accommodating a range of force profiles is preferable. For a -147 degree C initial ullage gas charge temperature, an acceleration rate of change of 2.5g per second is acceptable. A higher axial rate of change may be acceptable with the currently proposed -220 to -250 degree C pre-charge gas. Table 2 shows the predicted effect of lowering pre-charge gas temperature on the make-up gas required to recover from an ullage collapse. A change out of metering rods could adapt a set of struts to revised ullage requirements. Sloshing risk increases as the axial acceleration of the rocket diminishes. Surface tension and vibration force the fluid in the tank up the tank walls as shown in Figure 12. Stage separation with 356 kN of residual thrust assures that the average axial acceleration never drops below .12g. This is enough acceleration to force the ullage gas to remain in a hemispherical shape bubble. The MAG Strut system further mitigates the risk of ullage collapse by limiting the axial acceleration rate of change.

Table 2 – Hydrogen Tank Recovery Gas Requirements

Initial tanked He assumptions: T=-250 C; P=22,00 kpa					Supply assumption: Isentropic Blowdown P=6,895 kpa			
H2 pre-press temp	Mass for ullage recovery	Initial storage density	Final storage density	Delta density	Storage volume required	Bottle mass	Total loaded He mass	Total Mass
19 C	226.9 kg	192.38 kg/m^3	144.81 kg/m^3	47.58 kg/m^3	.486 m^2	1,390.0 kg	917.2 kg	3,642.2 kg
-181 C	115.7 kg	192.38 kg/m^3	144.81 kg/m^3	47.58 kg/m^3	.248 m^2	708.6 kg	467.5 kg	1,176.5 kg
-220 C	0.0	192.38 kg/m^3	144.81 kg/m^3	47.58 kg/m^3	0.00	0.0	0.0	0.0
-250 C	0.0	192.38 kg/m^3	144.81 kg/m^3	47.58 kg/m^3	0.00	0.0	0.0	0.0

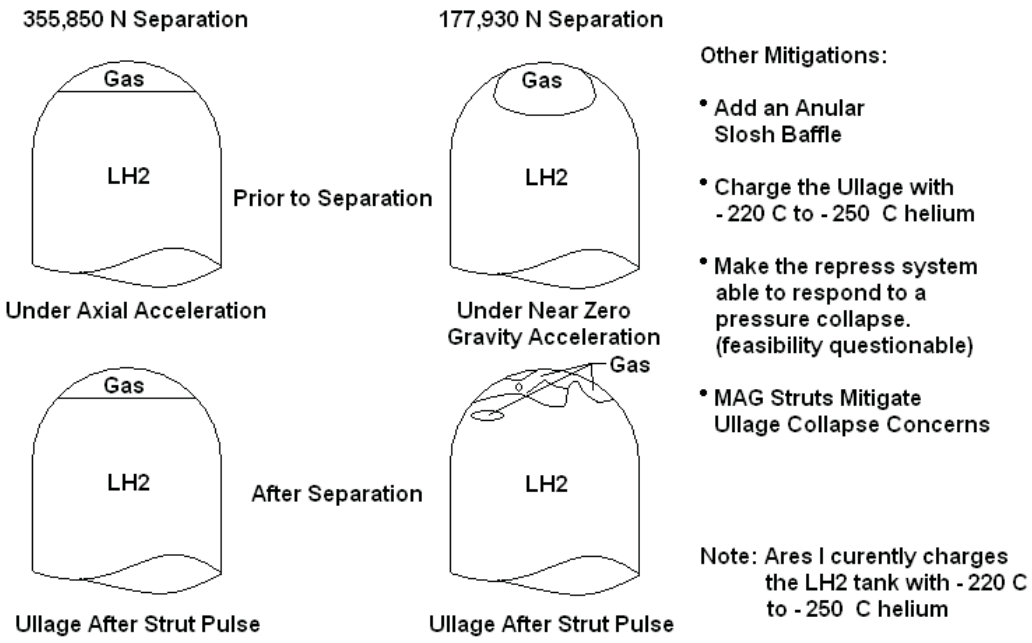

Figure 12 - Ullage Gas Collapse Mitigation Proposals

Real fluid analytical tools show that the smaller holes produce a force-profile that does not exceed 8,896.4 kN per second level as shown in Figure 13. The force-profile has some irregularities that can be eliminated through further refinement of the hole-pattern. The force spike at .4 seconds indicates that a few more holes are needed in the last 7.62 cm of stoke for the 3.18-mm diameter holes. If the first row of holes were exposed after 1.27 cm of stroke rather than 2.54 cm of stroke, more energy could be recovered from the expanding gas. If a few less holes were exposed in the middle part of the metering rod, the rate of change peak could be lowered. For Ares I, the 3.18-mm diameter holes shown in this plot meet a 2.5 g/sec jerk requirement if the decay of the thrust of the SRB is considered.

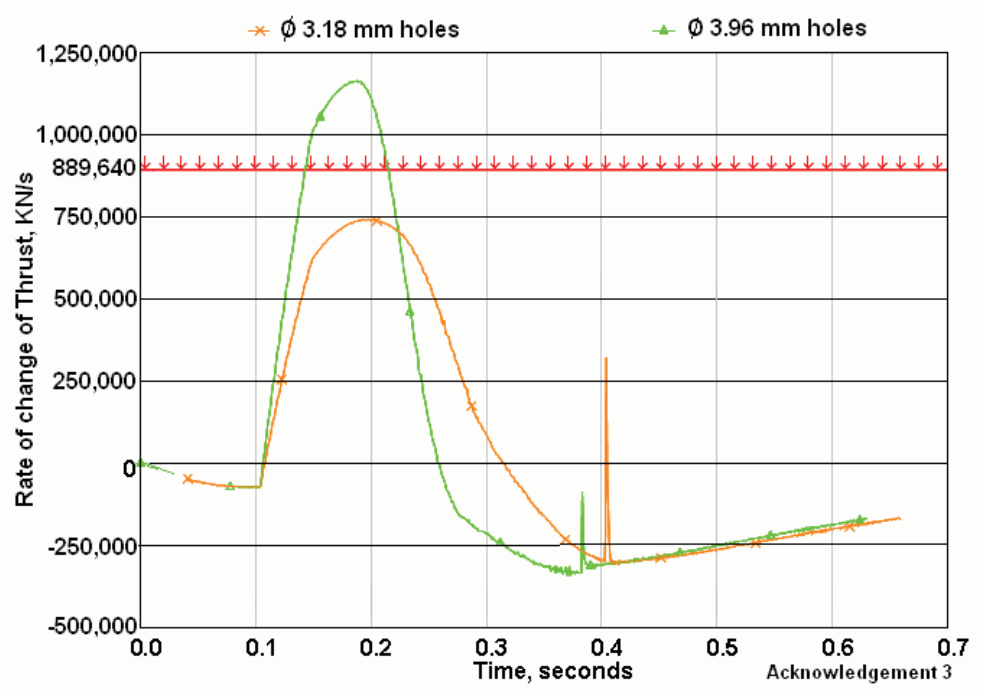

Figure 13 – Force Rate of Change Plot

Figure 14 and Figure 15 show the force profile analytical results for the same two hole-patterns as a function of stroke as well as a function of time respectively.

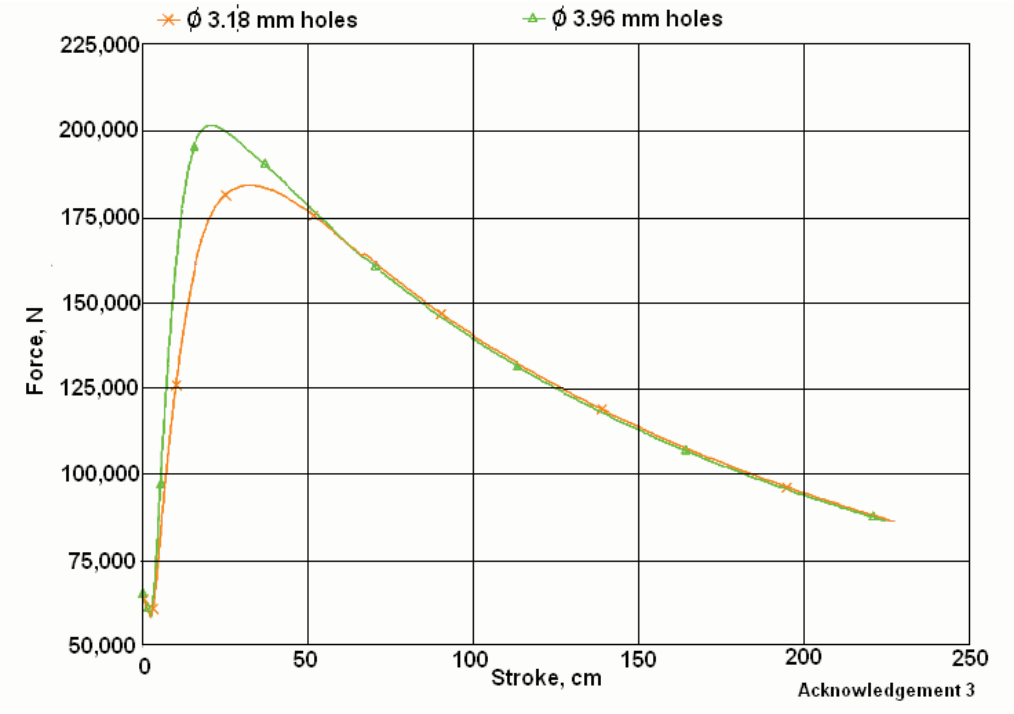

Figure 14 – Strut Force as a Function of Stroke

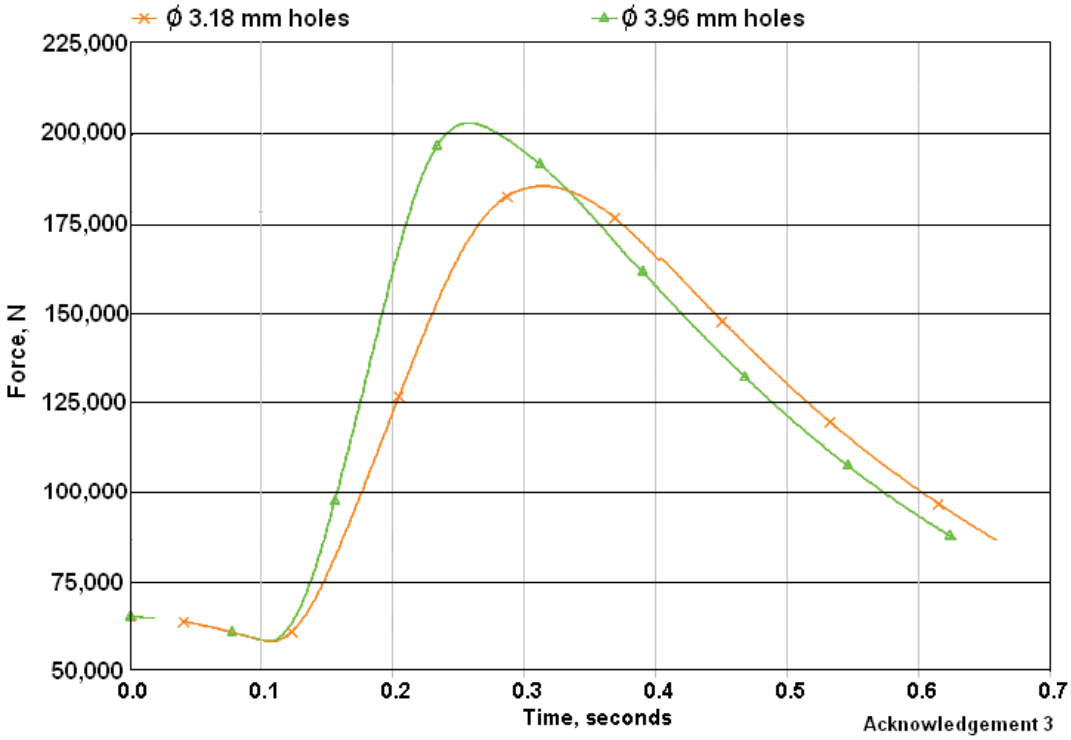

Figure 15 – Force as a Function of Time

Development Program Goals and Objectives

Since gas struts have not been used for separation on a manned vehicle, development testing is needed to mitigate risk. The risk falls into three categories; performance related risk, reliability related risk, and programmatic risk. Programmatic risk is in some ways a sub-set of the stated technical risk because technical issues that arise in the strut development program could threaten the schedule for the launch of Ares I flight tests. This concern is one of the chief objections to this technology. A realistic approach to address this programmatic risk is to carry both BDMs and struts in the program until struts have demonstrated their capability. The struts are a bolt-on technology, using the existing hole patterns on the upper part of the Ares I interstage attach ring and a direct bolt through on the upper stage aft skirt, so they can be installed with little impact on other systems. The recurring cost of the struts will not likely increase because of the development program. Because of development testing, the qualification program cost for a strut separation system will be substantially reduced. Programmatic-risks are addressed in this paper by eliminating technical risk through a robust development test program.

Resolving Performance Related Risk

The metering function of the MAG Strut system is determined by the size and pattern of holes along the metering rod. Development testing is required to characterize the strut performance with different metering rods under different conditions that simulate nominal operations and potential failures. Mathematical models provide solid indications of the flow rates for struts with various metering rods; however, their accuracy is not good enough to use for qualification by analysis. The development testing would provide data that would validate the analytical flow models. The best way to establish the force vs. distance performance characteristics of the struts is to test them with several different metering rods moving different masses. A range of pressures could also be investigated to establish the performance characteristics of the struts under nominal and degraded performance scenarios. A relatively simple test set-up as shown in Figure 16 is required to perform the development testing. In this performance test, a mass of approximately 22,680 kg is released to be pushed by the strut. It will accelerate to approximately 6.17 meters per second and then disengage from the fitting mounted on the mass. After disengagement, the moving mass must be stopped by a snubber. Side forces acting against the fitting will be simulated by attaching a spring to the mass that applies a side force as it rolls down the track on its metal wheels. High-speed video recording will measure any twang or motion oscillations.

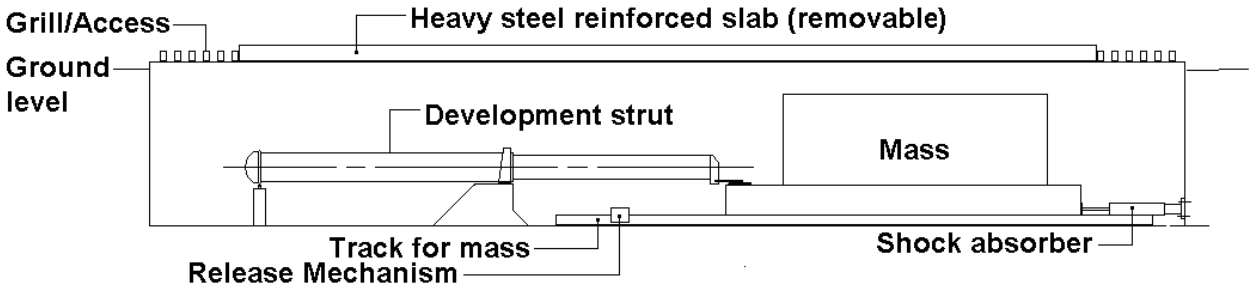

Figure 16 – MAG Strut Performance Development Test Set-up

The development program would seek to characterize the performance of the struts for several separate side force profiles that would represent a range of operational possibilities and off nominal load cases. The strut has Teflon slides on the piston and in the rod housing. If sufficient side force was present, a strut that was pressurized to less than 10% of the design pressure may bind at some point during the stroke of the strut. The mating conical interface of the rod fitting and the spike fitting on the upper stage is intended to gradually relieve side force as the struts disengage. If binding occurred on a partially charged strut, this side load relief action is intended to preclude disengagement of the strut from the fitting while pressurized. Figure 17 shows the strut rod fitting and the spike fitting that is mounted to the upper stage. Because no failure scenario has been identified that indicates that binding is a problem, development

testing will establish the amount of side loading required to cause the strut to bind such that the load relief action from the conical interfaces will not be adequate to relieve it.

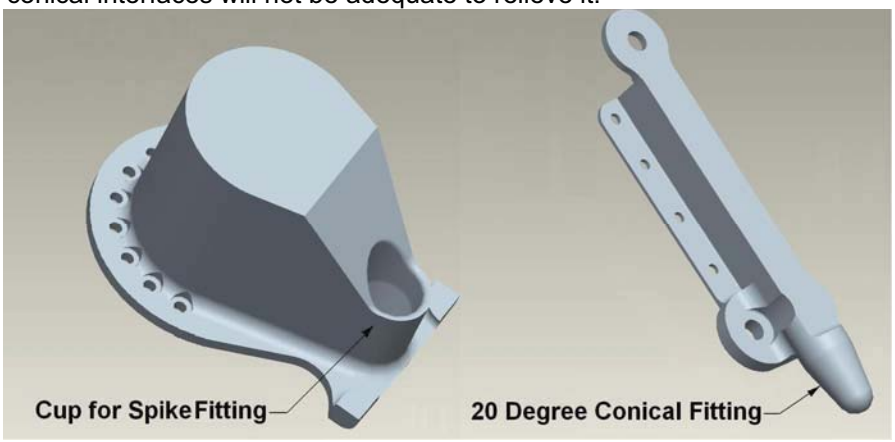

Figure 17 – Strut Fitting Aft Skirt Mounted Spike Fitting

Resolving Reliability Related Concerns

The safety of the struts must be demonstrated by test. The struts are designed to leak before burst; however, only testing can demonstrate this. If the leak before burst design is proven prior to qualification, the potential for a costly redesign and schedule slip is avoided. After completion of testing, one or more of the test struts would be subjected to extreme pressure until leakage or burst occurred. This burst test would be done with an oil or water charge to avoid the explosive hazards associated with gas.

All elastomeric seals leak a minute amount of gas because of permeation of the seal material. The expected performance of each seal must be bounded in order to establish launch commit requirements and pad operations. Nominal leak rates of the seals could be established without assembly into the struts by using a test fixture as shown in Figure 18. Different elastomer compounds could be evaluated for gas permeability at the pressures used in the strut. With this data the struts could be pressurized taking into account the number of days before launch. The low pressure chamber would gain a very small amount of pressure due to seal permeation during pad operations but not enough to exceed its required operating range.

Pressurizing the large volume chamber while leaving the low volume chamber at ambient pressure as discussed in the performance section of this paper would also be an option to eliminate uncertainties about rate of leakage into the low pressure chamber from the high pressure chamber. Figure 18 shows potential test configurations for two different seals. Testing 50 seals of each type would provide a large enough sample size to characterize the nature of the seals under ambient conditions. Temperature extremes could also be evaluated by placing the small seal test fixture in a thermal chamber.

Analysis Needed Prior to System Testing

An analysis of the integrated system would be required to establish the overall capability of the MAG Strut system to achieve separation under all potential operational scenarios. Initial analysis shows startling results with large positive clearance margins for the nozzle during separation. Revisiting this analysis is required prior to system testing to assure that an undiscovered disturbance force acting in the system will not cause the results to degrade.

To recover the first stage, the interstage with the extended struts must be separated from the first stage. However, no analysis has been done to establish the clearance between the first stage and the interstage. The struts extend about 2.44 meters from the interstage. Consequently, their presence will make it more difficult to gain adequate clearance between the first stage and the interstage after separation of the interstage from the first stage.

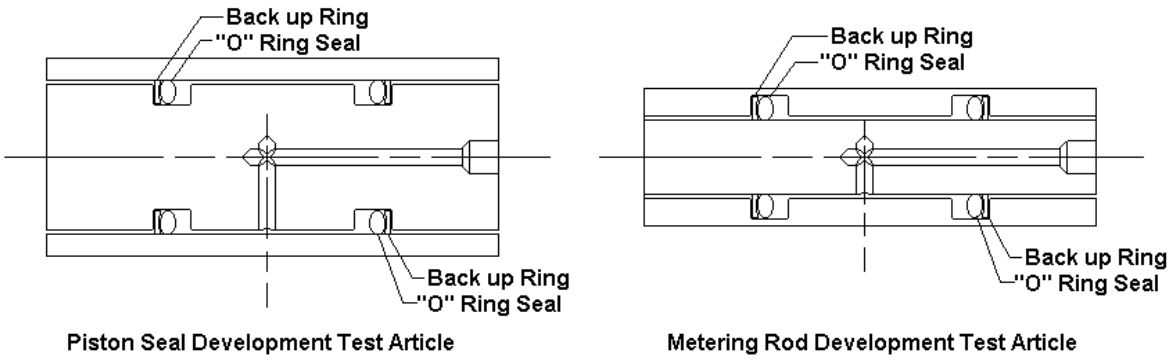

Figure 18 - Proposed Seal Test Configurations

Stress analysis of the second stage aft skirt interface with the spike fitting would provide a better understanding of the threat of buckling with a failed strut. If the high-pressure seal fails on a strut, the good strut will apply 68 kN of load to the structure while the failed strut will apply 236 kN of load. The safety factor is 1 for analyzing a failure case. However, the safety factor is 1.65 for buckling without a failure. Showing sufficient margin under all conditions is required prior to approving a final design configuration.

A stress analysis using finite element models of the struts themselves is required to assure adequate margin exists for all components. This analysis would allow for weight optimization of the strut prior to finalizing the design.

Integrated System Testing

Testing the integrated system has the decisive advantage of establishing the validity of the analytical models used to evaluate separation dynamics. A close match between the development testing and the analytical models will make it possible to qualify the separation dynamics by analysis, avoiding an expensive flight test dedicated to qualifying the separation system. Actually simulating the flight conditions is not practical considering the cost and complexity of such a test set up. A test setup that is capable of simulating any flight condition in one plane could be used to demonstrate the system incrementally. Figure 19 shows a proposed test setup that would be capable of simulating all of the most relevant conditions in the horizontal plane.

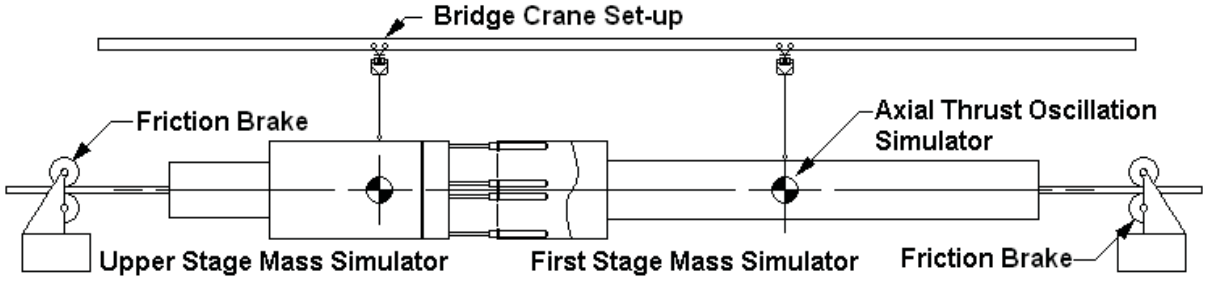

Figure 19- System demonstration test set up

Different asymmetric strut cases could be combined with various simulated thrust conditions. The simulations could be accomplished by placing many support points at the center of gravity of each of the mass simulators. The brake rod would have a ball joint attachment at the center-of-gravity and the brake body would be free to rotate on a pivot arrangement. When the separation joint is activated, the brakes would simulate the effects of the SRB thrust and the relevant component of gravity acting on the vehicle. This set up would simulate the mass and the mass-moment-of-inertia of each of the stages. Thrust vector side loads would be simulated by springs acting between the rod coming from the brake and the end of the first stage. The brakes would also arrest the motion of the two bodies after separation was

demonstrated. The axial thrust oscillation could be simulated by 2 large asymmetric counter-rotating masses near the center of gravity of the first stage. Demonstrating the ability to prevent re-contact after initial separation is a critical part of any separation qualification program. If the thrust oscillation was to slam the two stages back together after initial separation, impact loads would be transmitted to the sensitive avionics boxes on the aft skirt. Also, the structure of the aft skirt near the contact location could fail locally and unpredictable separation dynamics would be present.

MAG Strut Qualification

Qualifying the strut separation system will be a relatively quick, low cost program if a well-designed development test program is completed before hand. The separation dynamics will be qualified by analysis. The struts could be structurally qualified by analysis with the end fittings being considered qualified by test assuming that the qualification strut was pressurize with fluid that would generate sufficient force to subject the fitting to 1.4 times the limit load. Since the strut is designed with a safety factor of 2 for static pressure containments and a safety factor of 2.5 for dynamic pressure containment, the end fittings could be subjected to the limit loads without subjecting the struts to pressures that would yield the structure. The structure of the aft skirt and the interstage could be qualified by analysis. The development test would provide the data to validate the analytical models for both the struts and the structure. If some design changes were made to the flight struts that were not reflected in the development test articles, the qualification testing could be done using the same test set up used for development testing.

Conclusion

The MAG Struts are the ideal separation system for Ares I. No other separation system has the capability to separate with 356 kN of residual thrust on the first stage. This capability increases the Ares I payload lift capability significantly over a BDM separation system. Secondly, the MAG Strut system is mounted internally minimizing aerodynamic drag. Finally the MAG Strut system pushes the first stage and the second stage apart increasing the momentum transfer between the stages.

The struts reduce the potential for ullage collapse in two ways. Separating with 356 kN of residual thrust mitigates the potential for ullage collapse because the liquid hydrogen does not have the have the tendency to climb the walls of the tank as is possible when operating at very low levels of acceleration. The MAG Strut limits the amount of acceleration the vehicle experience to less than 2.5 g per second decreasing the potential to agitate the liquid hydrogen.

The MAG Strut limits the amount of load applied to the aft skirt during assent to 68 kN while they have the capability of stroking with a peak force 187 kN each.

The MAG Struts produce superior nozzle clearance under all conditions including one strut out cases. This means that the struts are inherently two-fault tolerant against pressure bleed down. The struts also greatly mitigate the effects of the SRB nozzle pointing accuracy and any other disturbances coming from another source because of the matching of the mass properties of the two separated stages.

Although struts have not been used on a manned vehicle, the struts can be brought up in design maturity in time to support later Ares I test launches assuming that the development test program is conducted concurrently with other Ares I development programs. Doing the development program facilitates the inclusion of the struts at a later date in the Ares program.

The authors of this paper would like to acknowledge the contributions of the following people:
Acknowledgement 1: Young Kim of Marshall Space Flight Center for fly-out analysis
Acknowledgement 2: Mike Hannan of Marshall Space Flight Center for performance analysis
Acknowledgement 3: Mike Martin of Marshall Space Flight Center for gas flow and pressure analysis
Acknowledgement 4: Mike Perry of Marshall Space Flight Center for computer aided design integration

Evaluation of Separation Mechanism Design for the Orion/Ares Launch Vehicle

Kevin E. Konno*, Daniel A. Catalano* and Thomas M. Krivanek*

Abstract

As a part of the preliminary design work being performed for the Orion vehicle, the Orion to Spacecraft Adaptor (SA) separation mechanism was analyzed and sized, with findings presented here. Sizing is based on worst case abort condition as a result of an anomaly driving the launch vehicle engine thrust vector control hard-over causing a severe vehicle pitch over. This worst-case scenario occurs just before Upper Stage Main Engine Cut-Off when the vehicle is the lightest and the damping effect due to propellant slosh has been reduced to a minimum. To address this scenario and others, two modeling approaches were invoked. The first approach was a detailed Simulink model to quickly assess the Service Module Engine nozzle to SA clearance for a given separation mechanism. The second approach involved the generation of an Automatic Dynamic Analysis of Mechanical Systems (ADAMS) model to assess secondary effects due to mass centers of gravity that were slightly off the vehicle centerline. It also captured any interference between the Solar Arrays and the Spacecraft Adapter. A comparison of modeling results and accuracy are discussed. Most notably, incorporating a larger SA flange diameter allowed for a natural separation of the Orion and its engine nozzle even at relatively large pitch rates minimizing the kickoff force. Advantages and disadvantages of the Simulink model vs. a full geometric ADAMS model are discussed as well.

Introduction

A component of the Vision for Space Exploration, Orion will be capable of carrying crew and cargo to the ISS, or rendezvous with a lunar landing module and an Earth departure stage in low-Earth orbit to carry crews to the moon and, one day to Mars-bound vehicles assembled in low-Earth orbit. Orion borrows its shape from the capsules of the past, but it takes advantage of 21st century technology in computers, electronics, life-support, propulsion, and heat protection systems. Orion will be launched into low-Earth orbit by the Ares I Crew Launch Vehicle. To maximize the crew's safety, Orion and its abort system will be placed at the top of the Ares I rocket. Other means of abort are available after the Launch Abort System is jettisoned at ~75 km (250,000 ft). The Orion vehicle will be able to remain docked to ISS for up to six months and have the ability to stay in lunar orbit untended for the duration of a lunar surface visit that could be up to six months.

A separation mechanism design is being developed to assure clearance between Orion (Crew Exploration Vehicle and Service Module) and the Spacecraft Adapter (SA), which stays fixed to the Ares upper stage as the two vehicle elements separate from each other during both normal post-launch staging or in an abort event. Figure 1 depicts the Ares/Orion stack configuration prior to separation.

The preliminary design of the separation mechanism requires the balancing of several competing design parameters most notably sufficient kickoff forces to ensure separation, highly reliable components, limited space to house these mechanisms, and a requirement to keep the mechanisms lightweight due to tight mass budgets. The abort case will typically drive the size of the separation mechanism design for a crewed vehicle. Activation of the separation mechanism cannot occur until the thrust levels of the Ares I Upper Stage (US) are significantly reduced. The potential hard-over gimbal abort case can induce a severe pitch over rate (often referred to as "dump rate") of up to 35 degrees/second on the stack if it were to occur just before Upper Stage Main Engine Cut-Off when the vehicle is the lightest and the damping effect due to propellant slosh has been reduced to a minimum. The transients of the controls and engine thrust tail-off (~ 3 sec total from hard-over to low thrust) are the main reason a large dump rate can be induced. A Residual Engine Thrust also continues to induce a small force at 5 degrees off the vehicle

* NASA Glenn Research Center, Cleveland, OH

centerline resulting in an applied moment to the Upper Stage after separation. This defines the worst-case environment that the separation mechanisms must overcome. Recontact during either an abort separation, or a nominal separation, can be catastrophic resulting in a Loss of Mission or a Loss of Crew event. A recent example of this type of detrimental recontact was observed during the March 2007 SpaceX Corporation Falcon I launch first stage separation event in which the first stage adapter inner wall contacted the second stage engine nozzle and induced a propellant slosh in the second stage tanks, prematurely shutting down the second stage engine before reaching the proper orbit [1]. The Orion separation system must be adequately sized to reliably separate the crew and vehicle safely for all design cases. Multiple types of mechanisms were evaluated including spring actuators, constant pressure pneumatic actuators, and pyrotechnic-actuated gas thrusters.

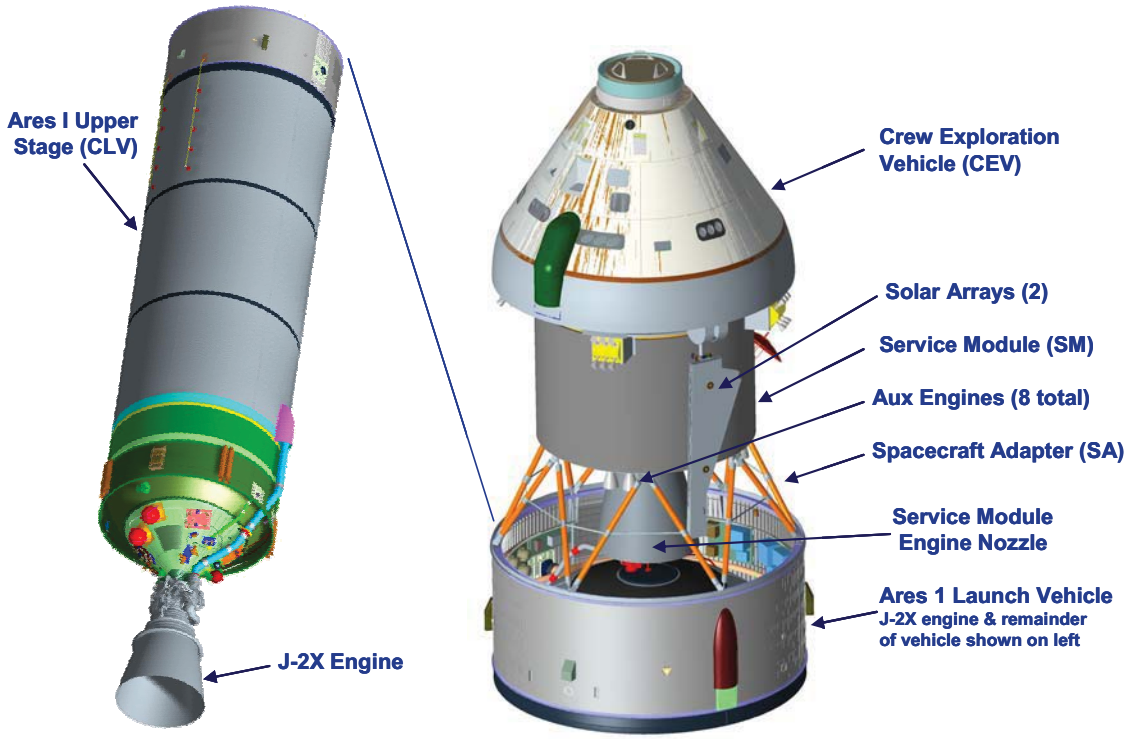

Figure 1. Ares I Upper Stage/Orion Spacecraft Configuration (Lockheed Martin Concept)

The Point of Departure separation system is shown in Figure 2. Unlike Apollo's Service Module, which was bolted to the top of a four piece faring and severed from it via a circumferential linear shape charge, this system incorporates compression kickoff springs and pyrotechnic separation bolts to join the Orion Vehicle to the SA. Separation is triggered by firing the pyrotechnic retention bolts, which allows the compression springs to push the SM away from the Upper Stage. The spring force must be sufficient to accelerate the separated bodies away from each other while maintaining a minimum clearance throughout separation.

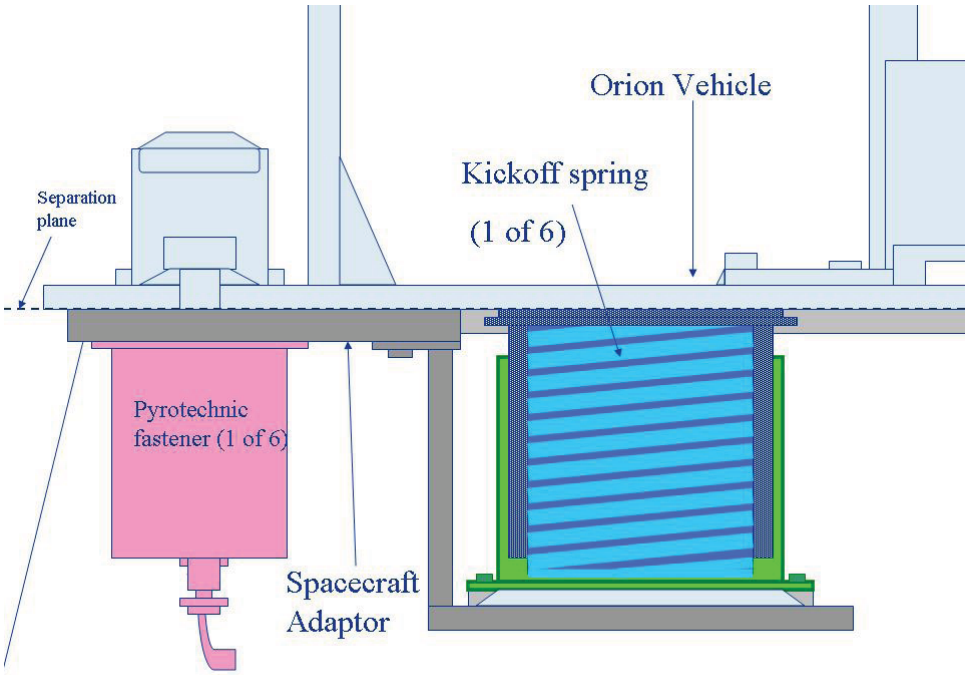

Figure 2. Separation Spring Concept

Separation System Hardware

The force needed for separation can be generated from various competed technologies, including mechanical springs, pneumatic actuators or gas thrusters. The other components of interest in the staging mechanism are the pyrotechnic fasteners through which the launch loads are transmitted.

Mechanical Springs: For this study open coiled, helical, compression springs were the preferred form of kickoff devices if the required energy level was low enough to warrant their use. Spring kickoff devices were incorporated in most of the models because the separation environment did not require large kickoff forces. Obviously, mechanical springs are used in countless terrestrial applications as well as space. They are highly reliable and when designed correctly can handle millions of cycles. Several papers detail the use of compression springs in spacecraft staging mechanisms [2], [3], [4], [5], [6], [7], [8]. For spacecraft mechanisms mechanical kickoff springs must be designed with the resistive force (F_r) and the force required for acceleration (F_a) of the bodies in mind. Where redundant springs are used instead of a backup mechanism, they should be designed to provide adequate force for a one-spring-out case [5].

Additionally, the spring system should have a 100% positive Margin of Safety on drive force over resistive force, as measured at acceptance or qualification testing. It is prudent to carry additional margin prior to testing. Also, spring systems are required, when practical, to have a dynamic force margin of safety over the required force F_a of 25%, as tested. Additionally, when sizing mechanical springs, spring material stress relaxation and residual stresses must be factored in, for which some test data exists [9]. These effects decrease the driving force a spring is capable of after prolonged storage, and can vary by greater than an order of magnitude depending on the material. 302 SS, a common aerospace spring material, can go through 3-5% stress/preload relaxation in 1000 hours of storage time.

The dynamic modeling of springs in this system always considered six compression springs located equidistant around the circumference of the SA interface flange. If incorporated in the final flight design, equivalent redundant pairs of springs will be used to improve reliability. It is important when designing mechanical redundancy to do so wisely as it has been shown that some redundancy can actually decrease overall system reliability, even in spring actuator designs [10], [11].

Pneumatic Actuators: Pneumatic actuators have extensive spaceflight experience, most notably on the Delta launch vehicle stage separation system. Pneumatic actuators possess larger specific force capability (N/kg) than mechanical springs, giving 4 to 5 times the kickoff force of springs of the same mass. Higher part count and pressurized components leads to potentially lower reliability than the simpler mechanical springs, making them less attractive for a crewed mission.

Gas thrusters: While compressed gas thrusters have aerospace flight heritage in solid rocket booster separation (Figure 3) they have no known experience as a spacecraft or payload separation device to this author's knowledge. Their benefit is in producing a large specific force giving very high drive capability, even greater than 10 times that of mechanical springs for the same mass. Where high kickoff forces are not required, their greater complexity and potentially lower reliability may make them less attractive. Gas thrusters are currently being traded against pneumatic actuators for the Ares 1 launch vehicle staging mechanism as well.

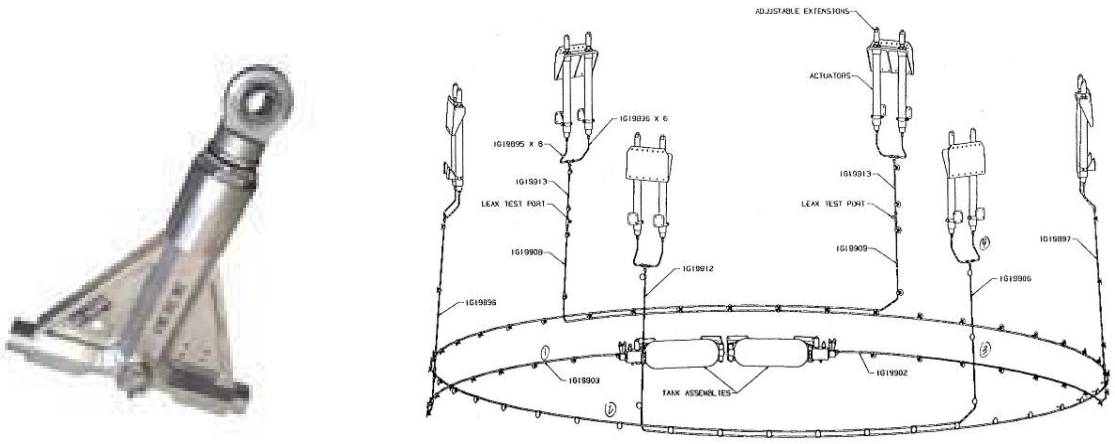

Figure 3. Pyrotechnic Gas Thruster/Actuator (left), Pneumatic Actuator System (right) (Used with permission of Scot, Inc.)

Modeling Approach

To address the mechanism design sizing, two modeling approaches were invoked. Each method allowed for easy evaluations as vehicle configuration changes occurred. The first approach was a simplified Simulink model to quickly assess the critical clearance between the Orion Engine nozzle and the SA. The second approach involved the generation of an ADAMS 3D geometric model to assess secondary effects due to offset mass centers of gravity, off-diagonal moment of inertia terms and other out of plane effects. It also captured any interference due to potential contact between other parts of the Orion Vehicle and the SA.

Simulink Model Approach

The Simulink model approach [12] for the abort simulation was based on the translation and rotational equations of motion, which are integrated through the time step function to determine the relative positions of the Ares Upper Stage and Orion. Figure 4 depicts the full Simulink model. The separation force is applied as either a constant pressure (as from a gas thruster) or a variable force (mechanical spring) over the length of the actuation. Assumptions of planar motion for the location of element centers of gravity and constant component masses for the duration of the separation event are incorporated. Capability has been added to the model to include the residual J-2X engine thrust acting on the Ares I US after separation and the contribution of Reaction Control System thrust to the separation acceleration.

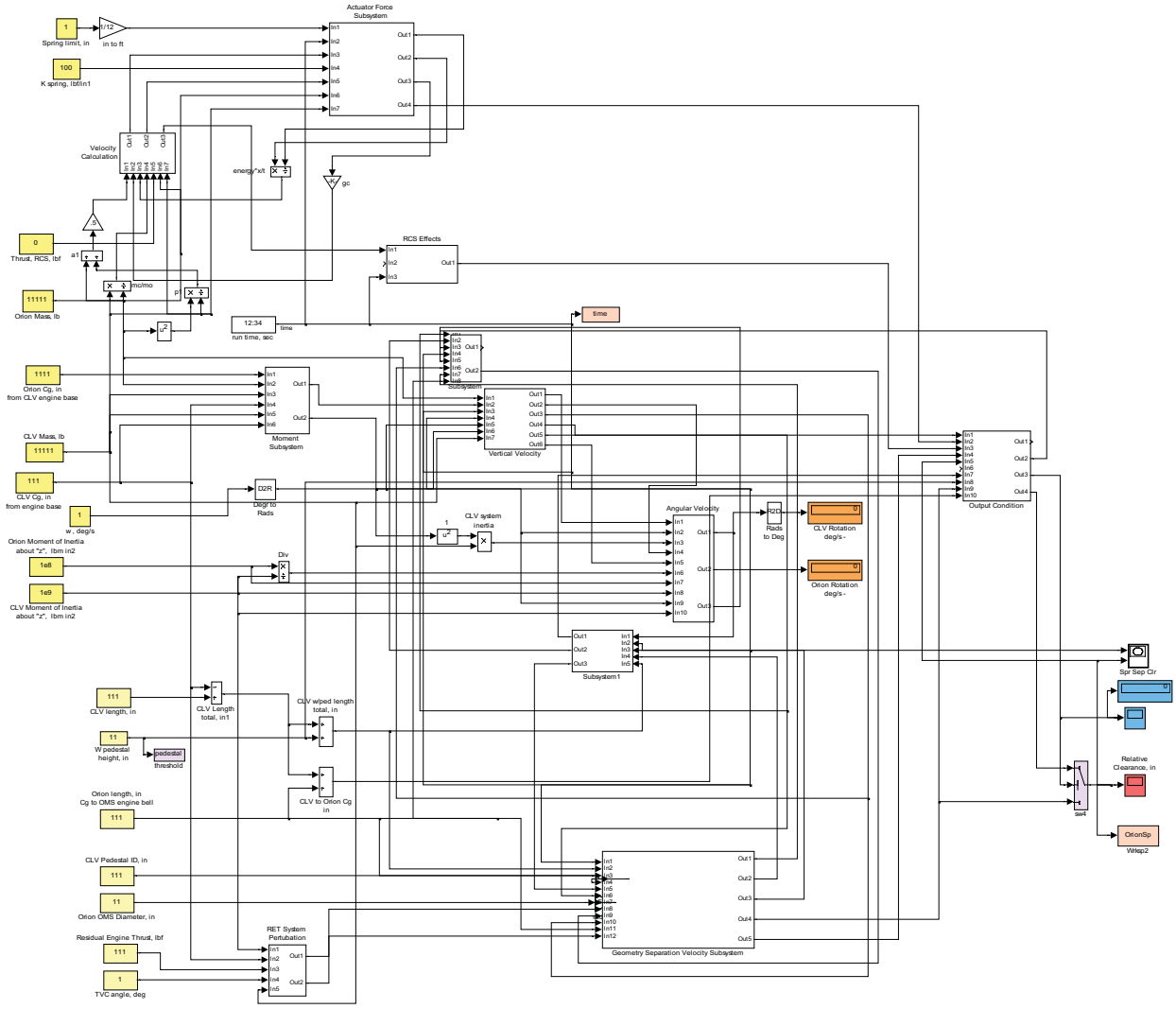

Figure 4. Simulink Separation Model

The basis of the Simulink analysis utilizes the conservation of momentum and kinetic energy equations shown below:

$$\left(I_{stack}\ \omega\right) = \left(I_c + m_c\ r_c{}^2\right)\omega_c + \left(I_o + m_o\ r_o{}^2\right)\omega_o$$

and

$$\left(\frac{I_{stack}\ \omega^2}{2}\right) = \left(\frac{m_c\ v_c{}^2 + I_c\ \omega_c{}^2}{2}\right) + \left(\frac{m_o\ v_o{}^2 + I_o\ \omega_o{}^2}{2}\right)$$

Where the variables are defined as:

I_{stack}	=	Stack (Orion + Ares 1 US) moment of inertia, kg-m^2
I_c	=	Ares 1 US moment of inertia, kg-m^2
I_o	=	Orion moment of inertia, kg-m^2
ω	=	body stack rate of rotation, deg/s
ω_c	=	Ares 1 US rate of rotation, deg/s
ω_O	=	Orion rate of rotation, deg/s
m_c	=	Ares 1 US mass, kg

m_O = Orion mass, kg
r_c = Ares 1 US c_g moment arm to system cg, m
r_0 = Orion c_g moment arm to system cg, m
v_c = Ares 1 US relative velocity to system, m/s
v_O = Orion relative velocity to system, m/s

The results of solving these equations are that the rotation rate of the separated components is maintained at the same rate as the stack rotation prior to separation. The addition of a residual engine thrust post separation does induce an additional moment onto the Upper Stage and results in an angular acceleration, reducing the clearance during separation.

ADAMS Approach

The SA/Upper Stage and Orion vehicles were also modeled using the ADAMS dynamic software code [13]. This is a motion simulation code that allows the user to create a mechanism model and then solves the simultaneous equations for kinematic, static, quasi-static, and dynamic simulations. Figure 5 depicts the ADAMS separation model during a simulation as Orion clears the SA. For the purposes of this study the Upper Stage and Orion were modeled as rigid bodies, each with six degrees of freedom. The SA was modeled as rigidly linked to the Upper Stage since it never separates from it. However the geometry of the SA, particularly the top flange was important for this analysis since the Orion engine nozzle needs to be extracted from this cavity and translate beyond the top flange of the SA without impact. The Crew Module and SM were modeled as a single rigid body (i.e. Orion) since, again, they never separate in this analysis. The modeling of the separation systems for the Orion to Ares 1 US included the single axis springs or actuators located around the SA top flange, between the SM and SA. These compression springs produce a translational motion when released. Once their free length is achieved they no longer impart any force onto the vehicle. The Ares 1 US's J-2X engine thrust is modeled at the bottom of the Upper Stage. Auxiliary engine thrust is also accounted for on several design studies and these are also modeled as point forces located at the current auxiliary engine locations near the separation plane. Vehicle "dump" or pitch rate is applied as an initial velocity condition to the Ares 1 US/Orion at the combined vehicle stack center of gravity (CG). Joints were added to the model as follows: a fixed joint was created between the Upper Stage and the CEV to allow them to pitch together at the start of the simulation (time = 0 sec.) and release when the separation event began arbitrarily at time = 1.0 sec.; a hinge joint was created at each solar array anchor point under the avionics ring to allow for flaring of the arrays in order to investigate different launch configurations to optimize array clearance from the outer fairings at launch as well as avoid impact with the SA upon separation.

Figure 5. ADAMS Separation Model

Results

The clearance requirement for this system was to provide a 5.1-cm (2-in) minimum clearance between the Orion vehicle (engine nozzle, solar arrays, and other protrusions) and the SA. Several analyses were completed to size the actuator forces, determine practical separation times and optimize the vehicle geometry (engine size, solar array placement, SA diameter, etc.). Figure 6 plots the time that the minimum clearance is reached versus the vehicle dump rate for a gas actuator system and for the case of no actuator forces, using the Simulink model. From this plot the two systems are seen to coincide at the higher body rates where the actuation force needed for the 5.1-cm (2-in) clearance is diminishing as the system approaches the no-force required condition.

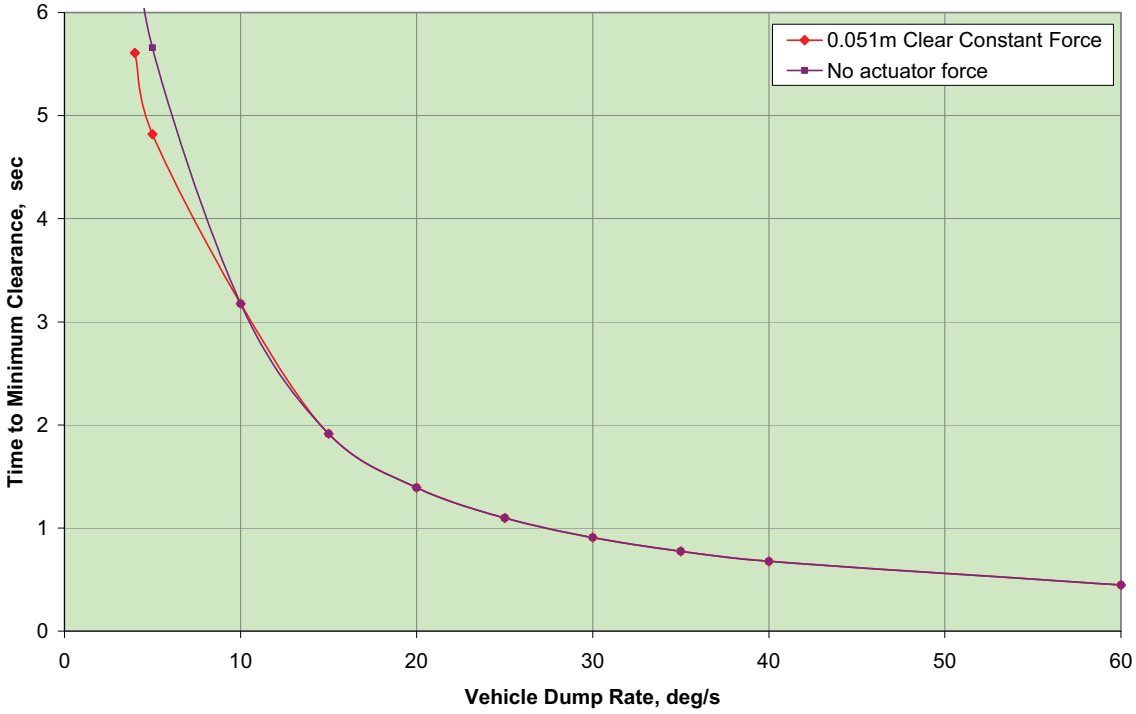

Figure 6. Clearance Time as a Function of Vehicle Body Rate

The initial actuation force required to meet the clearance requirement at the baseline 5 deg/s dump rate is shown in Figure 7. The curves in the figure are the Orion radial clearance (red), the Orion axial separation distance (green), and the actuator force line (blue) which shows when the actuator force is terminated (0.33 sec) and is reflected in the slope of the Orion separation distance curve which tends to be more linear after this force is removed. The jog in the clearance curve occurs when the Orion vehicle clears the SA at approximately 4.8 seconds, which is when the change in clearance becomes a positively sloped line as the vehicles move further apart from each other with no chance of contact.

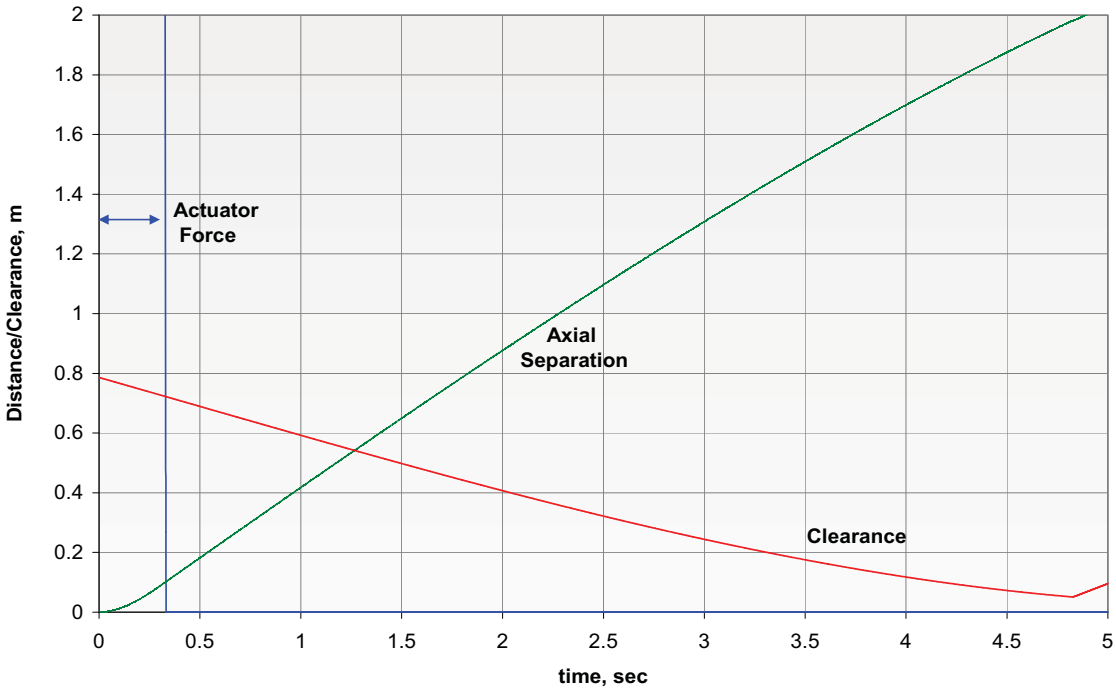

Figure 7. Time Required for Separation at 5 deg/s, (Simulink Model)

Figure 8 is a plot of the Simulink model separation force required to provide clearance at an initial dump rate of 5 deg/s for both types of actuators, springs and gas (or pneumatic) thrusters. In the spring type actuator the force is a function of axial displacement where the initial force is very high and then decreases along a power curve as a function of time. In the gas thruster system, which can be modeled as constant pressure through its full stroke, the force is maintained throughout the action time at a constant level. Both systems were sized to separate the vehicle with exactly 5.1-cm (2-in) clearance maintained at the engine nozzle. Duration of the constant pressure actuator is determined by the 10.2-cm (4-in) actuator stroke. The calculated time necessary to provide this clearance is shown to be independent of the actuation method, since the vehicles are rotating and translating at a rate as a function of dump rate and the residual engine thrust on the Upper Stage. The 5.1-cm (2-in) minimum clearance point in space or “gate” is reached at the same point in time, which varies from 24.0 deg (4.8 s) to 23.4 deg (0.39 s) of vehicle rotation for the 5 deg/s to 60 deg/s body rate respectively.

There is a very slight difference in the final velocity induced by the actuators since to make the clearance gate time, the spring actuator provides a higher initial acceleration and then coasts at the resulting velocity of 0.477 m/s (1.56 ft/s) with an acceleration rate of 0.144 g’s, while the constant pressure actuator provides an acceleration rate of approximately 0.118 g’s over a longer time period resulting in a higher 0.485 m/s (1.59 ft/s) final velocity imparted on the Orion system. Therefore, less energy is required for the spring actuator compared to the gas thruster mechanism.

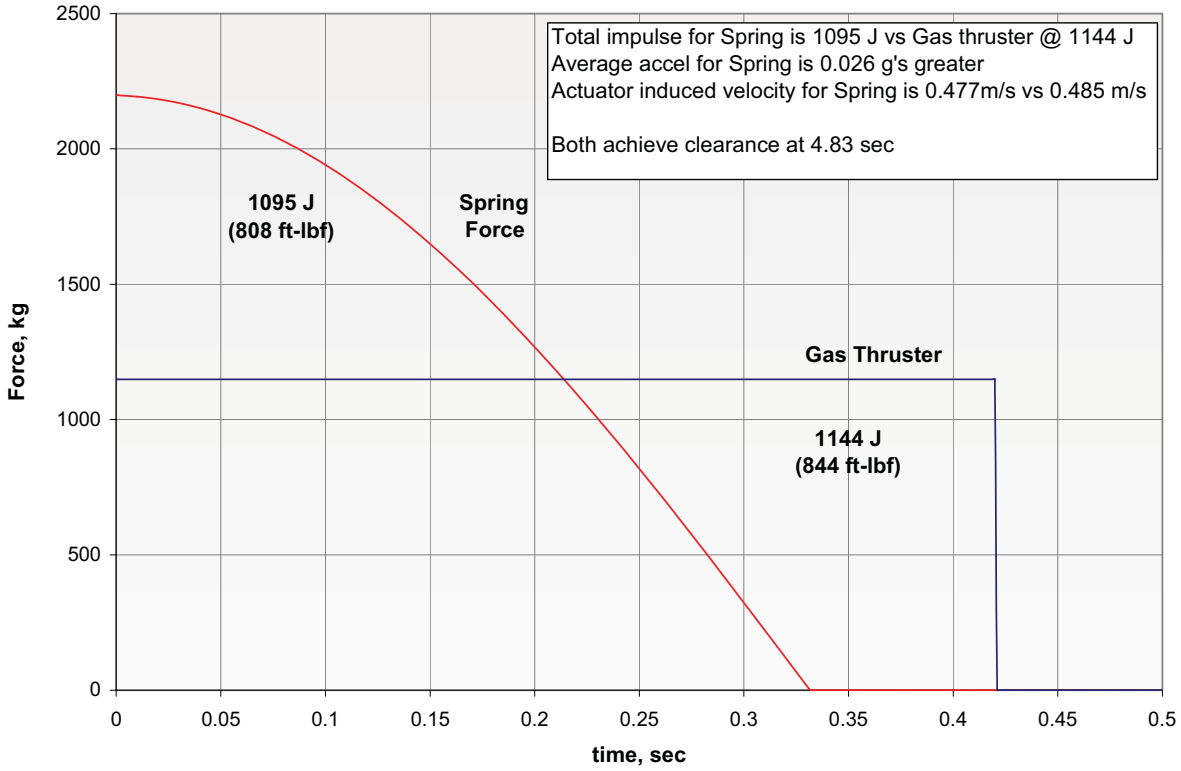

Figure 8. Separation Force Input for Spring vs. Gas Thruster

For the ADAMS model several cases and design studies have been run to determine the optimal separation system. The two critical considerations in these dynamics analyses are to ensure that the SM engine bell can get extracted from within the SA without bumping (avoiding a Falcon 1 type of hazard), and that the solar arrays, which are mounted down the sides can clear the SA without interfering from the outside. Using the given mass properties the resulting spring stiffness case results are shown in Table 1 as well as Figure 9. All cases are assuming there is no separation assistance from the Orion SM main engine.

Table 1. Summary of Parameters Analyzed

case #	dump rate (deg/s)	J-2X Residual Thrust	CEV RCS Thrust kg (lbf)	Spacecraft Adapter flange ID m (in)	Spring stiffness kg/m (lb/in)	Spring stroke length m (in)	min clearance, ADAMS model m (in)	min clearance, Simulink model m (in)	model delta m (in)
1	35	yes	0	3.4 (135)	0	0.102 (4)	0.14 (5.6)	0.11 (4.5)	0.03 (1.1)
2	0	yes	0	3.4 (135)	10,724 (600)	0.102 (4)	0.80 (31.5)	0.72 (28.3)	0.08 (3.3)
3	10	yes	0	3.4 (135)	178 (10)	0.102 (4)	0.07 (2.6)	0.08 (3.0)	-0.01 (-0.4)
4	10	no	0	3.4 (135)	178 (10)	0.102 (4)	0.15 (6.0)	0.13 (5.2)	0.02 (0.8)
5	20	no	0	3.4 (135)	178 (10)	0.102 (4)	0.15 (5.9)	0.13 (5.1)	0.02 (0.8)
6	20	yes	0	3.4 (135)	178 (10)	0.102 (4)	0.13 (5.2)	0.10 (4.1)	0.03 (1.1)
7	5	yes	0	3.15 (124)	4,147 (232)	0.102 (4)	-0.08 (-3.3)	-0.05 (-1.9)	-0.04 (-1.4)
8	35	no	0	3.15 (124)	0	0.102 (4)	0.01 (0.2)	0.01 (0.2)	0
9	5	yes	366 (808)	3.4 (135)	0	0.102 (4)	0.18 (7.2)	0.11 (4.5)	0.07 (2.7)
10	5	yes	0	3.4 (135)	4,147 (232)	0.102 (4)	0.05 (2.0)	0.08 (3.2)	-0.03 (-1.2)

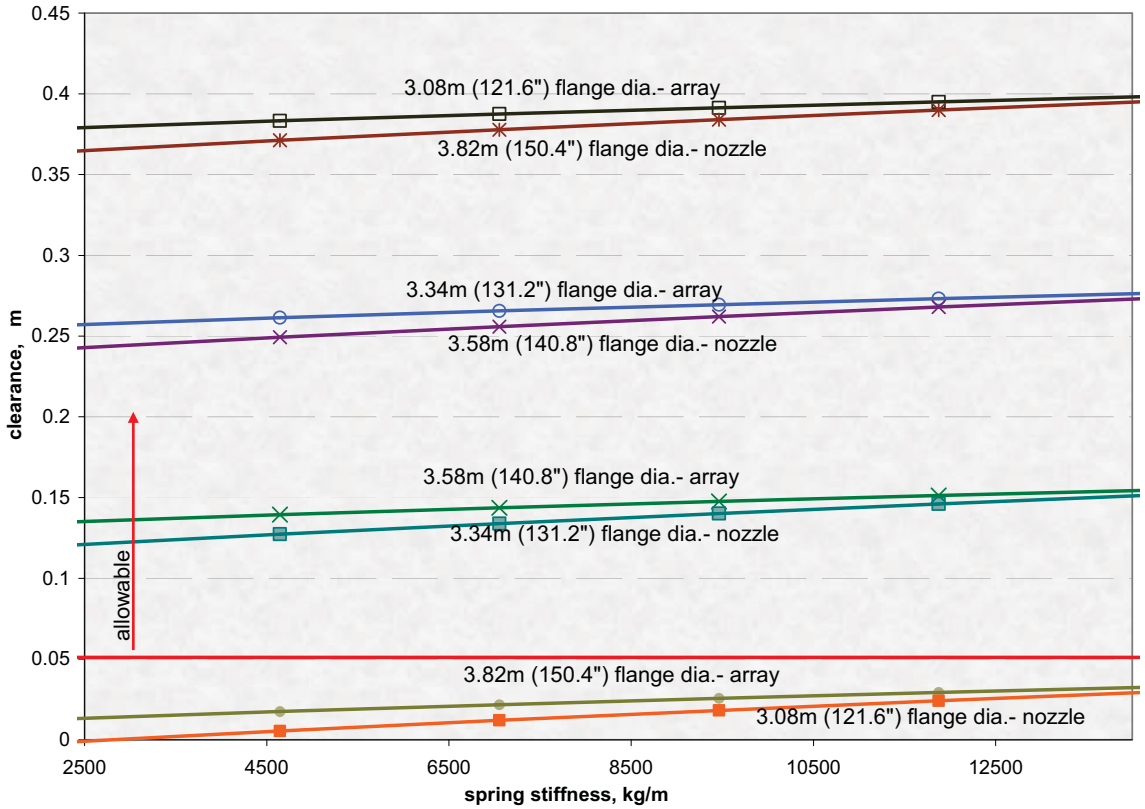

Figure 9. Engine bell and 6-m Array clearance for 5°/sec dump rate

Figure 9 depicts the results of several ADAMS cases using different SA flange diameters to assess clearing the solar arrays on the outside versus clearing the engine nozzle on the inside. Previous Orion designs incorporated a longer but narrower vehicle with a likewise narrower SA. The redesign of the vehicle allowed for a wider SA flange. As can be seen in the plot, the arrays have adequate clearance (>5.1 cm) for any SA inner diameter of 3.58 m (140.8 in) or less, while the engine nozzle will have adequate clearance for a SA diameter of 3.34 m (131.2 in) or greater. Thus an inside diameter of 3.34 – 3.58 m (131.2 – 140.8 in) satisfies both. In these cases it is assumed that the J-2X engine residual thrust is active and the flange width is 0.343 m (13.5 in) radially. A nominal separation system would include springs located at SA nodes as shown in Figure 2 outboard of the separation pyrotechnic device with a 10.2-cm (4 in) stroke and 3,842-kg/m (215-lb/in) stiffness. Six standard 1.27-cm (1/2 in) separation bolts located directly inboard of the push off springs at each node will transmit launch loads through the structure.

Figure 10 is a plot of the separation clearance as a function of time for the different models used for the baselined configuration at a body rate of 5 deg/s. The ADAMS model includes the Solar Arrays for additional clearance studies while the Simulink model only considers the clearance for the Engine Nozzle to the SA, which becomes the limiting parameter for both models after approximately 2.4 seconds.

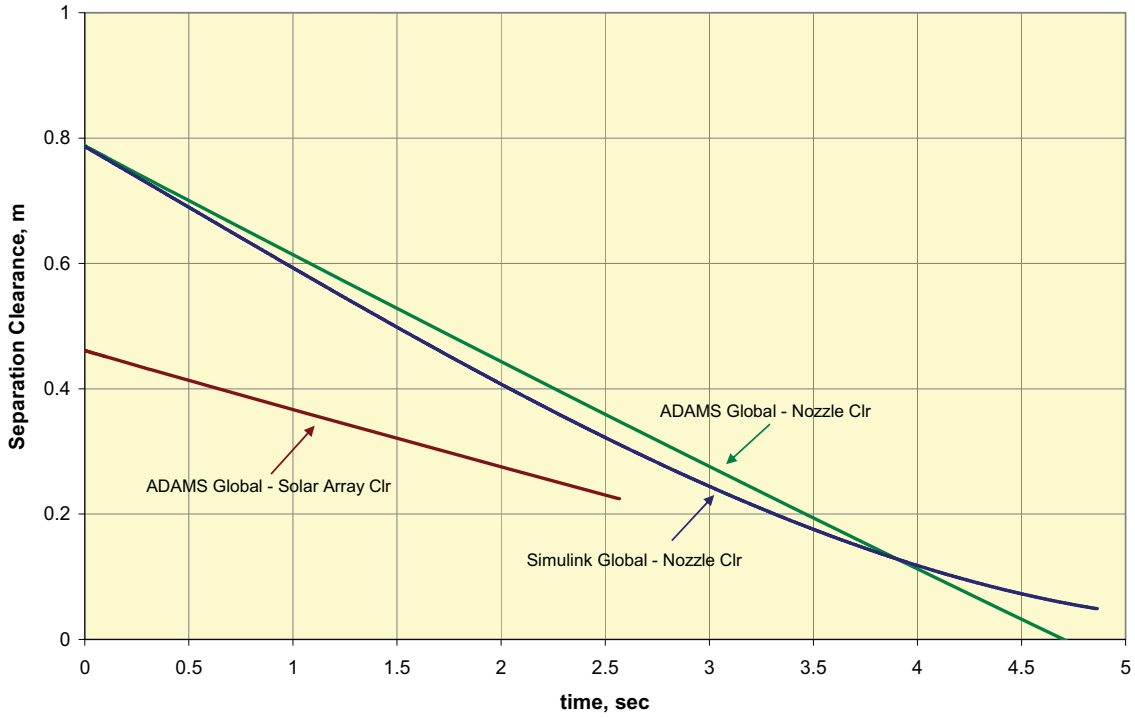

Figure 10. Separation Clearance at 5 deg/s Body Rate

Figure 11 depicts the clearance achieved as a function of actuator force for the Simulink and ADAMS models at a 5 deg/s dump rate. The interference at the low actuator force is due to the influence of the applied Residual Engine Thrust moment and to the longer separation time required for the low dump rates (<10 deg/s). This slower separation time allows the induced moment on the Upper Stage to rotate the SA reducing the clearance below the required limit. From the plot it is evident that an actuator force of greater than 3500 kg/m (196 lb_f/in) is required to assure the clearance is achieved and that use of a grossly oversized actuator has diminishing returns since the actual clearance is not a linear function of spring stiffness.

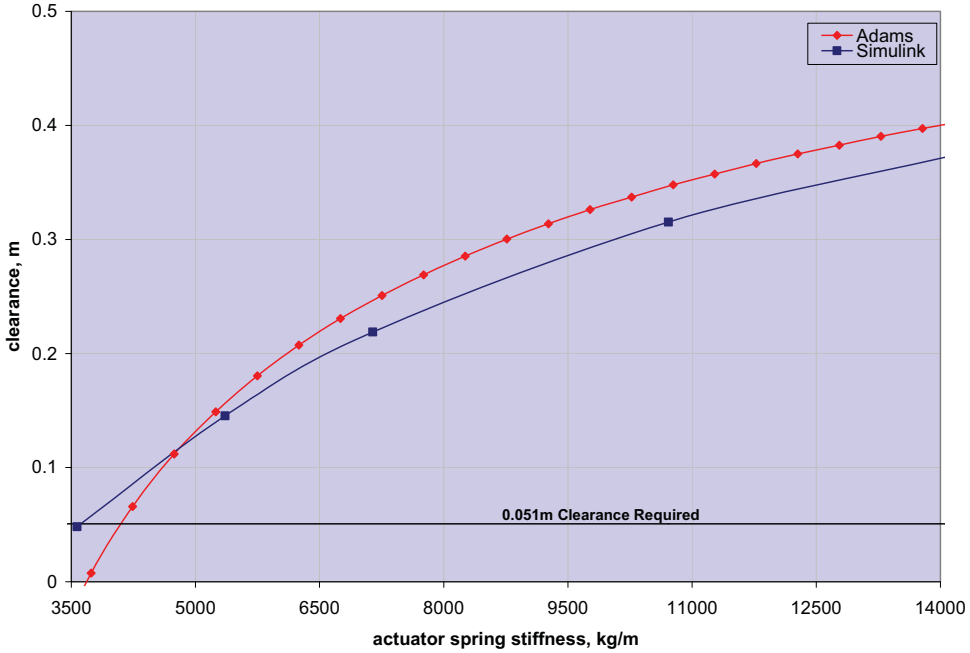

Figure 11. Comparison of Clearance vs. Actuator Force

Natural Separation

It has been learned through this analysis that for two bodies rigidly fixed together and undergoing rigid body rotational and translational motion which then separate, if body 1 has a protruding feature (like an engine bell) tucked inside a recessed area of body 2 (such as the SA cavity) that, due to the centrifugal forces naturally propelling them apart, there exists a relationship between the diameter and length of the protruding feature and the mating clearing radius Y_{B1} of the recess whereby for a recess radius greater than Y_{B1}, the vehicles will separate without collision at any dump rate with no additional kickoff force required nominally. Figure 12 depicts the geometry definitions used.

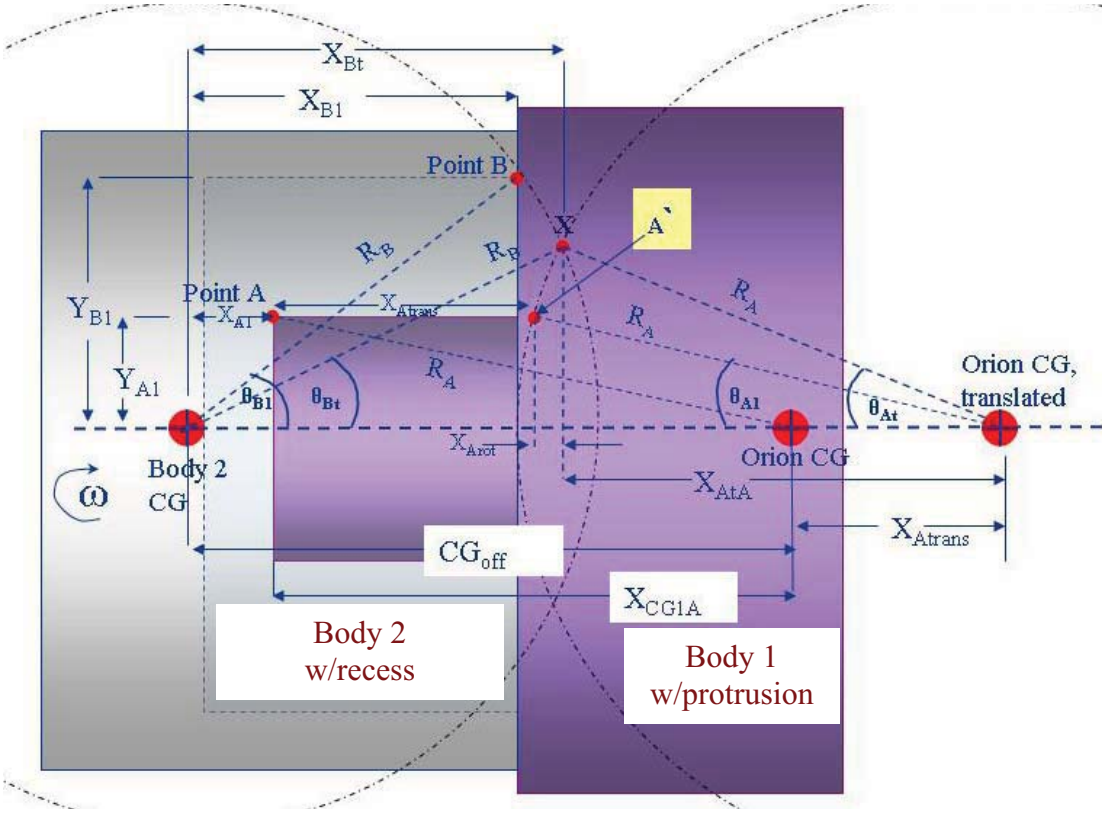

Figure 12. Ares I US/Orion Vehicle Geometry and Definition

R_B*COS(θ_{Bt}) = X_{A1}+X_{Atrans}+X_{Arot} ; *where X_{A1} is the initial axial distance from Body 2 CG to Protrusion point A, X_{Atrans} and X_{Arot} depict the axial & rotation motion components of point A, which represents the outermost point of the protrusion.*

$R_B = R_A$ *(SIN(θ_{At})/SIN(θ_{Bt}))

SIN(θ_{A1}) = YA_1/R_A

R_B = SQRT[(X_{B1})^2 + (Y_{B1})^2]

$X_{CG1A}+X_{A1} = CG_{off}$; CG_{off} *is the distance between Body 1 and 2 CG's prior to separation*.

$X_{Atrans} = \omega * T_{coll} * CG_{off}$; *T_{coll} is the time needed for pt. A to separate and pass thru pt. B at X.*

$X_{Arot} = R_a$ *[COS(θ_{A1}) - COS(θ_{At})]

$X_{Bt} = R_B$ *COS(θ_{Bt})

$X_{Bt}+X_{AtA} = CG_{off} + X_{Atrans}$

$\theta_{Bt} = \theta_{B1}-\omega * T_{coll}$

$\theta_{At} = \theta_{A1}+\omega * T_{coll}$

Thus, the minimal recess radius for natural separation, Y_{B1}, can be solved for easily, if X_{A1}, Y_{A1} (protrusion radius), and lengths X_{B1} (recess radius) and CG_{off} (distance between CG's) are known. This analysis

assumes the protrusion and recess are modeled as straight cylinder sections. This finding gives a designer a useful preliminary size for the vehicle recess diameter (such as in a spacecraft adaptor cone flange) or protruding diameter (such as an engine bell), and is independent of the vehicle's dump rate at separation. While this does not account for secondary effects like residual engine thrusts and separation event side loads, tank slosh or friction which can either help or hurt this clearance, these effects are typically secondary to the overall conic area that the bodies follow dynamically upon separation. For our case, assuming no external forces, the separation event has been determined to occur naturally for the approximately 28.5 degrees of rotation needed and will provide a minimum clearance of 0.173 m (6.8 in) for all significant body rates. This is primarily due to the location of the Vehicle Stack system Cg, which is located very close to the separation plane and is therefore very sensitive to any changes in that location.

Taking this concept further, separation cases were run (see Figure 13) in which the same conditions were applied to a vehicle with an adequately large recess diameter (SA flange diameter) and to an undersized flange diameter (124 in). As can be seen, cases were run with the US engine on or off for comparison. As the lowest curve shows for a smaller SA flange of 3.15 m (124 in), spring force is dependent on dump rate as the higher dump rates require much larger spring stiffness to clear upon separation, while for a SA flange ID of 3.4 m (top curve) no springs are required at any dump rate even with the US engine on (2nd curve). The vehicle separates naturally without help of any kickoff device.

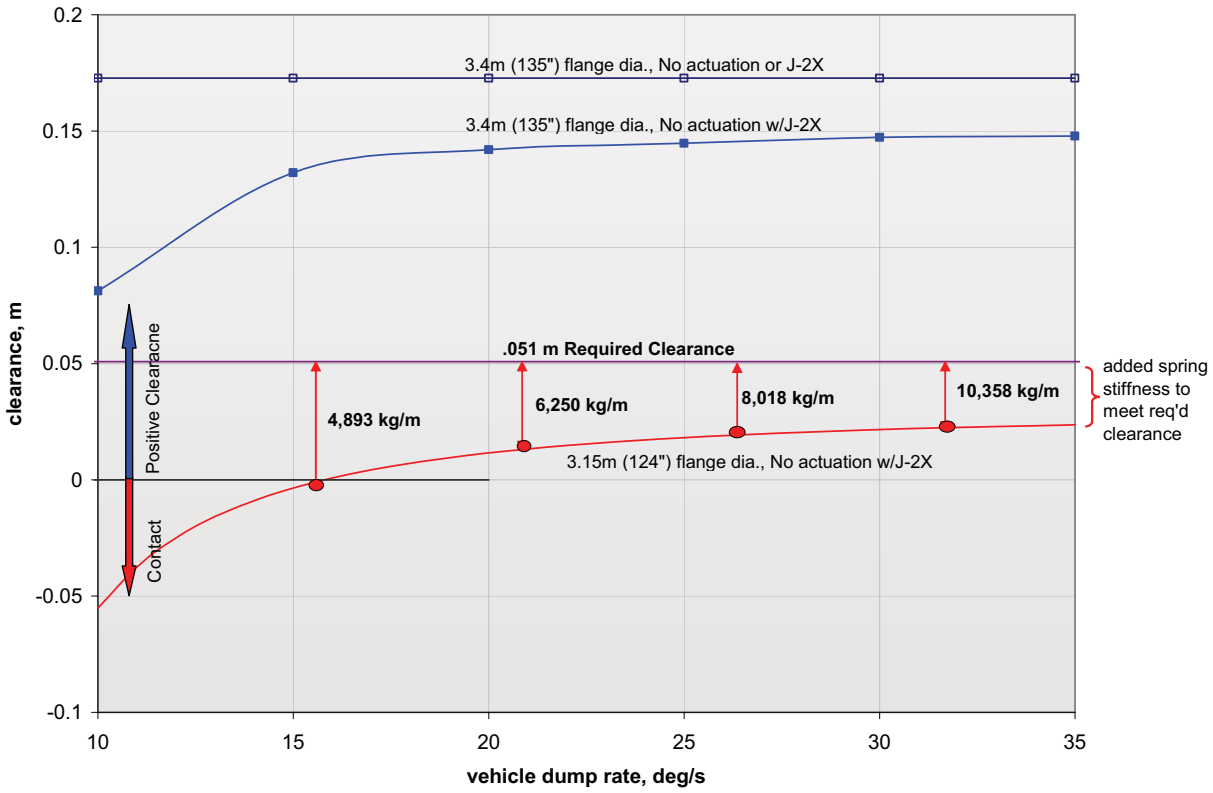

Figure 13. Engine Nozzle Clearance with No Separation Forces (no springs or actuators)

Lessons Learned

One of the lessons learned was that intelligent preliminary sizing of spacecraft geometry can greatly improve reliability and save on vehicle weight. Also for two connected bodies rotating at a fixed dump rate, that same angular rate will be maintained by each body after separation, as angular momentum is conserved. Another important lesson learned was that separation mechanism component mass can be

minimized and reliability maximized if the geometry is dimensioned to allow for “natural separation” concepts. However, the need for a controlled separation event necessitates the use of applied force actuators to overcome any potential external forces. The last lesson learned was that there exists a very steep curve between separation clearance and the vehicle main parameters of mass, inertia and geometry with that sensitivity often resulting in inadequate clearance dynamics.

Summary

The simulations conducted indicate that a low fidelity, 2-D equations of motion model can be useful in separation mechanism design. It provides insight into separation events and the many parameters and their relative sensitivities. A more detailed 3-D geometric dynamics model is also required to clearly define the actuator requirements while accounting for all factors in three dimensions and can also identify interferences due to other hardware on the vehicle. The overall design conclusions drawn are that a simple, dependable spring system can be used for the Orion crewed vehicle separation system. Minimizing the actuator force is preferred in terms of mass, reliability, and cost. However, ensuring the separation system controls the event and all potential external forces is still paramount. This is especially true in an abort scenario. Additional effort needs to be invested to assure second order effects due to propellant slosh or thruster imbalance does not violate the design criteria used in the analysis.

Acknowledgments

The authors would like to acknowledge the contributions, advice, and suggestions of Keith Schlagel and Lance Lininger of Lockheed Martin Corporation who aided in the development and compilation of this work.

References

1. http://www.spacex.com/media.php?page=57
2. Onoda, J. “The Development of Staging Mechanisms for the Japanese Launcher Mu-3SII,” 19th Aerospace Mechanisms Symposium, NASA Ames Research Center, August, 1985.
3. Harrington, T.G. “Compression Spring Separation Mechanisms,” First Aerospace Mechanisms Symposium, University of Santa Clara, Santa Clara, California, May 19-20, 1966.
4. Abdul Majeed, M. K., Matarajan, K., Krishnankutty, V. K. “Separation and Staging Mechanisms for the Indian SLV-3 Launch Vehicle,” 18th Aerospace Mechanisms Symposium, NASA Goddard Space Flight Center, May 1984.
5. AIAA-S-114-2005, *Movinq Mechanical Assemblies Standard for Space and Launch Vehicles*, American Institute of Aeronautics and Astronautics standard, July 2005.
6. Conley, Peter L. *Space Vehicle Mechanisms,* New York, John Wiley & Sons, Inc. 1998.
7. Brennan, Paul C., *NASA Space Mechanisms Handbook,* July 1999.
8. Purdy, W., Hurley, H., “The Clementine Mechanisms,” 29th Aerospace Mechanisms Symposium, NASA Johnson Space Center, May 1995.
9. Hanna, W. D., Chang, R. S., Sheckel, G. L., “Stress Relaxation of Spring Materials,” Fortieth Anniversary: Pioneering the Future, May 1998.
10. Chew, M. “On the Danger of Redundancies in Some Aerospace Mechanisms,” 22nd Aerospace Mechanisms Symposium, NASA Langley Research Center, May 1988.
11. Holmanns, W., Gibbons, D., “Misconceptions in Mechanical Reliability,” 34th Aerospace Mechanisms Symposium, NASA Goddard Spaceflight Center, May 2000.
12. Simulink program Ver.7.0.1.29704, The Math Works Corporation, September 2004.
13. ADAMS dynamic software code Ver. 2005 r2.0, MSC Software Corporation, August 2005.

Focus Mechanism for Kepler Mission

Kraig Koski*

Abstract

The Focus Mechanism built for the primary mirror on the Kepler mission provides a method for adjustment of the mirror position for the duration of the mission. The Focus Mechanism also provides structural support for the 87 kg primary mirror. The Kepler mission requirements provided some interesting and difficult design tasks for the Focus Mechanism. This paper will describe the development, design, function and testing of the Focus Mechanism.

Introduction

The goal of the Kepler mission is to survey our region of the Milky Way Galaxy to detect and characterize hundreds of earth-size and smaller planets near the habitable zone. The habitable zone encompasses the distances from a star where liquid water can exist on a planet's surface. The transit method will be used for detecting extrasolar planets. A transit is when a planet crosses in front of its star as viewed by an observer, resulting in a small change in the star's brightness for a repeatable amount of time. Once detected, the planet's orbital size and mass can be calculated using Kepler's Third Law of planetary motion ($T^2 = R^3$). The size of the planet is found from the depth of the transit (how much the brightness of the star drops) along with the size of the planet's star. From this information, the planet's characteristic temperature can be calculated.

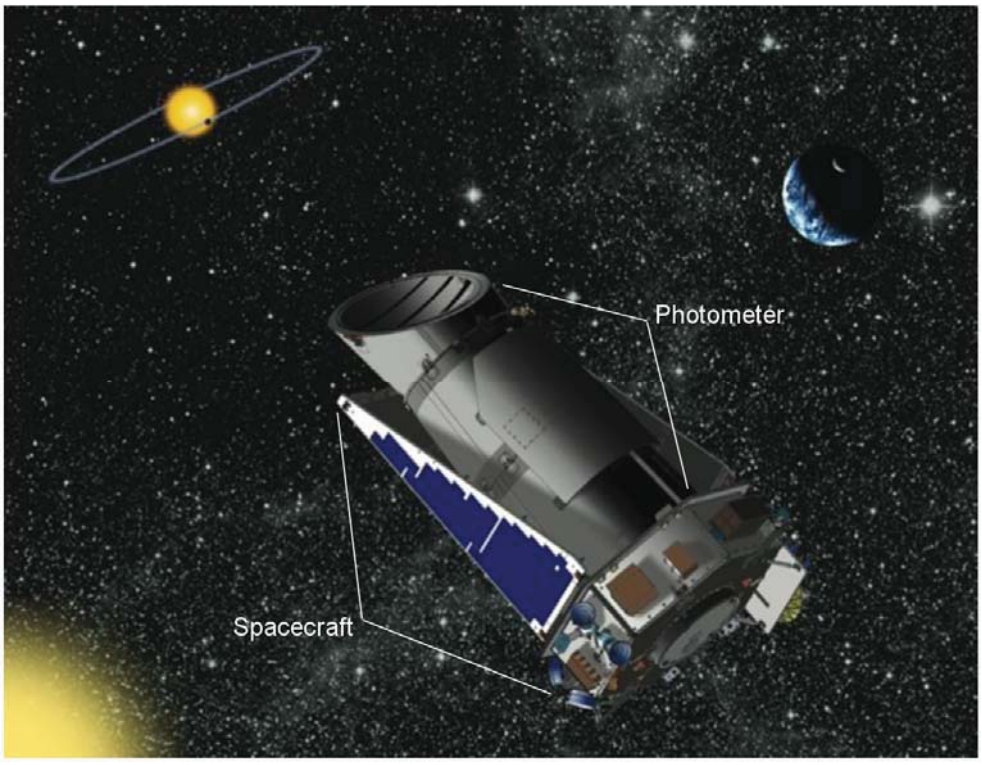

Figure 1. Kepler Flight Segment [1].

* Ball Aerospace & Technologies Corp., Boulder, CO

Kepler Mission Design

For a planet to create a transit visible from our solar system, the orbit must be lined up edgewise to us. The probability for a planet in an Earth-like orbit around a solar-like star to be properly aligned is 0.5%. For this reason, one must look at thousands of stars to determine if Earth-like planets are common or rare. The time between transits for planets in the habitable zone is around 1 year and to reliably detect a sequence, four transits are required. The Kepler instrument, called a photometer, has a large field of view (12° diameter) in order to observe more than 100,000 stars in the Cygnus Region of the Milky Way continuously for the entire 3.5 year mission as shown in Figure 2. Kepler is scheduled to be launched in February, 2009 on a Delta-II rocket into an Earth-trailing heliocentric orbit with a period of 372.5 days which provides the optimum Sun-Earth-Moon avoidance criteria [1].

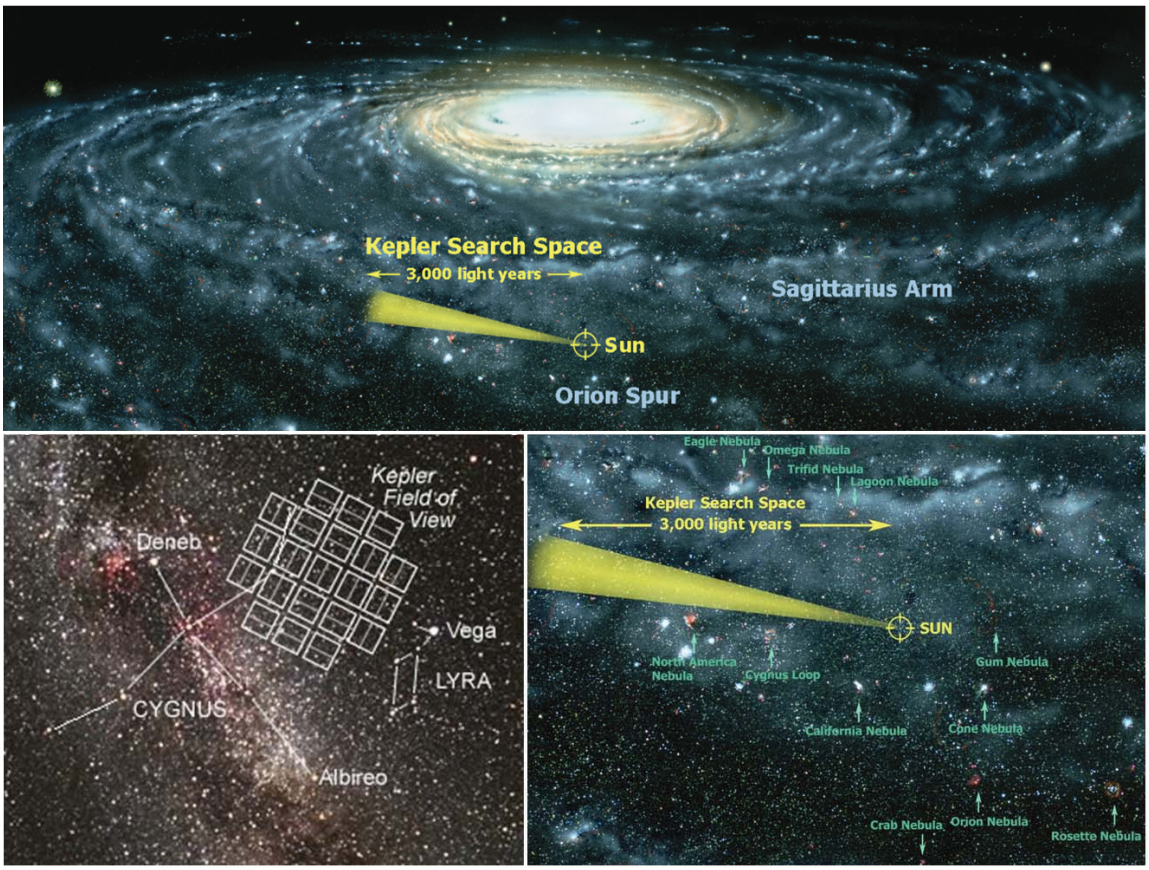

Figure 2. Kepler field of view in Milky Way Galaxy [2].

Kepler Flight Segment

The Kepler flight segment, which was designed and fabricated at Ball Aerospace & Technologies Corp., consists of the Photometer mounted onto a Spacecraft as shown in Figure 1. The Spacecraft provides power, pointing and telemetry for the Photometer. Pointing at a single group of stars for the entire mission greatly increases the photometric stability and simplifies the Spacecraft design. The Photometer, shown in Figure 3, is a specially designed Schmidt telescope with a 0.95-meter diameter aperture and an array of 42 CCD detectors. Each 50x25 mm CCD has 2200x1024 pixels, which are read every three seconds to prevent saturation. The CCD's are not used to take pictures and the images are intentionally defocused to 10 arc seconds to improve the photometric precision. The instrument has a spectral bandpass from 400 nm to 850 nm. Data is stored on the spacecraft and transmitted to the ground once per week [1].

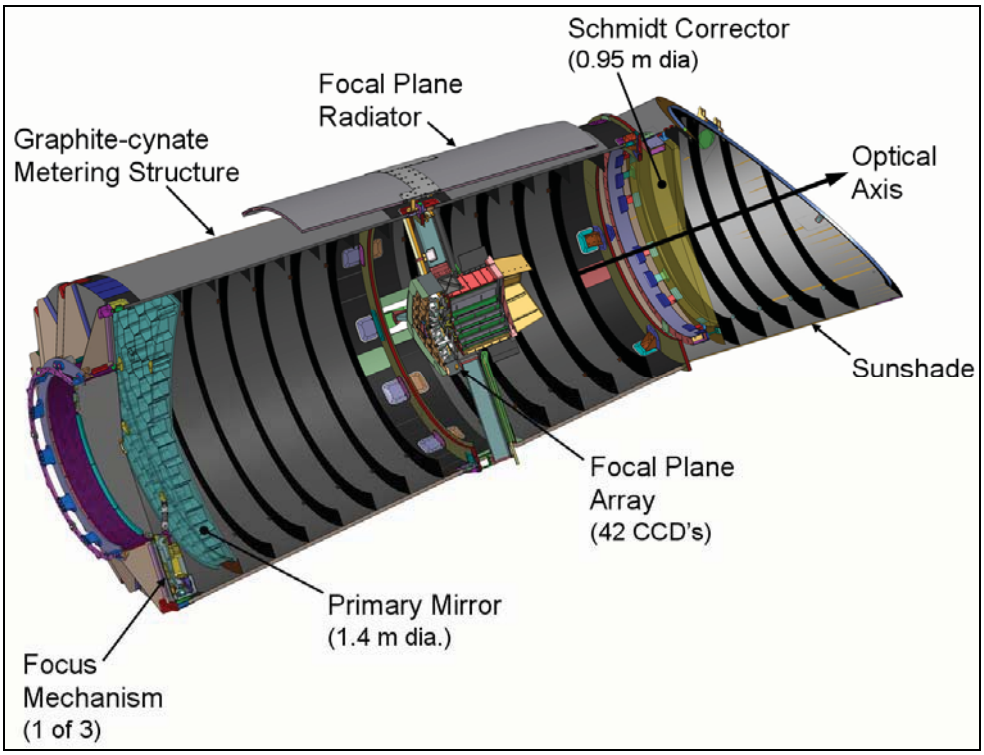

Figure 3. Kepler Photometer, Section View.

Primary Mirror

Three Focus Mechanism units are used to support and focus the primary mirror as shown in Figures 4 & 5. Each Focus Mechanism attaches to the primary mirror with two flexured struts resulting in a hexapod configuration. The low CTE FRIT bonded primary mirror is made from ULE Titanium Silicate and is 1.45 meters in diameter with a mass of 87 kg. The three Focus Mechanisms are situated at 120º to each other and mounted to invar inserts embedded in a composite bulkhead.

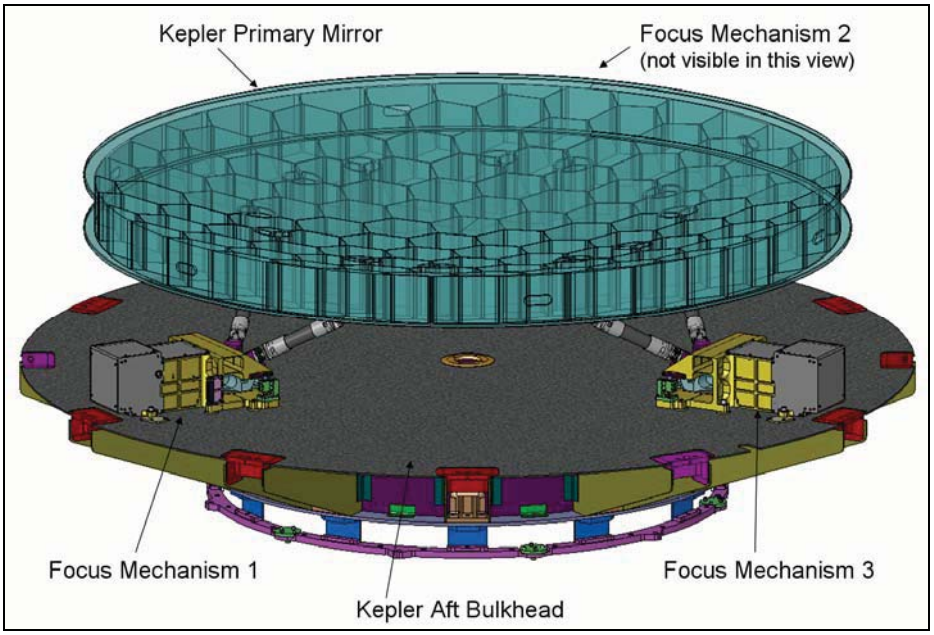

Figure 4. Solid Model of Kepler Primary Mirror/Focus Mechanisms/Aft Bulkhead Assembly.

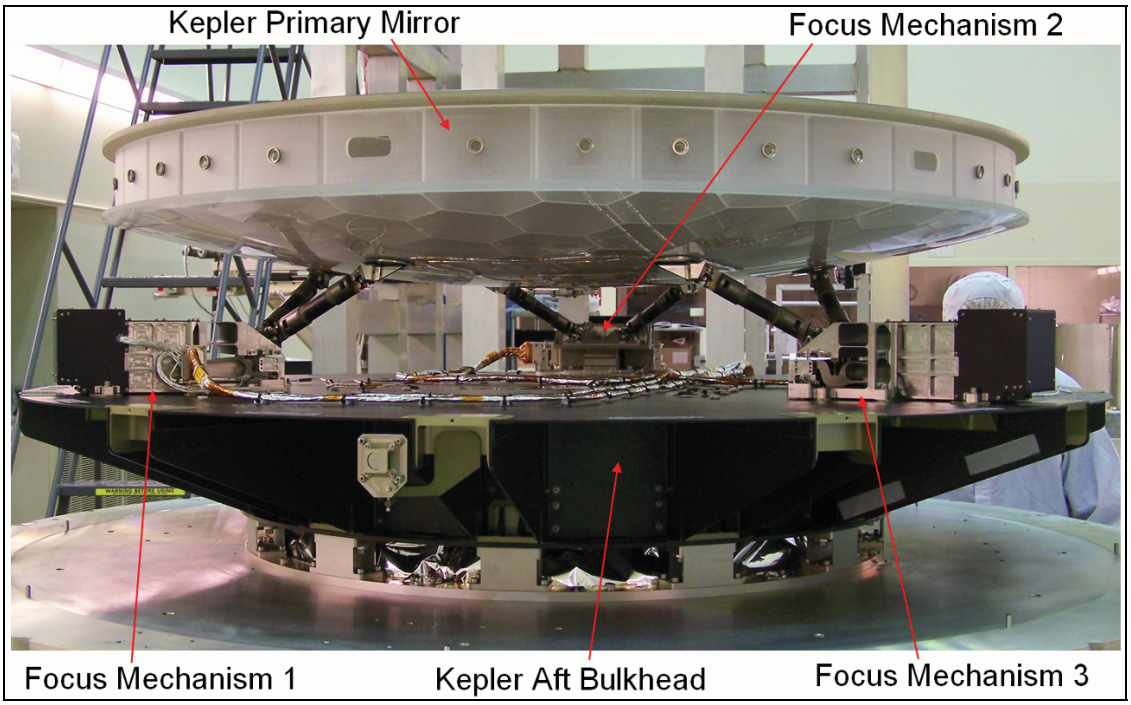

Figure 5. Kepler Primary Mirror Mounted onto the Focus Mechanisms.

Focus Mechanism Driving Requirements

Table 1 summarizes the requirements for the Focus Mechanism and shows the performance based on flight unit testing. The focus mechanism has the ability to tip and tilt the primary mirror, but this is not a mission requirement. Only axial focus displacement of the PMA is required.

Table 1. Focus Mechanism Key Driving Requirements.

Requirement	Value	Performance
Axial position knowledge	±1.4 µm	0.5 µm
Operating Temperature Range	-55C to +35C	Meets
Survival Temperature Range	-65C to +45C	Meets
Focus mech Motor Case Operational Temperature Range	-55C to +60C	Meets
Focus Mech Motor Case Survival Temperature Range	-65C to +70C	Meets
Range of Travel	±762 µm	±900 µm
Smallest increment of Travel	≤1.5 µm	0.4 µm
Unidirectional Repeatability	≤1.25 µm	Meets
Focus Mechanisms shall not require power during launch	n/a	Meets
4 Year Lifetime equates to mechanism cycles	112 cycles	Meets
Mass (1 Focus Mechanism)	≤4.9 Kg	4.13 Kg
1st Mode Frequency, Axial	>50 Hz	61.2 Hz
1st Mode Frequency, Lateral	>50 Hz	70.0 Hz
Maximum Launch Acceleration	41 g	Meets

Focus Mechanism Design Overview

A unique design was incorporated in order to meet the difficult resolution requirement of less than 1.5 microns over a range of at least 1500 microns. This design includes a variety of the classical moving mechanical components that were integrated into an elegant, robust and efficient system. Some of the key components of the Focus Mechanism include a stepper motor, gears, ball screw, bearings, lever arm and several flexures. Figures 6 and 7 show the front and aft views of one of the three flight Focus

Mechanisms. Redundant LVDT (Linear Variable Differential Transformer) sensors are mounted on both sides of the Primary Mirror Interface shelf and used for position sensing. The Stepper Motor, which drives the entire system, also has primary and secondary windings for redundancy.

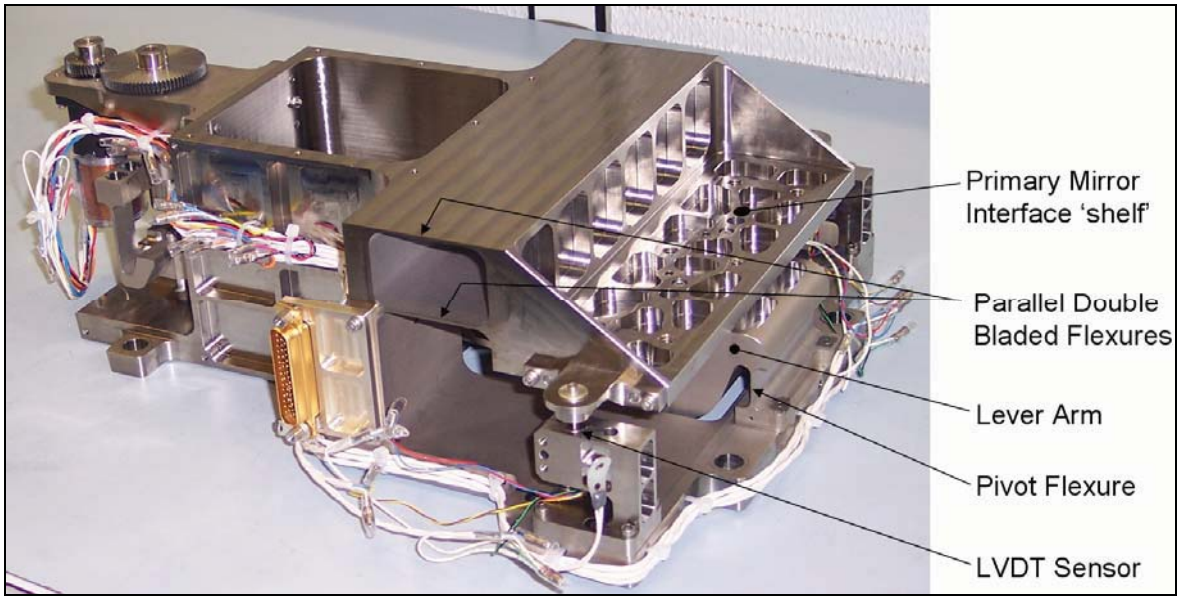

Figure 6. Kepler Focus Mechanism, Front View.

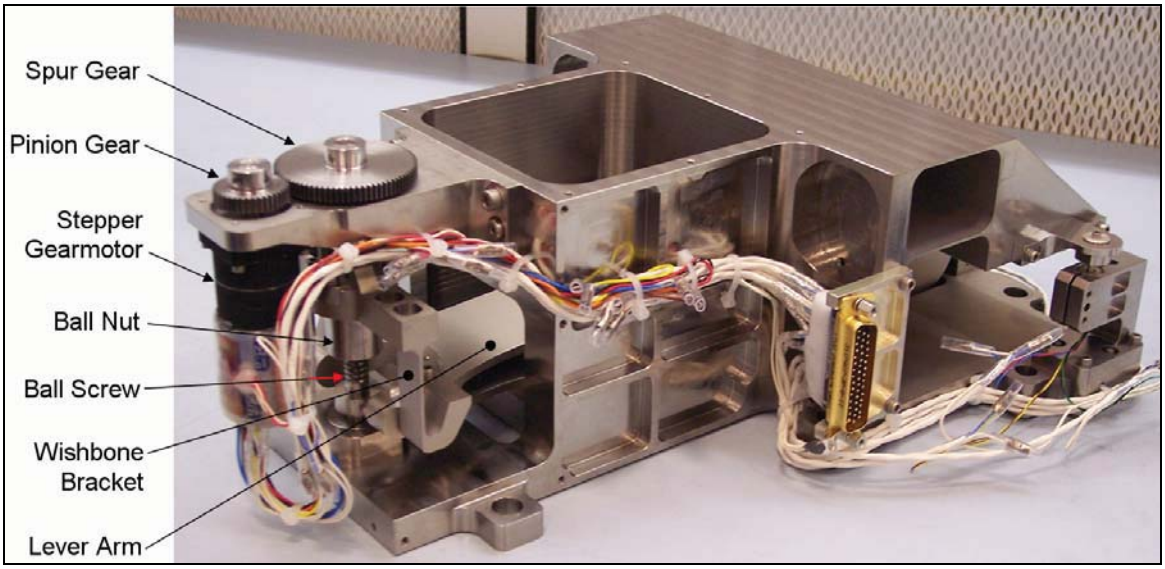

Figure 7. Kepler Focus Mechanism, Aft View.

Function

The Focus Mechanism is driven by a 30° stepper motor with an integral 100:1 gear head. The output shaft of the gearmotor attaches to a 2:1 pinion-spur gear reduction. The spur gear is attached to the shaft of a 2-mm pitch ball screw which is supported by duplex bearings at the base and a radial bearing on top. A titanium 'wishbone' bracket with flexures attaches the ball nut to the end of a titanium lever arm. As the ball nut moves up or down, the lever arm pivots on an integral pivot flexure while a 2nd drive flexure, also integral to the lever arm, moves the primary mirror interface shelf up or down. A parallel double bladed flexure provides nearly perfect up and down movement of the interface shelf. The 8.75:1 lever arm provides mechanical advantage by reducing load requirements and also allows finer displacements. Redundant LVDT sensors, mounted on both sides of the primary mirror interface, measure

displacements. Upper and lower hard stops are attached to the ball screw to prevent damage to the mechanism. Figure 8 shows a section view of the mechanism solid model.

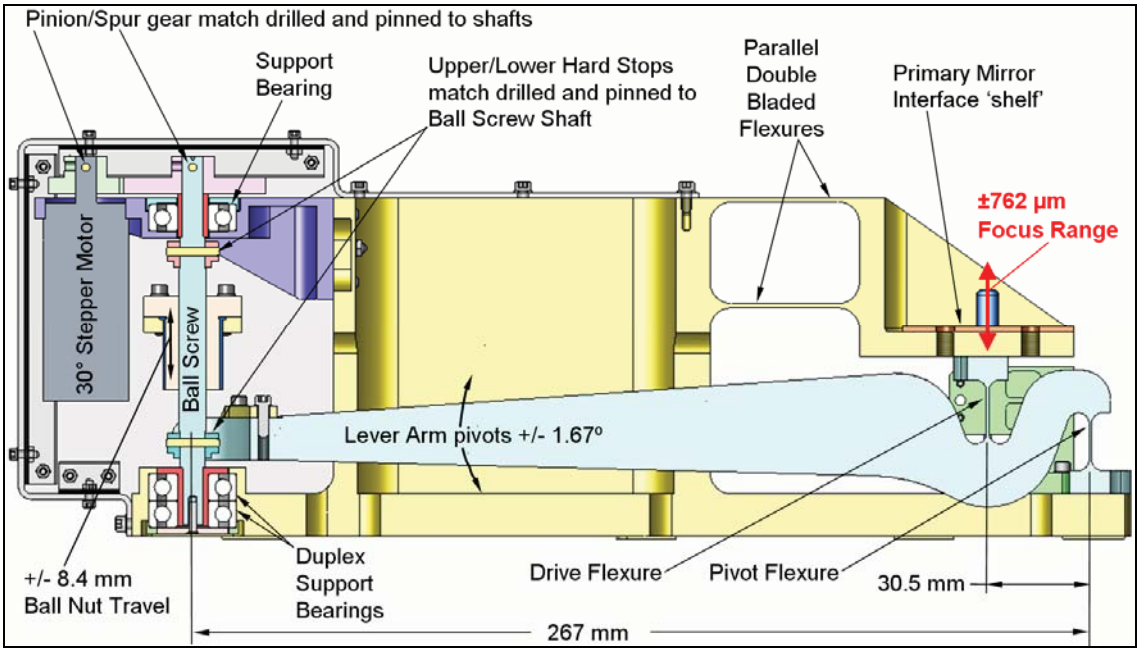

Figure 8. Section View taken from Focus Mechanism solid model.

Focus Mechanism Design Background

The initial conceptual development of the Focus Mechanism began at Ball Aerospace in September, 2002 by Robert Warden. The design concept (Figure 9) was based on the components of the Spitzer Space Telescope (formerly SIRTF) Secondary Mirror Cryogenic Focus Mechanism.

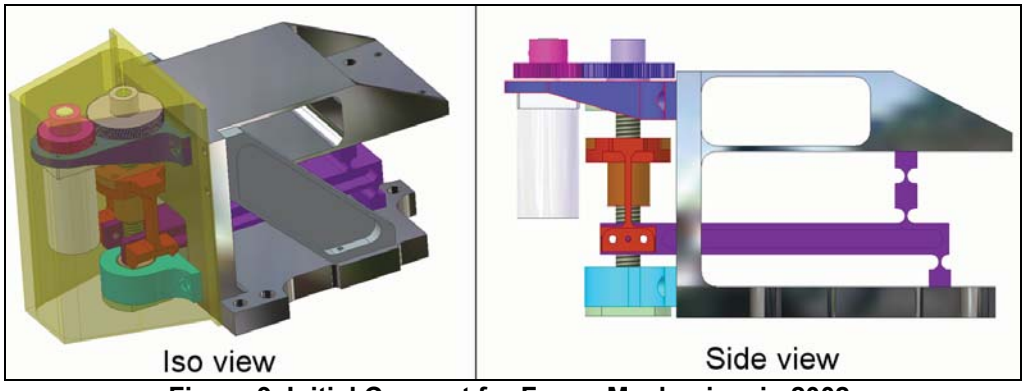

Figure 9. Initial Concept for Focus Mechanism in 2002.

Numerous developments and improvements were made to the mechanism from late 2003 to 2006. Some of these developments include:

1. The parallel double bladed flexure was made more compliant to decrease the torque requirements and stresses on the drive and pivot flexures.
2. The main flexure interface 'shelf' was widened to accommodate the interface to the primary mirror strut brackets.
3. The geometry of the lever arm was optimized to minimize bending and maximize mechanical advantage.
4. The geometry of the lever arm pivot and drive flexures was optimized to minimize stresses.
5. The ball nut flexure 'wishbone' design was optimized to eliminate 'wind-up' and minimize stresses.
6. Redundant LVDT sensors were added for 16 bit position sensing.

Design Discussion

Motor

The Focus Mechanism is driven by a 2-phase driven, bipolar, permanent magnet, redundantly wound, 30° stepper motor. The motor possesses a detent torque which prevents backdriving of the mechanism during launch. Integral to the motor is a 100:1 gear head which enhances mechanical advantage and helps meet the strict Kepler resolution requirements. The detent torque combined with the large gear ratio eliminates the need for a launch lock in the mechanism.

The Focus Mechanism is open-loop controlled by commanding the motor to move a specified number of steps. During actuation a 'commanded step' from the control electronics moves the motor rotor four 30° steps. This equates to 0.38 μm of axial movement at the primary mirror. The 'commanded steps' are used to start and stop the motor rotor in the same phase which increases step count accuracy. The resulting position of the primary mirror is verified with the LVDT sensors.

Transfer Gears

Both the 40-tooth pinion gear and 80-tooth spur gear are made from custom 455 stainless steel heat treated to condition H1050 to give adequate strength margins. Other than the special material callout, the gears are standard off-the-shelf parts. There is a small amount of backlash in the system due to the transfer gears and 100:1 motor gear head which results is a maximum vertical motion of 0.43 μm at the primary mirror interface shelf. This is well below the 1.25 μm repeatability requirement.

Ball Screw

The ball screw has an 8-mm diameter and 2-mm pitch and is preloaded with oversized balls to eliminate backlash. The balls, shaft, nut and deflectors are fabricated from 440C passivated stainless steel. The ball screw was sized to result in positive stress margins.

Hard Stops

The upper and lower hard stops are non-jamming and use a radial face-to-face design which minimizes stress on the ball screw. Figure 10 shows a close up view of the mechanism model with the lower hard stop engaged. The hard stops were fabricated from Titanium and designed to insure that the maximum torque delivered by the gear motor did not over stress them. The hard stops were positioned onto the ball screw during the build up of the focus mechanism so that they stop movement at approximately ±890 μm, well beyond the required ±762 μm range requirement. After the hard stops were correctly positioned, the ball screw was removed from the assembly and the hard stops were match drilled to it. The threads of the ball screw were completely covered to prevent contamination during this operation. The ball screw and hard stops were then reassembled into the mechanism after the match drilling operation.

Wishbone Bracket

The wishbone bracket attaches the ball nut to the lever arm. It contains two flexures that extend down on both sides of the ball nut. The wishbone flexures are designed such that they are compliant enough to bend without binding when the Ball Screw rotates and they translate rotary motion to linear motion. At the same time, the wishbone flexures are stiff enough to prevent 'wind-up' when the ball screw rotates. If the wishbone flexures are too compliant, the bracket will rotate along with the ball screw and then at an unexpected time it will 'unwind' causing unwanted movement and unfavorably affecting the step size and repeatability of the system. Figure 11 shows the titanium wishbone bracket and the tension joint attachment to the lever arm.

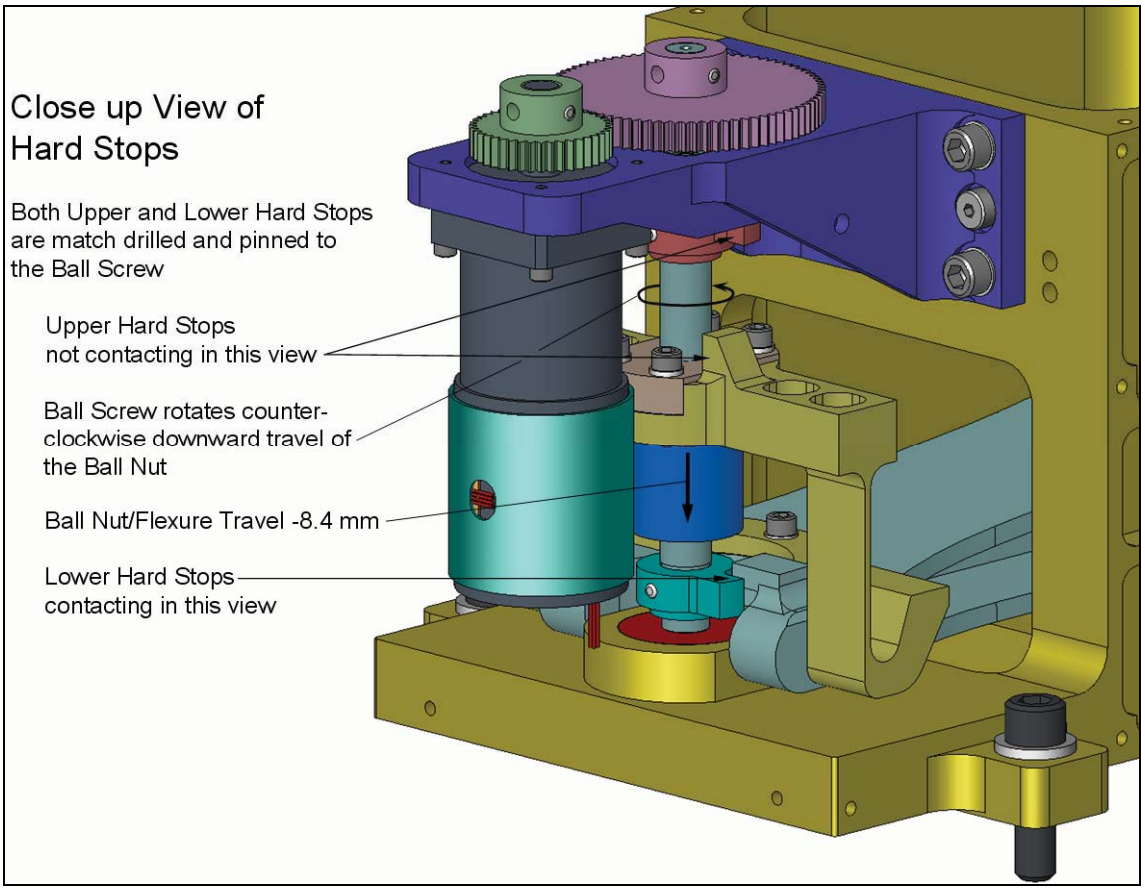

Figure 10. View of lower hard stop engaged.

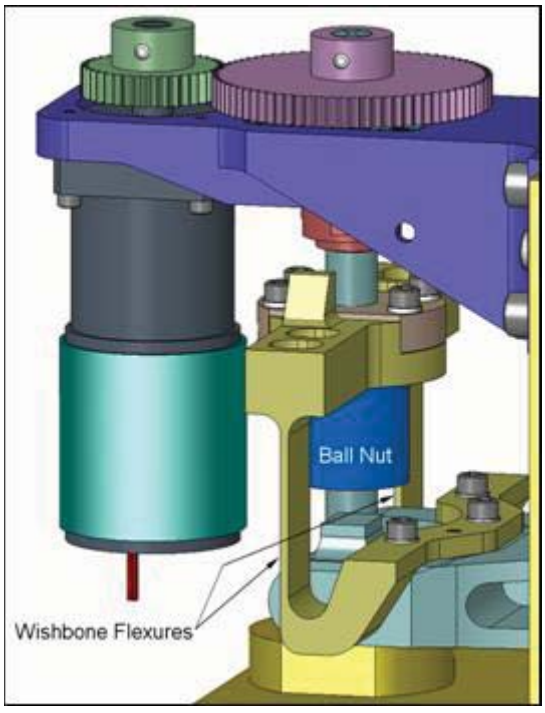

Figure 11. Wishbone Flexures/Bracket.

Bearings

The bearings used to support the ball screw are a duplex pair at the base and a radial ball bearing on top. The duplex pair uses face-to-face mounting to allow for slight misalignment and also to eliminate axial and radial play in the system. The preload in the duplex pair is 13.3-26.7 N (3-6 lb). As shown in Figure 12, the ball screw shaft is supported and rotates with the inner races of the duplex pair. The sleeve and retainer disk also rotate with the ball screw. The ball screw shaft is allowed to float axially on the upper radial bearing which prevents possible binding due to CTE mismatch. There is a 0.2-mm radial gap in the mounting design for both bearings to provide a labyrinth seal which keeps dust out and prevents the lube from migrating.

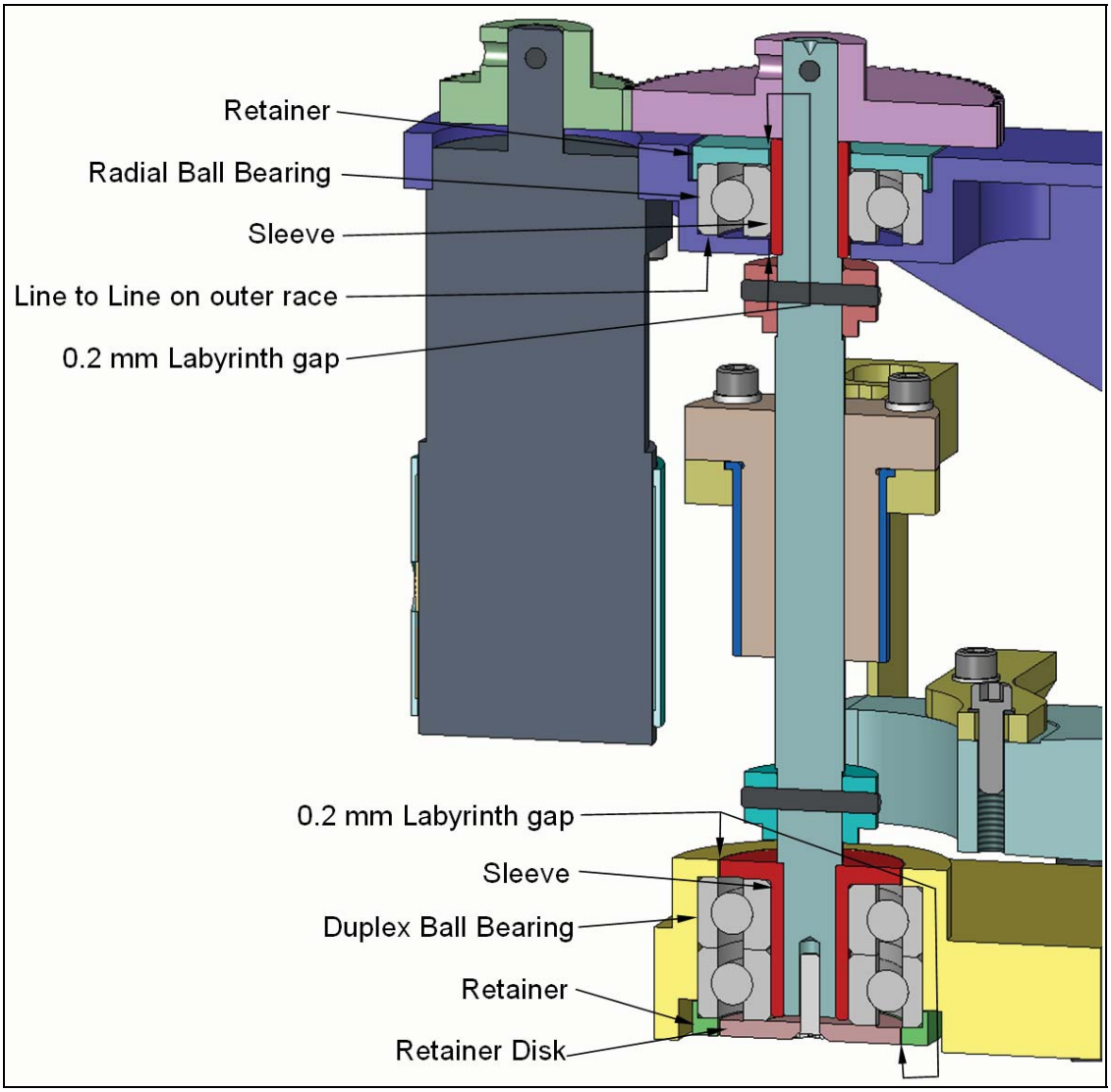

Figure 12. Section view of Bearings/Ball Screw

Lever Arm

The lever arm provides a mechanical advantage of 8.75:1 which helps achieve the required resolution and torque margin in the system. The shape of the lever arm resulted in analysis to optimize the design for minimum bending at the extents of travel. The bending forces on the lever arm increase as the mechanism approaches the hard stop positions due to bending of the flexures. This results in a system that is not perfectly linear. An identical amount of motor steps will result in approximately 5% less movement of the primary mirror at the extents of travel versus at the null position. This non-linearity is mitigated by the LVDT measurements. The lever arm was fabricated from titanium, like most of the

components in the focus mechanism, to minimize CTE mismatch and for optimum mechanical properties for the pivot and drive flexures which are integral to the lever arm.

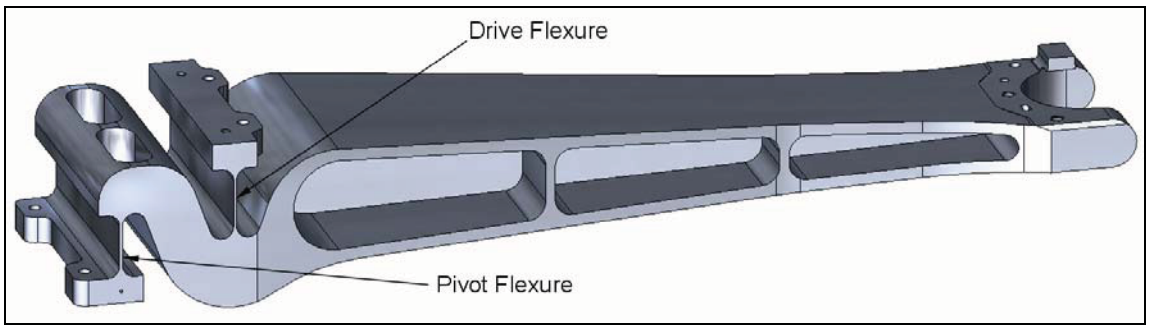

Figure 13. Lever Arm

Flexures

There are 4 flexures in the focus mechanism design. The pivot flexure, drive flexure, parallel double bladed flexure and wishbone flexure. All four are fabricated from Titanium 6AL-4V and have been analyzed and designed to have positive stress margins for launch loads and actuation cycles. A fatigue analysis showed that the flexures will survive 86 lifetimes of actuations.

The parallel double bladed flexures cause the primary interface shelf to rotate a very small amount during actuation of the focus mechanism. The movement of the interface shelf is not perfectly vertical. At the extents of travel, the maximum rotation of the interface shelf is 0.21° and the maximum out of plane displacement is 7.4 µm. This non-axial motion is mitigated with the compliant flexures in the struts that attach the focus mechanisms to the primary mirror.

Lubrication

The lubricated elements associated with the Focus Mechanism assembly are the motor-gearhead assembly, transfer gears, ball screw, and the ball screw support bearings. All elements were lubricated at Ball Aerospace, or in the case of the motor gears, under specific instructions from Ball. The selection of lubrication is highly dependent on operating temperature. The minimum operational temperature requirement for the Focus Mechanism originally was -75C. This made lubrication selection difficult because at this temperature, the wet lube becomes more viscous, increasing drag and friction in the system, which results in a lower torque margin. Dry lube is an alternative at extremely low temperatures, but restrictions in the operating environment for dry lube increase the cost and test set-up complexity. For this reason Braycote 601EF wet lube was chosen for all of the lubricated elements in the Focus Mechanism.

A torque test was performed on the ball screw and support bearings using the chosen lube at a temperature of -75C. The resulting rotating torques were determined to be acceptable and used in initial torque margin calculations.

Initially the Focus Mechanism design called for I^2R heating of the motor windings to warm the lube in the motor components, which decreases viscosity, if it was required at cold temperatures. Thermal analysis on the motor driver board later revealed that the driver chips on this board would heat up too quickly and reach dangerous levels. As a result of this, the design changed from I^2R heating to a foil heater wrapped around the motor body. Subsequent drag torque testing at the motor vendor revealed that heating the gearmotor with a foil heater at -75C resulted in ample torque margin. Ultimately the Kepler thermal model was refined and the minimum operational temperature requirement was increased from -75C to -55C, which resulted in even higher torque margins in the Focus Mechanism.

Redundancy

There are two LVDT sensors mounted on either side of the primary mirror interface shelf. Only one is required for position feedback. Figure 14 shows one of the LVDT sensors on the focus mechanism.

The stepper motor contains 2 sets of 2 phase windings, each capable of independently meeting the performance requirements. The motor heater foil contains two sets of coils, only one is required for normal operation.

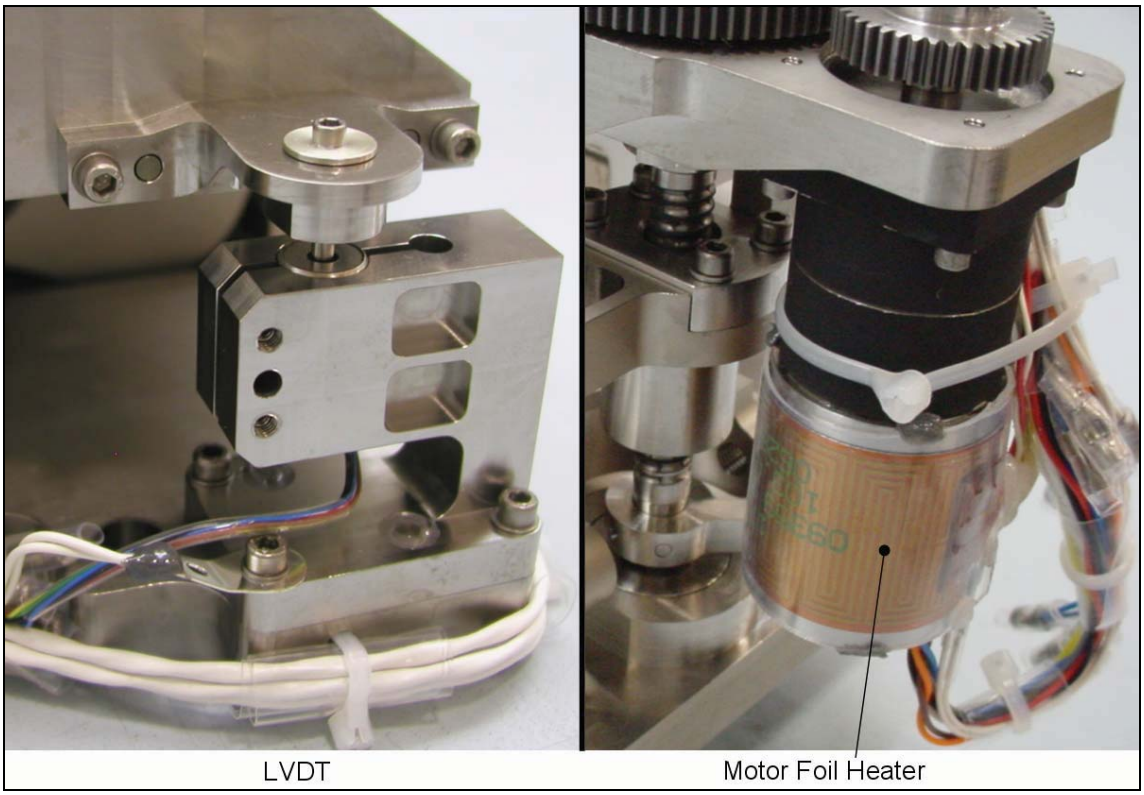

Figure 14. Focus Mechanism LVDT Sensor and Motor Heater.

Analysis

Detailed finite element models of the focus mechanism were produced to predict structural and thermal stresses along with modes during launch loads. As a result of this analysis, several features of the focus mechanism were adjusted as the design matured to produce positive safety margins. A surrogate primary mirror was mounted onto the three completed focus mechanisms and vibration tested. The finite element models were correlated to the vibration test data to more accurately predict the axial, lateral and rocking modes of the focus mechanism/primary mirror assembly during launch loads.

Testing

Static Load Test

On April 18, 2006 a static load test was performed to measure the stiffness of the focus mechanism in all 3 axes. An MTS Sintech Extensometer was used to apply a force on the focus mechanism in the area of the primary mirror interface and measure the resulting displacement. The forces applied were within the elastic limit of the unit and the data was used to correlate the finite element model of the focus mechanism. Figure 15 shows the Y-axis test.

Required Torque Test

In March, 2007 a required torque test at cold temperature was performed on the focus mechanism to determine the torque margin at the worst case temperature. The test was run in a climatic chamber that was cooled with liquid nitrogen. The motor was removed from the focus mechanism and replaced with a bearing/pinion gear/shaft assembly that was heated with a foil heater wrapped around the perimeter of the cylindrical housing. The torque to actuate the mechanism was measured with a torque watch. The results were within 20% of predicted values and the torque margin was acceptable.

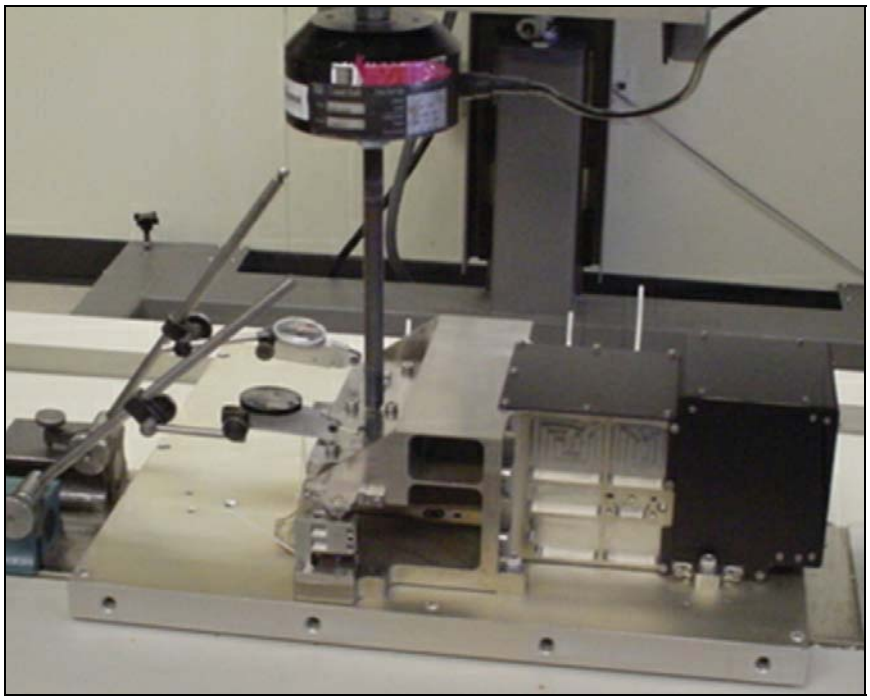

Figure 15. Focus Mechanism Static Load Test, Y-axis.

Functional Test

All three of the focus mechanisms underwent and passed extensive functional testing in the spring of 2007. Most of these tests were performed to show that the focus mechanism meets the requirements shown in Table 1. Some of these tests included range of motion, unidirectional repeatability, axial position knowledge and smallest increment of travel.

One issue that somewhat slowed testing was the requirement for the motor case maximum operational temperature. This requirement states that the maximum temperature that the motor case can operate at is +60C. The reason for this is to avoid warming the lubricant in the bearings. If the lube becomes too warm, the viscosity decreases and it can migrate out of the bearings. During testing the motor could only run for approximately one minute at a time before the case temperature became too high. Temperature sensors on the motor case were monitored closely to insure that this limit was not exceeded.

Figure 16 shows actual data from Focus Mechanism functional testing. The graph shows absolute position vs. LVDT counts for the entire range of motion. The X-axis is the absolute position, measured with a Ziess CMM (Coordinate Measuring Machine) and the Y-axis shows the corresponding primary and redundant LVDT counts. Each mechanism was fully characterized during this testing.

Vibration Testing

In April, 2007, all 3 focus mechanisms passed vibration testing with a surrogate primary mirror mounted to them. Figure 17 shows the test setup for one of the axes.

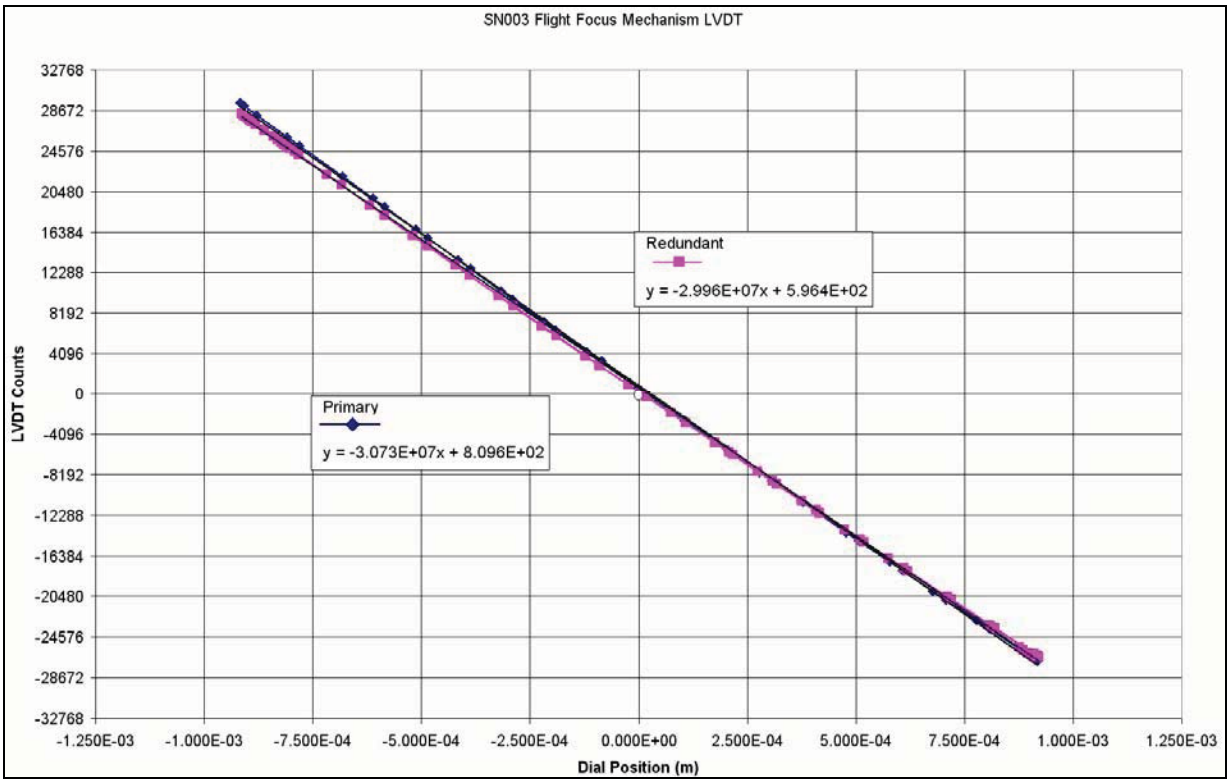

Figure 16. Range of motion test.

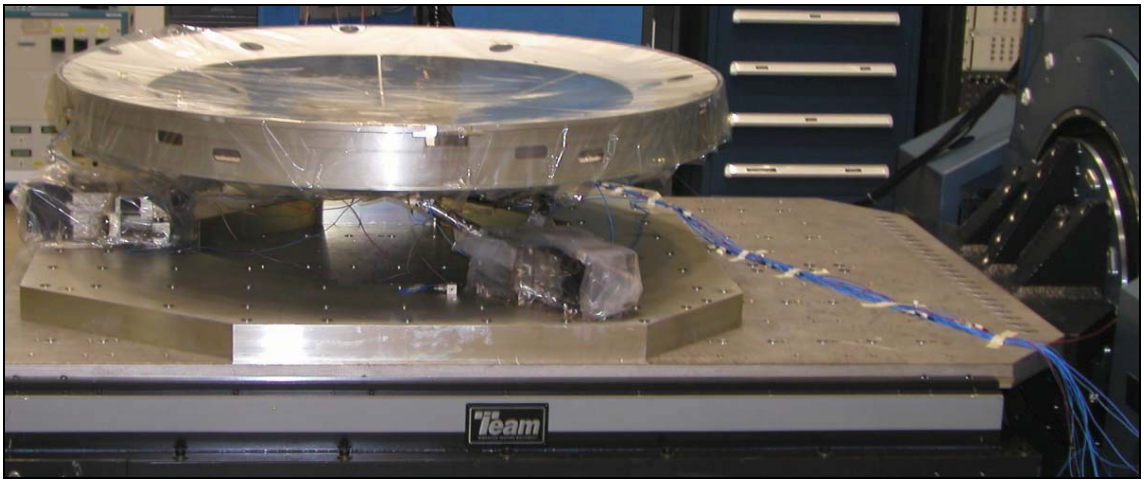

Figure 16. Vibration Test

Thermal Vacuum Testing

In May, 2007, all three focus mechanisms passed thermal vacuum testing. All three units were tested simultaneously as shown in Figure 17. Mass simulators, 1/3 the mass of the primary mirror, were mounted to the interface shelf to simulate the correct loads. Each focus mechanism was mounted to an Invar base plate to simulate the CTE of the composite aft bulkhead. Cooling boxes were mounted over the motor cover box to increase the cooling rate at the motors and speed up functional testing

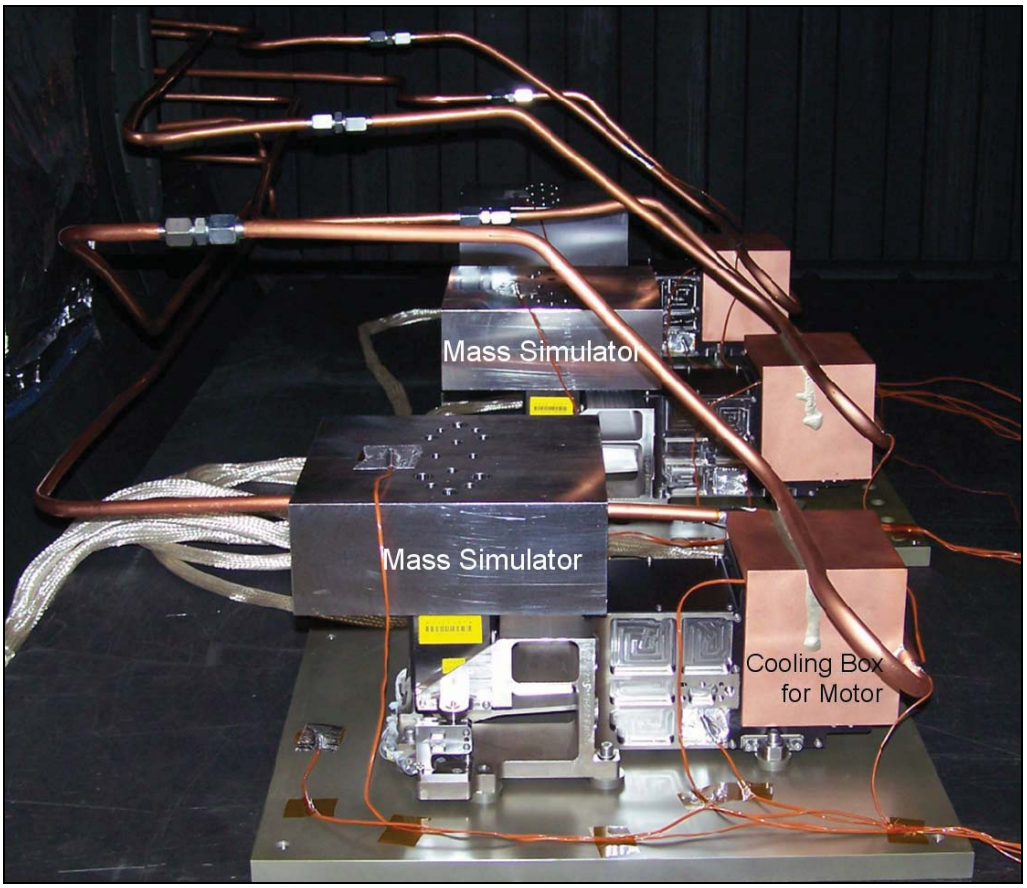

Figure 17. Thermal Vacuum Test

Conclusion

The design, fabrication, assembly and testing of the focus mechanism was successful due to the combined efforts of dozens of engineers, machinists and technicians at Ball Aerospace. It is impossible to list all of the lessons learned during this effort. One issue that caused a slight schedule delay involved the ball screw. When the ball screws were disassembled and lubricated at Ball Aerospace it was discovered that the ball sizes were oversized and the pre-load was too high. New balls needed to be ordered from the manufacturer which delayed schedule. It is recommended up front to order a spare set of balls, 2.5 & 5.0 µm (0.0001 & 0.0002") larger and smaller than the standard ball size to avoid delays.

The focus mechanism has successfully met all design and schedule requirements that it has faced and is currently operating flawlessly in the Kepler Telescope.

Acknowledgements

The author would like to thank all of the Kepler machinists, technicians, analysts, engineers and managers that played a role in developing the focus mechanism. The skill, hard work, passion and dedication of this team of people were vital to the success of this effort.

References

1. Kepler mission overview. Kepler/NASA website. http://kepler.nasa.gov/
2. Illustration of Milky Way Galaxy copyright Jon Lomberg. http://www.jonlomberg.com

Precision Linear Actuator for Space Interferometry Mission (SIM) Siderostat Pointing

Brant Cook*, David Braun*, Steve Hankins*, John Koenig* and Don Moore*

Abstract

"SIM PlanetQuest will exploit the classical measuring tool of astrometry (interferometry) with unprecedented precision to make dramatic advances in many areas of astronomy and astrophysics" (1). In order to obtain interferometric data two large steerable mirrors, or Siderostats, are used to direct starlight into the interferometer. A gimbaled mechanism actuated by linear actuators is chosen to meet the unprecedented pointing and angle tracking requirements of SIM. A group of JPL engineers designed, built, and tested a linear ballscrew actuator capable of performing submicron incremental steps for 10 years of continuous operation. Precise, zero backlash, closed loop pointing control requirements, lead the team to implement a ballscrew actuator with a direct drive DC motor and a precision piezo brake. Motor control commutation using feedback from a precision linear encoder on the ballscrew output produced an unexpected incremental step size of 20 nm over a range of 120 mm, yielding a dynamic range of 6,000,000:1. The results prove linear nanometer positioning requires no gears, levers, or hydraulic converters. Along the way many lessons have been learned and will subsequently be shared.

Introduction

SIM will improve "our understanding of the physical properties of stars, determining the mass, including the dark matter component, and its distribution in our Galaxy, observing the motions of the Milky Way's companions in the Local Group, and probing the behavior of supermassive black holes in other galaxies" (1). Using three interferometers, 1 science and 2 guides, SIM will deliver a dramatically more accurate mapping of our universe as well as a better understanding of the formation and evolution of other planetary systems outside our own. Accurate mapping using interferometers requires high precision actuation, pushing the limit of both the mechanical positioning realm and the electronics/control realms. The required lifetime of SIM is also extremely challenging with a need to meet performance requirements for no less than 5.5 (with a goal of 10) years of continuous science observation. This is approximately 3 million large angle gimbal moves.

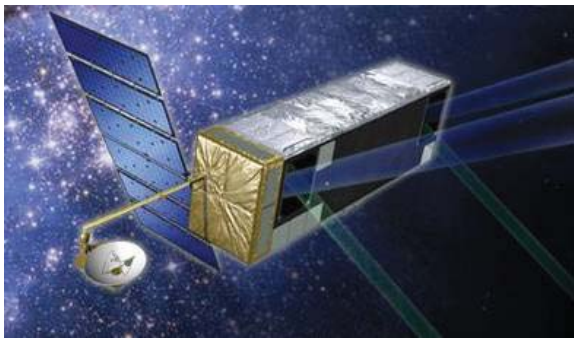

Figure 1: SIM PlanetQuest

While many precision mechanisms are required for SIM to deliver its science data, the Siderostat is the initial pointing mechanism used to direct starlight into the instrument. The Siderostat tips and tilts a 304.5-mm clear aperture optic across a 15-degree Field of Regard (on the sky) via a two-axis hexfoil flexured gimbal mechanism, with a required coarse accuracy of 1arc-second (as) and a fine accuracy of

* Jet Propulsion Laboratory, California Institute of Technology, Pasadena, CA

5 milli-arc-second (mas) on the sky. Implementing a pair of linear actuators approximately 300 mm from the gimbal axis yields a required linear coarse accuracy of approximately 1 micron and a fine linear accuracy of approximately 5 nanometers. See Figure 2, Potential Siderostat Configurations.

Figure 2: Potential Siderostat Configurations

This paper will discuss the design, build, and test of a linear actuator capable of repeatedly, over long periods of operation, performing submicron positioning maneuvers. The design successfully pushes the limits of mechanical positioning while remaining true to the JPL principles of heritage, simplicity, and robustness. Along the way interesting lessons were learned and will be put forth for the reader's benefit.

Mechanical Design

Generally speaking, design is a continuous balancing act to meet competing requirements. It requires the designer/engineer to carefully balance the design process between many conflicting requirements. In actuator design, if mutually exclusive positioning requirements are equally important a two-stage mechanism is often the solution. Unfortunately, multiple stages add to complexity, mass and cost. In our design, the need for large fast moves, trump the needs for fine positioning, and vice versa. It was originally thought that no single actuator could meet the large stroke, high speed, small incremental step size (actuator resolution), required by the Siderostat. The original intention of our Precision Linear Actuator, Direct Drive (PLADD) was to fill the role of a coarse actuator.

The design approach taken with PLADD is one of simplicity, heritage, and robustness. The initial design required at least 2000 incremental positions per revolution of the nut/motor in order to obtain a linear incremental step size of 1 micron. Figure 3 shows a cross section of the actuator.

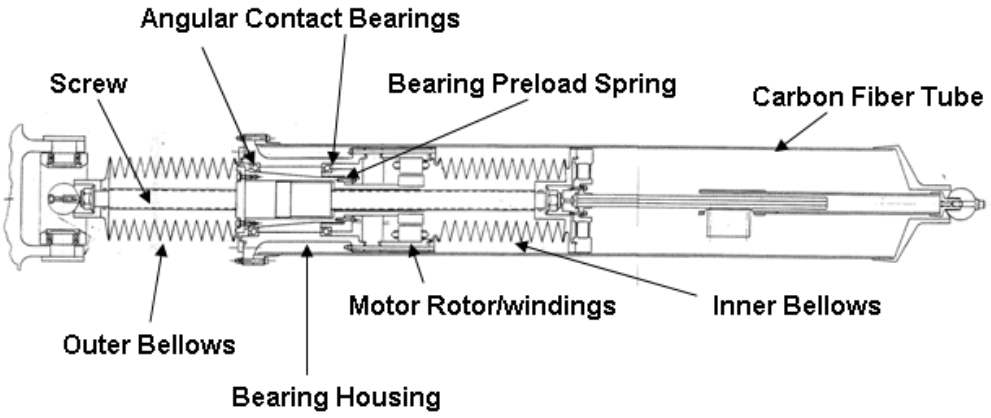

Figure 3: SID PLADD Cross Section View

The bearing housing, as shown in Figure 4, is the center of the actuator, housing the back-to-back duplex angular contact bearings, brake, and motor. Both sets of bellows are suspended from the bearing housing, while the housing bolts directly to the carbon fiber outer tube for thermal stability.

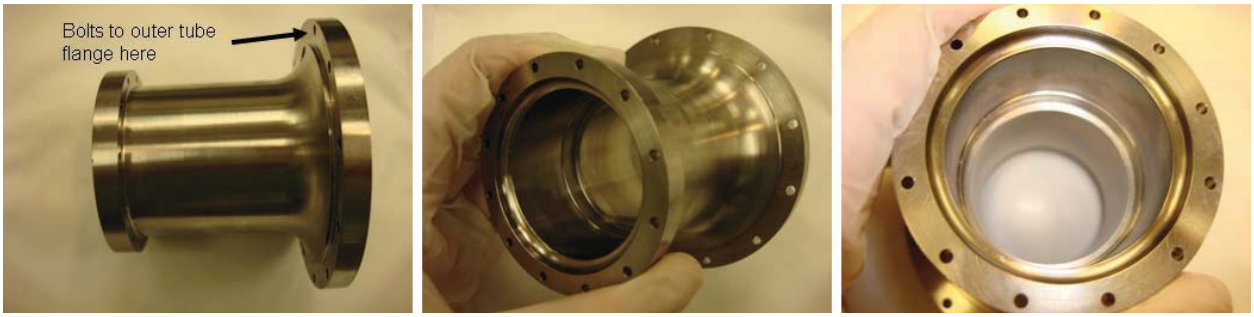

Figure 4: Bearing Housing

The angular contact bearings are assembled into the bearing housing from opposing ends of the housing. The housing is stepped, creating a bearing spacer against which the bearings can be preloaded. The bearings are thin section MPB (Miniature Precision Bearings) angular contact ball bearings with a phenolic retainer ball spacer. The bearings have 440C balls and races. The bearings are shown in Figure 5.

Figure 5: Timken MPB Angular Contact Ball Bearing

The bearing inner races are mated to the motor drive link. As depicted in Figure 6, the inner race of the inner bearing seats on a non-sliding preload flexure. The DC brushless motor rotor is assembled to the rear of the drive link via set screws. The ballnut is mounted to the front of the drivelink via bolts.

Figure 6: Bearing Preload Flexure and Rotor mounted to Drive Link

The motor is coupled to the NSK ballnut by way of an in-house designed and built drive link. The drive link is shown in Figure 7.

The complexity of the mechanism is reduced and backlash of a gear train is eliminated via a direct drive approach. By eliminating mechanical backlash in the actuator the control system is able to actively eliminate any mechanical imperfections in the actuator using feedback from the linear glass scale

encoder mounted to the actuators' output. The direct drive approach also greatly simplifies manufacturing and assembly of the actuator by lowering part count and complexity.

Figure 7: Motor Drive Link

The heart of the actuator is a 12-mm diameter, 2-mm lead, NSK ballscrew mounted onto an NSK Double nut utilizing a spring preload of 130 newtons. The combination can be seen in Figure 8.

Figure 8: NSK Ballnut

The ballnut is connected directly to the drive link via 8 bolts.

Figure 9: Ballnut bolted to Drive Link

The ballnut drive link combination is assembled into the bearing housing with the angular contact bearings, preload flexure, and finally the piezo brake as pictured in Figure 10.

Figure 10: Housing Assembly

The piezo brake consists of a set of flexured levers, preload springs, and guide flexures machined out of a single piece of titanium. The drive-link is radially compressed by the machined springs upon power-off. This constrains the drive link, and thus the ballnut, in rotation. The power must be applied in order to release the brake. The braking force is applied by the compressed preload springs via a wedged preload shim. The preload force is eliminated by the application of power to the piezo stacks.

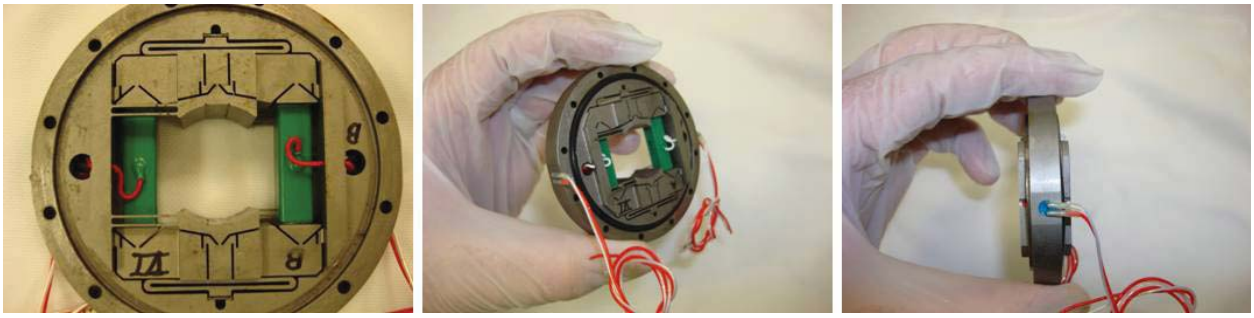

Figure 11: Piezo Brake

The actuators' driving torque is delivered via an off the shelf DC brushless motor from BEI/Kimco Magnetics as pictured below.

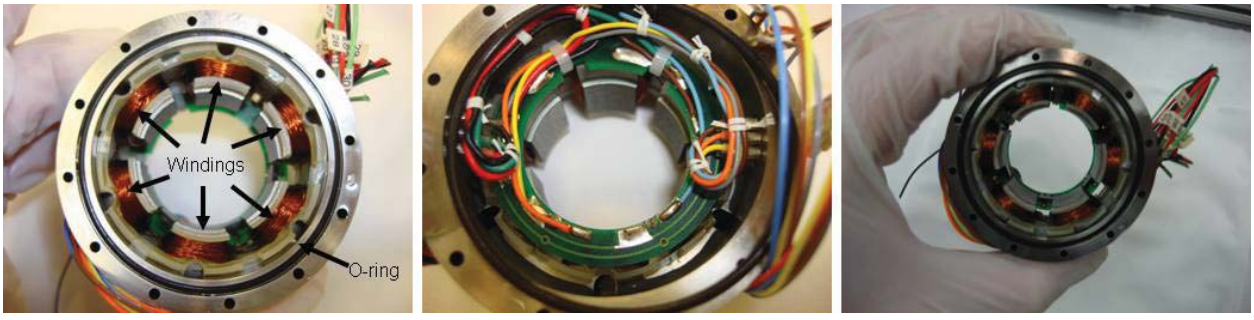

Figure 12: BEI DC Brushless Motor

Long life requirements along with a high correlation between lubricant consumption and life limitation led the team to immerse the mechanical drivetrain of PLADD in oil via a set of hermetically sealed bellows mounted to each end of the ballscrew. The bellows create a constant volume to house Brayco 815Z oil, and subjects the mechanical system to a continuous oil flush. The bellows additionally are used to hold the screw in rotation, thus allowing the rotating ballnut to produce linear motion at the screw. The continuous motion of oil through the mechanical system is conjectured to eliminate many failure modes. This hypothesis is being tested via life tests that are in progress.

The motor windings, piezo brake, and inner bellows are bolted to the outer housing via thru bolts.

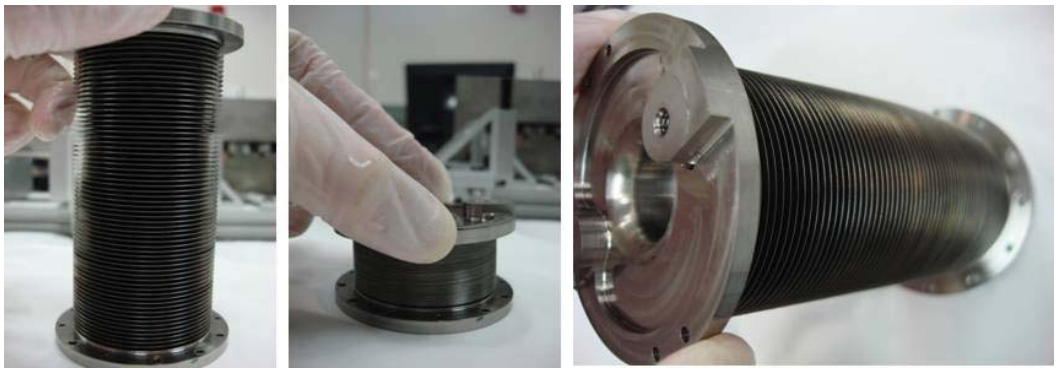

Figure 13: Inner Titanium Bellows

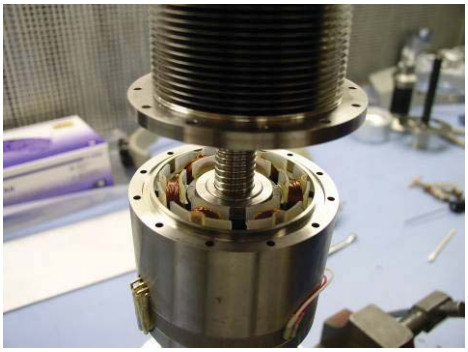

Figure 14: Motor Windings Mounted

A MicroE linear glass scale is connected to the end screw via a set of parallel motion flexures. These flexures provide a thermally stable mount for the glass scale via a low CTE metering rod. The scale is allowed to float relative to the inner tip of the ballscrew, minimizing the coupling of thermal drifts in the parts of the actuator not in the position path. The use of metering rods helps minimize false delta readings at the sensor head. The glass scale is mounted on a carbon fiber rectangular rod. A dummy glass scale is mounted opposite the operating scale to help eliminate bending in the scale due to changes in bulk temperature.

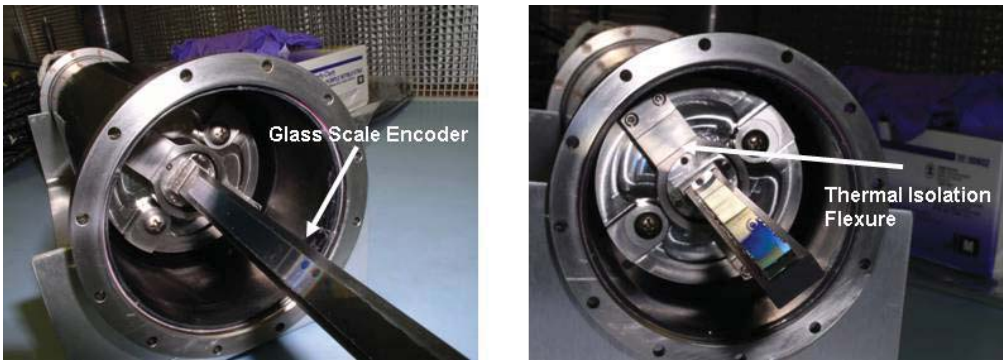

Figure 15: Glass Scale Encoder Mount via Flexures

The sensor head is mounted via a set of parallel motion flexures and the composite tube that acts as a metering rod. This completes the thermally stable sensor mount.

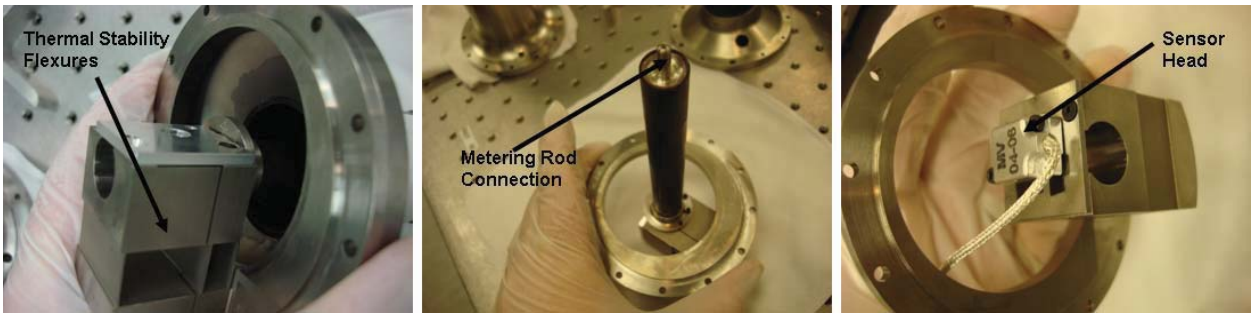

Figure 16: Sensor Mount

All component alignment is achieved via sets of self aligning slip fit radial diameter lips between mating parts. All components are thus axially self aligning to within the tolerances of the slip fits. O-rings are used at all interfaces to eliminate oil leaks.

The actuator connects to ground via a coaxial orthogonal flexure blade flange. The metering rods are hard mounted to each end joint.

Figure 17: Flexured End Joint

Results

The initial resolution requirements for the ballscrew actuator was ±1 micron which was not clearly achievable based on vendor data for ballscrew position as a function of rotation angle. The selection of the Micro-E linear encoder capable of 5-nm position feedback was expected to give position sensing feedback well beyond that which was needed to determine the limits of ballscrew positionability. The direct drive architecture and a preloaded ballnut minimized actuator windup and backlash that enabled maximal position control. Additionally, rather than control the motor commutation based solely on the hall effect sensor as with typical motor control schemes the team also utilized the output sensor data. Since a 3-phase DC brushless motor is being driven, a PID controller reads the linear encoder and outputs 3-phased sinusoidal voltage commands to the 3 motor windings.

Typical trapezoidal commutation uses only the Hall Effect sensors to apply the voltages in a rough way (24 steps per motor rotation). These 3 discrete sensors decode to 6 distinct points per pole, and since there are 4 poles per motor revolution that provides 24 points per revolution. Sinusoidal commutation makes use of the encoder data to fill in the gaps between the Hall Effect transitions and increase the points per revolution from 24 to 409,600. This allows the sinusoidal shape of the back-EMF waveform to be matched much more precisely.

The geometry of the motor is such that sinusoidal commutation converts all of the applied current into useful torque (in the ideal case), rather than into undesirable radial forces. Since all the current is being converted into torque, the variation in torque is minimized and thus torque ripple is reduced compared to

trapezoidal commutation. This is critical for the SIM project because torque ripple induces excess vibrations in the structure that affect other sensitive components of the interferometer.

The results of this architecture were surprising! The PID control loop utilizes 4 position sensor steps to start and stop the screw resulting in repeatable incremental step sizes of 20 nm! This means the DC brushless motor has to be capable of positioning to 100,000 distinct points around a revolution and the mechanical imperfections are beneath the control loop sensitivity. Furthermore, PLADD is able to track a prescribed profile over its entire range with a lag of approximately 16 ± 1.5 microns. However, with correct sequencing or control logic PLADD has an effective positional tracking error of ~3 microns peak to peak at a rate of approximately 3 mm/sec. Below is a short review of the results for a 10-mm move, a 1-micron move, and a 20-nm move. Also included is a discussion of the precision piezo brake effects, future work/improvements, and lessons learned.

10-mm Slew-Nominal Gains

Nominal gains are the gains chosen for well-rounded performance characteristics for a given move size. There is a nominal set of gains for both high resolution (less than 1 micron) moves and low resolution (greater than 1 micron) moves. The nominal gains were set based entirely by trial and error, and are thus not necessarily optimal in any specific sense.

Encoder resolution is increased for moves larger than 1 micron, down to 80 nm due to 22-bit electronics counting limitation. The electronics limitation is a designed in counter size on the FPGA that was not realized to be problematic until late in the build. It is in no way related to the commonly discussed 14-bit analog noise floor in most space electronics. This allows PLADD to cover the entire 120-mm range regardless of the initial zero point location chosen by the operator.

PLADD is able to track a prescribed profile over its entire range with a lag of approximately 16 ± 1.5 microns. However, with correct sequencing or control logic PLADD has an effective positional tracking error of ~3 microns peak to peak at a rate of approximately 3 mm/sec.

In Figure 18, the position command profile is created using constant acceleration to get up to speed, constant velocity for the main portion of the slew, and constant deceleration to approach the command position.

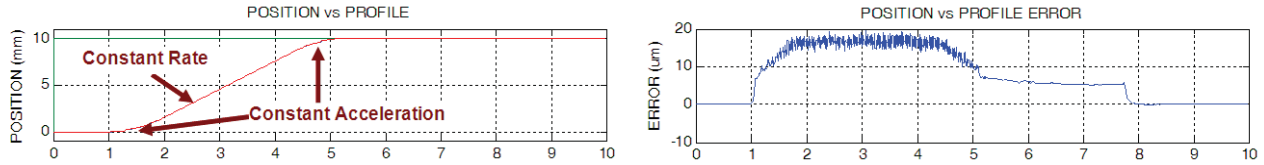

Figure 18: 10-mm Slew (Nominal Gains) - Entire Move

Figure 19 highlights the 16 micron lag during the constant velocity portion of the slew. It also shows the ~3 um error, peak to peak about the 16 micron offset. The sinusoidal commutation is also clearly displayed in this view.

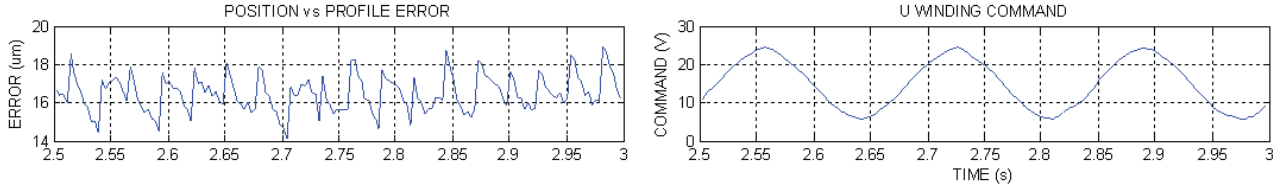

Figure 19: 10 mm Slew (Nominal Gains) - During Slew

Figure 20 illustrates the end of the slew and the initiation of the integral gain to reduce the steady-state error. The proportional gain primarily contributes to slew performance. However, it can only reduce the error down to ~5 um using the nominal gain value. Once within this 5-micron zone the controller's integral term integrates the error and creates the final step to its commanded position.

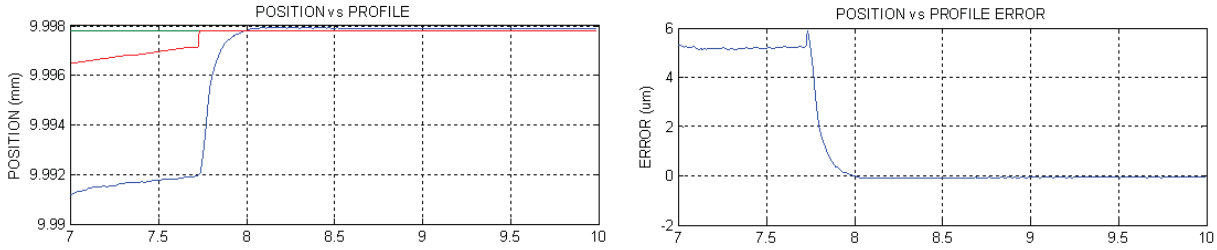

Figure 20: 10-mm Slew (Nominal Gains) -End of Slew

Finally, Figure 21 shows the final result of the integral action. There is a small overshoot, which is then reduced to within ±80 nm of the command position. This is the limit of the capability of low-resolution mode, since the PID controller does not see any motion less than 80 nm (due to the previously discussed 22-bit legacy hardware limitation). The actuator could now be commanded with a new set of high-resolution gains allowing the zeroing in of the actuator down to ±5 nm of the commanded position. It is important to note that for large moves, although the actuator can move to within ±5 nm of the commanded position, in reality the overall accuracy of the move is affected by many other contributors, and are not discussed in this paper. The contributors can be, but are not limited to, thermal drifts in the unmeasured structure during the move, grating accuracy of the glass scale, and inter-grating accuracy. Large move accuracies are extremely complex comprising many error sources and are beyond the scope of this paper.

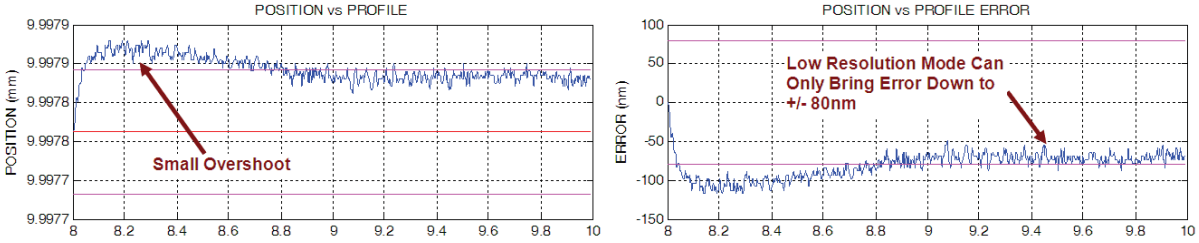

Figure 21: 10-mm Slew (Nominal Gains) - Steady-state Error

1-Micron Step-Nominal Gains

Full encoder resolution of 5 nm can be used for small moves of less than 20 mm. However, actuator velocity requirements generally lead to the use of high-resolution mode for moves only less than 1 micron. Using a different control resolution changes the scaling of the PID controller and thus a different set of gains are used in high-resolution mode versus the low-resolution mode used for large slews.

Figure 22 shows a 1-um move using nominal gains. Figure 23 focuses in on the last part of the move to show the steady-state error. The nominal gains provide a fast response with minimal overshoot. The steady-state error is improved over the low-resolution mode because the PID controller is able to respond to deviations from the commanded position as small as 5 nm. The background noise in the plot will be further addressed in the Noise and Vibration section of this paper.

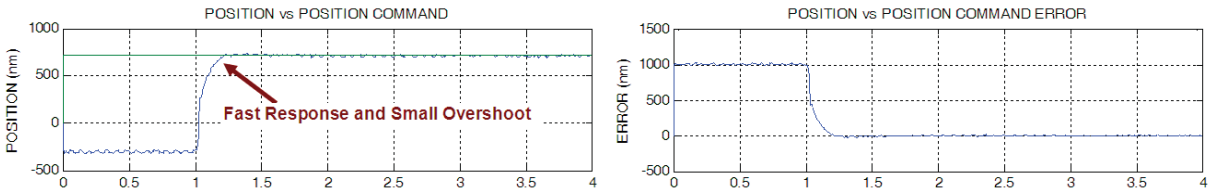

Figure 22: 1-um Step (Nominal Gains) - Entire Move

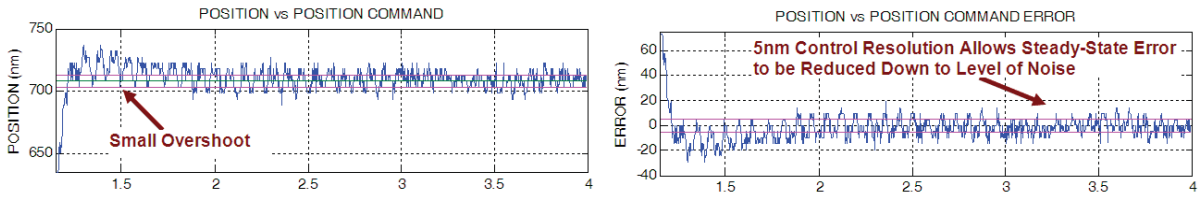

Figure 23: 1-um Step (Nominal Gains) - Steady-state Error

20-Nanometer Step-Nominal Gains

Due to a 4X minimum encoder resolution command limitation within the control system (a legacy piece of hardware originally intended for another use) 20 nm is the smallest incremental step that can be taken. The following series of plots will show 20-nm steps using the same nominal gains as the 1-um steps.

Figure 24 displays a 20-nm move. Overshoot is non-existent, with a move time of roughly one second. At this nanometer level of position control, the noise of the encoder position signal is significant. It has a noise of approximately ±5 to ±10 nm, with occasional spikes of ±20 nm. The nature of this noise is not fully understood, but is conjectured to be from a combination of mechanical (background vibration) and electrical (sensor and wiring noise) sources. Environmental noise and its potential elimination are discussed in the Noise and Vibration, Future Work, and Lessons Learned sections of this paper.

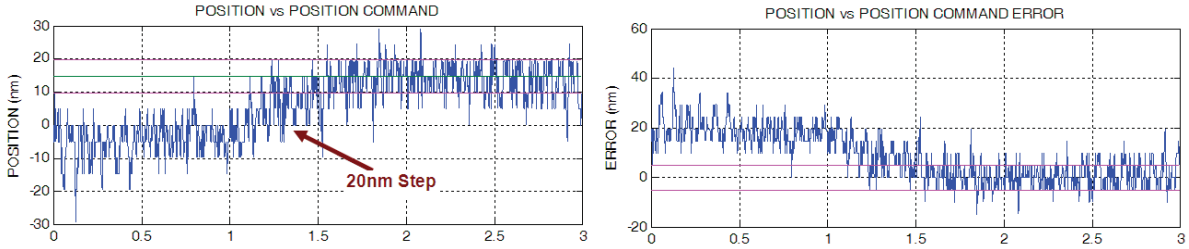

Figure 24: 20-nm Step (nominal Gains)

Noise and Vibration

Nanometer level work requires an extremely quite environment. Vibration and external noise sources can greatly affect test results. All test data was taken in Bldg 318 (Space Interferometry Test Lab), which is specifically designed to be a low noise test facility. The test was performed on an air table separated from the building via an isolation pad. In order to better understand the test noise environment, we sampled 1 second of high rate position data (approx. 1240 samples/second) with no power applied to the actuator. The measurement below is unfiltered data. It is clear that there is a noise disturbance identical to the noise seen when the actuator reaches its commanded position at steady state. This suggests that the noise seen in our position graphs is either environmental mechanical or the electrical noise of the sensor.

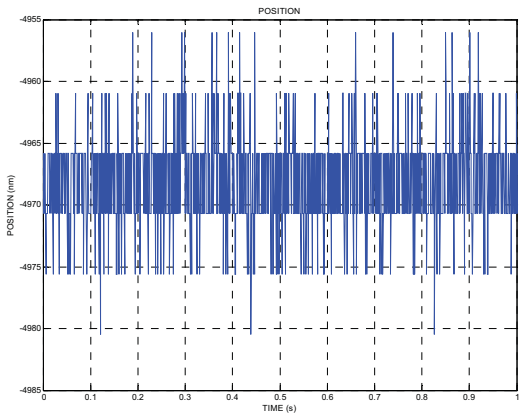

Figure 25: Vibration Measurement - Test Environment and Sensor Noise

Figure 26 shows a 30-point moving average of the steady state error of the actuator with the actuator powered on and attempting to hold a position. Averaging decreases the steady-state error down to ±4nm. The average position is -0.2 nm with a standard deviation of 1.14 nm.

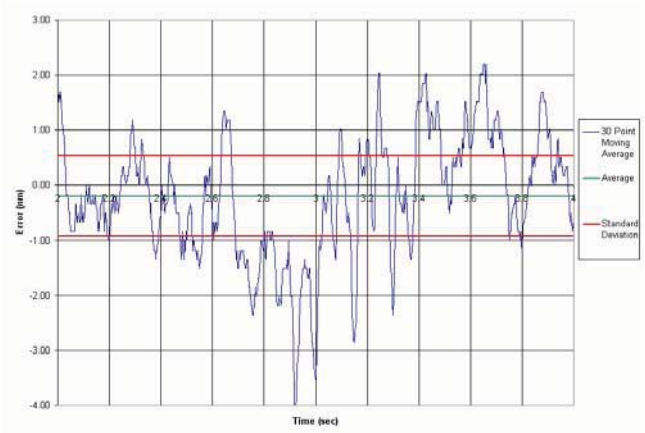

Figure 26: Steady State Error, 30-Point Moving Average

Piezo-Brake Effect

Creating a brake for an actuator performing nanometer size moves is not an easy job. In order to achieve high braking forces, PLADD is equipped with a piezo-actuated brake mechanism. This is required in a coarse stage/fine stage configuration where the coarse stage is turned off and locked while the fine stage operates. A brake is also a necessity when the actuator moves periodically. Through the use of a custom piezo brake and correct power shut off sequencing, the SID team was able to brake the actuator with minimum disturbance. The correct sequencing of the brake and actuator control power off must be performed in order to achieve the best results.

Figure 27 shows a 200-nm step at one second with the brake engaged at the third second. Since the PID controller remains on during the slow braking, it recognizes and corrects for the brake-induced drift, bringing the actuator back to its commanded position. At the ninth second, the power is removed from the motor.

The current brake design degrades the relative accuracy of the move and also requires much longer times to reach a position and stop. The SID team believes that some design alterations could create a brake with much less induced drift. Also, if the actuator were to be used as a fine actuator it could potentially always be powered on, thus requiring no brake.

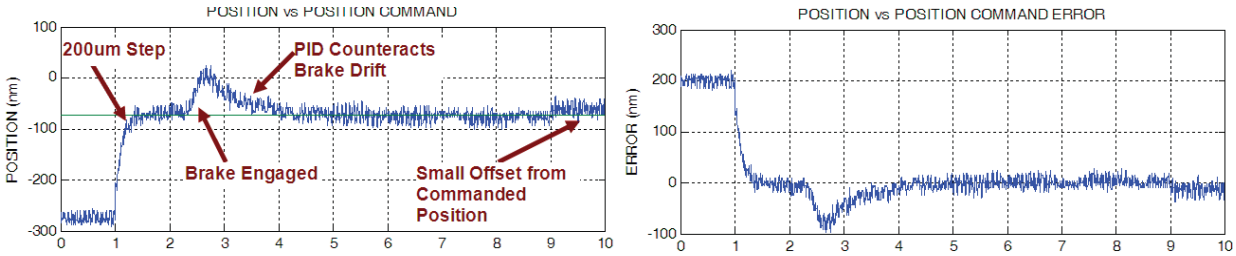

Figure 27: Brake Test (Good Sequencing)

Future Work

To potentially reduce the incremental step size of PLADD down into the 2-5 nm range, we plan on taking the following steps:

Mechanical Modifications

MicroE Mercury II Encoder—Micro E recently introduced its next generation Mercury II encoder capable of obtaining 1.2-nm LSB. Installing this improved read head would allow the controller to attempt moves as small as 4.8 nm.

Mechanical Disturbance Isolation—While the current test setup utilizes an extremely quiet building, an isolation pad, and an air table there are potentially further layers of isolation that could be added to the test setup. Potential gain can be had by installing an isolation layer of foam padding between the test fixture and the table. The row of actuators is also currently mounted along one edge of the air table.

Control Modifications

PLADD's control logic is derived from code developed by JPL's Ted Kopf for the Mars Exploration Rovers. Many elements of the code can potentially be improved to optimize PLADD's performance. The following is a list of potential adjustments.

Filter Encoder Count—The value read from the encoder has high frequency noise of +/- several bits. Currently, this value goes directly into the PID controller. Placing a filter in front of the controller would clean up the signal so that the PID command does not react to small noise variations. This could improve performance for very small step sizes.

Adjust Rate Filter—There is already a filter inside of the PID controller on the internally generated rate signal. However, the time constant of this filter was set for an entirely different application (MER motor control) that used very different encoders. Adjusting this filter could help make the derivative gain useful for this application.

Adjust Controller Scaling—The PID controller scaling was set for a very different application (MER motor control) and is not ideal for the SID ballscrew. Adjusting this scaling could result in performance benefits due to finer tuning of the PID gains.

Add Bits to PID Controller Position Value—The PID controller currently uses 22 bits for the position value. For this application, the limited number of bits forces a choice between high resolution and large range. Increasing the bits allocated for the position value would allow high resolution control over the entire ballscrew range. This modification is tied in with the scaling modification listed above, as the scaling is effected by the number of bits.

Control Down to Encoder LSB—The PID controller does not allow delta position commands less than 4x the encoder resolution. It might be worth investigating the reason for this in detail to figure out if it is feasible to remove that limitation. The idea is to find out just how far down we can push the incremental command resolution.

Reduce Encoder Noise—The encoder noise is probably due to a combination of mechanical and electrical sources. Investigation into the nature of this noise might lead to ways to reduce it. One idea is to improve the shielding of the cable between the encoder read head and the encoder interpolation module. This cable transmits sensitive analog signals that are susceptible to noise.

Gain Calibration—By calibrating gains for many different move sizes and adjusting the command software to generate such commands on a per move basis PLADD could improve many performance parameters such as response time, overshoot, lag, etc.

Lessons Learned

1. **Nanometers are really, really small.**
When working in small numbers it is easy to forget how small nanometers truly are. In real life mechanical terms a nanometer is approximately 1/50,000 of the diameter of a human hair. When dealing with numbers of this size, deflections of mechanical components can play a large role in performance. Movements may not be actual position changes, like one is familiar with, but instead a "wind up" or deflection of the mechanical components in the drive-train. A well-designed system should minimize these effects. The remaining system deflections can be actively eliminated by employing an encoder in a location such that it measures the output of the actuator that one is interested in controlling. Also, environmental noises, especially when not in a "quite" building may completely overwhelm any experimental results

2. **Nanometer incremental step size is achievable with no gears, levers, or hydraulic reducers.**
This one speaks for itself. It also was something I never expected possible.

3. **Sensor technology is the limiting factor for fine positioning when proper mechanical design considerations are taken.**
Sensor technology is a fast growing field. As the sensor technology progresses one should not hesitate to take advantage of technology. This especially applies to space-flight applications where a fear of the unknown can often be crippling, especially when attempting to actuate mechanisms with finer resolutions and more precision.

4. **A clear path for oil circulation/pumping shall be designed into the system to avoid excessive driving loads.**
In designing our actuator a clear path for the oil to pass was not considered. Upon complete assembly and operation it was discovered that much of our reserve torque was required to force the oil lubricant through the motor, screw, nut, bearing assembly. This leads to a reduced maximum velocity and an increased input of heat into to the actuator under continuous operation.

5. **Full alignment adjustability makes everyone's job easier. Access to the sensor without disassembly is vital to technician (or assembling engineers') sanity.**
The actuator's design requires that the sensor is housed inside a carbon fiber tube. The sensor cannot be tested for functionality or alignment until the actuator is assembled. There is also no way to easily adjust the sensor once it is determined it is not aligned properly (inevitable, as it is practically impossible to blind assemble the sensor in perfect alignment). This requires that the actuator be slightly disassembled, shims guessed on based on previous experience and the whole procedure repeated. This can be extremely frustrating and time consuming. This problem may be eliminated as sensor technology improves and alignment tolerances grow. However, until then be sure to design in alignment adjustability and allow for active alignment post-assembly.

6. **Instrument thin section bearing should be used with caution as they are extremely easy to damage.**
We ran into a few issues with the handling of the thin section bearings during disassembly of the actuators. More than one bearing was lost as a result of improper handling by technicians. Take caution with your technician choice and your handling procedures.

7. **Obtain external mechanical noise measurements to isolate electronics noise and environment noise.**
If external sensors are not used to measure the mechanical environmental noise it is impossible to troubleshoot noise issues between the mechanical and electrical systems. The use of a local mechanical

noise sensor can help in this process greatly. This is something we did not foresee, and thus we are still uncertain as to the root of our environmental noises.

8**. Be aware that bellows buckle in proportion to their linear stiffness. Be cautious when using them to react torque over a large stroke.**
PLADD's design uses titanium bellows to react out the rotational torque in the screw. Our bellows are extremely soft as they must travel 120 mm full stroke. The first buckling mode of the bellows occurs when a torque is applied. The bellows collapse down as it buckles. The torque required to induce buckling is directly related to the linear stiffness of the bellows. This phenomenon was ignored during design. Fortunately our actuator works at the bitter edge of buckling, but does not buckle. Rotational alignment of the bellows is also critical to buckling, as a misalignment, or initial rotational load lowers the buckling torque drastically.

Conclusion

The SIM Siderostat team successfully outperformed our initial goal of less than 1-micron repeatable incremental step size by a factor of 50. We strongly believe we will attain incremental step sizes of 2-5 nm for large ranges given the current sensor technology. Through the elimination of gears and their inherent backlash we have been able to show that the mechanical system is not the limiting factor in fine positioning applications, if appropriate design considerations are taken into account. We have realized that sensor technology more than any other factor is the limiter with regards to fine positioning over large ranges. We hope to be able to further develop this novel linear actuator concept and to eventually use it on SIM in our PLANETQUEST, and many other future projects.

Acknowledgements

The research described in this (publication or paper) was carried out at the Jet Propulsion Laboratory, California Institute of Technology, under a contract with the National Aeronautics and Space Administration. I would like to thank all involved with this effort for their hard work and dedication towards achieving our goals. Those involved beyond the authors were Rob Calvet, Yutao He, Bruce Scardina and Don Benson. I would finally like to thank Caltech and NASA for providing the great freedom to explore the unknown.

References

[1] Edberg, Stephen J, "SIM PlanetQuest: A Mission for Astrophysics and Planet Finding", NASA/JPL White Paper, May 2005
[2] Koenig, John, "SIM Siderostat Ballscrew Testbed Electronics Report", JPL, Feb 2007
[3] Moore, Don, "Actuator Logs and Assembly Notes", JPL, 1999

Development of a Low-Cost Fine Steering Mirror

Steven R. Wassom and Morgan Davidson*

Abstract

The Space Dynamics Laboratory has used internal funds to develop a prototype low-cost two-axis fine steering mirror (FSM) for space-based and airborne applications. The FSM has a lightweight 75 mm-by-150-mm high-reflectance mirror, high angular deflection capability for along-track ground motion compensation and cross-track pointing, and a 70-Hertz bandwidth for small amplitudes to help cancel unwanted jitter. It makes use of off-the-shelf components as much as possible. Key performance parameters are: Clear aperture, 75 mm; elevation angle, ±15 deg (mechanical); azimuth angle, ±60 deg (mechanical); slew rate, greater than 75 deg/sec; bandwidth, 70 Hz; steady-state average error, about 1 arcsec; average power dissipation, 0.4 Watts; mirror surface, figure, <0.1 waves RMS; and total mechanical mass, 1 kg. Key components for the elevation axis include a rotary voice coil and a unique patent-pending non-contact feedback sensor. The azimuth axis features a brushless DC motor and a high-resolution optical encoder. Rapid prototyping, autocoding, and real-time hardware-in-the-loop (HIL) testing were used to develop the control algorithms. Additional accomplishments include temperature mapping of the feedback sensor, inventing a successful passive launch lock, launch vibration testing, and subjecting the system to a space-like environment at pressures down to 1e-7 torr and temperatures down to 164 K.

Introduction

Over the past two years, Space Dynamics Laboratory (SDL) has used internal funds to develop a prototype low-cost two-axis fine steering mirror (FSM). This mechanism is intended to have a broad flexibility for both space-based and airborne applications.

The main purpose of this effort was to reduce the cost of a normally expensive technology while maintaining performance, thus enabling this capability for more applications. A $2 million price tag has not been uncommon. The first year's development effort required about $200,000 and resulted in a successful working prototype (Ref. 1).

This report will review the accomplishments of the first year and describe the additional progress of the second year that includes:

- Subjecting the system to a space-like environment at pressures down to 1e-7 torr and temperatures down to 164 K
- Verifying that the system will survive a typical launch vibration test profile
- Performing temperature mapping of the patent-pending feedback sensor
- Inventing a successful passive launch lock
- Mounting the system on a portable cart for demonstrations

Figure 1. Prototype FSM

* Space Dynamics Laboratory / Utah State University Research Foundation, North Logan, Utah

General Requirements

Although this FSM was not intended for a specific program, some general top-level requirements and performance goals were established. An angular position accuracy of about 1-2 arcsec was desired to minimize jitter. A clear aperture of 75 mm was chosen as a good starting point, with the intention that the design be scalable to larger or smaller apertures. An elevation axis deflection of ±15 deg (mechanical) was chosen to perform ground motion compensation (GMC) along the flight path, and the azimuth axis deflection was chosen to be ±60 deg to achieve both off-track pointing and the ability to rotate far enough to view an on-board calibration source. A high bandwidth approaching 70-100 Hz was desired to enable jitter control during pointing and scanning.

The final performance parameters achieved are tabulated in the section below describing the test results.

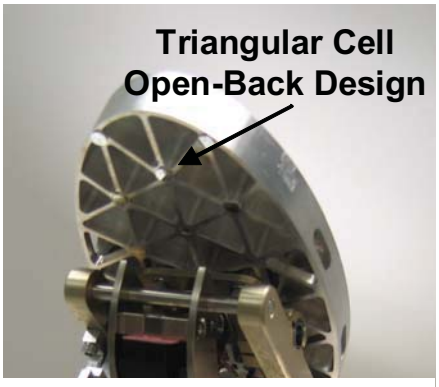

Figure 2. Back View of Mirror Showing Triangular Rib Structure

Design Description

Mirror Design

To meet the aperture and bandwidth goals, the mirror needed to be lightweight and low cost. Mirror trades included several materials (Be, Al, SiC) and shaft connections (bonded, bolted, or integral). The final selection was a lightweighted Al mirror to keep costs low, and a bolted connection to facilitate future design changes.

The flat mirror geometry provides a 75-mm aperture when scanned to a 60-deg optical angle (30-deg mechanical angle). The flat mirror is elliptical with a 75-mm-by-150-mm clear aperture. Thermal considerations coupled with the light-weighting requirement for high bandwidth necessitated the open back form shown in Figure 2, which provides a 60% reduction in mass compared with a solid mirror. Total mirror mass is 0.16 kg corresponding with a 17 kg/m^2 optical surface area mirror density.

Triangular cells were selected over hexagonal or square cells as they are considered to be the optimum cell geometry (Ref. 2). Triangular cells also work well in providing a uniform distribution of ribs across the part and structure for mounting features.

The mirror is mounted on four flexure-isolated pads in the center of the mirror back. The mounting pads require flexure isolation to reduce mounting distortion of the optical surface; however, the stiffness of the flexures must balance mounting distortion isolation and mirror modal response. Finite element analysis was used to find the optimum performance balance for the scan mirror application.

Mirror Surface Finish

The mirror surface is fabricated using single point diamond turning (SPDT) combined with post-polishing. An RMS surface roughness better than 20 angstroms is obtained utilizing a post-polishing method termed VQ for “Visible Quality”. This process aids in the removal of the grooves typical from SPDT.

The RMS surface figure of the mounted mirror was measured to be near 1/12 wave HeNe at 210K. This shows the capability of this mirror to hold good optical figure. Test and analysis results are discussed in detail later in the paper. Table 1 summarizes the optical performance specifications.

Table 1. Mirror Optical Performance Specifications

Description	Specification
Mirror Mass	0.16 kg
Operating Temperature	210K
Optical Aperture @60 deg Optical Angle	75 mm
RMS Surface Figure	< 1/10 waves HeNe
RMS Surface Roughness	< 20 angstroms

Elevation Axis

For the elevation axis bearing, options considered were flexures, flexural pivots, and conventional ball bearings. Flexural pivots were chosen based on their high deflection capability, negligible friction, and SDL's extensive experience with these devices in their Michelson interferometer.

Actuator choices for the elevation axis included piezo actuators, magnetostrictive actuators, voice coils, brushless DC motors, and stepper motors. A rotary voice coil was chosen primarily for its favorable ratio of rotation angle to package size, since only a limited rotation was required. Other advantages to the rotary voice coil are simplicity, low cost, and high bandwidth potential.

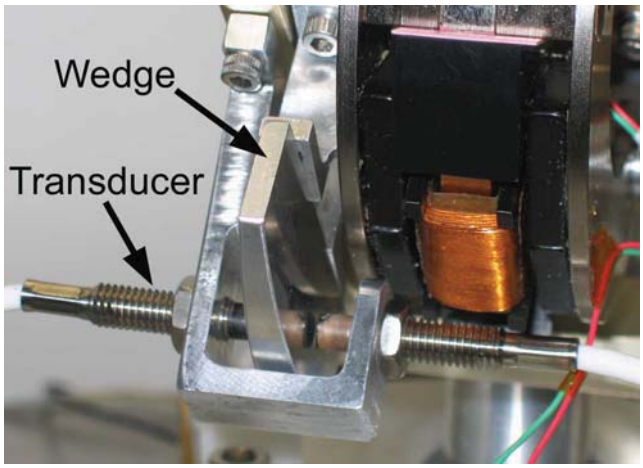

Figure 3. Close-up of Wedge Sensor, Showing Precision Wedge and Displacement Transducers

The moving coil of the elevation axis and the mirror are bolted to a mirror mount, which is supported on flexural pivots. The pivots and the voice coil magnets are mounted to a compact U-shaped yoke. The mounting scheme for the pivots is the same that is used in SDL's Michelson interferometers. The pivots were sized to support the rotating mass without failure during a representative launch load and to ensure virtually infinite life during on-orbit duty cycles.

The feedback sensor for the elevation axis was selected from the following options: non-contact proximity transducers (inductive or capacitive), strain gages, optical encoders, resolvers, and inductosyns. Inductive non-contact sensors were chosen for their low weight, compact packaging, low cost, high resolution, and SDL's related experience.

The feedback device for the elevation axis is unique and patent-pending. In this angular measurement device (called the wedge sensor), two non-contact inductive displacement transducers are arranged in opposition facing a moving target wedge made of aluminum (see Figure 3). These transducers exhibit excellent resolution and repeatability over a limited range. The precision wedge extends the range of the non-contact transducers by converting angular motion to limited linear motion. Using two opposed transducers minimizes the sensitivity of the device to relative displacements out of the plane of symmetry of the wedge (wobble, vibration, misalignments, etc). Nonlinearity in the wedge sensor over the large deflection angles was mapped using a theodolite. This map was incorporated into the elevation axis control algorithm.

Azimuth Axis

The azimuth axis requires much larger deflections and needs to move a larger inertia. Consequently, the bearing trades were more limited. Ball bearings were chosen due to their extensive heritage in space and SDL's experience base. Actuator options were brushless DC motors and stepper motors. Brushless DC was chosen for its high bandwidth and accuracy capabilities and typically long service life. Feedback device options were encoders, resolvers, and inductosyns. An optical encoder was chosen for high accuracy, low mass, and related experience.

The output shaft of the motor is connected to the yoke supporting the elevation axis. The optical encoder has a resolution of 4.5 arcsec per count. Although this drive system is not designed for space, it uses the same type of components as another SDL scan mirror drive system, which has been operating flawlessly for over six years in orbit. Upgrading the azimuth axis to space-worthiness has low risk.

Electronics

Two independent sets of electronics are used to drive the azimuth and elevation motors. The azimuth motor is driven using a commercial linear brushless servo amplifier. The elevation motor uses a simple amplifier circuit based on an operational amplifier.

Structural/Thermal Analysis

Mirror Modal Analysis

Finite Element Analysis (FEA) was used to predict the modes of the mirror. The high control system bandwidth near 70 Hz required the mirror modes to be considerably higher.

A normal modes analysis was run. Table 2 lists the mode shape descriptions. Figure 4 depicts the first mode: a torsional mode about the Z-axis at 270 Hz. The majority of the deformation and strain energy is in the flexure mount.

Figure 4. Mirror Mode 1, Torsional about Z-Axis, 270 Hz

Mirror Mounting Distortion Predictions

Some wave-front error (WFE) is caused when non-flat surfaces are mated together with a bolt preload, producing strain in the mated parts. FEA was again used to predict optical surface displacement.

The analysis assumed that the combined worst-case flatness tolerance of the two mating surfaces produces a Z-axis forced displacement of the mounting surface. The mounting pads on the mirror have a coplanarity requirement of 2 µm. The mating surface is assumed to have a coplanarity or flatness of 12.7 µm. Conventional machining can get surfaces as good as 7.6 µm in flatness. This approach conservatively assumes that all the strain occurs in the mirror as if it were mated to an infinitely stiff part.

Table 2. Mirror Modes Summary

Mode Shape Number/Description		Frequency (Hz)
1	Mirror torsional, about Z-axis	270
2	Mirror rocking, about Y-axis	390
3	Mirror vertical or Z-direction translation, with mirror bending (saddle mode)	1230
4	Complex X-direction side to side translation with mirror surface bending/waves	2700
5	Complex Y-direction side-to-side translation with mirror surface bending/waves	2900
6	Second saddle mode	3100

Optical surface deformations from each of the enforced displacements are then transformed into surface normal interferometric space using Zernike polynomial fitting. Piston and tilt can then be subtracted, resulting in WFE due to mounting distortion. The results show that distortion in the mirror is dominated by astigmatism and tetrafoil. Predicted surface normal displacements are shown in Figure 5 with the dominant aberrations identified in Table 3.

Mirror Thermal Elastic Predictions

Thermal simulation of the FSM in a representative orbit was used to evaluate expected performance. For the simulation, the representative orbit was a nadir-pointing low-Earth orbit. A typical baffle geometry was assumed. Standard minimum and maximum values were used for long-wave infrared heat from the earth and for reflected sunshine. Diurnal temperature profiles for the system as well as a detailed mapping of temperature variation across the face of the mirror were the principle outputs from the thermal simulation.

Table 3. Zernike Polynomial Coefficients Ordered by Highest Contributor

Standard Zernike No.	Zernike Description	RMS WFE (waves HeNe)
14	Second order Astigmatism y	0.018
6	First order Astigmatism y	0.017
27	Second order Tetrafoil y	0.005
26	Third order Astigmatism y	0.005

Table 4. Results of Thermal Analysis

	Units	Case 1	Case 2	Case 3
Azimuth motor / yoke isolation	W/K	0.019	0.007	0.007
Baffle temperature	K	160	160	180
Average mirror temperature	K	210	201	210
Mirror face gradient	K	0.11	0.08	0.07
Mirror face distortion Z-dir*	nm	43	27	22

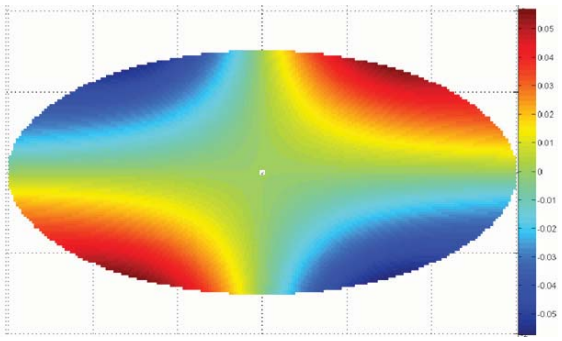

Figure 5. Predicted Surface Normal Deformations

Thermal analysis results showed the two most sensitive elements of the thermal design were the level of thermal isolation between the yoke and the azimuth motor and the baffle temperature. These parameters were the principle drivers in determining the operational temperature of the mirror. Because the gradients across the mirror are affected by the overall mirror temperature, the optical distortion was weakly coupled to the same parameters, showing small changes as the mirror temperature and baffle temperature varied. Table 4 shows various amounts of isolation and baffle temperatures and the resulting mirror temperature and optical distortion. A typical diurnal temperature profile during one orbit and the resulting thermal gradients across the mirror face are shown in Figure 6.

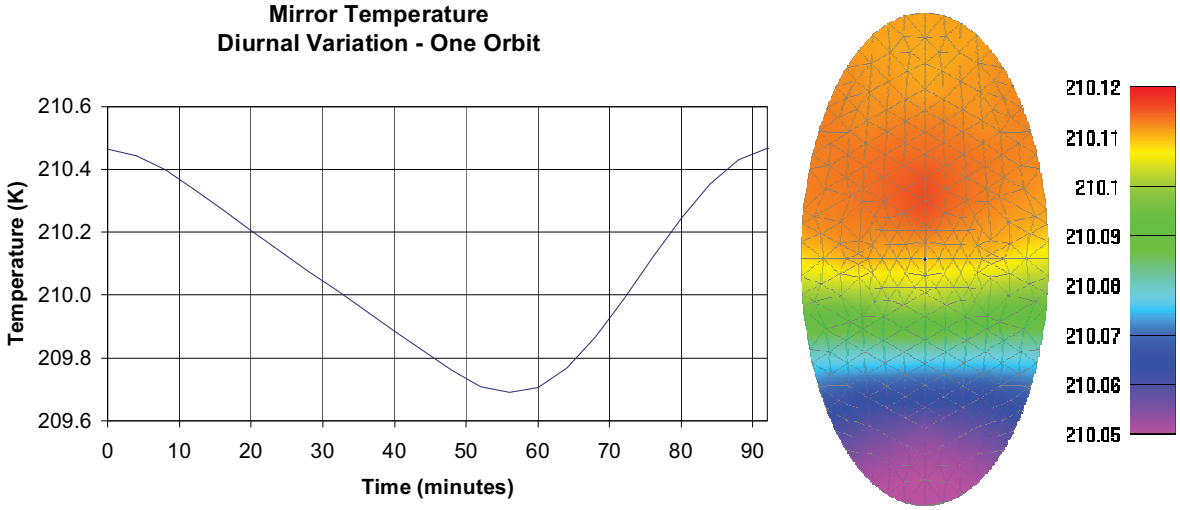

Figure 6. Typical diurnal temperature profile (left) and thermal gradients across mirror face (right)

FEA was again used to predict elastic distortion caused by thermal gradients across the mirror during operation in space. Coefficient of thermal expansion (CTE) mismatch at the mounting interfaces has no impact given that the mating materials are aluminum.

The thermal elastic analysis predicts a peak-to-valley sag (Z axis on a flat mirror) of 22 nm or 0.034-wave HeNe (see Figure 7). This distortion is very small and should not be a factor in maintaining a good optical figure in operation.

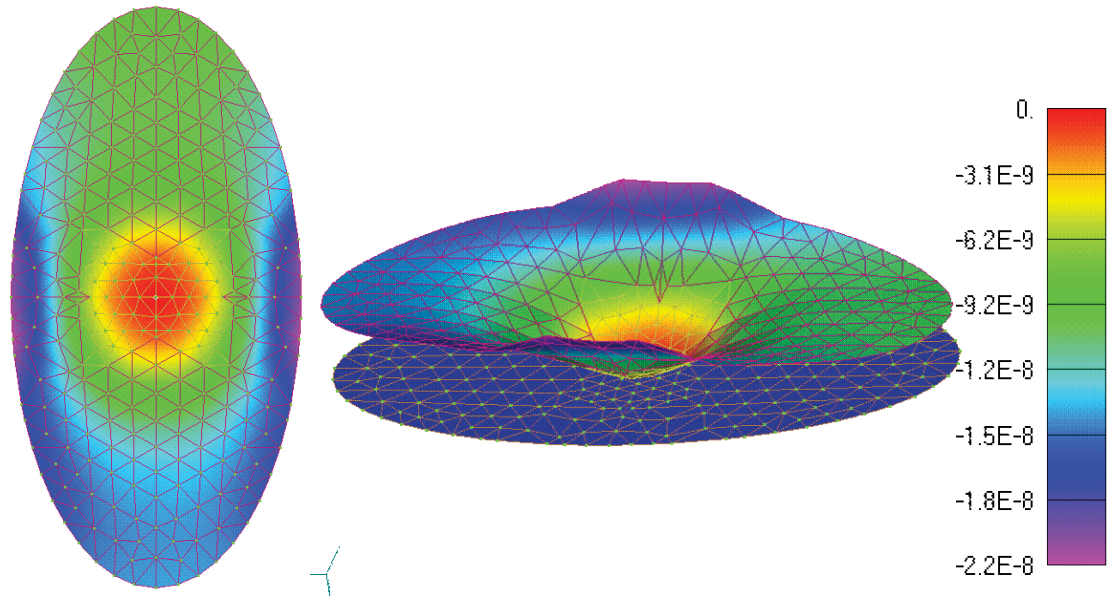

Figure 7. Sag (meters) of Optical Surface due to Thermal Elastic Deformation

Control System Development

Instead of following a traditional waterfall or serial development process for the elevation and azimuth closed-loop control algorithms, SDL used the Rapid Prototyping Methodology (RPM) spiral development process shown in Figure 8. This process can be quickly iterated due to its software-driven nature. Customized features for line-of-sight (LOS) optical pointing systems include: integrated end-to-end modeling, co-simulation, and 3-D visualization of structural and system dynamics, controls, and optics; automatic C-code synthesis from block diagrams; real-time hardware-in-the-loop (HIL) testing; dynamic automated ray tracing, and a customizable GUI to monitor testing and change control parameters "on the fly." Eventually, the block diagram transforms from a virtual model of the system to the complete integrated assembly. The control algorithm is then embedded in the actual computer.

The advantages of RPM include:

- virtually no software written by hand (except for occasional device drivers)
- substantial savings of time and money in code generation
- short iteration cycles that result in early problem identification and solution
- changes can be made early in the design cycle at the component level

The left side of Figure 9 shows the multi-body dynamic model of the FSM. This high-fidelity model includes flexible- and rigid-body representations of all major components (mirror, mirror flexure, flex pivots, actuators, etc.). The right side of Figure 9 shows the top-level hierarchy of the block diagram simulation of the FSM control system with the dynamic model embedded for co-

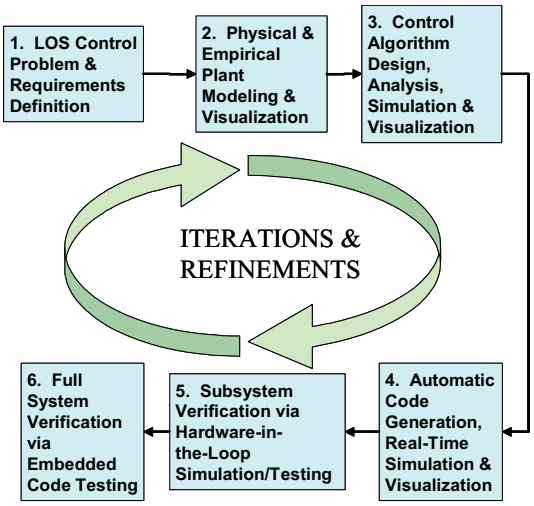

Figure 8. SDL's RPM for Control Systems

simulation. Each of the blocks shown has detailed algorithms and calculations within it. Analytical tools in the software were used to determine the control gains, shape the open- and closed-loop responses, and simulate the step response and frequency response.

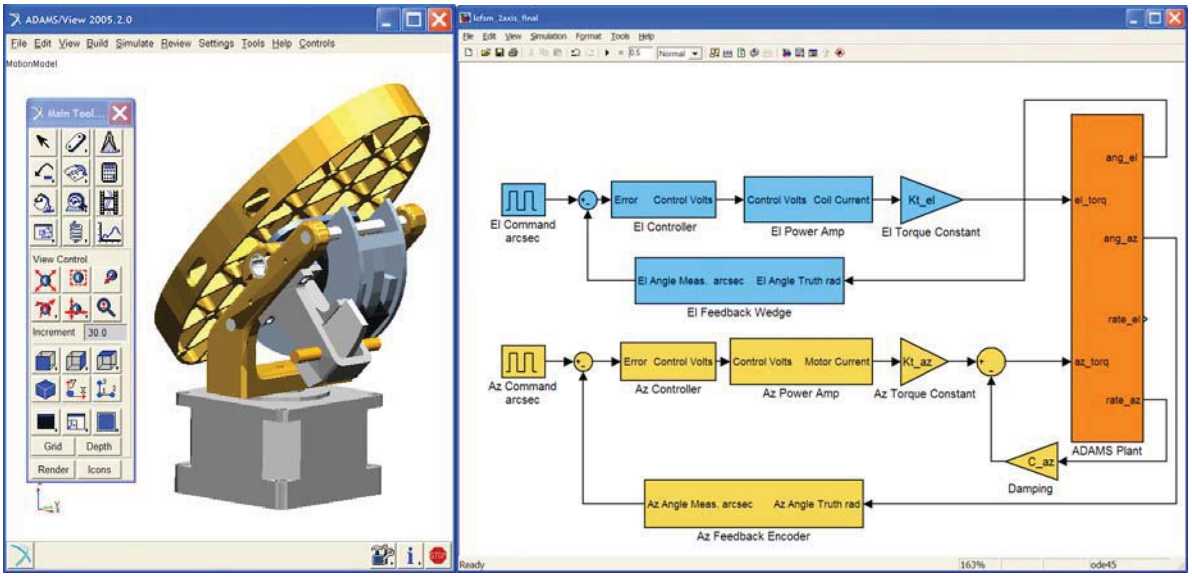

Figure 9. FSM Dynamic Model

Test Results and Model Validation

Mirror Surface Figure Testing

Surface figure tests were performed on the mirror to better understand the optical performance and validate the predictions. Mounting distortion and thermal elastic distortion at cryogenic temperatures were tested using a commercial Zygo Fizeau interferometer.

The test setup (see Figure 10) consisted of mounting the mirror in a bell jar test chamber on an optical bench. The mirror is insulated and baffled to reduce thermal gradients during testing. The mirror looks out the bell jar window. The interferometer is set up to view the test mirror through a fold mirror. The fold mirror is necessary to adjust tilt on the mirror, as it is very difficult to move the large bell jar or the interferometer in fine increments.

It should be noted when viewing the test results that the interferometer only spans 100 mm of the 150 mm elliptical test mirror aperture. The test mirror aperture outside the 100-mm center was tested separately with the results showing a more behaved WFE. Also, WFE from the fold mirror was not removed from any of the results.

Room temperature tests were performed with various mounting torques applied to the mirror. The interferometric results show very little distortion from mounting. Figure 11 shows the WFE after applying 0.68 N·m to the number 4 screws. The RMS WFE error is essentially 0.025 waves HeNe with or without the applied torque. The circular grooves noticeable in the interferogram are residual SPDT marks in the

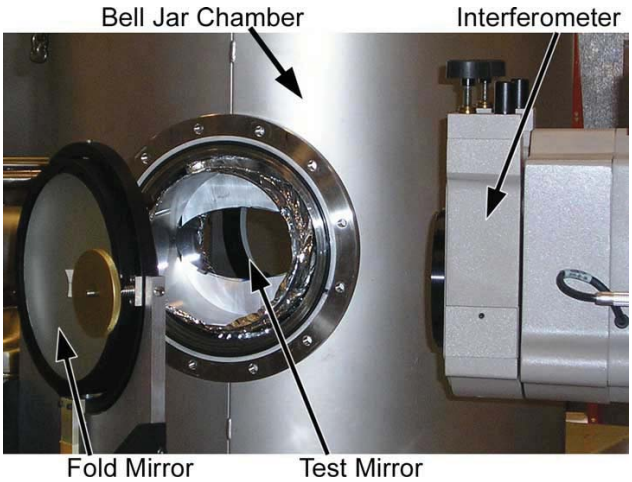

Figure 10. Mirror Surface Figure Test Setup

mirror. The polishing house is confident that these marks can be polished out of future mirrors.

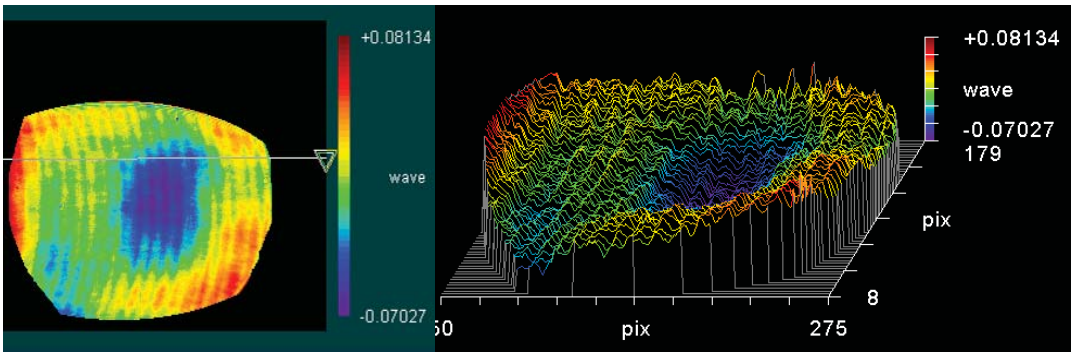

Figure 11. Mounting Distortion Test, 0.68 N·m Torque Applied

The mirror was then cooled with liquid nitrogen. Testing the mirror over temperature showed that WFE is dominated by the CTE mismatch of the VQ coating and the aluminum substrate producing bending in the mirror at the low cryogenic temperatures. The aluminum shrinks more at cold temperatures due to its larger CTE producing a slightly convex mirror. This bimetallic bending is much less than is typically seen with nickel-plated mirrors. Figure 12 shows how the mirror shape changed from concave at 292K to convex at 186K. RMS WFE error measured at 292K and 186K were 0.039 and 0.106 waves HeNe respectively.

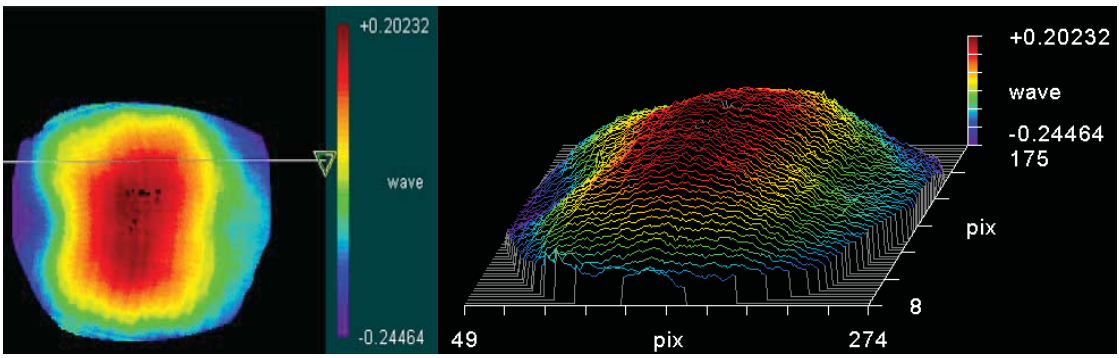

Figure 12. Interferometric Measurements at 186K

Figure 13 shows the RMS, PV, and Power WFE from 292K to 141K. Using this data, the RMS WFE at the required operating temperature of 210K is linearly interpolated to be nearly 0.083-wave HeNe.

The mirror retained a very good figure at 141K with a deformation shape nearly identical to the 186K measurement and a 0.125-wave RMS WFE. At temperatures lower than 141K, the WFE did not increase noticeably. Wave front measurements were measured as low as 92K with very similar performance as seen at 141K. Transient thermal gradients affected the accuracy of this data. Quilting or rib print-through was not detectable in the testing, even at temperatures as low as 92K. The mirror does however show substantial high order WFE.

The mirror surface figure exhibits great stability under mounting and cryogenic temperatures with some expected and very small bimetallic bending of the optical surface. At the 210K operating temperature the RMS WFE is near 0.083-wave HeNe.

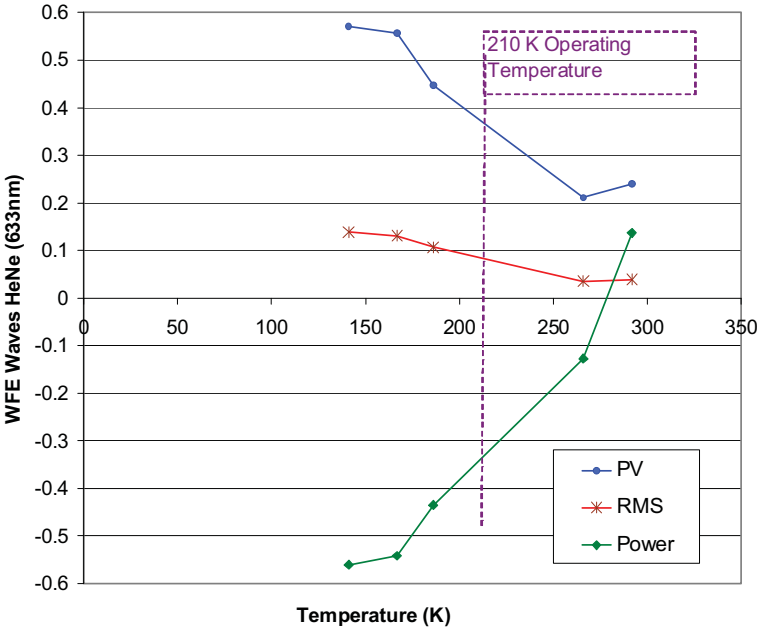

Figure 13. Mirror WFE at Cryogenic Temperatures

Control System Performance Testing

Considerable testing was performed to quantify the control system performance. The real-time HIL tools of the RPM process were used to test and optimize the control laws for both the elevation and azimuth control loops. A graphical block diagram was used to monitor the performance and change the control parameters "on the fly" as the tests were running.

Tests performed included large and small steps, and small-angle frequency response. The frequency response tests were performed using a control systems analyzer, which excited each axis with a sine sweep of 100 arcsec amplitude and a frequency range from 1 Hz to 1000 Hz, and analyzed the resulting waveforms for gain and phase shift. The analyzer was also used to test individual components and subsystems and thus obtain their open-loop transfer functions, which were then implemented in the model.

As an example of model validation, Figure 14 shows the response of the azimuth axis to a 30-deg step and compares it to the prediction from the simulation. The response is well behaved with little overshoot. The average slew rate from 0 to 100% of the commanded angle is 164 deg/sec.

Performance Summary

Table 5 summarizes the performance of the final prototype in key areas.

The mass total is only for the mechanism and does not include the electronics, since the electronics are only breadboard at this stage of the development.

The average power was determined from the simulation by commanding both axes to perform continuous simultaneous slow scans, as would be used for GMC. The peak power was obtained by commanding both axes to do a large-angle step simultaneously.

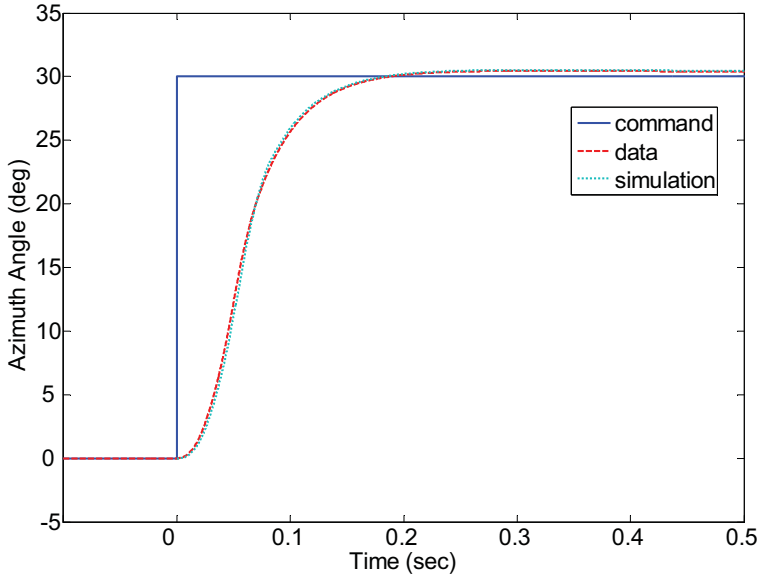

Figure 14. Azimuth Axis Large-Angle Step Response

Table 5. Performance Specifications of Final Prototype

Specification	Value
Aperture (mm)	75
Mass (electronics not included) (kg)	1.0
Avg. Power (W)	0.4
Peak Power (W)	30
Azimuth Rot. (mechanical deg)	±60
Elevation Rot. (mechanical deg)	±15
Azimuth Error Mean (arcsec)	<1
Azimuth Error Std. Dev. (arcsec)	<3
Elevation Error Mean (arcsec)	<0.05
Elevation Error Std. Dev. (arcsec)	<6.5
Azimuth Slew Rate (0-100%) (deg/sec)	160
Elevation Slew Rate (0-100%) (deg/sec)	75
Bandwidth (Hz, 100 arcsec amplitude)	70
Gain Margin (dB)	6

The error mean and standard deviations were calculated using the statistics of the angular position data at the end of a 10-second step-and-hold for both large and small steps. This is not absolute mirror pointing accuracy, but rather the tracking error between the commanded angle and the angle measured by the encoder for azimuth and the wedge sensor for elevation. Absolute pointing accuracy, as measured with the theodolite, was about 0.03 deg at room temperature.

The azimuth error is largely due to the limited counts of the encoder, 288000 counts over 360 deg of rotation, which results in 4.5 arcsec/count. The encoder toggles by one count during steady state, resulting in the error.

The elevation axis is extremely repeatable, as shown by the small mean error; however, the noise, represented by the error standard deviation, is larger than desired. The noise is attributed mainly to the 16-bit A/D computer card's peak-to-peak noise of over 15 counts, as claimed in the card manufacturer's specification sheet. This equates to about 25 arcsec of peak-to-peak noise, when the 16-bit resolution is applied to the full 30-deg mechanical angle of the elevation axis. Some noise is also generated by the wedge sensor electronics box. A digital moving average filter was applied to the wedge sensor feedback, which helped considerably. The control algorithm also contains a derivative term in the forward loop, which tends to enhance the noise.

The closed-loop bandwidth for each axis, as measured using the control systems analyzer, was about 70 Hz at the -3 dB point. The gain margin of 6 dB was verified by doubling the control algorithm gains in each axis and performing a step response test to determine that the system remained stable, which it did.

FSM Portable Demonstration

Figure 15 shows the FSM portable demonstration system, which includes the FSM, the breadboard electronics, the host and target computers, and a laser for "light show" demonstrations. The system was programmed to project a Lissajous figure and an "S" figure on the ceiling at high frequencies, and also to do slow scans for audience visualization.

Wedge Sensor Temperature Mapping

The current wedge sensor for feedback experiences drift with temperature, so a mapping was performed to show feasibility of achieving high absolute pointing accuracy. One possible application of the FSM requires a ±50-arcsec absolute pointing accuracy over a 0-40°C temperature range. The angle was measured using an autocollimator and mapped versus sensor voltage and temperature. Figure 16 shows that the results appear predictable and highly repeatable, verifying feasibility of mapping.

Figure 15. Portable Demonstration

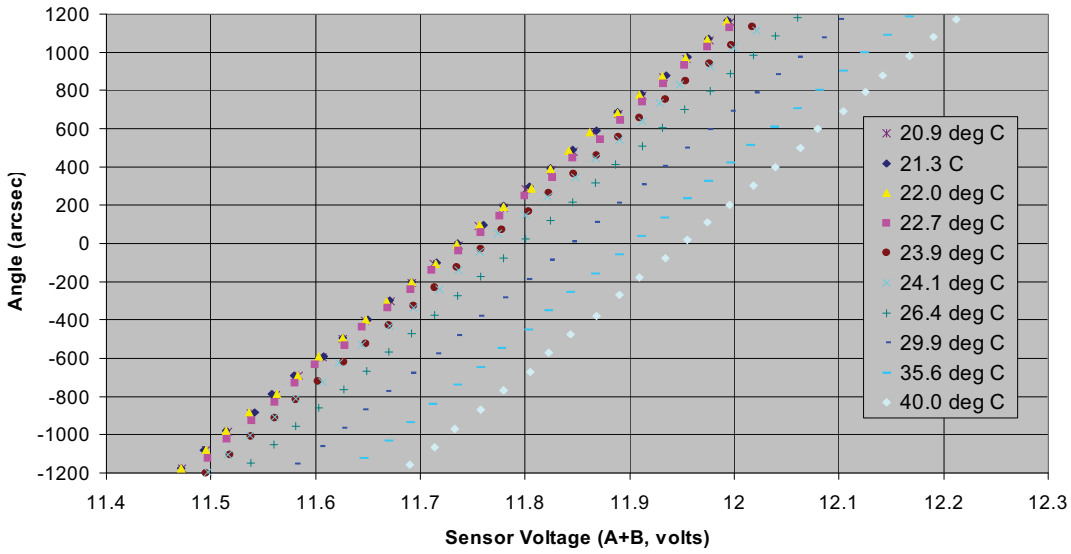

Figure 16. Temperature Mapping

Launch Lock

Launch lock options included a permanent magnet, a shape-memory alloy pin-puller, and a wax actuator. The magnetic concept was chosen based on simplicity and a 6-year on-orbit heritage with another SDL scan mirror.

The patent-pending launch lock is shown in Figure 17. The combination of a magnet with a cone-shaped receptacle provides restraint in all directions. The restraint force is adjustable by changing the air gap, which is done by screwing the cup holding the magnet in or out and locking it with the set screw. The holding force is high enough to restrain motion during external loads, but is low enough that the actuator can overcome the holding force to release the lock. For this particular prototype, the latch force can be about 2.2 N maximum, since it is limited by the maximum current (~1 amp) and torque of the voice coil actuator. Analysis was performed to validate the design by applying the launch vibration spectrum to the dynamic model of the FSM shown in Figure 9.

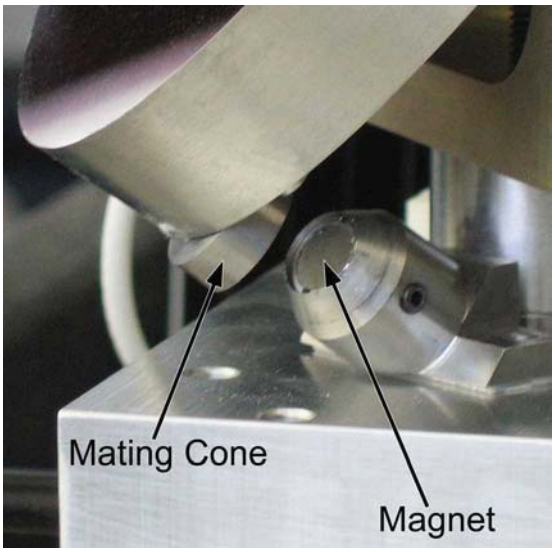

Figure 17. Magnetic Launch Lock

Vibration Testing

A vibration test was conducted to verify the performance of the launch lock and the survivability of the FSM. The 3-minute test was based on proto-qualification levels for the planned STP-SIV spacecraft,

Table 6. STP-SIV Spacecraft Vibration Spectrum

Frequency (Hz)	PSD – Acceptance (g2/Hz)	PSD – Protoqualification (g2/Hz)
20	0.005	0.01
100	0.012	0.024
800	0.012	0.024
2000	0.005	0.01
Overall (grms)	4.27	6.04

shown in Table 6, with the first minute at reduced power and two minutes at full power. The test consisted of the following duty cycle:

- -12 db for 15 sec
- -9 db for 15 sec
- -6 db for 15 sec
- -3 db for 15 sec
- 0 db for 2 min.

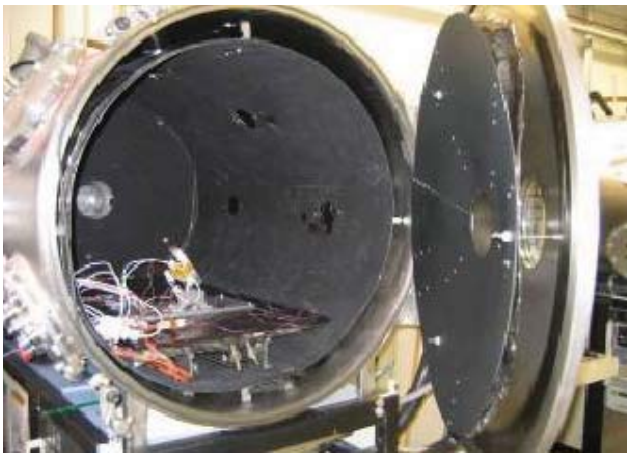

Figure 18. FSM Mounted in Thermal Vacuum Chamber

The launch lock magnetic force was set to about 1.5 N for the first vibe test. The launch lock released after 105 sec., but no violent mirror motions were observed. Measurement of the latch force after the test showed it to be about 1.4 N, so the set screw may have been loose. The latch force was increased to about 2.2 N for the second test. This test was successful. Before and after each test, the FSM was powered up and exercised with its nominal duty cycle of a Lissajous figure, an "S" figure, and slow scans. The performance appeared nominal before and after each test. The FSM was also repeatedly commanded to latch and unlatch positions, verifying that the voice coil could overcome the latch force.

Thermal-Vacuum Testing

Although the FSM prototype was not intended for harsh testing, it was mounted in one of SDL's thermal-vacuum chambers (Figure 18) and subjected to 55 duty cycles with pressures as low as 1e-7 torr and temperatures to 164 K (the lower limit of the chamber's capability). The azimuth axis worked for 26 runs as the temperature dropped, until the thermocouple on the azimuth motor housing reached 227 K. This axis then ceased working as expected due to the bearing lube freezing up, since its published range is 233 K to 423 K. The elevation axis operated for all runs, down to 164 K. Figure 19 shows how the elevation axis "rings" at cold temperatures due to a change in the plant resulting in improper gains. The feedthrough cables add considerable noise, as shown for small angles in Figure 20. The azimuth noise was noticeably worse than the previous year, possibly due to bearing abuse during the vibe test, or loss of lubricant during vacuum testing. The encoder optics could also be impaired due to outgassing on the lens. Figure 21 shows how the "before" and "after" performance of the elevation axis at ambient for large angles is nearly identical. Some outgassing was evident from the residue collected in the chamber's cold trap, although it was not analyzed after testing.

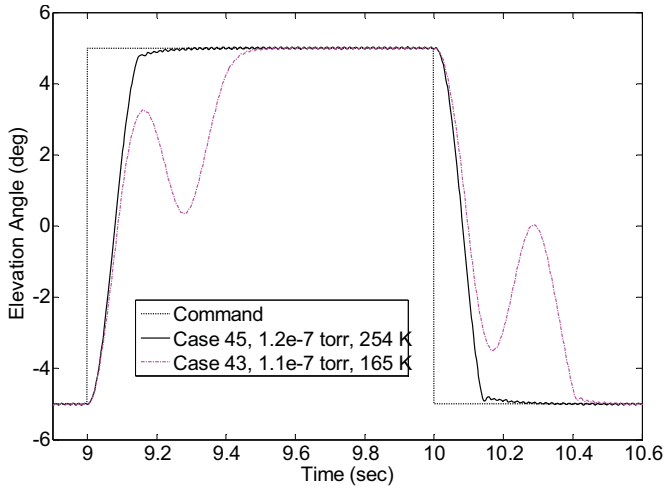

Figure 19. Effect of Temperature on Elevation Step Response

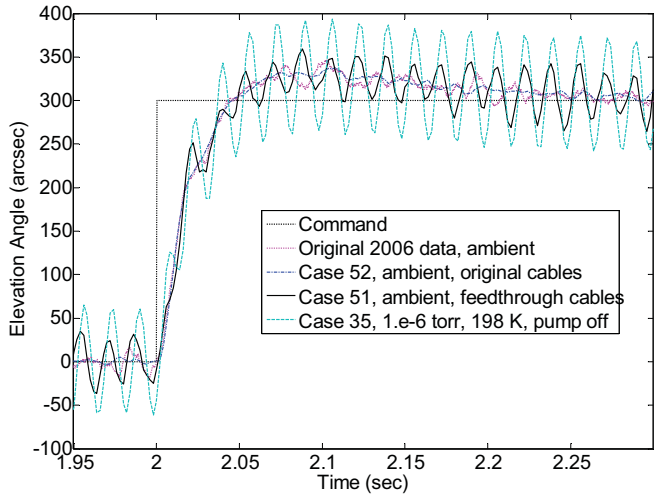

Figure 20. Effect of Cable Noise on Elevation Small-Angle Response

Lessons Learned and Future Work

The FSM prototype has been shown through testing to have the potential for robust performance in the harsh environment of space. The elevation axis operates at hard vacuum and cold temperatures down to 164 K. The "before" and "after" ambient performance of the elevation axis is virtually the same. The azimuth axis works down to 233 K until the current bearing lube freezes up. The launch lock successfully handles a typical launch environment.

Obviously, some materials changes would need to be made for space and/or cryogenic applications. The azimuth lubricant would need to be changed. Also, the gains for both axes should be scheduled based on temperature. The cause and corrective action for the cable noise in both axes would need to be identified.

The elevation axis circuit design could be modified to allow a slightly higher current limit of about 2 amps to provide additional latch force and stall torque margins.

The focus of future efforts are being centered more on the development of space-type electronics, as described in the following paragraphs.

The control algorithms and filters need to be further refined and optimized to reduce the noise, especially in the elevation axis. This may be done by moving the derivative term to the feedback loop, using optimal state-space methods with observers, etc.

The algorithms need to be implemented in low-cost space-qualified processing hardware, such as an FPGA, DSP, or microprocessor. This may necessitate conversion to fixed-point math, as was done for the radiation-hardened fixed-point microprocessor used to control a FSM in another SDL space payload (Ref. 3).

A protocol or set of operational codes needs to be defined to communicate digitally with the FSM, such as commanding it to move to a position, querying it for the current position, etc.

The D/As, A/Ds, wedge sensor electronics, and quadrature encoder functionality need to be implemented using space-rated components.

The autocoding feature of the RPM process needs to be evaluated to determine how much of the code automatically generated for the control algorithms can be used in the final product.

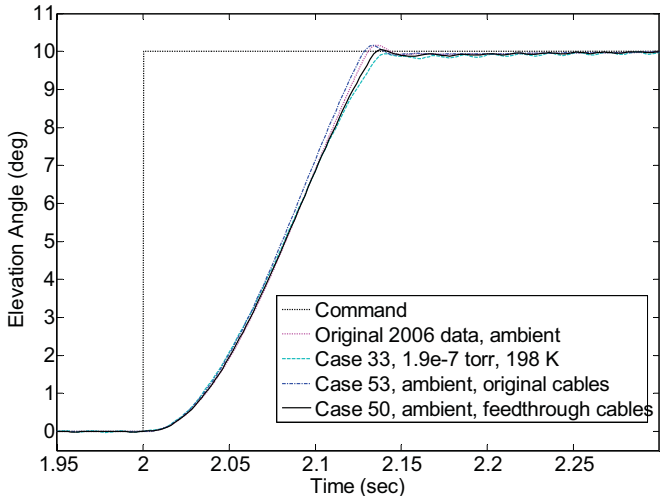

Figure 21. Ambient Data for Elevation Angle Large-Step Response

The input power interface needs to be defined to either use the spacecraft power to drive the motors or else have a customer supply the motor power.

Off-the-shelf space-rated three-phase motor amplifiers need to be evaluated.

It would also be desirable to develop an automated procedure for mapping the wedge sensor output against temperature and angle using optical techniques and precise temperature control.

Summary

A low-cost two-axis FSM has been successfully developed and demonstrated for air- and space-based sensors. The 75-mm aperture mirror is lightweight, isolated by flexures, and maintains a surface figure of less than 0.1-wave RMS down to a temperature of 210 K. The drive system uses an innovative combination of off-the-shelf components to achieve large angles, high slew rates, high bandwidth, and relative position error less than 1 arcsec. A rapid prototyping methodology has been used to develop the control laws. Temperature mapping has been employed to improve the absolute pointing accuracy. A passive patent-pending launch lock has been developed and demonstrated. Vibration testing has been performed to show the survivability of the FSM and the successful operation of the launch lock. The mechanism has been subjected to many duty cycles in a hard vacuum and at low temperatures. Areas for improvement include a lower-temperature azimuth lubricant, gains scheduled with temperature, noise reduction in the cables, a higher elevation axis current limit, and development of space-worthy electronics.

Acknowledgments

The authors express their sincere appreciation to the following individuals for their significant contributions: Richard Sanders and Melissa Draper, mechanical design; Trent Newswander, mirror design, analysis, and testing; Brent Jensen, structural analysis; Brian Thompson, trade studies and conceptual design; Steve Dansie, Andrew Little, and Scott Schicker, mechanical technologists; Duane Miles, optical technologist; Jeff Blakeley, analog and power electronics; James Cook and Zach Casper, electronics and software; Adam Shelley and Quinn Young, thermal design; Aaron Gilchrist, temperature mapping; and Jim Herrick, vacuum testing. The authors also appreciate the funding and support from the Research Division of SDL, directed by Dr. J. Steven Hansen and Dr. Scott Jensen.

References

1. Steven R. Wassom, Morgan Davidson, Trent Newswander, James Cook, Zach Casper, Adam Shelley, “Fine Steering Mirror for Smallsat Pointing and Stabilization,” 20th Annual AIAA/USU Conference on Small Satellites, Paper #SSC06-VIII-7, 17 August 2006.

2. Ahmad, Anees, *Optomechanical Engineering Handbook*, CRC Press, 1999.

3. Steven R. Wassom, Chad Fish, Mitch Whiteley, Dave Russak, Joel Nelsen, Brian Thompson, Glen Hansen, Jason Wooden, Larry Gordley, John Burton, Mark Hervig, Paul Cucchiaro, Dan Hammerle, “SOFIE Pointing Control System,” SPIE Proceedings Vol. 6297, *Infrared Spaceborne Remote Sensing XIV*, 7 Sep. 2006.

Cryogenic Focus Mechanism for the Spitzer Space Telescope

William C. Schade*

Abstract

A new focus mechanism was developed, tested, and flown for the Spitzer Space Telescope ("Spitzer"), one of NASA's "Great Observatories". Figure 1 shows the Flight Focus Mechanism (FLT-FM), now in Spitzer. The mechanism uniquely provides robust support and precise focus adjustment for the Spitzer secondary mirror, from 300 K to a 5 K cryogenic environment.

This paper summaries the requirements, performance, description, and testing of the focus mechanism, including key component level tests of a geared-stepper motor and ball screw. Also, a secondary mirror mount is described that minimizes mirror distortion and supports high loads. Several design and test challenges were overcome and lessons learned from this successful development include:

- Titanium is useful as a flexure material to liquid helium temperatures.
- Adhesive bonds at cryo-temperatures should be well understood and / or tested.
- Geared-stepper motor and ball screw components were simply modified to work to < 5 K.

Figure 1. Flight Focus Mechanism (FLT-FM)

* Ball Aerospace & Technologies Corp. (BATC), Boulder, CO

Introduction

The Spitzer observatory shown in Figure 2 includes the Cryogenic Telescope Assembly (CTA) that directs infrared signals to various instruments by means of a beryllium primary and secondary mirror. Ball Aerospace & Technologies Corporation (BATC) supplied the CTA as shown in Figure 3, with funding and oversight provided by NASA-JPL. Early in the program it was decided a focusing capability was desired, providing the cost and complexity to achieve it was reasonable and providing it could be developed on time. Fortunately these objectives were met, so the focus mechanism is included in the CTA as shown, mounted on a beryllium metering structure.

Spitzer was launched on August 25th, 2003 with the focus mechanism and other key telescope components at ambient temperature. The telescope components were later cooled in space to less than 5.5 K. This space-assisted cooling approach was beneficial in helping to preserve Spitzer's cryogen. Consequently, the observatory has surpassed its expected 2.5-year life and is approaching a 5 year life goal. Additional Spitzer facts are given on the next page, for reference.

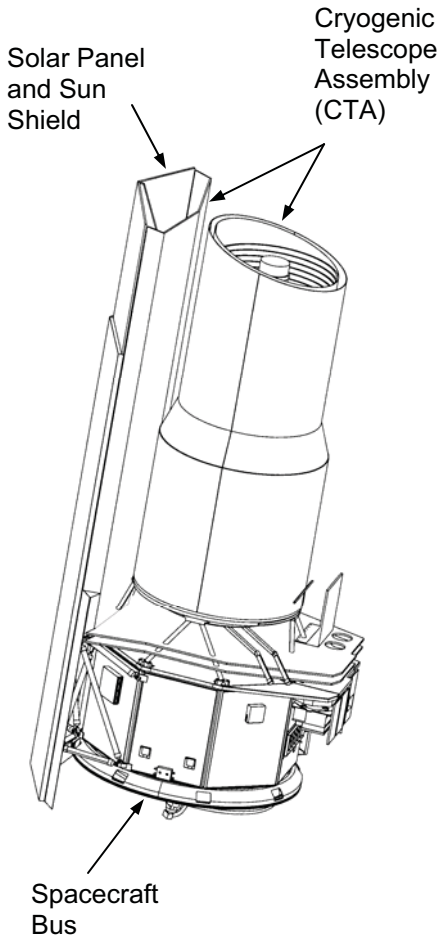

Figure 2. The Spitzer Observatory

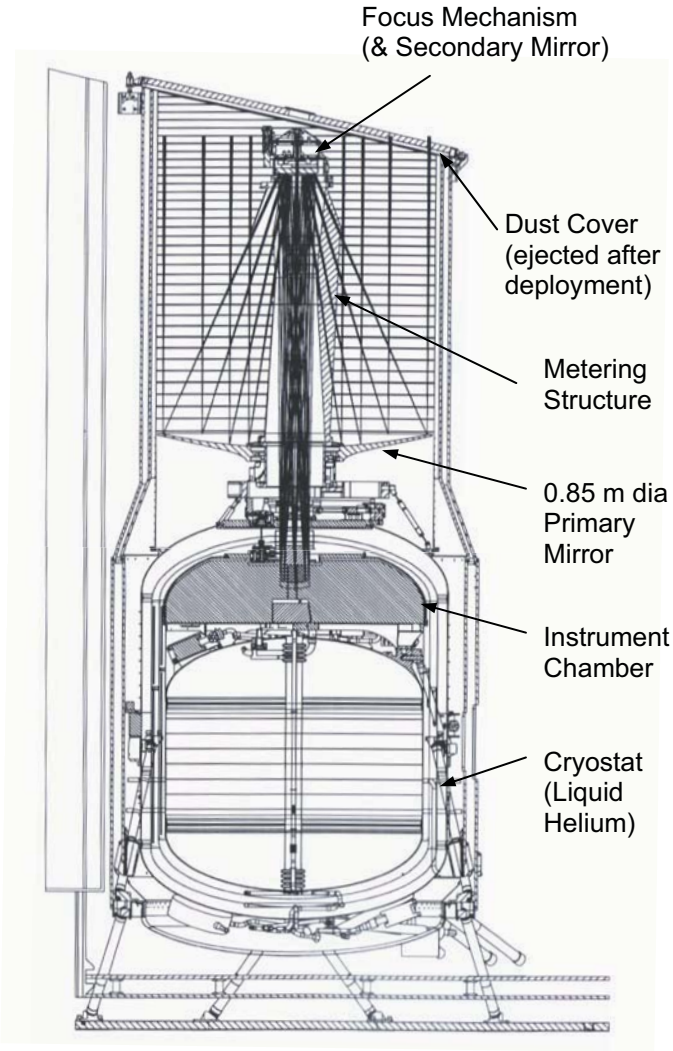

Figure 3. Cryogenic Telescope Assembly (CTA)

Spitzer “Fast Facts”

For reference, this page includes Spitzer “Fast Facts” from the California Institute of Technology web site http://www.spitzer.caltech.edu/about/fastfacts.shtml.

The Spitzer Space Telescope is a space-borne, cryogenically-cooled infrared observatory capable of studying objects ranging from our Solar System to the distant reaches of the Universe. Spitzer is the final element in NASA's, Great Observatories Program and an important scientific and technical cornerstone of the Astronomical Search for Origins Program.

Launch Date:	25 August 2003
Launch Vehicle/Site:	Delta 7920H ELV / Cape Canaveral, Florida
Estimated Lifetime:	2.5 years (minimum); 5+ years (goal)
Orbit:	Earth-trailing, Heliocentric
Wavelength Coverage:	3 - 180 microns
Telescope:	85-cm diameter (33.5 inches), f/12 lightweight Beryllium, cooled to less 5.5 K
Diffraction Limit:	6.5 microns
Science Capabilities:	Imaging / Photometry, 3-180 microns Spectroscopy, 5-40 microns Spectrophotometry, 50-100 microns
Planetary Tracking:	1 arcsec / sec
Cryogen / Volume:	Liquid Helium / 360 liters (95 Gallons)
Launch Mass:	950 kg (2094 lb) [Observatory: 851.5 kg, Cover: 6.0 kg, Helium: 50.4 kg, Nitrogen Propellant: 15.6 kg]

Major Innovations

- Choice of Orbit
- Warm-Launch Architecture
- New Generation of Large-Format Detector Arrays
- Lightweight, cryogenic optics

The Spitzer Team

- Jet Propulsion Laboratory
- Spitzer Science Center, California Institute of Technology
- Ball Aerospace and Technologies Corporation
- Lockheed Martin Space System Company
- Smithsonian Astrophysical Observatory
- NASA-Goddard Space Flight Center
- Cornell University
- University of Arizona

Focus Mechanism Key Requirements and Performance

The purpose of the focus mechanism is to maintain the Spitzer's secondary mirror position and, if desired, move it along the CTA optical axis for focus adjustment. As a single axis device, it must maintain mirror alignment with minimal de-center or tilt motion of the mirror due to launch, cool-down, or focus operation. This basic functionality is reflected in the key requirements and tested performance of the mechanism, as summarized in Table 1. And, since it must be controlled reliably and remotely, redundancy is required.

The performance results are for ambient and cryogenic temperatures, before and after exposure to launch vibration levels, and after life testing of a Focus Engineering Model (FM-EM) to 1X life. The FM-EM was built and tested to reduce risk and for life testing up to 4X life, prior to making the Flight Focus Mechanism (FLT-FM). The tests for the FLT-FM were more abbreviated, but performance was similar.

Table 1. Focus Mechanism Key Requirements and Performance

Key Requirements		Tested Performance (Meets all)
Range	≥ ± 0.25 mm ≤ ± 0.50 mm	≥ ± 0.25 mm (soft limits) ≤ ± 0.33 mm (hard stops)
Step size	≤ 2.5 μm	≤ 1.3 μm [a]
Repeatability	≤ ± 1.25 μm (unidirectional)	≤ ± 0.81 μm [a] (bi-directional) [b]
De-center over range [c]	≤ ± 5.0 μm	≤ ± 3.61 μm
Tilt over range [c]	≤ ± 58 μrad	≤ ± 41 μrad
Shift after launch [d]	≤ ± 12.5 μm de-center ≤ ± 116 μrad tilt	≤ ± 9.3 μm de-center ≤ ± 110 μrad tilt
Operating temperature	300 to 2.5 K	Meets
Operating pressure	Ambient to 10^{-6} Torr	Meets
Launch acceleration	70 G lateral 125 G axial	Meets
First mode frequency	> 150 Hz	330 Hz
Clear aperture of SM	∅ 120 mm min	∅ 123.8 mm min
Mass (with mirror)	≤ 4 kg	Meets

Notes pertaining to Table 1:
a) Mean and standard deviation values for these are given in the assembly test section.
b) Repeatability was met bi-directionally, while only unidirectional was required.
c) De-center and tilt over range refer to mirror motion along and rotation about any axis normal to the optical axis, respectively, over the mechanism's full range.
d) Shift after launch refers to mirror motion due to temperature repeatability and launch vibration combined. The former is any difference in mirror position from ground alignment at 5 K and after cooling again on orbit. The latter is any permanent shift due to launch.

Aside from the requirements, a goal was set to limit the focus shift of the mirror after launch to ≤ 2.5 μm. This was a goal only since the mechanism can correct for focus after launch and it was anticipated performance might slightly exceed this. Performance for this was measured at ≤ 3.2 μm, which was just over the goal, as was expected might happen.

The FM-EM also demonstrated a viable flight mechanism could be made on time. The FM-EM design was started in November 1997, it was built, and cryo-testing was started by June 1998, as required. This success paved the way for the build of the FLT-FM.

Focus Mechanism Description

Concept

An initial challenge was to select a concept that would efficiently constrain the mirror in all but one direction, yet provide for precise focus control. The concept in Figure 4 achieves this. The secondary mirror (SM) is held on a carrier and tube suspended on two diaphragm flexures, which are stiff in all but the focus direction. Focus is precisely controlled by a stepper motor acting though a lead screw, lever arm, and flexure system, as shown. Focus step size and position are simply determined by counting motor steps. Advantages of this concept are summarized as follows:

- Simplicity – *Minimizes cost*
- Effectiveness – *Meets requirements*
- Robustness – *Carries high launch loads*
- No free play in flexures – *Repeatable*
- Low actuation force – *Low screw loads*
- Symmetry of major supports – S*table over temperature*

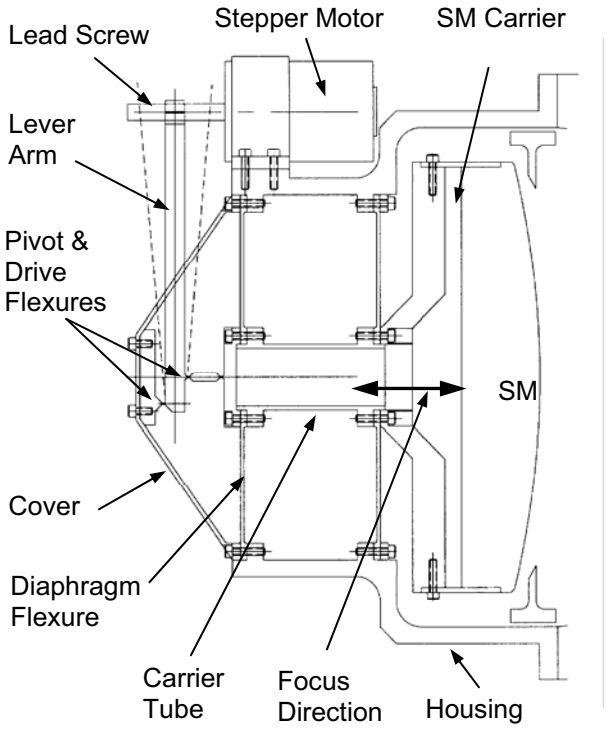

Figure 4. Focus Mechanism Concept

Focus Mechanism Engineering Model (FM-EM)

The FM-EM shown in Figure 5 was built and tested to mitigate risk early. Key challenges then were to find motor and lead screw components and a material suitable for flexures, for operation to 5 K.

A 2-phase stepper motor (Figures 8) was selected with a gearhead for further reduction to achieve the desired output step size. Motor detent torque and the overall mechanical reduction also prevent backdriving during launch. A ball screw (Figure 9) was selected to provide for a low friction, precision lead screw. Both these components were tested for operation near 5 K, as described in their testing sections.

Titanium was selected for all the flexures and major structure. Beyond its other desirable properties, it nearly matches the coefficient of thermal expansion (CTE) of the SM and metering tower (and flexures in the SM mount and main housing legs compensate for the small mismatch). The FM-EM used 6Al-4V, due to schedule. For flight, extra low interstitial titanium 6Al-4V (ELI) was chosen since it is generally tougher.

There was concern titanium may become too brittle at 5 K and not flex well over life. This was resolved by determining its plane strain fracture toughness (K_{IC}) was sufficient, as shown in the lesson learned below and with fatigue analysis. Cryo-life testing of the FM-EM to 4X life further alleviated this concern.

Lesson learned #1: Titanium is useful as a flexure material at cryogenic temperatures. 6Al-4V (ELI) predicted K_{IC} at 4 K is 54.9 MPa*$\sqrt{m}$ (50 ksi*$\sqrt{in}$) per the NASA/FLAGRO manual, JSC-22267A. This was more than sufficient to meet the focus mechanism requirements for flexure operations below 5 K. Additionally, 6Al-4V flexures were life tested in the FM-EM at 35 K to 4X life.

Other development included: For modularity of the SM mount and carrier, the carrier mounting screws are accessible from the cover side. A SM and carrier mass simulator (shown in the photograph) was made for FM-EM testing. The drive flexure passes through the lever arm before attaching to it, to reduce its deflection. Ball screw nut flexures provide compliance to prevent binding at the screw, yet are stiff in the drive axis and prevent excessive rotational windup of the nut. And non-jamming hard stops on the screw provide for range limits.

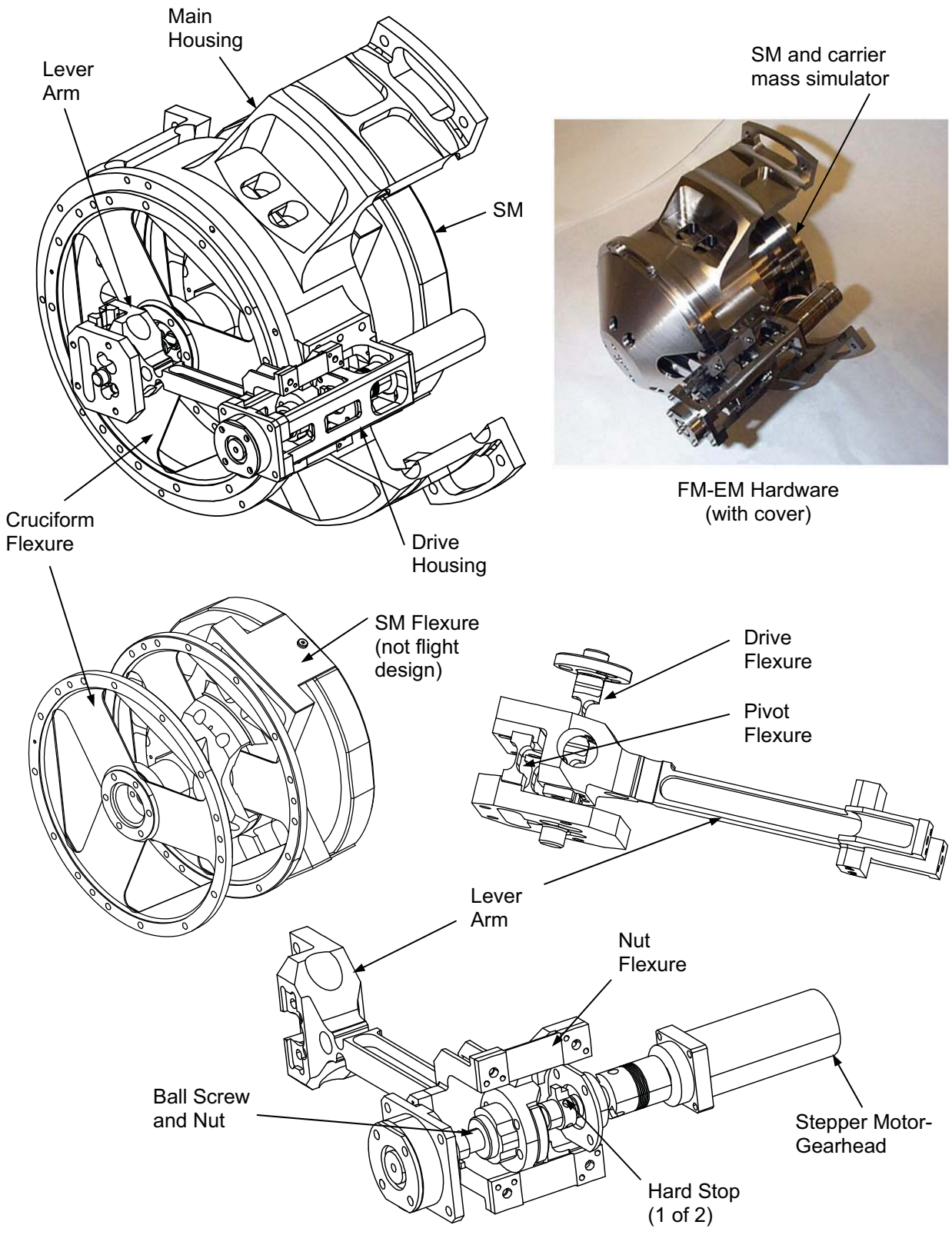

Figure 5. Focus Mechanism Engineering Model (FM-EM)

Flight Focus Mechanism (FLT-FM)
Figure 6 shows the Flight Focus Mechanism, which is much like the FM-EM except for some notable developments. Most notable is the addition of the flight secondary mirror and its mount, shown in the next section. Also, the motor is dual wound for redundancy.

The drive and pivot flexures were also significantly strengthened because the axial (focus) load requirement was changed from 70 G to 125 G and a “low risk fracture part” methodology was voluntarily imposed to enhance reliability. This methodology is defined in a JSC memo (June 1992), TA-92-013 and included designing the flexures to ≥ 10X their required fatigue life (including all vibe cycles).

Other developments included: The addition of the mirror mask and stray light baffle. A larger motor was provided for more torque margin. And Variable Impedance Transducer (VIT) sensors were added for “soft” limits.

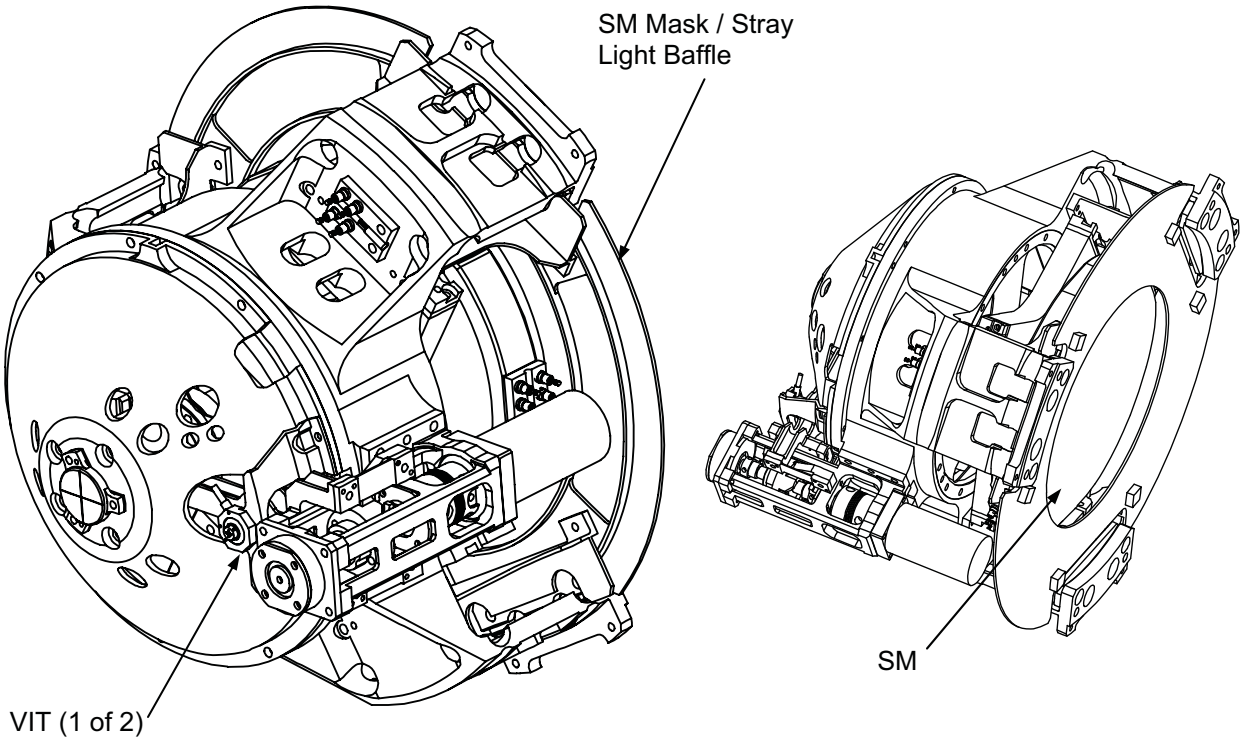

Figure 6. Flight Focus Mechanism (FLT-FM)

Secondary Mirror Mount
The secondary mirror mount approach is shown in Figure 7. The mirror is a convex hyperbolic front surface on a beryllium substrate. Beryllium spacers are bonded to the substrate and titanium bi-pod flexures are then conventionally attached. This approach helps to minimize mirror distortion and provides high load capacity. It also presented challenges due the bonds being used at cryogenic temperatures.

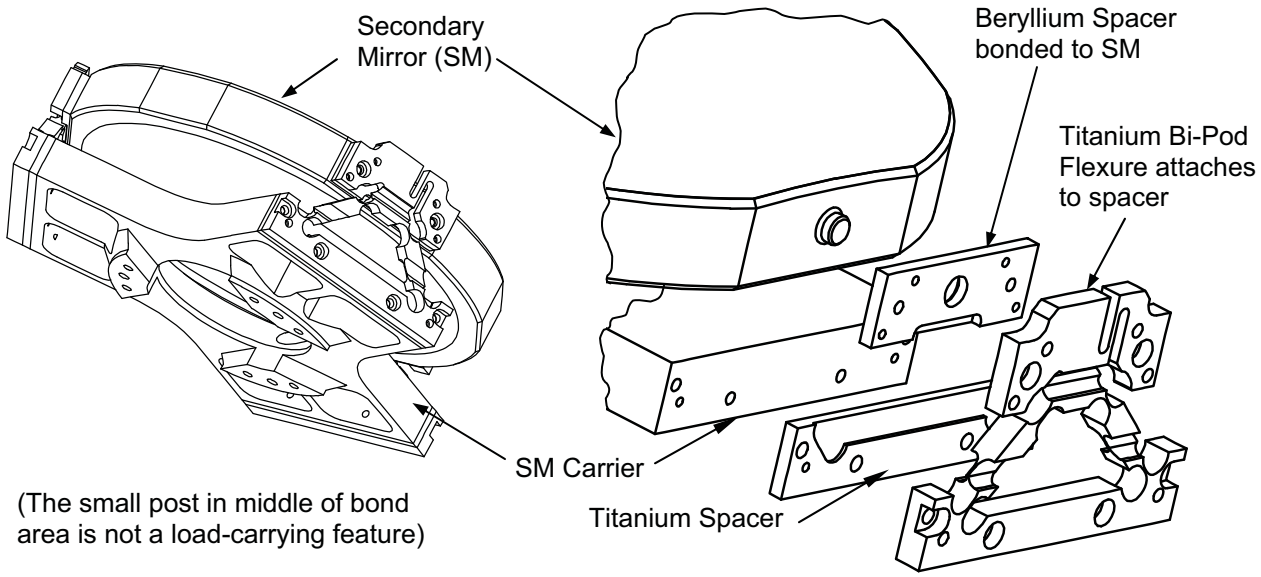

Figure 7. Secondary Mirror Mount

The beryllium spacers match the CTE of the mirror to minimize thermally induced strain in the bondline and to maintain mirror figure. The bondline also provides some isolation from flexure fastener preloads, which were light, to further minimize mirror distortion. Titanium spacers at the carrier interface were machined in thickness and wedge to achieve ideal flexure alignment and for optimal mirror figure at 5K.

High load capacity was achieved with epoxy bonds to beryllium (> three times better vs. titanium). Beyond strength, a specific epoxy was also chosen for its desirable CTE and modulus of elasticity vs. other adhesives, based on tests at room temperature to 5 K.

A challenge arose when finite element analysis (FEA) predicted high stress in the bond due to the epoxy shrinkage when cycled to 5 K. The high stress occurred around the exposed periphery of the bond, essentially independent of bond area. This raised concern micro-cracking could occur around the periphery and cumulatively degrade bond strength over multiple 5 K cycles. However, we realized the analysis could be too pessimistic in predicting the adhesive stresses, due to assumed linearity and stress infinity conditions at the bond edges often inherent in such FEA [1]. And BATC had successful use of adhesives to 5 K, which further suggested the FEA did not provide for sufficient understanding of this issue.

Testing was done to address this concern. Beryllium coupons were bonded and cycled ten times from room temperature to 4 K. They were then shear and leverage strength tested at room temperature to determine if any degradation resulted. There was essentially no difference in results between cycled and un-cycled samples. In fact, all the cycled sample actually showed slightly higher strengths (a pleasant surprise).

***Lesson learned #2*:** Adhesive bonds at cryo-temperatures should be well understood and / or tested. For the secondary mirror mount, FEA showed high stresses that suggested the bond joint strength could cumulatively degrade by thermal cycling to 5 K. To better understand if this was an issue or not, tests were done as described above. These tests showed no degradation in bond strength after thermal cycling to 5 K and provided the understanding we needed to proceed.

Stepper Motor Component Testing

A stepper motor-gearhead assembly was tested early, as a component, because it was considered a significant risk item to work at 5 K. We had one in house from a vendor that does a good job of matching the CTE of materials in their units and that would have a good chance of working. The following briefly summarizes the test of this motor.

Test Description
Measure power-off backdriving torque and operating output torques at room and cryogenic temperatures.

Motor Modifications
The stepper motor-gearhead is shown in Figure 8. This unit was disassembled and all its key bearing and gear surfaces were dry lubricated with a BATC proprietary process. The unit also had non-metallic parts that were replaced with metallic ones, as supplied by the vendor in another version of this unit. It was baked out to remove moisture and dry purged for testing.

Figure 8. Stepper Motor-Gearhead

Test Set-Up
See Figure 10 on the next page for the set-up description (also used for ball screw component testing).

Success Criteria
- Operate near 5 K.
- Show no big increase in backdriving torque (exhibit no to low binding).
- Show starting (pull in) torque ≥ 353 mN*m (50 oz*in).

Results
The unit met all the success criteria, as shown by the results in Table 2. Stall (pull out) torque and winding resistance were also measured for reference.

Table 2. Stepper Motor Component Test Results

Temperature of Unit	Operated?	Backdriving Torque (mN*m)	Starting (pull in) Torque (mN*m)	Stall (pull out) Torque (mN*m)
Room (pre-test)	Yes	212 - 233	466 - 480	508 - 530
7-14 K	Yes	247 - 268	395 - 565	424 - 706
Room (post-test)	Yes	212 - 247	438 - 480	480 - 530

(Tests were done at less than peak power, CW / CCW, and at multiple step rates)

An approximately 100:1 Relative Resistivity Ratio (RRR) was measured at 5 K, the RRR being the ratio of winding resistance at room temperature vs. 5 K. This lower winding resistance at cryogenic temperatures was not an issue since the motor was current limited by its drive electronics.

The flight motor was similarly tested to higher acceptance torque values, since it is larger.

***Lesson learned #3(a)*:** The stepper motor-gearhead needed only simple modification to work near 5 K. The modification was primarily dry lubrication, using a BATC proprietary process.

Ball Screw Component Testing

Ball screw testing was performed early because there was concern its running friction torque might change appreciably when rotating at 5 K. The following briefly summarizes the testing of the ball screw.

Test Description
Measure starting and running torque at room temperature and near 5 K. Two ball screws were tested, a smaller, preloaded, carbon steel unit, shown in Figure 9, and a larger un-preloaded 440C version.

Figure 9. Ball Screw

Ball Screw Modifications
The ball screws were disassembled and dry lubricated with a BATC proprietary process. Some internal plastic parts were changed to metal parts, for flight but not for this testing. The units were baked out to remove moisture and dry purged for testing.

Success Criteria
Max torque of 35.3 mN*m (5 oz-in), but a goal of 17.6 mN*m (2.5 oz-in) is preferred.

Results
The test was a success, as shown in Table 3. The larger, un-preloaded screw met the torque limit and was near to the preferred goal. The preloaded units torque was shown to be undesirable. So, a smaller un-preloaded screw was chosen for the FM-EM, which ultimately met the preferred goal.

Table 3. Ball Screw Component Test Results

Temperature at test	Smaller, preloaded screw max torque* (mN*m)	Larger, un-preloaded screw max torque (mN*m)
Room (pre-test)	21.2 - 35.3	8.8
At 4.8 – 5.2 K	35.3 - 67.1	22.0
Room (post-test)	21.2 - 28.2	11.3

* 6 balls missing (2 per track), lost in lubrication process

Test Set-Up (used for ball screw and motor)
The items were tested in a dewar with liquid helium, per Figure 10. They were held with a low thermal conductance outer tube and turned with or by another tube. A torque watch was used for ball screw testing, while the dynamometer shown was used for the motor testing.

***Lesson learned #3(b)*:** The ball screw needed only minor modification to work near 5 K. The modification was primarily dry lubrication, with a BATC proprietary process.

(Dewar not shown)

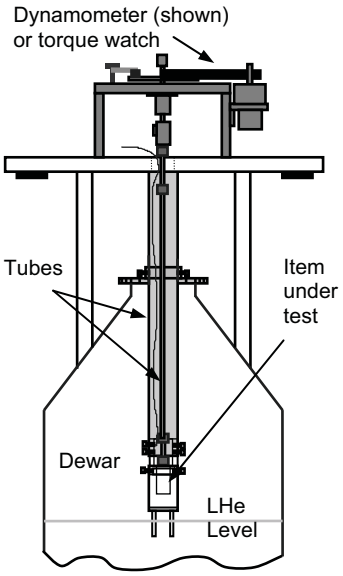

Figure 10. Component Test Set-Up

Focus Mechanism Assembly Testing

The FM-EM and FLT-FM assemblies were tested as described in this section, to evaluate how well the focus mechanism met its requirements over ambient and cryogenic temperatures, before and after vibration testing, and after life testing of the FM-EM.

Challenges overcame included precisely measuring the "mirror" (simulator) motion in a cryogenic environment. Also, the flight mechanism survived a severe over-test condition, as described herein. And relevant items that contributed to successful testing are also noted.

Test Description
All the key requirements per Table 1 were evaluated, and are summarized as follows:

- Focus range, step size, and repeatability
- De-center and tilt over the focus range
- De-center, tilt, and focus shift after launch vibe
- Vibration testing and determination of mode frequencies
- Life testing to 1X life and for up to 4X life

FM-EM performance testing was done in vacuum at cryogenic temperatures and in ambient conditions, both before and after vibration testing, and after life testing.

FLT-FM performance testing was done at ambient conditions, but it was later cryo-tested at the telescope assembly level. The FM-EM and FLT-FM are similar, except for the notable differences shown in Table 4.

Table 4. Differences between the FM-EM and FLT-FM

FM-EM	FLT-FM
SM mass simulator	Flight SM and mount
Smaller motor and single wound	Larger motor and dual wound
Flexures sized for 70 G in all axes	Flexures sized to 125 G in focus axis
Carbon steel ball screw	440C induction hardened ball screw
No limit sensors	Limit sensors

Test Set-Up Description
The FM-EM was tested in the dewar shown in Figure 11. The test measured mirror motion relative to the mechanism interface, using a mirror simulator. A brief description of the test set-up is as follows:

- The mechanism was mounted on a stable reference plate that was used for cryogenic or ambient testing and for vibration testing. It had position sensors on it that monitored the mirror simulator motion relative to the plate, hence, the mechanism interface.
- Legs (not shown) mounted the reference plate to the dewar and provided a conductive path to the dewar cold plate. The legs were removed so the plate could be used in vibration testing too.
- VITs (Variable Impedance Transducers) monitored the mirror simulator motion along the focus axis, in two axes of tilt, and in two lateral axes for decenter. The VITs were initially calibrated at room temperature and to 80 K, but not to lower temperatures.
- Anticipating the VIT calibration could change below 80 K, a secondary focus measurement technique was provided by using two laser interferometers on a stable base. One measured mirror simulator motion and the other measured the reference plate motion. The difference between these measurements represented the desired focus motion, relative to the plate.

- Likewise, another secondary measurement technique was provided for tilt of the mirror simulator in two axes (tip / tilt) using two quad-cell autocollimators, on a stable base. One measured mirror simulator tip/tilt motion and the other measured the reference plate tip/tilt motion. The difference between these measurements represented the desired tip / tilt motion, relative to the plate.
- The dewar has two stages, one for liquid nitrogen and one for liquid helium. It was modified to fit windows for the secondary measurement techniques.
- Thermocouples were used to monitor temperature at various locations.

Success Criteria
Meet the key performance requirements, as shown in Table 1, over ambient and cryogenic temperatures, before and after vibration testing, and over 1X life for the FM-EM, and as a goal for up to 4X life.

Results
The FM-EM met the above success criteria. Table 1 shows the FM-EM performance before and after launch vibration and over 1X life. Performance did not change appreciably for up to 4X life, meeting the goal to provide significant life margin.

Table 1 shows maximum values for step size and repeatability. The mean and standard deviation values for these over 1X life are provided in Table 5.

Table 5. Mean and Standard Deviation for FM-EM Step Size and Repeatability

Parameter	Mean	Standard Deviation
Step size	0.42 μm	0.17 μm
Repeatability (bi-directional)	0.0005 μm	0.29 μm

The FLT-FM performance was similar, based on abbreviated testing. A difficulty occurred during FLT-FM testing when it was erroneously vibration tested to 170 G in the lateral direction, due to a faulty control of the vibration table. This was far beyond the required 70 G.

The effects of the 170 G over-test were carefully evaluated. Fortunately, due to the robustness and conservatism in the design, there were relatively few issues. However, the ball screw was loaded beyond its rating. So we loaded a spare flight ball screw to the same over-test level and well beyond. Based on inspections of the overloaded spare ball screw, we concluded the flight ball screw was still acceptable for use. This 170 G over-test also reduced the fatigue life of the flexures from 10X to 6X. But this was deemed acceptable, with customer approval.

Notable Items Contributing to Successful Testing:
- The FM-EM was tested at 30 K to 49 K since the dewar had only one, liquid nitrogen shroud and due to parasitic radiation from the optical windows. This was accepted since the motor and ball screw components were tested near 5 K. Also, most material shrinkage occurs by these temperatures and the predicted toughness (K_{IC}) for titanium at 5 K was more than acceptable.

- Including secondary measurement techniques proved to be a prudent decision. As anticipated might happen, the VIT calibration changed below 80 K. Using interferometer and autocollimator data, it was found the slope of the calibration changed but the VITs retained good linearity. After accounting for this, the data between all the measurement methods agreed well. This also allowed for interpretation of VIT data measuring the lateral motions, which did not have the secondary measurements.

- Vibration testing without force limiting showed high magnification factors at resonant frequencies that would have resulted in over-testing the mechanisms capability, if vibrated to the required input levels on a standard shaker. As recommended by JPL, using force limiting [2] resolved this problem and it was successfully tested to its full levels. (Force limiting is now more routinely used at BATC)

Dewar with Laser Interferometers
(Quad-Cell Autocollimators not shown)

FM-EM on Reference Plate
(Without legs)

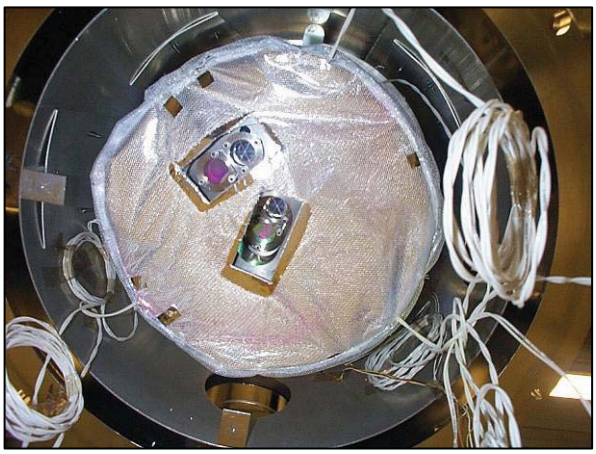

FM-EM Shrouded in Dewar
(Looking up at ref plate side)

Figure 11. FM-EM Test Set-Up

Conclusion

The new focus mechanism was completed and shown to provide repeatable focus positioning to 5 K. Its design and test challenges were successfully overcome, on schedule. The mechanisms concept and implementation have been shown to be simple, effective, and very robust. It is currently in service in the Spitzer Space Telescope, one of NASA's "Great Observatories".

After launch on August 25th, 2003, the new focus mechanism has performed as planned in flight. The observatory has surpassed its expected 2.5-year life and is now approaching a 5-year life goal. (The mechanism only needed operation twice during this time; once to verify its successful operation, and then to achieve the final focus position that is currently in use.)

Testing of the stepper motor and ball screw components significantly mitigated risk early in the program. The build and test of the mechanism engineering model further mitigated risk and allowed for verification of performance over and above the required life.

Lessons learned, resulting from this successful mechanism development, are summarized below.

Lessons Learned Summary

1. Titanium 6Al-4V (ELI) is useful as a flexure material to liquid helium temperatures since it has sufficient plane strain fracture toughness (K_{IC}) to < 5 K.
2. Adhesive bonds at cryo-temperatures should be well understood and / or tested. For the mirror mount, FEA did not provide sufficient understanding of the bond. Testing with coupons was required and showed the bond strength was acceptable after multiple cycles to 5 K.
3. The geared-stepper motor and ball screw components needed only slight modification to work at 5 K, which was primarily dry lubrication.

Subsequent Developments

This mechanism has provided heritage for other programs at Ball Aerospace, as follows:

- The James Webb Space Telescope (JWST): Similar geared-motors are planned for use in the cryogenic nano-actuators used to position its primary mirror segments.
- Kepler (another space-borne telescope): A derivative of this mechanism is planned to move the primary mirror for focus adjustment.

Acknowledgements

This device was developed with funding and oversight from JPL under contract 960669.

Thanks to Robert M. Warden (BATC) for developing the mechanism concept and to the BATC team and suppliers that supported this effort. And in memory of Mike Rice, an outstanding technician on the team.

References

1. MIL-HDBK-17-3F, section 6.2.3.6.
2. T. D. Scharton. Force Limited Vibration Testing Monograph. NASA Reference Publication RP-1403 (May 1997).

Development of a Spacecraft Antenna Pointing Gimbal

Charles Monroe* and Peter Rossoni*

Abstract

The development of the pointing gimbal in the high-gain antenna system (HGAS) of the Solar Dynamics Observatory spacecraft is described. The gimbal was designed for 5 years of service in Geo-Synchronous orbit. The hardware incorporates multiple levels of redundancy, allows harnessing and waveguide along its full length across its two axes of rotation and points with an accuracy of better than 0.065°. Significant issues with actuator alignment, Electrical Contact Ring noise, pointing budget, and waveguide failures are described, along with their respective resolutions.

Introduction

This paper outlines requirements, design and development activities of the SDO gimbal. Several hardware anomalies and their resolution are described. The critical reliability level was a driver for most of the issues uncovered during the gimbal development.

Significant design areas include the actuator and contact-ring mechanisms and waveguide. Unique events and lessons-learned include the encoder alignment to the actuators, noise during component-level testing, replacing flex waveguide and accommodating the harness.

Background

The Solar Dynamics Observatory (SDO), shown in Figure 1, is a NASA spacecraft that will collect data from the Sun during its 5-year life. The spacecraft was designed by and is being integrated at NASA Goddard Space Flight Center in Greenbelt, MD. Universities and industry provide its science instruments.

This observatory transfers 150Mbps (millions of bits per second) of solar imagery (with overhead) per day from its 28.5° inclination, geosynchronous orbit at 36,000 km (22,400 mile) altitude, to the ground station in White Sands, New Mexico. The gimbal geometry that is most conducive to this end is a two-axis azimuth/elevation configuration. The azimuth axis will rotate once per orbit (once per day), and the elevation axis will rotate up to ±65 degrees to allow the antenna to point to the desired Earth coordinates at the SDO Ground Station. To avoid excessive spacecraft roll maneuvers, a dual HGAS approach was taken, with antenna systems on opposite sides of the spacecraft, allowing selection of the optimum gimbal for downlink via scheduled hand-offs.

* NASA Goddard Space Flight Center, Greenbelt, MD

Figure 1. Solar Dynamics Observatory with One of Two High-Gain Antennas and Gimbals Circled

Driving Requirements

An important driver for the gimbal system is the downlink requirement. A rate of 150 MB/second is needed with 99.99 percent reliability over a 99 percent duty cycle.

The 99.99 percent reliability requirement reflects the transmission error rate. To achieve this percentage during periods of transmission, the azimuth axis must be able to rotate continuously without downtime for "rewinding" of the harness about the axis of rotation. This drives the need for an electrical contact ring assembly (ECRA), a slip ring or roll ring, to pass power and signal through the axis.

The 99 percent duty cycle addresses periods of fog and rain at the ground station. The spacecraft itself will occasionally occlude the view from a single antenna. A continuous downlink capability dictates two antennas—one on either side of the spacecraft. During portions of the year, a daily hand-off between antennas will be required.

These requirements lead to a highly reliable, 100% duty-cycle design, with no planned datalink interruption.

The characteristics of the antennas and the power available for transmission drive the need to keep RF throughput loss low—the gimbal itself was allocated a loss of less than 1.45 dB. To meet this requirement, an all-waveguide RF system was selected as opposed to the simpler coaxial cable approach. This necessitated waveguide rotary joints at each axis of rotation.

Also, minimizing loss drives the need for having a pointing capability of $\pm$0.30° to the ground station for all error sources, including spacecraft position and orientation. Of this amount, there is 0.14° budgeted for random and calibration errors of the gimbal.

Gimbal Design

The overall configuration is shown in Figure 2. The azimuth axis has unlimited rotation and the elevation axis has a ±69° range. The continuous azimuth rotation is made possible by having the power and signal transferred through the ECRA. For the elevation rotation, a rotary cable wrap wherein the cable is carefully spiraled through the center of the elevation actuator manages the harness.

There are two rotating sections of waveguide on this two-axis gimbal. An azimuth section rotates with the azimuth axis and extends from the azimuth actuator up to the elevation axis. An elevation section rotates with the elevation axis and extends from the elevation actuator up to the antenna.

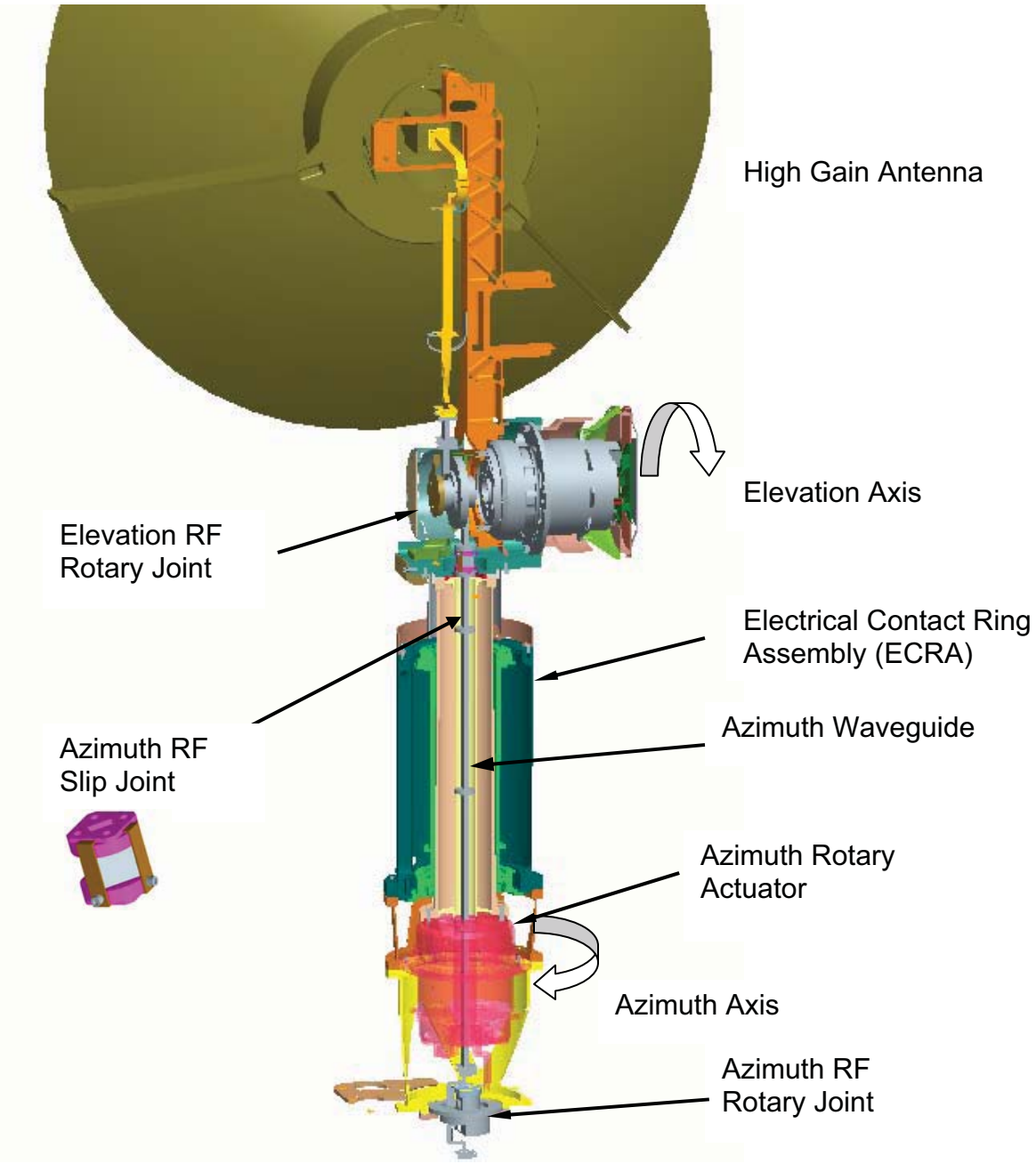

Figure 2. Gimbal Cross-section

Rotary Actuators

The rotary actuators for azimuth and elevation are identical except for hard stops on the elevation actuators limiting travel to ±69 degrees. Each commercial actuator consists of a stepper motor, hybrid optical encoder, and harmonic drive gear reducer in a titanium housing. Once delivered, the units were tested for compatibility with the GSFC-designed control electronics, and characterized for settling time, torque margin, encoder output and alignment. Then thermal hardware was applied, as shown in Figure 3, and the harnessing prepared for integration to flight hardware.

Figure 3. Rotary Actuator Shown During Thermal Hardware Application

Actuator Description

The three-phase stepper motors are redundantly wound. There are two redundant encoders: a coarse encoder on the output that determines hemisphere and home, and a fine encoder on the input that counts each step taken. The actuator details are summarized below:

Actuator Parameter	**Value**
Output step	0.0075 degree
Harmonic drive gear ratio	200:1
Motor step	1.5 degrees
Unpowered detent torque	34 N-m (300 inch-pounds)
Max required slew speed (under the following conditions at qualification temperatures)	30 degrees/min (66.7 pulses/sec)
Driven inertia	2 kg-m^2
Driven offset load	28 N-m (250 inch-pound)
Driven friction load	2.5 N-m (22 inch-pound)

Step Settling of Bearings

On orbit, a motor step will be taken roughly every two seconds. For the actuator life test, time constraints drive the need for more frequent steps, but the period between steps should be no less than the time required for bearing balls to settle. It was decided that after the ball motion decreased to a point where the magnitude of the oscillations is less than the width of the Hertzian contact patch, the bearings would be considered essentially settled. We believe this settling criterion to be consistent with ball-pass analysis for lubricant tribo-degradation. The time required to reach this point is 35 msec, so the actuator life test could be run at ~28 pulses per sec, which is an acceleration factor of ~57.

Actuator Encoder Alignment

Actuator position is determined by internal optical encoders. Alignment of the encoder is inferred from its output. Even though settling time and torques were within requirements, some actuators had marginal

alignment of their encoder discs to the step detents. The easiest way to test for alignment is by the quality of the encoder output during settling in its detent. A well-aligned encoder disc would have its Light-Emitting Diode (LED) centered in the disc aperture. Even at the beginning of settle, when the oscillations are highest, little or no light would be occulted by either edge, as shown in Figure 4a (each window is two steps wide). Encoders that are not optimally aligned would shadow a portion of the light while settling in a step detent. Of 10 potential flight actuators, 6 were aligned with less than optimal performance, as shown in Figure 4b by the encoder light output "hash" during characterization testing. The actuator specification called out static alignment only; as a result, all 10 flight actuators satisfied the specification requirements.

Just prior to delivery to the spacecraft, two of the flight actuators were damaged beyond repair by excessive heat in a Goddard thermal vacuum chamber. Two of the less-than-optimal actuators were brought to flight status. These passed the static alignment specification but during a high-rate slew operation could incur positioning errors of one step. This error is reset in the control electronics when the actuator passes through the "home" position, so the condition is tolerable during slews. Under normal tracking, there is adequate time for the encoder output to settle and the output to be verified. The only remaining issue is diode output over the mission life. As the diode response decays due to radiation effects and the normal degradation due to operation, the partial occulting could reduce margin on the encoder output.

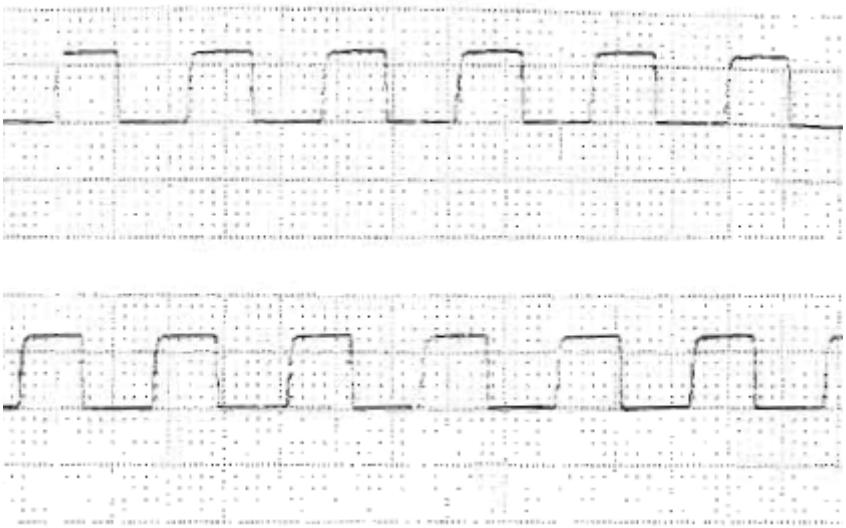

Figure 4a. Good Encoder Alignment – Two-Step Window

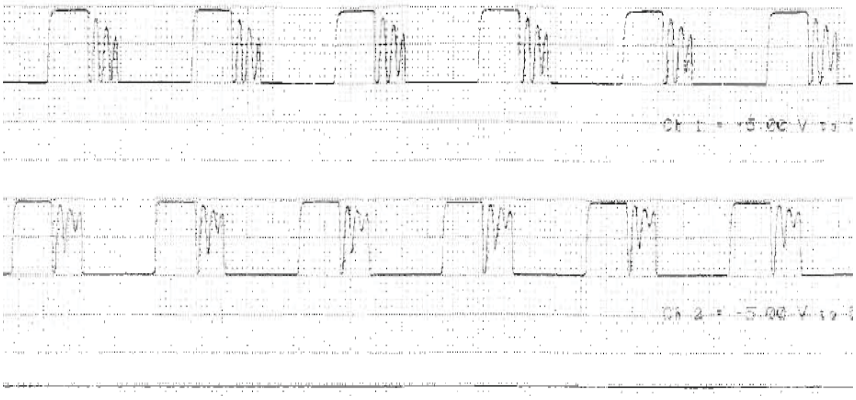

Figure 4b. Less than Optimal Encoder Alignment

Electrical Contact Ring Assembly (ECRA)

The elevation axis harness, which consists of 14 power circuits and 26 signal circuits, is routed through the ECRA. The outer structure of the ECRA, shown in Figure 5, is stationary and is hard-mounted to the same bracketry as the azimuth actuator stator. The inner structure of the ECRA is fully supported in the stationary section by a duplex set of angular contact bearings as well as a trailer bearing. A tooling ball mounted in the base of the rotating portion of the ECRA mates with a slot in the azimuth output shaft allowing the gimbal to transmit the rotary motion while permitting slight angular misalignment between the ECRA and the output shaft.

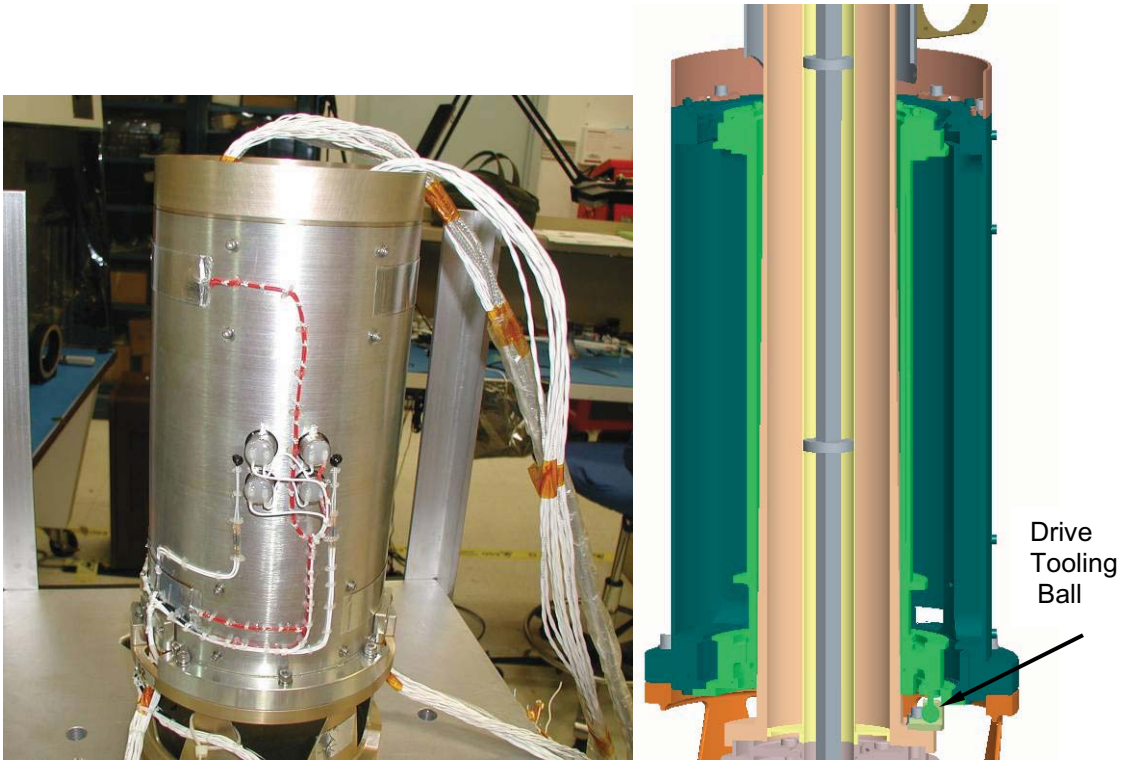

Figure 5. ECRA with Thermal Hardware Attached (prior to lead tape over wrap)

The structure consists primarily of aluminum and titanium components. The ECRA uses gold/silver/nickel alloy mono-filament brushes in gold-plated brass grooves. Two outer brush blocks that are part of the stator support brushes that span the gap between the stationary and rotary portions of the assembly. Each groove accommodates two brushes, one leading and the other trailing. The power circuits utilize a three-groove design while the lower-powered signal brushes utilize a two-groove design. The final result is a current-carrying margin in the power and signal circuits of three and four times respectively. This is in addition to the electrical redundancy in the gimbal itself.

Component-Level Test Issue

During component thermal testing, the ECRA exhibited higher than expected noise in the lines. While the ECRA exhibited acceptable noise performance at temperatures greater than 0°C, the noise levels on several circuits increased considerably at sub-zero temperatures. The primary cause was determined to be water contamination of the brush-groove lubricant. It was determined that the nitrogen environment in the thermal chamber was insufficient to purge the assembly of all water vapor. The primary solution was to perform the thermal testing in vacuum. Additional steps that were taken included a vacuum bakeout without the external housing installed before final assembly, a run-in before testing, and efforts to improve

the cleaning process and prevent contamination sources after cleaning. These changes to the assembly and test program resulted in power and signal circuit noise level well below the required values.

RF System

SDO's data downlink is carried out by a Ka-band RF transmission of 26.5 GHz from a ¾-meter (30 in) High-Gain Antenna to one of two 18-meter (60-ft) ground station antennas. WR-34 waveguides are used to transfer the signal from the transmitter to the HGA. They are aluminum, plated with silver. An anti-tarnish coating was applied over the silver plate. Rotary joints, shown in Figure 6, pass the RF signal with budgeted 0.2-dB insertion loss and allow rotations about the two axes. The stationary and rotating sections of each rotary joint are aligned by a duplex set of ball bearings. The rotating portion of the joint is driven similarly to the ECRA. A ball drives the movement through a slot arrangement, using a tooling ball and a clevis with a close-tolerance gap.

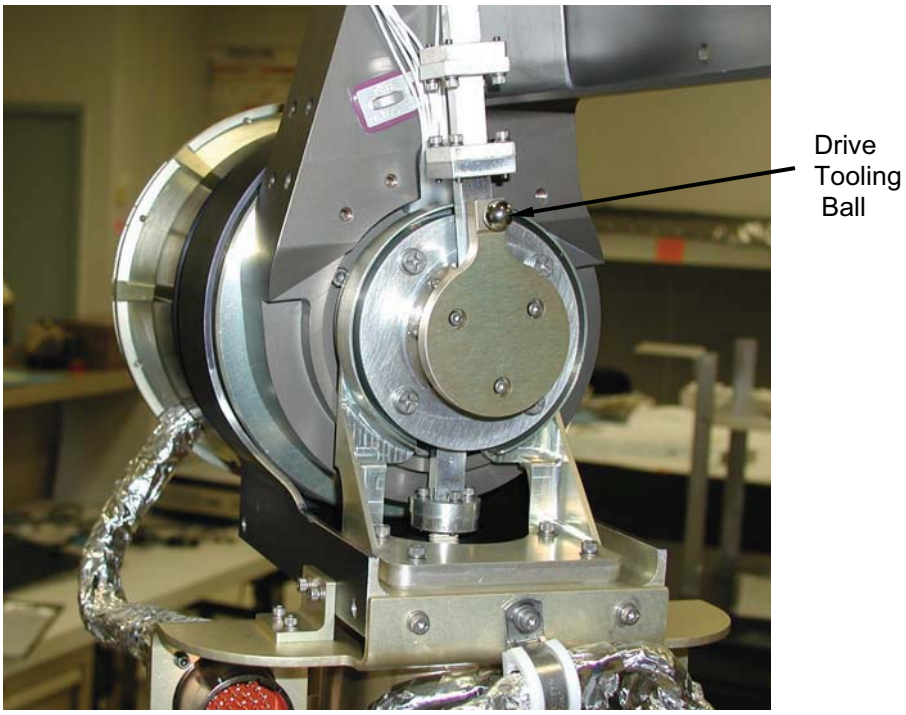

Figure 6 RF Rotary Joint with Drive Tooling Ball (Elevation Axis Shown)

Waveguide Failure

Originally, there were two 7- to 11-cm sections of corrugated flexible beryllium copper waveguide on the gimbal—one in the azimuth section and one in the elevation section. The design intent was that the accordion-style flexibility would compensate for tolerance stack-up and for slight variations in temperature or CTE mismatches. During initial Qualification Unit vibration testing, both of the flexible sections broke completely due to low-cycle fatigue.

One cause for this failure was insufficient waveguide support. Some rigid waveguide spans were 25 cm or more, while the manufacturer recommended 15 cm or less. During vibration, it was shown by analysis that the flex waveguide saw deflections well above the yield stress point.

The main cause for failure was improper heat treatment and fabrication steps of the delicate 100-µm thick corrugated sections. Metallographic analysis of the failed waveguide revealed a larger grain size than that associated with the certified heat treatment. There are multiple conditions that can result in excessive grain size. Regardless of its cause, this condition was a primary contributor to the low cycle fatigue failure

that occurred. There was also concern with the corrugation process, which led to variable thickness. The thickness before cold forming is 125 µm. After forming, it was to be no less than 100µm. The uncertainty added to the difficulty in analyzing the part.

Other problems with the waveguide related to the braze joints between the 1mm thick rigid sections and the flex sections, a 10:1 thickness ratio. Heat from the braze operation could also have increased brittleness in the proximal region where all failures occurred. The added thickness at the joint compounded the stress concentration on the thin section.

Figure 7. Waveguide Resolution - Elevation Waveguide with "P-Trap" section

Failure Resolution

For the elevation waveguide, analysis confirmed that the 90° bend in flex could be replaced with rigid waveguide in a slightly longer, convoluted path. The addition of two more 90° bends created a shape similar to a plumbing expansion section or a P-Trap, shown in Figure 7. The extra path mitigated misalignment and thermal effects. Tolerance stack-up in the axial direction away from the P-Trap was accommodated through the use of aluminum shims.

Because of volume constraints, the azimuth section could not have bends, so two approaches were explored. The first was to procure new flexible waveguides made with properly heat-treated material, and to redesign the structural supports. New waveguides were ordered and tested with sufficient supports, and this arrangement was deemed acceptable.

The second solution, shown in Figure 2, was to replace the flexible section of waveguide with a slip-joint section. This was also developed and tested, and it was found to work well. Ultimately this slip-joint approach was determined to be more robust with no discernible failure mode, and it was selected for use in the azimuth Waveguide.

RF Path Performance

The Ka band transmission performance was tracked throughout the development process. Individual waveguide sections were scanned at various points during manufacture, test and integration. Upon delivery from the vendor the RF performance, as measured by Insertion loss and VSWR, was part of the

End-Item Data Package. Prior to integration into the gimbal, the waveguide was assembled on the bench and throughput loss measured. The budgeted and actual losses are shown in Table 1.

Table 1. Gimbal Waveguide Total Throughput Loss

	Loss (dB)
Budgeted to each Gimbal	-1.45
Highest measured in Flight Unit 1	-0.86
Highest measured in Flight Unit 2	-0.92

Pointing Capability

The characteristics of the RF system, including the transmitting and receiving antennae and the power available for transmission, drove the need for an overall allowable random pointing error of ±0.30 degrees. This value includes spacecraft position knowledge, attitude knowledge and control. The gimbal portion of this pointing budget was 0.14 degree. This random error is measured on the ground to be 0.042 for the first gimbal and would have been 0.062 (not including boom-to-gimbal co-alignment) for the second.

The total budgeted error for the gimbal, including biases that can be calibrated out, is 0.87 degree. Based on ground measurements, this error is 0.175 degree for the first gimbal and would have been 0.356 for the second gimbal. The alignment budget and measurements are summarized below.

Table 2. Pointing Budget (Degrees)

	Budget				**Ground Measure**	
	Known on ground	**Ground-to-Orbit**	**Random**	**Budget Totals**	**Flight 1**	**Flight 2**
Hardware Alignment Errors						
Gimbal to boom axis co-alignment error	.13				.043	
Gimbal to HGA base l/f alignment error	.13				.162	.350
Gimbal Interaxial Orthogonality	.14				.007	.015
Gimbal actuator interface launch shift		.55**			.025	.018
Dynamic Pointing Errors						
Gimbal/boom dynamic interaction			.04		.011*	.011*
Gimbal tracking error			.08		.041	.061
Total on-orbit error (RSS)	.23	.55**	.09	.87	.175	.356
Total on-orbit error after compensation and on-orbit calibration (RSS)* **	--	.05	.09	.14	.042	.062

* from Qualification Unit Jitter testing
** Worst case assumption
*** Ignores 0.02 degree of thermal effects allowed in budget

The launch shift was budgeted based on worst case interface assumptions, the measured value were variations measured before and after vibration testing.

For gimbal/boom dynamic interaction, the gimbal was instrumented with force gages, and the forcing function was used to derive the jitter error measurements. The item tested was an engineering test unit, flight-like in all structural respects.

For the gimbal tracking error, the budgeted amount of 0.08 degree was calculated by summing estimates for the following for each axis: harmonic drive wind-up, gear error, step latency, and wobble of the actuator output. The results were added vectorially (Root-Sum Squared). For the measured value of 0.041 degree, the rotational error and the wobble were measured for each axis and added together vectorially. Due to 1-g effects, this error is greater than the value will be on orbit.

Harnessing and Multi Layer Insulation

Some more general lessons learned deal with leaving more space for harnessing and multi-layer insulation (MLI) and addressing these details earlier in the design effort. Since the gimbal is deployed away from the spacecraft body, it is exposed to the worst radiation environment and temperature extremes on the entire spacecraft, except perhaps for the instrument complement. Protecting against this onslaught required elaborate measures that were frequently at odds with the smooth operation of a high-precision pointing mechanism.

The volumetric demands for harnessing were especially great. Even though the Tefzel®-insulated wiring is resistant to radiation, the SDO system designers implemented a policy of over-wrapping exposed actuator wires with Kapton, Lead and Aluminum tape. Because of the reliability requirements for a 5-year mission at geo-synchronous orbit, the tape layers plus the 36 wires from a single actuator formed a bundle that was approximately 15.9 mm (5/8 inch) in diameter. After wrapping, the metallic layers were each electrically bonded to ground with silver-filled epoxy.

MLI over the entire spacecraft has an electrically conductive germanium black Kapton® (GBK) outer layer. MLI is usually a challenge to bend and position in small pieces and tight quarters. The extra layers brought additional concerns as the mechanism and thermal goals conflicted. The gimbal required ten separate MLI pieces in order to protect its various convoluted surface features, as well as allow for access to the various parts. Some MLI pieces were only 15 cm (6 in) on a side. The bends and seams, such as between moving parts, are potential heat leaks that could expose the actuators to dangerous extremes of temperature. In addition, GBK is sensitive to even light abrasion such as normal hand pressure from an accidental brush against its surface. All these factors contributed to a tough challenge of constructing accurate, intricate pieces of MLI, tightly positioned, and allowing free relative motion between close-tolerance parts.

Conclusion

The first flight gimbal, shown in Figure 8, has been tested and delivered to the spacecraft. The second gimbal will be replaced by a spare after being subjected to damaging temperatures during the post-thermal vacuum bake-out. Integration and testing of the re-built gimbal is scheduled to be complete in March 2008. Launch is scheduled for late 2008.

Acknowledgements

Richard Barclay, Carlos Lugo – gimbal electronics
Steven Wood – mechanical assembly
Richard Marriott – materials
Michael Dube – ECRA noise investigation
Javier Lecha, Joe Schepis – HGAS
Jason Hair – HGAS deployment
Ken Hersey – RF
SpaceDev/Starsys – actuators and ECRAs
Kevlin Corporation – RF rotary joints

Figure 8. SDO Gimbal Mated to Deploy Boom and High Gain Antenna, with MLI installed

Second Unit Shown Vertical in Background

REPORT DOCUMENTATION PAGE

Form Approved
OMB No. 0704-0188

1. AGENCY USE ONLY *(Leave Blank)*	2. REPORT DATE	3. REPORT TYPE AND DATES COVERED
	May 2008	Conference Publication

4. TITLE AND SUBTITLE
39th Aerospace Mechanisms Symposium

5. FUNDING NUMBERS

6. AUTHORS
E.A. Boesiger,* Compiler

7. PERFORMING ORGANIZATION NAME(S) AND ADDRESS(ES)
George C. Marshall Space Flight Center
Marshall Space Flight Center, AL 35812

8. PERFORMING ORGANIZATION REPORT NUMBER
M–1225

9. SPONSORING/MONITORING AGENCY NAME(S) AND ADDRESS(ES)
National Aeronautics and Space Administration
Washington, DC 20546–0001

10. SPONSORING/MONITORING AGENCY REPORT NUMBER
NASA/CP—2008–215252

11. SUPPLEMENTARY NOTES
*Lockheed Martin Space Systems Company, Sunnyvale, CA
NASA MSFC Point of Contact: Don McQueen
An electronic version can be found at http://ntrs.nasa.gov

12a. DISTRIBUTION/AVAILABILITY STATEMENT
Unclassified-Unlimited
Subject Category 37
Availability: NASA CASI 301–621–0390

12b. DISTRIBUTION CODE

13. ABSTRACT *(Maximum 200 words)*

The Aerospace Mechanisms Symposium (AMS) provides a unique forum for those active in the design, production, and use of aerospace mechanisms. A major focus is the reporting of problems and solutions associated with the development and flight certification of new mechanisms. Organized by the Mechanisms Education Association, NASA Marshall Space Flight Center (MSFC) and Lockheed Martin Space Systems Company (LMSSC) share the responsibility for hosting the AMS. Now in its 39th symposium, the AMS continues to be well attended, attracting participants from both the United States and abroad. The 39th AMS was held in Huntsville, Alabama, May 7–9, 2008. During these 3 days, 34 papers were presented. Topics included gimbals and positioning mechanisms, tribology, actuators, deployment mechanisms, release mechanisms, and sensors. Hardware displays during the supplier exhibit gave attendees an opportunity to meet with developers of current and future mechanism components.

14. SUBJECT TERMS
actuators, bearings, deployment, design, gimbals, mechanisms, release, test, tribology

15. NUMBER OF PAGES
436

16. PRICE CODE

17. SECURITY CLASSIFICATION OF REPORT	18. SECURITY CLASSIFICATION OF THIS PAGE	19. SECURITY CLASSIFICATION OF ABSTRACT	20. LIMITATION OF ABSTRACT
Unclassified	Unclassified	Unclassified	Unlimited

National Aeronautics and
Space Administration
IS20
George C. Marshall Space Flight Center
Marshall Space Flight Center, Alabama
35812